

# Simple models for complex questions on plant development

Eva Elisabeth Deinum

## **Thesis committee**

### **Promotors**

Prof. dr. Bela M. Mulder  
Professor of Theoretical Cell Physics  
Wageningen University

Prof. dr. Ton H.J. Bisseling  
Professor of Molecular Biology (Development Biology of Plants)  
Wageningen University

### **Other members**

Dr. Eric M. Kramer, Bard College at Simon's Rock, Great Barrington, USA  
Prof. dr. Paulien Hogeweg, Utrecht University  
Prof. dr. Dolf Weijers, Wageningen University  
Prof. dr. Pieter-Rein ten Wolde, VU University, Amsterdam

This research was conducted under the auspices of the Graduate School of Experimental Plant Sciences.

# Simple models for complex questions on plant development

Eva Elisabeth Deinum

## **Thesis**

submitted in fulfilment of the requirements for the degree of doctor  
at Wageningen University

by the authority of the Rector Magnificus

Prof. dr. M.J. Kropff,

in the presence of the

Thesis Committee appointed by the Academic Board

to be defended in public

on Monday 1 July 2013

at 11 a.m. in the Aula.

Eva Elisabeth Deinum  
Simple models for complex questions on plant development  
300 pages

Thesis Wageningen University, Wageningen, NL (2013)  
With references, with summary in Dutch

ISBN: 978-94-6173-631-4



# Contents

<b>1</b>	<b>Introduction</b>	<b>1</b>
1.1	We will do it the <i>wrong</i> way	1
1.2	Plant growth and development: different angles	2
1.2.1	I: Adaptive plant architecture	2
1.2.2	II: Coordination of cellular functions	3
1.2.3	III: The mechanics behind morphology	4
1.3	Root nodules and symbiotic nitrogen fixation	5
1.4	Integrating information	6
1.4.1	Auxin	6
1.4.2	Cytokinin	8
1.4.3	Symplastic transport	9
1.5	Cortical microtubules and wall mechanics	10
1.6	Outline	11
<b>I</b>	<b>Symplastic transport</b>	<b>13</b>
<b>2</b>	<b>Walking the back alleys: a modelling study of symplastic transport</b>	<b>17</b>
2.1	Introduction	18
2.2	Results	21
2.2.1	Basic properties of pure symplastic transport	21
2.2.2	Realistic tissues: effects of different anisotropies	25
2.2.3	Symplastic vs. apoplastic transport	26
2.2.4	Impact on pattern formation: a conceptual approach	32
2.3	Discussion	34
2.3.1	Symplastic transport and simple diffusion	34
2.3.2	Symplastic transport and auxin gradients	36
2.3.3	Options for asymmetry in symplastic transport	37
2.3.4	Biophysics behind different roles for symplastic and directed apoplastic transport	37
2.3.5	Impact of non-targeted symplastic transport on pattern formation	38
2.4	Conclusions	40
2.5	Methods	41
2.5.1	Overview	41
2.5.2	1D: analytical calculation of steady states	42
2.5.3	1D: time resolved solutions (approximation)	42

2.5.4	Numerical simulations	42
<b>3</b>	<b>Modelling symplastic transport: from single channels to effective wall permeability</b>	<b>47</b>
3.1	Introduction	48
3.2	Model and Results	50
3.2.1	Outline of the single channel model	50
3.2.2	Effective wall permeability	54
3.2.3	Reaching PDs: correction for inhomogeneity of the wall permeability	55
3.2.4	The acid test: comparing with measurements	56
3.3	Discussion	59
3.3.1	PD spacing	60
3.3.2	Plasmodesmata from a design perspective	61
3.3.3	Size exclusion limit	62
3.4	Conclusion	63
3.5	Methods	63
3.5.1	Diffusive flux through a single PD	63
3.5.2	Relative molar flow rate and average passage time	64
3.5.3	Numerical simulations for transport to the wall	64
<b>II</b>	<b>Primordium initiation</b>	<b>67</b>
<b>4</b>	<b>Modeling a cortical auxin maximum for nodulation: different signatures of potential strategies</b>	<b>71</b>
4.1	Introduction	72
4.1.1	Setting	72
4.1.2	Background	72
4.1.3	Approach	74
4.1.4	Key findings	74
4.2	Results	75
4.2.1	Signatures of increasing influx, decreasing efflux and local auxin production	75
4.2.2	Time evolution of auxin accumulation	77
4.2.3	Precise distribution of cortical PINs can shift the lateral position of the auxin maximum	81
4.2.4	Endodermal PIN layout strongly affects nodulation potential	83
4.3	Discussion	83
4.3.1	Auxin accumulation in nodulation	83
4.3.2	The accumulation mechanism affects the dimensions of the primordium	86
4.3.3	Steady state vs. transient patterns	86
4.3.4	Are cortical PINs distributed differently for determinate and indeterminate nodules?	87
4.3.5	Biological limits of the simple changes	87

4.3.6	On simple roots	88
4.3.7	The next step: a step back	89
4.4	Methods	89
4.4.1	General approach	89
4.4.2	Tissue geometry and PIN-layout	89
4.4.3	Boundary conditions	90
4.4.4	Changes are applied in the “controlled area”	90
4.4.5	Simulation method	91
4.4.6	Parameters	92
<b>5</b>	<b>Playing the auxin pipeline – consequences of different mechanisms for local auxin accumulation</b>	<b>99</b>
5.1	Introduction	100
5.2	Results	103
5.2.1	Solutions for a 1D pipeline	103
5.2.2	Local changes: reaching the target concentration?	106
5.2.3	Understanding the differences between 1D and 2D: changes in local fluxes	106
5.2.4	Changing the resting state/global flux	109
5.2.5	Strong symplastic connections diminish Infl $\uparrow$ pattern	111
5.3	Discussion	112
5.3.1	Different signatures and different contexts	112
5.3.2	Is (strong) symplastic connectivity a negative regulator of root lateral organ formation?	115
5.3.3	Recycling brings more wealth than depleting the environment	116
5.4	Conclusions	118
5.5	Methods	119
5.5.1	2D root segment	119
5.5.2	Numerical methods	119
5.5.3	Parameters	119
<b>6</b>	<b>Induction of the nodule primordium: from epidermal signal to interior response</b>	<b>121</b>
6.1	Introduction	122
6.2	Results	123
6.2.1	Symplastic transport affects spreading of [epidermal] CK	123
6.2.2	Linking CK and auxin distribution via PIN dynamics	123
6.2.3	Impact of symplastic transport	126
6.2.4	Competition for auxin	129
6.3	Discussion	130
6.3.1	Nodule primordium induction by an epidermal CK signal	130
6.3.2	Differential sensitivity of PIN proteins to CK	131
6.3.3	Impact of symplastic transport	132
6.3.4	Confinement of the auxin response	134
6.3.5	Auxin availability and autoregulation of nodule number	135
6.4	Conclusions	136

6.5	Methods	136
6.5.1	General setup	136
6.5.2	Numerical simulations	137
6.5.3	Parameters	137
<b>III</b>	<b>Self organisation of cortical microtubules</b>	<b>139</b>
<b>7</b>	<b>Taking directions: The role of microtubule-bound nucleation in the self-organisation of the plant cortical array</b>	<b>143</b>
7.1	Introduction	144
7.2	Methods	145
7.2.1	Simulation technique	145
7.2.2	Microtubule interactions	146
7.2.3	Dimensionless control parameter	146
7.2.4	Microtubule-bound versus background nucleation	147
7.2.5	Angular distribution of microtubule-bound nucleation	148
7.2.6	Quantifying the degree of alignment	148
7.2.7	Calculation of $G_c^*$ from simulations	149
7.3	Results and Discussion	150
7.3.1	CL nucleation leads to a large increase of the ordered regime and faster alignment compared to isotropic background nucleation	150
7.3.2	The co-alignment of nucleation with the parent microtubule is the main determinant ordering propensity	151
7.3.3	Focussed sideways nucleations appear to lead to a more homogeneous microtubule array	154
7.3.4	Rotation through nucleation of ordered microtubule domains requires a strong handed nucleation bias and a sufficiently “fluid” array organisation.	156
7.4	Conclusion and Outlook	157
7.5	Abbreviations list	159
<b>8</b>	<b>Cortical microtubule array initiation</b>	<b>161</b>
8.1	Abstract	161
8.2	Introduction	161
8.3	Results	163
8.3.1	After cytokinesis, microtubules reappear with a transient diagonal order	163
8.3.2	Transient diagonal ordering during recovery from oryzalin treatment	165
8.3.3	Diagonal ordering also occurs during array disassembly	165
8.3.4	Microtubule nucleation has a diagonal bias during array initiation	165
8.3.5	A large fraction of nucleations during array initiation are free of labeled $\gamma$ -tubulin complexes	168
8.3.6	Simulations	169
8.4	Discussion	169
8.5	Materials and methods	172

8.5.1	Plant material	172
8.5.2	Specimen mounting	173
8.5.3	Microscopy	173
8.5.4	Data analysis	174
8.5.5	Simulation methods	175
8.6	Acknowledgements	177
8.7	Supplementary information	177
<b>9</b>	<b>Which way to go? Role of CLASP and MAP65 in the orientation of the cortical array</b>	<b>183</b>
9.1	Introduction	184
9.2	Results	185
9.2.1	Edge-induced catastrophes can reliably orient the cortical array	185
9.2.2	The only MAP65 function relevant for orientation control is linking CLASP and MTs	187
9.3	Discussion	187
9.3.1	Bundling and orientation	187
9.3.2	CLASP based orientation mechanism and cell size	187
9.3.3	Chicken and egg: how to position CLASP?	191
9.4	Conclusions	192
9.5	Simulation methods	192
<b>IV</b>	<b>Concluding considerations</b>	<b>195</b>
<b>10</b>	<b>General discussion</b>	<b>197</b>
10.1	Biological systems from a design perspective	197
10.2	Reinventing the wheel: the systems biology cycle	198
10.2.1	A little historical context	198
10.2.2	Stereotypical systems biology	201
10.2.3	Beyond the stereotype	206
10.3	Comparing different scenarios – uses and limitations of this method	208
10.3.1	Case study: On determinate and indeterminate nodules	209
10.3.2	Case study: Different scenarios for cortical microtubule (re)orientation	210
10.4	The warders of our prison of space and time	211
10.4.1	Numbers	211
10.4.2	Scaling laws	213
10.4.3	Case study: Different mechanisms (and models) for auxin gradients in the plant root	214
10.5	What are realistic parameters? – Lessons from cortical microtubule simulations	216
10.6	Seeing the invisible	218
10.6.1	Case study: Symplastic transport: the rise of the conveniently ignored	218
10.6.2	Case study: Indirect markers and time series	219

10.7	Too <i>little</i> of a good thing can be wonderful	220
10.7.1	Case study: On dynamic PIN localization	221
10.8	A final word on hammers	224
<b>11</b>	<b>So, what was the use of all this?</b>	<b>225</b>
<b>A</b>	<b>Walking the back alleys: a modeling study of symplastic transport</b>	<b>229</b>
A.1	Mathematical derivations	229
A.1.1	1D analytical model: coordinate system	229
A.1.2	1D steady state profile for purely diffusive symplastic transport	229
A.1.3	1D: time resolved solution for purely diffusive symplastic transport (approximation)	234
A.1.4	1D steady state profile for combined symplastic transport and apoplastic transport	236
A.1.5	1D: Reconstructing intracellular gradients and local fluxes from analytical steady state profiles	239
A.2	Overview of mathematical symbols	241
<b>B</b>	<b>Playing the auxin pipeline – consequences of different mechanisms for local auxin accumulation</b>	<b>243</b>
B.1	1D model	243
B.1.1	Definition and notation	243
B.1.2	General steady state solution for a homogeneous tissue (no production or decay)	243
B.1.3	Resting state	245
B.1.4	Target concentration	247
B.1.5	Adding symplastic transport	248
	<b>References</b>	<b>251</b>
	<b>English summary</b>	<b>274</b>
	<b>Nederlandse samenvatting</b>	<b>277</b>
	<b>Acknowledgements</b>	<b>281</b>
	<b>List of publications</b>	<b>284</b>
	<b>Curriculum Vitae</b>	<b>285</b>

# 1

---

## Introduction

---

### 1.1 We will do it the *wrong* way

*“Essentially, all models are wrong, but some are useful.”* – famous words by statistician George E. P. Box.

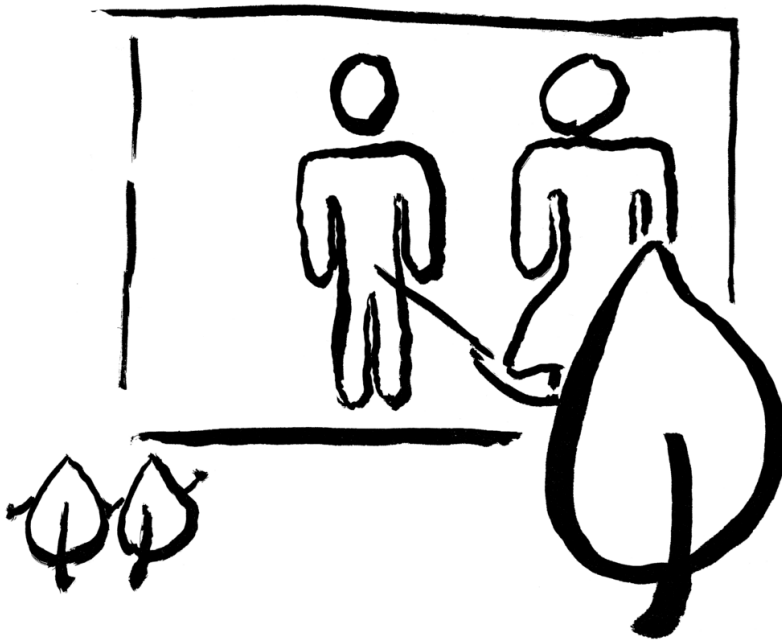
This thesis is about the use of models to better understand several aspects of plant growth and development. I distinctly remember a student asking me, during a mandatory course on modelling for biology students, about the use of models: “why care about models, as they are wrong anyway?”

Models are tools: tools to increase our understanding of a particular process. They are not meant as perfect representations of the process – the original system would be much more efficient for that. This is not a weakness, but a strength. Only by being simpler (faster, smaller, slower and/or larger) than the actual system of interest they can help us understand.

What is the “right” level of simplicity? One may think of the words often attributed to Einstein, that “everything should be made as simple as possible, but not simpler,” but this is hardly any answer. The most insightful level of simplification differs per problem, changes over time and even depends on the scientist asking the question. At the same moment it might be insightful to expand a model, make a simpler model of the model and contrast different models of the same thing.

In this thesis I will present several different models of different levels of complexity, applied at different stages of “the path towards understanding”. Together they show that there is not a single correct modelling approach. On the contrary, a (bio)diverse approach can be very powerful.

In a sense, a model is like a hammer. Very beautiful things have been made using hammers. And yet, anyone proclaiming that the hammer is a true miracle of civilization and the driver of creativity will be laughed at. A hammer is a hammer. The same goes for models. There are so many examples of how some model helped us better understand our world, that it is hard to pick the best one. Yet a model by itself is just a model. Without a good question, a model deserves gathering dust in a rusty toolbox in the attic.



## 1.2 Plant growth and development: different angles

The questions in this thesis are all related to plant growth and development. Contrary to animals, growth and development remain tightly coupled throughout the entire plant life. Plant growth and development can be understood on different levels, calling for different approaches. I will first present an overview of three different levels of thinking about plant growth and development, illustrated by several examples from the literature. After that I will introduce the specific scientific content of this thesis.

### 1.2.1 I: Adaptive plant architecture

Plant growth inevitably involves the continual formation of new organs, such as (side) roots, branches, leaves and flowers. There is no such thing as a complete plant body plan, that contains all organs in their “adult” number, as we are so used to in animals. Nevertheless, the organs are not formed in random positions. For each organ type, plants control both the spacing/positioning and timing of their initiation and maturation.

For example, the positioning of new leaves, phyllotaxis, is determined in the shoot apical meristem. The specification of where the next new leaf (primordium) will be formed occurs through the continual formation of local maxima of the plant hormone auxin within the shoot apical meristem [1, 2]. The number of concurrently initiated primordia and their relative position determines whether the leaves will occur in pairs, whorls, or spread. Currently, several hypotheses compete for best explaining the formation of these maxima and the occurrence of different phyllotactic patterns in different species or mutants. Computer models are used extensively on this “battleground”, to test whether the proposed



mechanism is actually capable of producing the observed patterns [3–8].

When a new leaf is formed, a so called axillary bud is formed at its base. When a new branch is formed, it originates there. Typically, branches do not develop immediately, nor from all nodes. Many axillary meristems remain dormant as long as the apical meristem (the one at the tip of the shoot/branch they occur on) remains active, a phenomenon called apical dominance. Several plant hormones interact in the control of apical dominance and bud dormancy, including auxin, cytokinin and strigolactone [9, 10]. Computer modelling has helped understand the together counterintuitive impacts of different mutations in auxin and strigolactone signaling on branching patterns [11].

A key question at this level is how different signals interact in the spatio temporal coordination of the initiation of specific developmental programs.

## 1.2.2 II: Coordination of cellular functions

The formation of a new organ is more than just deciding to make one. As the cells divide to create the building material of the new organ, they have to organize themselves into tissues. From the beginning the cells giving rise the different tissues have to differentiate in the correct relative position. The number of cells adopting a certain “faith” also has to be suitable to fulfil the later demands on that tissue. In *Arabidopsis* roots, the number of cell files with a particular function is normally tightly controlled. Mutations and misexpression studies in the TMO5/LHW system, key regulators of the number of vascular cell files, show that the mechanisms controlling differentiation into different vascular tissues are robust against a far greater degree of variation in the number of vascular cell files than normally occurs in these plants [12]. Even in normal, wild type, *Arabidopsis* root growth there is enough variation in the position of mature cells relative to their origin that researchers were able to show that a cell’s position rather than its lineage determines its fate [13].

These phenomena require the local coordination of developmental decisions, therefore some way of communication among cells is essential. A canonical example of cell-cell communication in animals is the Notch system [14], a system of a membrane bound receptor (Notch) and a membrane bound ligand (e.g. Delta) on the opposing cell membrane. The system exaggerates initial differences in the amount of ligand, eventually dividing cells in “Delta” and “Notch” types. This is used, for example, in selecting a single cell from a group of progenitors to become a neuron (that the others will support), a process called lateral inhibition [15]. This system is also crucial for the determination of boundaries, such as the dorsal-ventral boundary in the *Drosophila* wing or somite boundaries in vertebrate embryos [14, 15]. Another system with interacting transmembrane proteins are the planar cell polarity proteins. In *Drosophila*, the communicating complex contains, amongst others, Frizzled (Fz) on one side and Strabismus (Stbm) on the other side. The full complex inhibits the formation of complexes with the opposite orientation in the interface, sorting out into an Fz and an Stbm side. If a cell has Fz on one side, it will accumulate Stbm on the other side, thus locally propagating the planar cell polarity (e.g. distal (Fz) / proximal (Stbm) in the wing [16, 17]). Additional mechanism(s) seem to be required for global coordination over longer distances (noise and irregularities limit the number of consecutive cells that can be directed by this mechanism in isolation), for example mechanical forces in wing development [18], or tissue spanning gradients

[17]. Such local signaling systems do not exist in plants and could not function there, as plant cells are separated by their walls. A cell wall with a thickness of 200 nm is considered thin, whereas membrane anchored proteins – because of their size – typically reach no more than a few nm from the cell membrane. Thus, the wall disallows direct protein-protein interactions between neighbours across the wall: separated as Pyramus and Thisbe, but unable to talk.

Plants do have a different system of sending (protein) messages to their neighbours. Non-cell-autonomous messages are generated in one cell, but affect transcription in a different cell. One example is the GLABRA/WEREWOLF system, that is involved in the specification of root hair and trichome cell fate (that is: which cells make these appendages). Several components in this system move to the neighbouring cell, inducing the opposite cell fate in a neighbour [19]. In technical terms: these proteins act non-cell-autonomously. Non-cell-autonomous proteins can also act in the definition of boundary layers. One such example is SHORT ROOT (SHR). This is transcribed in the central cylinder, then moves to the layer surrounding it, where it together with SCARECROW (SCR) instructs one layer to become the endodermis, the layer that separates the cell wall continuum in an “inside” and an “outside” part [20]. In this process SHR is sequestered by SCR and moves to the nucleus. This is essential to limit the endodermis to a single layer. If SCR availability is artificially reduced, SHR/SCR becomes active in multiple layers [21].

A key question at this level is how local communication functions in the coordination of cell fate specification and subsequent isolation of determinants.

### 1.2.3 III: The mechanics behind morphology

Zooming in on the cells, the building blocks of the plant, growth becomes a highly mechanical process. It can be compared with the inflation of balloons (cells) [22]. The resistance of the cells to the (turgor) pressure inside makes them rigid. Contrary to ordinary balloons, the cell walls do not yield to pressure in the same way everywhere on the surface: cell walls are highly anisotropic. This anisotropy allows cells to grow into different shapes, in close relation with function: stomatal guard cells that open and close by changing their turgor pressure, leaf epidermal cells shaped as puzzle pieces to make the epidermis more resistant to tearing by the wind and cells with appendages such as root hairs for extra absorption surface. The list of examples could be much longer. Even the “simple” elongated cell shape found in many tissues of the root and shoot internodes are highly functional: this is what makes these plant parts cover the distance towards more light, water or nutrients. Plant cells can adopt a wide variety of shapes and yet, when the wall is chemically removed (in the creation of so called protoplasts), they all turn spherical.

The cell wall is highly functional in the control of plant growth, but it does come at a price. Because of their walls, plant cells are by and large unable to move relative to their neighbours. Cell migration, intercalation and tissue rearrangements are very important processes in animal morphogenesis, but unavailable to plants. Mechanisms available for plant morphogenesis are (oriented) cell divisions and (differential) expansion of cells and wall segments. Misorientation of cell division in crucial places, such as the root stem cell niche, can result in an abnormal number of cell layers and worse, the lack of whole tissues.

This is the case in the previously introduced (*shr*) mutant: the initials that should form cortex and endodermis, fail to divide periclinally. The single resulting layer differentiates into cortex, because it lacks the SHR signal [20]. The single round of periclinal divisions is induced by the SHR/SCR complex. If this complex is not restricted to a single layer, this results in additional rounds of periclinal divisions and thus additional cell layers [21].

An extreme example of the impact of local modification of the wall properties is seen in thread-like appendages such as root hairs. Highly localized expansion combined with a continuous supply of new wall material can sustain cell growth from their tips [23, 24]. The direction of this growth can change in response to external signals (e.g. Nod factors), resulting in root hair curling [23, 25].

A key question on this level is what controls the orientation of division planes and the mechanical properties of (parts of) the cell wall.

### 1.3 Root nodules and symbiotic nitrogen fixation

The original motivation behind much of this thesis' work comes from legumes, a plant family known for its symbiotic interaction with nitrogen fixing bacteria, rhizobia. The legume family contains many of the high protein crops in our diet: such as soy bean, peas, lentils, beans and peanuts. Other legumes, such as alfalfa and clover are used for organic nitrogen fertilization, saving energy that otherwise would have been spent on the production of artificial nitrogen fertilizer. The fixation of atmospheric nitrogen ( $N_2$ ) requires the breakage of a triple bond. This makes it energy expensive. Moreover, the enzyme the rhizobia use for this reaction, nitrogenase, is highly sensitive to oxygen. The symbiotic nitrogen fixation therefore takes place in specialized structures called root nodules. The presence of oxygen binding leghemoglobin consolidates two paradoxical demands: a low oxygen pressure for nitrogenase activity and a high oxygen supply to meet the metabolic demand of nitrogen fixation. The nodules are well connected to the plant's vascular system for transport of fixates and supply of fuel carbohydrates.

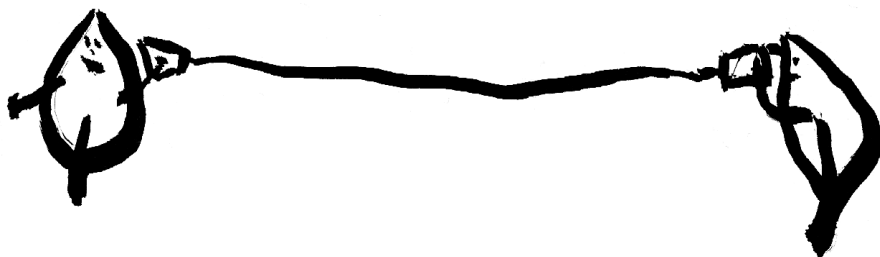
The formation of a root nodule starts with recruiting the right bacteria. When in need, legume roots attract symbiotic rhizobia by the secretion of flavonoid compounds. Most legume species can only be nodulated by specific strains of rhizobia. The plants recognize the correct strains by the specific nature of the signaling molecules, called NOD-factors, secreted by the rhizobia [26]. From the initial entry point in the epidermis, growing root hairs in model legumes *Lotus japonicus* and *Medicago truncatula*, infection threads are formed that will lead the rhizobia into their future nitrogen fixing location. At the same time, cell division starts from deeper tissue layers, initially the inner cortex, pericycle and to a lesser extent the endodermis in *Medicago* [27] and the middle cortex for *Lotus*. This corresponds with the two plant species producing different types of nodules, with different morphologies: *Medicago* produces indeterminate nodules, that maintain meristematic growth, whereas *Lotus* forms determinate nodules, in which the meristem terminates upon nodule maturation [28].

The nitrogen fixing symbiosis with rhizobia costs a lot of energy of the plant, so several mechanisms exist to adjust nodule number to nitrogen demand [29, 30].

As many other processes in plant development, the formation of the root nodule itself is under the control of plant hormones. After the initial signaling at the epidermis,

upon recognition of a suitable rhizobium strain, phytohormones are key to the plant side responses. The earliest discoveries pointing in this direction are the induction of nodule-like structures using auxin transport inhibitors [31] or cytokinin [32]. Cytokinin is thought to relay the signal from the epidermis to the site of the first cell divisions [33–35], which is itself marked by a local accumulation of auxin [36, 37]. These two hormones interact extensively, as cytokinin affects auxin transport [38, 39] and possibly production [40] and auxin in turn affects cytokinin metabolism [38].

A key question in this thesis is how these two hormones cooperate in the induction of root nodule primordia (part II). As central players, they will be introduced more extensively in the context of the more general theme of integrating information.



## 1.4 Integrating information

Most growth takes place from populations of dividing cells, called meristems. The specification, or activation, of new meristems and their rate of activity is coordinated plant wide to adapt the plant morphology to the demands of the environment. For the internal communication, the plant employs a range of interacting signaling molecules. A very important class of these are the phytohormones, such as auxin and cytokinin, but also RNA molecules [41–43], peptides and small proteins [44] acting in neighbouring cells (non-cell autonomous) confer internal messages. Even nutrients and sugars can perform signaling functions and alter the plant's patterns of growth [45]. All these molecules differ greatly in their range of action and modes of transportation. As development is a highly spatial process, it is important to understand how the relevant signals move through the tissue. A very interesting question related to this is how the transport mode(s) of a signal affect(s) the range and time scales of its action.

### 1.4.1 Auxin

The plant hormone auxin occurs in all three parts of this thesis. It has a research history in plant biology of over a century and has been found to be involved in virtually all major plant developmental decisions [46].

**Metabolism** The most abundant natural auxin, Indole-3-acetic acid (IAA), is derived from the amino acid tryptophan. Several routes of auxin synthesis have been described [47]. They may all play a role in some processes, but the consensus at the moment\* appears to be that most IAA is synthesised in the following two step process: first tryptophan is converted to indole-3-pyruvic acid by TAA1/TAR proteins [49], which is subsequently converted to IAA by YUCCA proteins (possibly in several steps) [47, 50]. YUCCA proteins, a family of 11 in *Arabidopsis*, show an expected amount of redundancy in this organism: no obvious phenotypes are reported for single mutants, but several higher order mutants show defects in for example flower development or specification of the basal (root) part of the embryo [50, 51]. Curiously, however, single “YUCCA” mutant *sparse inflorescence1 (spi1)* in maize is clearly affected: a strong reduction in axillary meristem number results in sparse inflorescences [52]. Auxin can be conjugated to other molecules, both reversibly (e.g. for temporal storage) and irreversibly (for degradation) [53].

**Transport** Auxin is a weak acid (IAA has  $pK_a \approx 4.8$ ). Its protonated form is uncharged and can therefore passively cross the cell membrane. The apoplast is mildly acidic and thus contains a fair fraction of protonated auxin (e.g. 24% at pH=5.3). The cytoplasm, however, is near neutral and thus hardly contains any protonated auxin (e.g.  $\approx 0.4\%$  at pH=7.2) [3]. As only the concentration of protonated auxin matters for the passive influx, the pH difference has the potential to drive a passive auxin influx against the difference in total auxin concentration. Its magnitude is mostly determined by the apoplastic pH as this is closest to the  $pK_a$ . Moreover, the influx can be enhanced by more than an order of magnitude by influx carriers such as the AUX1/LAX protein family, that exploit the proton gradient for the import of deprotonated auxin [54]. They are usually located homogeneously over the cell membrane, or at higher levels on both apical and basal sides [55–57]. Efflux of auxin occurs predominantly by active transport through efflux carriers such as the PIN [58, 59] and ABCB [60, 61] proteins. The membrane PINs often appear concentrated at specific sides of the cells, giving rise to directional auxin transport [62, 63].

**Perception** Auxin is perceived by the SCF(TIR1) complex. Upon auxin binding, this complex ubiquitinates Aux/IAA proteins [64, 65], targeting them for proteasome degradation. The Aux/IAAs are short lived proteins that repress ARFs, auxin responsive transcription factors, by dimerizing with them. The increased degradation of Aux/IAAs upon auxin perception thus rapidly releases the transcriptional block of the (positive) ARFs, resulting in auxin induced transcription [66]. Both the Aux/IAAs and the ARF protein families have many members, differentially expressed throughout the plant, allowing for diverse responses to the same signaling molecule [67–69]. This mechanism is not unique to auxin. A similar system functions in the perception of jasmonate, another plant hormone, with JAZ proteins instead of Aux/IAAs and COI1 in interaction with SCF forming the intracellular hormone receptor [70, 71]. Besides the intracellular auxin receptor system, an extracellular receptor exists: ABP1 (auxin binding protein 1). Auxin binding by

---

\*Opinion of a large fraction of the participants of the “auxin 2012” that this is the predominant pathway for IAA synthesis, at least in *Arabidopsis*. It is hard, however, to find this claim written in a reviews yet. Best so far: [48].

this protein affects the local endocytosis rates of PIN proteins and thus their subcellular localization [72–74].

**Experimental observation** Auxin is active in minute concentrations (typical measurements: tens to hundreds pg per mg fresh weight [75–77], i.e.  $0.1\text{--}10^1\ \mu\text{M}$ ). Several strategies have been developed to measure auxin. The shoot-to-root movement speed of a pulse of auxin can be measured using radioactively labelled auxin [78, 79]. Physical concentrations can be measured using mass spectroscopy, although the low concentrations limit the resolution of such approaches to slices of tissue (e.g. [76]) or, using cell sorters, groups of cells expressing a certain marker specific for their cell type and developmental stage [77]. Auxin responses can be monitored using the auxin responsive promoters GH3 or its synthetic derivative DR5 [80]. Recently, another auxin response marker has been developed, that operates further upstream in the auxin perception pathway. This marker is a fluorescent protein fused to part of an Aux/IAA protein, the proteins that are degraded upon increasing auxin concentrations. Hence, it is a negative marker of auxin concentration (increases) [81]. Despite recent advances, in many interesting developmental processes it is still impossible to live monitor auxin concentrations in the desired location, or not with the desired spatial and temporal resolution. Not surprisingly, computer models have become very valuable tools in auxin biology [82, 83]. The earliest models focussed on the propagation of radio-labeled auxin through “linear” tissue [84–86]. With increasing computer power a plethora of more complex developmental questions came within reach, on topics such as phyllotaxis [3–6, 87], venation [7, 88–90], apical dominance [11] and root gradients [54, 91–93]. In this thesis we use models to address the questions how auxin transport and gradient formation are affected by symplastic transport (chapter 2) and how different mechanisms for local auxin accumulation may function in the initiation of (root) lateral organs, with a particular emphasis on root nodules (part II).

### 1.4.2 Cytokinin

Cytokinin occurs in the textbooks as auxin’s antagonist. Evidence is accumulating, however, that the two interact and cooperate in many developmental processes, such as the aforementioned nodule formation, but also in the specification of xylem and phloem transport tissues [94], the control of root meristem length [38], control of shoot branching (together with strigolactone) [9].

**Metabolism** The rate limiting step in cytokinin biosynthesis is performed by adenosine phosphate-isopentenyltransferases (IPT) and the irreversible step in its degradation is controlled by cytokinin oxidase/dehydrogenase (CKX) [95]. IPT genes may be induced in response to auxin [38].

**Perception** Cytokinin is perceived by histidine kinases (HKs) at a membrane. The signal then is transferred to the nucleus by histidine phosphotransfer proteins (HPT). HPTs then activate a group of transcription factors called response regulators (RR). These RRs are split in two classes: negative (type A) and positive (type B) regulators of the cytokinin response [96]. The HKs involved in cytokinin perception were thought to be plasma membrane localized [96], but the most recent reports suggest localization on the ER [97].

**Transport** Contrary to auxin, not much is known about cytokinin transport [98]. Cytokinins are structurally related to nucleobases and nucleosides. Two families of transporters for these substances can also transport cytokinin with a low affinity: PUP for nucleobase cytokinins [99, 100] and ENT for nucleoside cytokinins [101, 102]. No specific cytokinin transporter has been reported and these non-specific ones are not present in all relevant tissues. No molecule with known cytokinin transporting function has been found in the cortex [100–102], for example, but a cytokinin signal does travel from epidermis to cortex and pericycle during the initiation of a nodule primordium in *Medicago* [33–35].

Inhibition of symplastic transport in the phloem can significantly reduce the local pool of cytokinin, e.g. in the root meristem [103], so this mode of transport may also be important in other situations. Moreover, the developmental defects caused by changes in callose deposition [104], which regulates the plasmodesmal aperture (“size exclusion limit”) [105], show that symplastic transport could be of general importance for the hormonal regulation of plant development.

### 1.4.3 Symplastic transport

At the tissue level, the available transportation modes can be split in two categories: symplastically and apoplastically.

The apoplast is all that is outside the cells, that is, mostly the cell walls. Apoplastic transport always consists of two components: getting out of the cell and back in. The available options include specific carriers (such as for auxin), exo- and endocytosis (secretion and internalization through small vesicles) and diffusion through the cell membrane. The transport through the wall itself is typically diffusive.

The symplast is everything inside the cell, including narrow channels connecting neighbouring cells, called plasmodesmata. Symplastic transport can occur by diffusion [106, 107] through the continuation of the cytoplasm, called the cytoplasmic sleeve. This is a generic mechanism, available to all sufficiently small molecules, including plant hormones [108], and therefore called non-targeted symplastic transport. Chaperone proteins could aid in the targeting of specific molecules to the plasmodesmata and/or their temporal modification to facilitate their movement through the plasmodesmata [109]. This is called targeted symplastic transport.

Although plants lack a fast circulation system as in larger animals, they do have specialized tissues for the long distance transport of nutrients, metabolites and water: the xylem, which is part of the apoplastic pathway and the phloem, part of the symplastic pathway. These can also function as a medium for long distance signals.

Viruses [110] and some other intracellular pathogens [111] exploit plasmodesmata for their movement to neighbouring cells. As viruses typically are too large to pass plasmodesmata unaided, they employ a range of so called movement proteins that help target (parts of) the virus to the plasmodesmata and enable their passage [110].

The amount of symplastic transport is heavily regulated. The opening and thus the amount of transport is mostly regulated through deposition and degradation of callose on both ends of the channel, in what is called the neck region, by callose synthase (CalS a.k.a. GSL gene family) and  $\beta$ -1,3-glucanase respectively (with further regulation by other factors) [112]. Modulation of the stability of actin, one of the proteins present inside

plasmodesmata, also affects their permeability [113] and is needed for the functioning of at least some viral movement proteins [114]. The proper regulation of symplastic transport is of such developmental importance, that mutations affecting this are often embryo or seedling lethal [115–117]. The number, properties and types of plasmodesmata are also developmentally regulated [118–121].

Non-cell-autonomous proteins are often so large that they have to move in a targeted way, although in heart stage *Arabidopsis* embryos, single GFP ( $\approx 240$  amino acids, 27 kDa) and 10 kDa F-dextran can move throughout the whole embryo [115, 122]. Later in development the movement of free GFP becomes more restricted [122]. A similar trend is observed in leaves: as they mature, they turn from carbohydrate sinks to sources and along with this development, the size limit for non-targeted mobility is reduced (from up to/over 50 kDa in sink leaves) [123]. Research on non-cell-autonomous transcription factor SHR (531 amino acids itself) shows that proteins that can move by non-targeted symplastic transport in early developmental stages, would require the targeted pathway later in development. Free GFP expressed under the SHR promotor remains in the vascular tissue (where SHR is expressed), but when fused to the SHR protein it is taken along to the endodermis [124]. This SHR:GFP movement to the endodermis can be blocked by local overexpression of callose synthase (CalS3), that is by decreasing the plasmodesmata aperture beyond what is normal for that developmental stage [104].

A large part of the research on symplastic transport is still in a rather descriptive stage, that is, there is almost no work on the biophysical behaviour of symplastic transport as a means of communicating molecular signals. We therefore started with a modelling study of the simplest (diffusive, non-targeted) form of symplastic transport, addressing basic questions concerning the biophysical properties of this transport mechanism (part I). This also serves as input for more complicated developmental questions in chapters 5 and 6.

## 1.5 Cortical microtubules and wall mechanics

The questions so far are mostly related to description I and II of plant growth and development. For the mechanical understanding (III), we turn to the cell wall structure and its control. The cell wall consists for a large part of cellulose microfibrils. These long fibers are deposited in highly aligned layers by cellulose synthase complexes. This is thought to dictate the anisotropic mechanical properties of the cell wall. The movement of these wall depositing complexes in turn is controlled by the orientation of cortical microtubules [125, 126]. In dividing cells, the orientation of the microtubule array is also a predictor of the next division plane.

Microtubules are highly dynamic protein filaments, continually switching between growing and shrinking states. They are hollow tubes with a diameter of approximately 25 nm, typically consisting of 13 protofilaments or strings of tubulin monomers. Microtubules grow and shrink by (de)polymerization: the addition (dissociation) of  $\alpha$ ,  $\beta$  subunits. This  $\alpha$ ,  $\beta$  structure of the monomers makes microtubules polar structures, with a +end and a –end [127]. This polarity also plays an important role in intracellular transport: motor proteins walking over the microtubules typically walk towards either the +end, or the –end [128]. Tubulin monomers are added as GTP-tubulin. After incorporation, this GTP is hydrolyzed to GDP. This stochastic process results in a GTP cap at the tip



of a growing microtubule. This GTP cap is thought to be very important for microtubule stability. This also explains how obstructing the growth of a microtubule can result in a catastrophe (switch to the shrinking state): without addition of new monomers its GTP cap disappears [129]. In cells, microtubules are decorated by many proteins, which affect their stability [130].

A very famous microtubule structure is the mitotic spindle. This structure pulls apart the chromosomes during cell division. In the mitotic spindle, all microtubules originate with their -end from one of two microtubule organizing centers. Plant cortical microtubules, however, have no such organizing center. Instead, microtubules are nucleated throughout the whole array [131]. They are attached to the cell membrane. As a result, their interactions take place in an effectively 2D environment. Consequently, they interact through frequent collisions [132]. These interactions can be sufficient for spontaneous alignment [133], and regulation of microtubule dynamics is a potential source of control over their alignment and array orientation. Array orientation can also be modified in response to wall stress [134] and familiar developmental signals, such as auxin [8, 135].

The first models of the cortical array assume isotropic microtubule nucleation. In reality, however, the  $\gamma$ -tubulin complexes nucleating the microtubules show a high affinity for existing microtubules [136] and nucleation angles relative to the parent microtubule show are strongly biased [137]. In chapter 7 we investigate the impact of nucleation from existing microtubules rather than uniformly distributed over the cortex and the effects of the specific distribution of nucleation angles as measured by [137]. In (near) absence of parent microtubules, for example right after cell division or chemical depolymerization, the distribution of nucleation angles is not uniform either. This is investigated in chapter 8.

An interesting protein linking microtubule orientation and cell divisions is the microtubule severing protein katanin. Although severing at random locations reduces the average microtubule length and only has detrimental effects on their alignment [138], this protein actually promotes microtubule alignment and is important for array reorientation. Loss of function mutants show decreased microtubule alignment. This results in less elongated cells and resulting stunted plant growth. Also, the nice organisation in cell files in the root is disrupted, with many oblique division planes, which also results in misexpression of genes that are normally limited to a single cell layer (cylinder) in the root [139–142].

With interphase array and division plane orientation so tightly linked, what controls the orientation of the cortical microtubules becomes a very important question. In chapter 9 we investigate one possible mechanism.

## 1.6 Outline

The first part of this thesis is about symplastic transport, addressing basic questions about its biophysical properties: how fast, how far and what are its consequences? We approach these questions on a tissue level (chapter 2) and by explicitly considering diffusive transport through individual channels (chapter 3). The results and simulation platform extensions of this also appear in the second part, which focuses on the formation of root lateral organ primordia for nodulation (chapters 4 and 6) and in general (chapter 5). The

third part is about the self organisation of cortical microtubules. It starts with two chapters on their spontaneous alignment, addressing the roles of directed microtubule bound nucleation of new microtubules (chapter 7) and a diagonal bias on microtubule nucleation in the early steps of array formation (chapter 8). The final chapter (9) is about a mechanism for array orientation and through this division plane control. This mechanism is under the control of auxin signaling, thus providing a link between the “biological” and “physical” control mechanisms of plant growth.

## **Part I**

# **Symplastic transport**



Plant development is not only a temporal, but also an inherently spatial process, orchestrated by developmental signals. To understand how these usually biochemical signals interact, it is essential to understand how they move through the various plant tissues. In potential, this movement can be facilitated by specific transporters. For some important regulatory molecules, however, such specific transport systems are not known, or not present in the relevant tissues. All sufficiently small molecules, however, can move from cell to cell through plasmodesmata, a process called (non-targeted) symplastic transport. In this part we will investigate the basic biophysical properties of non-targeted symplastic transport: How fast, how far, and in what way do these depend on the size of the signal molecule? We will also discuss the potential and actual developmental impact of symplastic transport.





---

## **Walking the back alleys: a modelling study of symplastic transport**

---

*In collaboration with Veronica Grieneisen and Yoselin Benitez-Alfonso*

Development is not only a temporal, but also an inherently spatial process. To understand how specific biochemical signals can interact to control development, it is essential to understand how they move through tissues.

One mechanism for such movement is often overlooked: (non-targeted) symplastic transport. Nevertheless, many small substances can move symplastically and mutations affecting the regulation of symplastic transport are often lethal. Here we present a modelling study of its biophysical properties and their implications.

We will first study the transport mechanism in isolation, comparing it with similar mechanisms. Next, we will investigate how it interferes with the much more thoroughly studied directed apoplastic transport. We also address its pattern generating properties in a conceptual way using a Turing-like mechanism. Together this provides an overview of the biophysical properties of non-targeted symplastic transport and illustrates its major biological impact.

## 2.1 Introduction

Development is not only a temporal, but also an inherently spatial process. To form different tissues, cells have to differentiate and follow different developmental paths. Plant cells are by and large unable to move relative to each other, so the cell types must differentiate in the correct position relative to each other. This requires both coordination of developmental decisions among cells and cell types and subsequently the isolation of these decisions to individual cell(type)s. For this coordination plants use a wide range of signaling molecules. To understand how specific signals can interact to control development, it is essential to understand how they move through tissues.

Plants and animals employ quite different systems for intercellular communication. Animals have several membrane located systems for direct communication between neighbouring cells, such as the Delta-Notch system for lateral inhibition [14, 15] and the planar cell polarity proteins for local coordination of cell polarity [16, 17]. These systems rely on protein-protein interactions at the cell membranes of neighbouring cells. Such direct interactions are impossible among plant cells, as they are separated by thick cell walls.

Plants, however, can perform similar tasks using a range of non-cell-autonomous proteins: protein signals that are transcribed in one cell and affect transcription in another. Examples are CAPRICE and GLABRA3 (both involved in root hair and trichome specification) [19], KNOTTED1 (KN1) (involved in leaf development) [143] with its *Arabidopsis* homolog SHOOTMERISTEMLESS (STM) and SHORT ROOT (SHR) (involved in endodermis specification) [124]. These proteins move symplastically, that is through narrow channels connecting the cytoplasm of neighbouring cells called plasmodesmata.

Symplastic transport can be divided into two types. The first is generic: the passive movement of all sufficiently small molecules. This is called *non-targeted symplastic transport* and is diffusion driven [108, 144]. The second is specific and therefore called *targeted symplastic transport*. This is a container term for a variety of different mechanisms that allow symplastic movement of molecules that, typically, would not be able to pass in absence of the mechanism [145]. It includes the intercellular transport of transcription factors KN1 and STM, for example, which requires the chaperonin complex [146]. Another example of targeted transport is the movement of plant viruses, which express their own “movement proteins” to facilitate the crossing [110]. This process may involve structural alterations of the plasmodesmata, which affect the non-targeted transport properties [147].

Molecules moving by non-targeted symplastic transport may include plant hormones, small RNAs and small proteins, as long as they are small enough [108]. The boundary for being “small enough” is conceptually referred to as the “size exclusion limit” (SEL) and mostly depends on a molecule’s hydrodynamic dimensions [106, 107]. The SEL is developmentally regulated and varies among different tissues, developmental stages and different cell faces, as does the density of plasmodesmata [118–121, 148]. The aperture of plasmodesmata is controlled through the deposition and degradation of callose, by callose synthase (CalS a.k.a. GSL gene family) and  $\beta$ -1,3-glucanase respectively, with further regulation by other factors [112]. Callose deposition is assumed to be a fast process and is also involved in the closure of plasmodesmata in response to wounding [105]. The proper regulation is essential for plant development and mutants defective in this regulation are often embryo or seedling lethal [115–117].



As fairly large molecules, such as the 27 kDa GFP, can move throughout the whole embryo in the heart stage [122], reduction of the SEL is required for the isolation of cell fate determinants. For example, in the mutant *chorus*, a weak allele of *GSL8* = *CalS10*, the stomatal fate marker *SPEECHLESS* (364 amino acids in *Arabidopsis thaliana*) moves to neighbouring cells. This results in clusters of – normally isolated – stomata [149]. Normally the SEL is reduced while leaves mature, which has been shown in tobacco leaves [123]\*.

Here, we will focus on the non-targeted transport of generic small molecules. On a molecular level, this transport mechanism has no bias for any specific direction. In the presence of a (turgor) pressure gradient, the direction of non-targeted transport could be biased by the pressure induced hydrodynamic flow. For a rigorous description of the hydrodynamic flow through single plasmodesmata we refer to [150]. We shall not consider such flow, as it has been reported that the non-targeted transport is diffusion driven [108], implying that hydrodynamic flow plays at most a minor role, except in few specific contexts, such as in nectar secreting trichomes [151, 152] and in the phloem [153, 154].

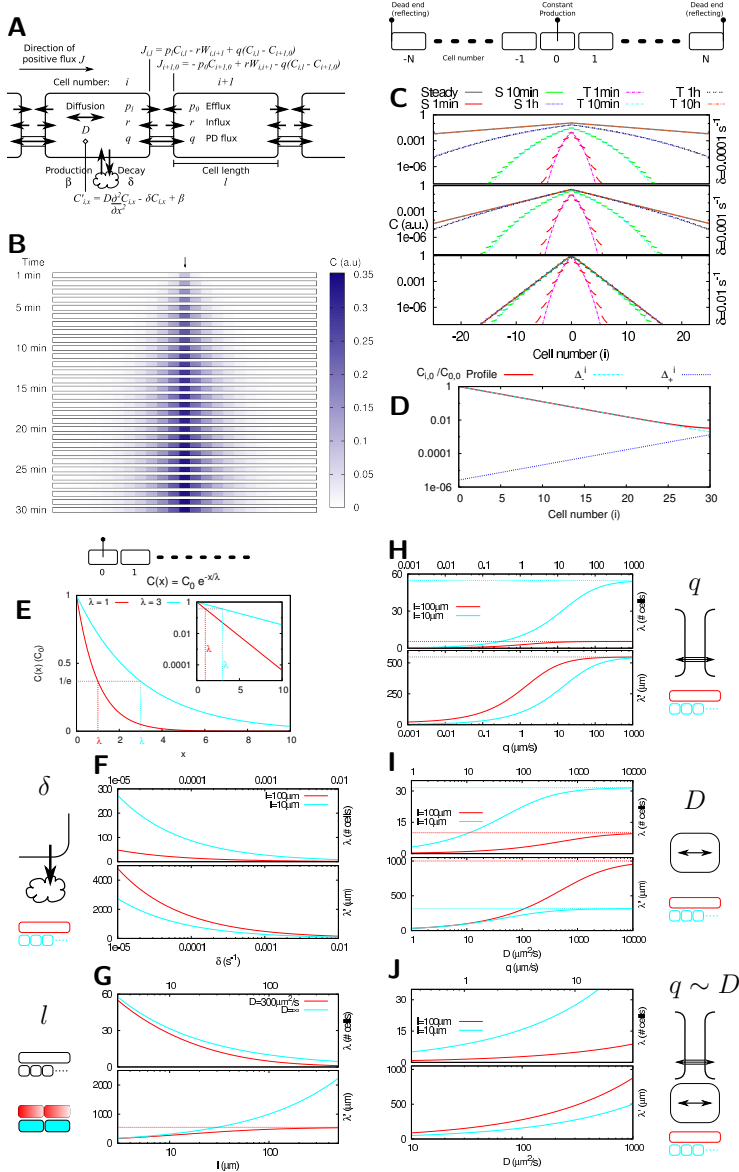
The different mechanisms mentioned are used for local communication. Both plants and animals employ concentration gradients for the coordination of development over longer distances. A very famous animal example is the bicoid gradient in the *Drosophila* embryo, a protein gradient originating from maternal RNA deposited at the anterior end of the embryo [155–157]. Gradient formation takes place in early stages of *Drosophila* development, before individual nuclei are surrounded by their own cell membrane. This morphogen gradient has received much attention from modelers and has long been modelled as a simple diffusion process in a homogeneous medium [158, 159]<sup>†</sup>. Many long range gradients in plants are gradients of the plant hormone auxin [46]. It has been suggested that, because auxin is such a small molecule, symplastic connections may strongly reduce the efficiency of (apoplastic) auxin transport, depending on cell size [163]. As directed auxin transport is essential for auxin pattern formation, we will further investigate this interaction.

Diffusion has traditionally played a central role in the modelling of and conceptual thinking about developmental patterning in animals [164–167]. Contrary to studies on animal systems, intracellular diffusion is often neglected completely in auxin models, specially in studies of shoot processes, such as phyllotaxis and veination [82]. In studies of root tissues, which typically contain strongly elongated cells, intracellular gradients are more often (e.g. [54, 91]), but not always, considered.

Symplastic transport often relies on diffusion also for the *intracellular* movement of the signal, as in most tissues there is little or no net hydrodynamic flow. We will therefore consider both the cellular compartmentalization and intracellular diffusion together. In the discussion we will reflect on the importance of both aspects (2.3.1). The few published measurements on diffusive permeability through plasmodesmata [163, 168, 169] will serve as a guideline in searching the relevant parameter spaces.

\*Bombardment; Sink leaves/cells (immature) showed a SEL of  $\approx 50$  kDa for proteins.

<sup>†</sup>This has then been replaced by a model based on mRNA transport, with the bicoid gradient as a direct readout of the mRNA gradient [160, 161], which was disputed again by more precise measurements of the mRNA gradient, which restored the need for bicoid diffusion, or another form of bicoid transport [162] *et cetera*...



**Figure 2.1: Basic properties of symplastic transport.** **A:** model outline. All fluxes through the walls are modelled as effective permeabilities (with units  $\mu\text{m/s}$ ). Concentrations are given as  $C_{i,x}$  in cell  $i$  at location  $x$  and  $W_{i,i+1}$  in the wall between cell  $i$  and  $i+1$ . Model parameters: decay constant  $\delta$ , cell length  $l$ , effective wall permeability  $q$  and diffusion constant  $D$ . **B:** time series for a 1D tissue with a single producing cell (with rate  $\beta$ /volume =  $2\delta$  a.u.) in the middle ( $q = 1 \mu\text{m/s}$ ,  $\delta = 0.001 \text{ s}^{-1}$ ,  $l = 100 \mu\text{m}$ ,  $D = 300 \mu\text{m}^2/\text{s}$ ). **C:** Dependence of profile steepness and time scales on  $\delta$  (other parameters as in **B**). Simulation profiles are indicated with "S", analytical predictions with "T". **D:** Example steady state profile (solid red) with source left and reflecting wall right. This is the sum of two exponential functions (dashed): a decreasing one (cyan) and approximately the continuation of its reflection on the wall (blue). **E:** The steepness of the concentration profiles can be expressed using the characteristic length, the length over which the concentration drops with a factor  $1/e$  ( $\approx 0.37$ ). This can be expressed in number of cells ( $\lambda$ ) or physical length ( $\mu\text{m}$ ;  $\lambda'$ ).

**Figure 2.1** (continued): **F-J**: dependence of  $\lambda$  (upper panel) and  $\lambda'$  (lower panel) on individual parameters, as indicated with symbols and cartoons at the sides, for two cell lengths (**F,H-J**) or with (red) or without (cyan) intracellular gradients. Default parameters:  $q = 10\mu\text{m/s}$ ,  $\delta = 0.001\text{s}^{-1}$ ,  $l = 100\mu\text{m}$ ,  $D = 300\mu\text{m}^2/\text{s}$ . As both  $q$  and  $D$  depend on particle size, we also calculated the characteristic lengths keeping the ratio  $q/D$  fixed (**J**).

## 2.2 Results

### 2.2.1 Basic properties of pure symplastic transport

When thinking about the importance of symplastic transport, the first questions that come to mind are how fast can a signal move by symplastic transport and how far will it get? To address them we built a tissue level model of non-targeted symplastic transport.

The plasmodesmata allow for diffusion of sufficiently small particles through them. This can be captured as a diffusive permeability  $q$  for each interface separating two cells. The value of  $q$  will be substance dependent, with a very strong influence of the particle's hydrodynamic dimensions [106, 107]. For the small (0.5 kDa) molecule fluorescein, measured values are reported in the range of 1-10  $\mu\text{m s}^{-1}$  [163, 168, 169]. We started with a description in 1D, as this is easiest to tackle analytically and explain, and later extended this to 2D (first in section 2.2.2).

In 1D, the effective permeability results in a flux  $J_{i,i+1} = q(C_{i,l} - C_{i+1,0})$  over the wall between consecutive cells  $i$  and  $i+1$ , with  $C_{i,l}$  the concentration at the far wall of cell  $i$  and  $C_{i+1,0}$  the concentration at the near end of cell  $i+1$  (figure 2.1A). Within each cell the substance moves by diffusion (with diffusion constant  $D$ ), with decay (with rate  $\delta$ ) occurring everywhere in the cell. Production (with rate  $\beta$  per volume) may take place in designated cells.

For our initial questions we opted for a setup of a long line of identical cells, with the continuous production of substance in the middle cell only and degradation everywhere. Conceptually this is similar to monitoring the spread of a locally induced signal (hormone, transcription factor, tracer molecule). An example is shown in figure 2.1B.

When using parameters reasonable for a small molecule (like most phytohormones or dyes like fluorescein), we found from our simulations that the steady state distribution can be approached within minutes or may need hours, depending on the turnover of the molecule (figure 2.1C). From the same figure it becomes clear that the parameter  $\delta$  (degradation or other removal from the mobile pool of the substance) has a strong influence on the range of the signal, with steeper gradients for higher  $\delta$ .

For a more systematic understanding of model, we calculated an analytical expression describing the steady state profile, in the shape of a smooth profile matching the concentration at one point per cell, e.g., the edge closest to the production source. The mathematical structure of the steady state solution is the sum of two exponential functions ( $\Delta_-^i$  and  $\Delta_+^i$  in figure 2.1D). One of these ( $\Delta_-^i$ ) dominates the profile, the other is only needed to accommodate the effect of the boundaries (appendix A.1.2). Based on the dominant part only, we could derive an analytical approximation for the dynamics (see appendix A.1.3), also plotted in figure 2.1C. In this, time ( $T$ ) always occurs in a factor  $\sqrt{\delta T}$ , explaining why turnover is a key determinant of the time scales for reaching

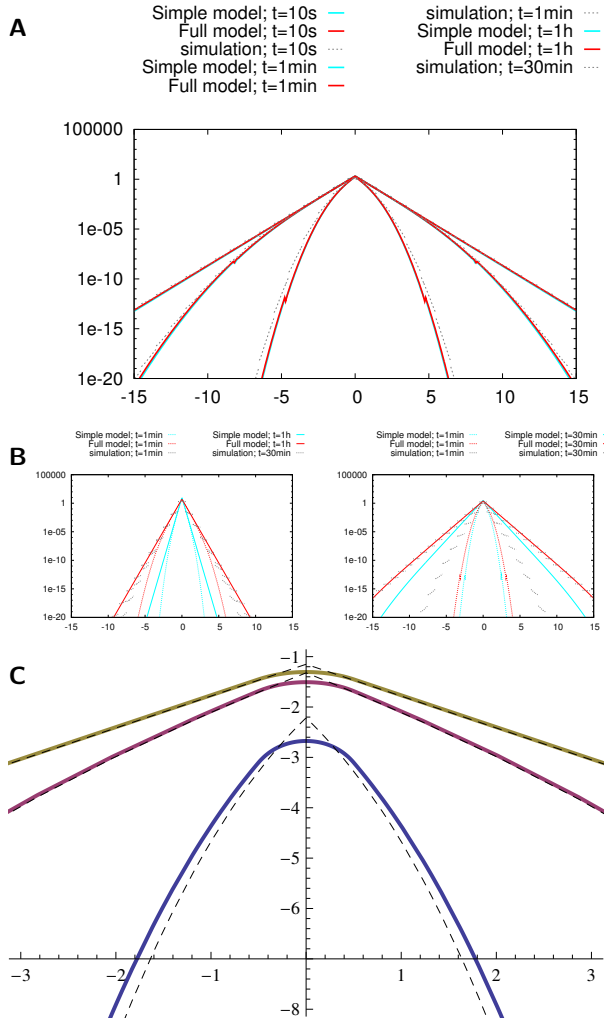


Figure 2.2: **(Supplementary) – Comparison of full cell based calculations (red/dark) and simplified model (cyan/light) with numerical simulations ((gray) dotted).** For a large range of parameters the two yield very similar predictions, e.g. **A** ( $q = 10\mu m/s$ ,  $\delta = 0.1s^{-1}$ ,  $l = 100\mu m$ ,  $D = 300\mu m^2/s$ ). Only towards large  $l$  and  $\delta$ , specially with smaller  $q$ , the two diverge and the full model performs better, e.g. **B** ( $q = 0.1\mu m/s$ ,  $\delta = 0.1/0.01s^{-1}$ ,  $l = 100\mu m$ ,  $D = 300\mu m^2/s$ ). In both cases, the tails of the distribution, that is, farther away from the source, are underestimated. This underestimation decreases quickly with time and the full model always converges to the correct steady state. This error is structural and results from the assumption that all signal is produced in a single point. (Without this assumption, it is impossible to obtain an analytical expression for the temporal solution.) Assuming that production takes place in an entire cell corrects for this (**C**: point source in dashed lines, whole cell  $(-0.5$  to  $0.5)$  in solid lines. This is a proof of principle with arbitrary values.)

a steady state. The production rate ( $\beta$ ), on the other hand, has no influence on the time scales. This means that the concentration at any point and any moment depends linearly on  $\beta$  (because we assumed a constant production rate, i.e. no regulation).

Not counting the production rate, the model has four free parameters:  $\delta$ ,  $l$ ,  $q$ ,  $D$ , too many to obtain a good overview of the model's behaviour by studying how the full profile changes with each of them. To better understand how the range of the signal is affected by different parameters, we therefore used the concept of a characteristic length, here defined as the distance over which the (steady state) concentration drops with a factor  $1/e \approx 0.37$  (illustrated in figure 2.1E). A characteristic length is, for example, often used to describe morphogen gradients.

It is not a priori clear what is more limiting to the spread of a signal: the physical distance it has to travel, or the number of walls it has to cross. We therefore computed the characteristic length in two different ways. When distance is expressed in the number of cells, we denote it by  $\lambda$  and for physical distance ( $\mu m$ ) by  $\lambda'$ . Figure 2.1F-I shows the effect of each parameter on the characteristic lengths for two different cell lengths per graph. The two curves never overlay, indicating that both cellular scale and the physical distance are important for the range of the signal. For cell length  $l$  the most extreme picture emerged: with increasing  $l$  the average number of cells travelled decreases, but the distance increases (figure 2.1G). Even with infinitely fast intracellular diffusion  $\lambda$  decreased with increasing  $l$ , because the signal is slowed down at each wall (barrier) and the total degradation per cell is proportional to its volume. Only in the case of effective wall permeability  $q$  (figure 2.1H), the two cell lengths share the same upper limit for the characteristic length in physical distance ( $\lambda' \rightarrow \sqrt{D/\delta}$ ). In this limit, the walls pose no longer any barrier, which is equivalent to diffusion/decay in a homogeneous medium.

Reflecting on this, we defined an effective diffusion constant ( $\delta$ -dependent)  $D_{eff} = \lambda^2 \delta$ , the full expression quite complicated (equation A.53). Taking the limit of  $\delta \downarrow 0$  of this expression, however, we arrived at a much simpler result:  $D_S = \frac{Dq}{l(D+q)}$  with distance expressed in cell length. Converted to physical distance this is:  $D'_S = \frac{Dql}{D+ql}$  (appendix A.1.2), a result also found in other contexts, e.g. morphogen gradients in embryogenesis [166]. Using this “simple” effective diffusion constant in results derived for ordinary diffusion/decay systems, we obtained very good approximations of the tissue profiles over a wide range of parameters. In extreme cases, however, the complicated  $D_{eff}$  performed better than the simplified  $D_S$  (figure 2.2A,B). This illustrates a common trade-off between precision on the one hand and insight and simplicity on the other hand.

The formulas of  $D_S$  and  $D'_S$  nicely explain that the characteristic lengths can not be increased indefinitely by increasing the particle's diffusion constant  $D$  (employing smaller molecules; 2.1I) or the effective permeability  $q$  (increasing PD density and/or aperture; figure 2.1H) in isolation. Although plants can regulate  $q$  independent of  $D$ , the two are not fully independent. As diffusion is the major driving force of non-targeted symplastic transport,  $D$  and  $q$  are both functions of the size of the signal molecule. We varied them together with a fixed ratio  $\frac{D}{q} = 30 \mu m$  (based on measurements in [163]) as a proxy for inverse particle size, which we assume is reasonable for particles much below the SEL (figure 2.1J). In this case mathematical limits are replaced by physical bounds on  $D$  and  $q$ . As a reference: the diffusion constant of water in water is  $\approx 2300 \mu m^2/s$  [170].

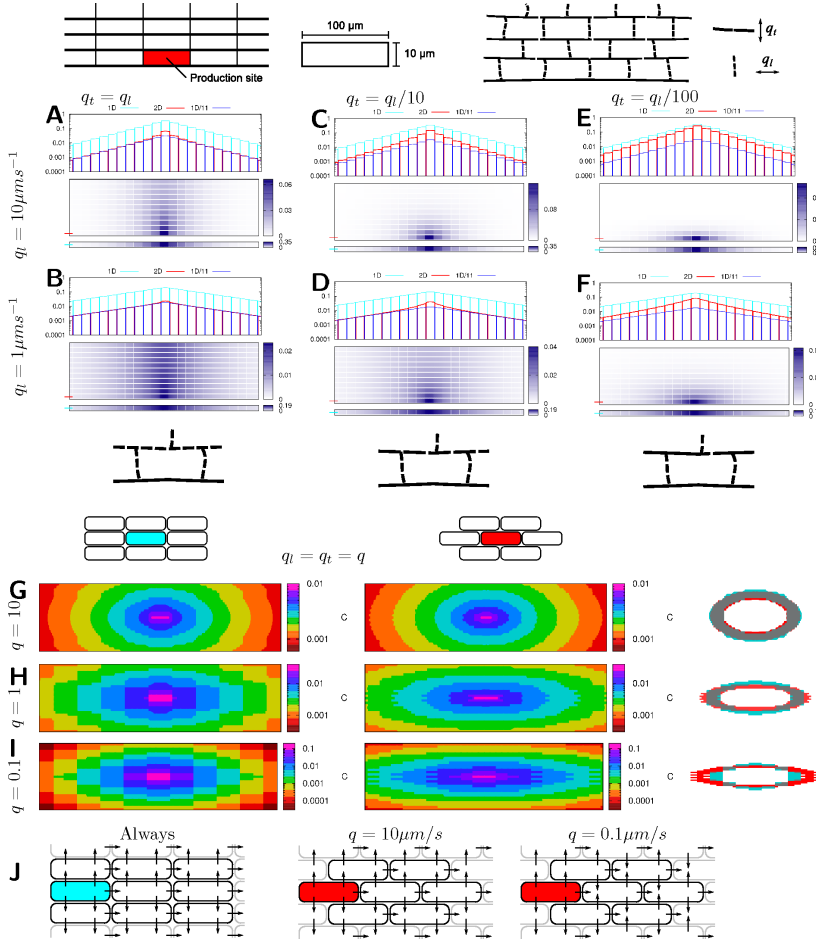


Figure 2.3: **Tissue anisotropy.** **A-F:** spread of a signal produced in a single cell at the edge of an 11 cell files wide linear tissue with effective permeability  $q_l$  within cell files (longitudinal transport) and  $q_t$  between cell files. Gaps in the lines in the cartoons are an intuitive indication of the ratio  $q_l : q_t$ . The profile through the producing cell (red) is bound between a 1D profile (cyan) with the same parameters ( $q = q_l$ ) and this 1D profile divided by 11 (blue). The distance required to converge to the latter profile depends much stronger on the  $q$ -value between files ( $q_t$ ) than the ratio  $q_t/q_l$  (see also figure 2.4). **G-I:** another kind of tissue anisotropy originates from the alignment of the cells. Production occurs in a single cell in the center of the tissue. Concentrations are indicated with different colors using a step function. An overlay of a ring representing the same concentration range for both alignments (cyan: “square”, left; red: “brick”, middle) is shown on the right (gray: overlap). The brick alignment shows a stronger longitudinal transport. Differences are largest with the smallest values of  $q$  (I), indicating that low transport creates greater sensitivity to geometrical anisotropies. **J:** directions of net symplastic flux. With the brick alignment this depends on  $q$  (compared to D). Parameters:  $D = 300 \mu\text{m}^2 \text{s}^{-1}$ , cell length:  $l = 100 \mu\text{m}$ , cell width:  $10 \mu\text{m}$ ,  $\delta = 0.001 \text{s}^{-1}$ ,  $\beta/\text{volume} = 2\delta$ ,  $T = 10h$  (A-F) or  $T = 1h$  (G-I).

### 2.2.2 Realistic tissues: effects of different anisotropies

Building on the understanding from the 1D model, we could then move to more realistic (2D) tissues. These have more degrees of freedom, resulting in anisotropies due to cell aspect ratios, possibly different effective permeabilities for different faces of the cell, and the alignment of cells and cell files. How do such tissue anisotropies affect the spreading of a biochemical signal?

Inspired by the observation by Zhu *et al.* that the longitudinal walls in the young root zones have a lower PD density than the transverse walls [119], we selected a long strip of 2D tissue, with different  $q$ -values for transport within cell files ( $q_l$ : for longitudinal transport) and between ( $q_t$ : for transverse/radial transport), for a first “tissue” investigation. The rectangular tissue of 11 cell files wide can be seen as a caricature of an elongated plant part. Locally this is a real 2D environment (3D in the actual plant), but globally it can be considered as 1D. To probe the spatial scales of this transition in dimensionality, we investigated the spread of a signal produced in a single cell on the side (fig 2.3A-F) with varying  $q_l$  and ratio  $q_l : q_t$ , the latter illustrated by the density of gaps in the cartoons.

Close to the production site the steady state profile declined faster than expected from 1D, even if  $q_l \gg q_t$ . Further away from the production site, however, the 2D profile converged to the 1D profile, corrected for the relatively smaller production volume (by dividing the concentration in 1D by 11, the number of layers in 2D). We changed both the ratio of  $q_l : q_t$  (A→C→E and B→D→F in fig 2.3) and the value of  $q_l$  itself (top→bottom in fig 2.3). Comparing how fast the profile converted to a 1D-like profile, we found that the value of  $q_l$  was more important for this than the ratio  $q_l : q_t$  (fig 2.4). This implies that the strength of the coupling between cell files is the most important factor in the transition from local (2D/3D) to global (1D) behaviour of a signal spreading in elongated organs.

Real plant tissues are not aligned in a rectangular pattern as in figure 2.3A-F, but at most in files only. We compared the two extreme possibilities for rectangular cells in files: a “square” and a “brick” alignment (fig 2.3G-I). We used a stepwise color gradient to visualize the concentration profiles around a single producing cell in the center. This resulted in a set of “rings”, each representing an arbitrary concentration range. By overlaying a single equivalent ring of both alignments we found that with a square alignment the signal could spread relatively easier to the sides (= crossing the long walls) and relatively easier in the longitudinal direction (= crossing the short walls) with the brick alignment. With high transport ( $q = 10\mu\text{m/s}$ ) this difference was small, but it became more pronounced with decreasing  $q$ .

Recalling from figure 2.1H and I, this can be understood as follows:  $q$  and  $D$  mutually bind the spread of the signal. If  $q$  is large compared to  $D$ , diffusion is the limiting process and the local concentration will mostly depend on the physical distance from the source, which is the same for both alignments. If, on the other hand,  $q$  is small compared to  $D$ , the transport over the wall is limiting and the number of walls to cross and the connectivity of the cells becomes important. In this respect the two alignments differ, as the square alignment has a square grid topology, whereas the brick alignment has a hexagonal grid topology. A key difference between the two topologies is illustrated in figure 2.3J: the directions of the net symplastic fluxes are always the same for the square alignment, but depends on the relative importance of transport and diffusion for the brick alignment.

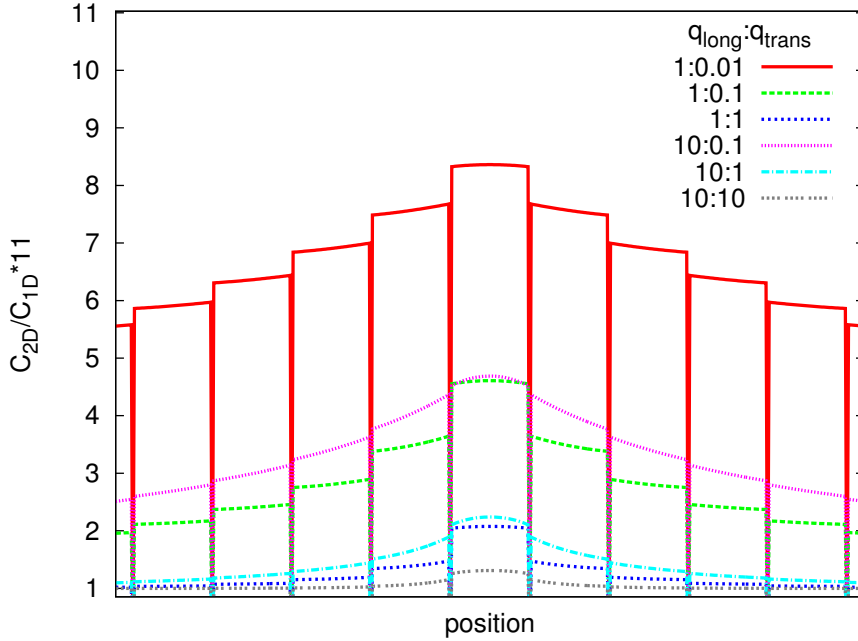


Figure 2.4: **(Supplementary) – Comparison of impact of  $q_l$  and  $q_t$**  on how, moving away from the source, the profile relaxes to a 1D profile with the same parameters ( $q_{1D} = q_l$ ). Curves are calculated based on figure 2.3A-F: concentration in 2D in the cell file containing the producing cell divided by the concentration in 1D, multiplied by 11. As a result of this multiplication, a value of 1 signifies local equivalence to the corresponding 1D profile. Note that the spatial relaxation to the 1D equivalent for equal  $q_t$  is more similar than for equal  $q_l : q_t$ .

### 2.2.3 Symplastic vs. apoplastic transport

We next compared symplastic and apoplastic transport, addressing two questions: (i) to what extent can (symmetrical) apoplastic transport behave the same as symplastic transport and (ii) how do symplastic and apoplastic transport interact?

Assuming that the apoplastic system operates far from saturation, it can be modelled using effective permeabilities, possibly different for influx ( $r$ ) and efflux ( $p$ ) and for different faces of the cell (fig 2.7A). Using the same method as before, we calculated the 1D analytical steady state profile (appendix A.1.4). This has the same mathematical structure as with symplastic transport, i.e. the sum of two exponential functions.

The influx permeability  $r$  does not occur in this solution, implying that in 1D the influx capacity does not affect the intracellular steady state concentrations, provided that  $r$  is the same for both sides of the wall (and  $r > 0$ ). This was indeed the case (fig 2.5A, compare blue and cyan curves).

For symmetrical apoplastic transport (the same efflux permeability on both sides of the



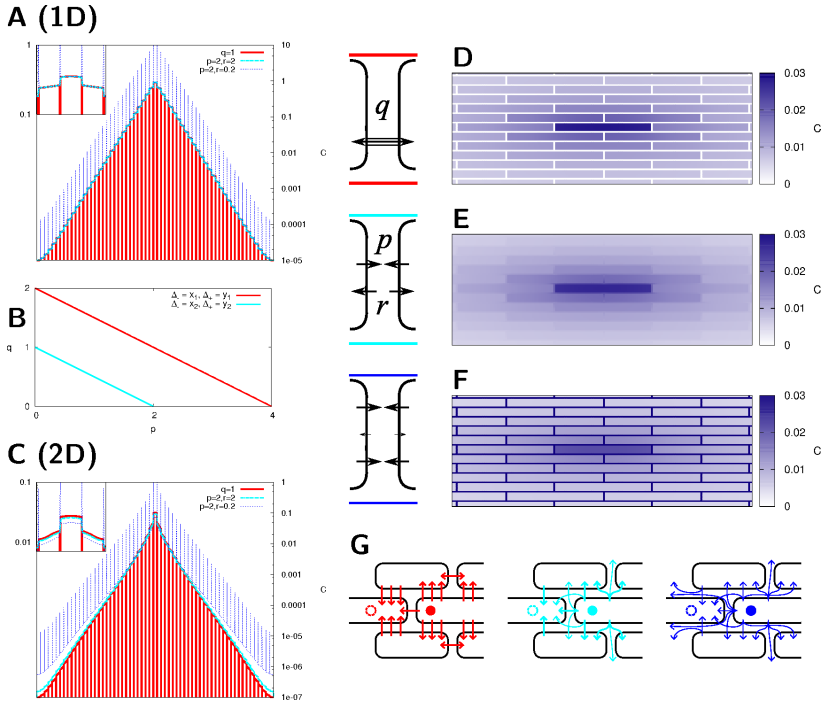


Figure 2.5: **Bypassing cells through the apoplast: a novelty of higher (2+) dimensions.**

**A:** 1D steady state profiles: for parameters satisfying  $y = 2p + q$  (see **B**), only the wall concentrations differ between symplastic (red) and symmetric apoplastic (cyan: equal effective influx and efflux permeabilities  $r = p$ , blue: reduced effective influx permeability  $r = p/10$ ) transport. **C:** with the same parameters on a 2D tissue (brick alignment: see **D-F**) the intracellular concentrations are no longer the same (though profiles remain similar), because it is possible to bypass cells through the apoplast (see **G**). Parameters:  $D = 300\mu\text{m}^2\text{s}^{-1}$ ,  $l = 100\mu\text{m}$ ,  $\delta = 0.001\text{s}^{-1}$ ,  $\beta = 0.002[C]\text{s}^{-1}$ ,  $q = 1\mu\text{m}/\text{s}$  (**D**: symplastic only),  $p = 2\mu\text{m}/\text{s}$ ,  $r = 2$ ,  $0.2\mu\text{m}/\text{s}$  (**E,F**: both apoplastic only).

wall:  $p_0 = p_l = p$ ), the analytical solutions were the same for symplastic and apoplastic transport along lines obeying  $y = 2p + q$  (figure 2.5B). Under these conditions, we indeed found only differences in the wall concentrations (figure 2.5A).

The reason behind these identical intracellular profiles is that in 1D the apoplast does not form a continuous network surrounding all cells. In higher dimensions, it is possible to move around cells through the apoplast (fig 2.5G). In 2D, this movement through the apoplast resulted in somewhat increased dispersal of the signal compared to symplastic transport (with the same parameters as in 1D; figure 2.5C vs. A). This effect was more pronounced with decreased influx efficiency (lower  $r$ ). Lower  $r$ -values result in a longer average distance travelled by a secreted signal molecule before (re)entering a cell (e.g. see [82]). This way apoplastic diffusion has the potential to function as a “blurring factor”, most strongly when the spread of the signal is strongly limited by the transport across the

wall/membrane in combination with low re-entry (low  $r$ ) (figure 2.5G).

### Interaction of symplastic and directed apoplastic transport

Although no longer identical 2D, the differences between symplastic and symmetrical apoplastic transport were not that large. A key differentiating feature of apoplastic transport, however, is that it can have a strong directionality resulting from different effective efflux permeabilities (in 1D:  $p_0 \neq p_l$ ). It has been argued that the efficiency of directed apoplastic transport could be greatly reduced if the signal can move back through plasmodesmata, for example in the case of auxin [163]. This plant hormone is well known for its directed transport and based on its size is likely to move symplastically as well.

Mathematically, a directional bias in the apoplastic transport does not change the formulas describing the steady state. Contrary to the previous profiles, however, the positive exponential part now plays an important role in the steady state solution: it describes the effect of substance heaping up against the far end of the tissue (see figures 2.6A and 2.7C). We now have two important characteristic lengths (figure 2.6A):  $\lambda_{source}$  and  $\lambda_{end}$ . The former describes the flat part of the solution, which functions in transport towards the end. From a design perspective, little losses in this part are desirable, so  $\lambda_{source}$  should be large. The latter describes the ascending part of the profile, that is, from a developmental perspective, the informative gradient.  $\lambda_{end}$  should therefore be neither too large (impossible to reliably retrieve the information at a cellular level) nor too small (steep, but probably very short gradient). This model, without symplastic transport, has been studied extensively before, so we present an overview of the impact of the different parameters on both characteristic lengths (expressed in the number of cells) as a supplementary figure (figure 2.6). From this overview it is interesting to note that with the fairly large value of degradation constant  $\delta = 0.01s^{-1}$  (which is sometimes used in models describing auxin transport), the ascending part of the gradient had almost disappeared (figure 2.6A), even though the value of  $\lambda_{end}$  was hardly affected (figure 2.6B). The loss of signal during transport, however, was so large with this value of  $\delta$ , that the “high” concentration at the far end was much lower than at the arbitrary(!) starting point. Moreover, with the default value of  $p_l$  or the default ratio  $p_l/p_0 = 20$ ,  $\lambda_{end}$  was always smaller than 0.4, meaning a very steep gradient (probably stretching only a small number of cells). An online [notebook/.cdf] file is available for the interactive exploration of the characteristic lengths and matching profiles.

Combining symplastic transport with apoplastic transport, we found that allowing for a symplastic backflux resulted in a less steep (= larger  $\lambda_{end}$ ), but several fold longer informative gradient (figure 2.7B). As we had observed a similar possibility with decreasing  $p_l$  (that is, reducing the efficiency of the forward flux; figure 2.6E) as well as very similar behaviour of symplastic and symmetrical apoplastic transport (figure 2.5), we wondered to what extent we could achieve the same results by increasing the symplastic (back) flux (increasing  $q$ ) and the apoplastic backflux (increasing  $p_0$ ).

As we found from figure 2.6 that  $\lambda_{source}$  and  $\lambda_{end}$  together aren't fully informative, we compared the two with regard to the length of the informative gradient and the total concentration difference over it.

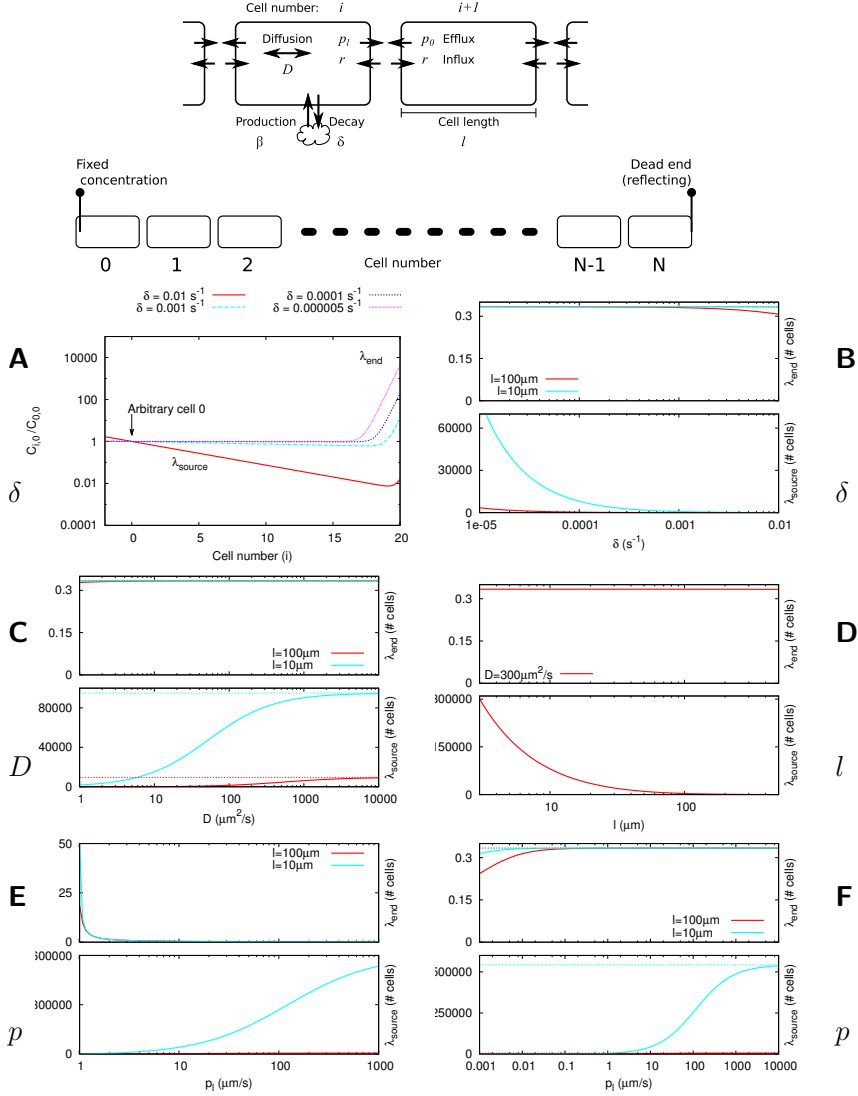


Figure 2.6: **(Supplementary) Purely apoplastic transport ( $q = 0$ ).** **A:** example profiles for different values of  $\delta$ . Note that with high  $\delta$  only little substance reaches the far end. Similar to figure 2.1, we introduce two characteristic lengths ( $\lambda_{source}$  and  $\lambda_{end}$ , both expressed in number of cells). Note that a “heaping up” effect at the far end is only possible if  $\lambda_{source}$  is large. **B-E:** dependence of  $\lambda_{source}$  and  $\lambda_{end}$  on single model parameters. **F:** dependence of  $\lambda_{source}$  and  $\lambda_{end}$  on  $p_l$ , with a fixed ratio  $p_l/p_0 = 20$ . Default values:  $p_l = 20\mu\text{m/s}$ ,  $p_0 = 1\mu\text{m/s}$ ,  $D = 300\mu\text{m}^2/\text{s}$ ,  $l = 100\mu\text{m}$ ,  $\delta = 0.00001\text{s}^{-1}$ .

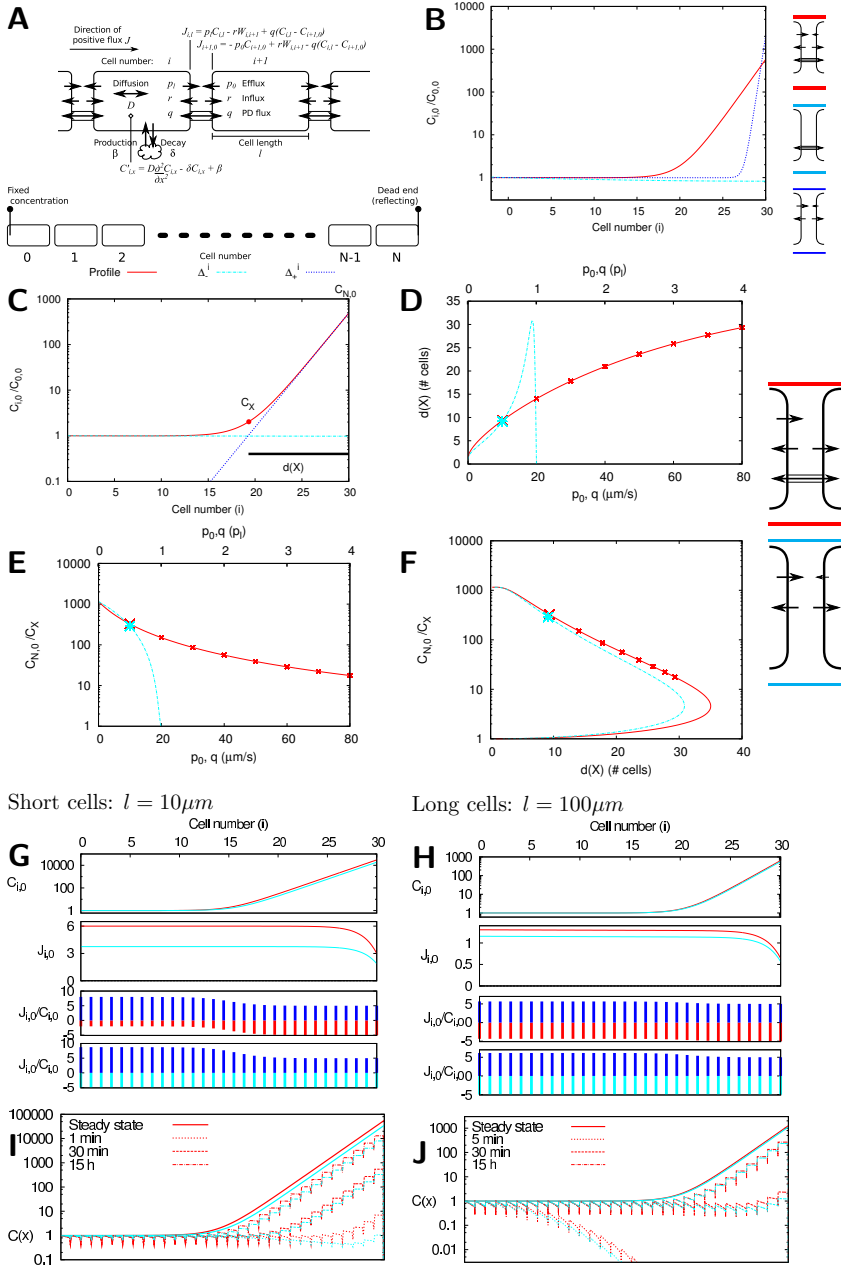


Figure 2.7: **Directed apoplastic flux: symplastic vs. apoplastic backflux.** **A:** model overview including symplastic and apoplastic transport. **B:** Purely apoplastic profile (blue), Purely symplastic profile (cyan) and the combination of the two ( $\delta = 1 \cdot 10^{-5} \text{s}^{-1}$ ,  $D = 300 \mu\text{m}^2/\text{s}$ ,  $q = 10 \mu\text{m}/\text{s}$ ,  $p_0 = 1 \mu\text{m}/\text{s}$ ,  $p_l = 20 \mu\text{m}/\text{s}$ ,  $l = 100 \mu\text{m}$ ). **C:** length of the informative gradient ( $d(X)$ ) and relative concentration increase ( $C_{N,0}/C_X$ ) over this distance. **D:**  $d(X)$  as a function of  $q$  (red:  $p_0 = 0$ ) and  $p_0$  (cyan;  $q = 0$ ). Markers occur every  $10 \mu\text{m}/\text{s}$ .  $p_0$  can not increase in a biologically meaningful way beyond  $p_l = 20 \mu\text{m}/\text{s}$ . **E:** idem for  $C_{N,0}/C_X$ . **F:** combined curves. The markers show that the values of  $q$  needed to complete the curve far exceed the maximum in **D,E** and the progression along the curve slows down with increasing  $q$ .

**Figure 2.7** (continued): **H**: steady state profiles for symplastic (red) and apoplastic (cyan) backflux for parameters as indicated with the large markers in **F** (top), corresponding flux through every cell wall (second) and the relative forward (directed apoplastic, blue) and backward (symplastic: third, red; apoplastic: bottom, cyan) fluxes through every cell wall. **G**: idem, but with short cells ( $l = 10\mu m$ ). Note that in this case the symplastic relative backflux is much lower in the first (flat) half of the profile, whereas it is constant with apoplastic backflux, explaining the almost two fold difference in net flux for the largest part of the profile. **I,J**: time plots: profiles from numerical simulations towards the steady states also shown above.

We exploited the mathematical structure of the steady state profiles to define and quantify the length of the informative gradient. We defined the point  $X$  as the point where the ascending ( $\lambda_{end}$ ) and descending/flat ( $\lambda_{source}$ ) part of the solution meet and  $d(X)$  as the distance from this point to the far end (figure 2.7C). This distance is independent of the length of the tissue (see appendix A.1.4). With this notation,  $C_{N,0}/C_X$  is the relative concentration difference over the gradient.

When looking only at these quantities separately as functions of  $q$  or  $p_0$ , the impact of symplastic fluxes or apoplastic backfluxes seemed completely different (figure 2.7D,E). For one thing, it is impossible (i.e. biologically meaningless) to increase  $p_0$  beyond  $p_l$ , which shows up as a horizontal asymptote in both graphs, whereas the upper limit to  $q$  is not a priori clear.

When combining both quantities into a single plot (changing  $q$  or  $p_0$  to walk along the curve), however, the two became a lot more similar (figure 2.7F). We consistently found that the symplastic ( $q$ ) curve was laying outside the apoplastic backflux ( $p_0$ ) curve (figure 2.10), indicating that a symplastic flux performs consistently “better” than an apoplastic backflux in optimizing both  $d(X)$  and  $C_{N,0}/C_X$  at the same time. In biological terms that means that with a symplastic backflux the (distance to the) reflecting end of the 1D tissue could be communicated over a greater distance from this end wall and/or with a steeper gradient (i.e. easier detection). The difference was larger with short cells than long cells. We found that, depending on the other parameters, it could take very large values of  $q$  to actually complete the curve  $d(X)$ ,  $C_{N,0}/C_X$ -curve, far larger than biologically reasonable. To illustrate how the progress along the curve slows down as  $q$  increases, we plotted 8 points at equal  $q$ -distance in figures 2.7D-F and 2.10. Although the highest  $q$ -value of this set (coinciding with the maximum on the x-axis of figures 2.7D,E) was probably much higher than realistic for most signaling molecules, it was insufficient to reach the maximum possible  $d(X)$  in figure 2.7F, but not in figures 2.10E,G,I, which had larger  $\delta$  and/or lower  $p_l$ .

To better understand why symplastic backflux always outperformed apoplastic backflux, we focussed on the fluxes over each interface. We derived an expression for calculating these fluxes (at steady state) from the steady state profile (appendix A.1.5). With this, we compared the two mechanisms at a point where their resulting profiles are very similar, indicated with a large cross in figure 2.7D-F. We found that throughout the tissue, the net flux towards the end was larger for symplastic than for apoplastic backflux (fig. 2.7G,H). When splitting the flux over each interface in a forward apoplastic ( $p_l$ ) and backward (either  $q$  or  $p_0$ ) part, we found that the normalized backflux by the apoplastic pathway was the same everywhere, whereas the symplastic backflux was smaller in the “flat” part of the profile. Towards the end it reached the same level as with  $p_0$ , because

the parameters were selected such. This difference and hence its impact on the net flux was strongest with small cells (figure 2.7G).

Reasoning that the net forward flux could well affect the time scales of building up the profile, we compared the dynamics of the two mechanisms using numerical simulations (fig. 2.7I,J). Indeed, with symplastic backflux the steady state was approached faster than with apoplastic backflux. This difference was larger with small cells (fig. 2.7I), which also showed a larger difference in the net flux (figure 2.7G) and the largest difference between the  $d(X)$ ,  $C_{N,0}/C_X$ -curves (figure 2.10).

Once again, the 1D model offered mathematical ease. It has been shown, however, that a single linear flow is not suitable for generating a sufficiently long, but fast established gradient as found/assumed in the root [171]. We therefore also tested the impact of symplastic transport in a realistic root context based on [92] (figure 2.8) using the same PIN/efflux permeability distribution and similar cell sizes. For symplastic transport, we split the walls in three groups: H (“horizontal”: radial transport), V (“vertical”: longitudinal transport) and C (“columella”: all walls within the 3 layers of the columella). We compared two cases (red), high radial (figure 2.8A,C) and high longitudinal (figure 2.8B,E) symplastic transport, with a reference case without any symplastic transport (cyan, figure 2.8D). Strikingly, the radial symplastic transport had a much larger impact on the shape and length of the gradient. Nevertheless, upon closer inspection, the average concentration in whole simulation root was remarkably similar and auxin accumulation occurred on the same time scales in both cases (figure 2.11G). Adding high symplastic transport to the columella did not change these results (figure 2.11), possibly because of the high efflux permeability into all directions of these cells.

## 2.2.4 Impact on pattern formation: a conceptual approach

Let’s assume that the concentration of some molecule ( $A$ ) affects the PD aperture, either directly or indirectly. What could be the consequences?

First of all, this will affect the effective wall permeability ( $q$ ) and thus the effective diffusion constant for all molecules. This change will depend on particle size, in a necessarily *non-linear* way. Therefore, the effective diffusion constants for different molecules could, from a certain starting point, be differentially sensitive to changes in the PD aperture. This is particularly interesting, because for the formation of Turing patterns, an extensively studied class of pattern generating mechanisms, the ratio of the diffusion constants of the “activator” ( $A$ ) and “inhibitor” ( $H$ ) determines if and what patterns can form starting from the tiniest disturbances of a homogeneous equilibrium. As a starting point we will use a system with an activator and inhibitor, with a saturation term in the production of the activator based on [167]. Because of this saturation term, the system can yield both spotted and striped patterns on the same domain, depending on parameters [167].

$$\begin{aligned}\frac{\partial A(x,y,t)}{\partial t} &= \nabla \cdot D_A \nabla A(x,y,t) + \frac{\rho A(x,y,t)^2}{H(x,y,t)(1 + \kappa A(x,y,t)^2)} - \mu_A A(x,y,t) + i_A \\ \frac{\partial H(x,y,t)}{\partial t} &= \nabla \cdot D_H \nabla H(x,y,t) + \rho A(x,y,t)^2 - \nu_H H(x,y,t) + i_H\end{aligned}\quad (2.1)$$

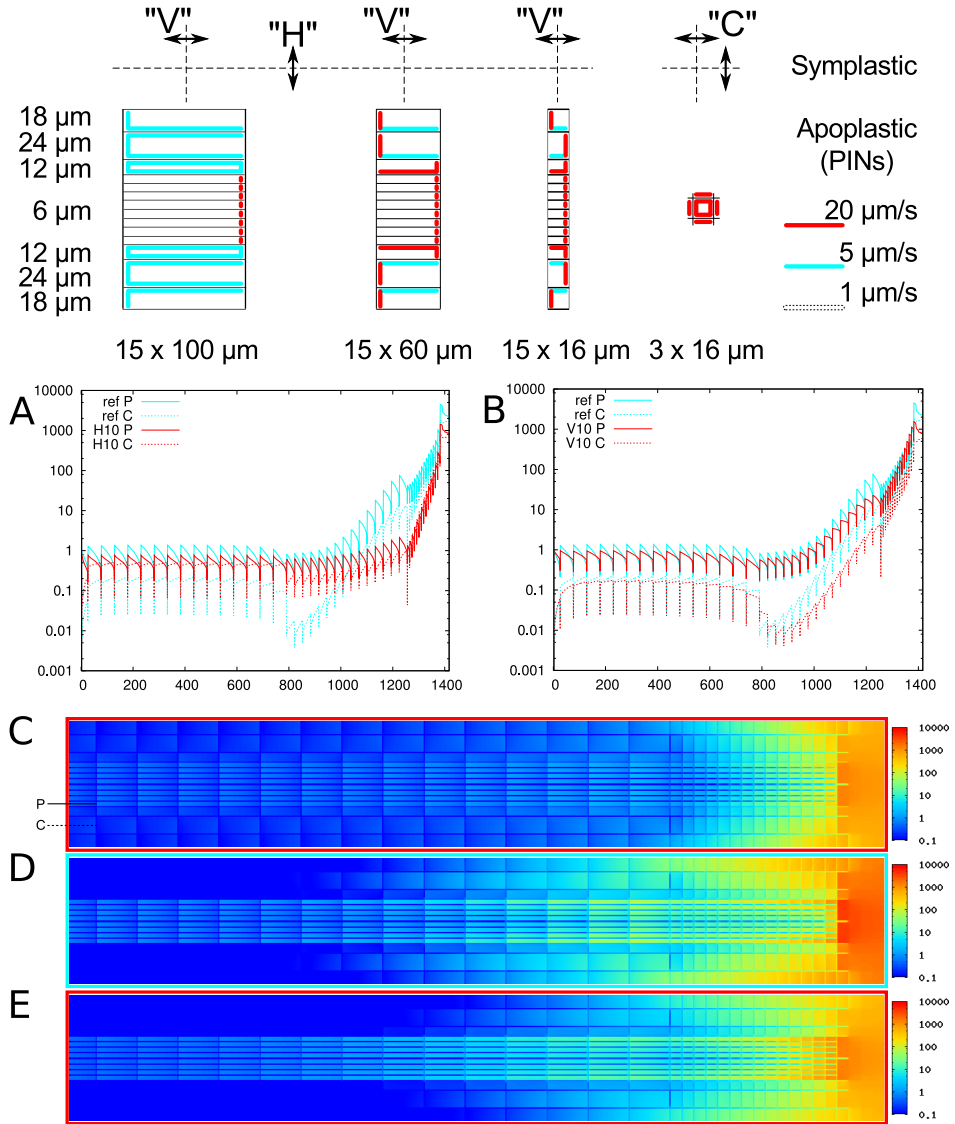


Figure 2.8: **Impact of symplastic transport on root gradients.** Symplastic transport is possible in the radial direction:  $H = 10\mu\text{m/s}$  (A,C) or longitudinal direction  $V = 10\mu\text{m/s}$  (B,E) of the root (red profiles). Control roots without symplastic transport (D) in cyan. A,B: Profiles in the pericycle (indicated “P” in C) with solid lines, cortex (indicated “C” in C) with dashed lines. No symplastic transport in the columella ( $C = 0$ ). Roots based on [92], with slightly altered cell sizes.

On sufficiently large domains, the following patterns could form with our reference system: starting from a low ratio  $D_A : D_H$  and increasing it, the patterns obtained go from spots of high  $A$ , via stripes of  $A$  to spots of low  $A$  and end with a stable homogeneous equilibrium (“no pattern”) if the ratio is above a critical value (fig. 2.9B,E,H,K).

Because of the complex dependence of effective diffusion constants for different molecules on PD dimensions, it is not a priori clear which of the two particles responds strongest to a change in PD aperture. We therefore performed numerical simulations making either  $D_A$  or  $D_H$  decrease with an increasing concentration of  $A$  (then denoted as  $D_x(A)$ , with  $x$  either  $A$  or  $H$ ). This corresponds to either  $D_A$  or  $D_H$  being most sensitive to changes in PD aperture (after a minor spatial rescaling). For the most stringent comparison, we have chosen the dependence of  $D_x(A)$  such that in the homogeneous equilibrium  $D_x(A) = D_x$ .  $D_x(A)$  is the following decreasing function of  $A$  (i.e. increase of  $A$  leads (directly or indirectly) to a decrease of  $D_x(A)$ ).

$$D_x(A) = D_x \frac{2\bar{A}^2}{A + \bar{A}^2} \quad (2.2)$$

with  $\bar{A}$  the value of  $A$  in the homogeneous equilibrium.

We found that in both cases, the dependence of  $D_x(A)$  on  $A$  could change the type of patterns formed given the homogeneous diffusion constants ( $D_A$  and  $D_H$ ; see fig. 2.9). (Strongest) sensitivity of  $D_A(A)$  showed the potential for switches from spots of low  $A$  to stripes of  $A$  (figure 2.9K to J) and from stripes of  $A$  to spots of high  $A$  (figure 2.9E to D), whereas (strongest) sensitivity of  $D_H(A)$  showed the potential for the reverse switches (figure 2.9K to L and 2.9H to I). We also noted that in the regime that all three cases resulted in (mostly) spots of high  $A$ , the spots were smallest with (strongest) sensitivity of  $D_A(A)$  and largest with (strongest) sensitivity of  $D_H(A)$ , making it harder for patches of high  $A$  to merge in the former case than in the latter. These trends were similar as changing the ratio of static  $D_A : D_H$ . As we started our simulations from the homogeneous equilibrium (with small noise added), we only observed pattern formation if the ratio of parameters  $D_A : D_H$  was small enough. In the  $D_A(A)$  case, it was possible to induce pattern formation somewhat above the critical ratio using a large initial disturbance from the homogeneous equilibrium in the shape of a large peak of  $A$  in the center of the domain. The minimal magnitude of the initial disturbance rapidly increased moving beyond the critical ratio (not shown).

## 2.3 Discussion

### 2.3.1 Symplastic transport and simple diffusion

Plant cells are surrounded by both membranes and cell walls, that function as barriers to free diffusion of molecules, even though the walls are perforated by plasmodesmata. That does not mean, however, that a more coarse grained description of symplastic transport – very useful in understanding its generic properties – is impossible. On the contrary, we were able to derive effective diffusion constants that over a very large range of parameter combinations very accurately capture the system’s behaviour as predicted by the version of the model with subcellular precision. With these effective diffusion constants we can



fully exploit the large body of analytical work on diffusion processes to increase our understanding at the (coarse grained) tissue level. A few simple consequences are that the average time required to traverse a certain distance  $L$  scales with  $L^2$  and the time scales for reaching the steady state strongly depend on degradation parameter  $\delta$ . It also opens the door to conceptual models on pattern formation to approach the impact of symplastic transport on plant development on a more abstract level, which is further discussed in section 2.3.5.

In studying the effects of tissue alignment (figure 2.3G-J) we found two different regimes: diffusion limited spread of the signal, with relatively high effective wall permeability  $q$ , or wall traversal limited spread, with relatively high diffusion constant  $D$ . In the latter regime the distribution of the signal was most sensitive to various tissue anisotropies, such as cell aspect ratios and their alignment. This finding is of particular interest, as square tissue layouts are still used quite often in simple models of plant development (e.g. [54, 91–93]). The transition between these two regimes also depends on cell length, as diffusion times scale quadratically with cell length. Both the existence of the two regimes and the impact of cell length can also be inferred from the simple expressions for the effective diffusion constant<sup>‡</sup>. In the limit of  $D \rightarrow \infty$ , the cytoplasmic diffusion constant  $D$  disappears from the equation, meaning that the spread of the signal then is fully determined by effective wall permeability  $q$  and vice versa in the limit of  $q \rightarrow \infty$ . The latter of these two limits should be regarded somewhat critically, though. Whereas it is well possible to make  $q$  arbitrarily small compared to  $D$ , it cannot become arbitrarily large, as the transport through the plasmodesmata themselves is diffusion driven too [108]. With both expressions the cell length determines the ratio of  $D : q$  at which both parameters contribute equally to the effective diffusion constant.

We also derived a more complicated expression for the effective diffusion constant, dependent on turnover constant  $\delta$ . This expression yielded more accurate results for high  $\delta$ , specially for large cell length ( $l$ ) and small  $q$ . In the homogeneous diffusion/decay system, a signal spreads by diffusion and its range is limited by the degradation. The increased spreading with large  $\delta$ ,  $l$ , and low  $q$  could be interpreted as an additional “pulling force”, and thus increased symplastic flux, resulting from an “extra” increase of the concentration difference over the wall. This can only occur because of the cellular structure of the tissue. This example illustrates how understanding the discrepancy between coarse grained and detailed models can provide new insights into the underlying mechanism. A more elaborate model can have even more benefits: for example, our calculation of the fluxes over the wall and their different components requires the full subcellular derivation and we would not have found the two regimes (diffusion limited and permeability limited) for signal spreading if we had ignored intracellular diffusion in our simulations. Starting simple is also valuable, because it helps in understanding what happens in more complicated situations. In many cases the 1D model offered a lot of understanding because it is analytically tractable. Some phenomena, however, cannot occur in 1D and for those the 1D model cannot even predict the right trends. Our most striking example we found in assessing the impact of (non-targeted) symplastic transport on directed apoplastic transport, as in the case of auxin. This is elaborated in the next section.

<sup>‡</sup>These simple expressions are:  $D_S = \frac{Dq}{l(D+q)}$  (length in number of cells (which have length  $l$ ), see appendix A.1.2) and  $D'_S = \frac{Dql}{D+ql}$  (length in normal units; see also [166] and appendix A.1.2).

### 2.3.2 Symplastic transport and auxin gradients

Rutschow *et al.* commented on the impact of symplastic transport on directed auxin transport at the level of a single cell [163]. To observe the “global” implications we assessed the impact of symplastic transport on directed transport in the context of a simple 1D tissue (figures 2.7 and 2.10) and in a realistic root context with a reflux loop structure (figures 2.8 and 2.11).

In 1D we found that the backflux through plasmodesmata resulted in an increase of the gradient length ( $d(X)$ ) and a decrease of the relative concentration increase over this distance ( $\frac{C_{N,0}}{C_X}$ ; see figure 2.7C). The same trends could be achieved through addition of an apoplastic rather than symplastic backflux. Compared to an apoplastic backflux, however, a symplastic backflux performed consistently better in terms of maximizing both  $d(X)$  and  $\frac{C_{N,0}}{C_X}$ . The reason for this is that whereas a (non-saturating) apoplastic backflux is always proportional to the concentration at the wall, a symplastic (back)flux depends on the concentration difference over the wall and can thus be relatively smaller in part of the tissue (fig 2.7G,H). In the flat part of the profile, the concentration difference over the wall is very similar to the concentration difference between both ends of a cell and thus increases with cell length. As a result, the difference between symplastic and apoplastic backflux is most pronounced with short cells (figs 2.7G-J and 2.10) and increases with decreasing forward transport ( $p_l$ ; compare fig 2.10B-E vs F-I).

Recently, Grieneisen *et al.* presented a biophysical comparison of different mechanisms for the formation of developmental gradients in “plant roots” [171]. We can add the combination of directed apoplastic transport and symplastic backflux to this overview as a new mechanism that in mathematical terms performs similar, but “better” than purely apoplastic directed transport. One important note to this is that for apoplastic backflux the whole curve of  $d(X)$ ,  $\frac{C_{N,0}}{C_X}$  combinations (figures 2.7F and 2.10) is available with realistic parameter choices, whereas – depending on parameters – only the part of the curve with the largest  $\frac{C_{N,0}}{C_X}$  can actually be reached with symplastic backflux. In biological terms this implies that symplastic transport can affect, but far from abolish gradients arising from directed apoplastic transport. In line with Rutschow *et al.* we do find that the impact of symplastic transport is larger with longer cells [163].

Interestingly, in a full root context, the addition of symplastic fluxes did not increase the length of the gradient. Moreover, the time scales of auxin accumulation in the whole root were remarkably unaffected by symplastic transport, showing that the root patterning mechanism is far more robust than expected from a simple 1D model. Strong symplastic connections in the direction of the main auxin transport (through the transverse walls) hardly affected the gradient length (figure 2.8B) and orthogonal to the main flow (through the tangential walls) the symplastic connections reduced the gradient length and resulted in a steeper gradient in the most apical (“MZ”) part of the root (figure 2.8A). Together with the strong inward orientation of the MZ PINs, radial symplastic transport may increase the ratio of inward/shootward auxin flux in the (MZ) cortex. Such a change in the ratios of PIN based efflux also results in a steeper gradient [91]. Interestingly, in the MZ of *Arabidopsis* roots, the tangential walls contain far fewer plasmodesmata than the transverse walls [118, 119], which may aid in maintaining a relatively long auxin gradient in the root.

### 2.3.3 Options for asymmetry in symplastic transport

Diffusive transport is in principle symmetrical: it will always occur down a gradient. There are, however, a few possibilities of symmetry breaking in symplastic transport. A hydrodynamic flow could impose a bias in the direction of the transport, as is the case in a few specific tissues including the phloem (measured linear flow velocities e.g. up to 0.4 mm/s in main stems [153] and down to 0.05 mm/s and less in small organs such as leaf petioles and seedling stems [154]) and secreting (e.g. nectary) trichomes [151, 152]. In most tissues, however, this does not play a significant role. A different way of enabling symplastic transport against a gradient of the target molecule is by changing it in the sink location to an immobile form. Such is the case in SHR, which is transcribed in the stele and following symplastic movement sequestered by SCARECROW (SCR) in the (developing) endodermis [124]. Developmentally, this complex functions as a transcription factor in the nucleus, inducing endodermis fate [20]. At the level SHR transport, it maintains a low concentration in the endodermis, so the transport is still occurring down the gradient of *free* SHR. If too little SCR is formed, e.g. in a RNAi knockdown, SHR is not restricted to a single endodermal layer, but moves to farther layers, with developmental consequences [21]. SHR is a 531 AA protein that moves by targeted transport, even with an additional GFP fused to it, whereas single GFP (238 AA) would remain in the stele [124]. The same is possible, however, for small molecules. This happens for example in symplastic phloem loading: polymerization of sugars to short polymers results in their trapping to the phloem and drives passive symplastic transport of monomers down the monomer concentration [172].

*Apparently* passive movement against a gradient occurs in many contexts, including the chemiosmotic model for auxin transport: the pH difference between the apoplast (slightly acidic) and cytoplasm (neutral) potentially drives the import of protonated auxin (IAAH) against the total auxin gradient, because in the apoplast a fair fraction of the auxin occurs as IAAH (e.g. 20-25%) and much less ( $\ll 1\%$ ) in the cytoplasm [85, 173]. These cases have in common that the transport *sec* is passive, but energy *is* spend on maintaining the conditions for transport, in our examples by sequestration (i.e. expressing additional proteins), controlled polymerization or maintaining a pH difference.

### 2.3.4 Biophysics behind different roles for symplastic and directed apoplastic transport

We have considered the (impact of) symplastic transport in two different contexts: local and long range signals. Concurrently, we have used different default values for the degradation parameter  $\delta$ , depending on the process under study. For purely symplastic transport we typically used a fairly high value of  $\delta = 0.001s^{-1}$  and the much lower  $\delta = 10^{-5}s^{-1}$  for the interaction with directed apoplastic transport.

With this we implicitly assumed a local role for purely symplastic transport and a long range range for directed (apoplastic) transport (for example thinking of long range auxin signaling/gradient formation). As we have seen in figures 2.1C,F, a signal could get quite far by purely symplastic transport if  $\delta$  is low, although it might take very long to reach steady state far away from the source, and conversely, even with strong directed transport a signal will not get far if  $\delta$  is too high (fig 2.6AB).

This seems to imply that  $\delta$  is closely correlated with the signal's functional range. This does not necessarily mean that the molecules for short range signals are very quickly degraded. Other processes that remove them from the mobile pool can mimic a high  $\delta$  with regard to the amount of signal available for the next cell(s). Coppey *et al.* have shown, for example, that (nuclear) trapping of the signal can produce the same exponential bicoid gradient as typically modelled with (high) degradation. This mechanism also offers greater gradient stability after the source of the signal is removed [174].

Along the same lines we would like to consider the diffusion constant of a signal in relation to its function(s). The Stokes-Einstein relation gives an inverse relationship between particle size and diffusion constant. In crowded environments, such as cells, the diffusion constant may even decrease exponentially with particle size [175]. Signals with a larger diffusion constant have a larger range (larger  $\lambda$  in figure 2.11,J) and at a given distance from the source, the steady state is approached faster (see equation A.70 in appendix A.1.3). Plant hormones, which may be involved in long range signaling, are small molecules with sizes in the order of 1-3 amino acids (the smallest plant hormone, ethylene, is even smaller). As a result, they have large diffusion constants. Contrary to plants, animals such as the vertebrate *Homo sapiens* also employ proteins for long range signals<sup>§</sup>. They have an actively driven circulation system, however, so diffusion plays a negligible role in long range (body wide) transport of hormonal signals. Because proteins are larger, they can contain functional domains that directly perform certain signaling tasks, without additional receptor systems (e.g. they could be transcription factors themselves) and because of that much more easily allow for an (evolutionary) diversification of the signals transmitted. Their larger size makes them diffuse slower, but even in plants they will still be fast enough for many local roles. For non-cell-autonomous communication in plants, (aided or unaided) movement through plasmodesmata puts some limits on the size of such signaling proteins, but much less stringent than on signals that should diffuse as fast as possible.

### 2.3.5 Impact of non-targeted symplastic transport on pattern formation

Throughout we have compared non-targeted symplastic transport with free diffusion/decay processes and exploited the similarities between the two. Thinking of diffusive processes, one easily thinks of smooth gradients and smoothing out of patterns rather than their creation. We have shown, however, that through differentially affecting the effective diffusion constants of different molecules, regulation of symplastic transport has the potential to qualitatively alter developmental pattern formation (figure 2.9). We used a Gierer-Meinhardt model as a proof of principle, because this class of models has been well studied [176]. However, it is likely that symplastic transport can affect also other patterning mechanisms in which the mobility of components plays a role. The interaction of symplastic transport with known patterning mechanisms offers a rich potential for interesting further research.

The relevance of such research would be much increased if we could already find examples of pattern formation in plants which are affected by symplastic transport in

<sup>§</sup>For example, in humans the most important bioactive form of prolactin is 22kDa / 198 amino acids and the most abundant form of growth hormone 22kDa / 191 amino acids long.

line with the model predictions. The first case study is *chorus*, a weak allele of callose synthase (GSL8 / CalS10). This mutation results in larger than usual plasmodesmata aperture. The phenotype includes clusters of – normally isolated – stomata, coinciding with spreading of stomatal fate marker SPEECHLESS (SPCH). Stomata clustering is even more pronounced in a different, stronger allele of the same callose synthase, *gsl8-2* [149]. Interpreting markers such as SPCH as (readout for) high activator levels, this follows the trend in figure 2.9A-C of small to large spots with increasing  $D_A/D_H$  inside spots of high A. That an activating/inhibiting patterning mechanism is at work is further supported by the observation that stomata occur in relatively small clusters in the *chor* mutant, but cover a large fraction of the epidermis when negative regulator TOO MANY MOUTHS (TMM) is also lacking (double mutant *chor tmm*) [149]. Stomatal patterning defects are also observed in a different mutant allele of the same callose synthase, *gsl8-4* [177]. Interestingly, in these plants an additional layer of root tissue (interpreted as additional cortex) is observed [177], reminiscent of the effect of increased SHR movement in SCR-RNAi knockdown plants (see 2.3.3) [21].

A second case study is the patterning of root hairs and trichomes. The two types of epidermal appendices are controlled by a similar set of transcription factors, the GLABRA-/WEREWOLF system [19], but they occur in very different patterns: trichomes occur isolated (“dots”), whereas root hairs (in *Arabidopsis*) occur in files either fully with, or fully without hairs (“stripes”). These different patterns have previously inspired the comparison with a Gierer-Meinhardt type activator-inhibitor model [178].

The first question in mapping the system to such a model is: what are activator and inhibitor. These authors choose GLABRA2 (GL2), the first stable pattern established in this system [179, 180], as a direct readout of the activator activity. This links trichomes and non-hair cells to the high activator state. This indicates as activators GLABRA1 (GL1) (leaf) and WEREWOLF (WER) (root), GLABRA3 (GL3) and ENHANCER OF GLABRA3 (EGL3) and possibly TRANSPARENT TESTA GLABRA1 (TTG1). The corresponding inhibitor role is fulfilled by TRIPTYCHON (TRY) (leaf) and CAPRICE (CPC) (root) and the related ENHANCER OF TRIPTYCHON AND CAPRICE1 (ETC1), ETC2, ETC3 and TRICHOME-LESS (TCL) [19, 178]. Although several of these components normally are active in the root or leaf only, they do show genetic redundancy. The effects of mutations in these proteins are in line with the described division of roles and GL2 expression as the relevant readout [178].

Of these proteins, it has been demonstrated that the inhibitors TRY/CPC/ETC1 ( $\approx 100$  AA) move symplastically, as do activators GL3/EGL3 ( $\approx 600$  AA) [19]. Given their sizes, these inhibitors may move in a non-targeted fashion, but for these activators that is highly unlikely, at least in the root, because in *Arabidopsis* the symplastic permeability of the root epidermis is strongly reduced (just) before root hairs are formed (as measured by microinjection of carboxyfluorescein [181]). In immature (sink) leaves, the state in which trichomes are formed, symplastic movement of proteins up to  $\approx 50$  kDa is possible [123]. Moreover, also mature trichomes maintain a high density of plasmodesmata [151] and a larger “basal SEL” (compared to mesophyll cells [152]).

If these observations are to be in line with our conceptual model, the difference between trichomes and root hairs would have to be explained as a variation on line D-E-F in figure 2.9. Effectively, this means that [in the locations of high activator] the effective diffusion constants of activator and inhibitor are more similar in the root hair case ( $\approx F$ )

than in the trichome case ( $\approx D$ ). This could be the case if in the leaf epidermis the inhibitor(s) (predominantly TRY) can easily move non-targeted, but this movement is much restricted (perhaps only targeted?) in the root epidermis. In the latter case both activator and inhibitor would be strongly permeability ( $q$ ) limited, making their effective diffusion constants more similar.

Interestingly, all cell files produce root hairs in *Arabidopsis* mutant *ise1* (“increased size exclusion limit”), a mutant impaired in plasmodesmata closure [115]. This would correspond to a homogeneous state of the Gierer-Meinhardt like model, which occurs if the effective diffusion constants of both types are too similar. The relevant question is if it is possible to have going from wild type root hairs, to trichomes of *ise1* root hairs first more dissimilar and then more similar effective diffusion constants than in the wild type root epidermis by increasing and further increasing the SEL. This would imply that in the *ise1* root epidermis the plasmodesmata are opened so far that both activator and inhibitor are in/closer to the diffusion limited regime for spreading. This is dominated by the free diffusion constant, which scales with  $1/R_h$  (1/hydrodynamic radius) and the radius scales with approximately  $R_h \sim \sqrt[3]{L}$  (for globular proteins), this difference may be too small for spontaneous pattern formation. Another option is that other, normally immobile fate markers, are moving symplastically in *ise1*. If this is the case, it would be interesting to see if *ise1* also develops clusters of trichomes – if the seedlings develop far enough to develop trichomes at all.

In conclusion, the effects of callose synthase mutation *chor* are well in line with our model. For the root hair/trichome system, however, several assumptions are required to reconcile all data with our caricature model – which remain to be tested.

As a final note on the Gierer-Meinhardt like model, we would like to remark that also if the change in effective symplastic permeability is not locally induced [by the activator], but caused in a homogeneous way by a parallel developmental process, a shift of pattern type is still possible if the effect of changes in plasmodesmatal aperture is different for different molecules (e.g. because of size differences). This would correspond to vertical shifts in figure 2.9. Such a difference in response is certainly conceivable if the size of one molecule is close to the SEL.

## 2.4 Conclusions

Plants require a proper regulation of symplastic transport for their normal development. This is the first rigorous attempt of modelling diffusive symplastic transport. Starting from a multi level description, explicitly including intracellular diffusion, we have found that on a coarse grained (tissue) level the problem can be mapped to diffusion/decay processes in a homogeneous medium using some effective diffusion constant. This determines the large scale spatio-temporal behaviour of non-targeted symplastic transport, explaining why purely diffusive symplastic transport is more suitable for local signals than for long range communication. Both intracellular diffusion and effective wall permeability limit the spread of the signal, with cell length determining the transition between two regimes. We found that towards the permeability limited regime the spread of signals is affected most by the tissue anisotropy and cell alignment. Inspired by the same mapping to homogeneous diffusive processes, we have shown in a proof-of-principle manner that the

potential developmental impact of non-targeted symplastic transport is much larger than naively expected from such a “passive” mechanism.

Symplastic transport does not interfere so strongly with directed apoplastic transport that it is likely to destroy its potential to form ascending gradients. In the context of a reflux loop it does not even have a strong impact on the time scales of gradient formation. Nevertheless, it has the potential to alter the length and steepness of the gradient, so developmental control of the symplastic wall permeability is important for the proper communication of spatial position (e.g. relative to the QC) and the developmental consequences of its readout.

Symplastic transport affects so many processes in plant development that many open questions remain. What we have presented here also provides tools to address many of them, from the level of very specific contexts up to generic mechanisms.

## 2.5 Methods

### 2.5.1 Overview

We use a combined analytical and numerical approach, in both cases incorporating the cell walls and intracellular gradients. Inside cells there is diffusion and (if applicable) homogeneous production and degradation. We assume that cell walls are so thin that gradients over the wall’s width are negligible. Model equations are included in figures 2.1A (also appendix A.1.2) and 2.7A (also appendix A.1.4).

Conceptually, we tackle two different problems. (1) The biophysical properties of a locally produced or introduced signal, that moves only via non-targeted symplastic transport. This can easily be mapped to typical experiments used in the estimation of the tissue parameters of symplastic transport [163, 168, 169]. (2) Interference of symplastic transport with the directed (apoplastic) transport of a signal such as auxin. Because of the different functions these signals perform within a plant, some parameters are necessarily in different ball parks (see table A.1). This is further discussed in section 2.3.4 of the discussion.

In 1D the two approaches have an exact overlap in the steady state, which is useful for debugging. The analytical solutions provide more insight in how the solutions depend on the underlying parameters, whereas the numerical simulations are more precise for the temporal solutions and easily allow for inhomogeneous tissues (i.e. different parameters for different cells).

We use the numerical simulations on 2D tissues to investigate the effects of signal dilution to other cell files, the impact of tissue layout on the anisotropy and range of signal propagation and the impact of symplastic transport on auxin transport in a realistic root context (based on a published model description of the *Arabidopsis* root [92]).

All analytical calculations are included in the appendices; here we only sketch our approach. An overview of all model parameters and mathematical symbols used is given in table A.1.

### 2.5.2 1D: analytical calculation of steady states

From the mass flux equations over cell membranes and within cells we compute a general formula for the steady state intracellular gradient and derive how flux and concentration at the end of one cell are related to the same quantities in its neighbouring cells. This results in a system of equations that closes with two boundary conditions: two times a flux or concentration at any point in the system (provided that the two are not redundant).

If all cells are the same, it is possible to calculate formulas for the tissue scale steady state profile. For this we compute the ratio ( $\Delta_i$ ) of the concentration at a particular point in one cell ( $i$ ) and the same point in the previous cell ( $i - 1$ ), given the relations described above. It turns out that there are two “homogeneous” solutions for which, on an infinite system, the ratio  $D_i$  is the same for all cells. Any possible profile is a combination of these two solutions, which can be found from the boundary conditions.

The actual calculations are shown in appendix A.1.2 for purely symplastic transport and appendix A.1.4 for symplastic and apoplastic transport together.

Taking into account that these functions give the intracellular concentration at only one point in the cell, these solutions are exact. As such, they should match exactly with the numerical simulations, providing clues about numerical error, or earlier in the process about errors in the calculation or bugs in the code.

From the calculations for purely symplastic transport we were able to define an effective diffusion constant describing the behaviour of symplastic transport on a coarse grained (tissue) level, as shown in appendix A.1.2.

### 2.5.3 1D: time resolved solutions (approximation)

For our scenario of purely symplastic transport of a substance produced in one central cell we managed to find an approximation for the time resolved solution, neglecting the boundaries of the system (that is, on an infinite system). For this we exploit the similarity of the previously found steady states to the solutions for diffusion in a homogeneous medium (the “heat equation”). We use that the limit for  $t \rightarrow \infty$  should be our previously found steady state on an infinite domain to find the constants appearing in the time resolved solution.

The actual calculations are shown in Appendix A.1.3.

### 2.5.4 Numerical simulations

All numerical simulations are performed on 2D grids, using the same finite volume description of the tissue as in [182]. We use the Alternating Direction Implicit (ADI) algorithm [183], adapted to a band-5 diagonal matrix to guarantee matrix invertibility under all possibly relevant conditions. Although it is possible to use a standard tri-diagonal matrix in for example the case of purely symplastic transport by skipping some points while solving the system, the use of slightly different algorithms for different conditions is a potential source of error in batch simulations and parameter sweeps. Moreover, the situation with efflux on only one side of the wall, combined with symplastic transport over it, can not be solved that way. For such reasons we opted for an approach that uses slightly more memory (scaling the same as the original algorithm), but is guaranteed to work.



For figures 2.2C and 2.9 we used Wolfram Mathematica versions 7 and 8 for numerical integration.

## Acknowledgements

The authors thank Bela Mulder and Ton Bisseling for helpful discussions.

The work of EED is funded within the research program of the Netherlands Consortium for Systems Biology (NCSB), which is part of the Netherlands Genomics Initiative (NGI)/the “Nederlandse Organisatie voor Wetenschappelijk Onderzoek” (NWO). Her stay at the John Innes Centre was funded by the European Molecular Biology Organization (EMBO) short term fellowship ASTF 105-2011.

## List of Abbreviations

PDs	plasmodesmata (plural!)
SEL	Size exclusion limit
AA	amino acid residues (for protein size)

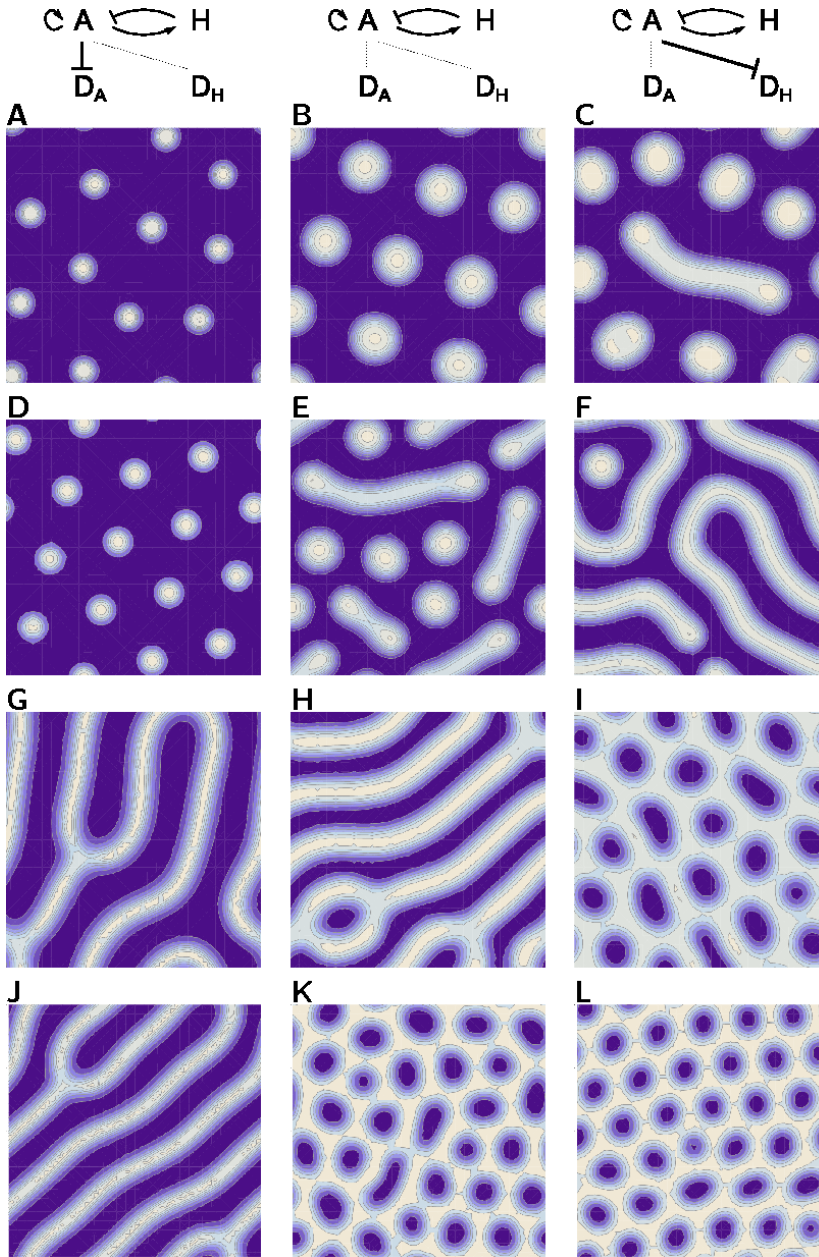


Figure 2.9: **Impact of regulated symplastic transport on a Turing-like mechanism.**

In a conceptual framework, the activator concentration ( $A$ ) could have, through changes of PD aperture, a stronger impact on the tissue level effective diffusion constant of  $A$  ( $D_A$ ; left) or on  $D_H$  (belonging to inhibitor  $H$ , right). The middle column shows patterns without changes in either  $D_A$  or  $D_H$ , in the other columns the least affected constant is assumed fixed for simplicity. Parameters: **A-C**:  $50 \times 50 \mu\text{m}$ ,  $T=1000\text{s}$ ,  $D_a = 0.5 \mu\text{m}^2/\text{s}$ ; **D-F**:  $100 \times 100 \mu\text{m}$ ,  $T=10000\text{s}$ ,  $D_a = 2 \mu\text{m}^2/\text{s}$ ; **G-I**:  $150 \times 150 \mu\text{m}$ ,  $T=10000\text{s}$ ,  $D_a = 5 \mu\text{m}^2/\text{s}$ ; **J-L**:  $200 \times 200 \mu\text{m}$ ,  $T=10000\text{s}$ ,  $D_a = 6 \mu\text{m}^2/\text{s}$ , defaults (see table A.1C).

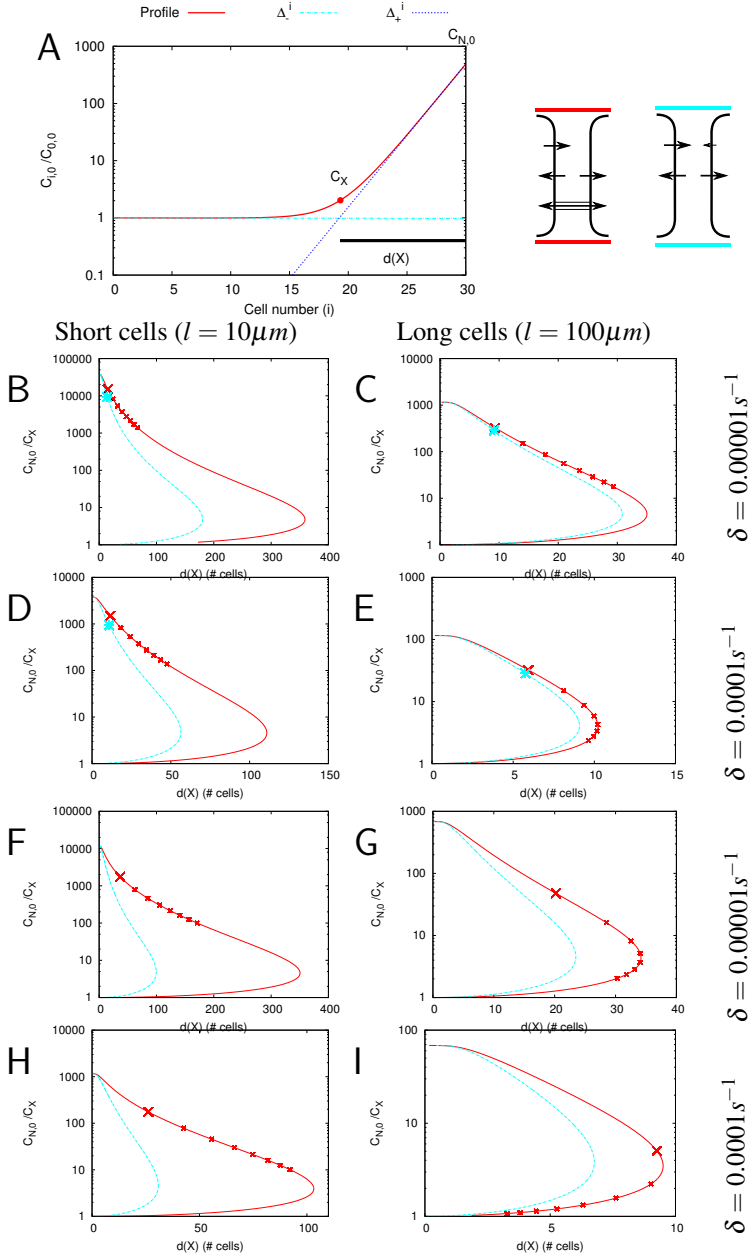


Figure 2.10: **(Supplementary) Symplastic vs. apoplastic backflux for different parameters.** Curves show the length of the informative gradient ( $d(X)$ ) and relative end-concentration ( $C_{N,0}/C_X$ ), as explained in A, for symplastic (red curves) and apoplastic (cyan curves) backflux. The crosses on the symplastic curves occur every  $10 \mu\text{m/s}$  until  $80 \mu\text{m/s}$ , showing how progression along this curve slows down with increasing  $q$ . Parameters:  $p_l = 20 \mu\text{m/s}$  (B-E) or  $p_l = 5 \mu\text{m/s}$  (F-I),  $D = 300 \mu\text{m}^2/\text{s}$ ,  $r = 20 \mu\text{m/s}$ .

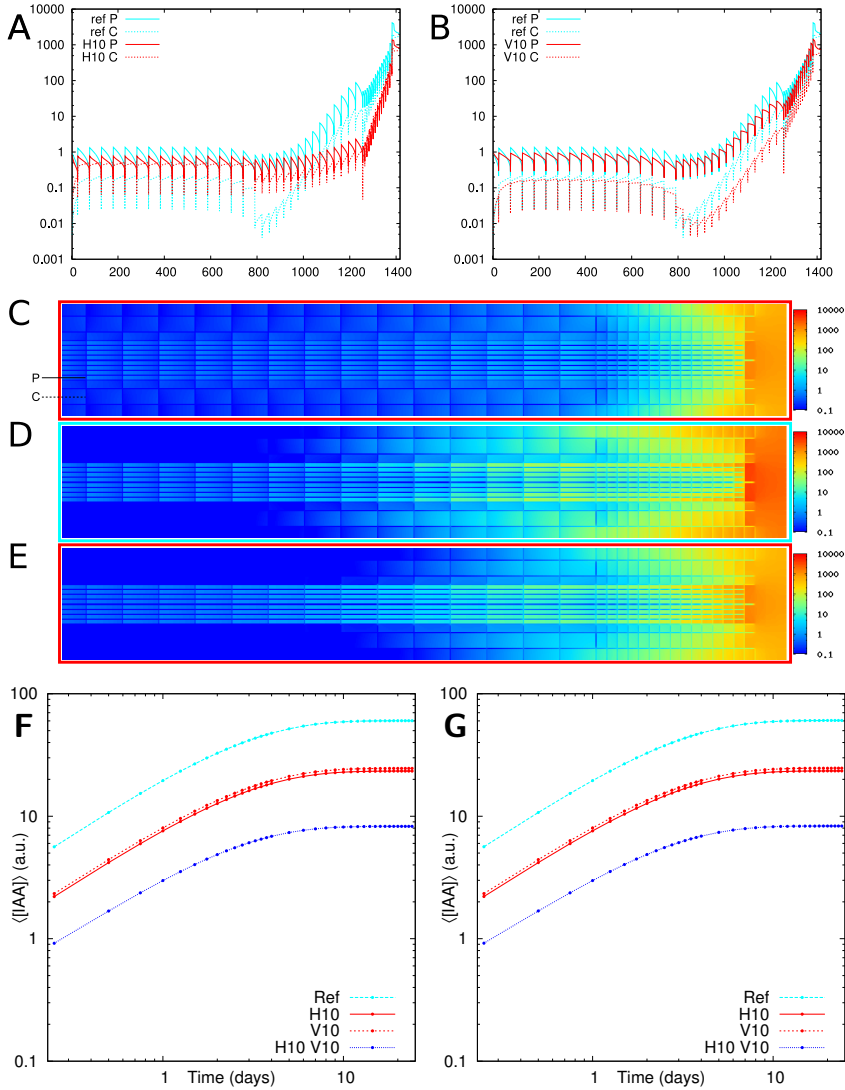


Figure 2.11: **(Supplementary) Impact of symplastic transport on root gradients.** Symplastic transport is possible in the radial direction (A,C) or longitudinal direction (B,E) of the root (red profiles). Control roots without symplastic transport (D) in cyan. A-F: Also symplastic transport over all columella walls ( $C = 10\mu m/s$ ). F,G: dynamics of auxin accumulation, as measured by the average concentration over the whole simulation domain. Note the remarkably similar shapes on the log-log plot, indicating that the time scales of auxin accumulation are not affected by symplastic transport, only the shape of the gradient and the total concentration difference. Solid red curves correspond with C, dashed red curves with E. G:  $C = 0$ .

---

## Modelling symplastic transport: from single channels to effective wall permeability

---

*With Yoselin Benitez-Alfonso and Bela Mulder*

The regulation of symplastic transport – the cell-to-cell movement of sufficiently small molecules through plasmodesmata (PDs) – is extremely important for normal plant development, both for the coordination of cell fates among neighbouring cells and the subsequent isolation of developmental decisions. Key in both processes is (the regulation of) the effective wall permeability, which strongly depends on molecule sizes. Experimentally this has been probed on a tissue level by assessing the mobility of different dyes and on a much smaller length scale using ultrastructural data. In this work we aim to build a theoretical bridge between the two experimental approaches by calculating the effective wall permeability from a geometrical description of individual PDs, also considering the flux towards them. This approach allows us to assess the impact of different experimentally observed PD features such as the neck region and the desmotubule. It also allows us to compare, from a design perspective, plasmodesmata with similar channel-like structures occurring in animals, such as gap junctions. As a validation of our method, we used reasonable PD dimensions as input parameters to reproduce experimentally measured effective permeabilities from first principles. Our approach provides a framework that facilitates the assessment of the impact of microscopic changes in PD architecture, number and dimensions on macroscopic scales.

### 3.1 Introduction

An essential part of plant development is spatial pattern formation, which requires the interaction of molecular signals. This has two key aspects: the sharing of information with neighbouring or more distant cells, to coordinate cell fate decisions over multiple cells, and the isolation of cell fate determinants within a cell or group of cells on the same developmental path. Long distance signals may be carried by small molecules such as nutrients and plant hormones. A clear example of more local exchange are the non-cell-autonomous transcription factors, such as CAPRICE and GLABRA3 (both involved in root hair and trichome specification) [19], SHORT ROOT (SHR) (involved in endodermis specification) [124], and KNOTTED1 (KN1) [143] and its *Arabidopsis* homolog SHOOTMERISTEMLESS (STM) (involved in leaf and meristem development).

It has been shown experimentally that these molecules move symplastically: through plasmodesmata (PDs) [19, 124, 143]. These are narrow channels that connect the cytoplasm of neighbouring cells. They allow for the passive exchange of sufficiently small molecules, such as hormones, sugars, small proteins, etc. This process is called *non-targeted symplastic transport*. Non-targeted transport is a mostly diffusive and thus symmetrical process [108, 144], although in specific tissues a hydrodynamic flow can create directionality, for example in secreting trichomes [151, 152] and the phloem. For a theoretical description of the hydrodynamic flow through single PDs we refer to [150] and to [184] for the flow through phloem sieve tubes.

Not all symplastic transport is of a generic nature. So called *targeted symplastic transport* is the specific transport of molecules that, judging from their size alone, would not be able pass otherwise. This may involve additional proteins that temporarily modify their substrate and/or target it to the PDs. Molecules may also induce modifications of the PDs to allow for the passage of larger molecules. In short, the mechanisms of targeted transport are highly substrate dependent [145]. This includes the intercellular transport of transcription factors KN1 and STM, for example, which requires the chaperonin complex [146] and viral movement proteins, that may alter PDs in several ways [110].

A cartoon of a simple PD is provided in figure 3.1A. PD dimensions are dynamically controlled by the cell, mostly through deposition and degradation of callose on both ends of the channel, in what is called the neck region, by callose synthase (CalS a.k.a. GSL gene family) and  $\beta$ -1,3-glucanase respectively (with further regulation by other factors) [112]. The center of the PD is occupied by a narrow membrane tube, called desmotubule (DT), which connects the ER of both cells. The space between the wall lining membrane itself and the DT is called the cytoplasmic sleeve, which is considered the most relevant space for symplastic transport.

Opinions differ about transport through the DT. Conflicting observations include the absence of ER lumen filling stain in the DT [185] and the cell-to-cell spread of small ER confined fluorescent molecules (much smaller than single GFP) [186], suggesting that this may be tissue/context dependent. We will therefore focus on the cytoplasmic sleeve. Our approach, however, is easily amendable to the DT lumen, which we will address in the final section of the results.

The dimensions of the cytoplasmic sleeve at the PD opening – typically being the narrowest part – determine the maximum size of molecules that can pass through the PD

[106, 107]. This is often referred to as the “size exclusion limit” (SEL)\*. Size, shape and number of PDs are under developmental control [121, 148, 187]. Proper regulation of symplastic transport is essential for normal plant development. Several known mutants affected in this regulation are embryo or seedling lethal [115–117].

Two experimental routes have been used in quantitative studies of symplastic transport. On the one hand, ultrastructural studies can provide insight into the dimensions, densities and distributions of plasmodesmata. The diffraction limit makes it impossible to resolve different features within PDs using classical light microscopy [188]. Although recent advances in super resolution techniques allow for the discrimination of coarse features, such as different orifices of complex shaped PDs, electron microscopy remains the only tool with sufficient (nm) resolution to determine PD dimensions [188, 189]. On the other hand, the effective wall permeability resulting from the presence of PDs can be probed in tissue level experiments with marker molecules [163, 168, 169]. Both approaches have their limitations/difficulties. A fundamental issue with electron microscopy is that the fixation procedure somewhat affects the observed sizes (e.g. see [190]) and the relevant dimensions are pushing the limits of certain electron microscopy techniques. Needless to say that getting statistically reliable measurements by this approach is very labour intensive. The concept of the tissue level studies is simple: release (or bleach) a fluorescent molecule in a certain location and derive the effective wall permeability from the dynamics of the spread of this signal. In practise, however, these techniques are limited to specific molecules (such as the small fluorescein derivatives and fairly large GFP) and often to the surface layers (in case of microinjection, bombardment and photobleaching/activation in single cells). Moreover, microinjection and bombardment are invasive and plants quickly respond to damage stress by reducing PD aperture. As a result, different techniques using the same dye molecule can give very different estimates of the symplastic permeability (e.g. see [42] or the almost order of magnitude difference between [163] and [168]). A non-invasive approach that can target the inner tissues is using fluorescent proteins driven by promoters with a very specific expression pattern (e.g. SUC2, expressed in the phloem companion cells) [120, 122]. Unfortunately, as these do not allow control over moment the marker is released, they only provide information on which cells are symplastically connected for molecules of similar size (so called symplastic domains).

Although – or because – neither approach is all powerful, they can complement each other. In this paper we describe the biophysical properties of diffusive transport through single channel PDs. This approach allows us derive from single channel calculations how tissue level characteristics depend on the molecule size (for given PD dimensions) and what the impact of characteristic geometrical PD features such as the neck region is. We aim to improve the general understanding of the implications of ultrastructural PD features and changes therein for the cell-to-cell spreading of molecules of interest and increase the applicability of tissue level measurements as a calibration tool against fixation artefacts in electron microscopy.

---

\*We will use this term because of its familiarity, although the concept is somewhat problematic when it comes to a proper definition in a biologically meaningful way (see discussion 3.3.3).

## 3.2 Model and Results

The problem of obtaining an effective wall permeability due to symplastic transport can be split in two parts: the movement through a channel and the approach of the channel from the cytoplasmic bulk. We will address them in this order.

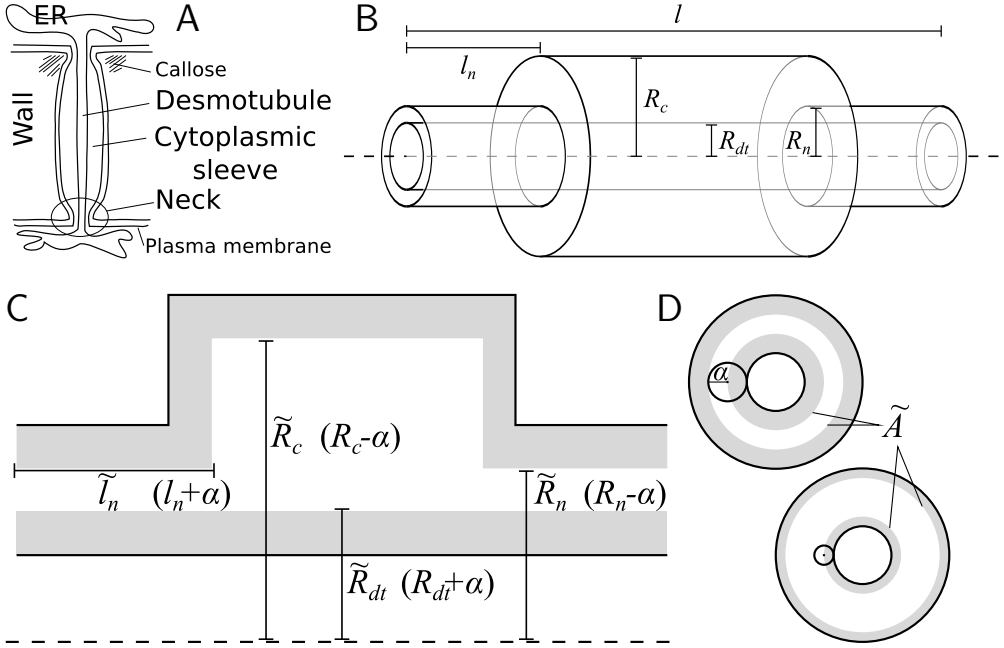


Figure 3.1: **Model PD geometry.** **A:** sketch of a simple PD. **B:** sketch of a single PD channel as modelled. It has length  $l$ , neck (inner) radius  $R_n$ , central cavity (inner) radius  $R_c$  and DT (outer) radius  $R_{dt}$ . **C,D:** illustration of the available volume for particles of radius  $\alpha$  on longitudinal (**C**) and transverse (**D**) sections. The gray areas can not be reached by the center of the particle with radius  $\alpha$ . For an intuitive description of the available volume and cross section area we use the rescaled lengths  $\tilde{l}_n = l_n + \alpha$ ,  $\tilde{R}_c = R_c - \alpha$ ,  $\tilde{R}_{dt} = R_{dt} + \alpha$  and  $\tilde{R}_n = R_n - \alpha$ . **D:** The area available for diffusion on a transverse section we call  $\tilde{A}$ , which depends the particle radius ( $\alpha$ ).

### 3.2.1 Outline of the single channel model

We modelled non-targeted transport through PDs as diffusion of hard spherical particles (i.e. they can not overlap with the wall, but otherwise no interaction) through hard pores with cylindrical symmetry. We chose the hard interaction potential, because the actual potential describing wall-particle interactions is unknown. Moreover, it would be highly particle dependent. Fortunately, measurements with molecules of different size and charge show that the hydrodynamic dimensions are the main determinant of PD transport characteristics, leaving behind, amongst others, particle charge [106, 107]. Obtaining



good EM data of PD dimensions is notoriously hard. We therefore opted for the simplest possible geometrical description, with as few parameters as possible, that captures the essential spatial PD features (see 3.5.1). We modelled a single PD as a 3-part cylindrical channel (figure 3.1B), with total length  $l$  (equal to the local wall thickness). The ends of the channel were modelled by narrow cylinders representing the plasmodesmal “neck” constriction. These have length  $l_n$  and radius  $R_n$ . The middle part, the “central cavity” has radius  $R_c$ . Over the whole length the center of the channel is occupied by a “desmotubule”: a cylinder of radius  $R_{dt}$ . The part available for diffusive transport, the cytoplasmic sleeve, is the space between the outer cylinder wall and the DT.

The space between the wall of the neck and the outer surface of the DT is so small, that we have to take into account the size of the particles (figure 3.1C,D). To describe the reduced volume available to (the center of) particles of radius  $\alpha$  we rescaled the geometrical parameters:  $\tilde{l}_n = l_n + \alpha$ ,  $\tilde{R}_c = R_c - \alpha$ ,  $\tilde{R}_{dt} = R_{dt} + \alpha$  and  $\tilde{R}_n = R_n - \alpha$ . With these, the available surface area (figure 3.1D) is  $\tilde{A}_x(\alpha) = \pi(\tilde{R}_x^2 - \tilde{R}_{dt}^2)$ , ( $2\alpha < R_x - R_{dt}$ ) (with  $x = n$  for the neck and  $x = c$  for the central cavity. Particles can not pass without available area, which results in a natural and straightforward definition for the SEL for a single channel (or a population of identical channels) and spherical particles (assuming the neck is the narrowest part of the channel):

$$\text{SEL} = \bar{\alpha} = (R_n - R_{dt})/2. \quad (3.1)$$

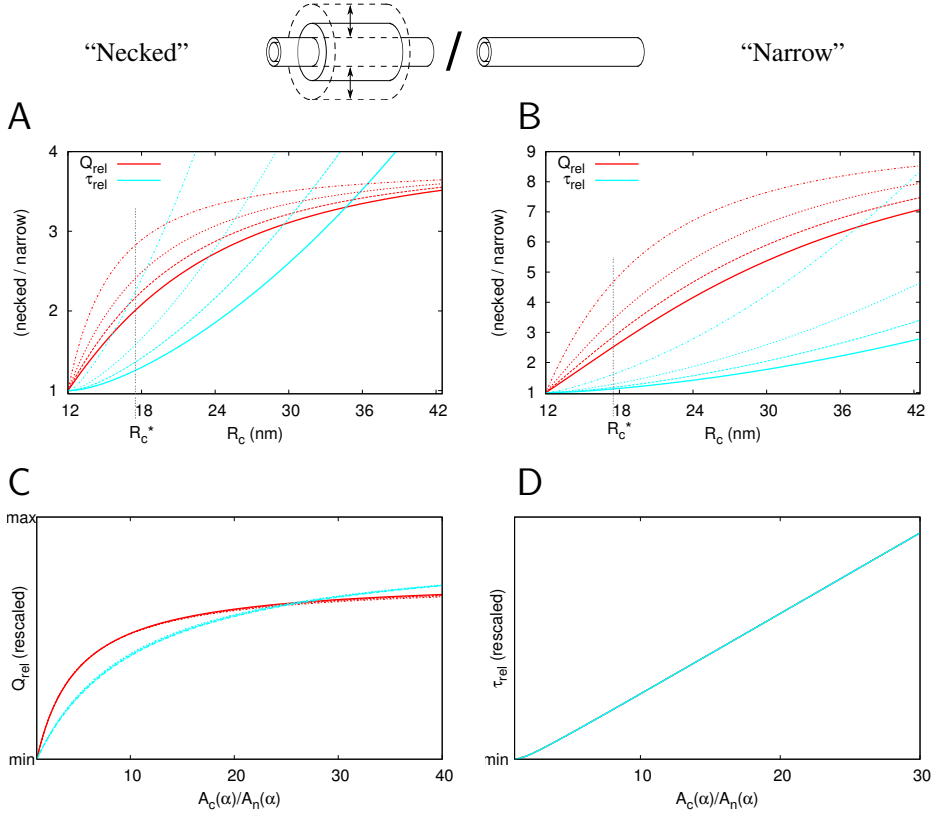
Assuming a homogeneous distribution of particle flux over (the available part of) each channel cross section, the local flux is proportional to the inverse of the available surface area ( $J(x, \alpha) \sim 1/A_x(\alpha)$ ; see 3.5.1 for a discussion of this approach). This leads to a steady state molar flow rate  $Q(\alpha)$  through each channel of

$$Q(\alpha) = \frac{D(\alpha)\tilde{A}_n\tilde{A}_c}{2\tilde{l}_n\tilde{A}_c + (l - 2\tilde{l}_n)\tilde{A}_n}\Delta C \quad (3.2)$$

with  $\Delta C = C_l - C_0$  the concentration difference over the channel and  $D(\alpha)$  the particle’s diffusion constant (inside the PD).

### Neck constrictions affect molecular flux through PDs

With this formula we could assess the impact of different PD features on the spreading of a signal (of a given size). Given the severe effects of mutations affecting the regulation of PD aperture, we can safely assume that size selectivity is a property under selection. To assess the impact of the narrow-wide-narrow PD architecture, we compared our full channel with a narrow channel with uniform radius ( $R_n$ ) (i.e. with DT, but no central cavity). Increasing the radius of the central cavity ( $R_c$ ) from this narrow starting point resulted in an increased molar flow rate (figure 3.2A). This was no free lunch: the average passage time  $\tau(\alpha)$  of individual particles increased with  $R_c$  (figure 3.2B). With increasing  $R_c$ , the molar flow through a single channel saturates (the maximum increase is a factor  $\frac{l}{2l_n}$ ), whereas the average passing time scales quadratically with  $R_c$  (see 3.5.2). In economic terms: the incremental benefits of further increasing  $R_c$  decrease, but the incremental costs keep increasing. Although a limited increase of the passage time may or



**Figure 3.2: Impact of neck on molar flow rate ( $Q$ ) and average passage time ( $\tau$ ) through the PD.** **A:**  $l = 200\text{nm}$ , **B:**  $l = 500\text{nm}$ ; Red/black curves:  $Q_{rel} = Q_{necked}(R_n, R_c)/Q_{narrow}(R_n)$ ; cyan/gray curves:  $\tau_{rel} = \tau_{necked}(R_n, R_c)/\tau_{narrow}(R_n)$ . Parameters:  $l_n = 25\text{nm}$ ,  $R_n = 12\text{nm}$ ,  $R_{dt} = 8\text{nm}$ . The broken curves show how the curves shift with increasing particle size for the same channel (solid:  $\alpha = 0$ , dashed:  $\alpha = 0.5\text{nm}$ , sparse dashed:  $\alpha = 1\text{nm}$ , dash-dotted:  $\alpha = 1.5\text{nm}$ ). **C:** curves for different  $\alpha$  almost collapse when plotted as function of  $\tilde{A}_c/\tilde{A}_n$  and rescaled from the minimal value of 1 to the maximum of  $Q_{rel} = l/(2\tilde{l}_n)$ . The curves for different  $l$  do not collapse (red/black:  $l = 200\text{nm}$ , cyan/gray:  $l = 500\text{nm}$ ). **D:** curves for  $\tau_{rel}$  fully collapse (for different  $l$  and  $\alpha$ ) with rescaling function  $\tilde{\tau}_{rel} = (\tau_{rel} - 1)l^2/(2\tilde{l}_n(l - 2\tilde{l}_n))$ .

may not be biologically relevant, the scaling behaviour is such that the slow down will have physiological effects beyond some  $R_c$ . This means that increasing the radius of the central cavity too far would be detrimental to diffusive transport through the cytoplasmic sleeve.

We then tried to gain a better understanding of these results by rescaling the curves for  $Q_{rel}$  and  $\tau_{rel}$ . The idea behind this is that if we can find a function to collapse the curves, this function can tell us more about the physical quantities governing the increase of molar flow rate and passing time. As the local flux is inversely proportional to the available cross section, the ratio  $\tilde{A}_c/\tilde{A}_n$  of the necked channel was a good candidate for the x-axis. Using the limit for  $Q_{rel}$  it is possible to almost completely collapse the curves for different particle sizes for a single  $l$ ,  $l_n$  combination (figure 3.2C). Moreover, for large  $R_c$ ,  $\tau_{rel}$  becomes proportional to  $\tilde{R}_c^2$  (equation 3.11:  $\tau_{rel} \sim \tilde{R}_c^2$ ). From this we derived a rescaling the relative average passage time:  $\tilde{\tau}_{rel} = (\tau_{rel} - 1)/(\tilde{f}_c(1 - \tilde{f}_c))$  with  $\tilde{f}_c$  the fraction of PD length occupied by the central cavity (adapted for particle size). With this we could fully collapse the curves for  $\tau_{rel}$  for all  $\alpha$  and  $l$  (figure 3.2D). The rescaling factor for the x-axis,  $\tilde{A}_c/\tilde{A}_n$ , increases faster for larger particles. The reason is that  $\tilde{A}_n$  decreases relatively faster with particle size than  $\tilde{A}_c$ , which becomes intuitively clear from figure 3.1C,D. This difference explains why the curves for the largest particles lay above the others prior to rescaling (figure 3.2A,B). The  $\tau_{rel}$ -rescaling factor implies that the average passage time increases fastest if the central cavity occupies approximately half of the length of the channel. With our choice of a constant  $l_n = 25nm$  that would be for a wall thickness of  $l = 100nm$ , suggesting that perhaps the optimal  $R_c$  – optimizing molar flow against average passage time, given size selectivity ( $R_n$  and  $R_{dt}$ ) – is larger for thick walls than for thin walls.

### Novel considerations on the relevance of the DT

The DT blocks a significant amount of space: therefore it is straightforward to assume that its removal would greatly increase the SEL of a channel, as well as the wall permeability for particles of a given size ( $< \bar{\alpha}$ ). Indeed this route is exploited by certain viruses that target the DT to facilitate their cell-to-cell spreading [110]. We asked ourselves whether the DT would also offer possibilities to increase the efficiency of symplastic transport. Assuming that SEL and net flux are under selection, we compared the number of circular channels that would offer the same orifice area ( $\approx A_n$ ) as a single channel with a DT of radius  $R_{dt} = 8nm$  and the same SEL. This number  $n_c(\bar{\alpha})$  is given by (figure 3.3A):

$$n_c(\bar{\alpha}) = \frac{(R_{dt} + 2\bar{\alpha})^2 - R_{dt}^2}{\bar{\alpha}^2} = 4 \frac{R_{dt} + \bar{\alpha}}{\bar{\alpha}} \quad (3.3)$$

So, with  $\bar{\alpha} = 2nm$ , 20 cylindrical channels without DT would be needed to match the orifice surface area of a single channel with DT (with  $R_{dt} = 8nm$ ). For the passage of actual particles, the available surface area matters, not the total surface area. Figure 3.3B shows that the available surface area  $A_n(\alpha)$  is larger with DT, even if the total surface area ( $A_n(0)$ ) is the same as the group of channels with circular cross section. This difference becomes very large for  $\alpha$  close to the limit (diverges for  $\alpha \uparrow \bar{\alpha}$ ). This implies that having a DT allows for a much more efficient passage of particles with a radius close to the SEL.

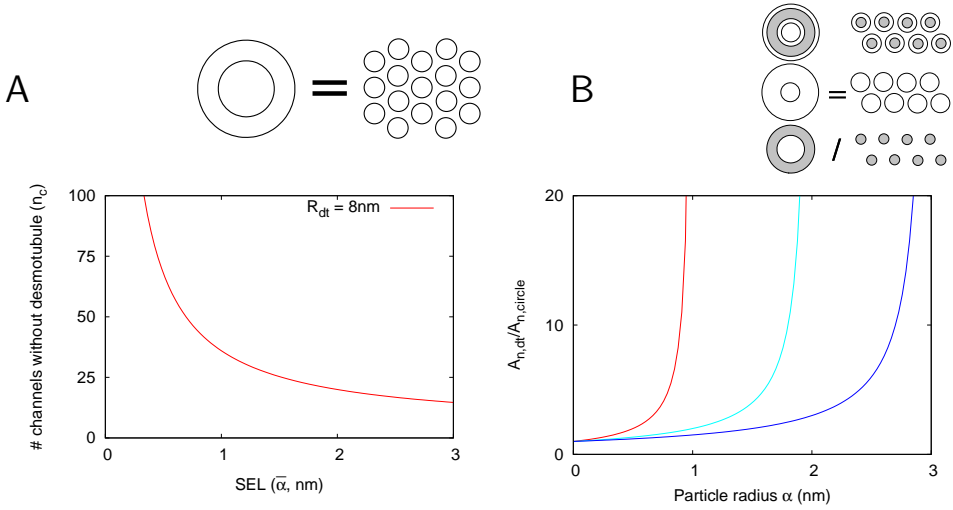


Figure 3.3: **Impact of DT on available surface area (given SEL).** **A:** number of channels without DT ( $R_{dt} = 8\text{nm}$ ) that would have the same total entrance surface for a given SEL (expressed as particle radius). **B:** Ratio of available area ( $A_n(\alpha)$ ) for particles that can pass ( $\alpha < \bar{\alpha}$ ) for channels with DT or without, with same total surface.  $\bar{\alpha} = 1, 2, 3\text{nm}$  drawn with red/solid, cyan/dash-dotted and blue/dashed, respectively. In the cartoon on top, only the gray part of the cross section is available to particles of given size.

### 3.2.2 Effective wall permeability

The flux through an interface can be computed as  $J = P\Delta C$ . From this we can define the effective wall permeability as  $P(\alpha) = f_{ih}\rho Q(\alpha)/\Delta C$ , with  $\rho$  the number density of PDs per unit wall area ( $/\mu\text{m}^2$ ) and  $f_{ih}$  a correction factor for the inhomogeneity of the wall permeability. This must be a function of the distribution of the PDs. As the diffusive path from “far away” to specific (permeable) spots on the wall is longer than to any position on the wall, we intuitively expect that  $0 < f_{ih} < 1$ . This issue will be addressed in more detail later on.

$$P(\alpha) = \frac{f_{ih}\rho D(\alpha)\tilde{A}_n\tilde{A}_c}{2\tilde{l}_n\tilde{A}_c + (l - 2\tilde{l}_n)\tilde{A}_n} \quad (3.4)$$

Note that with the usual choice of  $P(\alpha)$  in  $\mu\text{m}/\text{s}$ ,  $D(\alpha)$  in  $\mu\text{m}^2/\text{s}$  and the PD and particle dimensions expressed in nm, this has to be multiplied by a factor  $10^{-3}$  to correct for the different units of length used.

Being a diffusive process, the transport through the channel linearly depends on the particle’s diffusion constant  $D(\alpha)$  (inside the PD). So far, we have considered this as a given parameter. In reality, however, it is size dependent. According to the Stokes-Einstein equation, the diffusion constant for spherical particles (with radius  $\alpha$ ) in low Reynolds number liquids is given by:  $D(\alpha) = \frac{k_B T}{6\pi\eta\alpha}$ , with  $k_B$  the Boltzman constant,  $T$  (absolute) temperature and  $\eta$  the viscosity of the medium. Rewriting this as  $D(\alpha) = D(1)/\alpha$ , with  $D(1)$  the diffusion constant for a particle with unit radius, an inverse relation

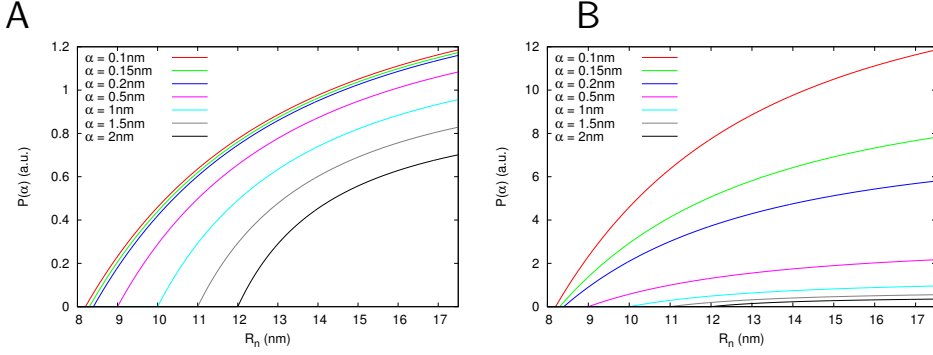


Figure 3.4: **Impact of particle size (radius =  $\alpha$ ) on effective permeability  $P(\alpha)$ .** **A:** Same diffusion constant for all particle sizes. **B:** From Stokes-Einstein formula:  $D(\alpha) = D(1)/\alpha$ . Parameters:  $l = 200nm$ ,  $l_n = 25nm$ ,  $R_{dt} = 8nm$ ,  $R_c = 17.5nm$ ,  $f_{ih} = 1$ .

between size and diffusion constant appears. Figure 3.4 shows how incorporation of this general trend made effective wall permeability more sensitive to particle size (for the moment ignoring  $f_{ih}$ , assuming that  $f_{ih}$  is (nearly) independent of  $\alpha$ , and therefore expressing  $P(\alpha)$  in arbitrary units).

### 3.2.3 Reaching PDs: correction for inhomogeneity of the wall permeability

Our considerations from single channels left us with one last unknown, correction factor  $f_{ih}$  for the inhomogeneity of the wall permeability. Plasmodesmata can be considered as discrete spots of (locally homogeneous) wall permeability, with a non-permeable wall in between the channels. To investigate how this affects the flux over the wall, compared to a homogeneous permeability, we numerically compared the steady state flux towards the boundary in 3D box (figure 3.5A). This has a fixed concentration  $C_h$  at a distance  $h$  from the target plane. The target plane is a radiating plane with rate  $\kappa D$ . This rate is either homogeneous (“reference”) or concentrated in a patch representing the PD orifice. The latter was implemented as an annulus (“ring” with inner radius  $R_{dt} = 8nm$  and outer radius  $R_n = 12nm$ , with corresponding surface area  $A_{ann}$ ) with  $\kappa = 1/\mu m$  and  $\kappa = 0$  elsewhere. The reference had a rate according to the surface area occupied by the patch:  $\kappa = \frac{A_{ann}}{A_{tot}}/\mu m$ . We used periodic boundary conditions for the lateral walls of the box, corresponding to regularly spaced plasmodesmata.

Comparing the average of the flux component towards the wall, we found that annular patches (PD with DT in the center) resulted in less loss of transport due to boundary inhomogeneity than a circular patches with equal surface area (figure 3.5B). Circular patches with the same (outer) radius as the annular ones, but with a reduced rate ( $\kappa_c = A_{ann}/A_{circ}$ ), however, showed the same reduction as the annular patches (figure 3.5B). This implies that results for circular patches can be used to study PDs, using a simple correction factor  $\xi = A_{ann}/A_{circ}$ .

We found a more or less linear dependence of the permeability reduction on the distance between the permeable patches. This is in contrast with the findings of Berezhkovskii *et al.* [191]. They studied a boundary homogenization problem for a surface with regularly spaced absorbing traps. They found that the flux through the homogenized boundary only depended on the fraction of the surface occupied by traps, but not their spacing [191], in line with results for the flux towards spheres with small absorbing disks [192, 193]. A major difference is that in none of these the concentration is fixed at a finite distance (such as our source plane) from the target (plane/sphere). We therefore investigated how our results depended on the distance  $h$  between source and target planes. We found that the reduction of the effective permeability due to patchiness decreased with  $h$ , but maintaining a near linear dependence on the distance  $d$  between the patches (figure 3.5D).

Consequently, it seems that our results will converge to agreement with the results for (partially) absorbing patches [191–193] for  $h \rightarrow \infty$ . In cells, of course with a finite length  $L_{cell}$ , the results for  $h = L_{cell}/2$  will probably be a good estimate for the permeability reduction due to patchiness. This implies that for long cells and/or high PD densities the correction factor  $f_{ih} \approx 1$ , i.e. it can safely be ignored.

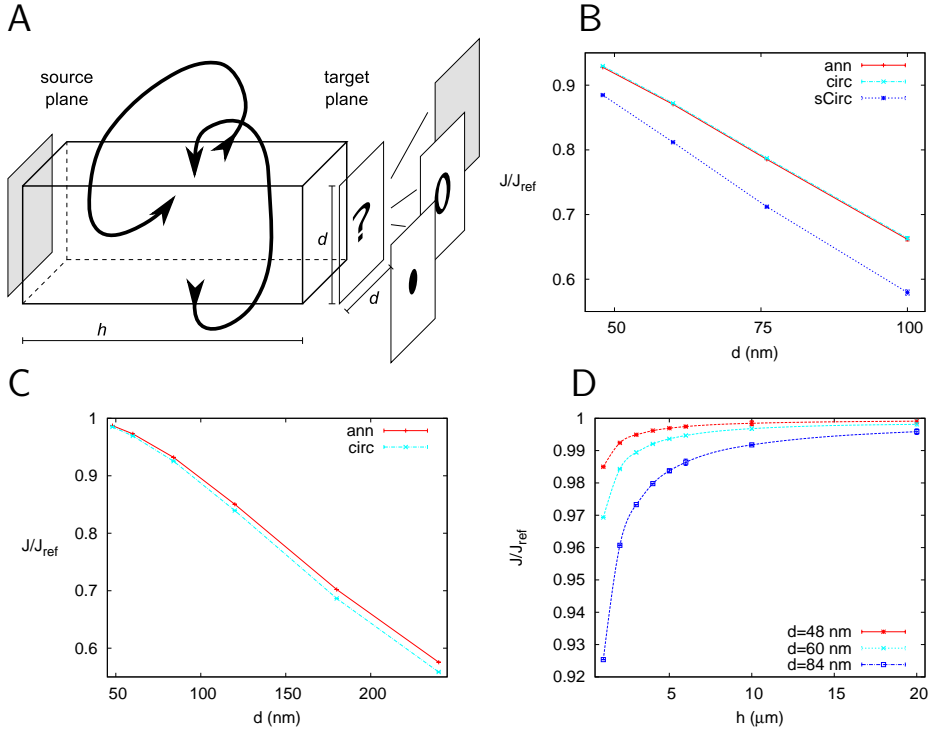
### 3.2.4 The acid test: comparing with measurements

In a system where non-targeted symplastic transport is indeed fully driven by diffusion (so no (significant) active transport or hydrodynamic flow), our calculations should give at least the experimentally measured values for reasonable PD dimensions and densities. As a test case we used the measurements by Rutschow *et al.* [163], because their measured values are among the highest reported, and PD density estimates are available [118]. The authors estimated that the effective permeability of the transverse walls in the root meristem zone (measured  $\approx 200\mu\text{m}$  from the QC) for fluorescein is  $6\text{--}8.5\mu\text{m/s}$ . Fluorescein has a Stokes radius of approximately  $0.5\text{ nm}$  [194, 195]<sup>†</sup>. The authors use a cytoplasmic diffusion constant of  $D = 162\mu\text{m}^2/\text{s}$ , one third of its water value. For simplicity we copy that for inside the PD. This is probably an overestimation of reality, but as the cytoplasm is also a molecularly crowded environment, the difference may be small. From the biochemistry of the fluorescein used in their experiments, we can safely assume that it is fully contained in the cytoplasm and uses the cytoplasmic sleeve only for transport. Using these numbers and our defaults for the PD dimensions, we only obtain their measured values for the permeability with a PD density in the order of  $\rho = 10\mu\text{m}^{-2}$  (figure 3.6A) and a relatively wide open neck. This density is in line with measured PD densities in transverse walls of immature Arabidopsis vascular tissue and cortex [118]<sup>‡</sup>. Although it is not a systematic study, it is worth noting that the relevant electron micrographs in this paper do not show clear neck constrictions. Increasing the radius of the central cavity by  $5\text{ nm}$  to  $R_c = 22.5\text{ nm}$  increased the values for a given  $R_n$  by about 50%, with a higher maximum as we use  $R_c$  as an upper limit for  $R_n$  (figure 3.6B).

The agreement between measured and calculated values is so close, that we can conclude that diffusion as a sole driver of symplastic transport is sufficient to explain the highest measured effective permeabilities under physiological conditions and that a more

<sup>†</sup> Several other authors mention values of  $0.4\text{ nm}$  e.g. [196, 197] or  $0.45\text{ nm}$ , but without reference to actual measurements. This difference has little impact on our calculated values.

<sup>‡</sup> Numbers: vascular:  $9.92 \pm 0.58$ , inner cortex:  $12.58 \pm 0.67$ , outer cortex:  $9.08 \pm 0.5$  [118].



**Figure 3.5: Supply to channel: comparison of discrete (PDs) and homogeneous permeability.** **A:** setup (see main text). Bold arrows illustrate the periodic boundary condition in the  $x$  and  $y$  direction. **B:** Relative average net flux in direction of trap (component along the box) for PDs with DT (“ann”: red) and circular channels with the same apparent surface (“sCirc”: blue) and same outer radius, but trapping efficiency decreased according to surface ratios (“circ”: cyan),  $h = 300\text{nm}$ . For both, the flux is compared with a homogeneous trap with efficiency  $\kappa = \frac{A_{\text{ann}}}{A_{\text{tot}}}$ . **C:** Impact of coarse grid: a small difference between annular and matched circular patches ( $h = 1002\text{nm}$ , colors as in B). We therefore used the circular patches for **D**. **D:** The difference between homogeneous and patchy permeability decreases with increasing distance  $h$  between source and target planes. The relative distance between the curves for different distances between patches ( $d$ ) was (almost) constant, implying a linear relationship between distance and permeability reduction for all  $h$ . Error bars represent the quality of the numerical estimate by minimum and maximum possible values.

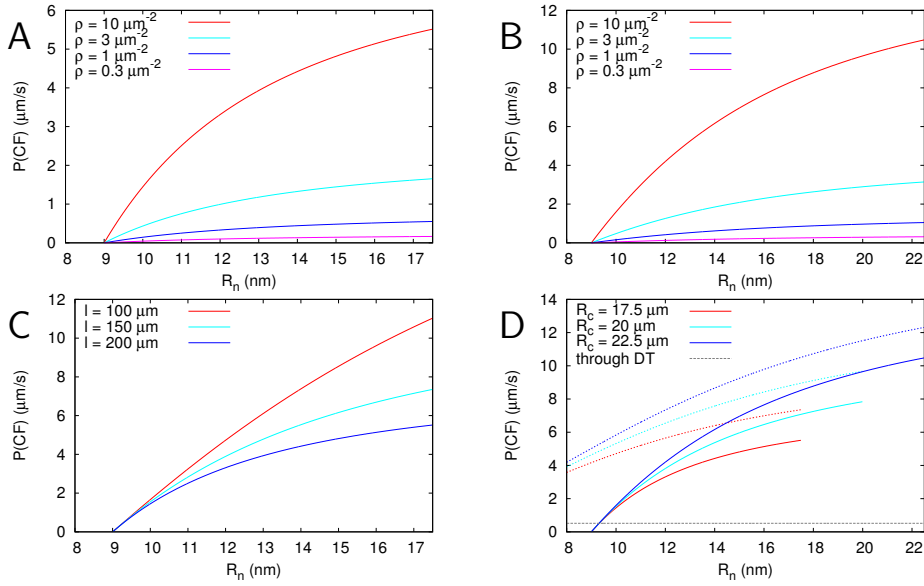


Figure 3.6: **Calculated effective permeabilities for carboxyfluorescein (CF)** as a function of PD aperture at the neck  $R_n$ . **A,B:** for different PD densities ( $\rho$ ). **C:** for different wall thickness ( $l$ ). **D:** impact of removing the DT (dashed curves). For comparison, transport through the DT lumen ( $R = 5 \text{ nm}$ : “wide open”) is indicated with a dashed gray line. Default parameters:  $\alpha = 0.5 \text{ nm}$ ,  $D = 162 \mu\text{m}^2/\text{s}$ ,  $l_n = 25 \text{ nm}$ .  $R_c$ : 17.5 nm (**A,C**) or 22.5 nm (**B**);  $l = 200 \text{ nm}$  (**A,B,D**),  $\rho = 10 \mu\text{m}^{-2}$  (**C,D**). TEMP: no correction for supply factor  $f_{ih}$ . TODO. (strongest impact with the lowest densities, but only an estimated 6-11% reduction  $P(\text{CF})$  for  $\rho = 10/\mu\text{m}^2$ .)



rigorous test would require consistent measurements on permeabilities, PD densities and dimensions in the same system, as even growth conditions [198] and light [199] affect PD conductivity.

Rutschow *et al.* also reported an increased effective permeability of around  $25\mu\text{m/s}$  after treatment with a low concentration of  $\text{H}_2\text{O}_2$  (and a strong decrease to  $\approx 1\mu\text{m/s}$  with a higher concentration of  $\text{H}_2\text{O}_2$ ). An increase in branched and twinned PDs has been found in *ise1* and *ise2* mutants or with silencing of gene function [200–202]. This effect has been attributed to an increase of reactive oxygen species (ROS) in the cell [202]. An increase of branched and twinned PDs can be interpreted as an increase of PD density. Starting from the  $\rho = 10\mu\text{m}^{-2}$  PD density and  $R_c = R_n = 22.5\text{nm}$  channels from figure 3.6B, we would need an over 2-fold increase of PD density to obtain the measured value. To our knowledge, no one has ever measured the time scales of PD twinning, but such an increase seems high given the 2 hour incubation time in the Rutschow experiment.

A much smaller increase of PD density would be needed if the starting density would be higher, or central cavities wider (larger  $R_c$ )<sup>§</sup>, but with more constricted neck regions (smaller  $R_n$ ) in the control situation. In that case a large(r) increase of the effective permeability would be possible through callose degradation, which is assumed to be a fast process.

Transport through the DT lumen can be possible for small molecules (demonstrated up to 10.4 kDa) [186]. To quantitatively assess the potential contribution of this route, we approximated the DT as a straight cylindrical channel with a radius of  $5\text{ nm}$ <sup>¶</sup>, the maximum of the range of 3.5-5 nm reported for “open” DTs [151, 206]. The resulting effective permeability for a fluorescein sized molecule is shown as a straight line in figure 3.6D. Only for an almost closed neck (for this particle size), the transport through the ER lumen was of a similar order of magnitude. For more open necks the cytoplasmic route allowed for more than an order of magnitude higher effective permeabilities. Considering the symplastic spread of a signal on a tissue level, the difference between cytoplasmic sleeve and DT lumen will probably be larger, as the confined reticulate structure of the ER probably results in a much lower effective intracellular diffusion constant for the same substance in the ER than the cytoplasm. Crick’s effective diffusion constant for (linear) animal tissues suggests that the impact of this difference in intracellular diffusion constants will depend on the effective wall permeability:  $D_{eff} = \frac{D_{cell}PL_{cell}}{D_{cell} + PL_{cell}}$  [166] and chapter 2.

As the membrane itself occupies a large fraction of the DT cross section, complete removal of the DT resulted in a much larger increase in the effective permeability than expected from the (maximum) contribution of the DT lumen (figure 3.6D).

### 3.3 Discussion

We have derived a method for calculating the effective wall permeability for symplastic transport directly from the dimensions of individual PDs and their distribution over the

<sup>§</sup>[150] mentions an inner diameter of 30-60 nm ( $R_c$  15-30 nm), easily justifying a wider cavity.

<sup>¶</sup>Note that if an inner radius of 5 nm should be compatible with an outer radius of  $R_{dt} = 8\text{nm}$ , only 3 nm would be available for the membrane, requiring very short fatty acid chains [203, 204]. Data on the movement of ER lumen located GFP in the presence of TMV movement protein shows that the DT dimensions are probably dynamic too [205].

wall. The match between calculated and measured values supports the claim that non-targeted symplastic transport is diffusion driven [106, 107]. The effective permeability values we were able to calculate (see 3.2.4) using literature based parameter estimates were so close to experimentally measured ones [163], that a more stringent test of our model would require a very consistent set of micro- and macroscopic measurements from the same system, grown under the same conditions [198, 199].

In our model we have made two assumptions that probably lead to a mild overestimation of the actual effective permeability: with our choice for a hard interaction potential we ignore a slowing effect due to molecular friction with the PD lining and we do not explicitly take into account the proteins present inside the cytoplasmic sleeve [207, 208]. These effects, however, are at least partially accounted for by using a (cytoplasmic) diffusion constant that is much lower than in water. If the protein density inside the PDs is so much higher than in the cytoplasm that a much further reduction of the plasmodesmal diffusion constant is required, this most likely implies that the estimated PD radii – conservatively based on ultrastructural studies – that we used in our calculations are too small with respect to unperturbed living plants. Given the impact of fixation methods [190], this may actually be the case. (Improved) measurements of either PD dimensions or the difference between cytoplasmic and plasmodesmal diffusion constant of the same molecule could be used to improve estimates of the other quantity.

### 3.3.1 PD spacing

Our formula for the effective wall permeability includes a correction factor (reduction of the effective permeability) for the discreteness of the permeable spots in the wall:  $f_{ih}$ . We have found that the impact of this discreteness decreases if with increasing distance between walls (figure 3.5D). From this it can be concluded that the correction  $f_{ih}$  can be ignored for large cells, as the effect will be small compared to other sources of uncertainty. This is in line with the finding of Jensen *et al.* in their study of the hydrodynamic flow through phloem sieve plates that inhomogeneities in the linear flow velocity due to the sieve pores disappear in a short distance from the sieve plates [184].

If PDs were regularly spaced on a rectangular grid, they would occur at distances  $d = 1/\sqrt{\rho}$ , with spacing correction factors  $f_{ih}$  of 0.89-0.94 to 0.6-0.8 for  $\rho = 10\mu m^{-2}$  to  $\rho = 1\mu m^{-2}$  for cells of  $10\mu m$  length<sup>||</sup>. In reality, PDs do not occur on a regular grid. Deviations from a regular grid could result in a larger effective distance between PDs with respect to  $f_{ih}$ . Moreover, PDs are often observed in pairs (“twinned PDs”), which is thought to have a (PD) developmental origin [121, 209, 210]. Observations by Faulkner *et al.* of pit fields showed almost two distinct length scales in the PD distribution: short distances in the order of 100-200 nm between closest neighbours and larger distances between small clusters of PDs [210]. A numerical strategy for assessing the impact of such a spacing pattern could involve a two step procedure: high resolution simulations to determine the size (probably similar to the average cluster radius) and rate of a replacement patch, followed by coarser simulations using this replacement patch and the inter cluster distance. The formulation of this strategy already suggests that the largest length scale of

---

<sup>||</sup> Estimated by linear extrapolation of points in figure 3.5D for  $h = 5\mu m$  (lower bound) and  $h = 10\mu m$  (upper bound)

the distribution will likely have the strongest impact on the effective wall permeability for non-targeted symplastic transport.

### 3.3.2 Plasmodesmata from a design perspective

In our calculations we have considered two desirables for symplastic transport: the amount of molecules passing and control over the maximum size of molecules that can pass (SEL). From these we found that the neck/central cavity structure allows for increased transport per channel, whilst keeping control over the SEL (figure 3.2). The desmotubule also allowed for more transport per channel, decreasing the number of channels needed for a given total available surface area at the entrance (for some particle size) by more than an order of magnitude (figure 3.3). This effect is much stronger than the increase of effective permeability that could have been achieved by the finer distribution of permeable spots possible with more smaller channels (figure 3.5D).

These properties could be considered advantages of the existing PD architecture, but that does not mean that that is the reason they are this way.

In this light it is interesting to compare PDs with gap junctions, their animal equivalent. These symplastic connections are protein based channels that open and close in response to the intracellular  $\text{Ca}^{2+}$  concentration. They have been found in almost every tissue [ ] and are essential for normal embryonic development [211].

Contrary to PDs, gap junctions do not have a DT and thus can be viewed as “simple” cylindrical channels. This suggests that limiting the number of channels is not a universal selection criterion. Turning the question: is it even possible to create symplastic connections in plant cells as cylindrical channels? A first difference between gap junctions and PDs is that gap junctions always bridge an intercellular distance of 2-4 nm, whereas PDs have to cross the cell wall. The very thin cell walls are typically are  $> 100\text{nm}$  thick and cell wall thickness is not constant over time. The membranes lining the PD are fluid, allowing for stretching of the channel by pulling in phospholipids from the plasma membrane if the channel is stretched. Addition of protein subunits to elongate a channel while the wall thickens, is much more complicated, if possible at all.

For this reason, cylindrical “plant-channels” would probably need to be membrane lined. Several examples exist of very narrow protein based channels, such as the aforementioned gap junctions (inner diameter  $\approx 1.5\text{ nm}$  [212]) and protein import channel in mitochondria (inner diameter  $\approx 2\text{ nm}$  [213]). The nuclear pore complex allows for passive import of larger molecules, with a diameter up to  $9\text{ nm}$  [214].

The generation of a membrane channel with an inner radius in the order of  $3\text{ nm}$ , however, is not trivial. Even the inner radius of the DT membrane, estimated  $3.5\text{-}5\text{ nm}$  for “open” DTs [151, 206], is larger than this and the recently discovered tunneling membrane tubules in animal systems have a radius of  $25\text{-}100\text{ nm}$  or more [215, 216]. From theoretical calculations, the axial force required to sustain a membrane tube is found to be proportional to the inverse of the tube’s radius (i.e.  $\sim 1/R$ ) [217], which also shows in experiments using optical tweezers to pull membrane tubes from giant unilamellar vesicles (e.g. [218] for tube radii of  $\approx 200\text{--}400\text{ nm}$ ). This inverse linear relation might break down for very narrow tubes, in which case the forces required will scale even less favourable. Certainly, the narrower the membrane channel, the higher the energetic costs of maintaining its shape. This makes reversible size regulation of really narrow membrane

lined channels very hard, if not impossible. Moreover, the desmotubule requires specific membrane proteins, likely including reticulons, to obtain such a small radius [208]. This is not a matter of just a few proteins scattered over the membrane: simulations of a protein ring-membrane system estimate that a tube with an outer diameter of 17.4 nm requires a 2 nm distance between constricting protein rings [219]. To put this in perspective: the modelled rings themselves were chosen to be 4 nm wide, based on reticulon dimensions [219], i.e. 2/3 of the tube volume would be occupied by reticulon and still the tube diameter is larger than values typically reported for the desmotubule.

The PD architecture involving a DT allows for more flexible regulation of size selectivity, as the DT allows for a dilated state of the PD by its displacement or removal [145, 220] and thus temporarily or permanently enable transport of larger molecules/particles. It also creates a weakness – larger holes in the cell wall – that is exploited by viruses [110] and other intracellular parasites such as the fungus *Magnaporthe oryzae* [111] for movement to neighbouring cells. PDs are so important in the normal development of the plant, that it is – to certain extent – defenseless against such exploitation.

Why do PDs have (in certain states) a neck region? We found that, compared to narrow channels without a central cavity, a central cavity/neck structure can allow for several fold more transport through a single PD without a large increase of the average passage time. Is this “benefit” selected for? (Regulation of) size selectivity does not require a uniform diameter, as long as a sufficient constriction is present. Callose deposition in the neck region is sufficient for that. It requires less material (and energy) than regulating the width of the whole channel and is therefore probably faster. This can be seen as another benefit of the neck constriction, making it impossible to tell which is *the* reason (if this question makes sense at all). There might be an even simpler reason why callose based restriction of PD aperture is confined to the neck region. CalS1, one of the callose depositing enzymes, has a molecular weight of  $\approx 226$  kDa [221], compared to 27 kDa of single GFP [222], with similar sizes for other CalS proteins. In other words: the callose depositing enzymes would not fit all the way into the PDs, so they are unable to regulate PD diameter all along the channel. This is in line with our casual observation that neck length appears to be similar in different existing PD electron micrographs, suggesting that it is independent of PD length/wall thickness.

In summary, considering PD features from a design perspective can not reveal the true reason that these features exist as they do. Nevertheless, studying the effects of particular PD features makes it possible to assess the impact of observed differences in PD shape, number, etc.

### 3.3.3 Size exclusion limit

The size exclusion limit (SEL) is an often used concept in the plasmodesmata field. It is often used in hand waving ways, such as “a large SEL ( $>67$  kDa) for the plasmodesmata connecting SEs and CCs” or “a peripheral SEL of about 27-36 kDa” [223]. At this level it is comprehensible: single GFP molecules were detected away from the production site, double GFP molecules were not. When comparing different classes of molecules it becomes more difficult: the molecular weight turns out to be a bad predictor of the SEL. A molecule’s hydrodynamic radius has much more predictive power [107]. Using this as a guideline, we could easily define the SEL of a single channel for our spherical particles

(SEL =  $\bar{\alpha}$ , the maximum radius  $\alpha$  that actually fits through the PD neck).

The picture gets more complicated for elongated molecules (such as the barrel shaped GFP), which may fit only with certain orientations, albeit at a high entropic cost due to the loss of orientational freedom. A replacement sphere with matching hydrodynamic radius probably would not fit at all. Now consider increasing the aspect ratio of this molecule while fixing its shortest dimension. The result will always fit through the channel, but the entropic cost would increase so much, that the actual chances of such a molecule entering the channel will become vanishingly small. Where should we draw the line for the SEL?

Moreover, not all PDs will have exactly the same dimensions. A literal interpretation of the SEL would point to the single PD with the largest opening for the SEL. That way, the definition would be based on outliers rather than the general population of (“open”) PDs, whereas the latter probably have a much stronger effect on the spread of molecules, specially if their size is not very close to the SEL (figure 3.4).

On the one hand the SEL lacks important factors determining the wall’s effective permeability (apart from PD number density), such as central cavity dimensions (figure 3.2) and particle diffusion constant (figure 3.4B). On the other hand if a particle size is such that it could (just) cross a PD, this does not necessarily imply that the substance will be detected across the wall. For such particles movement to a neighbouring cell must be considered as a stochastic process, specially if particle numbers are low. In conclusion: the SEL concept loses its value at the microscopic level, because it is imprecise and when taken very literally is not very informative for the actual movement of molecules.

## 3.4 Conclusion

In this work we have derived a method for calculating the effective wall permeability due to non-targeted symplastic transport from the dimensions and distribution of plasmodesmata and the particle size of the substance of interest. Our approach provides a framework that facilitates the assessment of microscopic changes in PD architecture, number and dimensions on the movement of a biochemical signal on a macroscopic scale. We have shown that this depends on particle size in a highly non-linear fashion. The framework could be extended to accommodate more complex PD architectures, such as branched PDs. This would allow to assess the functional consequences of such often observed architectures and that way help answer the long standing question whether these PD morphologies are mere consequences of developmental constraints or have been (strongly) selected for.

## 3.5 Methods

### 3.5.1 Diffusive flux through a single PD

Similar to [224] we assumed the flux is distributed homogeneously within each cross section along the axis of the channel. This results in a very simple mapping to a 1D channel, i.e. that the average local flux (per unit area of cross section)  $\sim 1/\text{available cross section surface}$ . Actually, this assumption does not hold close to the transition between neck and central cavity / narrow and wide cylinders. [225] offers an approximation for the

effective diffusion constant in cylindrical pores with varying diameter, but this is not valid for the abrupt changes of the diameter. This problem could be solved by describing the outer PD wall more gradually, but that would have required the introduction of at least one additional (hard to determine) geometry parameter. Fortunately, numerical simulations showed that the error introduced by the assumption of homogeneous flux turned out to be less than 4 percent for the shortest ( $l = 200nm$ ) channels (i.e. the ones where we expected the largest effect, as the relative size of “transition zones” decreases with channel length, see fig 3.7). This can be considered irrelevant given the quality of available data on PD dimensions and the many molecular aspects of PD functioning that are necessarily neglected in a simple model.

### 3.5.2 Relative molar flow rate and average passage time

For assessing the impact of the neck constriction on PD transport, we defined two relative quantities:  $Q_{rel} = Q_{necked}/Q_{narrow}$  and  $\tau_{rel} = \tau_{necked}/\tau_{narrow}$  (figure 3.2). Using equation 3.2 for  $Q(\alpha)$ ,  $Q_{rel}$  is well defined:

$$Q_{rel}(\alpha, R_c) = \frac{l\tilde{A}_c}{2(\tilde{l}_n)A_c + (l - 2\tilde{l}_n)A_n} \quad (3.5)$$

$$= \frac{l((\tilde{R}_c)^2 - (\tilde{R}_{dt})^2)}{2\tilde{l}_n((\tilde{R}_c)^2 - (\tilde{R}_{dt})^2) + (l - 2\tilde{l}_n)((\tilde{R}_n)^2 - (\tilde{R}_{dt})^2)} \quad (3.6)$$

$$\lim_{R_c \rightarrow \infty} Q_{rel}(\alpha, R_c) = \frac{l}{2\tilde{l}_n} \quad (3.7)$$

For  $\tau_{rel}$  we first need an expression for  $\tau$  itself. Using a steady state mass balance argument this can be calculated as the number of particles in the channel divided by the number leaving (or entering) per unit of time ( $= Q(\alpha)$ ).

$$\tau(\alpha) = \int_0^l C(x)\tilde{A}_x(\alpha)dx/Q(\alpha) \quad (3.8)$$

$$= \frac{C_l + C_0}{2D(\alpha)\Delta C} \frac{(2\tilde{l}_n\tilde{A}_n + (l - 2\tilde{l}_n)\tilde{A}_c)(2\tilde{l}_n\tilde{A}_c + (l - 2\tilde{l}_n)\tilde{A}_n)}{\tilde{A}_n\tilde{A}_c} \quad (3.9)$$

Unfortunately, this depends on the concentration difference over the channel. We are interested, however, in how the passage time changes with increasing  $R_c$ . In our definition of  $\tau_{rel}$ , the concentration difference cancels from the equation, solving the problem:

$$\tau_{rel}(\alpha, R_c) = \frac{(2\tilde{l}_n(\tilde{R}_n^2 - \tilde{R}_{dt}^2) + (l - 2\tilde{l}_n)(\tilde{R}_c^2 - \tilde{R}_{dt}^2)) (2\tilde{l}_n(\tilde{R}_c^2 - \tilde{R}_{dt}^2) + (l - 2\tilde{l}_n)(\tilde{R}_n^2 - \tilde{R}_{dt}^2))}{l^2(\tilde{R}_c^2 - \tilde{R}_{dt}^2)(\tilde{R}_n^2 - \tilde{R}_{dt}^2)} \quad (3.10)$$

$$\tau_{rel}(\alpha, R_c) \approx \frac{2\tilde{R}_c^2\tilde{l}_n(l - 2\tilde{l}_n)}{l^2(\tilde{R}_n^2 - \tilde{R}_{dt}^2)}, \quad (R_c \rightarrow \infty) \quad (3.11)$$

### 3.5.3 Numerical simulations for transport to the wall

Numerical simulations for assessing the effect of discrete patches of permeability rather than a (by ratio decreased) homogeneous permeability were performed using the Douglas

DT	Desmotubule
PDs	Plasmodesmata (plural!)
SEL	Size exclusion limit (mathematical symbol $\bar{\alpha}$ )

Table 3.1: List of abbreviations

method for 3D alternating direction implicit diffusion [226]. In the  $x$  and  $y$  direction, we used periodic boundary conditions. In the  $z$  direction we fixed the concentration on side of the domain (“source plane”) and used a radiating boundary condition with a mixed rate  $\kappa(x, y)D$  on the other side (“target plane”). We chose the rate proportional to the diffusion constant, as the flux and molar flow rate through single PDs ( $Q(\alpha)$ ) are proportional to  $D$  (equation 3.2). For PDs the target plane contained the “front view” of a single channel: an annulus with inner radius  $R_{dt}$ , outer radius  $R_n$  and surface area  $A_{ann}$ . Within this annulus  $\kappa(x, y)$  was set to unity ( $\kappa(x, y)|_{PD} = 1/\mu m$ ) and 0 outside. For the corresponding homogeneous target plane  $\kappa_{hom} = \frac{A_{ann}}{A_{total}}/\mu m$ . At the grid level, the pixels at a boundary of the annulus had  $\kappa$  proportional to the fraction of their surface falling inside the annulus. As we found in figure 3.5 that the annular patches gave the same result as circles with radius  $R_n$  and  $\kappa(x, y)|_{circ} = \frac{A_{ann}}{A_{circ}}/\mu m$ , i.e. that the outer radius of the patch was most important, we used a small pixel size of  $d_p = 1nm$  as a reference and used the same pixel size within each set of simulations. For the larger simulation domains, to reach as large  $h$  as possible, we used a pixel size of  $d_p = 6nm$ , chosen to prevent “bleeding” of the permeable patch to a new ring of pixels with the outer radius used ( $R_n = 12nm$ ). This coarse grid gave a small difference between circular and annular patches (figure 3.5C), whereas they gave +/- identical results with a finer grid. Given the importance of the outer dimensions of the patches, we decided to use the circular patches for this set of simulations, as they have the lowest  $\kappa$  in the corner pixels (i.e. the ones farthest from the patch center).

To be able to reach as large  $h$  as possible, we used a coarser grid. This resulted in a small deviation between the annular and circular patches that gave the same results before, with a stronger reduction with the circular patches. We therefore used the circular patches for further increasing  $h$ .

The reference flux was computed analytically, exploiting that within each plane at a given distance  $z$  from the target plane, the concentration is the same everywhere. This allows for a trivial mapping to a 1D system. With the (partially) radiating boundary condition, the driving force behind the transport is the concentration difference between the wall and the box close to the target plane. Therefore, we can assume without loss of generality that the concentration in the wall  $C_w = 0$ . If we write  $C_0$  for the concentration at the boundary, but inside the box, the flux through the boundary wall is given by  $J_b = C_0 D \kappa_{hom}$  and the diffusive flux towards the boundary is  $J_d = -\frac{\partial C}{\partial x} D$ . At steady state, the latter is the same everywhere within the box, so  $J_d = \frac{C_h - C_0}{h} D$ . This yields  $C_{0,ref} = \frac{C_h}{h\kappa + 1}$  and  $J_{ref} = \frac{\kappa C_h D}{h\kappa + 1}$ . Note that because the rate of the radiation boundary condition is proportional to the diffusion constant, it cancels from the equations for the concentration profile. Hence, we do not need to explore different diffusion constants.

To save computation time we used the analytically calculated reference profile as an initial condition for the simulations.

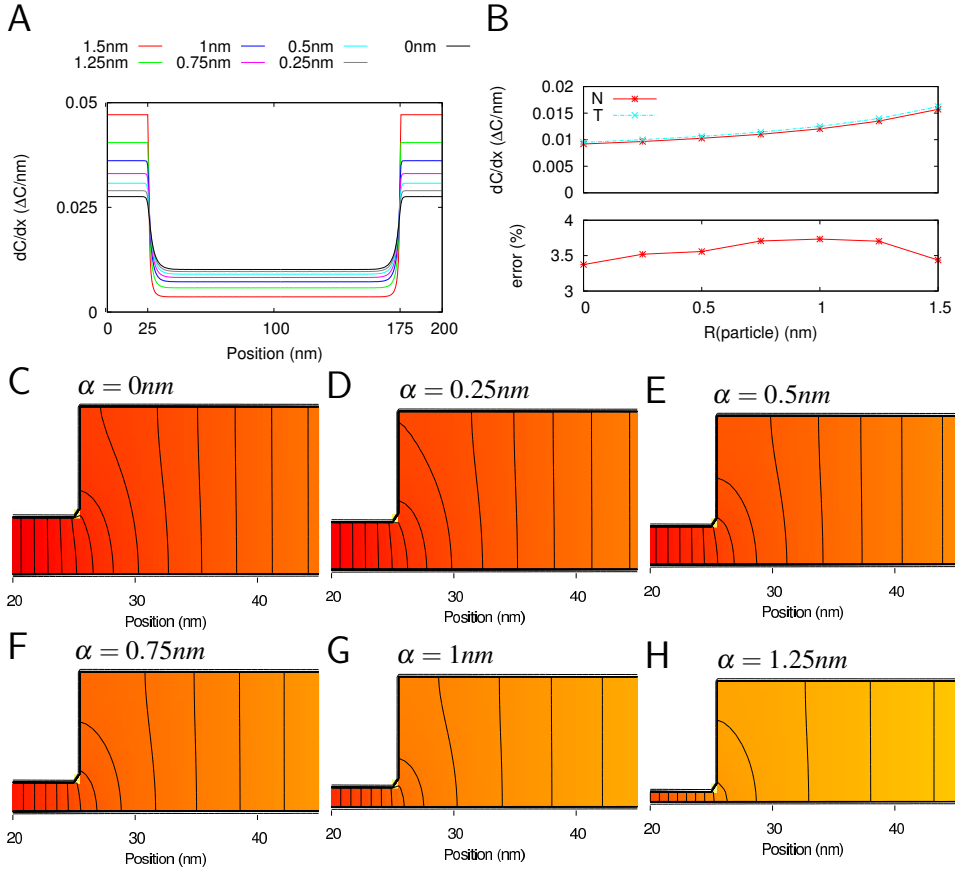


Figure 3.7: **(Supplementary) Error of homogeneous flux approximation (all 2D).** **A:**  $\partial C/\partial x$  from numerical calculations (2D) along a straight line through the middle of the available neck region for different particle sizes ( $\alpha$ ). **B:** top:  $\partial C/\partial x$  at neck entrance (proportional to the channel flux) from numerical calculations (N; solid red line with asterisks) and from 3-cylinder model with homogeneous flux assumption (T; dashed cyan line with crosses). The 3-cylinder model results in a consistent over estimation of  $< 4\%$  (bottom). **C-H:** concentration heat maps for available part of the channel, focus on the neck/central cavity transition. Particle size is accounted for by removing lines of (0.5 nm) pixels from the simulation grid (neglecting the impact of  $\alpha$  on the effective neck length  $\tilde{l}_n$ , as here we are only interested in the impact of the sharp transition of the channel radius). The same color gradient is used for all six graphs. Black isolines are spaced at 1% of the total concentration difference over the channel.

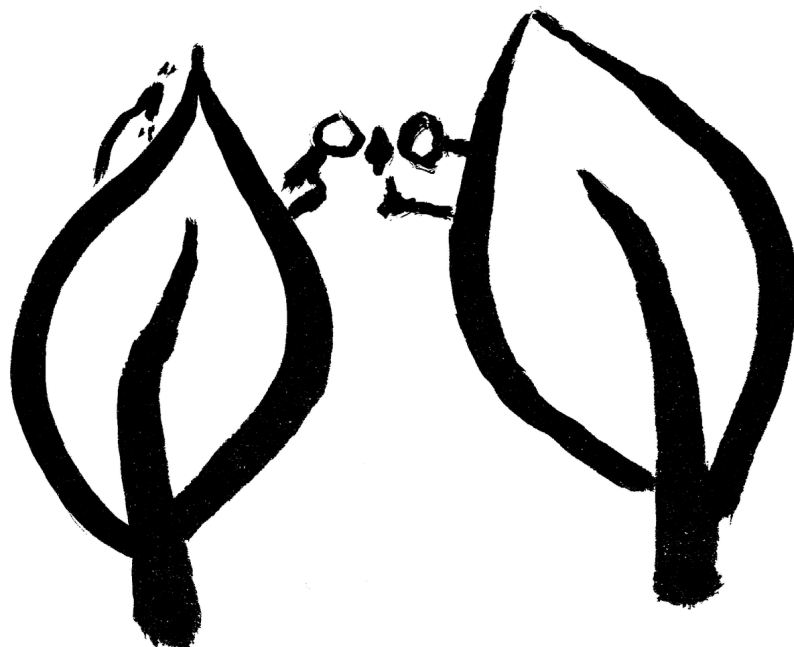


## **Part II**

# **Primordium initiation**



The formation of a new plant organ starts with the initiation of a primordium. The plant hormone auxin plays an elemental role in this process. It accumulates at the site where the cells from which the new organ will develop, start dividing. In this part we will investigate conceptually different options resulting in local auxin accumulation. These options all produce their own characteristic spatial and spatiotemporal signatures. We will look into these different signatures, their biophysical properties, and the developmental consequences of our findings. We will conclude with investigating the induction of a nodule primordium by a signal of epidermal origin.





---

## **Modeling a cortical auxin maximum for nodulation: different signatures of potential strategies**

---

*This chapter is based on [182].*

Lateral organ formation from plant roots typically requires the *de novo* creation of a meristem, initiated at the location of a localized auxin maximum. Legume roots can form both root nodules and lateral roots. From the basic principles of auxin transport and metabolism only a few mechanisms can be inferred for increasing the local auxin concentration: increased influx, decreased efflux and (increased) local production. Using computer simulations we investigate the different spatio-temporal patterns resulting from each of these mechanisms in the context of a root model of a generalized legume. We apply all mechanisms to the same group of preselected cells, dubbed the controlled area. We find that each mechanism leaves its own characteristic signature. Local production by itself can not create a strong auxin maximum. An increase of influx, as is observed in lateral root formation, can result in an auxin maximum that is spatially more confined than the controlled area. A decrease of efflux on the other hand leads to a broad maximum, which is more similar to what is observed for nodule primordia. With our prime interest in nodulation, we further investigate the dynamics following a decrease of efflux. We find that with a homogeneous change in the whole cortex, the first auxin accumulation is observed in the inner cortex. The steady state lateral location of this efflux reduced auxin maximum can be shifted by slight changes in the ratio of central to peripheral efflux carriers. We discuss the implications of this finding in the context of determinate and indeterminate nodules, which originate from different cortical positions. The patterns we have found are robust under disruption of the (artificial) tissue layout. The same patterns are therefore likely to occur in many other contexts.

## List of abbreviations

IAA	Indol-3-acetic acid (an auxin)
EZ	Elongation zone
DZ	Differentiation zone
Effl↓	Scenario in which the efflux permeability is decreased in the <i>controlled area</i> (see <b>figure 4.1A</b> )
Infl↑	Scenario in which the influx permeability is increased in the <i>controlled area</i>
Prod↑	Scenario in which all cells of the <i>controlled area</i> produce auxin

## 4.1 Introduction

### 4.1.1 Setting

Legume roots can form two kinds of lateral organs: lateral roots and root nodules, the latter in response to Rhizobium-secreted signaling molecules named Nod factors. Although these organs are induced in different ways and their primordia originate from different cell layers, in both cases local accumulation of the hormone auxin coincides with the site of primordium initiation [36, 37, 227–229]. In this light it is not surprising that the number of lateral roots can be increased by exogenous auxin application [53, 230]. For root nodules, however, this is not the case. Auxin’s textbook antagonist, cytokinin, plays an important role in nodulation: a cytokinin receptor is essential for nodulation [33, 34, 231, 232] and exogenously applied cytokinin can induce nodule-like structures [32], as can auxin transport blockers [31]. In contrast, cytokinin has an inhibitory effect on lateral root formation [233], possibly by removing PIN1, an auxin efflux carrier upregulated in lateral root primordia, from the membranes of primordium cells [39].

This apparent paradox hints at different mechanisms causing the initial auxin accumulation in either case. We hypothesize that the Nod factor activated cytokinin signaling causes the accumulation of auxin in the cortical cell layers of the root that form the nodule primordium. We investigate the possibilities for inducing local auxin accumulation by modeling three conceptually different mechanisms. We start with an unbiased analysis of their generic properties, then continue with the best candidate for nodulation. In the discussion we come back upon the likelihood that cytokinin can activate the proposed mechanism.

### 4.1.2 Background

To date **lateral root** formation is studied most extensively in the model organism *Arabidopsis thaliana* (Arabidopsis). In this plant the lateral root originates exclusively from a few pericycle cells, called founder cells [234, 235]. The first auxin accumulation occurs in these cells [236]. Arabidopsis roots contain only a single cortical layer. In model legumes, which all have a multi-layered cortex, the lateral root primordia are also predominantly of pericycle origin [237] and the first auxin accumulation is observed in the pericycle [227, 228].

**Nodules** can be induced upon contact with a compatible Rhizobium strain, recognized by the plant through the precise chemical structure of the Nod factors the particular Rhi-

zobium species produces [26]. Two major types of legume nodules exist: indeterminate and determinate, discerned by the presence of a persistent meristem in the former [28]. The model legume *Medicago truncatula* (Medicago) makes indeterminate, whereas *Lotus japonicus* (Lotus), the other model legume, forms determinate nodules. Of special interest is that indeterminate nodules are formed from cell divisions induced in the inner cortical layers, while determinate nodule formation starts with divisions in more outer cortical layers [28]. Studies in Lotus and white clover have shown local auxin accumulation at the site of the cortical cell divisions [36, 37], [229] respectively.

In legumes, lateral roots and root nodules originate in approximately the same zone of the root. The zone for nodule induction is called the susceptible zone [238]. Cortical cells in the susceptible zone have fully differentiated and will de- and redifferentiate in the process of nodule formation. Epidermal cells start developing root hairs from the youngest part of the susceptible zone. In this paper we sometimes refer to the susceptible zone of a legume using DZ (standing for “differentiation zone”) to stress the origin of the parameters we use (see methods).

The phytohormone **auxin** is active in minute concentrations (typical measurements: tens to hundreds pg per mg fresh weight [75–77], i.e.  $1\text{--}10^2 \mu\text{mol ml}^{-1}$ ) and no methods exist for live monitoring of the actual auxin concentration. All available techniques for auxin detection are either indirect, or kill the plant, or both. This is a key reason why analytical and computational models of auxin transport have become an important tool for studying the implications of auxin related hypotheses with high spatial and temporal resolution (see [82, 83, 239, 240] for some reviews). The earliest models focussed on the propagation of radio-labeled auxin through “linear” tissue [84–86]. With increasing computer power a plethora of more complex developmental questions came within reach, on topics such as phyllotaxis [3–6, 87], venation [7, 88–90], apical dominance [11] and root gradients [54, 91–93].

Here, we will use a model of auxin transport and metabolism to investigate different possible scenarios for local auxin accumulation in the root cortex and relate the resulting patterns of auxin accumulation to those observed upon Rhizobium Nod factor induced signaling. To infer the possible scenarios we recapitulate the basics of auxin transport and metabolism. Auxin is a weak acid (The most abundant active natural auxin, indol-3-acetic acid (IAA), has  $pK_a \approx 4.8$ ). Its protonated form is uncharged and can therefore passively cross the cell membrane. The apoplast is mildly acidic and thus contains a fair fraction of protonated auxin (e.g. 24% at pH=5.3). The cytoplasm, however, is near neutral and thus hardly contains any protonated auxin (e.g.  $\approx 0.4\%$  at pH=7.2) [3]. As only the concentration of protonated auxin matters for the passive influx, the pH difference has the potential to drive a passive auxin influx against the difference in total auxin concentration. Its magnitude is mostly determined by the apoplastic pH as this is closest to the  $pK_a$ . Moreover, the influx can be enhanced by more than an order of magnitude by influx carriers such as the AUX1/LAX protein family, that exploit the proton gradient for the import of deprotonated auxin [54]. They are usually located homogeneously over the cell membrane, or at higher levels on both apical and basal sides [55–57]. Efflux of auxin occurs predominantly by active transport through efflux carriers such as the PIN proteins [58, 59]. The membrane PINs often appear concentrated at specific sides of the cells, giving rise to directional auxin transport [62, 63]. For information about the production of auxin we refer to some reviews [53, 241].

### 4.1.3 Approach

Reasoning from this overview of auxin transport and metabolism we arrive at three major scenarios for increasing the auxin concentration inside a cell: increasing the amount of influx carriers, decreasing the amount of efflux carriers and (activating) local auxin production. These scenarios we will refer to by (n-fold)  $\text{Infl}\uparrow$ ,  $\text{Effl}\downarrow$  and  $\text{Prod}\uparrow$ , respectively. In this “n-fold” refers to the factor of increase or decrease compared to the starting situation, respectively.

For  $\text{Infl}\uparrow$  we specifically focus on the carriers, as changes in the passive influx (such as resulting from changes of the apoplastic pH) will be practically the same on both sides of the wall. As a result the change in the influx capacity will be almost fully compensated by an opposite change in the apoplastic concentration, with hardly any change in the intracellular concentration in either cell (c.f. For the same reason Grieneisen *et al.* found no noticeable effect of the, in their case uniform, influx permeability on the intracellular auxin concentrations, despite large variations in the values tested [91]).

We will not consider a decrease of auxin degradation, because this part of the root has to support the passage of auxin from shoot to root tip. To increase the local auxin concentration through a decrease of degradation by any significant degree, a large base degradation rate is required. This is inconsistent with auxin’s function as a long range signal. We will neither consider (the reversible forms of) conjugation and deconjugation of auxin, as this would either complicate the model by having separately to account for the conjugate concentrations, next to active concentrations, or, without this, reduce to a combination of decay and production that need to (almost completely) balance each other on the cell level in order to sustain long range auxin signaling.

Starting from these scenarios we aim to tackle the following questions: Which changes in auxin transport/metabolism in the cortex of the DZ can create a sufficiently strong cortical auxin maximum as is observed in root nodule initiation? Furthermore, how do the different scenarios relate to observed patterns of auxin accumulation in nodulation and lateral root formation?

### 4.1.4 Key findings

We find that these three scenarios produce clearly different spatial signatures, of which  $\text{Effl}\downarrow$  is most compatible with nodulation. The time scales of auxin accumulation under  $\text{Infl}\uparrow$  and  $\text{Effl}\downarrow$  are comparable and both sufficiently fast to be compatible with the experimentally observed timing of early nodulation events.

We also find that the lateral position of a cortical auxin maximum can be shifted by minor changes in the distribution of cortical PINs. Based on this observation we formulate the tentative hypothesis that differences in the distribution of cortical PINs could determine the lateral position of the early cell divisions in nodulation. This in turn is correlated with the nodule type.

The signatures we have found occur consistently and robustly. We therefore argue that the understanding of these different signatures is of general importance for the area of plant development.



## 4.2 Results

### 4.2.1 Signatures of increasing influx, decreasing efflux and local auxin production

Lacking the relevant PIN data for model legumes we have created an *in silico* DZ root segment based on the Arabidopsis model by Laskowski *et al.* [92] by adapting the tissue geometry. The resulting segment has five cortical layers, which is typical for the model legumes Lotus and Medicago (**figure 4.1A**). The PIN layout of the DZ root segment is shown in **figure 4.1B**. This layout results in a strong rootward flux in the stele and a shootward flux in the cortex and epidermis. The equal amount of PINs on the inner and outer sides of the cortical cells, results in a flat transverse auxin concentration profile in the cortex. More details on the creation of the root segment and the verification of the boundary conditions are provided in the Methods section (4.4.3).

From the available knowledge on auxin transport and metabolism we have identified three scenarios that could in theory lead to a local auxin maximum (Infl $\uparrow$ , Effl $\downarrow$  and Prod $\uparrow$ ). To assess whether these scenarios actually are compatible with the events that occur during nodulation we applied each scenario separately to a block of cells on one (lateral) side of the DZ fragment, dubbed the **controlled area**. It has a length of 500  $\mu\text{m}$  (in the simulations 5 cells long), which corresponds well with the typical length of a nodule primordium. The controlled area includes all cortical layers and the epidermis, as indicated in **figure 4.1A**. For simplicity we assume that the parameter change as a reaction to Nod factor perception is the same for all cells in the controlled area.

*In this text, the word **segment** is reserved for the whole simulation domain (figure 4.1A). A segment without any (additional) change in the controlled area is called a **reference segment**.*

We first focussed on the steady states of each scenario as obtained from evaluating the model. Although all three scenarios resulted in at least some increase of the local auxin concentration, their effects were remarkably different.

With an **increase of the influx permeability**, we observed a strong increase of the auxin concentration only in the most shootward cells of the controlled area (**figure 4.1C**). Considering the main flow directions of auxin through the controlled area (i.e. through cortex and epidermis), this corresponds to its downstream side. This strong focus on the most downstream cells inside the controlled area was independent of the length (number of cells in the longitudinal/(y)-direction) of the controlled area (data not shown). This means that the area of the strong(est) auxin accumulation can be much smaller than the area with increased influx activity. A 10-Fold (but not a 4-fold) Infl $\uparrow$  change was sufficient for increasing the cortical auxin concentration above the vascular auxin concentration in the reference segment  $C_v$ , which throughout we use as our unit of concentration.

A **decrease of the efflux permeability** on the other hand resulted in a fairly homogeneous increase throughout the whole controlled area, independent of the reduction factor (**figure 4.1D**). In all cases the auxin accumulation showed a slight maximum on the downstream (shootward) side in the area. This bias, however, was much weaker than with an increase of auxin influx. A 10-Fold (but not a 4-fold) Effl $\downarrow$  change was sufficient for increasing the cortical auxin concentration above the vascular level  $C_v$ .

**Local auxin production** in the controlled area led to a ill confined increase of the

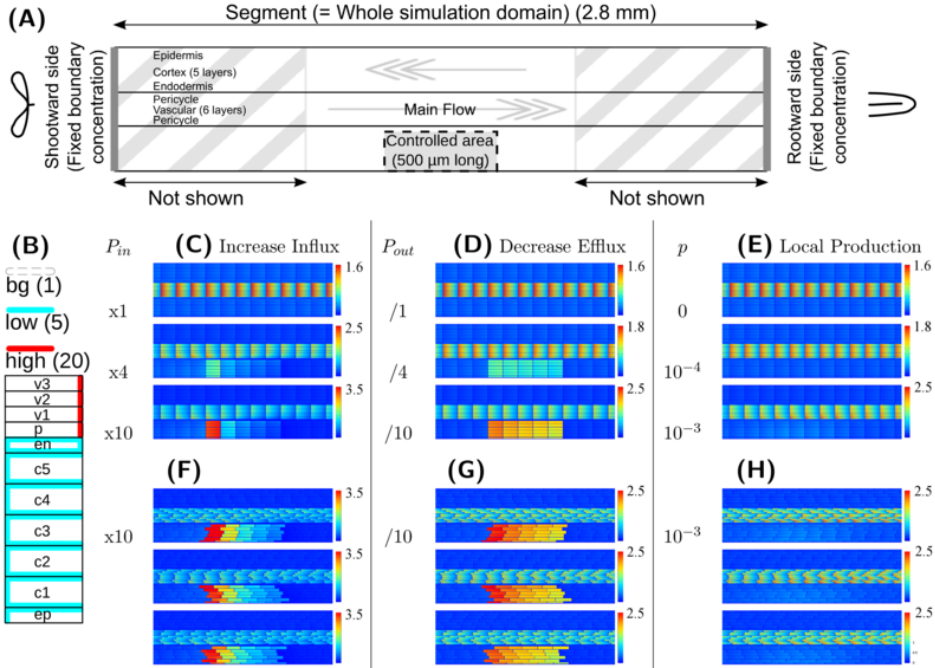


Figure 4.1: **Effect of single changes** in the controlled area on steady state auxin concentrations. **A**: layout of the root segment and the main directions of auxin flow. Throughout the text the word “segment” refers to the whole simulation domain, including the parts not shown in the figures. The same parameter change is applied to all cells in the controlled area (indicated by a gray block). The gray arrows indicate the main flow direction in the stele and cortex. Stylized leaves and root tips are used throughout the manuscript to indicate the orientation of the root segments. **B**: effective efflux permeabilities for each cell from center to periphery. Following [92] we distinguish three levels: high, low and bg (background). **C,F**: increase of influx permeability ( $P_{in}$ ) by an increasing factor (as shown left of the pictures). **D,G**: reduction of all efflux permeabilities ( $P_{out,x}$ ). **E,H**: local auxin production with rate  $p$  (in  $C_V s^{-1} \mu\text{m}^{-3}$ ). **F-H**: the strongest change from each category was repeated on randomly generated realistic tissue layouts, with an average cell length of  $100 \mu\text{m}$ , normally distributed with  $\sigma = 4 \mu\text{m}$ . The controlled area consists of all cells that fall in the desired area with more than 50% of their volume. **C+F, D+G**: Note that with increasing the influx the effect concentrates on the downstream side of the controlled area, whereas the effect of decreasing all efflux with the same factor is much more homogeneous over the controlled area. For maximum information the auxin concentration color gradient is rescaled for each picture. The gradient always starts from 0 and the maximum value is indicated per picture.

local auxin concentration, reaching at most a small fraction of the resting state vascular concentration  $C_v$  (**figure 4.1E**), even with what we considered a high production rate (estimated from gas chromatography and mass spectroscopy measurements by [75, 76]). This cannot be contributed to a too low production rate, but happened because the locally produced auxin is transported away and accumulates somewhere else. With the highest production rate tested ( $p = 10^{-3} C_v \mu\text{m}^{-3}\text{s}^{-1}$ ) the absolute increase of the auxin concentration was larger in the vascular tissue rootward from the production site than in the controlled area itself. This is in marked contrast to the other two scenarios, in which the changes of the auxin concentration were limited to the controlled area and a small surrounding region.

In biological tissues the cells are not aligned in a square pattern as in our idealized root segment. We therefore also tested our scenarios on randomly generated root segments without lateral alignment between cell files and with variable cell lengths. All signatures were conserved (**figure 4.1F-H**).

From the three mechanisms tested, only the reduction of the efflux permeabilities ( $\text{Effl}\downarrow$ ) resulted in a strong auxin accumulation that was fairly homogeneous along the length of the controlled area, as is observed in nodulation. Increased influx ( $\text{Infl}\uparrow$ ) resulted in a too narrow (single cell wide) maximum and local auxin production *alone* could not yield a local auxin maximum in the cortex at all. We therefore focussed on  $\text{Effl}\downarrow$  for the rest of this study.

We next asked how fast auxin accumulates under this scenario, what determines the time scales of auxin accumulation in this case and where the accumulation starts. The final steady state auxin maximum spanned all layers of the cortex, whereas the cell divisions founding a nodule occur either in the inner, or the outer cortex, depending on the legume species. To gain insight into this lateral confinement of the auxin accumulation we looked into both the dynamics of auxin accumulation after a change in the controlled area and the impact of slight changes of the lateral cortical PINs on the lateral position of the steady state auxin maximum.

## 4.2.2 Time evolution of auxin accumulation

### Auxin accumulation following $\text{Effl}\downarrow$ is sufficiently fast

After studying the steady state patterns the first important question was: is auxin accumulation following reduction of the efflux fast enough to explain the Rhizobium induced cortical cell responses? To be compatible with the formation of a nodule primordium, a scenario should yield a sufficient increase in auxin concentration at least several hours prior to the first cortical cell divisions. For this a time window of at most 20 hours is available: cortical cells show cytoskeletal signs of activation for division after 18-24 hours after inoculation [27] and no cortical cell divisions are observed within 20 hours after inoculation [242]. The actual time window is probably even shorter, as we start the clock at the moment the cells change with respect to auxin dynamics (which is instantaneously in this model). In reality, the transcription and translation of regulatory genes likely reduces the available time window by a few hours.

We only investigated the dynamics for the strongest ( $= 10$ -fold)  $\text{Effl}\downarrow$  and  $\text{Infl}\uparrow$  changes

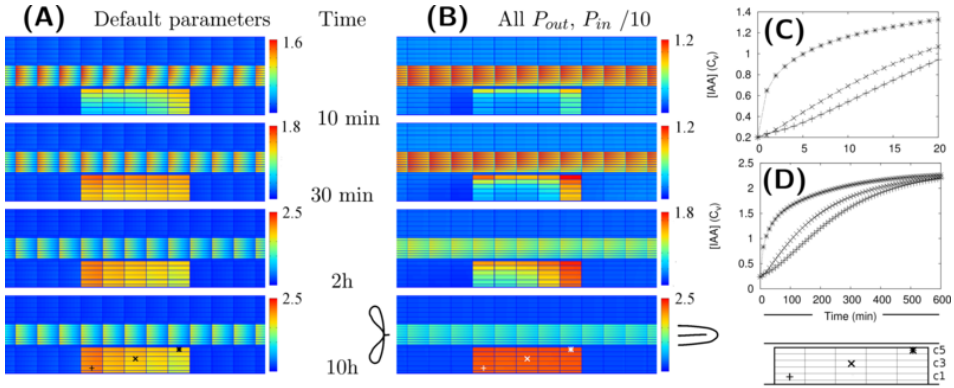


Figure 4.2: **Auxin accumulation after efflux reduction starts from the inner cortex.** The change in the controlled area, a 10 fold reduction of the effective efflux permeabilities (10-fold  $\text{Effl}\downarrow$ ), takes place at  $T = 0s$ . **A** and **B** show the auxin concentration at several time points afterwards. **A**: default parameters. **B**: “slowed down” parameters: the effective (influx and efflux) permeabilities of the whole root segment are reduced by a factor 10 (the  $\text{Effl}\downarrow$ -reduction comes on top of this). **C,D**: concentration in the three marked cells during the first 20 minutes (default parameters, **C**) or 10 hours (slowed down, **D**). Note how the concentration increases first from the inner cortex and the rootward/upstream side of the controlled area. This corresponds with the locations of possible auxin sources.

from **figure 4.1D and C**, respectively, because they have the longest adaptation times. With  $\text{Effl}\downarrow$ , a fairly homogeneous elevated concentration over the whole controlled area was observed within 30 minutes and almost no further changes occurred after 2 hours (**figure 4.2A,C** and supplementary movie 1). Adaptation to a 10-fold  $\text{Infl}\uparrow$  was even faster (**figure 4.7A,B**). Both processes happened much faster than strictly required, implying that either our dynamics is too fast, or that the time scales for auxin accumulation are dominated by other processes, such as the induction and buildup of the changes in efflux (or influx) permeabilities that are implemented as instantaneous changes in our simulations.

We have calculated (wherever possible) or estimated the effective influx and efflux permeabilities used by other authors [3, 4, 6, 54, 85, 90–92, 243]. We found values ranging over more than two orders of magnitude for both influx and (high) efflux. Our values for (high) effective efflux permeability,  $P_{out,high}$ , and effective influx permeability,  $P_{in}$ , are somewhere in the middle of these ranges. We expected that lower values would slow down the time scales of the response to changes. To assess how much, we also tested the model’s dynamic response in a new reference segment. This was created by reducing all effective permeabilities (influx ( $P_{in}$ ) and efflux ( $P_{out,high}$ ,  $P_{out,low}$  and  $P_{out,bg}$ )) by a factor 10. In this case a 10-fold  $\text{Effl}\downarrow$  (i.e. a further reduction of the effective efflux permeabilities in the controlled area only) resulted in a fairly homogeneous elevated concentration ( $> C_v$ ) inside the controlled area within 5 hours, the steady state concentration was almost reached at 10 hours and hardly any further increase was observed after 20 hours (**figure 4.2B,D** and supplementary movie 2).

Even with 10-fold reduced effective permeabilities, auxin accumulation after reduction of the efflux occurred fast enough to be compatible with the observed onset of nodulation. With both parameter sets the accumulation is so fast, that sufficient time is left for the part we did not explicitly consider (i.e. the actual induction of the changes).

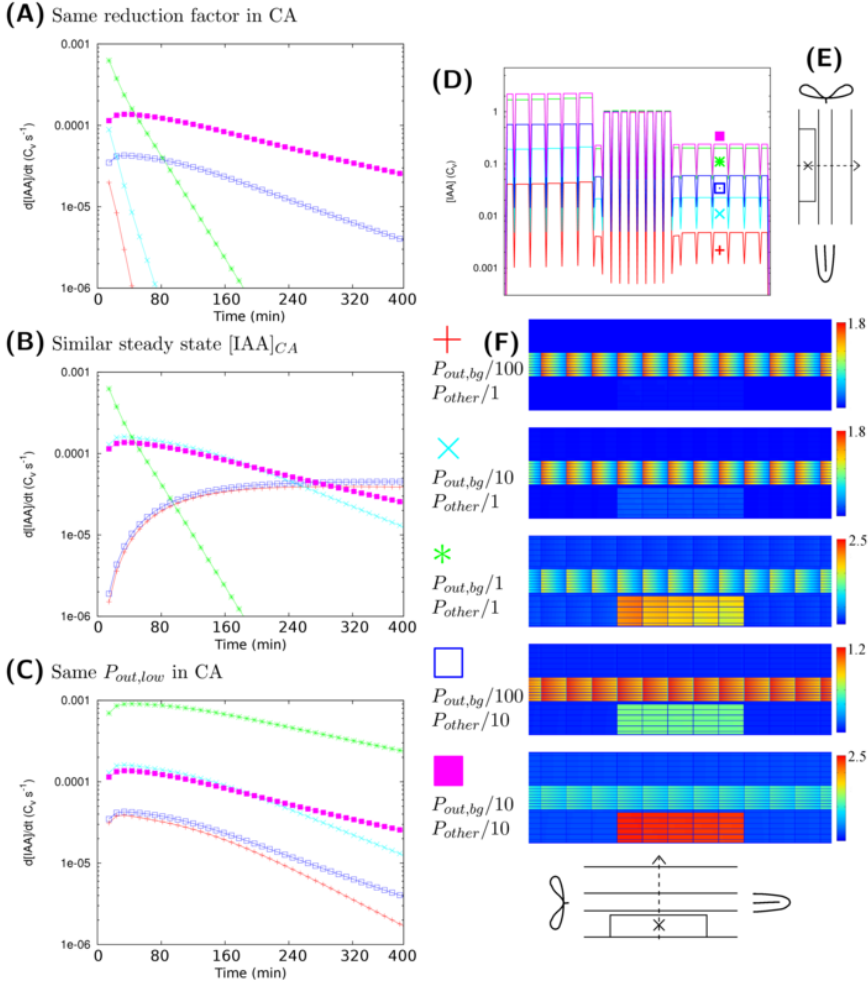
### **Auxin distribution over the controlled area sets the time scale of local auxin accumulation under Effl↓**

Given that we do not have perfect knowledge of the PIN layout in the susceptible zone (caricatured by the DZ segment) or the real values of the effective efflux permeabilities, we performed a robustness analysis of the system's dynamics with respect to the effective efflux permeabilities. To that end we enquired which process was the dynamic bottleneck of auxin accumulation under Effl↓. Was it the supply of auxin to the controlled area, its subsequent distribution over the controlled area, or the total amount accumulated in the whole controlled area?

With the DZ parameters the cortical cells have an effective efflux permeability of  $P_{out,bg}$  on the upstream (rootward) side and of  $P_{out,low}$  on the remaining three sides (**figure 4.1B**). To separate the effects of both we split the effective permeabilities in two groups: “background” ( $P_{out,bg}$ ) for the lowest efflux level resulting from mislocalized PINs and “other” ( $P_{out,low}$ ,  $P_{out,high}$  and  $P_{in}$ ) (**figure 4.1B**, **equation 4.2** and **table 4.1**). We created additional reference segments in which the “other” and “background” permeabilities were reduced by a factor of 1, 10 or 100 independently (reducing “background” at least as much as “other”). The reduction factors are shown in **figure 4.3F**. We applied Effl↓ to this whole set of five reference segments.

To monitor the time scales of this change we calculated the time derivative of the auxin concentration (i.e. the instantaneous change of the auxin concentration) in the most central cell of the controlled area (this cell is indicated in **figure 4.3E**) in all individual simulations. These curves tell how fast the local auxin concentration changes at each moment, making their shape a good proxy for the time scales of the concentration changes. If the course of the time derivatives is similar for the whole set of five, the time scales of auxin concentration changes are dominated by a common feature and conversely, if a certain quantity dominates the time scales, the shape of the time derivatives should be similar in all cases that share the same value of this quantity.

We first applied the same factor, 10-fold, efflux reduction to the set. We found two quite different shapes for the time derivatives, meaning that within the set of five, the auxin concentration in the controlled area increased on different time scales with a change of the same factor (**figure 4.3A**). Additionally, the final concentrations inside the controlled area differed by orders of magnitude (**figure 4.3D,F**). The further the background was reduced relative to the other permeabilities, the lower the steady state concentrations in the controlled area became (**figure 4.3D**). We found an explanation for this effect in the transverse concentration profiles of the reference segments. Actually, in all five cases the cortical concentration in the controlled area increased with a similar factor, but the starting level, or resting state cortical concentration, varied. As we always normalized the vascular concentration to  $1C_v$  for ease of interpretation (see methods), the resting state cortical concentration necessarily differed among these segments. From a 1D calculation along a transverse (x-direction) section with the DZ PIN-layout we obtained a first order



**Figure 4.3: Determinants of time scales.** To determine what factor governs the time scales of auxin accumulation in the controlled area (CA in the scope of this figure) under  $\text{Effl}_\downarrow$  we followed the changes in the auxin concentration over time in five different reference segments, created by reducing the effective permeabilities with different factors for  $P_{\text{out},bg}$  and all others ( $P_{\text{other}} = \{P_{\text{out},low}, P_{\text{out},high}, P_{\text{in}}\}$ ). **A-C:** each graph shows simulations that share a common factor. If all five curves have a similar shape, this common factor is the most likely key determinant of the auxin accumulation time scales. **A-C:**  $\frac{d[\text{IAA}]}{dt}$  in the most central cell of the CA (indicated with “X” in **E**). **A:** 10-fold (further) reduction of efflux inside the CA. Steady state profiles and overviews matching these curves in **D** and **F** respectively. **B:** Similar steady state  $[\text{IAA}]_{CA}$ :  $[\text{IAA}]_{CA} \approx 2\text{--}6 C_v$ . **C:**  $P_{\text{out},low} = 0.05 \mu\text{ms}^{-1}$  inside the CA. **D:** Steady state  $[\text{IAA}]$  profile along the dotted line in **E** for all curves in **A**. **F:** legend for all:  $P_{\text{out},bg}/100$ ,  $P_{\text{other}}/1$  red pluses,  $P_{\text{out},bg}/10$ ,  $P_{\text{other}}/1$  cyan crosses,  $P_{\text{out},bg}/1$ ,  $P_{\text{other}}/1$  (original DZ segment) green asterisks,  $P_{\text{out},bg}/100$ ,  $P_{\text{other}}/10$  blue open squares,  $P_{\text{out},bg}/10$ ,  $P_{\text{other}}/10$  magenta filled squares, next to steady states for the curves in **A**. Note that only in **C** all five curves show a similar shape. This implies that the value of  $P_{\text{out},low}$  in the CA, which governs the distribution of auxin over the CA, is the key determinant of the time scales of local auxin accumulation under  $\text{Effl}_\downarrow$ .

estimate for the resting state cortical concentration:  $\frac{P_{out,bg}}{P_{out,low}} C_v$ . Any deviations from this must result from diffusive transport through the apoplast, which is always part of our model. The impact of diffusive transport will be larger for lower (influx) permeabilities, as auxin molecules will then typically remain longer in the apoplast before re-entering a cell.

We also calculated 100 and 1000-fold  $\text{Effl}\downarrow$  for the set of five segments and plotted their time derivatives with (**figure 4.3B**) similar steady state concentrations and (**figure 4.3C**) equal  $P_{out,low}$  in the controlled area. Only in the last case, the course of the time derivatives was very similar for all five segments. Revisiting **figure 4.3A,B** with this observation in mind, it became clear that also in the other two cases the curves of root segments with equal  $P_{out,low}$  in the controlled area have a similar shape.

In summary: The amount of auxin available in the cortex determines the level of auxin accumulation with a given degree of efflux reduction. This is a property of the PIN layout of the whole segment, especially its lateral components. The efflux level inside the controlled area (which in this case is mostly set by  $P_{out,low}$ ) determines the time scales of auxin accumulation, apparently independent of the supply from outside the controlled area. This implies that the final efflux level in the controlled area (the region of the nodule primordium in biological terms) is important for predicting the time scale of local auxin accumulation, rather than the reduction factor compared to the unaffected root.

#### Auxin accumulation under $\text{Effl}\downarrow$ starts close to auxin sources

Looking closer at **figure 4.2** and **supplementary movies 1 and 2** we observe that despite the homogeneous change in the parameters, the initial auxin accumulation is strongest on two sides of the controlled area: the inner cortex and the rootward (=upstream) side. This is most pronounced in the reference segment with 10-fold reduced parameters (**figure 4.2B,D**). This is particularly interesting, as in legumes forming indeterminate nodules the formation of the primordium occurs predominantly in the inner cortex.

To assess the importance of this transient phenomenon we repeated the analysis from section 4.2.2 for the inner cortex (middle of the controlled area; data not shown). We found that also in the inner cortex the time scales are dominated by the efflux level inside the controlled area /  $P_{out,low}$ . The finding that the initial rate of auxin accumulation was faster in the inner cortex than in the central cortex was consistently retrieved in all reference segments and for different reduction factors (**figure 4.8**). The duration of the period with faster auxin accumulation in the inner cortex than in the middle cortex strongly depended on the value of  $P_{out,low}$  in the controlled area, rather than the factor of efflux reduction (compare both parts of **figure 4.8**). The lower  $P_{out,low}$  in the controlled area, the longer this period, so the greater the importance of the inner cortex dominated transient state.

#### 4.2.3 Precise distribution of cortical PINs can shift the lateral position of the auxin maximum

Determinate and indeterminate nodules differ in the radial position of the root cortical cell divisions from which they originate and (most likely) also in the position of the correlated auxin maximum. The formation of indeterminate nodules starts in the inner cortex,

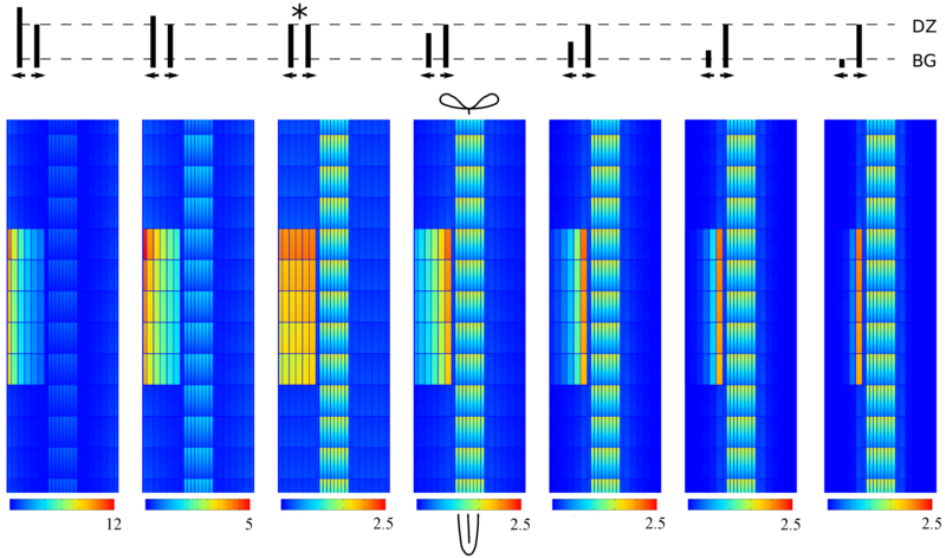


Figure 4.4: **Shifting the auxin maximum by changing the ratio of lateral PINs in the cortex.** All maxima are induced by 10-fold decreased efflux ( $\text{Effl}\downarrow$ ). The cartoon on top shows the ratio of peripheral to central lateral PINs in each cortical cell of the root segment. The original DZ segment is indicated with \*. Note that in all cases the highest concentration in the controlled area is well above the vascular concentration  $C_v$ .

whereas determinate nodule formation occurs in the outer cortex [27, 36, 37, 229, 244]. Despite an early increase from the inner cortex (and upstream edge), in our simulations so far the system reached a steady state with a homogeneous increase of the auxin concentration over the full width of the cortex. Coincidentally, the lateral PINs in our DZ reference segment are equally strong on the central and peripheral sides. We wondered if a bias in the lateral PIN positioning in the cortex, either to the periphery or the center, could shift the lateral position of the auxin maximum resulting from  $\text{Effl}\downarrow$  and if this would still allow for a sufficiently strong maximum.

To test this we created a set of reference segments based on the original DZ segment but with a varying ratio of inward to outward effective efflux permeability in the lateral walls of the cortical cells. We fixed the inward effective efflux permeability at  $P_{\text{out},\text{low}}$  and varied the outward efflux permeability. We then applied a 10-fold  $\text{Effl}\downarrow$  to these segments (figure 4.4). Indeed the lateral position of the maximum shifted along with the changes of the effective efflux permeability: most auxin accumulated on the side of the controlled area (inner/outer) of the largest effective efflux permeability. In all cases the maximum cortical concentration was well above the vascular level  $C_v$ .

Our scenario  $\text{Effl}\downarrow$  for the reduction of the effective efflux permeability preserves the inward to outward ratio inside the controlled area. As a consequence, changes in this ratio can shift the lateral position of the resulting cortical auxin maximum from inner to outer cortex. This means that the same change of effective efflux permeabilities can result in cortical auxin maxima in different positions, depending on the PIN layout of the root



segment concerned. In the discussion we will return to the importance of transient and steady state patterns relative to each other.

#### 4.2.4 Endodermal PIN layout strongly affects nodulation potential

The DZ PIN layout was the obvious choice for the susceptible zone, but as we did not start from actual legume PIN localization studies in the susceptible zone we asked ourselves if the EZ layout would also allow for the creation of a cortical auxin maximum. If yes, this would imply that the location of the susceptible zone is likely determined independent of the PIN layout (e.g. by the presence of growing root hairs only). If not, we could perhaps identify the feature of the PIN layout responsible for the difference in behavior.

We compared the response to 10-fold  $\text{Infl}\uparrow$  and  $\text{Effl}\downarrow$  in the DZ and a similarly created EZ segment. To make the EZ root segment we changed the PIN-layout (but not the cell sizes) of the DZ root segment, again according to the layout from Laskowski *et al.* [92] (**figure 4.5I**). This layout differs in two ways from the DZ layout: In the EZ segment the endodermis has a PIN level at the inward and rootward side, rather than ubiquitous and low as in the DZ segment. Additionally, the PIN level at the shootward side of the cortex cells is high in the EZ segment and low in the DZ segment.

Contrary to the DZ root segment (**figure 4.5C,D**), strongly increasing influx or decreasing efflux in the controlled area of the EZ segment showed little effect (**figure 4.5K,L**). The auxin concentration in the controlled area did increase (**figure 4.5G,H**), but the highest concentration reached was low compared to the vascular auxin concentration  $C_v$  (**figure 4.5K,L**).

This can be understood from the (resting state) auxin profiles: they arise as a direct consequence of the segment's PIN layout (**figure 4.5A,I**). Compared to the DZ segment, the EZ segment contained far less auxin in the cortex and the auxin concentration declined towards the outer cortex (**figure 4.5J and G,H**). The DZ segment, on the other hand, showed a flat transverse cortical profile (**figure 4.5B and E,F**). As in the case with reduced permeabilities (**figure 4.3D**) the profile within the controlled area always resembled the reference profile, apart from a certain offset (**figure 4.5E-H**).

These results show that the creation of a cortical auxin maximum is much harder with the EZ PIN layout than with the DZ PIN layout. As the only difference in PIN layout between the EZ (with little auxin increase upon 10-fold  $\text{Effl}\downarrow$ ) and the rightmost segment in **figure 4.4** is in the endodermis, this has to be the differentiating element. The transverse concentration profiles show that the difference in the endodermal PINs results in a much lower amount of auxin in the cortex (**figure 4.5B,J,E-H**), explaining the different nodulation potential.

### 4.3 Discussion

#### 4.3.1 Auxin accumulation in nodulation

Our simulations have yielded distinct auxin accumulation signatures for all conceptually different scenarios for creating a local auxin maximum along a root (increasing influx ( $\text{Infl}\uparrow$ ), decreasing efflux ( $\text{Effl}\downarrow$ ) and local auxin production ( $\text{Prod}\uparrow$ )). One of these,  $\text{Effl}\downarrow$ ,

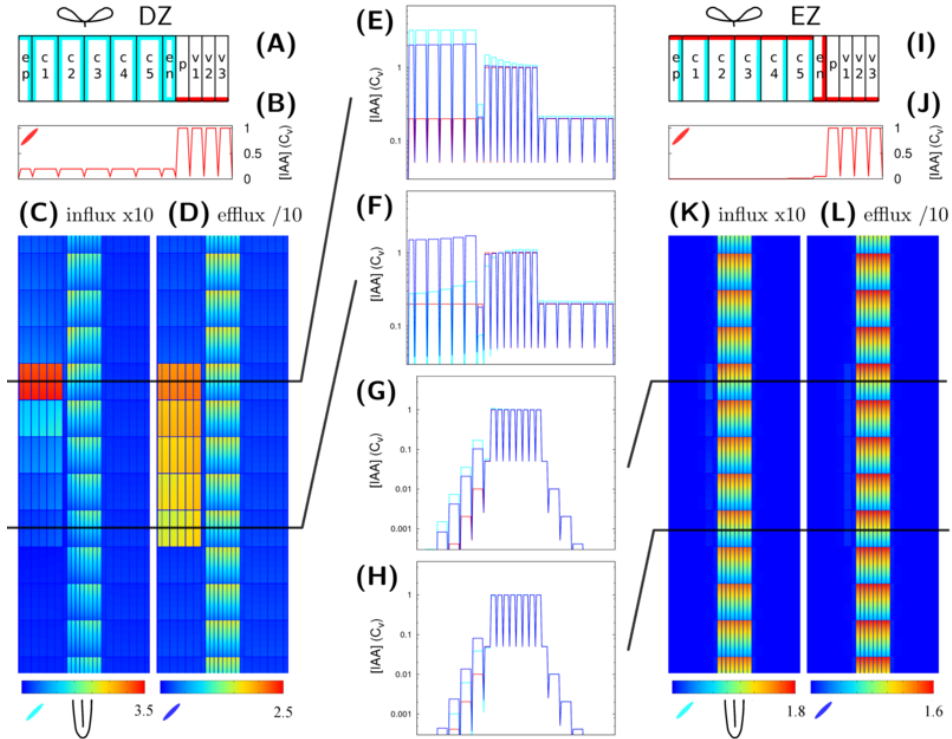


Figure 4.5: **Increased influx and decreased efflux in different zones of the root.** The same change in parameters has a different impact with different PIN-layouts (but equal tissue geometry). **A-F:** DZ, **G-L:** EZ parameters. Parameters for the left half of the root (**A, I**) on top ( $P_{out}$ -levels: red for “high”, cyan for “low” and white for “bg” as in figure 4.1B). The EZ PIN-layout results in a much lower auxin concentration in the cortex (compare reference profiles **B** and **J**). As a result, the impact of increasing the influx (**C, K**) or decreasing the efflux (**D, L**) is hardly visible with the EZ parameters (**K, L**). **E-H** show transverse concentration profiles on a logarithmic scale through the middle of the rows of cells indicated in **C, D, K, L** at the shootward and rootward side of the controlled area (Infl↑: cyan, Effl↓: blue). Note how the shape of the profiles in the controlled area largely resembles the shape of the respective reference profiles (in red).

provides a scenario that is most compatible with Nod factor induced cortical cell divisions, which form the start of nodule formation.

At the start of nodule primordium formation auxin accumulates either in the inner or outer cortex with a homogeneous concentration in a region of several cells long [36, 37]. Of the three simple scenarios  $\text{Effl}\downarrow$  is the only one that yields an auxin concentration that is both strong and fairly homogeneous along the length of the root (**figure 4.1D**). Moreover, the lateral location of this position can be shifted by small changes in the lateral PINs in the cortex (**figure 4.4**), allowing for both “Lotus” and “Medicago” locations of the induced auxin maximum. The downregulation of PIN proteins ( $\text{Effl}\downarrow$ ) as the mechanism behind auxin accumulation in the cortical cells that will form a nodule primordium is also compatible with several lines of experimental evidence: The induction of nodule-like structures with auxin transport blocker NPA [31, 245], a decrease of polar auxin transport 24 hours after treatment with *Rhizobium* [246].

A cytokinin response is observed early in nodulation [34, 247]. A gain of function mutation of a specific cytokinin receptor results in spontaneous pseudonodule formation [232] and several cytokinin response regulators are induced in nodule primordia [34, 35]. Moreover, this key nodulation hormone caused a reduction of PIN expression and/or membrane localization in several *Arabidopsis* tissues [38, 39, 248–250].

Therefore we argue that cytokinin is a likely candidate for inducing a removal of PIN proteins from the membrane in nodulation, leading to local auxin accumulation.

In our simulations auxin accumulation through efflux reduction was fast enough to be compatible with the known timing of nodulation events [27, 242]. Interestingly, the auxin accumulation started from the inner cortex (**figure 4.2** and movies 1 and 2), even though the change (reduction of efflux) occurred simultaneously in all cells of the controlled area. This “head start” for the inner cortex became more pronounced if the effective efflux level in the cortex was reduced to a lower value (**figures 4.2B,A, 4.8**).

The current view, in which Nod factor signaling induces cytokinin production, which reduces the amount of PIN in the membranes and thus invokes local auxin accumulation, invokes a naive question: why has the pathway evolved such that it includes cytokinin? Is this contingent, or necessary? In other words: would it be possible to create a cortical auxin maximum without a secondary signal such as cytokinin, but with a direct auxin signal?

First thing to note is that such a scenario is similar to our local production scenario ( $\text{Prod}\uparrow$ ). Most of the auxin signal (whether of epidermal or rhizobial origin) would be transported away from the production site and the little local increase will be ill confined (as in **figure 4.1E,H**). Moreover, due to the net shootward flux in the cortex the strongest accumulation will occur longitudinally shifted relative to the production site. These issues are further illustrated in **figure 4.10**. The use of a second signal, that is not transported away like auxin, bypasses this problem. Such a signal could induce local changes in the auxin transport system, which would then result in local auxin accumulation. Indeterminate nodules such as those of *Medicago* species are also in another way incompatible with a direct auxin signal. These nodules are formed from the inner cortex [27]. A direct auxin signal, if effective at all, would always induce divisions starting from the outer cortex. We have observed that under  $\text{Effl}\downarrow$ , auxin accumulation naturally starts from the sources of auxin, notably the inner cortex (**figure 4.2**).

From this we hypothesize that a secondary signal, in this case cytokinin, is required to induce a cortical auxin maximum in the vicinity of the original epidermal *Rhizobium* infection.

### 4.3.2 The accumulation mechanism affects the dimensions of the primordium

We have observed that in *Medicago* nodule primordia have a typical width of 5-6 undivided cortical cells which is much broader than a lateral root primordium (data not shown). Could this be a consequence of the mechanism underlying the local auxin accumulation?

Several authors have shown that in *Arabidopsis* the influx carrier AUX1 is strongly upregulated in the pericycle cells founding the lateral root primordium and their descendants, including the early primordium stages [76, 92]. We observed from our simulations that with increased influx a much narrower auxin maximum is formed than with decreasing efflux. This maximum can even be much narrower than the zone of Aux1/Lax expression. Data by Hirota *et al.* actually show an auxin maximum that is more focussed than the known area of AUX1 expression [236].

This combination of experimentally observed morphologies and auxin accumulation patterns together with the distinct patterns resulting from different scenarios for auxin accumulation lead to the hypothesis that the mechanism used for local auxin accumulation in a given case affects the dimensions of the emerging organ.

### 4.3.3 Steady state vs. transient patterns

We have identified two mechanisms that affect the lateral position of the Effl $\downarrow$  induced local auxin maximum. A possibility for shifting the steady state maximum towards either the inner or the outer cortex is changing the inward : outward ratio of lateral PINs in the cortex. In that case the steady state maximum will occur on the side of the largest effective efflux permeability (**figure 4.4**). From the dynamics we have observed that without such a lateral bias, the inner cortex accumulates auxin faster than the outer and middle layers (**figures 4.2 and 4.8**). Specially for strong reductions of the efflux transient patterns could become more important for development than the steady state. How do these two findings interact?

For an auxin maximum in the inner cortex we found two possibilities. The first is a very strong reduction of the efflux, to such a low level that the transient state becomes the only relevant one. The second comprises any reduction that is strong enough to obtain a sufficiently high steady state concentration at the location of the maximum, combined with an inward bias of the lateral cortical PINs. In that case the steady state and transient patterns will be similar, both with the strongest accumulation in the inner cortex. Moreover, with less auxin available in the outer cortex, the vascular tissue will become practically the only auxin source. This would strongly reduce the auxin accumulation from the upstream / rootward side of the controlled area we observed in **figure 4.2**, reducing the dynamical rootward/shootward differences in the process of the local auxin accumulation.

For an auxin maximum in the outer cortex, on the other hand, it seems important that the minimal efflux level in the region of the primordium does not become too low, as that would probably result in a long lived transient maximum in the inner cortex, something that has not been reported in auxin reporter studies in *Lotus* [36, 37]. Therefore it is more likely that in this case the steady state dominates the development. A slight efflux bias towards the outer side could further increase the auxin accumulation in the outer cortex.

#### 4.3.4 Are cortical PINs distributed differently for determinate and indeterminate nodules?

A key difference between determinate and indeterminate nodules is the main site of the primordial cell divisions: the outer or the inner cortex respectively. This has also been observed in the location of auxin accumulation [36, 37, 229]. Under the strict, but not necessarily fully true, assumption that the location of auxin accumulation perfectly predicts the division site and this turn perfectly predicts nodule type, we like relate our findings for the formation different nodule types.

The phylogenetic distribution of determinate and indeterminate nodule types within the legumes can not be explained by a single transition from an ancestral to a derived type [251, 252]. From this we conclude that the distinguishing difference must be relatively easy to “invent”. Additionally it has to be root autonomous, as grafting experiments show that the shoot does not affect the nodule type formed [253].

We have shown that changing the ratio of inward to outward PINs can be sufficient for shifting the axial position of the Effl $\downarrow$  auxin maximum. Slight differences in the PIN positioning appear to us as relatively easy changes in an evolutionary sense. Under the assumption that the position of the initial auxin maximum and resulting cell divisions is the key determinant for (in)determinate nodule type, we tentatively hypothesize that the lateral PIN localization in cortex of the DZ could differ between legumes making either nodule type, with a bias towards the center for indeterminate and no bias or a slight bias towards the periphery for determinate nodules.

Phosphorylation and dephosphorylation of PIN proteins by PINOID and PP2A respectively plays an important role in the polar targeting of PIN proteins [254, 255]. It has been shown that changes in PINOID activity impact the central/peripheral lateral distribution of PINs in another context [256]. Differences among legumes in the lateral PIN positioning in the cortex could perhaps result from differential regulation of these players.

#### 4.3.5 Biological limits of the simple changes

Although in our simulations we are essentially free to give any value to the effective influx- and efflux permeabilities, in reality they are bound by biological constraints. What does this mean for our results?

The increase of influx under Infl $\uparrow$  must result from a stronger expression of influx carriers. Of course, a plant can and will only produce a certain amount of these proteins. A frequently used value for AUX1 based influx ( $p_{\text{AUX1}} = 0.55 \mu\text{ms}^{-1}$  [4, 54]\*) permeability results in a carrier based influx that is 15 times higher than passive diffusive influx [54].

---

\*Note: this is not the same quantity as our effective influx permeability  $P_m$ .

Taking into account the strong upregulation of AUX1 observed in lateral root founder cells [76, 92], a difference between cells of up to two orders of magnitude can be considered reasonable. The model by Laskowski *et al.*, our starting point, assumes (initially) homogeneous AUX1 expression [92]. Under this assumption the maximum increase we used under  $\text{Infl}\uparrow$  is still reasonable, but could be close to the upper bound.

Under  $\text{Effl}\downarrow$  the decrease of efflux has to originate from a decrease of PINs or other efflux carriers from the membrane and/or a reduction of their activity. Our implementation of using the same reduction factor for all sides of the cell assumes that the efflux is facilitated by a single type of carrier, or, if it results from multiple types, that these all show the same response to the initial signal. Following current studies on PIN proteins, which show that they can disappear almost completely from the membrane upon addition of large amounts of cytokinin (see e.g. [250]), our approach is probably the most reasonable one, barring the explicit consideration of PIN activity regulation and localization dynamics.

However, a different type of efflux carriers, known as PGP, or ABCB [60, 61] has been suggested to give rise to a small but significant base efflux permeability even in the absence of PINs [257]. Additionally, some suggestions for a minimal efflux permeability in absence of efflux carriers appear in the literature [54, 258].

The importance of such a minimal efflux permeability will only surface with strong reductions of the efflux carriers. In that case the ratios between  $P_{out,high}$ ,  $P_{out,low}$  and  $P_{out,bg}$  will necessarily change inside the controlled area, resulting in transverse profiles that are flatter than the reference profile. How this affects the auxin accumulation throughout the cortex makes an interesting topic for further research.

### 4.3.6 On simple roots

The root segments used in our work are a generalization of PIN-layouts measured and modelled in Arabidopsis [92]. Lacking clear PIN layout data of the relevant zones of any legume's root this starting point is the best we have. It is likely that the rootward flux in the stele and the shootward flux in the cortex, which set the directional bias in the patterns we observe, are conserved. If more precise quantitative predictions are desired, however, actual legume PIN-data are needed.

This does not mean that our simple approach is but a poor man's choice. Its simplicity is also one of its strengths. The first recognition of the typical signature of each scenario is easier with a simple PIN- and tissue-layout than with a more "realistic" layout. In a next step we checked that they are also well distinguishable on a "realistic" layout (**figure 4.1F-H**). From this we conclude that the signatures we have discovered are general phenomena with a scope well beyond this pseudo-legume.

The way these signatures are affected by certain aspects of the PIN-layout sets requirements on the actual PIN-layout of diverse legumes. These observations brought us to the tentative hypothesis that differences in the distribution of cortical PINs in the lateral walls might distinguish determinate and indeterminate legumes. We also found a very important role for the endodermal PIN-layout on the overall nodulation potential of a stretch of root, as it is pivotal in determining the amount of auxin available in the (inner) cortex.

Our approach is based on the strong link between the positions of auxin carriers and the steady state auxin concentration distribution. We use differences in the patterns result-

ing from different scenarios (Infl $\uparrow$ , Effl $\downarrow$  and Prod $\uparrow$ ) to address the differential likelihood of these scenarios in a particular situation. This approach may also prove useful in elucidating PIN positioning information from fluorescence data. This data can be hard to interpret, because cell membranes from neighbouring cells are usually less than a wavelength apart. When available, information on the auxin accumulation pattern could be used to find the most likely positioning scenario that fits the fluorescence data.

### 4.3.7 The next step: a step back

In this work we applied all changes in an all-or-nothing manner to a well defined block of cells (the controlled area). This proved a very powerful approach for recognising different patterns and their distinguishing features. No plant in its right (absence of) mind, however, will ever show exactly such a precise and all-or-nothing change. This brings forth a very natural follow-up question: how is, upon contact with *Rhizobium*, such a confined local change in the auxin transport/metabolism induced? What mechanism(s) can spatially confine the response to the signal (likely cytokinin) originating from a single epidermal cell to the correct area? The dynamic localization of PIN proteins [259] will most likely play an important role in the establishment of a local auxin maximum.

## 4.4 Methods

### 4.4.1 General approach

We have simulated auxin diffusion and transport on a static root tissue using conventional numerical methods (4.4.5). We explicitly model intracellular auxin concentrations. This is customary for models describing root tissue [54, 91–93, 243], as, assuming realistic diffusion constants, the relatively long cells give rise to significant concentration differences between the ends of the cell [82]. Following these previous works we also use a static influx/efflux/production parameters within individual simulations (4.4.2), focussing on the consequences of our different scenarios (4.4.4). For ease of interpretation we normalize auxin concentrations with the average vascular level (4.4.6) of the respective reference segment (a segment without any change in the controlled area).

### 4.4.2 Tissue geometry and PIN-layout

Our simulations are carried out on a 2D root segment representing the susceptible zone of a generalized legume. Current model legumes typically have 4–6 cortical layers, so we have created a segment with five cortical layers. Cell sizes were chosen to match the typical length of cortical cells in the susceptible zone, a representative root diameter and the right ratio between cortical and vascular tissue, see **table 4.1** and **figure 4.1A**.

Lacking good PIN position data for the susceptible zone of model legumes (*Medicago* or *Lotus*), we used the DZ part of the *Arabidopsis* model by Laskowski *et al.* [92] as a starting point, as the differentiation zone comes closest to the susceptible zone. *Arabidopsis* has only a single cortical layer, so we copied the parameters for the cortical layer to four additional layers. All cells of the same type (e.g. cortex, epidermis, vascular) have the same PIN distribution, as in [92]. The resulting PIN layout of the DZ root segment

is shown in **figure 4.1B**. We also used the EZ PIN layout from the same paper (shown in **figure 4.5I**).

### 4.4.3 Boundary conditions

The biological root continues on both (rootward and shootward) ends of the segment (**figure 4.1A**). We modelled these edges with an open boundary consisting of a row of open cells of half the normal length. The concentration at the boundary grid points is fixed. Lateral boundaries have a no-flux boundary condition: no auxin leaves from the epidermis into the surroundings.

The full root simulations from Laskowski *et al.* show almost no longitudinal gradient within the DZ. Based on this we chose the same concentration profile on both the rootward and shootward side of the segment. In this situation the transverse concentration profile settles at a fixed profile, which is to a very large extent dictated by the PIN layout of the segment. This transverse concentration profile we call “**resting state**”, because in theory one could create an infinitely long segment with the same concentration profile everywhere along its length by forever repeating the same transverse building blocks (as long as decay is negligible). The rootward and shootward boundaries are fixed at this resting state. Although the concentrations at these boundaries are fixed, a net flux of auxin through the segment does occur.

Considering the whole root, it is conceivable that at the edge of the DZ the resting state is not fully reached yet and the actual concentrations at the boundary are different. A small deviation from the resting state is perhaps far more likely than none at all. For this reason we tested the impact of deviations from the resting state profile at the boundaries of the DZ segment. Looking at a transverse line through the middle of the cells (all at the same distance from the rootward boundary) the resting state profile has the same concentration in all vascular cells including the pericycle. As explained in 4.4.6, this level is normalized to  $1C_v$ . In the DZ fragment all peripheral layers (i.e. epidermis, cortex and endodermis) have a resting state concentration of  $0.2C_v$  (**figure 4.5A,B**).

We changed the boundary conditions of the DZ segment by changing the ratio between the vascular and the peripheral auxin concentration ( $C_v$  and  $X$  in **figure 4.9A**). After equilibration we renormalized the total amount of auxin with the transverse row of cells with a profile closest to the resting state. We found that in the shootward direction the deviation from the resting state transverse profile (integrated over the whole line) decayed exponentially  $\sim e^{-n/4.3}$  (with  $n$  the cell number counted from the rootward edge of the segment). This decay constant implies that the deviation from the resting state is halved every 2.9 cell lengths in the shootward direction (**figure 4.9B**). In the opposite direction deviations decay even faster.

With this we are confident that a segment without a longitudinal gradient, settled at the resting state transverse concentration profile is a very reasonable model of the DZ situation.

### 4.4.4 Changes are applied in the “controlled area”

We investigate both dynamic and steady state effects of homogeneous changes of a block of cells situated on one side of the root, dubbed controlled area. It consists of all five



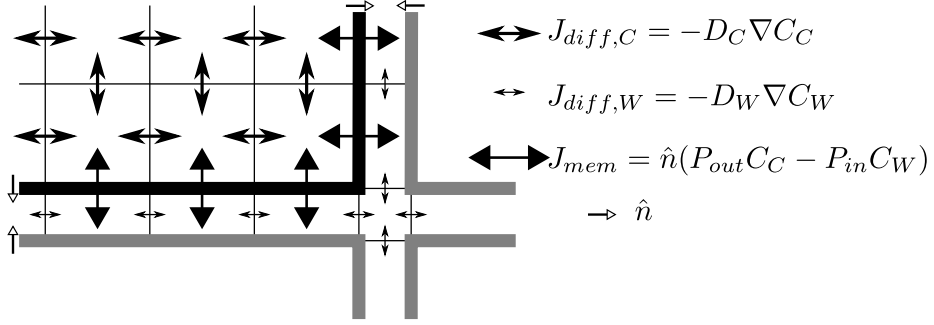


Figure 4.6: **Simulation details.** The figure shows the simulation grid of a small corner section of a cell and the surrounding apoplast. Membranes are indicated with thick lines, the grid with thin lines. Different types of arrows indicate the different equations: diffusion inside the cell and within the apoplast (differing only in the value of the diffusion constant) and active + passive transport over the membrane.  $\hat{n}$  is a unit length vector pointing out of the cell. Note that the apoplast thickness is not drawn to scale.

cortical layers and the epidermis and is five cells ( $5 \times 100 \mu m$ ) long (figure 4.1A). This corresponds well with the typical length of a nodule primordium. The same change is applied to every cell in the controlled area:

- (n-fold) Inff $\uparrow$ : increase the effective influx permeability ( $P_{in}$ ) (n times)
- (n-fold) Effl $\downarrow$ : decrease the effective efflux permeabilities ( $P_{out,bg}$ ,  $P_{out,low}$  and  $P_{out,high}$ ) (n times)
- Prod $\uparrow$ : local auxin production with the given rate (per volume) in  $C_v s^{-1} \mu m^{-3}$

#### 4.4.5 Simulation method

We use in house developed C++ code for simulating the transport and metabolism of auxin. Our simulations are carried out on a 2D longitudinal slice through the center of a generalized root segment, in most cases representing the DZ (figure 4.1A,B). We simulate auxin diffusion (in cells and walls separately) and transport (over membranes) with subcellular precision (figure 4.6; pixel sizes in table 4.1). The apoplast is considered as a separate continuous compartment. Spatial coordinates are denoted with  $x$  (transverse) and  $y$  (rootward or longitudinal) with coordinates in  $\mu m$ .

Within a compartment auxin moves by diffusion, with different diffusion constants for cells (C) and walls (W):

$$J_{diff,CW}(x,y) = -D_{CW} \nabla C(x,y) \quad (4.1)$$

with  $C(x,y)$  the auxin concentration at a given position and  $D_{CW}$  the respective diffusion constant. The combined effects of active transport and passive permeability are grouped into a single parameter for effective efflux permeability  $P_{out}$  and effective influx permeability  $P_{in}$ . In principle  $P_{out}$  can be set for each face of a cell independently, whereas a cell

always has a single value of  $P_{in}$  for all four faces. These parameters control the flux over the membrane:

$$J_{mem}(x, y) = (P_{out,xx}C_C(x, y) - P_{in}C_W(x, y)) \cdot \hat{n} \quad (4.2)$$

Here  $P_{out,xx}$  is the relevant effective efflux permeability. In the reference segment three different levels are used: high, low and bg for strong and weak PIN expression and a background level due to ubiquitously expressed PINs respectively. In the choice of three levels we follow [92].  $\hat{n}$  is a unit length normal vector pointing out of the cell. We follow [92] in assuming a single value of  $P_{in}$  for the whole reference segment.

These equations are solved using the Alternating Direction Implicit (ADI) algorithm [183] using a 2D finite volume description of the tissue. We use a rectangular grid topology with different volume sizes within the cell and wall compartments and at junctions. This allows us to use a realistic cell wall width without wasting excessive memory on the cells' interiors.

The integration time step is chosen depending on the interval between measurements, with typical values of 0.5, 1 and 2.5 seconds. Results were checked for numerical artifacts and if necessary the time step was adapted.

#### 4.4.6 Parameters

When thinking of the root segment as a thin 3D slice with unit thickness ( $1\mu\text{m}$ , much thinner than a cell's diameter) all parameters and quantities can be used in their usual dimensions. For reasons of familiarity we present them as such, although our simulations are carried out on a strictly 2D template.

For an overview of all model parameters, see **table 4.1**.

#### Normalization of IAA concentration units

By lack of a real 3D volume, concentrations units are arbitrary. This means all concentrations can be multiplied with an arbitrary constant without affecting the model's behaviour. (The only parameter that contains concentration units is the auxin production rate. Thus, this is the only parameter that scales with the actual concentration). For the ease of interpretation we choose to scale all concentrations such that the average auxin concentration in the centre of the vascular cylinder of a reference root segment without a longitudinal gradient is  $1 C_v$ . Without information about the cells', likely differential, sensitivity to changes in the auxin concentration and/or the absolute concentration it is probably most insightful to compare concentrations to a known level. Nevertheless, it is important to bear in mind that cells could show different responses to the same auxin concentration or change.

### Disclosure/Conflict-of-Interest Statement

No conflicting interests

Parameter	(Default) value	Description
$D_C$	$300 \mu m^2 s^{-1}$	Auxin diffusion constant inside cells [92]
$D_W$	$44 \mu m^2 s^{-1}$	Auxin diffusion constant in apoplast [93]
$P_{out,high}$	$20 \mu m s^{-1}$	Effective efflux permeability, high value [91, 92]
$P_{out,low}$	$5 \mu m s^{-1}$	Effective efflux permeability, low value [91, 92]
$P_{out,bg}$	$1 \mu m s^{-1}$	Effective efflux permeability, background value (due to misplaced PINs) [91, 92]
$P_{in}$	$20 \mu m s^{-1}$	Effective influx permeability [91, 92]
$C_v$	concentration	The average auxin concentration in the vascular tissue is normalized to 1 $C_v$ . (Strictly speaking, $C_v$ is not a parameter.)
$p$	$0(C_v \mu m^{-3} s^{-1})$	Auxin production rate; Default: no production. Estimate for reasonable rates based on [75], scaled relative to total concentrations [76]: order $10^{-4} C_v \mu m^{-3} s^{-1}$ .
$l$	$100 \mu m$	Cell length
$w_C$	$20 \mu m$	Width of cortical cells
$w_x$	$10 \mu m$	Width of other cells
$d_W$	$0.2 \mu m$	Wall thickness [93]
$d_p$	$2 \mu m$	Pixel size for the cells' interior
$t$	0.5, 1, 2.5 s	Integration time step (dependent on interval between measurements)

Table 4.1: Overview of model parameters

## Acknowledgement

We thank both reviewers for their constructive feedback on the manuscript.

**Funding:** The work of EED is funded within the research program of the Netherlands Consortium for Systems Biology (NCSB), which is part of the Netherlands Genomics Initiative (NGI)/NWO, RG is funded by NWO VIDI grant 864.06.007 and the work of BMM is part of the research program of the “Stichting voor Fundamenteel Onderzoek der Materie (FOM)”, which is financially supported by the “Nederlandse Organisatie voor Wetenschappelijk Onderzoek (NWO)”.

## Supplemental Figures

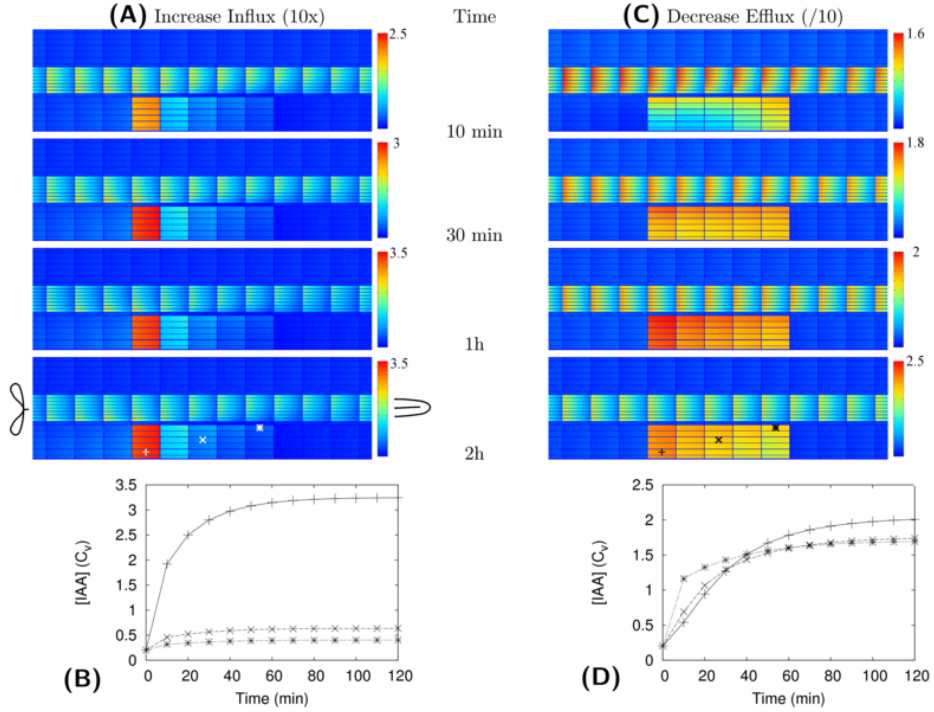


Figure 4.7: **Dynamic response to influx and efflux changes compared.** At  $T = 0s$  the influx is increased 10-fold (Infl $\uparrow$  **A**, **B**) or the efflux is decreased 10x (Effl $\downarrow$  **C**, **D**) in the controlled area. The top part shows snapshots of selected time points (**A**, **C**). Graphs **B** and **D** show the auxin concentration in the three indicated cells (see lowest snapshot) over the first 2 hours. Note that under Infl $\uparrow$  the new steady state is reached faster than under Effl $\downarrow$ , but the reverse is true for the most rootward inner cortex cell of the controlled area (marked \*).

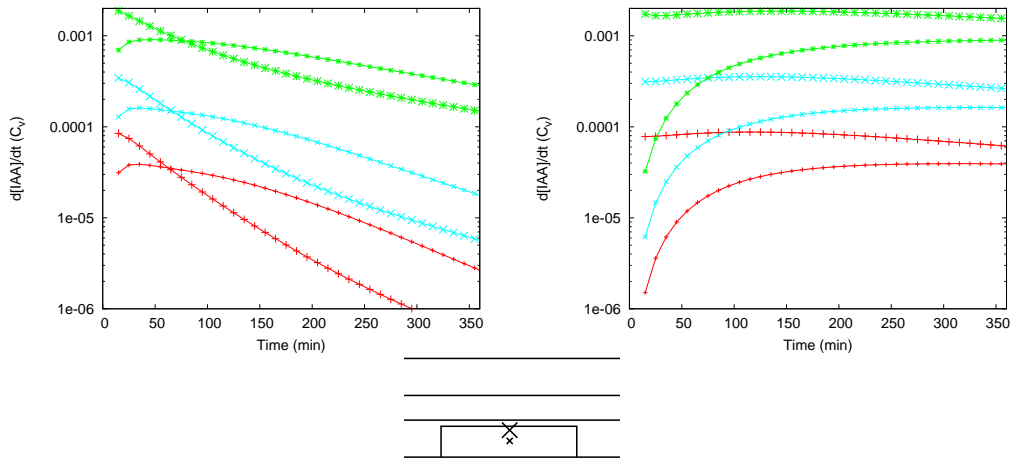


Figure 4.8: **Faster auxin accumulation in the inner cortex with  $Effl_{\downarrow}$ .** Time derivatives of the auxin concentration in two different cells in the (longitudinal) middle of the controlled area: inner cortex (large symbols) and central cortex (small symbols). Colors and symbols as in **figure 4.3** (For clarity of the graphs the two cases with  $P_{other}/10$  are omitted. In both cases they are very similar to their respective matches from the lower two pairs of curves, as in figure 4.3C). In all segments,  $P_{out,low}$  in the controlled area is reduced to the same value:  $P_{out,low} = 0.05 \mu ms^{-1}$  (top),  $P_{out,low} = 0.005 \mu ms^{-1}$  (bottom). In the beginning the auxin concentration increases faster in the inner cortex than in the central cortex, as can be seen from the higher rate of change of the auxin concentration. With a stronger reduction the efflux this period of faster increase in the inner cortex was longer.

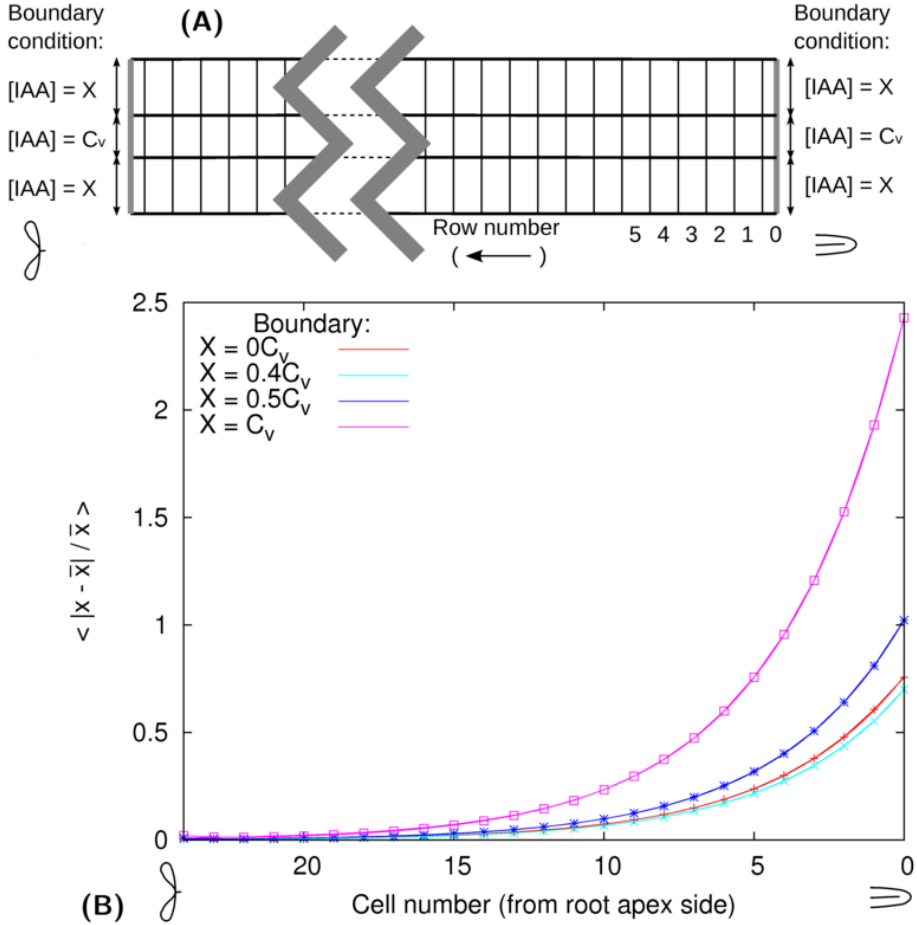


Figure 4.9: **Test of DZ parameters with respect to disturbed boundary conditions.** The cortical auxin concentration at both edges is clipped at different values ( $X$ ) relative to the vascular concentration at the edge, as shown in **A**. After equilibration with these boundary conditions and normalization with the central vascular auxin concentration the transverse profile through the center of the cells is compared to the resting state profile for four values of  $X$  (**B**). In the resting state profile  $X \approx 0.2C_v$ . For each value of  $X$  the deviation from the reference decays exponentially according to  $e^{-n/\tau}$ , with  $\tau = 4.3$  and  $n$  the number of the cell counted from the rootward edge (curves fitted to the data). This means that the deviation from the resting state profile is halved every 2.9 cells.

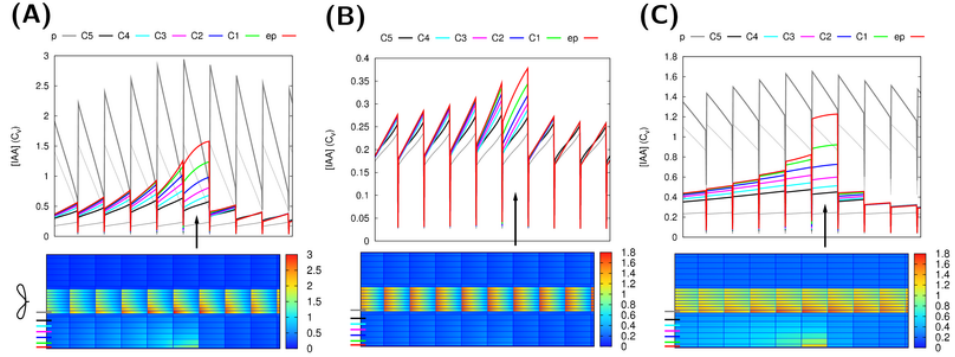


Figure 4.10: **Auxin is not suitable as a direct signal.** In all three cases auxin is produced in a single epidermal cell (position is indicated with an arrow in the line graphs). For a notable increase of the auxin concentration in some parts of the segment, very high production rates are needed, even with slowed down transport. Moreover, in the inner cortical layers the auxin concentration increases a bit over a wide region and the maximum increase does not occur closest to the production side, but shootward of it (downstream considering the cortical flow direction). The bottom images show steady state auxin concentrations. The graphs on top show the concentrations in the indicated layers (thick lines: pericycle, 5x cortex and epidermis). The resting state concentrations (i.e. before production started) are plotted in thin black (vascular) and grey (cortex) lines. **A,B**: default parameters, **C**: “slowed down” parameters from **figure 4.2B**: all effective permeabilities are reduced by a factor 10. Production rates are much higher than in **figure 4.1E,H**, as here only a single cell produces:  $0.1 C_v \mu m^{-3} s^{-1}$  (**A**),  $0.01 C_v \mu m^{-3} s^{-1}$  (**B,C**). Note that in **A** the producing epidermal cell produces the full amount of auxin present in a vascular cell (both have the same size) of the reference segment every 10 seconds. The total amount produced per second is slightly more than half of the total in **figure 4.2E** and consequently from several cells rootward of the production site onwards the auxin concentration is significantly increased in all cell files. We consider this value (**A**) absurdly high, but use it because hardly any change is seen with the already high production rate of **B**. This is because the auxin is very efficiently transported away from the production site. Reducing the efficiency of this transport by reducing all effective permeabilities of the whole segment (“slowing it down”, **C**), a less absurd production rate is enough to support an obvious accumulation, but the issues of ill confined auxin accumulation and a shift of the maximum in the inner cortical layers (C5 - C3) remain.





---

## **Playing the auxin pipeline – consequences of different mechanisms for local auxin accumulation**

---

The formation of a new root lateral organ requires the formation of a primordium, which is marked by the formation of an auxin maximum.

On an abstract level, the largest part of the root can be seen as a pipeline, facilitating the transport of (mostly) shoot-derived auxin to the root tip(s). Formation of root lateral organs happens along this pipeline.

Different mechanisms for local auxin accumulation along a pipeline, increased influx, decreased efflux and local production, can produce strikingly different spatial signatures.

We use a 1D model alongside a more realistic root model, functioning as a null model to assess how the tissue context influences the different signatures.

We also investigate the impact of (non-targeted) symplastic transport on these signatures.

Translating our results to a developmental context, we find that enhancement of local reflux is a potentially more powerful source of extra auxin (compared to 1D) than redistribution of flux density and that this makes most difference with increasing the influx. We also discuss the impact of symplastic transport on the potential for root lateral organ initiation.

Controlled area (CA)	Part of the tissue where a local change of parameters is applied (see figure 5.1B).
Embedding tissue	All modelled tissue outside the CA (see figure 5.1B).
Infl $\uparrow$	Scenario with an increase of the effective influx permeability ( $P_{inf}$ ) in the CA.
Effl $\downarrow_0$	Scenario with a reduction of the effective efflux permeabilities ( $P_{eff,x}$ ) in the CA. $P_{eff}$ is reduced by the same factor at all faces of a cell.
Effl $\downarrow_{base}$	Scenario with a reduction of the effective efflux permeabilities ( $P_{eff,x}$ ) in the CA, with a certain minimum ( $P_{eff,base}$ ). The remaining part, $P_{eff} - P_{eff,base}$ is reduced by the same factor at all faces of a cell.
Prod $\uparrow$	Scenario with local auxin production with rate $Q$ in the CA.
Resting state	Relation between average concentration ( $\bar{c}$ ) and steady state flux ( $\bar{J}$ ). An infinite (OR: sufficiently long) tissue without production or decay settles at this relation
Target concentration	Steady state concentration that would be reached in the CA after a change, if it were long enough. Similar to the resting state for a homogeneous tissue.

Table 5.1: List of abbreviations and concepts

## 5.1 Introduction

The phytohormone auxin plays an important role in plant development. From the formation of the embryonic axis to the adult processes of phyllotaxis and root lateral organ formation, a local auxin maximum is found at the site of meristem/organ initiation [36, 260].

Conceptually, a few obvious options exist for increasing the local auxin concentration in a cell: increasing its influx capacity, decreasing its efflux capacity and switching on/increasing local auxin production [182]. Previous work showed that these options all show their own characteristic signatures in the context of a root, which serves as a shoot-to-root auxin pipeline [182].

That work was focussed on the specific context of the legume-rhizobium symbiosis, but auxin plays many roles in many contexts (e.g. see [46, 260]). Other examples involving local auxin accumulation along the root pipeline include lateral root initiation [228] and the formation of root galls by parasitic nematodes [261, 262]. For wider applicability of this knowledge, we now investigate in a more generic context under what conditions different mechanisms produce experimentally distinguishable signatures. This could be used for making inferences about either a mechanism for local auxin accumulation from flux patterns in the tissue, or vice versa, whenever either one is easier to address experimentally. We address the question under what conditions the different mechanisms for local auxin accumulation are (most) effective, aiming to better understand why evolution has “chosen” different mechanisms for local auxin accumulation in different developmental programmes such as lateral roots and root nodules.

In this study we also investigate the impact of symplastic transport, because auxin is so small it can easily move through open plasmodesmata. Recent measurements in the root meristem zone have found rates that could drastically reduce the efficiency of polar

auxin transport [163], specially in long cells. Perhaps not surprisingly, the regulation of symplastic transport is of such great developmental importance that several known mutations affecting this regulation are lethal [115–117, 263]. As symplastic fluxes are hard to monitor *in planta*, models are an ideal tool to assess the potential effects of symplastic transport.

The primary context of our study is a “pipeline” for auxin transport between different parts of the plants, for example from the shoot to the root apex. This function requires that net decay of auxin within the tissue is very small. For simplicity we assume there is no decay.\*

The easiest model of such a plant “pipeline” is a 1D model of a single line of cells, all pumping auxin in the same direction. This would be in line with the first models of auxin transport [84, 85]. Other modelling studies have shown, however, that even in long stretched tissues such as roots the layout of the whole tissue can dramatically affect the model’s behaviour (e.g. [91–93]). We will therefore use a combined approach. We will use a 1D model for analytical simplicity, deriving the “core” patterns, and use these as a null-model to better understand what happens in a full root context. As an example for the full root we will use a previously used 2D model of a generalized (Legume) root [182].

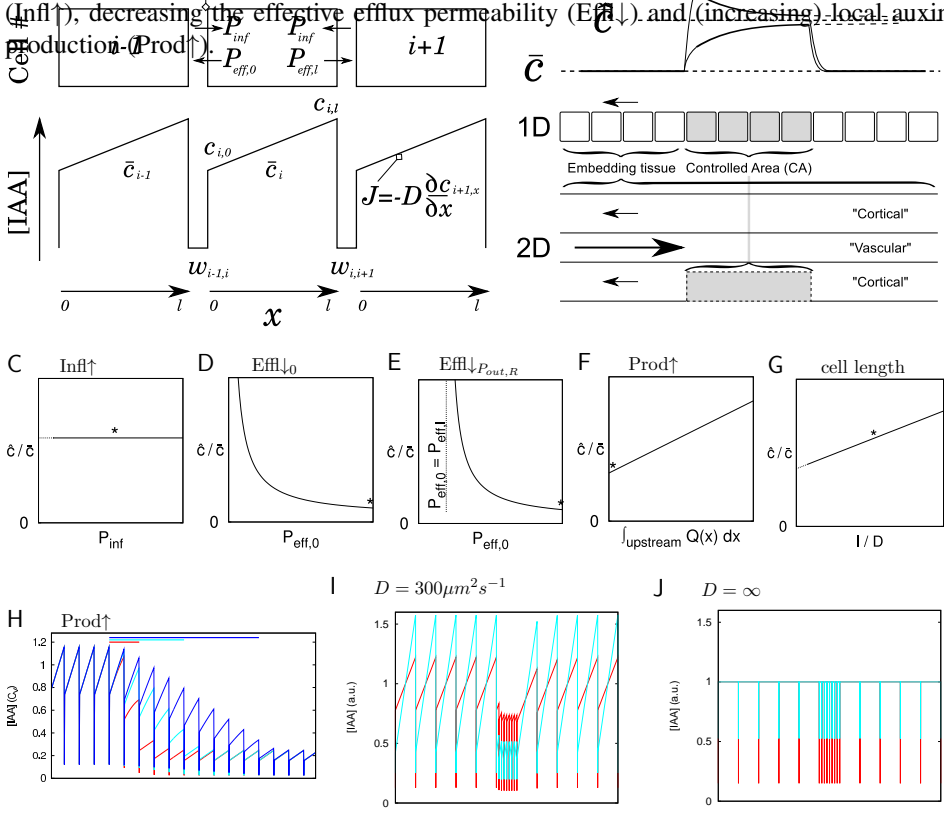
Both versions of the model are based on the biochemistry and physiology of auxin transport. Auxin is a weak acid (for the most abundant natural auxin, IAA,  $pK_a \approx 4.8$ ). The protonated form (IAAH) can passively cross membranes, whereas the charged form ( $IAA^-$ ) hardly can. Because the pH is much lower in the apoplast (e.g. pH=5.3) than in the cytosol (e.g. pH=7.2), auxin transport into the cell is possible against the difference in the total auxin concentration ( $IAAH + IAA^-$ ). This is the basis of what is called the chemiosmotic model [79]. The auxin influx can be enhanced by more than an order of magnitude by influx carriers (AUX1/LAX family, [54]). The high cytosolic pH makes efflux almost fully dependent on efflux carriers, as from the PIN [58, 59] and PGP/MDR families [60, 61].

Figure 5.1A shows a schematic overview of the model components and parameters. Assuming that the carriers operate far from saturation (supported by e.g. [264]), we model all auxin transport over membranes using effective permeabilities for total influx and total efflux (similar to [91] and many others), denoted  $P_{...}$ . For the influx we use a single value  $P_{inf}$  for all sides of the cell, because the influx carriers are typically found homogeneously distributed or at elevated levels on both the apical and the basal end of a cell [55–57]. The extensively studied PIN proteins often show a polar localization [62, 63], so we use a different value  $P_{eff}$  for each face of the cell. In the 1D version of the model, they are indicated  $P_{eff,0}$  (left side of the cell) and  $P_{eff,l}$  (right side of the cell). Inside the cell the auxin moves by diffusion, giving rise to an intracellular gradient. For this reason we write  $c_{i,x}$  for the concentration in cell  $i$  at position  $x$  inside the cell ( $x = 0$  indicates the left end of the 1D cell) and  $\bar{c}_i$  for the average concentration in the cell. We assume that walls are so thin, that no gradients are formed over the width of the wall. A more detailed model description and an overview of the default parameter values is provided in 5.5.

With this model we will investigate the effect of local changes in the auxin transport and metabolism. For this we homogeneously change parameters in a block of cells, which we call the *Controlled Area* (CA). The other cells will be referred to as *Embedding Tissue*.

\*Adding a small decay will complicate the mathematical appearance of the formulas and the validity of concepts we use in infinite pipelines, but hardly affect the way the local patterns will look to the eye.

Following [182] we will investigate the following scenarios (summarized in table 5.1) for locally increasing  $J$  and  $P_{\text{auxin}}$  concentration: increasing the effective influx permeability ( $\text{Infl}\uparrow$ ), decreasing the effective efflux permeability ( $\text{Effl}\downarrow$ ) and (increasing) local auxin production ( $\text{Prod}\uparrow$ ).



**Figure 5.1: Model description (A), setup for local changes (B) and target concentration (C-G).** **A:** Model equations and parameters. We explicitly take into account intracellular diffusion and the apoplast. Note that we use  $P_{\text{eff},0} > P_{\text{eff},l}$ , resulting in a flux to the left. **B:** Setup. Changes are applied to the controlled area (CA; indicated in gray). The number of cells in the CA varies. The resting state concentration ( $\bar{c}$ ) and target concentration ( $\hat{c}$ ) are illustrated above. **C-G:** Impact of changing individual parameters inside the CA. The starting point (default parameters) is indicated with a \* in each figure. For  $\text{Prod}\uparrow$  (F), the resting state concentration upstream and downstream of the CA are compared. For the change in concentration, the total amount produced in the CA matters, i.e.  $\int_{\text{upstream}} Q(x) dx$  (H). Reduction of cell size leads to a decrease of the average concentration (I). This effect disappears when intracellular diffusion is ignored (mathematically:  $D \rightarrow \infty$ ) (J).

In the implementation of  $\text{Effl}\downarrow$  we take a somewhat different approach than [182]. Several classes of auxin efflux carriers exist and even among the plasma membrane PINs the response to certain stimuli (e.g. application of cytokinin) is different for different PINs [39]. We therefore split the effective efflux permeability in two parts:  $P_{\text{eff}} = P_{\text{eff},\text{resp}} + P_{\text{eff},\text{base}}$ . Of this, only the first part,  $P_{\text{eff},\text{resp}}$  responds to the change we apply. It is reduced

by the same factor for all faces of the cell. We use the same  $P_{eff,base}$  on all sides of the cell, with short notation  $\text{Effl}\downarrow_{base}$ . Using this notation,  $\text{Effl}\downarrow_0$  indicates the original  $\text{Effl}\downarrow$  scenario used in [182] without a separate base level. The mechanistic effect of this split of the efflux parameter is that the ratios of efflux over individual faces of the cell can change, which will have important consequences.

We find that in many cases the polarity of the pattern is dependent on the direction of the local auxin flux. It turns out that the asymmetric (polar) positioning of the auxin carriers (efflux carriers) inside and outside the CA is essential for distinct patterns. Without this asymmetry, the differences between influx and efflux based accumulation vanish. Moreover, the different mechanisms for local auxin accumulation differ in their (in)ability enhance local recycling of auxin (“reflux loops”), explaining how their tissue signatures differentially differ from their respective 1D core pattern. They also differ in their sensitivity to symplastic connections between cells. We discuss the potential developmental importance of these findings in the context of root lateral organ development.

## 5.2 Results

### 5.2.1 Solutions for a 1D pipeline

As a null-model for understanding the complex situation of plant organs, we started with a simple 1D model of an “auxin pipeline”.

The consists of a chain of equations, with the transport over the wall (in two steps) linking the end of one cell to the beginning of the next and the intracellular transport linking both ends of a single cell. For a steady state profile, we can plug in the (flux dependent) steady state solution for the intracellular profile of a single cell. This system closes with two non-redundant boundary conditions in the form of concentration or flux at a specific location. In principle, this approach will yield a solution for any system with consistent boundary conditions<sup>†</sup>, no matter how diverse the individual cells.

In specific cases it is possible to derive a more explicit formula for the overall profile of (part of) the tissue. As we are interested in the pipeline, we assume that production and decay along the way are negligible. Under these conditions, the intracellular profile is a straight line with slope  $\frac{-J}{D}$  and the tissue level profile of the average concentrations is an offset exponential within parts consisting of identical cells (same length and other parameters; see appendix B.1.2 and equation B.18)<sup>‡</sup>. The steepness of this profile depends, amongst others, on the flux through the tissue. The implications of this observation will be discussed in more detail in section 5.2.4. A complete description at the tissue level then follows from joining partial profiles.

<sup>†</sup>Not every combination of boundary conditions imaginable is consistent. For example: without any production or decay, mass conservation requires that the flux through the tissue is necessarily the same at every position.

<sup>‡</sup>Some authors report coarse graining to a single (rather than offset) exponential profile (e.g. [171]). This is an effect of not considering intracellular gradients in the coarse graining calculation.

### Resting state and target concentration

If the tissue of identical cells is long enough, the concentration will settle a particular level. We will call this the *Resting State* concentration ( $\bar{c}$ ), which linearly depends on the resting state flux ( $\bar{J}$ ). Note that this concept only makes sense without net decay/production in the relevant area.

$$\bar{c} = J \frac{\frac{l}{2D}(P_{eff,l} + P_{eff,0}) + 2}{P_{eff,l} - P_{eff,0}} \quad (5.1)$$

In our setup we use an embedding tissue at resting state, which sets the steady state flux everywhere in the tissue. A local change of parameters in the middle of this, in the controlled area (CA; see figure 5.1B), could result in a local change of the concentration. If the CA area would be large enough, also there the concentration would at some particular level. This can be seen as the potential impact of a (local) change. We define the *Target Concentration*  $\hat{c}$  as the concentration reached in an infinitely long CA (figure 5.1B), stressing that this is the *potential* impact.

$$\hat{c} = \bar{c} \frac{P_{eff,l} - P_{eff,0}}{\hat{P}_{eff,l} - \hat{P}_{eff,0}} \cdot \frac{\frac{l}{2D}(\hat{P}_{eff,l} + \hat{P}_{eff,0}) + 2}{\frac{l}{2D}(P_{eff,l} + P_{eff,0}) + 2} \quad (5.2)$$

In this, the parameters of the CA are designated with a “hat” (^) and those of the embedding tissue without. Figure 5.1C-G shows how different changes in the CA affect the target concentration.

Changing the effective influx permeability  $P_{inf}$  has no impact on the target concentration (figure 5.1C). The reason is that (within a homogeneous tissue segment)  $P_{inf}$  is the same on both sides of the wall and therefore cancels from the equations (see appendix B.1.2).

Decreasing the efflux permeability showed a hyperbolic relation with the actual efflux permeability. The target concentration tends to infinity when approaching  $P_{eff,x} = 0$  ( $x = 0$  or  $x = l$ ; figure 5.1D:  $\text{Effl}_{\downarrow 0}$ , keeping a constant ratio  $\frac{P_{eff,0}}{P_{eff,l}}$ ), or  $P_{eff,x} = P_{eff,base}$  (figure 5.1E:  $\text{Effl}_{\downarrow base}$ ; going towards the same  $P_{eff,x}$  on both sides of the cell).

Production is not included in the resting state formula, as the concept of a resting state only makes sense in absence of net production/decay. It is possible, however, to calculate the impact of production by comparing the resting state on both sides of the production site. For this we choose to fix the upstream concentration at unity and measure the increased concentration as a function of the total amount of auxin produced in the CA (figure 5.1F). The rationale behind this was that, without decay, all matter produced has to be transported away, so directly adds to the total flux. This implies that the size of the production site (the CA) doesn't matter, only the total amount produced. Varying the number of producing cells, but keeping the total production constant confirmed this (figure 5.1H).

The target concentration also depends on cell length ( $l$ ) or more precisely on  $l/D$  (figure 5.1G). Figure 5.1I shows how cell divisions could decrease the average auxin concentration at the division site, if the cells are otherwise identical to their parents / the embedding tissue. This effect is a direct consequence of the concentration differences between both ends of the cell and thus disappears completely when ignoring intracellular

gradients (the same as assuming infinitely fast diffusion:  $D \rightarrow \infty$ ; figure 5.1J). As the steepness of the steady state intracellular gradient is given by  $\frac{\partial c}{\partial x} = -\frac{J}{D}$ , the effect is larger with larger net fluxes and the effect of cell length per se larger with smaller diffusion constants.

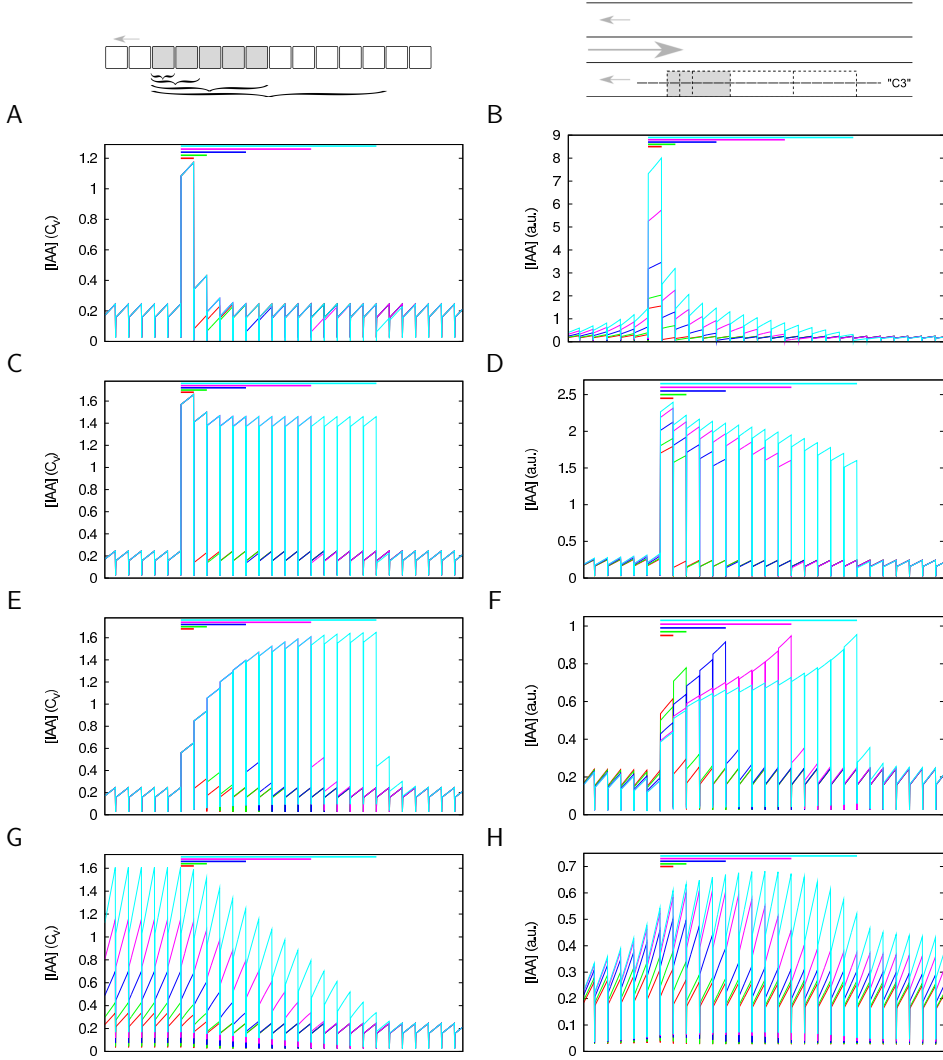


Figure 5.2: **Signatures of changes in a specified area (CA) along the auxin transport pipeline.** The different scenarios respond differently to increase of the length of the CA (lengths: 1 cell (red), 2 cells (green), 5 cells (blue), 10 cells (magenta) and 15 cells (cyan), as indicated with colored bars at the top of each graph). Left: 1D; Right: 2D (cortex + epidermis of a generalized root; the concentrations are measured in a single cell file indicated “C3” through the middle of the CA). Changes: **A+B:**  $\text{Infl}\uparrow (P_{inf} \times 10)$ , **C+D:**  $\text{Effl}\downarrow_0 (P_{eff,resp}/10)$ , **E+F:**  $\text{Effl}\downarrow_1 (P_{eff,resp}/10)$ , **G+H:**  $\text{Prod}\uparrow (Q = 0.001 \text{ a.u./s})$ .

### 5.2.2 Local changes: reaching the target concentration?

For investigating the effects of local changes, we used an embedding tissue at resting state outside (and sufficiently far away from) the location of the change (called CA: see figure 5.1B). Figure 5.2 shows the specific signatures of changes in the CA.

Although the influx permeability does not affect the resting state or target concentration (figure 5.1C), increasing  $P_{inf}$  in the CA did lead to an increase on the downstream side of the CA (in this case, on the left side of it; figure 5.2AB). Similarly, we observed a decrease of the auxin concentration just upstream of the CA. For this reason we call the  $\text{Infl}\uparrow$  pattern an “edge detect” pattern. In 1D, the concentration increase was independent of the length of the CA (figure 5.2A). In the 2D root context, however, the maximum increase in the down stream cell did increase with a larger CA (figure 5.2B). Moreover, the concentration increased everywhere in the CA, albeit to a much lesser extent than in the most downstream cell.

For  $\text{Effl}\downarrow$  we tested the two extreme possibilities:  $\text{Effl}\downarrow_0$ : no limits to the efflux reduction ( $P_{eff,base} = 0$ ); and  $\text{Effl}\downarrow_1$ : the lowest level (right side) already at the base level ( $P_{eff,base} = P_{eff,l}$ ). In 1D, with both options, the concentration increased to the target concentration in the largest part of the CA. The main difference was in the transition at the downstream side: an increase above the resting state level for  $\text{Effl}\downarrow_0$  (figure 5.2C) and a sloping increase from below the resting state level for  $\text{Effl}\downarrow_1$  (figure 5.2E). With the longest (15 cell) CA, both reached the target concentration, which was slightly higher for  $\text{Effl}\downarrow_1$ . In 2D, the two scenarios showed a more different profile in the CA. With  $\text{Effl}\downarrow_0$ , increasing the CA length increased the concentration everywhere inside the CA. With  $\text{Effl}\downarrow_1$ , on the other hand, increasing the length of the CA decreased the concentration in cells that were also part of the shorter CA.

Local production ( $\text{Prod}\uparrow$ ) resulted in 1D in a linear concentration increase over the CA, which persisted downstream of it (figure 5.2G). In 2D, however, the concentration decreased again downstream of the CA (figure 5.2H). The two differ in the possible routes an auxin molecule can take after production: in 1D the only possibility is down the pipeline, but in 2D it is also possible to “escape” to other parts of the tissue. Consequently, in 2D the concentration increase per cell decreased in the downstream direction. This also explains why for a short CA the highest concentration was reached on the downstream side of the CA, which shifted towards the center with increasing CA length.

### 5.2.3 Understanding the differences between 1D and 2D: changes in local fluxes

Although the distinct signatures of our different scenarios occurred both in 1D and 2D, we did observe several differences between 1D and 2D (figure 5.2). To understand these differences, we investigated the consequences of a fundamental difference between 1D and higher dimensions. In 1D, the steady state flux has to be the same everywhere in all cells (in absence of production / decay). In 2D, this is not necessarily true. The net flux through a cross section has to be constant, but it is possible to laterally redistribute the flux density over the cross section, for example, to (partially) bypass an obstruction. Figure 5.3AB shows two options for redistribution. To investigate the potential and actual impact of both, we plotted the local flux component along the pipeline for the different



changes (figure 5.3).

With  $\text{Infl}\uparrow$  we observed a strong relative increase of the local flux through the CA, increasing with every row of cells with increased  $P_{inf}$  (individual profile in figure 5.3C), accompanied by an increased local flux in the opposite direction in the vascular part. Sufficiently far upstream and downstream from the CA, the local fluxes returned to their respective reference levels.

With  $\text{Prod}\uparrow$  (figure 5.3F), on the other hand, we observed a pronounced lasting increase of the local flux magnitude of about 50% in both the vascular part sufficiently downstream of the CA/production site (i.e. to the right, as the vascular flux is in the opposite direction of the cortical flux). In that area, this coincided with a similar increase of the flux magnitude in the cortical part as well as the concentration in all cells. Towards the downstream (left) side of the CA and downstream of it, the local fluxes, although still increased, in the cortical part became progressively smaller than in the 1D case. Both trends are explained by the observation that the excess auxin is redirected to the vascular part, instead of being trapped in line downstream (left) of the CA. In both 1D and 2D, the result is a lasting increase of the flux and concentration, only on different sides of the production site when considering the flow direction in the cortical part (but in both cases downstream when considering the overall net flow direction).

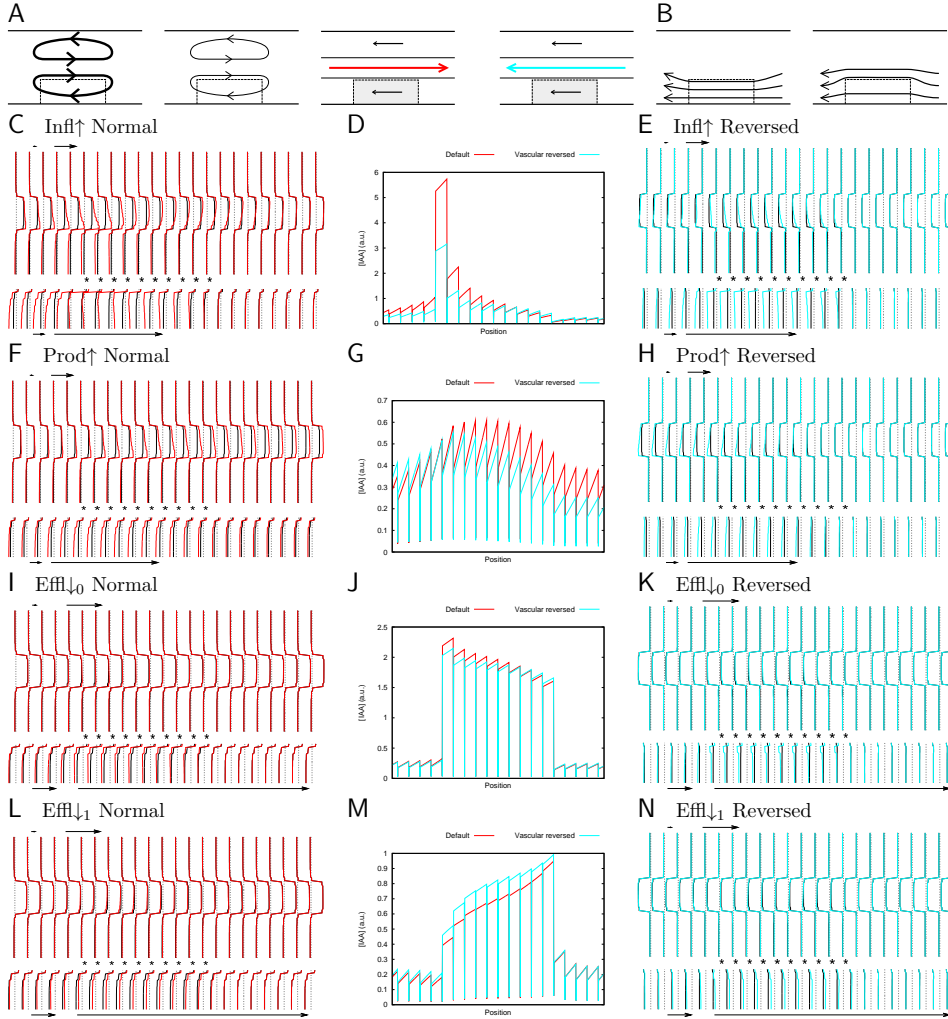
For the efflux scenarios we found a different picture. With  $\text{Effl}\downarrow_0$  (figure 5.3I), the local flux through the CA increased, but very mildly compared to  $\text{Infl}\uparrow$ . With  $\text{Effl}\downarrow_1$  (figure 5.3L), the local flux actually decreased, down towards about one half of the resting state flux close to the downstream (left) side of the CA. This was accompanied by a mild decrease of the reverse flux through vascular part.

Taken together, we observed increased local fluxes whenever the increase of the auxin concentration in the 2D pipeline was stronger than in 1D (figure 5.2) and decreased local fluxes with weaker concentration increases. The increase or decrease of fluxes, however, was not due to attracting fluxes to or diverting them around the CA (figure 5.3B). What increased or decreased was the local recycling of the auxin (figure 5.3A; c.f. the “reflux loop” in [91, 92]).

An increase or decrease of the concentration along with the flux, *without changing any parameters*, is also in line with the linear relation of concentration and flux for the resting state (equation 5.1).

The observed changes of the flux through the CA could also impact how the different scenarios interact. To investigate this interaction we applied the changes in pairs, both in 1D (figure 5.7A,C) and the 2D root (figure 5.7B,D). Typically, the joint scenarios resulted in a larger auxin accumulation than the sum of the two respective changes in isolation. The relative contribution of the three scenarios changed from 1D to 2D in accordance with their effects on the local flux through the CA:  $\text{Infl}\uparrow$  made a larger contribution in 2D and had an effect over the whole CA, rather than only the downstream end; whereas the contribution of  $\text{Effl}\downarrow_{base}$  (figure 5.7C,D) was much weaker in 2D (specially when compared with  $\text{Effl}\downarrow_0$  (figure 5.7A,B)).

With the root model and CA we used, changes in the amount of local recycling were only option in our setup (or almost, as the “endodermis” does not share the strong reverse flow of the vascular). We therefore wondered how effective the other strategy, attracting or diverting flux from somewhere else in the plane, would be if that were the available option. To this end we created a root segment with a reversed flow in the vascular part



**Figure 5.3: Fluxes in 2D roots.** In principle two options exist for changing the flux through a block of cells, while maintaining a constant total flux through an interface / cross section: increasing / decreasing the strength of a reflux loop (A) and attracting extra flux / diverting part of the flux to another part (B). Graphs on both edges (C-E, F-H, I-K, L-N) show the local fluxes along the long axis of the root with one flux profile per line of cells (measured along the middle of the cells). Steady state fluxes in a reference segment (i.e. a root without a change in the CA) are depicted with black lines, with the short and long black arrows representing a flux of  $1 \text{ a.u.} / \mu\text{m}^2/\text{s}$  and  $10 \text{ a.u.} / \mu\text{m}^2/\text{s}$ , respectively. The steady state fluxes after the given change in the CA are shown with red lines (original roots, **CFIL**: see figure 5.8C) or cyan lines (roots with reversed vascular flux, **EHKN**: see figure 5.8D). The level of 0 flux is indicated with dashes gray lines. As the net fluxes are a lot smaller in the cortical part than in the vascular part, the cortical part is repeated on a different scale, as indicated with larger black arrows. The flux profiles including the CA are indicated with \*. The graphs in the middle (**DGJM**) show the actual concentration profiles along the root, through the middle of the CA. Changes: **C-E**:  $\text{Inffl}\uparrow (P_{\text{inf}} \times 10)$ , **F-H**:  $\text{Prod}\uparrow (0.001 \text{ a.u.}/\text{s})$ , **I-K**:  $\text{Effl}\downarrow_0 (P_{\text{eff}}/10)$ , **L-N**:  $\text{Effl}\downarrow_1 (P_{\text{eff,resp}}/10)$ . Note: for enhanced visibility of the changes the graphs for  $\text{Effl}\downarrow$  (**I-N**) are plotted on a different scale.

(details in figure 5.8D). This would leave no other option for changing the flux in the CA than redistribution (figure 5.3B). In these segments we applied exactly the same changes to the CA as before. In all cases, the resulting flux diagrams (figure 5.3E,H,K,N) showed less extreme changes. At the same time, less auxin accumulated in the CA of the reversed segments if there was an increase of the net flux through the CA ( $\text{Infl}\uparrow$ ,  $\text{Prod}\uparrow$  and  $\text{Effl}\downarrow_0$ : figure 5.3D,G,J respectively). Only in case of  $\text{Effl}\downarrow_1$ , the concentration in the CA was higher in the reversed segment (figure 5.3M). In this case the reversal of the vascular flux decreased the strength of the local flux reduction due to asymmetrical reduction of effective efflux permeabilities.

## 5.2.4 Changing the resting state/global flux

From the preceding investigation of the local flux changes in a 2D root context it can be concluded that a local increase of the flux results in an extra increase of the concentration with changes of the transport parameters (scenarios  $\text{Infl}\uparrow$  and  $\text{Effl}\downarrow$ ). This is supported by the resting state formula, in which concentration and flux are linearly related. Considering the whole tissue, however, the resting state flux is not an independent quantity, but typically arises as a consequence of the model parameters in the embedding tissue (and with the simple changes we investigate thus depends on the parameters in the CA as well). So, how do changes in the embedding tissue flux affect the auxin accumulation in the CA?

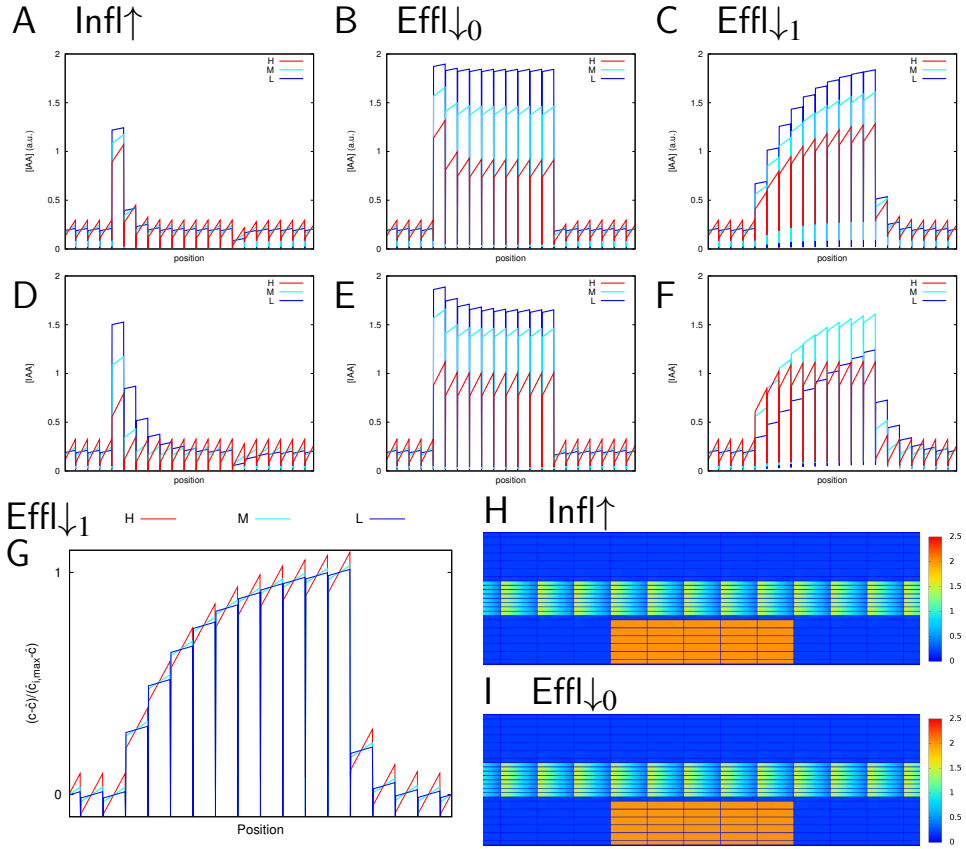
In essence, two options exist for changing the total flux that survive normalization of the resting state concentration (in 1D): 1: changing both  $P_{eff,0}$  and  $P_{eff,l}$  together, while keeping their ratio constant (fig 5.4A-C) and 2: change  $P_{eff,0}$  only (figure 5.4D-F). In both cases the target concentration is highest with the lowest (non-zero) flux. In the second case, i.e. with decreasing difference between  $P_{eff,0}$  and  $P_{eff,l}$ , the relaxation to the target concentration inside the CA needed more space (more cells) with a lower magnitude flux (figure 5.4D-F). With  $\text{Infl}\uparrow$  and  $\text{Effl}\downarrow_0$ , this resulted in a longer transient above the target concentration, whereas with  $\text{Effl}\downarrow_{base}$  this transient was below the target concentration (figure 5.4F). As this trend did not occur, or was hardly visible, with a fixed ratio  $\frac{P_{eff,l}}{P_{eff,0}}$ , we conclude that this ratio has a much stronger impact than the flux magnitude itself.

To understand this, we took a closer look at the general expression for the tissue level concentration profile (over a series of identical cells: equation B.18). For  $P_{eff,l} \neq P_{eff,0}$ , this has the following general shape:

$$\bar{c}_{i+n} = \left( \frac{P_{eff,l}}{P_{eff,0}} \right)^n \bar{c}_i + \bar{J} \left( 1 - \left( \frac{P_{eff,l}}{P_{eff,0}} \right)^n \right) K \quad (5.3)$$

with  $K$  some constant depending on the model parameters. It is not hard to see that if  $\frac{P_{eff,l}}{P_{eff,0}} \approx 1$ ,  $\bar{c}_{i+n} \approx \bar{c}_i$  for small  $n$ : the average concentration could only change slowly in that case.

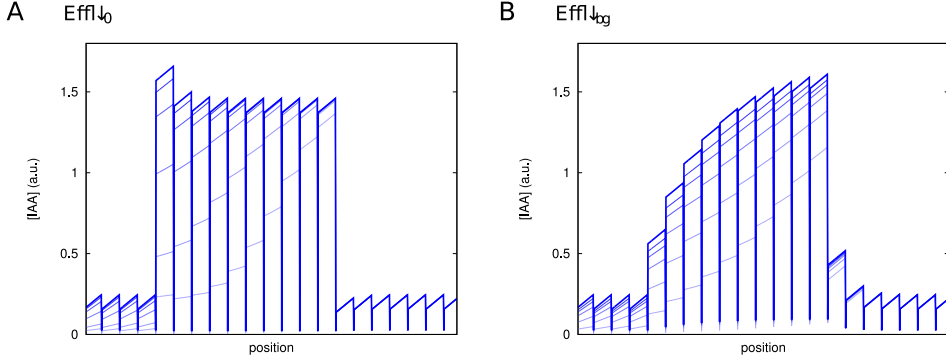
All else being equal, a higher resting state flux should result in more (spatially) confined relaxation towards the resting state/target concentration ( $\bar{c} = \bar{J}K$ ). As changes in the resting state flux are caused by changes in the embedding tissue, it turned out that the opposite was the case. When we used the resting state and highest average cell concentration to normalize several profiles of figure 5.4C, i.e.  $\text{Effl}\downarrow_{P_{eff,l}}$  with fixed  $\frac{P_{eff,l}}{P_{eff,0}}$ , it turned



**Figure 5.4: Impact of changing the resting state flux on the patterns in the controlled area.** The resting state flux can be changed in two conceptually different ways: by keeping a fixed ratio of effective efflux permeabilities ( $\frac{P_{eff,l}}{P_{eff,0}} = 0.2$ ) (**A-C – H**:  $P_{eff,0} = 20\mu\text{m/s}$  (red/black), M:  $P_{eff,0} = 5\mu\text{m/s}$  (cyan/dark gray), L:  $P_{eff,0} = 1\mu\text{m/s}$  (blue/light gray)), or changing this ratio (with fixed  $P_{eff,l} = 1\mu\text{m/s}$ ) (**D-F – H**:  $P_{eff,0} = 20\mu\text{m/s}$ , M:  $P_{eff,0} = 5\mu\text{m/s}$ , L:  $P_{eff,0} = 2\mu\text{m/s}$ ). Changes: **A,D**: Infl↑ ( $P_{inf} \times 10$ ), **B,E**: Effl↓₀ ( $P_{eff}/10$ ), **C,F,G**: Effl↓ $_{P_{eff,l}}$  ( $P_{eff,resp}/10$ ). **G**: the shape of the profiles in **C** is the same for all different levels of the resting state flux under this operation: 1 subtract resting state concentration; 2 divide by the highest average concentration in a cell. **H,I**: with a symmetrical PIN distribution, the difference between Infl↑ (**H**) and Effl↓₀ (**I**) with the same factor disappears. This implies that the two scenarios are indistinguishable in regions with symmetric localization of the auxin efflux carriers.

out that *in this case* the effect of a larger flux was (for all practical purposes) cancelled out by the other parameters not being equal (figure 5.4G).

From equation 5.3 it follows that the concentration does not change among identical cells (= with identical parameters) if  $P_{eff,0} = P_{eff,l}$  in absence of a net flux. This would



**Figure 5.5: (Supplementary) Dynamics of auxin accumulation under both scenarios for efflux reduction.** Although at steady state the highest concentration is found on different sides of the CA (downstream for  $\text{Effl}_{\downarrow 0}$  (A) and upstream for  $\text{Effl}_{\downarrow 1}$  (B)), the two scenarios are more similar in their dynamics. In both cases the controlled area fills up from the upstream side, i.e. where a source is available. Time scales of auxin accumulation are also very similar. Thin lines show the concentration every 30 minutes for the first 2.5 hours from the change in the CA. The thick line shows the steady state. Default 1D parameters.

make it impossible to reach the target concentration, which is anyway ill defined under these circumstances (division by zero in equation 5.2). So, what does happen in this case?

A 1D pipeline without a net flux does not make much sense, but in 2D/3D it is possible that the pipeline flux is confined to part of the root, likely the vascular, without much/no net (longitudinal) flux outside of that part. We created a virtual root without cortical flux by setting equal  $P_{eff}$  on all four sides of the cells in the cortical part. In this case, the difference between  $\text{Infl}_{\uparrow}$  and  $\text{Effl}_{\downarrow}$  (with the same factor) disappeared completely (figure 5.4H,I). This implies that a sufficiently strong polarization of the efflux carriers (sufficiently large relative difference between  $P_{eff,0}$  and  $P_{eff,l}$ ) in the relevant cell file is required for distinguishable  $\text{Infl}_{\uparrow}$  and  $\text{Effl}_{\downarrow}$  patterns.

### 5.2.5 Strong symplastic connections diminish $\text{Infl}_{\uparrow}$ pattern

Plant cells are connected symplastically by plasmodesmata. These narrow channels typically allow for the passage of small molecules such as auxin. We therefore tested to what extent the patterns we have found are effected by the presence of symplastic connections. To this end we introduced an effective permeability  $P_{sym}$  for diffusive (non targeted) symplastic transport between neighbouring cells. First of all, this affected the resting state through a reduction of the net flux (when keeping  $\bar{c}$  fixed):

$$\bar{c} = \bar{J} \frac{\frac{l}{2D}(P_{eff,l} + P_{eff,0} + 4P_{sym}) + 2}{P_{eff,l} - P_{eff,0}} \quad (5.4)$$

Given the resting state concentration  $\bar{c}$ , the target concentration in the CA ( $\hat{c}$ ) becomes:

$$\hat{c} = \bar{c} \frac{P_{eff,l} - P_{eff,0}}{\hat{P}_{eff,l} - \hat{P}_{eff,0}} \cdot \frac{\frac{l}{2D}(\hat{P}_{eff,l} + \hat{P}_{eff,0} + 4P_{sym}) + 2}{\frac{l}{2D}(P_{eff,l} + P_{eff,0} + 4P_{sym}) + 2} \quad (5.5)$$

with, as before,  $\hat{P}_{eff,l}$  etc parameters for inside the CA and  $P_{eff,l}$  etc for the embedding tissue. As before, this does not include the effective influx permeability ( $P_{inf}$ ). For  $\text{Effl}\downarrow$  the target concentration increases with increasing  $P_{sym}$ .

We again checked whether this increased target concentration would actually be reached. For all scenarios we investigated how the patterns changed with increasing symplastic connectivity (increasing  $P_{sym}$ ; figure 5.6).

We found that with  $\text{Infl}\uparrow$ , the pattern would almost vanish with a high symplastic effective permeability (figure 5.6A). With these parameters ( $P_{eff,0} = 5$ ,  $P_{eff,l} = 1$ ,  $P_{sym} = 10\mu\text{m/s}^{-1}$ ), the steady state flux was reduced by 69%, but the increase of the peak concentration (increase from  $\bar{c}$ , measured in the middle of the cell) by more than 95%.

As the resting state flux was reduced by the symplastic connections, the impact of  $\text{Prod}\uparrow$  increased with increasing the symplastic effective permeability (figure 5.6B).

The impact of symplastic transport on  $\text{Effl}\downarrow$  was less strong (figure 5.6CD) compared to  $\text{Infl}\uparrow$ , although the highest symplastic effective permeability,  $P_{sym} = 10\mu\text{m/s}$ , also lead to a strong reduction of the actual concentration in the CA, specially on the downstream side, or with a short CA. The patterns of  $\text{Effl}\downarrow_0$  tended more towards  $\text{Effl}\downarrow_{base}$ : even with a small  $P_{sym}$  the small peak on the downstream side of the CA disappeared and in stead the concentration at the downstream end was below the target concentration ( $\hat{c}$ ).

As the symplastic transport competes with the directed transport (see also equation 5.5), the impact of symplastic connections was less pronounced with a higher global flux magnitude (figure 5.6E-H  $P_{eff,0} = 20\mu\text{m/s}$  in stead of the default  $P_{eff,0} = 5\mu\text{m/s}$ ). In this case it was also visible within the length of the CA that the symplastic connections resulted in an increased target concentration ( $\hat{c}$ ) for both  $\text{Effl}\downarrow$  scenarios 5.6GH.

## 5.3 Discussion

### 5.3.1 Different signatures and different contexts

The formation of an organ primordium along the root (or shoot) requires the formation of a local auxin maximum. We have tested different scenarios for locally increasing the auxin concentration along a pipeline of directed auxin transport. These scenarios yielded different patterns for local auxin accumulation. Moreover, the conditions for effective auxin accumulation differed per pattern.

Scenario  $\text{Infl}\uparrow$ , the increase of the effective influx permeability  $P_{inf}$ , resulted in a marked concentration increase on the downstream side of the controlled area (CA), the group of cells to which we applied changes in our setup (figure 5.1B), but no, or a relatively very minor, increase further upstream in the CA. Changes in the effective influx permeability therefore act as an “edge detect” operation. Our analytical calculations show that this is the case because of the (assumed) symmetrical carrier localization on both ends of the cell (see appendix B.1.2). In the context of a real (2D/3D) tissue,  $\text{Infl}\uparrow$  has the potential to substantially increase the flux through the relevant cells/cell file(s). This results in a stronger auxin accumulation than expected from a similar 1D calculation. We found

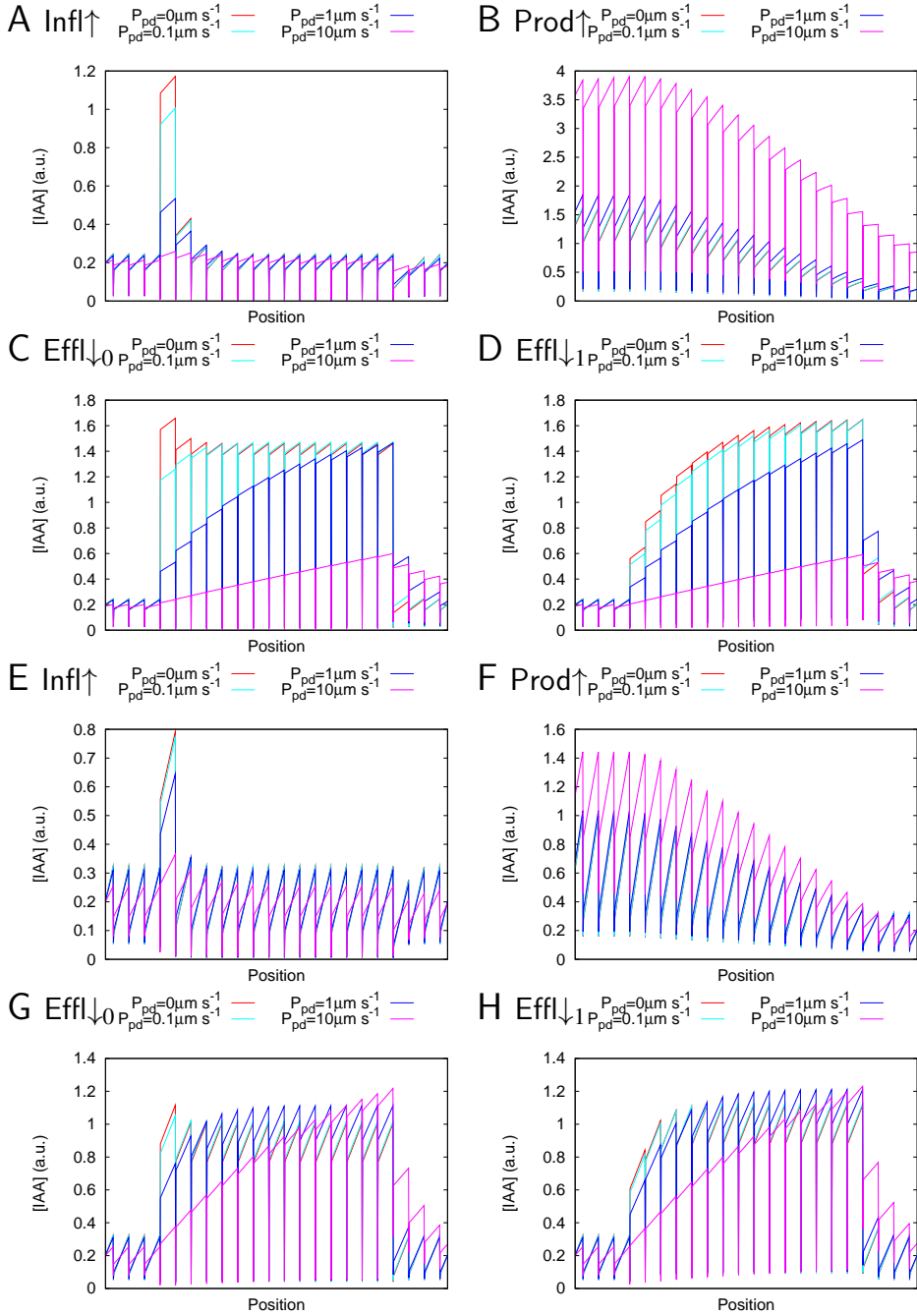


Figure 5.6: **Impact of symplastic transport (1D).** Increasing symplastic connectivity ( $P_{\text{sym}} = 0 \mu\text{m/s}$  (red),  $P_{\text{sym}} = 0.1 \mu\text{m/s}$  (cyan),  $P_{\text{sym}} = 1 \mu\text{m/s}$  (blue),  $P_{\text{sym}} = 10 \mu\text{m/s}$  (magenta)) diminishes the auxin accumulation under  $\text{Infl}\uparrow$  ( $P_{\text{inf}} \times 10$ ) (A,E) and reduces the accumulation under  $\text{Effl}\downarrow_0$  ( $\text{Effl}\downarrow_0$ :  $P_{\text{eff},0}/10$  (C,G) and  $\text{Effl}\downarrow_1$ :  $P_{\text{eff},\text{resp}}/10$  (D,H)). Only under  $\text{Prod}\uparrow$  in 1D the auxin accumulation increases, coinciding with a strong reduction of the net flux through the tissue (B,F). The effects are stronger with lower  $P_{\text{eff},0}$ , the largest effective efflux permeability of the two cell edges, compare A-D:  $P_{\text{eff},0} = 5 \mu\text{m/s}$  (default) and E-H:  $P_{\text{eff},0} = 20 \mu\text{m/s}$  (all:  $P_{\text{eff},l} = 1 \mu\text{m/s}$ ).

that this enhancing effect was strongest in locations that allowed for local recycling of auxin through a local reflux loop. Of all the scenarios investigated,  $\text{Infl}\uparrow$  was affected the strongest by symplastic connections between the cells (figure 5.6). Lateral root initiation is known to involve an increase of influx carriers [76, 92]. The edge detect pattern we find with our  $\text{Infl}\uparrow$  scenario results in a single cell in a cell file with by far the strongest increase (figure 5.2A,B, 5.4A), whereas lateral roots (in the model organism *Arabidopsis*) have two founder cells (per cell file) [265, 266]. Although contradictory at first glance, this may be an actual intermediate stage, as heat shock induction of auxin production in a single cell proved sufficient for lateral root initiation [267], from which the authors conclude that a single founder cell can induce its neighbour to become its partner founder cell.

Local auxin accumulation over a much broader area can be obtained with  $\text{Effl}\downarrow$ , a reduction of the effective efflux permeabilities. At a first glance, the steady state patterns of the two scenarios for efflux reduction appear quite different. If only considering the cell with the largest concentration (increase), it seems like the polarity of the patterns is reversed (figure 5.2CD vs. EF). This, however, is not the case, as can be seen from the dynamics of auxin accumulation (in both cases from the upstream side, figure 5.5). Moreover, when introducing symplastic transport as an interfering mechanism, the patterns of both scenarios become remarkably similar, both showing an undershoot at the downstream side of the CA (figure 5.6). The presence of a minimal efflux level (not responding to some change inducing signal) and symplastic connections have in common that the ratio of total outward fluxes of both ends of the cell comes closer to one when the effective efflux permeability is reduced. This explains the similarity between the corresponding  $\text{Effl}\downarrow$  patterns. As this ratio strongly affects how much the concentration can change between two neighbouring cells with identical parameters (away from their resting state) (section 5.2.4 and equation 5.3), a large number of cells can be required to reach the target concentration with an efflux reduction ( $\text{Effl}\downarrow_{\text{base}} \gg 0$ ) if (within the CA) the effective efflux permeabilities of both ends of the cell are similar. Under such conditions,  $\text{Effl}\downarrow_{\text{base}}$  is more effective with a larger CA. *Note that in reality,  $\text{Effl}\downarrow_0$  and  $\text{Effl}\downarrow_{p_{\text{eff},l}}$  are not the only two options for efflux reduction, but the extreme ends of the spectrum, with a gradual change of the patterns from one end to the other.*

Local auxin production,  $\text{Prod}\uparrow$ , by itself was not effective for local auxin accumulation along a pipeline: most auxin was transported away from the production site (figure 5.2G,H, 5.3F-H). Another striking example of this effect can be found in [91]. They show an artificial example of a single cortical cell supplying all auxin for the virtual root. In this case, the auxin concentration in the quiescent center, the normal location of the root's auxin maximum, soon is orders of magnitude higher than in the producing cell itself.

Upon (local) reduction of the efficiency of the auxin transport, the same production rate resulted in a larger increase of the local concentration. For this,  $\text{Effl}\downarrow_0$  was more effective than  $\text{Infl}\uparrow$  (and  $\text{Effl}\downarrow_{\text{base}}$ ) (figure 5.7). Strong symplastic connections had a similar effect (in 1D), as they too reduce the efficiency of the polar transport (through a passive back flux of auxin), but – as other global reductions [182] – did not confine the resulting auxin accumulation to the proximity of the production site (figures 5.6B,F).

For experimental differentiation between the increased influx (“edge detect”) and decreased efflux (“uniform”) patterns, a **sufficiently strong polarization of the auxin transport** is important. With decreasing ratio between both edges, the  $\text{Infl}\uparrow$  induced con-



centration increase was less confined to the boundary between CA and embedding tissue. Consequently, the pattern became more similar to  $\text{Effl}_{\downarrow 0}$  (compare “H” (strong polarization) and “L” (weak polarization) in figure 5.4D,E). They will become identical if the effective efflux permeability is the same on both ends of cells (within a cell file) (figure 5.4H,I). More particularly, this net flux should be present in the cell files of interest themselves. This is well illustrated by figure 5.4H,I, in which an increase of the influx and an equally strong decrease of the efflux in the cortex and epidermis gave an exactly identical pattern, because these hypothetical roots had no cortical flux. This was despite a strong rootward flux in the nearby vascular tissue.

### 5.3.2 Is (strong) symplastic connectivity a negative regulator of root lateral organ formation?

The formation of a lateral root primordium is signaled by a strong increase of auxin influx carriers in the founder cells [76, 92], leading to highly localized increase of the auxin concentration [236]. In this light it is interesting to note that in our model, the  $\text{Infl}_{\uparrow}$  pattern was most sensitive to a strong symplastic permeability (figure 5.6A). The largest value we used for this effective permeability,  $P_{\text{sym}} = 10 \mu\text{m}/\text{s}$ , is a realistic estimate for auxin based on measurements using the somewhat larger molecule fluorescein in a zone at  $\approx 200 \mu\text{m}$  from the quiescent center [163].

The effective permeability for symplastic transport, however, is not constant in a developing root [118, 119, 121, 163]. It is very high within cell files of the root meristematic region (with a lower effective permeability for the cells of the quiescent center), but decreases with the maturation of the root tissue [118, 119, 181]. The initiation of lateral root formation occurs in what is often called the differentiation zone, i.e. only at a certain distance from the root tip. These observations together lead us to the hypothesis that strong symplastic connections act as a suppressor of lateral root formation. In line with this, although by itself insufficient support, the activity of auxin responsive markers (measured by specific promoters driving luciferase) at so called “prebranch sites” appears to show a temporal minimum between initial oscillation and establishment of the prebranch site (see [268], specifically the movies). In some species, though, lateral root initiation already starts in the meristematic zone ([269] and references therein). If a high symplastic permeability indeed serves as a suppressor of lateral root initiation, it would be very interesting to compare the symplastic connectivity of these species against more “canonical” species.

Legumes may form an interesting case in this respect. They can produce two kinds of root lateral organs: lateral roots and nitrogen fixing root nodules. Primordium formation of both types of lateral organs is thought to require local auxin accumulation along the pipeline, but with different mechanisms [36, 37, 182, 227, 228]. For lateral roots, the local auxin concentration is increased by extra influx carriers, whereas an efflux reduction is thought to underly the auxin accumulation for nodule primordia.

In many legumes, such as the model species *Lotus japonicus* and *Medicago truncatula*, the susceptible zone for nodule formation [238] starts closer to the root tip than the zone of lateral root initiation<sup>§</sup>

<sup>§</sup> Although this is considered common knowledge within the field of legume-rhizobium interaction, we are not aware of any published quantitative comparison of both zones within a single species. The observation can be

Here we observed that symplastic transport decreases the efficiency of local auxin accumulation both with  $\text{Infl}\uparrow$  and  $\text{Effl}\downarrow$ , but that the effect was much stronger on  $\text{Infl}\uparrow$  (figure 5.6). In combination with the different onsets of susceptibility in relevant legumes, this supports the more general hypothesis that strong symplastic connections can suppress the initiation of new lateral organs and through this helps maintain the meristematic zone of the root.

### 5.3.3 Recycling brings more wealth than depleting the environment

We have used our 1D model as an easy tool for wide parameter explorations (e.g. figures 5.4 and 5.6). Real roots of course are more complex than 1D pipelines. It follows directly from a mass conservation argument that in a 1D pipeline, the flux has to be the same everywhere in the tissue (modulated only by the difference between production and decay between two points of observation). In actual roots the same holds for every cross section along the root, but it is possible to laterally redistribute the flux density, potentially varying the local flux within a cell file.

Such changes of the local flux were specially pronounced when locally increasing the effective influx permeability ( $\text{Infl}\uparrow$ ). This attracted more flux to the CA and through this resulted in a stronger increase than expected from the same change in a 1D pipeline. Conversely, when locally decreasing the efflux towards a certain minimum ( $\text{Effl}\downarrow_1$ ), the local flux decreased and the resulting increase of the concentration was smaller than expected from 1D. We applied these changes in two different 2D roots: a “normal” one with opposite flow directions in the vascular and cortical parts of the tissue and a “reversed” one with both flows in the same direction. In the normal root, the mechanism available for changing the flux locally was changing the extent of local recycling through altering the strength of a local reflux loop (figure 5.3A), whereas in the reversed root, the only possible mechanism was attracting flux from or diverting to the surrounding tissue (figure 5.3B). It turned out that changes in the amount of local recycling of auxin had a much stronger effect on the flux through the CA / a piece of the cortical part, both positive ( $\text{Infl}\uparrow$ ,  $\text{Prod}\uparrow$  and, to a lesser extent,  $\text{Effl}\downarrow_0$ ) and negative ( $\text{Effl}\downarrow_1$ ). The effectiveness of  $\text{Infl}\uparrow$  in allocating auxin to specific tissues also shows in the (*Arabidopsis*) root epidermis: AUX1 expression the non-hair cell files results in an increased auxin concentration in all epidermal cell files and a longer concentration gradient over the root [93].

This means that the potential impact of a change depends on the tissue context and specially for  $\text{Infl}\uparrow$  it is largest when different flow directions are nearby to facilitate local recycling through enhancing a reflux loop, as is the case in lateral root formation [92]. When there is a significant basal level for the efflux, efflux reduction ( $\text{Effl}\downarrow_{\text{base}}$ ), on the other hand, is more effective in a region of unidirectional flux.

---

supported by combining the published observations that the susceptible zone starts with cells not yet displaying root hairs at the time of inoculation [238] (several relevant legume species; this does not hold for infection by “crack entry” such as in peanut, as in that case the wounds of lateral root emergence serve as bacterial entry points) and that root hairs were present in a zone closer to the root tip than the first observed signs of lateral root initiation [270] (radish). Another observation perhaps supporting this is: “The highest nodule on the primary root usually developed 1-2 cm behind the root tip and more than two lateral primordia below the lowest lateral visible at inoculation.” (*Medicago tribuloides*) [271].

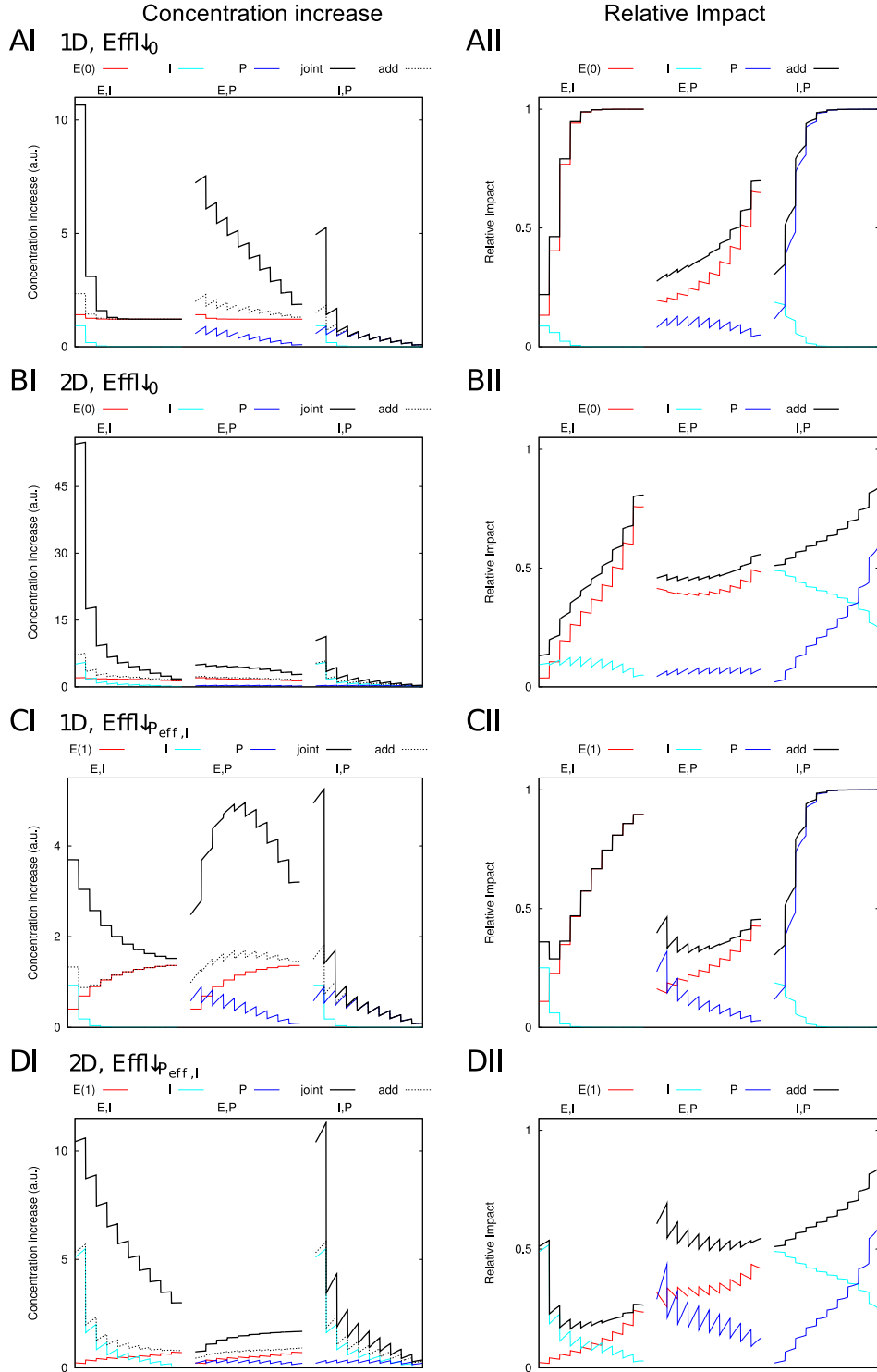
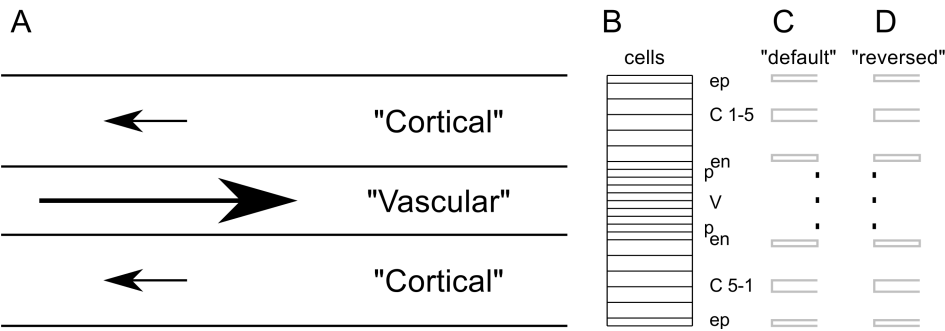


Figure 5.7: (Supplementary) Interaction of changes

**Figure 5.7: (Supplementary) Interaction of changes.** All figures compare a simultaneous (“joint”) change of two factors ( $\text{Effl}\downarrow$  and  $\text{Infl}\uparrow(\text{E},\text{I})$ ;  $\text{Effl}\downarrow$  and  $\text{Prod}\uparrow(\text{E},\text{P})$ ;  $\text{Infl}\uparrow$  and  $\text{Prod}\uparrow(\text{I},\text{P})$  respectively) with the corresponding single changes ( $\text{Effl}\downarrow$ : red,  $\text{Infl}\uparrow$ : cyan and  $\text{Prod}\uparrow$ : blue) and the sum of their concentration increase (**I** – black dotted) or relative impact (**II** – black solid). The concentration increase of the joint change is only shown in **I** (solid black), as it is by definition a straight line at 1 in **II**. Two  $\text{Effl}\downarrow$  scenarios are used:  $\text{Effl}\downarrow_0$  (**A,B**) and  $\text{Effl}\downarrow_{P_{eff,l}}$  (**C,D**). We used both 1D (**A,C**) and 2D (**B,D**).

5.4 Conclusions

Different mechanisms for local auxin accumulation not only have distinct signatures when invoked along an “auxin pipeline”, they moreover respond differentially to specific features of the tissue. An increase of the influx was most able to strengthen a local reflux loop at the interface of different flux directions, whereas a reduction of the efflux was more resistant against symplastic transport between cells. Because of these differences, the most suitable mechanism (or combination of mechanisms) for local auxin accumulation is process dependent and the mechanism used codetermines the developmental zone for organ initiation and infection. Combined with an understanding of how hard/easy it is to induce a particular change autonomously (e.g. for lateral roots) or ectopically (e.g. for nodules or host/pathogen interactions) the biophysical understanding of the different mechanisms opens the door to evolutionary questions about why particular mechanisms are used in specific processes.



**Figure 5.8: Outline of 2D roots.** Generalized legume root from [182] (“default”). Main direction of auxin flow in the default root are indicated in **A**. A single row of cells (drawn with the correct aspect ratio) is shown in **B** (length  $100\ \mu\text{m}$ , width  $10$  or  $20\ \mu\text{m}$ ). The root is built by joining many of these rows of cells. Cell layers: ep: epidermis, **C**: cortex, en: endodermis, p: pericycle, V: vascular. The effective efflux permeabilities in the embedding tissue of the default (**C**) and reversed (**D**, only used in figure 5.3) are grouped in three levels: high (black line; default  $P_{eff} = 20\ \mu\text{s}$ ), low (gray line; default  $P_{eff} = 5\ \mu\text{m/s}$ ) and background/bg (no line, default  $P_{eff} = 1\ \mu\text{m/s}$ ).

## 5.5 Methods

### 5.5.1 2D root segment

The 2D root segments used in this paper are based on previously used root segments [182]. The default root segment represents the DZ of a generalized legume root (based on *Arabidopsis* PIN positioning data in [92] and anatomical data of model legumes *Medicago truncatula* and *Lotus japonicus*). This segment has a 5-layered cortex and is represented in figure 5.8. The 1D pipeline is chosen to match the cortex of the default 2D root.

### 5.5.2 Numerical methods

Numerical solutions were obtained using the Alternating Direction Implicit (ADI) algorithm [183] and a 2D finite volume description of the tissue as described in [182]. As this is a 2D algorithm, we used a strip of at least 3 pixels wide for the 1D simulations (computational efficiency was not an issue for 1D). For the few simulations with symplastic connections (figure 5.6) we used a band-5 diagonal matrix to assure matrix invertibility.

The integration time step is chosen depending on the interval between measurements, with typical values of 1 and 2.5 seconds. Results were checked for numerical artifacts and if necessary the time step was adapted.

### 5.5.3 Parameters

Parameter	Default	Comments
$P_{inf}$	$20\mu\text{m/s}$	Effective influx permeability; [91, 92, 182]
$P_{eff,0}$	$5\mu\text{m/s}$	Effective efflux permeability 1D; [91, 92, 182]
$P_{eff,l}$	$1\mu\text{m/s}$	Effective efflux permeability 1D; [91, 92, 182]
$P_{eff,high}$	$20\mu\text{m/s}$	Effective efflux permeability 2D; [91, 92, 182]
$P_{eff,low}$	$5\mu\text{m/s}$	Effective efflux permeability 2D; [91, 92, 182]
$P_{eff,bg}$	$1\mu\text{m/s}$	Effective efflux permeability 2D; [91, 92, 182]
$P_{eff,base}$	$1\mu\text{m/s}$	Base level of effective efflux permeability under $\text{Effl}_{\downarrow base}$
$P_{sym}$	$0\mu\text{m/s}$	Effective wall permeability through symplastic connections. For auxin in the <i>Arabidopsis</i> MZ a value of $P_{sym} = 10\mu\text{m/s}$ in the longitudinal direction seems reasonable based on measurements with fluorescein [163]
$Q$	$0\text{a.u./s/volume}$	Auxin production rate. Default no production. Default used if $Q > 0$ : $0.001\text{a.u./s/volume}$ (10 times higher than the default in [182], for increased visibility of trends)
$l$	$100\mu\text{m}$	Cell length; [182]
	$20\mu\text{m}$	Width of cortical cells (2D); [182]
	$10\mu\text{m}$	Width of other cells (2D); [182]
$D$	$300\mu\text{m}^2/\text{s}$	Cytoplasmic auxin diffusion constant; [92, 182]
$D_w$	$44\mu\text{m}^2/\text{s}$	Apoplastic auxin diffusion constant (2D); [93, 182]
$d_w$	$0.2\mu\text{m}$	wall thickness; [93, 182]
$d_p$	$2\mu\text{m}$	pixel width in the cell's interior; [182]

Table 5.2: Overview of parameters & default values



---

## **Induction of the nodule primordium: from epidermal signal to interior response**

---

*With René Geurts, Ton Bisseling and Bela Mulder*

The local accumulation of auxin in the formation of a nodule primordium is most likely the result of a reduction of the effective auxin efflux permeability. From previous computer simulations we observed that if this reduction is induced instantaneously in a full “controlled area”, the first auxin accumulation occurs in the inner layers, because they are closest to the (predominant) auxin source. In reality, the cells respond to some signal of epidermal origin, likely cytokinin. We therefore asked under what conditions an epidermal signal can induce an interior auxin accumulation.

Using a very simple direct interaction between the epidermal signal and auxin efflux carriers, based on the documented negative effect of cytokinin on PIN proteins, we found that it was surprisingly easy to find the experimentally observed interior auxin response to the epidermal signal, provided we used the root PIN layout that emerged from our previous study as the most compatible with indeterminate nodule formation. This way of inducing the auxin accumulation naturally yielded a transient decrease of the auxin concentration rootward (“downstream”) of the induction site, as observed in experiments.

This simple interaction could easily be tuned to produce the observed patterns of auxin accumulation in both determinate and indeterminate legumes, but was not very robust against fluctuations in the production rate and variations affecting the free movement of the epidermal signal, e.g., the extent of symplastic movement. We extensively discuss how different aspects of the auxin-cytokinin interaction, which have so far been excluded from the model, could increase the robustness of the patterning mechanism and the developmental process relying on it.

## 6.1 Introduction

In chapter 4 we have studied different hypothetical mechanisms for the initiation of nodule primordia in response to a local signal. Of the different mechanisms tested, a reduction of the auxin efflux carriers produced auxin accumulation patterns most similar to what is observed/expected for nodule primordia. This mechanism is also in agreement with several lines of experimental evidence. In chapter 4 we applied instantaneous and homogeneous changes to a predefined group of cells, dubbed “controlled area” (figure 6.1A) [182]. This approach was very useful for studying the properties of the different mechanisms, but no plant in its right (absence of) mind would function exactly like this. In reality, the local change is induced by a signal of epidermal origin (figure 6.1B). Several lines of evidence points towards cytokinin (CK) fulfilling this role. Local application of CK induces nodule-like structures [32]; CK accumulation [272] and a CK response are observed early in nodulation [34, 247]; a gain of function mutation of a specific CK receptor results in spontaneous pseudonodule formation [232] and several CK response regulators are induced in nodule primordia [34, 35].

Although CK appears in textbooks as “auxin antagonist”, the interaction of these two hormones is more involved. Recent discoveries suggest that CK has the potential to induce auxin accumulation. In *Arabidopsis*, CK has been shown to reduce the transcription of the genes coding for PIN proteins through SHY2, an Aux/IAA protein [38, 273]. These proteins are an integral part of the auxin perception system. Moreover, CK can drastically reduce the amount of membrane localized PIN proteins, with differential sensitivities among the different PINs [39]. A reduction of the auxin efflux seems to play an important role in nodulation, too: nodule-like structures can be induced with auxin transport inhibitor NPA [31, 245], and a decrease of polar auxin transport is observed 24 hours after inoculation with *Rhizobium* [246].

In chapters 4 and 5 we showed that a reduction of the effective efflux permeability, as can be induced by CK, can give rise to a local auxin accumulation. With the predefined controlled area, this increase started in the inner cortex, even if there was no bias, inward or outward, of the cortical efflux carriers and eventually also no such bias in the resulting auxin maximum.

This transient inward bias was a particularly interesting finding with respect to legumes such as *Medicago truncatula*. These legumes produce indeterminate nodules, predominantly originating from the inner cortex, with also contributions of endodermis and pericycle [27]. Auxin accumulation is consistently observed at the site of the cell divisions [274, 275]. If the first cell divisions occur in a different location, e.g., middle or outer cortex, auxin accumulation is observed at the corresponding different sites [36, 37].

In all cases, the nodules are induced by epidermal contact with compatible rhizobia. This poses a very interesting question: how is it possible that in *Medicago* a signal of epidermal origin induces the first and strongest effects in the inner tissue layers (inner cortex – pericycle)? With instantaneous induction in all responding cells, the first auxin accumulation is observed in the inner layers, because they are closest to the (predominant) auxin source. Could this effect be strong enough to overrule the bias of the origin? Under what conditions is that possible?

Much is known about the intercellular transport of auxin (reviewed in 1.4.1). Little is known, however, about CK transport (see 1.4.2). We will therefore test several options



for CK transport. From its chemical properties, it is conceivable that the plasma membrane is somewhat permeable to CK. This permeability will necessarily be the same for all regions of the cell membrane. From its size, it is also likely that CK can move symplastically. Effective permeabilities for symplastic transport could be different for different cell-cell interfaces, as large differences in plasmodesmata densities have been reported for different wall segments [118, 119, 121]. We will start with an exploration of how a CK signal, produced in a single epidermal cell, spreads through a root depending on different assumptions on its transport mechanism(s) and the alignment of neighbouring cell layers.

We will then link CK concentrations to membrane PINs using a simple interaction based on observations in *Arabidopsis*. The effect of CK on PIN membrane localization depends on receptor AHK4/CRE1, and may be relayed by B-type response regulators AtARR2 and AtARR12 [39], transcription factors activated upon CK perception [96]. The receptor AHK4 is a membrane bound receptor. According to the latest insights it is located in the endoplasmatic reticulum (ER) [97]. Taken together these findings suggest that the CK concentration of the whole cell has a similar effect on the PIN proteins on all sides of the cell. We will therefore base our CK-PIN interaction on the average cellular CK concentration. We will explore the behaviour of this simple mechanism first in terms of primordium initiation and then in terms of interaction between consecutively initiated primordia. Although the mechanism is crude compared to what is known about the auxin-cytokinin interaction, it is sufficient to reproduce auxin accumulation patterns as actually observed in different legumes. We will discuss how several experimentally indicated relevant components which are currently omitted from the interaction mechanism can increase the robustness of primordium initiation against variations in the intervening tissue and in epidermal signal intensity.

## 6.2 Results

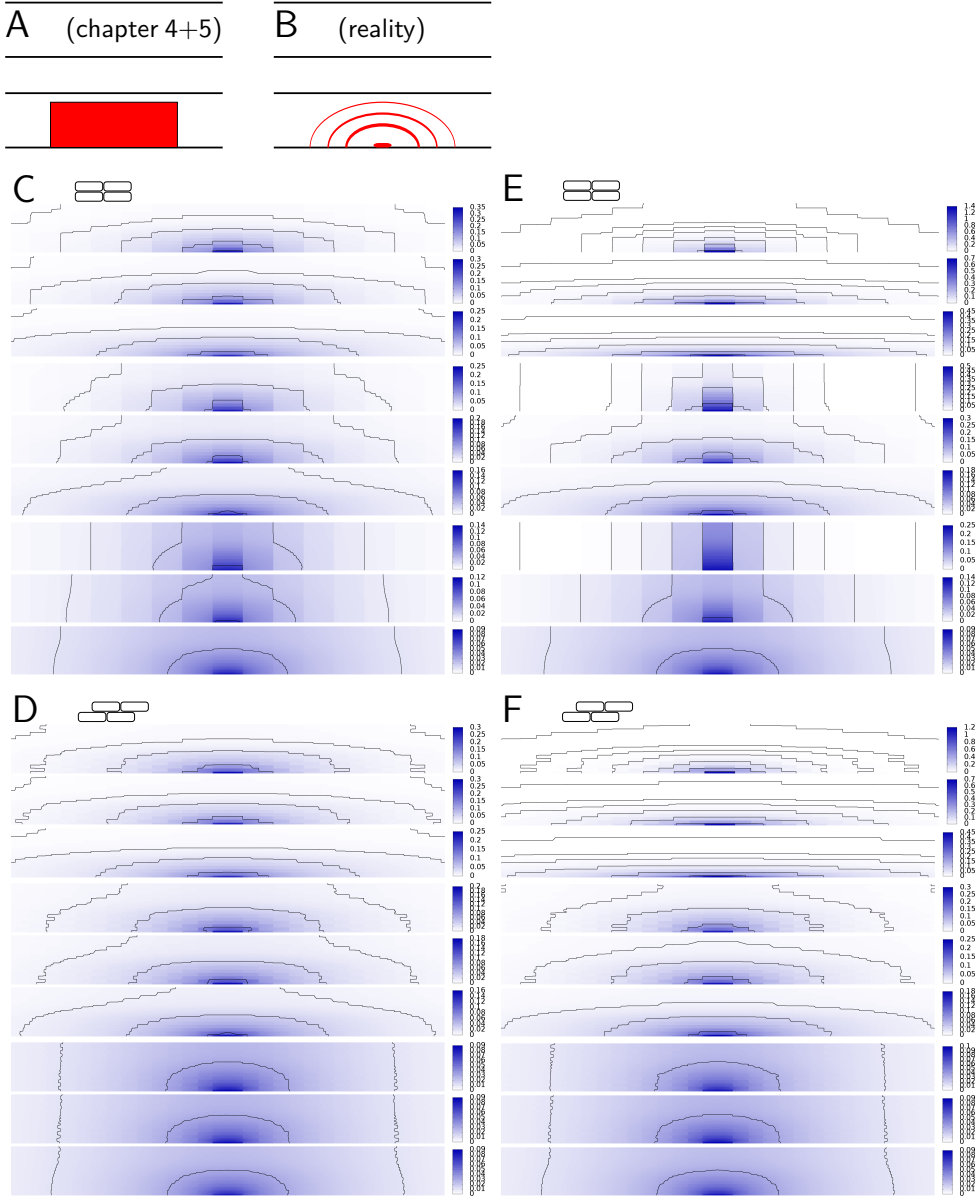
### 6.2.1 Symplastic transport affects spreading of [epidermal] CK

Before studying the interaction of CK and auxin, we first studied the impact that different assumptions on CK transport have on the shape of the resulting CK profiles, the “input” for the interaction. Figure 6.1 shows the spread of a steady CK signal produced from a single cell in the epidermis (indicated in 6.1B). Cell file alignment and assumptions on symplastic permeability both affected the slope of the CK gradient and the ratio of axial:longitudinal spread, but the maximum always coincided with the CK source.

The alignment of cell files in an alternating fashion (D,F) resulted in more longitudinal and less axial spread of the signal than with a “Manhattan” alignment (C,E). This was most pronounced if the symplastic permeability of transverse walls, i.e. relevant for longitudinal symplastic transport, was lowest (rows 1,4,7). This difference was smaller with (C,D) than without (E,F) membrane CK permeability. Conversely, the impact of membrane permeability was largest with low symplastic transport.

### 6.2.2 Linking CK and auxin distribution via PIN dynamics

CK has an inhibiting effect on membrane localized PINs, but the precise functional dependency is unknown. We, therefore, chose the following function for the effective auxin



**Figure 6.1: Spread of an epidermal signal.** Contrary to our previous approach (A, chapters 4 and 5), the change in auxin transport is induced by a signal of epidermal origin (B). C-F A signal produced in a single cell (bottom, middle) is always strongest in the producing cell. The spread of the signal is less sensitive to symplastic structure if the membrane is permeable to the signal ( $P_{mem} = 1\mu\text{m/s}$ ; C,D) than with only symplastic transport (E,F). Walls are divided into two groups for symplastic permeabilities: “L” (transverse; relevant for longitudinal transport) and “R” (tangential; relevant for radial transport). Within each set C,D,E,F:  $(P_{sym,L}, P_{sym,R}) = (0.1, 0.1), (1, 0.1), (10, 0.1), (0.1, 1), (1, 1), (10, 1), (0.1, 10), (1, 10), (10, 10)\mu\text{m/s}$ .  $T=1\text{h}$ .

efflux permeability  $P_{eff}$  as a function of the average CK concentration in the cell:

$$P_{eff} = P_{eff, intr} / (1 + (\kappa[CK])^p) \quad (6.1)$$

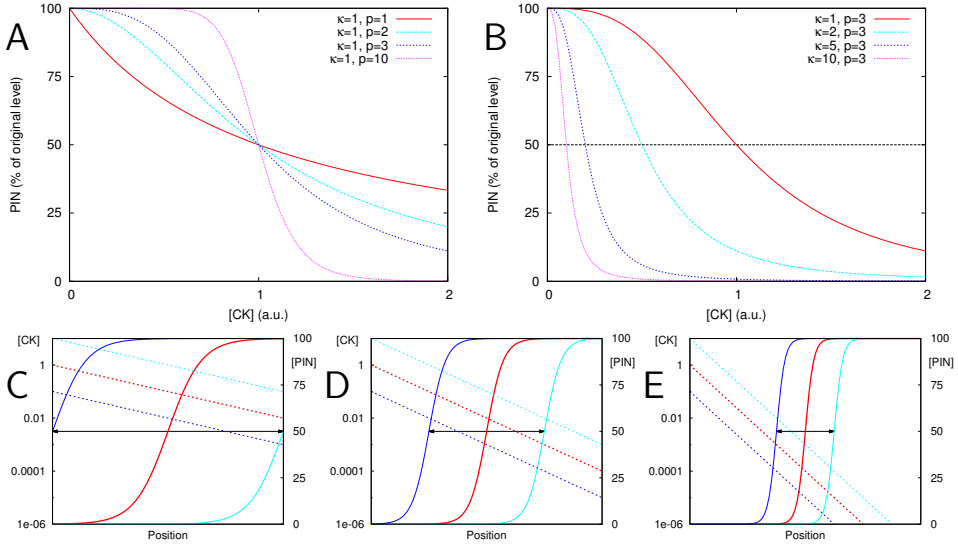
This function has two degrees of freedom: parameters  $p$  and  $\kappa$ . The exponent  $p$  determines whether the response to CK is gradual  $p = 1$ , or switch-like (large  $p$ ) around a threshold concentration  $[CK] = 1/\kappa$  (figure 6.2A,B). For a response in the inner cortex and pericycle,  $\kappa$  should be such that the CK signal that reaches these interior layers is sufficiently strong to trigger a large reduction of the effective efflux permeability in these layers. At first glance, it seems well possible to match the  $\kappa$  and  $p$  to any monotonic CK gradient. In reality, however, there will be some degree of noise, for example in the amount of CK produced. We, therefore, tested how much the response curve will shift upon a 10-fold increase or decrease of the production rate. For this we calculated the PIN reduction as a function of the distance from a CK source in a simple 1D model. We assumed an exponential steady state CK gradient – as both symplastic and symmetrical apoplastic transport yield such gradients after coarse graining (for homogeneous 1D tissues: see chapter 2) – and computed the percentage of PIN left in the membrane (figure 6.2C-E). The steeper the CK gradient, the smaller the shift upon a change of the CK production rate, but the fewer molecules will be available, and so the larger the sensitivity  $\kappa$  has to be to keep the 50% response in the same position (figure 6.2C-E).

Starting without symplastic transport, we investigated the auxin accumulation in response to a CK signal produced in a single epidermal cell. We studied this response in two different unperturbed PIN layouts (figure 6.3A), called “Lotus” and “Medicago” for their steady state auxin accumulation pattern in response to a homogeneous decrease of the effective efflux permeability (see chapter 4, figure 4.4). With the “Lotus” layout we observed a first auxin accumulation in the epidermis/outer cortex, which either remained strongest close to the source (figure 6.3B), or was later dominated by a much stronger accumulation in the vascular tissue (figure 6.3D,E), depending on  $p$  (gradual (B) vs switch-like (E) response). With the “Medicago” layout on the other hand, the response was always strongest in the inner cortex and vascular tissue (figure 6.3G-J). Interestingly, the auxin concentrations in both the innermost cortical layer (C5) and the pericycle were typically\* higher than in the endodermis, the layer in between these two layers. Similarly, the number of cells showing a clear increase of the auxin concentration was larger in C5 and the pericycle. The difference between the “Lotus” and “Medicago” layout most likely results from the auxin availability in the outer layer, which is much higher in the “Lotus” layout. Moreover, with increasing  $p$  we observed an increasing transient decrease of the vascular auxin concentration downstream of the induction site (to the right). With high  $p$  the vascular PIN levels were also reduced further than with low  $p$ .

A mismatch between overall sensitivity  $\kappa$  and the CK gradient resulted in “unnatural” auxin accumulation patterns (figure 6.3K-O). Too small  $\kappa$  resulted in a purely cortical response with the “Lotus” layout, or hardly a detectable response with the “Medicago” layout. Too large  $\kappa$ , on the other hand, resulted in a response that was strongest almost a millimeter (up to 8 cells) upstream of the induction site. With increasing  $\kappa$ , the downstream auxin depression became more pronounced, coinciding with a larger responding area in the vascular tissue.

---

\*The one exception was the “freak” case with  $p = 10$  (figure 6.3J).

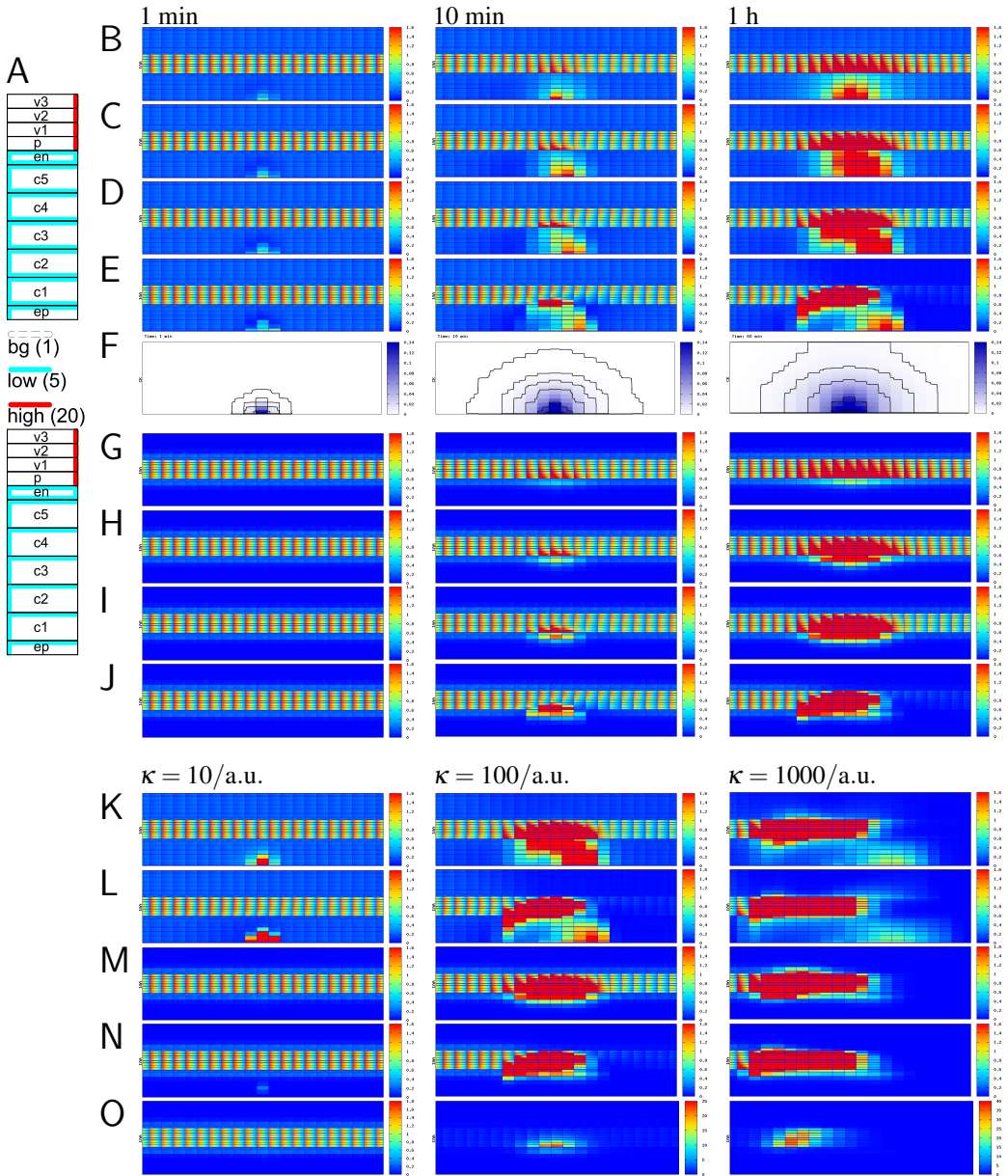


**Figure 6.2: CK response curves for membrane PINs.** **A,B:** Sensitivity of membrane PIN concentration to [CK] depending on model parameters  $p$  (**A**) and  $\kappa$  (**B**). **C-E:** Sensitivity to changes in CK production depends on the steepness of the CK gradient (dashed lines). The spatial shift (horizontal arrow) of the PIN response curve (solid lines) with a 10-fold change in the production rate is proportional to the gradient's characteristic length  $\lambda$ . All three graphs are plotted with the same axes lengths. As  $\lambda$  decreases 4-fold from **C-E**, a 10000-fold increase of  $\kappa$  is needed to keep the 50% point ([CK]=1/ $\kappa$ ) of the default response curve (thick red lines) at the same distance from the CK source. Default:  $p = 3$ .

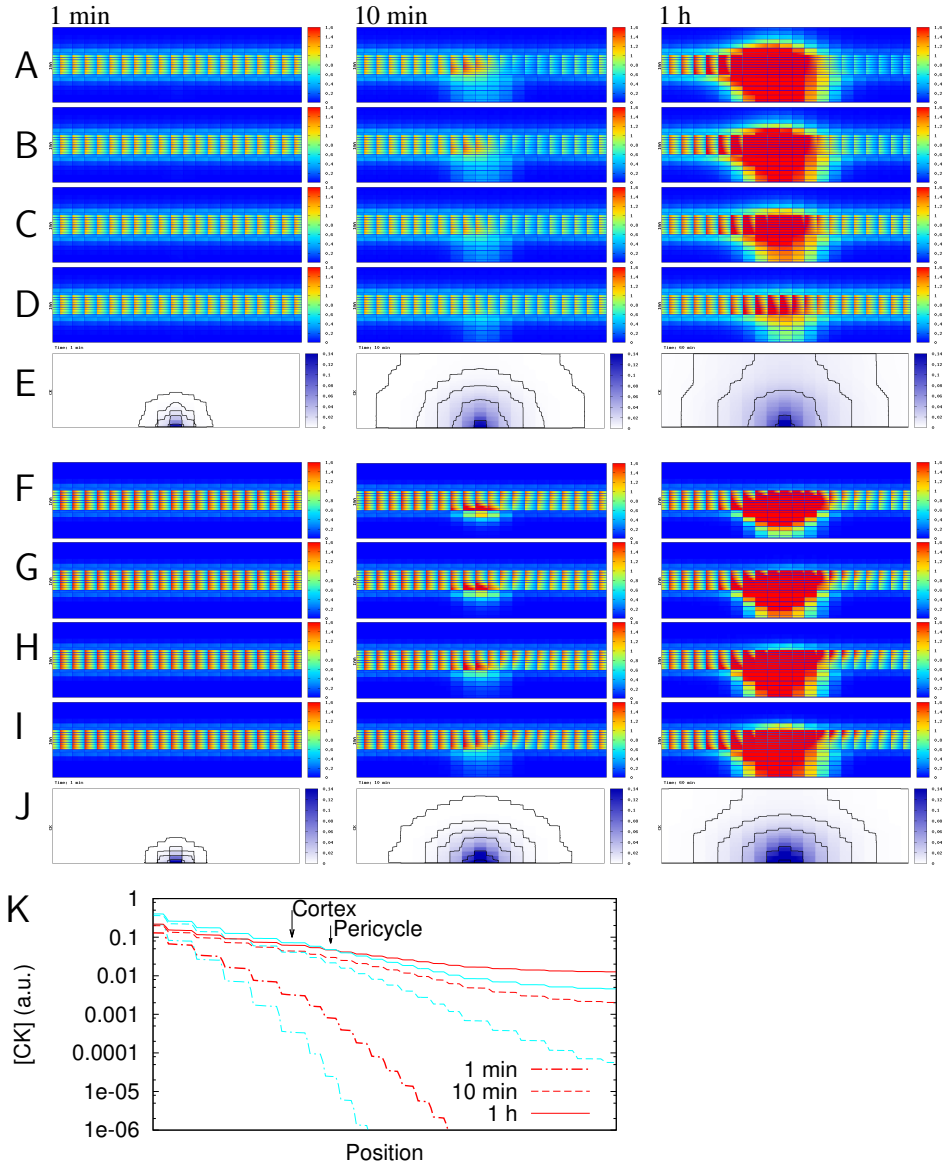
### 6.2.3 Impact of symplastic transport

From the differences in the CK gradients found with different symplastic permeabilities and cell file alignments (figure 6.1), we expected that changes in symplastic transport could affect the shape of the induced primordium (the number of cells in the relevant files showing auxin accumulation above a certain level). We therefore induced auxin accumulation in roots with an effective symplastic permeability of  $P_{sym} = 1 \mu m/s$  in all walls (figure 6.4A-E). We found that symplastic transport affected more than just the length of the primordium (number of cells per cell file showing auxin accumulation). With otherwise the same conditions as in figure 6.3I, the induced auxin accumulation not only was less strong, but also spread through the whole cortex, as well as the inner cortical layers on the other side of the vascular bundle (figure 6.4A).

In chapter 2 we found effective diffusion constants to describe the symplastic movement of signal in a 1D tissue. These could be adapted to include both symplastic and membrane (effective) permeabilities:  $D_{eff} = \frac{D(\frac{1}{2}P_{mem} + P_{sym})l}{D + (\frac{1}{2}P_{mem} + P_{sym})l}$  with  $D$  the cytoplasmic diffusion constant and  $l$  the cell length/width (see figure 2.5). Not all the cell widths are the same in our *in silico* roots, but this expression does explain why the CK gradient was flatter with symplastic transport (figure 6.4K). The amount of CK accumulated in the “near”



**Figure 6.3: Auxin response to epidermal signal depends on PIN layout and response function.** **A**: initial PIN distribution for “Lotus” (top, for **B-E,K,L**) and “Medicago” (bottom, for **G-J,M,N**) roots, illustrated by 1/2 of the root layers (effective efflux permeabilities in  $\mu\text{m/s}$ ). The difference is in the outward PINs in the cortex (c1-c5). **F**: CK input signal (no symplastic transport). Parameters:  $\kappa = 100/\text{a.u.}$  (**B-J**),  $p = 1$  (**B,G**),  $p = 2$  (**C,H**),  $p = 3$  (**D,I,K,M**),  $p = 10$  (**E,J,L,N**),  $T=1\text{h}$  (**K-N**). **O**: same as **M** but with adapted color gradient. With  $\kappa = 1000/\text{a.u.}$  the strongest auxin accumulation at 1h occurs far upstream of the induction site, i.e., to the left in this figure.



**Figure 6.4: Symplastic transport: shallower gradient and less confined response.** **A-E:** With symplastic transport. With the default sensitivity  $\kappa = 100$  a.u., the region of auxin accumulation extends beyond the vascular tissue (A). This effect can be compensated by reducing  $\kappa$  to 80, 60, 40 a.u. respectively (B-D), which results in less induced auxin accumulation. **F-J:** No symplastic transport, but basal efflux permeability. This also results in more auxin in the (outer) cortical layers and a decrease of the total accumulation.  $P_{eff,base} = 0.1, 0.2, 0.5, 1 \mu\text{m/s}$  respectively (F-I). The CK gradient (J) is unaffected, so the same as in figure 6.3. **K:** The CK gradient is flatter with (red, E) than without (cyan, J) symplastic transport. Default parameters:  $P_{sym,IAA} = 1 \mu\text{m/s}$ ,  $P_{sym,CK} = 0.7 \mu\text{m/s}$  (A-E),  $p = 3$  (all),  $\kappa = 100$  a.u. (A,F-I), PIN layout: "Medicago".

cortex and pericycle was very similar with and without, but at the other side of the vascular bundle the CK concentration was higher with symplastic transport. In line with this, a decrease of overall sensitivity  $\kappa$  was sufficient to greatly reduce the “bleeding” to the other side of the vascular bundle (figure 6.4B-D). Concurrently, we observed a decrease of the amount of auxin accumulating. This could be understood with the help of figure 6.2C-E: The response curve, as a function of distance from source, is less steep with shallower gradient. This suggests that the decreased accumulation could be compensated by increasing  $p$  (not shown).

Besides an effect on the steepness of the CK gradient, symplastic transport also results in altered ratios of total efflux per side of the cell when the effective efflux permeabilities are reduced. A different way of changing the ratios of efflux between cell faces is by introducing a basal efflux level  $P_{eff,base}$ , as discussed in chapter 5.

$$P_{eff} = P_{eff,base} + P_{eff,extra} / (1 + (\kappa[CK])^p) \quad (6.2)$$

In this case the starting value is split into a CK responsive ( $P_{eff,extra} = P_{eff,intr} - P_{eff,base}$ ) and a non-responsive ( $P_{eff,base}$ ) part. As this only concerns the auxin transport, the CK gradient is the same as in figure 6.3. Nevertheless, this altered response also resulted in a spread of the auxin accumulation towards the outer cortex (figure 6.4F-J). With increasing  $P_{eff,base}$  the pattern better resembled the one with symplastic transport and even a little bleeding across the vascular bundle could be observed (figure 6.4(I),J).

## 6.2.4 Competition for auxin

In our results so far we observed a transient decrease of the vascular auxin concentration downstream of the induction site, in line with experimental observations [229]. As changes in auxin transport and/or content have been observed in both hypernodulating *Medicago truncatula* mutants *sun* [246] and *sickle* [276], we decided to investigate to what extent the induction of one primordium would hinder the induction of a second primordium. For this we induced a second primordium downstream with respect to the net (=vascular) auxin flux (rootward/right; figure 6.5A,B) or upstream (shootward/left; figure 6.5A,B) of the first. The CK producing cells in the epidermis were separated by 8 non-producing cells. We found that the upstream one of the two primordia was virtually unaffected by the presence of a second primordium, as measured by the auxin concentration in the pericycle and inner cortex (C5) cell closest to the epidermal CK source (figure 6.5E). The downstream primordium, however, was always affected by the upstream one (figure 6.5F). If it had been induced first, the concentration in the pericycle could even show a temporal decrease (upstream induced 30min or 1h later). If it had been induced second, the concentration in both cortex and pericycle would rise slower than without upstream hindrance. The longer the downstream primordium was induced after the upstream one, the smaller the impact on the increase of the auxin concentration. In line with this, the transient decrease of the auxin concentration was largest after about 20-30 minutes, followed by a slow increase over the following few hours (figure 6.5G).

## 6.3 Discussion

### 6.3.1 Nodule primordium induction by an epidermal CK signal

In both *Lotus* and *Medicago*, nodulation starts with an epidermal encounter with compatible rhizobia. Next, an epidermal signal induces cell divisions in the plant host [26]. The radial position of the divisions differs between the two species, in relation to the type of the nodules they form [28]. Our simulations show that the PIN distribution in the susceptible zone of the root together with the CK-membrane PIN response function determines the location of the induced auxin maximum. Varying these we could reproduce the auxin accumulation patterns of both nodule types.

With the “*Medicago*” PIN layout, the resulting auxin maximum always occurred in the interior layers: inner cortex - pericycle, in line with experimental observations. Interestingly, for all combinations of response parameters  $p$  and  $\kappa$  that gave realistic results, the auxin accumulation in the inner cortex and pericycle was larger than in the endodermis (figure 6.3G-J). This is in line with the later onset of endodermal cell divisions (unpublished observations: T. Xiao *et al.*, in preparation) and the omission of the endodermis in published detailed descriptions of the early stages of indeterminate nodule formation [27]. With increasing radial symplastic transport of auxin, more auxin would accumulate also in the more exterior cortical layers (figure 6.4A-E). The same happened with an increasing non-CK-responsive base auxin efflux level ( $P_{eff,base}$ ), as this resulted in the inward and outward auxin efflux becoming more similar with increasing [CK] (figure 6.4F-J). In both cases, however, the first and strongest auxin accumulation occurred in the interior layers (figure 6.4).

With the “*Lotus*” PIN layout, on the other hand, the first auxin accumulation was always observed close to the epidermal source (figure 6.3B-E). Towards a more sensitive PIN response (high  $\kappa$  and/or  $p$ ), the auxin accumulation pattern at later time scales was dominated by the pericycle or vascular tissue (figure 6.3B-E,K,L).

With both layouts we observed a transient decrease of the downstream (rootward) auxin concentration, in line with experimental observations [229, 277]. The stronger the decrease of PINs and resulting auxin accumulation in the vascular tissue, the more pronounced this depression, independent of the PIN layout used (figure 6.3).

A different way of obtaining an interior, i.e. *Medicago*-like, auxin accumulation pattern in response to an epidermal signal could be that only the cells of the interior layers respond to the signal. In *Medicago*, however, the nodulation related (A-type) cytokinin response factor MtRR9 is induced in all cortical layers [35], showing that all layers respond to the CK signal as it moves from epidermis to the inner root layers. Also the expression of D27, marker for strigolactone biosynthesis, occurs in all cortical layers (W. Liu *et al.*, in preparation). Strigolactone is indicated as a reducer of auxin efflux [278, 279]. Its effect on lateral root density involves SHY2 [280], an Aux/IAA protein also involved in cytokinin’s effect on auxin efflux [38]. Taken together, this does not support the idea that only cells of the interior layers are sensitive to the CK signal, and supports the previous hypothesis that auxin availability is an important factor in the radial positioning of the nodule primordium [182].



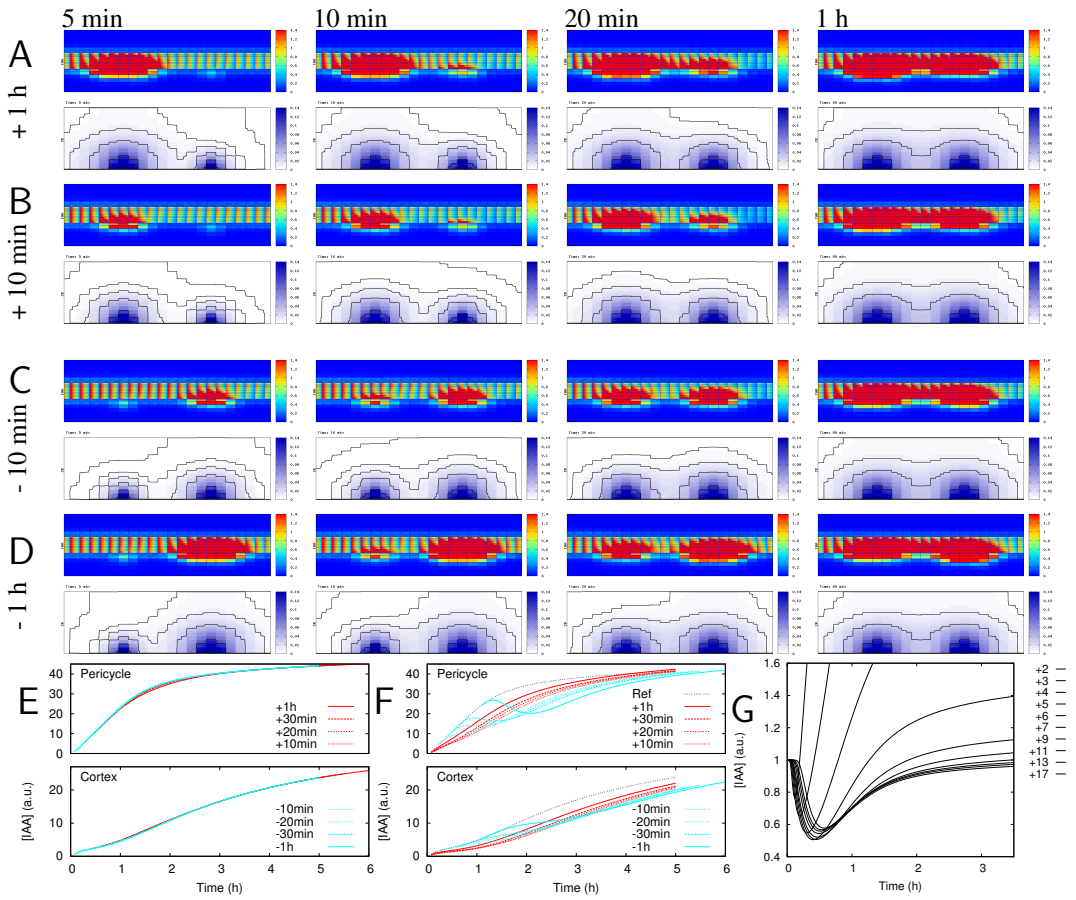


Figure 6.5: **Auxin competition among primordia.** Labels indicate how long before the downstream (right) primordium the induction of the upstream (left) primordium was started. **A,B:** Upstream primordium induced first. **C,D:** Downstream primordium induced first. **E,F:** Auxin concentration in (the center of) the pericycle cell and C5 inner cortical cell closest to the CK production site upstream (**E**) or downstream (**F**). The concentration increase in absence of a second primordium is indicated by dotted-dash gray lines in **F**. **G:** Quantification of the reduction of the auxin concentration in the pericycle downstream of the induction site (labels indicated the distance in number of cells; the position where the second (downstream) primordium would be induced is indicated with a thick line (“+9”). PIN layout: “Medicago”.

### 6.3.2 Differential sensitivity of PIN proteins to CK

In *Arabidopsis*, not all PINs respond to CK treatment in the same way [38, 39, 249]. For example, AtPIN1 rapidly disappeared from the membrane, AtPIN2 was less sensitive, and the amount of AtPIN7 even increased initially, with a strongest increase 4-6 h after CK (BAP) treatment [39]. Most PINs are transcriptionally downregulated by extended CK ex-

posure [38, 249], with the possible exception of vascular AtPIN7, which is upregulated in some [249], but not all [38, 249] reported measurements. If these findings in *Arabidopsis* generalize to legumes, this would imply that the presence of PINs in the membrane is less sensitive in the cortex, predominantly AtPIN2 in *Arabidopsis* and MtPIN2 in *Medicago*, than in the vascular tissue, at least for AtPIN1 in *Arabidopsis* and its *Medicago* equivalent. This would affect the relative strength of the vascular and cortical response. In the situation in which we obtained a “Lotus-like” auxin accumulation pattern, i.e. strongest accumulation in the outer/middle cortex, the downstream decrease of the auxin concentration was much less pronounced than with “Medicago-like” patterns, i.e. dominated by the inner cortex and pericycle, because the vascular transport was much less affected. If the vascular PINs were much more sensitive than the cortical ones, it would be possible to have both a cortical response restricted to the outer layers and a strong temporal reduction of the vascular flux. The observations of a temporal downstream minimum have so far been made in *Medicago* [229] [277]<sup>†</sup>, so a very relevant question is if this also happens in *Lotus* and other legumes with an even more peripheral site of primordium initiation. AtPIN7 is expressed in the vascular tissue. If a vascular PIN is upregulated after a number of hours, this could shorten the duration of the transient auxin depression downstream of the induction site. It would also result in a less extreme local auxin accumulation in the vascular tissue, which can be very high in our simulations, particularly with response parameters leading to high CK sensitivity, and no basal auxin efflux or symplastic transport.

### 6.3.3 Impact of symplastic transport

Because both auxin and CK are small molecules, symplastic transport affects our primordium initiation mechanism in two ways: first through the shape and steepness of the CK gradient (“input”) (figure 6.1) and second by altering the auxin accumulation pattern (figure 6.4). The latter depends on a change of the ratios of efflux over different wall faces and can be reproduced, at least partially, by introducing a basal effective efflux permeability level  $P_{eff,base}$  (figure 6.4F-I; see also chapter 5). The impact of symplastic transport in this respect seemed more severe, but it should be noted that in a symmetrical 1D case, similar profiles were found for parameter combinations  $2P_{mem} + P_{sym} = y$ , implying that the impact of symplastic permeability is twice that of membrane permeability (chapter 2, figure 2.5), and thus that the symplastic permeability used in figure 6.4A-E is high compared to the highest  $P_{eff,base}$  in 6.4I. It is hard to tell whether the value of  $P_{sym} = 1\mu\text{m/s}$  is high for the relevant region of legume roots, as all published studies on effective permeabilities are performed in different systems [163, 168, 169]. It is about five fold lower than what could be expected based on measured values for transverse walls in the meristem zone of the *Arabidopsis* root [163] or cucumber leaf mesophyll cells [169]. These cell types are both known, however, for their high symplastic conductivity, which in roots decreases as the tissues mature [163, 181].

In principle, the part of the interior tissues responding to the CK signal – i.e. the location of the  $[CK] = 1/\kappa$  contour and the width of the region showing a partial response (e.g. 10-90% PIN reduction) – can be tweaked to any gradient steepness by adapting  $\kappa$  and  $p$ . The shallower the gradient, however, the larger  $p$  has to be for a localized

<sup>†</sup> Describes measurements at only a single time point, i.e. 24h after spot inoculation, finding a reduction of auxin transport.

response – i.e. strong in the inner cortex and pericycle on one side of the root, but not “bleeding” through to the other. In biochemical terms, increasing  $p$  means increasing some mechanism, such as a positive feedback in detection, that enhances detection above the (arbitrary!) threshold  $[CK] = 1/\kappa$ , but not below. This implies that a minimal gradient steepness is needed – and the shallower the “input” gradient, the stronger the requirements on the additional mechanism(s) that prevent(s) the CK signal from moving too far beyond the desired site of primordium initiation or confine(s) the response.

We started with an overview of how the root structure – in terms of symplastic permeability – could affect the shape of the CK gradient (figure 6.1). After that, however, we did not include all these symplastic structures of the tissue when studying the CK-auxin interaction. A key reason is that, because the CK gradient is different for every case and our crude interaction between CK and membrane PINs is not very robust against such changes, a large number of simulations would be required to come to a full overview of the combined effects. By combining the insights of figures 6.2C-E and 6.4, however, we could predict from figure 6.1C,E the impact of symplastic transport in the longitudinal and radial directions on auxin accumulation in the inner cortex/pericycle (at least for the square cell file alignment as used in figures 6.1C,E and 6.3-6.5). It appears that the effective symplastic permeability of tangential walls,  $P_{sym,R}$ , has the strongest effect on the gradient steepness from epidermis to pericycle and beyond. Whether radial symplastic transport increases or decreases the robustness of the lateral position of the primordium depends on the starting situation: in principle a steeper gradient allows for larger robustness against fluctuations in the production rate (figure 6.2C-E), but if the starting gradient already is so steep that very few CK molecules would reach the inner cortex and pericycle, a less steep gradient would result in more reliable positioning due to less finite number noise [158]. The effective symplastic permeability of the transverse walls,  $P_{sym,L}$ , on the other hand, would mostly affect the length of the primordium through affecting the curvature of the  $[CK] = 1/\kappa$  and other relevant contours close to the vascular tissue.

The two directions are more coupled in case of a “brick wall” alignment of the cell files. In that case a high symplastic permeability of the tangential walls also promotes longitudinal transport of the CK signal (bottom of figure 6.1D,F) by enabling a “zig-zag” movement between cell files, bypassing the barriers formed by the transverse walls (see also figure 2.3J). As this alignment is probably closer to the cell file alignment in real roots than the square alignment (figure 6.1C,E), this suggests that a limited value of  $P_{sym,R}$  is important for confinement in both directions: with (too) high  $P_{sym,R}$ , the resulting CK gradient may be too shallow for a reliable interior response close to the epidermal induction site.

An interesting observation with respect to symplastic transport and nodulation comes from transgenic *Medicago* plants expressing a viral (TMV) movement protein. This movement protein increases the effective wall permeability for non-targeted symplastic transport by increasing the opening of the plasmodesmata [281]. These plants show increased nodulation [282]. Whether this results from increased overall auxin availability, more effective CK transport, or decreased autoregulation through less auxin retention in the vascular tissue near the primordium (or something altogether different), remains to be elucidated. The authors [282] only report the number of nodules per plant, not their spatial distribution or any changes therein, which complicates the interpretation of their results. Their observation nevertheless marks symplastic transport as an interesting factor

to consider in the study of the control of nodule numbers, if not because of a direct regulating role, then at least because different hypothetical mechanisms might be differentially affected. This problem should be within reach with the tools outlined in this chapter.

### 6.3.4 Confinement of the auxin response

A single infection event should result in no more than one primordium, with reasonable dimensions and in the correct position relative to the bacterial entry point, i.e., in the correct layers and centered as close as possible to the bacterial entry point. In our model, some degree of confinement results from the homogeneous degradation of the CK signal throughout the tissue. The larger decay parameter  $\delta$ , the steeper the “input” gradient and the easier a reliable readout can be achieved. Moreover, the higher  $\delta$ , the faster the steady state distribution is approached. In the “medicago” setup, i.e. with an inward directed bias of the cortical PINs, the auxin accumulation in the inner layers on one side of the root could easily be obtained by a switch like (high  $p$ ) PIN response function to the position of the steady state contour  $[CK] = 1/\kappa$ .

There are limits, however, to the robustness of this design with respect to signal detection in the inner cortex/pericycle and with respect to primordium size. On the one hand, a higher  $\delta$  creates a steeper gradient, which results in less displacement of the  $[CK] = 1/\kappa$  contour with a fixed change of the production rate, or other noise affecting signal propagation (figure 6.2). On the other hand, a higher  $\delta$  results in far fewer CK molecules reaching the inner cortex/pericycle target site and, hence, in an increase in the noise from detecting the CK concentration. There are, in short, fundamental limits to the precision of communicating positional information using a single gradient [158]. Diverse experimental observations suggest that indeed additional regulating mechanisms exist. For instance, in *Lotus*, homogeneous exposure to CK induces several distinct nodule-like structures and not a homogeneous response throughout the (susceptible part of the) root [283],

Interestingly, the A-type RRs, negative regulators of the CK response, are much smaller proteins than the B-type RRs, which are positive regulators of the CK response<sup>‡</sup> (e.g. [284] (rice)). This implies that there exists a regime of plasmodesmata dimensions allowing the non-targeted symplastic movement of A-type RRs, but not of B-type RRs. This could result in a combination of a local positive feedback enhancing a weak CK signal (B-type) and a wider range suppression of the response (A-type). This would combine increased sensitivity – i.e., a larger chance of detecting the incoming signal – with robustness of the primordium size, similar to the inhibitor in Turing-like models. Locally this would function in a “winner takes all” fashion.

It is important to note, however, that, although conceptually interesting in the light of symplastic transport and pattern formation, this size difference may not be relevant in the context of nodulation. The A-type RRs are of similar size as single GFP molecules (238 aa), which are able to move symplastically in some situations, e.g., heart stage embryos [122] and sink leaves [123], but far from always. A new symplastic domain for single GFP is formed during nodulation, but happens after rather than before specification of the

<sup>‡</sup>NUMBERS: In *Arabidopsis*, the A-type RRs range from 186 (AtRR6) to 225 (AtRR8) and the B-type RRs from 521 (AtRR11) to 690 (AtRR1) aa. Similar values hold for rice: A-type RRs range from 121 (OsRR8, OsRR12, OsRR13) to 252 (OsRR2) and B-type RRs range from 582 (OsORR6) to 696 (OsORR2) aa [284]. (source: pubmed protein, 25/02/2013).

primordium site [282].

A more likely candidate for confining the response would, therefore, be ethylene, a known negative regulator of nodulation [285, 286]. It has been demonstrated that the production of ethylene from the phloem poles is important for the positioning of nodules opposite xylem poles in *Vicia sativa* (vetch) [287]. This could also solve a problem that arises when considering this auxin-cytokinin interaction in 3D. In 3D the epidermal signal could move around the central cylinder, so strongly hindered CK movement through the central cylinder would produce a much less effective barrier to CK spreading than expected from a 2D model. In *Arabidopsis*, auxin is not equally distributed over the vascular cylinder, but is higher in the (proto)xylem than in the (proto)phloem [94]. Given the importance of auxin availability for the ease of inducing its local accumulation, this radial bias in the auxin distribution could contribute to the radial confinement of nodule primordia, although it would require ethylene for reinforcement of this bias [29, 287]<sup>§</sup>.

### 6.3.5 Auxin availability and autoregulation of nodule number

Changes in auxin transport and/or content have been observed in both hypernodulating *Medicago truncatula* mutants *sun* [246] and *sickle* [276], suggesting auxin could play a role in the autoregulation of nodulation. Moreover, local auxin depletion resulting from transport towards auxin maxima in the shoot apical meristem has been shown to function as a “long range inhibitor” that regulates the location of new primordia. Mathematically this functions equivalent to a diffusing inhibitor molecule in a classical Turing model [288].

We found that a primordium that is induced upstream, i.e. shootward, of another primordium is hardly affected by the presence of the downstream induction site, whereas the downstream one is always affected, even if it was founded first (figure 6.5). The transient decrease of the auxin concentration occurs downstream and thus can only affect primordium formation there. At first glance this may appear to contradict that auxin availability is a suitable mechanism for nodule regulation, however, as the root continuously grows and develops, the susceptible zone follows the root tip. This enforces (by and large) new primordia to be initiated downstream of previous ones, that is, on the side of the transient auxin depression.

Thus, the combination of transient downstream (rootward) auxin depression and the developmental rootward progression of the susceptible zone produces a timer-like mechanism for nodule number control. If a minimum amount of auxin is required for the initiation of the primordium program, the overall auxin availability will affect nodule number. This is in line with the increased auxin content in hypernodulator *sun* [246]. Although ethylene affects the total reduction of auxin transport (stronger reduction upon addition of ethylene precursor ACC to wild type roots) [276], the different responses show that ethylene also has a different effect on spacing [29]. The proposed mechanism further

<sup>§</sup>In vetch, about 10% of the nodules formed across phloem poles in the presence of ethylene inhibitors, compared to less than 1% without [287]. In the ethylene insensitive *Medicago* mutant *sickle*, however, there was almost no bias (56% across xylem poles versus 81% in wild type)[29]. This could be explained in two ways: 1: the ethylene inhibitors reduced, but did not abolish ethylene signaling in vetch or 2: the slight bias in *sickle* is significant, but small because of the overall much weaker bias in *Medicago*. The difference in the strength of the bias could perhaps result from the differences in cortex thickness between both species and/or the larger number of xylem poles in *Medicago* (4 vs 3).

predicts that upon first inoculation of a several day old root, nodule initiation will tend towards the oldest, i.e. shootward/upstream, end of the susceptible zone, temporarily suppressing nodulation towards the younger side of the susceptible zone. This suggests that the apparent susceptible zone would extend farther rootward with spot inoculation than with systemic inoculation. Experimentally this may be hard to test, as the (locally) applied *Rhizobia* may simply “wait” until the spot has matured enough to be susceptible and inducing a primordium with some delay. Given variations in development, such a delay might be hard to detect.

In the literature the duration of the auxin depression was longer than the about 2 hours we observed in figure 6.5G [229, 277]. This duration, however, will depend on parameters: the strength of the reduction of the effective efflux permeability determines how much more auxin is required to reach the new local steady state and thus the time it will take before the new steady state is reached, as the supply (normal flux through the root) is constant; for the same reason time scales are affected by the steady state flux through the unaffected root (a function of the effective efflux permeabilities), etc. Moreover, we have modelled the response to CK as instantaneous, whereas in reality it may take several hours before the maximum PIN reduction is reached [39]. We did not tune our parameters to the correct timing of such events, as this was not our (primary) aim, but with our model we are able to predict in what way parameter changes will affect the strength of the responses and the time scales of the phenomena we describe.

## 6.4 Conclusions

Using computer simulations we have shown that a mobile signal produced in the epidermis can induce an accumulation of auxin that occurs first and strongest in the inner cortex/pericycle. This finding resolves the paradox between the interior location of the primordium of indeterminate nodules as formed by *Medicago* and the epidermal origin of the primary signal that induces it. We have discussed several mechanisms that could improve the robustness of the proposed mechanism for primordium initiation, with promising directions for future investigations.

## 6.5 Methods

### 6.5.1 General setup

In our simulations, CK is produced in a single epidermal cell on one side of the simulation domain, usually in the middle of a 48 cell long *in silico* root. This root is the same as the DZ root used in chapter 4 (figure 4.1(A)B), with “low” (DZ) or “bg” (figure 4.4, \* and rightmost, respectively) starting level for the effective efflux permeability in the abaxial walls of the cortical cells, but twice as long. Effective efflux permeabilities in absence of CK for both roots are summarized in figure 6.3A. For easy reference we call the root with “low” effective efflux permeability in the abaxial walls of the cortical cells “Lotus” and the one with “bg” in these walls “Medicago”, based on the location of the steady state auxin maximum in previous work (chapter 4, figure 4.4).

### 6.5.2 Numerical simulations

We used the Alternating Direction Implicit (ADI) algorithm [183], when applicable using a pentadiagonal matrix to accommodate symplastic transport (see chapter 2). Diffusion, degradation, production and transport were calculated for auxin and CK separately. To minimize discrepancy between concentrations and transport parameters, the auxin transport parameters were updated using the average CK concentration per cell after every half-time step of the ADI algorithm. We used a full time step of 1s.

### 6.5.3 Parameters

Default auxin transport and metabolism parameters were the same as in [182]<sup>¶</sup>. The default was no symplastic transport. Where applicable, effective wall permeabilities for symplastic transport are mentioned in the main text. CK was produced with rate  $0.01 a.u./s$ , in designated cells only, and degraded with rate  $0.001/s$  in all cells. CK diffusion constants were  $200 \mu m^2/s$  in cells and  $30 \mu m^2/s$  in walls, which is  $2/3$  of the diffusion constants used for auxin. As symplastic transport is diffusive [108, 144], a molecule's diffusion constant affects its respective symplastic permeability values (chapter 3). We therefore used a factor 0.7 to calculate the values for CK from the corresponding values for auxin (except for figure 6.1, which only includes CK). For CK we used a default membrane permeability value of  $1 \mu m/s$ , almost twice the value typically used for protonated auxin (IAAH) (e.g. see [54]).

---

<sup>¶</sup>= chapter 4





## **Part III**

# **Self organisation of cortical microtubules**



Plant growth and development is also a story of mechanics. The mechanical properties of the building blocks, the cells, originate from a combination of turgor pressure in the cells pushing against the, typically highly anisotropic, cell walls. The deposition of the wall fibrils is guided by cortical microtubules, a population of often strongly aligned microtubules attached to the inside of the cell membrane. They can also affect cell shape directly by withstanding mechanical forces. This is particular important for young or thin walls.

Individual microtubules are highly dynamic protein filaments, which frequently switch between growing and shrinking states. Because of their attachment to the cell membrane, these cortical microtubules form a quasi-2D system and therefore interact through frequent collisions. The collision angle determines the possible outcomes of these collisions: for small angles zippering occurs, i.e., continued growth along the obstructing microtubule, for larger angles induced catastrophes, i.e. a switch to a shrinking state, or continued growth along the same path resulting in a cross over occur. Previous studies have shown that these ingredients can be sufficient for spontaneous alignment.

Although so few ingredients can already produce self organization, in reality many proteins and other particulars have been found to be important for the correct alignment and orientation of the cortical array. In this part we will investigate the impact of several experimental observations regarding the nucleation of new microtubules and interaction with the cell geometry on the alignment and orientation of the cortical microtubule array.





---

## **Taking directions: The role of microtubule-bound nucleation in the self-organisation of the plant cortical array**

---

*This chapter is based on [289].*

The highly aligned cortical microtubule array of interphase plant cells is a key regulator of anisotropic cell expansion. Recent computational and analytical work has shown that the non-equilibrium self-organisation of this structure can be understood on the basis of experimentally observed collisional interactions between dynamic microtubules attached to the plasma membrane. Most of these approaches assumed that new microtubules are homogeneously and isotropically nucleated on the cortical surface. Experimental evidence, however, shows that nucleation mostly occurs from other microtubules, and under specific relative angles. Here we investigate the impact of directed microtubule-bound nucleations on the alignment process using computer simulations. The results show that microtubule-bound nucleations can increase the degree of alignment achieved, decrease the timescale of the ordering process, and widen the regime of dynamic parameters for which the system can self-organise. We establish that the major determinant of this effect is the degree of co-alignment of the nucleations with the parent microtubule. The specific role of sideways branching nucleations appears to allow stronger alignment while maintaining a measure of overall spatial homogeneity. Finally, we investigate the suggestion that observed persistent rotation of microtubule domains can be explained through a handedness bias in the microtubule-bound nucleations, showing that this is possible only for an extreme bias and over a limited range of parameters.

## 7.1 Introduction

The so-called cortical microtubule array is a cytoskeletal structure unique to plant cells that plays a pivotal role in the determination and maintenance of cell shape. In elongating cells the cortical array develops a high degree of microtubule alignment oriented transverse to the direction of growth [290]. This specific alignment of the array indirectly controls cell shape by coordinating the transverse deposition of fibrillar structures in the plant cell wall [125, 126]. Although the cortical array is highly ordered, its organizational principle differs from other functional microtubule structures such as the mitotic spindle: it lacks specific organizing centers such as centrosomes [131] and motor proteins do not appear to play a role in its generation or maintenance [291].

Following the observations of Dixit and Cyr [132], it is now widely accepted that the observed organization is due to direct collisional interactions between microtubules, henceforth abbreviated to MTs. Microtubules are long and stiff polymer tubes that show dynamic instability [292]: the so-called plus-end of MTs stochastically switches between a growing and a shrinking state in events called catastrophes and rescues respectively. Their less dynamic minus-end typically retracts on average. The combination of these two effects can result in a net motion, called hybrid treadmilling [291]. In the cortical array MTs appear to be attached to the cell membrane by as yet unidentified linking protein complexes [290]. The cortical array is therefore an effectively 2-dimensional structure in which growing MTs can frequently collide into others. The results of these collisions depend on the relative collision angle. For small collision angles a growing MT almost always bends and continues its growth along the obstructing microtubule, a process called *zippering*. At larger angles there are two possible outcomes. Either the incoming MT will start shrinking shortly after a collision, undergoing an *induced catastrophe*, or it may slip over the obstructing MT and continue growing along its original path, an outcome called a *cross-over*. Several recent studies, using computer simulations [133, 293, 294] and mathematical models [295] have shown that these collisions can indeed explain the spontaneous self-organization of a 2D MT array into an aligned state.

In most of the modelling work it was assumed that new MTs are nucleated at random locations in the cortex in random directions. Detailed microscopic observations, however, reveal that a large majority of cortical MTs is in fact nucleated from nucleation complexes attached to pre-existing MTs and at specific angles with respect to the parent MT [136, 137]. To date only two studies have briefly addressed the issue of MT-bound nucleation [293, 294]. These studies were both limited to investigating MT-bound nucleation with just one or two parameter sets and use a fixed fraction of MT-bound nucleation events. Clearly, the presence of the MT-bound nucleations implies that the state of the array itself influences the distribution of nucleation angles. This creates an additional feedback mechanism, with potential impact on both the degree of alignment and the rate at which this ordering is established. The importance of this aspect, however, may depend both on the details of the nucleation pattern as well as the relative importance of MT-bound and unbound nucleations. This is underscored by the widely diverging results of the two simulations mentioned above.

In the light of the above, we here undertake to provide a comprehensive analysis of the role of MT-bound nucleations in their full complexity. To do so, we extend the theoretical framework [295] and simulation software [133] we have previously developed.

Specifically, this approach allows us to identify a number of key effects not touched upon by previous studies. We dissect the influence of specific features in the pattern of orientations in MT-bound nucleation by using a tailored parametrization of the distribution of nucleation angles that can fit both the experimental nucleation data by Chan and Lloyd [137], as well as other relevant variants. To assess the relative importance of MT-bound versus background nucleation, we implement a physically plausible binding equilibrium of the nucleation complexes with the MTs. This latter mechanism also solves the “bootstrap” problem one faces when evolving the system from an initially MT-free state, as is the case in plant cells after division. Finally, we address the hypothesis touched upon in [137, 296] aimed at explaining the persistent rotations of aligned microtubule domains observed in dark-grown hypocotyl cells [297]. To this end we investigate the impact of a left-right asymmetry in the MT-bound nucleation pattern.

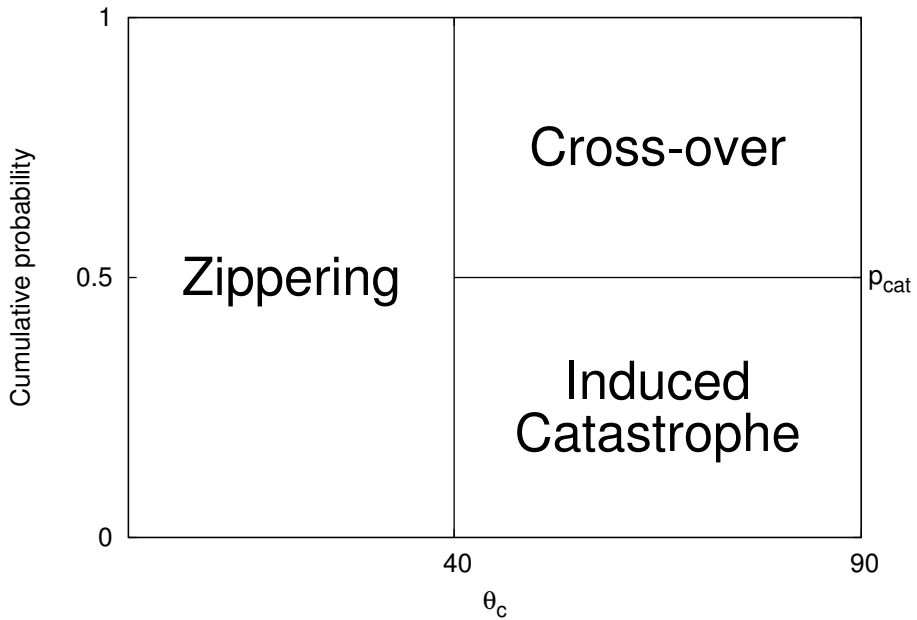


Figure 7.1: **Interaction function:** Zippering occurs for relative collision angles  $\theta_c < 40$ . For larger angles induced catastrophes occur with probability  $p_{cat} = 0.5$  and cross-overs with probability  $1 - p_{cat}$ .

## 7.2 Methods

### 7.2.1 Simulation technique

Simulations of the cortical microtubule array are performed using the event-based algorithm also employed in [133]. We use the same default values for the MT dynamic

parameters as in that work, which are based on [298] (growth speed  $v^+$ , shrinkage speed  $v^-$ , and rescue rate  $r_r$ ) and [291] (treadmilling speed  $v^t$ ). The nucleation rate of  $r_n = 0.001 s^{-1} \mu m^{-2}$  is based on casual observations of interphase cells, and is equal to that in [294]. It gives rise to an ordered state in combination with the chosen instability parameters. A summary of these parameters and their values is provided in table 7.1.

We use a 2D domain of  $80 \mu m \times 80 \mu m$  with periodic boundary conditions. The choice for a periodic simulation domain implies that we focus exclusively on the process of alignment of the array, but not on its orientation with respect to an externally imposed axis.

## 7.2.2 Microtubule interactions

For the MT interactions we follow the simplified scheme first adopted by [293] and followed by [294]: all collisions with angles below  $\theta_c = 40^\circ$  result in zippering. For collision angles larger than  $\theta_c$  the result is either an induced catastrophe, with probability  $p_{cat}$  or a cross-over (see figure 7.1). Different values of  $p_{cat}$  have been reported [132, 299] and different values have been used in the simulations published so far. In the absence of further information we adopt the intermediate value  $p_{cat} = 0.5$ , which falls between the reported values. Analytical calculations in absence of branched nucleation [295] show that the exact choice of  $p_{cat}$  does not affect the sign of the critical value of the control parameter  $G_c^*$  (to be introduced below). We therefore expect to find qualitatively similar results for any particular choice of  $p_{cat} > 0$ .

## 7.2.3 Dimensionless control parameter

Our previous theoretical work [295] has shown that the effective strength of the interactions between cortical microtubule can be characterized by a single dimensionless control parameter  $G$ , which subsumes the individual effects of all dynamical parameters governing the behaviour of isolated microtubules. Here we adopt a generalization of this dimensionless control parameter, suitably adapted to include the effect of minus-end treadmilling, which will allow for a straightforward comparison of the effects of different nucleation parameter settings.

$$G_c = \left\{ \frac{2(v^+ - v^t)^2(v^- + v^t)}{r_n v^+ (v^+ + v^-)} \right\}^{\frac{1}{3}} \left( \frac{r_r}{v^- + v^t} - \frac{r_c}{v^+ - v^t} \right) \quad (7.1)$$

Here  $v^+$  and  $v^-$  are the growth and shrinkage speed of the microtubule plus-end,  $v^t$  is the treadmilling (retraction) speed of the microtubule minus-end ( $\mu m s^{-1}$ ),  $r_r$  is the rescue rate of shrinking microtubules,  $r_c$  is the spontaneous catastrophe rate of growing microtubules (both  $s^{-1}$ ) and  $r_n$  is the nucleation rate ( $\mu m^{-2} s^{-1}$ ). This formula readily follows from the one presented in [295], if one takes into account that the effective growth speed of the MTs is renormalized to  $v^+ - v^t$  and the effective shrinkage speed to  $v^- + v^t$ . The number of collisions of a growing plus-end, however, does not depend on the treadmilling speed, so the renormalization does not apply to the first  $v^+$  in the denominator. Of the two factors in the definition of the control parameter, the second factor is most readily interpreted as minus the inverse mean length of the microtubules *in the absence of collisions*.



When this quantity becomes positive, the intrinsic length of the microtubules becomes unbounded. In that case the system can in general not support a stationary state. For this reason we will restrict ourselves to the regime  $G_c < 0$ . In view of the results obtained in [295], the absolute value of the control parameter can be interpreted as the inverse coupling strength of the system. For values close to zero ( $|G_c| \ll 1$ ), achieved e.g. when the spontaneous catastrophe rate  $r_c$  is relatively small or when the nucleation rate is large, the system is strongly coupled and we can expect orientational order to develop. In both cases the number of collisions between microtubules per unit of time is high, either because nearly all microtubules grow sufficiently long to encounter other microtubules, or because many microtubules are present in the system simultaneously. This control parameter has been thoroughly verified in the situations with either zippering or treadmilling. Although the use of  $G_c$  as an independent quantity, in the situation with both treadmilling and zippering, strictly speaking needs validation, we use it as a convenient phenomenological parameter to present our results. In practice we chose to vary this parameter by changing the spontaneous catastrophe rate  $r_c$ , keeping the remaining parameters fixed, which we explicitly acknowledge through the subscript  $c$ . This choice is based on the fact that this quantity is perhaps least well determined experimentally, as spontaneous catastrophe events are not always easy to distinguish from induced catastrophes or shrinkage after MT severing. This choice also has the advantage of allowing us to probe higher interaction strengths ( $G_c \uparrow 0$ ) in the sense explained in [295], without major changes in the number of MTs, which would be the case if we changed the nucleation rate. Given the values of our default parameters the explicit dependence of the control parameter on  $r_c$  is given by

$$G_c \approx -63.2s r_c + 0.182. \quad (7.2)$$

## 7.2.4 Microtubule-bound versus background nucleation

It is known that new cortical MTs are nucleated from  $\gamma$ -tubulin complexes [136]. We assume that the number of available complexes remains constant over time, so that also the overall nucleation rate remains constant. Given a specific affinity of the complexes for MTs the ratio of bound to free nucleation complexes, however, will depend on the total MT length density  $\rho$ . We model this partitioning by a simple saturating chemical equilibrium, so that the rate of MT-bound nucleations is given by

$$r_{n,\text{bound}} = r_n \frac{\rho}{\rho + \rho_{\frac{1}{2}}} \quad (7.3)$$

which introduces the single equilibrium constant  $\rho_{\frac{1}{2}}$  that sets the density at which half of the nucleations are MT-bound. This mechanism ensures that, in accordance with observations, the first nucleations in the initially MT-free cortex are all unbound [291], while even at high densities a small remaining fraction of nucleations will occur in the background [137, 300]. In practice we used the value of  $\rho_{\frac{1}{2}} = 0.1 \mu\text{m}^{-2}$ . The location of each MT-bound nucleation event was chosen uniformly along the length of all available MTs. All unbound background nucleations were homogeneously distributed and isotropically oriented.

### 7.2.5 Angular distribution of microtubule-bound nucleation

We chose to model the angular distribution of microtubule based nucleations based on the data by Chan & Lloyd [137]. Their data falls into three components, which we adopted for our model (“CL nucleation”): *forward*, towards the plus-end of the parent MT, with fraction  $f_{\text{forward}} = 0.31$ , *backward*, towards the minus-end of the parent MT, with fraction  $f_{\text{backward}} = 0.07$ , and the remaining fraction *sideways*. The more recent work by Nakamura *et al.*[300] suggest a slightly lower fraction of co-aligned nucleations ( $f_{\text{forward}} + f_{\text{backward}} = 0.33$ ), but unfortunately does not provide any details on the angular distribution of the sideways nucleations. The sideways component was modelled by fitting elliptically shaped polar distributions, with one of their foci on the nucleation site, to the data, yielding a distribution of the form

$$v_{\text{sideways}}(\theta) = \frac{(1 - \varepsilon^2)^{\frac{3}{2}}}{2\pi} \left\{ f_{\text{left}} \left( \frac{1}{1 - \varepsilon \cos(\theta - \theta_b)} \right)^2 + f_{\text{right}} \left( \frac{1}{1 - \varepsilon \cos(\theta + \theta_b)} \right)^2 \right\} \quad (7.4)$$

The full nucleation distribution function is thus given by

$$v(\theta) = f_{\text{forward}} \delta(\theta) + f_{\text{backward}} \delta(\theta - \pi) + v_{\text{sideways}}(\theta) \quad (7.5)$$

The best fits to the data were found (see figure 7.2) for a value of  $\varepsilon = 0.89$  for the ellipse eccentricity and  $\theta_b = 35^\circ$  for the mean branching angle. This nucleation mode with these fitted parameters we call CL. Our parametrized form of the angular distribution, however, lets us readily explore a number of other nucleation modes, obtained by varying both  $\varepsilon$  and  $\theta_b$ . An overview of all nucleation modes used is presented in table 7.2. Each nucleation mode in table 7.2 is illustrated with a cartoon, which we also use in the figures for easy identification of the mode(s) used.

### 7.2.6 Quantifying the degree of alignment

The degree of alignment in the system is defined using a nematic order parameter that takes into account the relative weight of individual microtubule segments in the orientational ensemble, which is proportional to their length. We define the 2D second rank tensorial order parameter

$$\mathbf{S} = \begin{pmatrix} \langle\langle \cos 2\theta \rangle\rangle & \langle\langle \sin 2\theta \rangle\rangle \\ \langle\langle \sin 2\theta \rangle\rangle & -\langle\langle \cos 2\theta \rangle\rangle \end{pmatrix} \quad (7.6)$$

where  $\theta$  is the angle an MT segment makes with the X-axis of the external reference frame. The double angle brackets denote the ensemble average

$$\langle\langle \mathcal{O} \rangle\rangle = \left\langle \frac{\sum_i l_i \mathcal{O}_i}{\sum_i l_i} \right\rangle \quad (7.7)$$

where the sum runs over all MT segments in the system. We define the positive eigenvalue of the tensor order parameter

$$S_2 = \sqrt{\langle\langle \cos 2\theta \rangle\rangle^2 + \langle\langle \sin 2\theta \rangle\rangle^2} \quad (7.8)$$

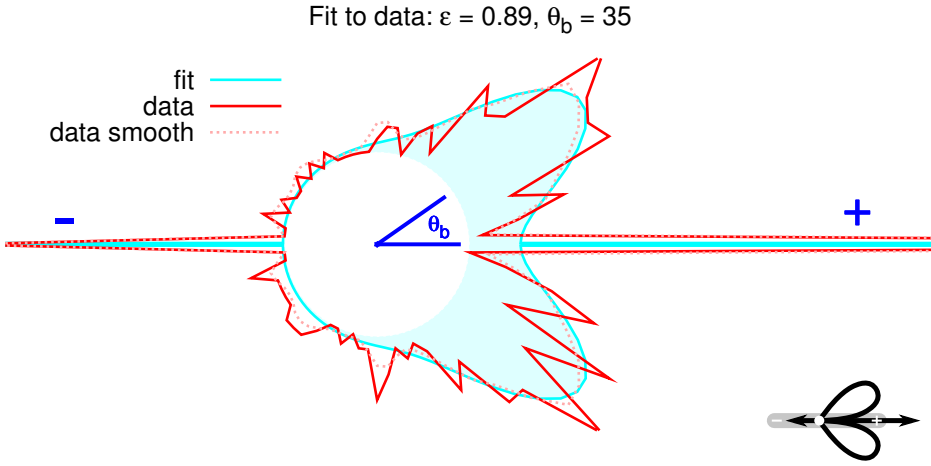


Figure 7.2: **CL nucleation angles (cyan/light) shown together with the data in [137] (red/dark).** The dotted line is created by smoothing the data across neighbouring points and assuming a symmetrical distribution ( $\hat{f}_i = \frac{1}{8} \sum_{z=\{left, right\}} f_{zi-1} + 2f_{zi} + f_{zi+1}$ ). (0 and  $180^\circ$  are excluded from smoothing.) In CL nucleation the angles of microtubule bound nucleations are drawn randomly according to this distribution.

as the scalar order parameter. This has the value  $S_2 = 0$  for a perfectly isotropic system and the value  $S_2 = 1$  if all microtubules are aligned in the same direction. This measure is insensitive to the polarity of the microtubules, which is appropriate, as microtubule polarity does not affect the result of collisions and all our simulations start from an empty system in which initially only isotropic background nucleation occurs. This implies that on average these systems cannot develop and sustain a net polarity. We can extract the overall orientation of the array by considering the so-called director, the unit eigenvector of  $\mathbf{S}$  corresponding to the eigenvalue  $S_2$ , which we parametrize as  $\hat{\mathbf{n}} = (\cos \Theta, \sin \Theta)$ . The preferential angle  $\Theta$  is then given by

$$\Theta = \arctan \frac{\langle \langle \sin 2\theta \rangle \rangle}{\langle \langle \cos 2\theta \rangle \rangle + S_2}. \quad (7.9)$$

### 7.2.7 Calculation of $G_c^*$ from simulations

The graph of the order parameter  $S_2$  as a function of the control parameter  $G_c$  as obtained from our simulations typically has a sigmoidal shape (see figure 7.3A). To extract the critical value  $G_c^*$  of the control parameter, above which the system spontaneously reaches at least some degree of order, we adopt the following procedure: the sigmoidal curve is approximated using least square fitting by 3 linear pieces, fitting the isotropic phase, the ascending part and the high density plateau respectively. We use several sets of initial parameters and manually check for convergence. If  $G_c^*$  is close to 0 (the maximum value considered), the plateau part is dropped from the fitting procedure. The  $G_c$  coordinate of the intersection of the isotropic and ascending line then is our operational definition of

$G_c^*$ .

We calculate average statistics over fits to the  $G_c$ ,  $S_2$  curves of 21 time points between  $T=10000$  s and  $T=20000$  s. The  $G_c^*$  measurement reaches steady state long before 10000 s.

## 7.3 Results and Discussion

### 7.3.1 CL nucleation leads to a large increase of the ordered regime and faster alignment compared to isotropic background nucleation

We start out with a direct comparison of CL nucleation and isotropic background nucleation (ISO). In figure 7.3A we show the degree of order as a function of the control parameter  $G_c$  for both cases. In general the system does not align for small  $G_c$ . When  $G_c$  is increased towards 0 the average number of plus-end collisions an MT experiences during its life time increases, leading to an increased “interaction strength”. When  $G_c$  is increased beyond its critical value  $G_c^*$ , the system will align. As MT length and density are unbounded for  $G_c \geq 0$ , the biologically meaningful parameter regime for alignment (at steady state) is  $G_c^* \leq G_c < 0$ . The mean length of the microtubules varies from  $\approx 4\mu m$  at  $G_c = -1$  to  $\approx 25\mu m$  for isotropic nucleation or to  $\approx 60\mu m$  for CL nucleation as  $G_c$  tends to zero. For both types of nucleation we find that the system is appreciably ordered for mean microtubule lengths between  $10\mu m$  and  $20\mu m$ , values not inconsistent with the admittedly scarce existing data (see e.g.[301]).

The critical value  $G_c^*$  is significantly lower for CL nucleation (-0.59) than for ISO (-0.24). This difference implies a 2.5 fold increase of the regime of parameters for which the system is able to achieve order. Moreover, for any given value of  $G_c$  the system with the CL nucleation mode reached a higher final degree of alignment than the one with isotropic nucleation. CL nucleation also leads to faster alignment: during the whole run and for all relevant values of  $G_c$ , the average degree of alignment was larger for CL. To enable a fair comparison we remove the effect of the shift in critical value by scaling the  $G_c$  axis using  $|G_c^*|$  of the respective nucleation modes. As the results in figure 7.3B) show the system with CL nucleation is ordered stronger at  $T = 6000$ s than with isotropic nucleation at  $T = 10000$  s, over the whole range of reduced control parameters.

We recall that Eren *et al.* reported no significant differences between isotropic nucleation and their implementation of CL-type nucleation [294]. Their simulations, however, were limited to one specific set of MT dynamic parameters, for which a small number of runs was performed. Unfortunately, they do not provide values for the order parameter, but based on the histograms presented (Figure 6B in [294]) it is clear that they are in a strongly ordered state, for which our results suggest that the differences are harder to resolve. Moreover, in their implementation of CL-type nucleation the proportion of bound versus unbound nucleations was arbitrarily fixed to be 50%. This constraint removes a potential order enhancing positive feedback effect: with increasing order the relative frequency of induced catastrophes decreases, resulting in a larger MT density. This leads to a larger fraction of MT bound nucleations (by a shift of the binding equilibrium of the nucleation complexes), which, by the directional bias of the nucleation angles, further

increases the degree of order. This issue is the subject of the next section.

### 7.3.2 The co-alignment of nucleation with the parent microtubule is the main determinant ordering propensity

In the theoretical description of [133], the ordered microtubule array appears through a continuous dynamical phase transition when the isotropic solution loses its stability against spontaneous orientational fluctuations ( $G_c > G_c^*$ ). This indeed suggests that a distribution of nucleation angles that reinforces chance fluctuations in the angle distribution of the array could have a larger ordered regime.

To assess the importance of the angle distribution, we compared the CL nucleation to microtubule bound nucleation with much simpler angle distributions. In the so-called nF mode (see table 7.2),  $n\%$  of the nucleations are along the parent MT. Whether this is in the forward or the backward direction is actually moot, as the system starts out isotropically, and the interactions are agnostic to MT-polarity, so by symmetry the system is unable to develop a persistent net polarity. The remaining  $(100 - n)\%$  of the bound nucleations has a uniform angular distribution.

A convenient measure that quantifies the degree of co-alignment of nucleation with the parent MT is provided by the second fourier coefficient of the nucleation distribution

$$v_2 = \int_0^{2\pi} d\theta \cos(2\theta) v(\theta) \quad (7.10)$$

This measure has a maximum of  $v_2 = 1$  for completely co-aligned nucleation (either forward or backward), a minimum of  $v_2 = -1$  for purely perpendicular nucleations and vanishes for uniform nucleation angles. For our parametrized nucleation distribution Eq.(7.5) we can determine  $v_2$  analytically, yielding

$$v_2 = (f_{\text{forward}} + f_{\text{backward}}) + (f_{\text{left}} + f_{\text{right}}) \left\{ 3 - 2\sqrt{1 - \epsilon^2} + \frac{2(\sqrt{1 - \epsilon^2} - 1)}{\epsilon^2} \right\} \cos 2\theta_b \quad (7.11)$$

We thus readily find that  $v_2(\text{CL}) = 0.53$ . Given that the forward and the backward nucleations together contribute  $0.38 (= 0.31 + 0.07)$  to this measure, the contribution of the sideways nucleations is limited to  $0.16$ . For the forward nucleation mode nF we simply have  $v_2(\text{nF}) = n/100$ .

In figure 7.4 we plot the value of the critical control parameter  $G_c^*$  for various nF systems, parametrized by their value for  $v_2$ . As expected, increasing the degree of co-aligned nucleations, decreases the value of  $G_c^*$ , thus increasing the region where the system spontaneously orders. The comparison with the CL result (square in the figure), which is virtually on top of the line through the nF data points, strongly suggests that  $v_2$  is the main determinant of the location of the transition. Finally, the small difference between the mode 0F (all MT-bound nucleation fully isotropic) and ISO (isotropic background nucleations only) shows that just the localization of the nucleations to MTs by itself does not strongly influence the ordering propensity, if it is not accompanied by some degree of co-alignment with the parent MT.

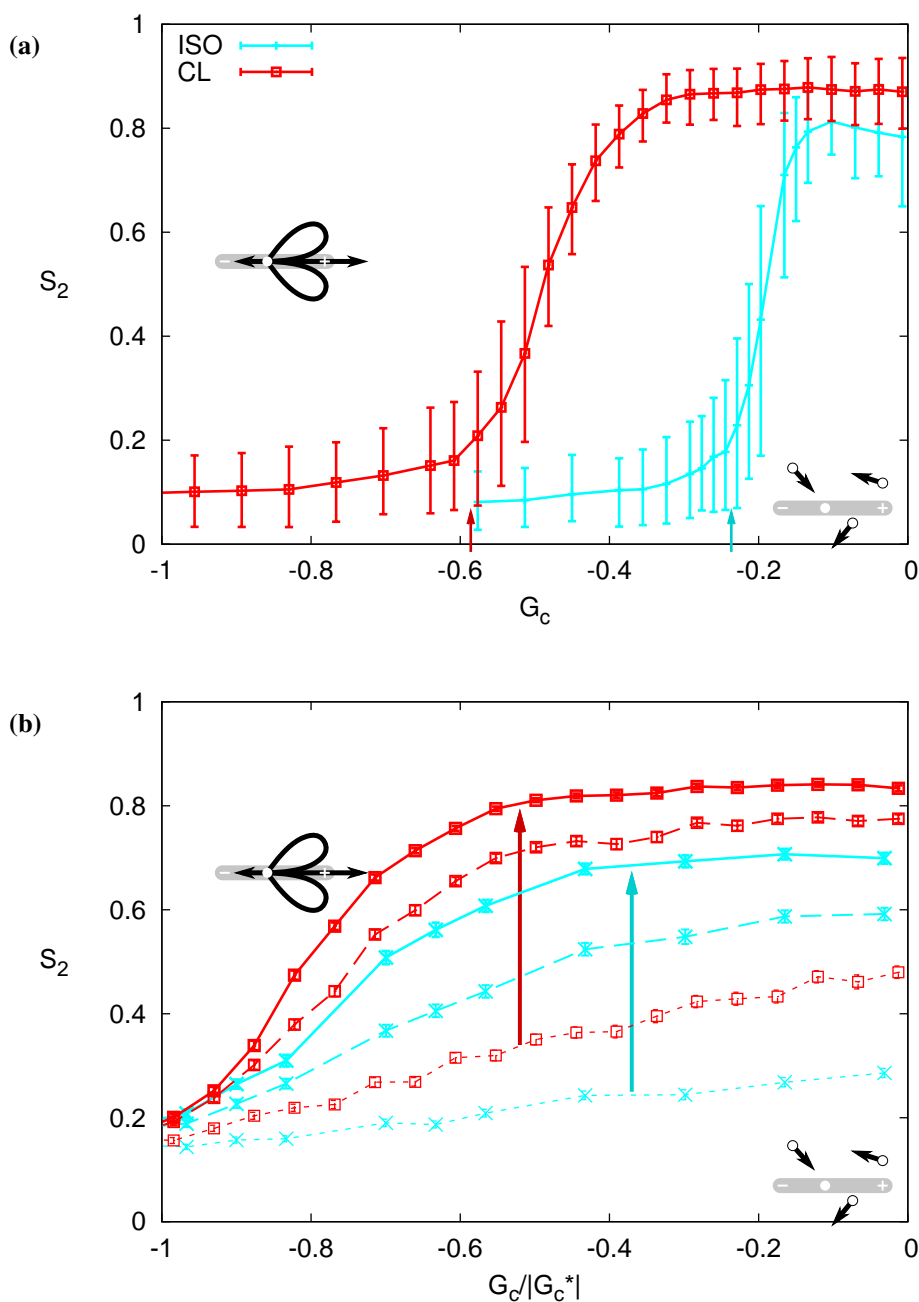


Figure 7.3: **CL and isotropic nucleation compared.** (a): final  $S_2$  as a function of  $G_c$  ( $T = 20000$  s). Arrows indicate the calculated value of  $G^*$ . (b):  $S_2$  at different times as a function of  $G_c/|G_c^*|$  (solid lines:  $T = 10000$  s, long dash:  $T = 6000$  s, short dash:  $T = 2000$  s) with isotropic (cyan/light with crosses) or CL (red/dark with squares) nucleation. CL nucleation leads to much faster alignment than isotropic. Errorbars: 10-90% interval (a) or SEM (b) ( $N=192$  runs).

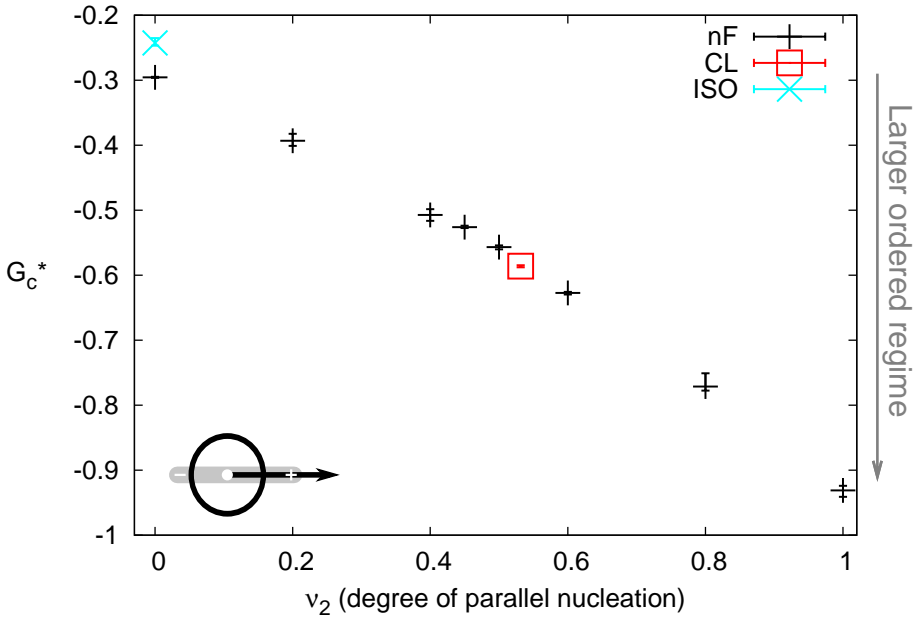


Figure 7.4: **CL nucleation (red/dark square) compared to n% Forward MT bound nucleation (black plusses)**. Note that for the latter  $v_2 = f_{\text{forward}}$ . As a reference the isotropic nucleation is included (cyan/light cross). The graph shows  $G_c^*$  values from simulations. Errorbars indicate the error from the fitting procedure alone (N=21 curves (different time points) per point).

As an extreme test that indeed the degree of co-alignment of the direction nucleation with the parent MT as expressed by the measure  $v_2$  determines the ordering propensity, we perform simulations in the sideways-only nucleation mode (SO), where there is no forward or backward directed nucleation, but we can vary the degree of co-alignment by changing the width of the side lobes, through the parameter  $\varepsilon$ , and the mean branching angle  $\theta_b$ . If our assumption is correct the data for the critical values  $G_c^*$  for all these simulations, when parametrized by their respective  $v_2$ 's, should also collapse onto the result for the nF mode presented earlier. Figure 7.5 shows that this is indeed the case.

Intriguingly, the measured preferred branching angle of  $\approx 40^\circ$  [137, 300], as well as our best fit value of  $35^\circ$ , are close to the “magic angle”  $45^\circ$  for which the sideways branching nucleations do not contribute to the value  $v_2$  (cf. Eq. (7.11)). Together with the observations above, this suggests that in nature they have only a small effect on the propensity for ordering, which is dominated by the fully co-aligned nucleations.

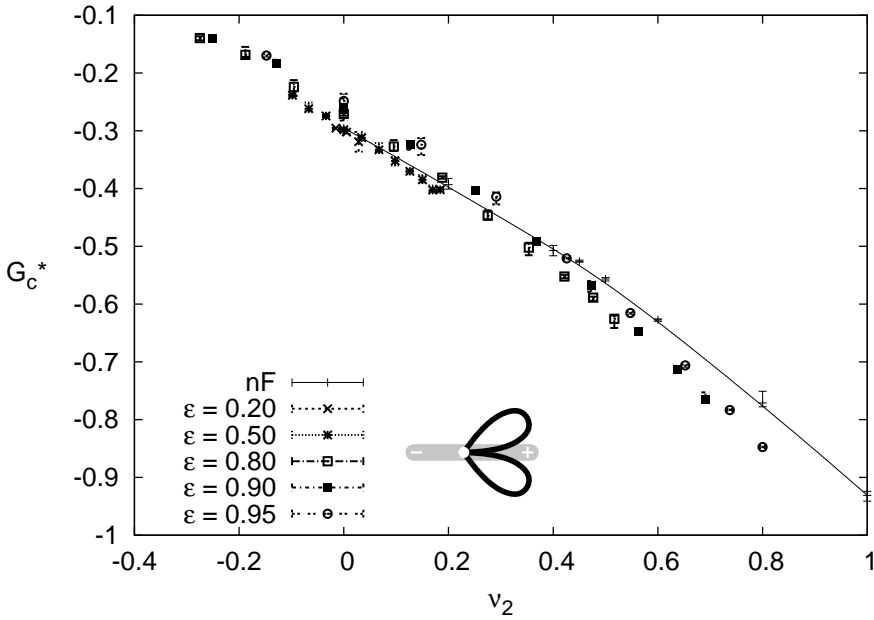


Figure 7.5: **The value of  $G_c^*$  is determined by  $v_2$ .** SO simulations with  $\theta_b$  varying from 10 to 60 degrees and the width parameter  $\epsilon$  ranging from 0.2 to 0.95 plotted as function of the degree of co-alignment  $v_2$  compared to the results from the nF simulations. (The solid line is a bezier fit to nF)

### 7.3.3 Focussed sideways nucleations appear to lead to a more homogeneous microtubule array

The results above indicate that as far as the propensity to spontaneously form ordered arrays is concerned there is no special role for sideways branching nucleations. This raises the question whether they have an impact on the properties of these system at a level not visible in the global statistical measures. We have therefore analyzed individual configurations (“snapshots”) from our simulations in more detail. To facilitate a fair comparison between the different nucleation modes, we compare them at a value of the control parameter  $G_c = \frac{1}{2}G_c^*$  half-way between the onset of ordering for the specific mode and the state of saturated order reached at  $G_c = 0$  effectively defining a non-equilibrium generalization of the concept of ‘corresponding states’ (see e.g. [302]). We chose to compare purely isotropic background nucleation, CL nucleation and 53% forward nucleation (53F), the latter chosen as it has the same degree of co-alignment,  $v_2 = 0.53$ , as CL. Some representative results are shown in figure 7.6.

At first glance it appears that the density of the microtubule array drastically decreases when going through the sequence of modes  $\text{ISO} \rightarrow \text{CL} \rightarrow 53\text{F}$ . This, however, is not the case: the actual MT length density is similar in all nucleation modes and roughly  $2\text{-}3 \mu\text{m}^{-1}$ . The marked visual differences are caused by differences in the spatial homogene-



ity of the arrays in the different modes.

Isotropic nucleation resulted in the most evenly spaced arrays. In this case, the process of overall alignment was sometimes slowed down by the formation of subdomains with different orientations. These domains can be very persistent and often coexisted until the end of the run ( $T=20000s$ ).

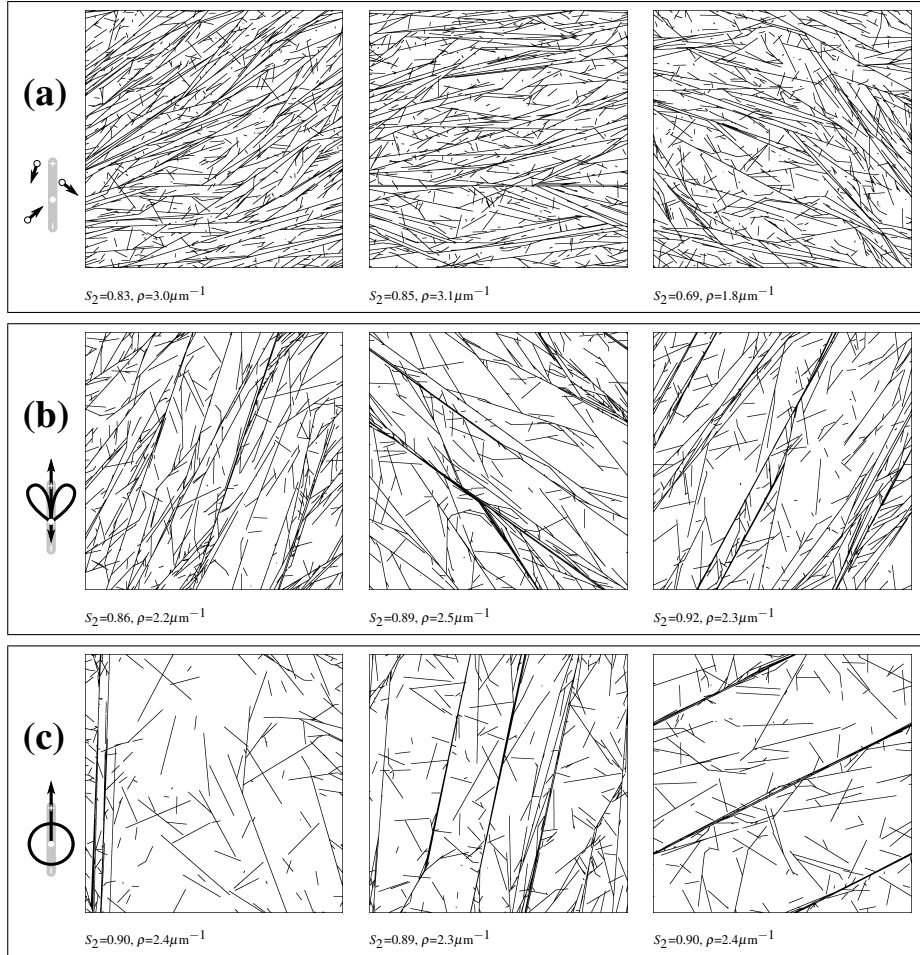


Figure 7.6: **Snapshots of different nucleation modes.** Each line shows three representative snapshots with the same parameters at  $T = 20000s$ . Nucleation modes: (a): Isotropic; (b): Chan-Lloyd; (c): 53% Forward (see table 7.2).  $G_c = \frac{1}{2}G_c^*$  ((a): -0.12, (b) and (c): -0.29).

The 53F mode on the other hand, resulted in highly inhomogeneous arrays, in which a significant fraction of MTs resides within very dense bundles with very sparse areas in between. In some cases almost all MTs were concentrated in one or two very thick “super bundles”. This was most pronounced for almost perfectly horizontal or vertical bundles, and thus in part a finite system-size effect, as with these orientations the bundle

wraps back onto itself after crossing the simulation domain only once. In many other runs the – then less pronounced – super bundles also turned out to eventually wind back on themselves after a limited number of traversals of the simulation domain. It should be noted that such finite-size effects also apply to the real system, in which bundles can span the circumference of a cell.

CL nucleation appears to be an intermediate case. On the one hand, it results in much more evenly spaced arrays than 53F, albeit not quite as homogeneous as with isotropic nucleation. On the other hand, it shares the increased ordering propensity of 53F, and typically achieves a higher degree of net alignment. This prompts us to speculate whether the biological role of focussed branching nucleation is indeed to achieve a balance between spatial homogeneity of the array and degree and rate of ordering, arguably both desiderata in the context of uniaxial cell expansion.

### 7.3.4 Rotation through nucleation of ordered microtubule domains requires a strong handed nucleation bias and a sufficiently “fluid” array organisation.

Chan *et al.* have reported the observation of “rotating” ordered domains of cortical MTs in *Arabidopsis* hypocotyl epidermal cells [297]. This led [296] to propose that either a left- or right handed bias in the relative nucleation angles with respect to the parent MT could give rise to a coherent rotation of an ordered cortical array. Indeed, from symmetry considerations alone one would infer that without such a bias sideways nucleations cannot give rise to persistent rotations. To study this potential effect in its most extreme setting, we considered CL-like nucleation fully biased towards counter-clockwise sideways nucleations, i.e.  $f_{\text{left}} = 0.62$  and  $f_{\text{right}} = 0$ . To track the orientation of the the array over time we employed the preferential angle  $\Theta$  (Eq. (7.9)). The results from a number of simulations are shown in figure 7.7.

This strong nucleation bias could indeed induce persistent rotation of the cortical array in the direction of the bias. Upon *decreasing* the value of the control parameter from  $G_c = -0.07$ , an almost fully ordered system, to  $G_c = -0.32$ , a value just above the ordering transition we observe the following: A steady increase in both the average rotation speed  $\frac{d\Theta}{dt}$  and the fraction of time individual systems spend in a rotating state. Note, however, that even at the smallest  $G_c$  value, some individual runs still do not develop rotating states. We can rationalise why the more ordered systems are less likely to show domain rotation, as the mean life-time of MTs in these states is longer (fewer catastrophe inducing collisions) leading to relatively long MTs. Locally ordered domains of MTs then are more resistant to changes in orientation, especially changes of the collective type leading to rotation. Only the less ordered systems, closer to the limit of stability where both orientational and spatial fluctuations are more pronounced — rendering them effectively more “fluid” — can support persistent rotation.

In the light of these observations it is unlikely that a few percent of handedness bias, such as the one reported in [137] is sufficient to lead to observable effects. Finally, Chan *et al.* [297] reported both clockwise and counter clockwise rotations. A nucleation bias originating from a handedness of the nucleation complex can by symmetry arguments only lead to either one of these rotation directions. The most likely alternative explanation

for these observations are actually slow fluctuations of the local orientation, which are ubiquitous in systems with broken orientational symmetry (cf. Goldstone modes [303]).

## 7.4 Conclusion and Outlook

Using computer simulations we have investigated the effects of MT-bound nucleation on the alignment of a model cortical MT array. Based on the experimental data of Chan *et al.*, we have found that the type of nucleation patterns observed in nature can serve to enhance the degree of alignment of the array and the speed of reaching this alignment, as well as widen the range of MT dynamical parameters for which alignment can be achieved. Further analysis shows that this effect is not due to the spatial localization of the nucleation events, but almost fully determined by a positive feedback effect on the global alignment process when newly nucleated MTs are relatively co-aligned to pre-existing MTs. We have also shown that achieving this effective co-alignment partly through sideways branching leads to spatially more homogeneous arrays, than when new microtubules are nucleated strictly in the same direction as their parent MTs. Finally, we have explored whether handedness of the MT-bound nucleation could lead to persistent rotations of an ordered array. The results indicate that this is possible for an extreme degree of biasing, but only in a limited regime of parameter space where the system is not too strongly ordered and “fluid” enough in a dynamical sense.

We have explicitly kept our model as simple as possible to be able to focus on the specific impact of the nucleation mode on alignment, leaving out biologically relevant aspects such as the influence of cellular boundaries on orienting the array as a whole and katanin induced severing [304]. As katanin preferentially severs at cross-over sites [299] and bundles are the best surviving structures in overexpression mutants [305], severing may have a stronger positive effect on MT ordering with MT-bound nucleation than expected from the effects of katanin alone. This is an interesting topic for future research.

Two of our assumptions regarding the details of the nucleation processes that occur deserve further attention. First, we let the ratio of MT-bound to background nucleation depend on the MT length density through a chemical equilibrium assuming a finite pool of nucleation complexes. The recent work of Nakamura *et al.* [300] provides the first quantitative data on this ratio, but only in cells with a fully developed cortical array. Ideally, the dynamics of this ratio should be studied in post-division cells while the array is built up starting from an initially MT depleted cortex, tracking its value as a function of time and increasing MT density. Second, we assume that the overall rate of nucleation is constant over time. This assumption actually has two components: not only do we assume that the total number of nucleating complexes and their nucleation properties remain constant, but also that the nucleation rate of bound complexes is equal to that of the unbound ones. Especially this last assumption bears scrutiny, as the results in [300] suggest that the bound nucleation rate may actually be an order of magnitude larger than the unbound one. The expected effect, however, is that in reality the positive feedback between (relatively co-aligned) MT-bound nucleation and alignment will be stronger than in our simulations. In other words, our simple implementation of the nucleation rates forms a worst-case scenario with respect to the impact of MT-bound nucleation.

In summary, using a rigorous approach we have demonstrated that MT-bound

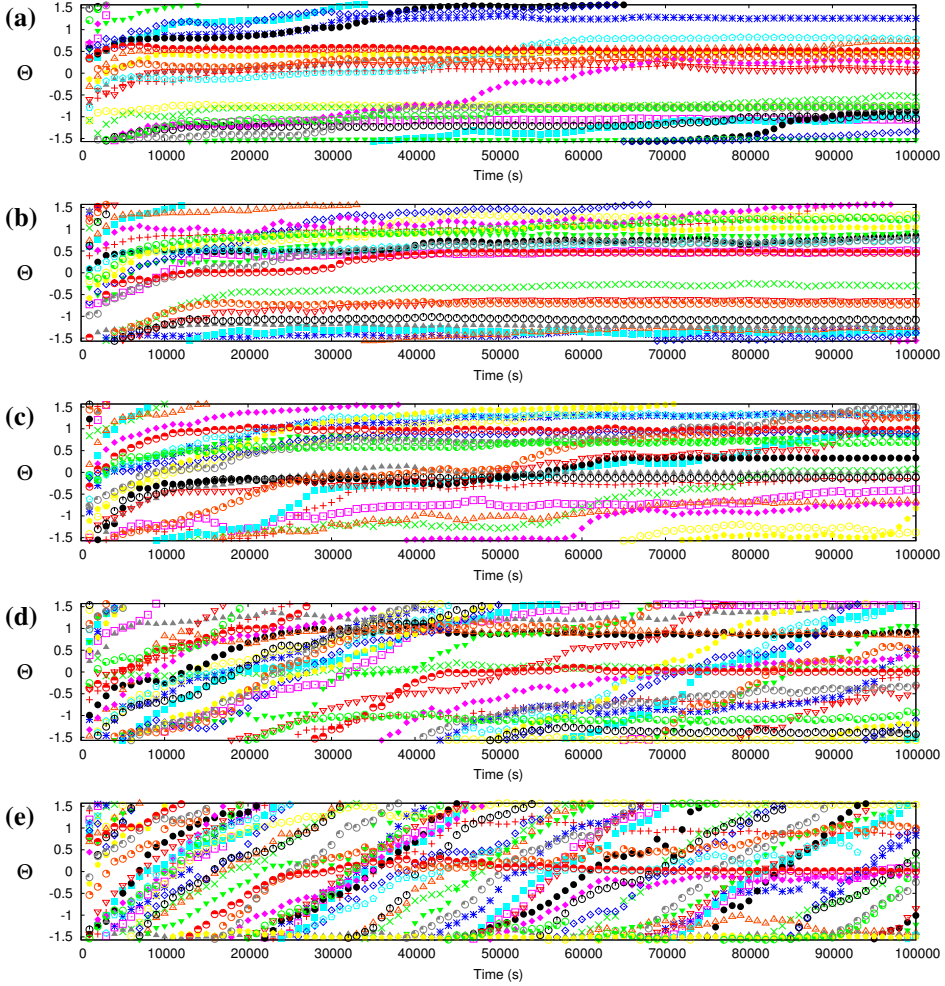


Figure 7.7: **Rotation of domains through nucleation bias only occurs for  $G_c$  sufficiently small** (i.e. close enough to the disordered parameter range). All graphs show the orientation of the global alignment ( $\Theta$ ) as a function of time. The slope of the lines is the rotation speed. Each of 20 runs is depicted with a different symbol and colour/shade. The nucleation bias is very strong: all sideways nucleations occur to one side left of the parent (Nucleation mode CL-I:  $f_{\text{left}} = 0.62$ ,  $f_{\text{right}} = 0$ ). A:  $G_c = -0.07$ , B:  $G_c = -0.13$ , C:  $G_c = -0.20$ , D:  $G_c = -0.26$ , E:  $G_c = -0.32$ .

nucleation has a strong impact on the cortical array. The analysis has revealed that the degree of co-alignment of newly nucleated microtubules with their parent microtubules determines the strength of the positive feedback that enhances the ordering propensity of these systems. This paves the way for using the “branching nucleation module” here developed as an integral component of future work in which we aim for a full quantitative understanding of the plant cortical microtubule array.

**Acknowledgements** The authors thank Jan Vos and Jelmer Lindeboom for insightful discussions and Jordi Chan and Clive Lloyd for kindly providing their data ahead of publication. This work is part of the research program of the “Stichting voor Fundamenteel Onderzoek der Materie (FOM)”, which is financially supported by the “Nederlandse Organisatie voor Wetenschappelijk Onderzoek (NWO)”. SHT was supported by a grant from the NWO program “Computational Life Science” grant CLS 635.100.003 and by the EU NEST network CASPIC grant 28974.

## 7.5 Abbreviations list

MT	Microtubule
ISO	See table 7.2 (nucleation modes)
CL	See table 7.2 (nucleation modes)
nF	See table 7.2 (nucleation modes)
SO	See table 7.2 (nucleation modes)
CL-1	See table 7.2 (nucleation modes)

Table 7.1: **Simulation parameters**

Parameter	Description	Value
$v^+$	growth speed	$0.08\mu m s^{-1}$
$v^-$	shrinkage speed	$0.16\mu m s^{-1}$
$v^t$	treadmilling speed	$0.01\mu m s^{-1}$
$r_r$	rescue rate	$0.007s^{-1}$
$r_c$	catastrophe rate	variable: $0.003 - 0.020s^{-1}$
$r_n$	nucleation rate	$0.001s^{-1}\mu m^{-2}$
$\theta_c$	Zippering occurs for all collisions with a relative angle $< \theta_c$	$40^\circ$
$p_{cat}$	probability of induced catastrophe for larger collision angles	0.5
$W \times H$	2D system size (periodic)	$80 \times 80\mu m$
$\rho_{\frac{1}{2}}$	microtubule affinity of nucleation complexes	$0.1\mu m^{-1}$

Overview of all parameters and variables with their default values (when applicable). The dynamic instability parameters are taken from [298] and rounded and the value for  $v^t$  has been approximated from the data by [291]. The nucleation rate is equal to that used in [294].

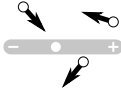

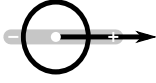
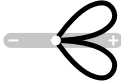

Name	Acronym	Description
Isotropic 	ISO	unbound isotropic background nucleation only (independent of microtubule density)
Chan-Lloyd 	CL	bound nucleation, based on data by Chan & Lloyd [137] (reproduced in figure 7.2, along with our fit to the data): $\varepsilon = 0.89$ , $\theta_b = 35$ , $f_{\text{forward}} = 0.31$ , $f_{\text{backward}} = 0.07$ , $f_{\text{left}} = f_{\text{right}} = 0.31$
n% forward 	nF	bound nucleation: $f_{\text{forward}} = n/100$ , $f_{\text{backward}} = 0$ , and the remainder with uniform relative angle, $\varepsilon = 0$ , $f_{\text{left}} = f_{\text{right}} = \frac{1}{2}(100 - n)/100$
Sideways only 	SO	bound nucleation, only sideways: $f_{\text{forward}} = f_{\text{backward}} = 0$ , $f_{\text{left}} = f_{text{right}} = 0.5$ with $\varepsilon \in [0.2, 0.95]$ , $\theta_b \in [10, 60]$
Left-handed CL 	CL-l	bound nucleation, like CL but with sideways nucleation only to left side of the parent MT: $\varepsilon = 0.89$ , $\theta_b = 35$ , $f_{\text{forward}} = 0.31$ , $f_{\text{backward}} = 0.07$ , $f_{\text{left}} = 0.62$ , $f_{\text{right}} = 0$

Table 7.2: Overview of nucleation modes

---

## Cortical microtubule array initiation

---

*This chapter is based on [306], with thanks to Jelmer Lindeboom for the conversion to  $\LaTeX$ .*

### 8.1 Abstract

The ordered arrangement of cortical microtubules in growing plant cells is essential for anisotropic cell expansion and hence for plant morphogenesis. These arrays are dismantled when the microtubule cytoskeleton is rearranged during mitosis and reassembled following completion of cytokinesis. The reassembly of the cortical array has often been considered as initiating from a state of randomness, from which order arises at least partly through self-organizing mechanisms. However, some studies have shown evidence for ordering at early stages of array assembly. To investigate how cortical arrays are initiated in higher plant cells, we performed live cell imaging studies of cortical array assembly in tobacco BY-2 cells after cytokinesis and drug-induced disassembly. We found that cortical arrays in both cases initiated non-randomly, but with significant over-representation of microtubules at diagonal angles with respect to the cell axis. A bias that simulation studies indicated could account for the observed evolution of array ordering. Surprisingly, during initiation only about half of the new microtubules were nucleated from locations marked by GFP-GCP2 tagged gamma-nucleation complexes ( $\gamma$ -TuRC), therefore indicating that a large proportion of early polymers was initiated by a non-canonical mechanism not involving  $\gamma$ -TuRC. Consistent with this observation, simulation studies indicate that the initial diagonal ordering of the cortical array is not a barrier to array organization, but rather, that the high rate of non-canonical initiation of new microtubules has the potential to accelerate the rate of array re-population.

### 8.2 Introduction

Higher plant cells feature ordered arrays of microtubules at the cell cortex [307] that are essential for cell and tissue morphogenesis, as revealed by disruption of cortical arrays by drugs that cause microtubule depolymerization (Green, 1962) or stabilization [309], and by loss of function mutations in a wide variety of microtubule associated proteins (MAPs) [310–313]. The structure of these arrays is thought to control the pattern of cell

growth primarily by its role in the deposition of cellulose microfibrils, the load-bearing component of the cell wall [314]. Functional relations between cortical microtubules and cellulose microfibrils have been proposed since the early sixties, even before cortical microtubules had been visualized [308]. Recent live cell imaging studies have confirmed that cortical microtubules indeed guide the movement of cellulose synthase complexes that produce cellulose microfibrils [125] and have shown further that microtubules position the insertion of most cellulose synthase complexes into the plasma membrane [126]. These activities of ordered cortical microtubules are proposed to facilitate the organization of cell wall structure, creating material properties that underlie cell growth anisotropy.

While organization of the interphase cortical array appears to be essential for cell morphogenesis, this organization is disrupted during the cell cycle as microtubules are rearranged to create the preprophase band, spindle and phragmoplast during mitosis and cytokinesis (reviewed by Wasteneys, 2002). Upon completion of cytokinesis, an organized interphase cortical array is regenerated, but the pathway for this reassembly is not well understood.

The plant interphase microtubule array is organized and maintained without centrosomes as organizing centers (reviewed in Wasteneys (2002), Bartolini and Gunderson (2006) and Ehrhardt and Shaw(2006) and microtubule self-organization is proposed to play an important role in cortical microtubule array ordering [132]. In electron micrographs microtubules have been observed to be closely associated with the plasma membrane [317] and live cell imaging provides evidence for attachment of microtubules to the cell cortex [291, 298]. The close association to the plasma membrane restricts the cortical microtubules to a quasi two-dimensional plane where they interact through polymerization-driven ‘collisions’ [132]. Microtubule encounters at shallow angles ( $< 40$  degrees) have a high probability of leading to bundling, while microtubule encounters at steeper angles most likely result in induced catastrophes or microtubule crossovers [132]. Several computational modeling studies have since shown that these types of interactions between surface-bound dynamical microtubules can indeed explain spontaneous co-alignment of microtubules [133, 293–295].

The question of how the orientation of the cortical array is established with respect to the cell axis is less well understood. One possibility is that microtubules are selectively destabilized with respect to cellular coordinates [290]. Indeed, recent results from biological observations and modeling suggest that catastrophic collisions induced at the edges between cell faces, or heightened catastrophe rates in cell caps could be sufficient to selectively favor microtubules in certain orientation and hence determine the final orientation of the array [135, 293, 294, 318].

To date, all models of cortical array assembly assume random initial conditions. However, experimental work by Wasteneys and Williamson (1989a, b) in *Nitella tasmanica* showed that, during array reassembly after drug-induced disruption, microtubules were initially transverse. This was followed by a less ordered phase and later by the acquisition of the final transverse order. A non-random initial ordering was also observed in tobacco BY-2 cells by Kumagai et al. (2001), who concluded that the process of transverse array establishment starts with longitudinal order, but did not provide quantitative data for the process of array assembly. The initial conditions for the cortical microtubule array formation are important to consider, as they may strongly influence the speed at which order is established, and could even prevent it from being established over a biologically relevant



time scale.

In the present study, we used live cell imaging to follow and record the whole transition from the cortical microtubule-free state to the final transverse array and used digital tracking algorithms to quantify the microtubule order. Nucleation stands out as a central parameter to define during array initiation. Lacking a central body to organize nucleation complexes, the higher plant cell has nucleation complexes [136, 291, 319, 320, 322–324]. Therefore we performed high time resolution observations to quantify nucleation complex recruitment, nucleation rates and microtubule nucleation angles. We found evidence for a highly non-random initial ordering state that features diagonal microtubule orientation and an atypical microtubule initiation mechanism. Simulation analysis indicates that these atypical nucleations have the potential to accelerate the recovery of cortical array density.

The angles of microtubules with respect to the cell elongation axis were measured and visualized in a contour plot (Figure 8.1c). Time is presented along the x-axis and the angular distribution over the interval from  $0^\circ$  to  $180^\circ$  along the y-axis (20 bins). The color range represents the fraction of the total microtubule length, so that orientation patterns at both low and high microtubule densities can be compared. Surprisingly, the majority of the microtubule length was diagonally oriented at  $45^\circ$  and  $135^\circ$  angles to the elongation axis in the early stages of array reformation, forming two clear peaks in the angular frequency histogram.

To quantify the transition from the diagonal to the transverse cortical microtubule order, the angular distribution data were filtered to produce the weighted diagonal order parameter  $D$  and the weighted transverse order parameter  $T$  (see Supplementary Information). From the means of the  $D$  and  $T$  order parameters over time, we infer that the diagonal ordering was dominant for the first  $\sim 25$  minutes after which it was replaced by transverse ordering (Figure 8.1d).

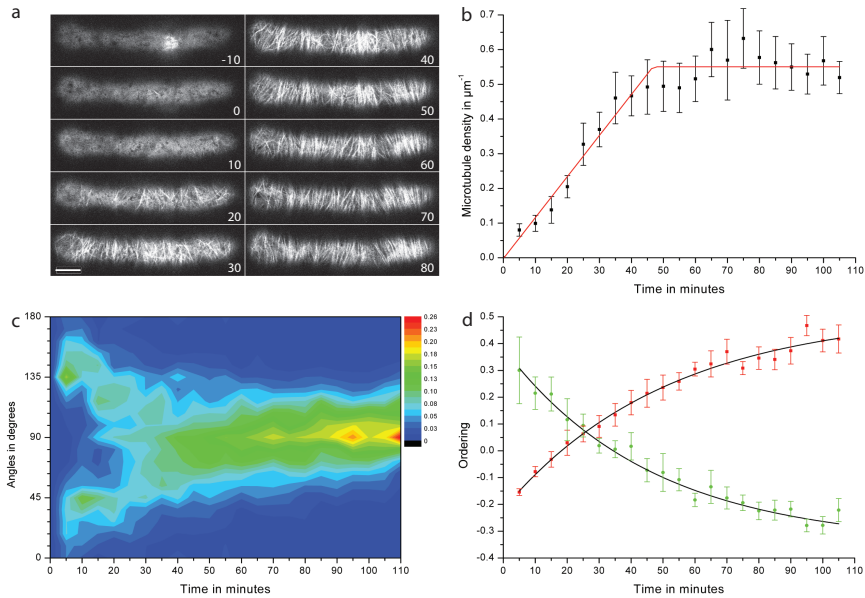
## 8.3 Results

### 8.3.1 After cytokinesis, microtubules reappear with a transient diagonal order

To investigate array initiation, we used tobacco Bright Yellow 2 (BY-2) suspension cells expressing GFP fused to tobacco  $\gamma$ -Tubulin (GFP-TUA). These cells feature highly ordered arrays oriented transversely to the axis of growth, have a relatively high mitotic index, and are ideal for drug treatment in flow cell experiments. Furthermore, the potential crosstalk with neighbors is limited because BY-2 cells generally grow in cell files that break up into individual cells [325–327].

Using point-scanning confocal microscopy, we acquired images from the plane of the cell cortex every 3–5 minutes and measured microtubule length density and ordering after cytokinesis. The first visible microtubules appeared in the cortex after the phragmoplast reached the optical plane of the cell cortex (Figure 8.1a, Figure S8.1 and Movie S1) and within  $\approx 45$  minutes the length density, defined as microtubule length per square micrometer, leveled at around  $0.5 \mu\text{m}/\mu\text{m}^2$  ( $= \mu\text{m}^{-1}$ ), mean of 6 cells; Figure 8.1b). With the increase in length density, the microtubules also became increasingly bundled, as in-

licated by increases in the fluorescence intensities of individual microtubule structures. As our focus was on microtubule orientation, we treated bundles the same as individual microtubules.



**Figure 8.1: Return of cortical microtubules after cell division in BY-2 cells.** (a) Cortical microtubules in two daughter cells after cytokinesis. The first frame ( $T_{-10}$  minutes) shows the late phragmoplast in the cortex. Time is indicated in minutes, scale bar is  $10\ \mu\text{m}$ . (b) Microtubule length density increase over time after cytokinesis (mean of 6 cells). The mean density plateaus at  $\sim 0.54\ \mu\text{m}^{-1}$  and is reached after  $\sim 46$  minutes, based on linear curve fitting of the individual data points of 6 cells (red line). Bars represent standard error (SE). (c) Angular distribution over time presented as the fraction of the total microtubule length at each measurement (mean of 6 cells). The first microtubules are ordered along the diagonal cell axes of  $45^\circ$  and  $135^\circ$ . (d) Diagonal (green circles) and transverse (red squares) microtubule order parameters,  $D$  (green error bars) and  $T$  (red error bars), after cell division (means of 6 cells  $\pm$  SE) and the exponential curve fittings (black lines, based on all individual data points). At  $\sim 25$  minutes after  $T_0$  (last measurement before microtubules became visible) the transverse microtubule ordering became dominant over the diagonal microtubule order.

### 8.3.2 Transient diagonal ordering during recovery from oryzalin treatment

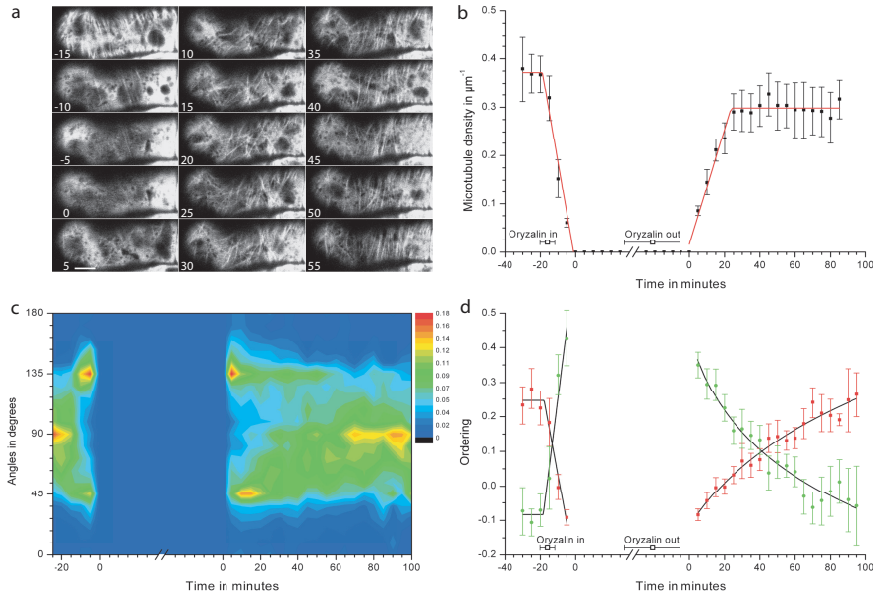
To establish if the mechanism of transverse microtubule ordering via a transient diagonal phase is generic or cell cycle dependent, we immobilized BY-2 cells expressing GFP-TUA in flow cells and treated them for 1 hour with 20  $\mu$ M oryzalin to reversibly depolymerize the cortical microtubule array [328](Figure 8.2a and Movie S2). This concentration and duration of oryzalin treatment was sufficient to eliminate all detectable GFP-TUA labeled microtubules. Both the microtubule length density increase and the development of ordering after oryzalin wash out were similar as observed after cell division (Figure 8.2b). The average plateau density was reached  $\sim$ 25 minutes after appearance of the first cortical microtubules, which is  $\sim$ 45 minutes after the start of the oryzalin wash out (mean of 8 cells). The first microtubules reappeared at diagonal angles to the elongation axis ( $45^\circ$  and  $135^\circ$ ; Figure 8.2c). On average, the transient diagonal ordering was replaced by the final transverse ordering after  $\sim$ 40 minutes (Figure 8.2d). Thus, it appears that both the pattern and kinetics of assembly and ordering are similar whether the array is disassembled by native mechanisms during the cell cycle, or by drug treatment.

### 8.3.3 Diagonal ordering also occurs during array disassembly

Interestingly, a diagonal bias for microtubule orientation was also observed during late stages of array disassembly as cells exit interphase and form preprophase bands (Figure S8.2). Likewise, the same bias was observed in late stages of microtubule depolymerization caused by oryzalin application (Figure 8.2c and d). The microtubule length density started to decrease less than a minute after drug application and reached zero microtubules after  $\sim$ 16 minutes. Within 2 minutes after oryzalin addition, a diagonal microtubule order took over the dominant transverse order and lasted until the last microtubules were depolymerized (Figure 8.2d). Thus diagonal biasing of microtubule orientation appears to be a feature both of the last stages of array disassembly and the first stages of array re-assembly, whether arrays are taken apart by cellular mechanisms or by drug treatment.

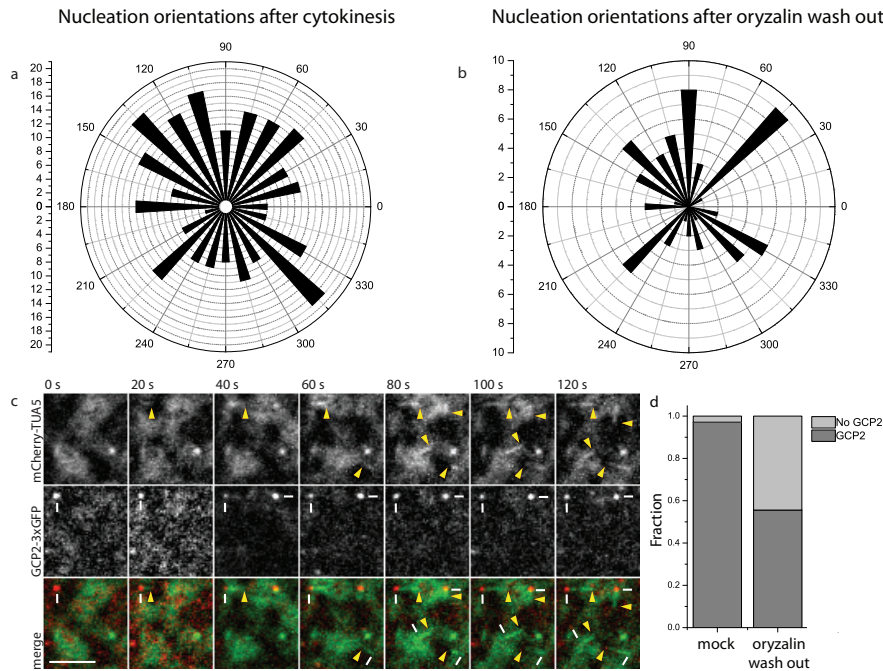
### 8.3.4 Microtubule nucleation has a diagonal bias during array initiation

A bias in microtubule orientation might occur because microtubules are preferentially created in specific orientations, or because they are selectively destabilized, or if they are reoriented once initiated. To assess the origin of the diagonal microtubule ordering, we made movies at high time resolution (2s intervals) of BY2 cells expressing GFP-TUA cytokinesis and oryzalin wash out (Movie S3). We observed that in the first 30 minutes the majority of new microtubules were nucleated at the cell cortex at locations free of other detectable microtubules. In fact, the majority of nucleations during this period were free nucleations (274 out of 352, 77%, in 6 cells after cytokinesis, and 73 out of 117, 62%, in 5 cells after oryzalin wash out). These observations are in contrast to those of interphase nucleation, where microtubule-associated microtubule nucleations have been observed to comprise greater than 99% of nucleations in wild type *Arabidopsis* cells [136, 324, 329]. We measured the angles of these free nucleations with respect to



**Figure 8.2: Treatment of GFP-TUA expressing BY-2 cells with oryzalin.** (a) Cortical microtubules before, during and after incubation with 20  $\mu\text{M}$  oryzalin in a flow cell. Oryzalin was added at  $T_{-15}$  minutes and washed out again after 60 minutes by continuous washing with BY-2 culture medium. Scale bar is 10  $\mu\text{m}$ . (b) Microtubule length density in oryzalin treatment over time (mean of 8 cells). The individual cells of the oryzalin treatments were aligned relative to the observation point at which no microtubules were visible after oryzalin addition, and to the point at which no microtubules were yet visible after oryzalin wash out. Both are referred to as  $T_0$  in the text and figures. Imaging was continued during depolymerization and all images were checked for microtubules. At  $-16 \pm 2$  minutes (mean  $\pm$  SE), 20  $\mu\text{M}$  oryzalin was added and washed out again after 60 minutes. About  $21 \pm 6$  minutes (mean  $\pm$  SE) after oryzalin washout, the first cortical microtubules started to reappear. (c) Averaged angular distribution over time presented as the fraction of the total microtubule length at each measurement (mean of 8 cells). Just after addition of oryzalin at the start of recovery after wash out, diagonal microtubules are dominant. (d) Diagonal and transverse cortical microtubule ordering parameters,  $D$  (green error bars) and  $T$  (red error bars), over time in oryzalin treatment experiments (means of 8 cells  $\pm$  SE). Less than 2 minutes after oryzalin addition,  $D$  (green circles) became dominant over  $T$  (red squares) based on the intercept of the linear curve fittings of the individual data points (black lines). After oryzalin wash out, diagonal ordering became apparent and remained dominant for  $\sim 36$  minutes, based on the intercept of the exponential curve fittings (black lines), followed by dominance of the transverse microtubule array.

the cell axis after both cytokinesis (Figure 8.3a) and oryzalin wash out (Figure 8.3b). We did not analyze microtubule nucleations in the same orientation as the microtubule they nucleated on, as they do not give rise to new microtubule orientations. A Bayesian statistical analysis of these data (see Materials and Methods) revealed a significant bias for nucleations to occur along the diagonal directions both after cytokinesis and oryzalin wash out.



**Figure 8.3: Free nucleations after cytokinesis and oryzalin wash out.** (a and b) Polar histogram nucleation angles within the 30 minute period after the first cortical microtubules appear after cytokinesis in tobacco BY-2 cells (274 nucleations, 6 cells) (a) and oryzalin wash out (117 nucleations in 5 cells) (b). Angles in degrees, histogram scale is in number of observations. (c) Example of free nucleations after oryzalin wash out in *Arabidopsis* root epidermal cells. Dashes indicate microtubule minus-ends, arrowhead indicate microtubule plus-ends. Two out of four nucleations in this image sequence show a GCP2-3xGFP signal. Scale bar is 3  $\mu$ m. (d) Bar graph of the fraction of nucleations where GCP2-3xGFP signal was detected or not. Results are shown for untreated cells *Arabidopsis* root epidermal cells (70 nucleations) and after oryzalin wash out (81 nucleations).

### 8.3.5 A large fraction of nucleations during array initiation are free of labeled $\gamma$ -tubulin complexes

We found it remarkable that the nucleation bias had the same orientation as the cortical microtubule order just before disappearance. This suggested that a ‘memory’ of the previous array organization might be maintained at the cell cortex. We could imagine three alternative models. First, nucleation complexes recruited to the previous array might persist at the cell cortex, retaining orientational information. Second, there might be other orientational information at the cell cortex that acts to orient newly recruited nucleation complexes as they initiate the next array. Finally, a subset of the previous array might be resistant to disassembly either by native mechanisms or by drugs, and they may be either small enough (or be of altered alpha tubulin isoform composition) to evade detection by GFP-TUA6 labeling. These disassembly-resistant remnants might act as orientated seeds for initiating new polymerization during array reassembly.

To distinguish among these hypotheses, we assayed the localization and dynamic behavior of  $\gamma$ -tubulin complexes and their relationship to new nucleations using *Arabidopsis* plants expressing both a  $\gamma$ -tubulin complex marker (GCP2-3xGFP, Nakamura et al., 2010) and a compatible tubulin marker (mCherry-TUA5, Gutierrez et al., 2009, see Movie S4). To facilitate our analysis, we used a 1 hr treatment of 20  $\mu$ M oryzalin to dissemble existing cortical arrays. After drug washout, we acquired images of the cell cortex at high time resolution (2s intervals). We observed no evidence for persistent GFP-labeled nucleation complexes at the cell cortex, thus refuting the first hypothesis; that nucleation complexes recruited to the previous array might persist at the cell cortex to initiate the new array.

We then scored all observed nucleation events in the field of view, asking if GCP2-3xGFP was present at the position of microtubule nucleation. As labeled complexes are present and motile in the streaming cytosol [324], we required that punctae GFP signal be present at the position of nucleation for at least two consecutive image frames to be scored positively. In control cells that were not pretreated with oryzalin, we found that 68 out of 70 nucleations (97%) colocalized with the GCP2-3xGFP label (Figure 8.3c and Movie S5, data acquired from 6 cells on 6 plants), a frequency in good agreement with the  $\sim$ 98% found by Nakamura et al. (2010) in hypocotyl cells. By contrast, in oryzalin treated cells, only a little over half of the observed nucleations (45 out of 81, 56%) colocalized with the GCP2-3xGFP label in the first 20 minutes after the start of oryzalin wash out, a dramatically lower proportion ( $p \ll 0.0001$ , one-tailed binomial test, 8 cells). Thus, while only  $\sim$ 3% of nucleations was not observed to be accompanied by GCP2-3xGFP in mature arrays, this frequency raised to  $\sim$ 44% during early stages of array assembly (Figure 8.3d). The lack of detectable  $\gamma$ -TuRC label at nearly half of the early nucleations argues strongly against the second hypothesis for diagonal nucleation orientation; that orientational information at the cell cortex directs the orientation of new nucleation complexes recruited to the cell cortex during early array assembly. We also found no evidence for involvement of two candidates for such orientational information, the cortical actin cytoskeleton and cellulose microfibrils, by disruption experiments with latrunculin B or isoxaben (Figure S8.3).

On the other hand, the marked reduction in GCP2-3xGFP co-localization was consistent with the third hypothesis; that a large and significant proportion of nucleations during early array recovery arise from seeds not associated with  $\gamma$ -tubulin complexes. We term

these nucleation events non-canonical nucleations because they lack association with detectable  $\gamma$ -TuRCs as determined by GCP2-3xGFP labeling, an essential subunit of the core  $\gamma$ -TuRC.

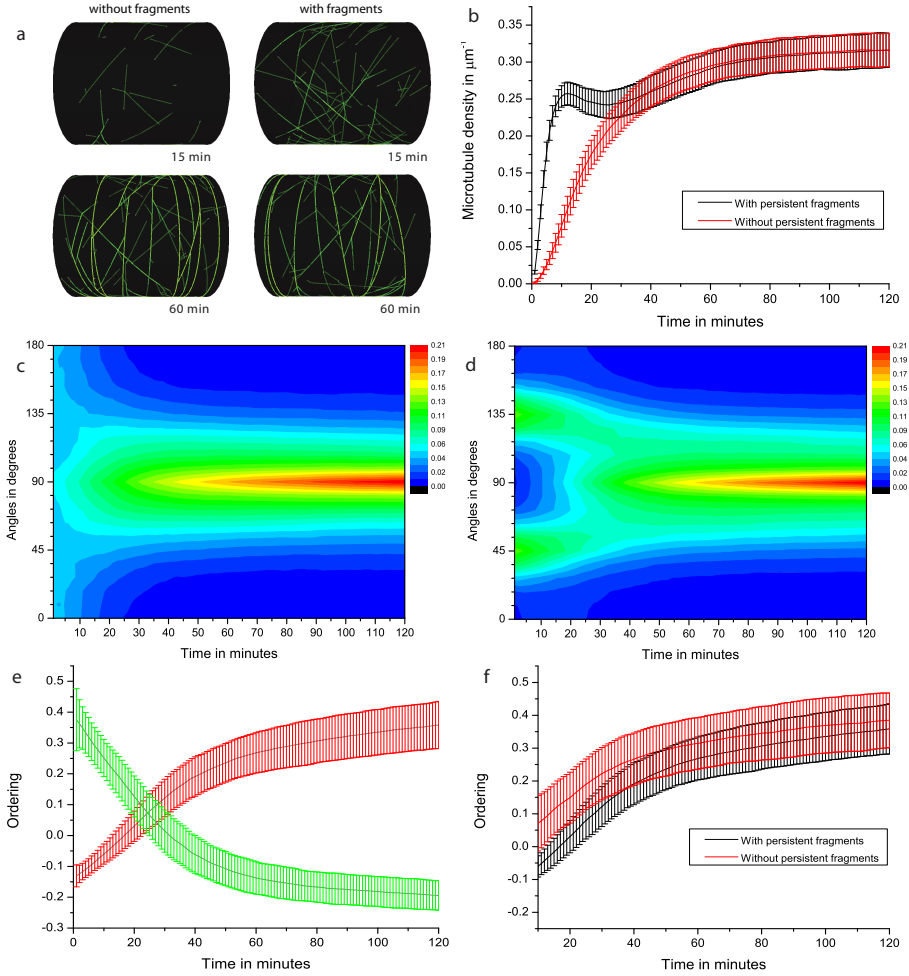
### 8.3.6 Simulations

We performed mechanistic simulations to ask if the observed prevalence of diagonal microtubule nucleation was sufficient to explain the degree of observed diagonal ordering during the initial stages of array assembly and to ask what affect these non-canonical nucleations might have on the evolution of array density and ordering. In the simulations, cortical microtubules interact on a cylindrical cell-shaped surface of dimensions similar to that of the tobacco BY-2 cells used in our *in vivo* experiments (Figure 8.4a)[133, 289]. To test for the influence of the non-canonical nucleation events, these nucleations were treated as a separate class, their density and orientations was chosen to match the distributions determined from the live cell experiments (see the Materials and Methods section for further details on the simulation technique and the parameters employed). In simulations that include all nucleation events the length density initially rises steeply, reaching  $\sim 80\%$  of the final density in just 10 minutes, then transiently leveling off (Figure 8.4b and illustrated in Figure 8.4a at 15 min.). By contrast, in simulations without the non-canonical nucleation class, the length density rises more gradually and steadily, reaching 80% of the final density only after about 40 minutes (Figure 8.4b). Thus, the non-canonical nucleations appear to have the potential to significantly accelerate the recovery of array density during array re-assembly.

When simulations were run without the non-canonical nucleation class there was no initial bias of the angular distribution (Figure 8.4c). As expected, when these nucleations were added to the simulation, a clear initial bias at 45 and 135 degrees is created (Figure 8.4d), markedly similar to our experimental observations (Figure 8.1c). The diagonal and transverse order parameters  $D$  and  $T$  as a function of time for the simulations with the non-canonical nucleation class (Figure 8.4e) both qualitatively and quantitatively match the values we found experimentally (Figure 8.1d). Thus, the inclusion of the diagonally biased nucleation events observed in living cells have the potential to explain both the initial diagonal ordering and the observed evolution of array ordering in these cells. While non-canonical nucleations had the effect of lowering the initial transverse ordering state of the simulated arrays, the difference is not significant and the order parameters level off to the same value (Figure 8.4f), indicating that biased non-canonical nucleations did not present a barrier to array ordering.

## 8.4 Discussion

The transverse arrangement of the cortical microtubule array is essential for anisotropic growth, yet little was known about how it arises from a disassembled state, a situation that arises at each cell division during the life of the cell. The currently accepted self-organization models for transverse cortical microtubule array establishment, based on microtubule interactions [133, 293–295], assume random initial conditions. We found that the first microtubules in new arrays of tobacco BY-2 cells were in fact not randomly



**Figure 8.4: Results of the simulations.** (a) Snapshots of representative microtubule configurations at 15 and 60 minutes after the start of the simulation both with (right) and without (left) persistent fragments. (b) The time evolution of the average (optical) density of microtubules for the simulations with (black) and without (red) persistent fragments, error bars show one standard deviation. (c and d) Averaged angular distribution over time presented as the fraction of the total (optical) microtubule length from simulations without (c) and with (d) persistent microtubule fragments. (e) The time evolution of the average diagonal  $D$  (green error bars) and transverse  $T$  (red error bars) cortical microtubule ordering parameters with persistent fragments. The gray lines represent the average value and the error bars represent one standard deviation. (f) The time evolution of the average transverse  $T$  cortical microtubule ordering parameter with and without persistent fragments. All simulation results are combined for 500 individual simulations.



oriented but showed significant ordering, at orientations of both 45 and 135 degrees. This was true both for array assembly during the cell cycle as well as reassembly of arrays after oryzalin washout. Organization in these arrays did not evolve by gradual ordering from a disorganized, random state, but by a transition from one ordered state to another.

Exploration of the cause for the non-random initiation of array establishment revealed that there was a significant bias in the orientation of early microtubule nucleations, sharing the same 45° and 135° bias relative to the cell axis that was observed for array ordering. Results from simulation studies incorporating these oriented nucleations matched experimental observations very closely, indicating that this population of directionally biased nucleations is sufficient to explain the fast-forming initial diagonal ordering state of new arrays, and together with self-ordering based on microtubule interactions, is sufficient to explain the transition from this array into the final transverse array.

We considered several alternative ideas for the mechanism of nucleation orientation. In interphase cells, the majority of nucleations at the cell cortex occurs from the sides of existing microtubules with a major peaks at about 40° [136] and a secondary peak at 0° (parallel to the mother polymer) [322, 324, 329]. Thus, in the interphase arrays studied to date existing microtubules largely determine the orientation of new microtubule nucleation. The vast majority of the nucleation events occur at gamma tubulin nucleation complexes as visualized with tagged components of the core complex (>98%, Nakamura et al., 2010; Kirik et al., 2012). However, at the start of array assembly there are no obvious existing microtubules (this study, Wasteney and Williamson, 1989, 1989) to recruit and position nucleation complexes [324], therefore it was necessary to consider other mechanisms for nucleation orientation. One possibility was that oriented  $\gamma$ -TuRC complexes are simply retained at the cell membrane from the previous cortical array, an idea that was contradicted by our observation that  $\gamma$ -TuRCs in *Arabidopsis* root cells were not retained at the cell cortex from the previous array. A second possibility was that newly recruited  $\gamma$ -TuRCs are positioned by cryptic orientational information at the cortex. Surprisingly, however, we found that labeled  $\gamma$ -TuRC complexes failed to be detected at ~44% of the nucleation events observed during array initialization compared to ~3% at steady state microtubule density. This result both effectively eliminated a mechanism based solely on oriented  $\gamma$ -TuRCs and revealed that many early nucleations apparently arise from non-canonical nucleation sites that lack a  $\gamma$ -TuRC.

The above results, together with the observation that cortical microtubules were oriented diagonally not only during the buildup of the cortical microtubule array but also during the last stages of breakdown during oryzalin treatment and preprophase band formation, were consistent with a third possible mechanism - that segments of the previous array survive or are resistant to disassembly, whether by oryzalin or by native mechanisms during mitosis. Segments that could then act as oriented seeds that participate in initiation of the next array. Consistent with the idea of disassembly-resistant microtubule seeds, deactivation of  $\gamma$ -tubulin complexes in several organisms does not abolish all microtubule nucleation in vivo (reviewed by Job et al., 2003) and nucleation free of  $\gamma$ -TuRCs is well known to occur in vitro at high enough concentrations of free tubulin dimers [331]. Previous studies by Wasteney and Williamson (1989b) in *Nitella* are also consistent with this possibility. These investigators observed that while *Nitella* microtubules returned in their original transverse orientation during recovery from oryzalin, orientation was random after longer, and presumably more complete, oryzalin treatment (Wasteney and

Williamson, 1989, 1989). In our studies, incomplete drug action cannot explain observations of array re-assembly following cytokinesis, since there was no drug treatment in these cells and the extremely similar mode and kinetics of array reassembly we observed between these cells and those recovering from oryzalin treatment suggest that similar mechanism are responsible in both situations.

If the latter hypothesis is true, a couple of puzzles remain. First, microtubule seeds from the previous cell cycle were not readily detected by imaging of GFP-TUA. However, this might be easily explained if the seeds are small enough to contain only a few labeled subunits (only a portion of alpha subunits in the cell are tagged), a degree of labeling that may well lie below the high background of unpolymerized subunits in the cytosol. It is also formally possible that the seeds may have a composition that does not include the labeled tubulin isoform used for imaging. A second puzzle is why the presumed source of the oriented seeds - the last cohort of microtubules at the end of array disassembly - has a diagonal bias to the cell axis. One possibility is that the bias arises from the normal formation of the newest microtubules by branching nucleation at about 40 degrees to their mother polymers [136, 137, 319, 320, 324]. In a transversely oriented array, these nucleations would lie approximately at 45° and 135° to the cell axis, and would have a high likelihood of interacting with the dominant population of transverse microtubules. These interactions can lead to incorporation into bundles by treadmilling motility [132, 291], or catastrophe ([132], both of which would tend to diminish the population of diagonally oriented polymers. However, as the microtubule array is broken down and microtubule density drops, encounters would be predicted to be less frequent and therefore the likelihood of aligning or eliminating branching microtubules will be reduced.

Whether the source of oriented nucleation in early array assembly is due to seeds from the previous array or another mechanism, our observations reveal the existence of a substantial class of non-canonical nucleations not associated with  $\gamma$ -TuRCs that contribute to the initiation of the cortical array. In simulation studies we explored how these non-canonical nucleations may affect array reassembly and found this class of oriented nucleations to have the potential to significantly accelerate recovery of array density without significantly impeding the acquisition of ordering driven by microtubule interactions. The existence of this mechanism may address a fundamental dilemma the plant cell faces in rebuilding an array from scratch. In interphase cells, nucleation from  $\gamma$ -TuRC complexes was observed to be approximately 10-fold more likely when they are localized to microtubules than to other locations at the cell cortex [324]. If this reflects a fundamental property of  $\gamma$ -TuRC activation, then the cell may face limitations in how fast it can initiate new arrays when there are no existing cortical microtubules to recruit  $\gamma$ -TuRCs and contribute to their activation. Our live cell observations and simulation studies reveal a class of nucleations that do not require  $\gamma$ -TuRC recruitment and activation at cortical microtubules may act as a primer to accelerate the assembly of the new array.

## 8.5 Materials and methods

### 8.5.1 Plant material

Tobacco (*Nicotiana tabacum* L.) Bright Yellow-2 (BY-2) suspension cultured cells were grown according to standard protocols (Nagata et al., 1992). We stably transformed

BY-2 cells using *Agrobacterium tumefaciens* LBA4404 mediated procedures with a reporter construct consisting of the enhanced green fluorescent protein fused to tobacco  $\alpha$ -tubulin (sGFP-TUA) under control of the CaMV 35S promoter, kindly provided by Dr. S. Hasezawa, University of Tokyo, Japan (Kumagai et al., 2001). The BY-2 cell line expressing eGFP-FABD was generously provided by Dr. T. Ketelaar (Wageningen University) [332]. We used *Agrobacterium tumefaciens* to transform the pGCP2-GCP2-3xGFP construct, kindly provided by Masayoshi Nakamura and Takashi Hashimoto (Nara Institute of Science and Technology, Ikoma, Japan), into an *Arabidopsis thaliana* Col-0 expressing 35S-mCherry-TUA5 [126].

### 8.5.2 Specimen mounting

Transformed cells were imaged in thin  $\sim 10$  to  $20\ \mu\text{L}$  gas permeable micro-chambers lined on one side with Biofoil (VivaScience, Hannover, Germany) and a  $24 \times 24\ \text{mm}$  coverslip on the other side as described earlier (Vos et al., 2004). Slides were sealed with VALAP (1:1:1 Vaseline : lanolin : paraffin). For oryzalin treatments, cells were immobilized in plastic flow cells (1 channel of  $100\ \mu\text{L}$  with a height of  $0.4\ \text{mm}$ ; Ibidi, Munich, Germany) that were pretreated with  $1\ \text{mg/mL}$  poly-L-lysine solution in  $\text{dH}_2\text{O}$  for 30 min at room temperature. Ten flow cell volumes of  $20\ \mu\text{M}$  oryzalin (from  $20\ \text{mM}$  stock in DMSO) in BY-2 medium were perfused through the channel with cells and after 1 hour, washed out with constant perfusion of BY-2 medium at a flow rate  $> 0.1\ \text{mL/min}$ . For latrunculin B and isoxaben experiments,  $10\ \text{mL}$  of a BY-2 culture was incubated for at least 3 hours in  $0.5$  or  $1.0\ \mu\text{M}$  latrunculin B or at least 24 hours in  $10\ \mu\text{M}$  isoxaben before adding  $20\ \mu\text{M}$  oryzalin and cell immobilization in a flow cell. Washes with latrunculin B or isoxaben were initiated after 1 hour to allow the microtubule cytoskeleton to recover, but not the actin cytoskeleton or the cellulose microfibril production. The immobilization, the perfusion of medium with  $0.1\%$  DMSO,  $0.1\%$  ethanol and the confocal imaging did not influence the cytoarchitecture or microtubule organization of the tobacco BY-2 cells (data not shown).

The *Arabidopsis* plants were grown on standard Hoagland's medium and gently mounted between an objective slide and coverslip spaced by two strips of double sided Scotch tape. For the oryzalin treatment, the plants were transferred to a six well plate containing  $1.0\ \mu\text{M}$  oryzalin for an hour to depolymerize the microtubules. Oryzalin was washed out at a flow rate of  $\sim 0.5\ \text{mL dH}_2\text{O/min}$ .

### 8.5.3 Microscopy

For the long-term microtubule analysis we used confocal laser scanning microscopy (CLSM). Images and time-lapse movies were produced with a  $63\times / 1.4\ \text{NA}$  oil immersion DIC lens on an Axiovert 200M microscope equipped with a Pascal CLSM unit (Zeiss, Jena, Germany). The GFP was excited with the  $488\ \text{nm}$  argon laser and a  $505\ \text{nm}$  long-pass emission filter. To see all microtubules in the cortex, a pinhole of  $1.5$  to  $2$  airy disc units ( $1.0$  to  $1.4\ \mu\text{m}$  in the Z-axis) was used. The scan time was  $4$  to  $8\ \mu\text{sec/pixel}$  and the temporal resolution was  $3$  to  $5$  minutes. Alternatively, time-lapse Z-series of  $2.5\ \mu\text{m}$  thickness were made on a Leica DM IRB microscope equipped with the perfect focusing system, a CSU22 spinning disk set up (Yokogawa, Tokyo, Japan) and a C9100 EM-CCD camera

(Hamamatsu Photonics, Hamamatsu City, Japan). We used a 100x / 1.4 NA objective lens and excited the GFP with a 488 nm argon laser. Five 0.5  $\mu\text{m}$  optical sections, each taking 250 ms, were typically obtained at 3-minute intervals. The visible area with cortical microtubules varied from about 200 to 600  $\mu\text{m}^2$ .

For the nucleation analysis we used a confocal spinning disk microscope described earlier [126], except that a Nikon Eclipse Ti microscope with the perfect focusing system and a 100x 1.45 NA oil objective replaced the Zeiss Axiovert 200. Alternatively, we used a total internal reflection fluorescence (TIRF) microscopy on a Nikon Eclipse Ti microscope with the perfect focusing system. We used a 100x 1.49 NA TIRF oil objective and excited with a solid-state 478 nm laser (Cobolt AB) and using a Semrock 535/39 emission filter. The microscope was equipped with a manual Nikon TIRF arm and a QuantEM EM-CCD camera (Photometrics). We used 800 ms exposure time and a 2 or 2.14 s time interval for the spinning disk and TIRF microscope respectively.

### 8.5.4 Data analysis

Time-lapse images were converted into 8-bit tiff file stacks with ImageJ (W. S. Rasband, U. S. National Institutes of Health, Bethesda, Maryland, USA, <http://rsb.info.nih.gov/ij/>, 1997-2007). Z-stacks were converted to average or maximum projections of 3 to 5 sections. The ImageJ StackReg plug-in was used to align the images of a stack [333]. All visible microtubules in the images were traced using the semi-automatic ImageJ plug-in NeuronJ (v1.01) [334]. The microtubule tracings were stored as a series of x and y pixel coordinates with a maximum distance of 5 pixels in both the x and y direction between subsequent points. A Perl script was used to extract the line segments and distribute their lengths over 20 evenly spaced bins according to their angle with the x-axis. The script corrects for the uneven distribution due to discrete pixel values of possible segment angles produced by NeuronJ (see Supplementary information and Figure S8.4 for the verification procedure). As we could not distinguish between the plus and minus ends of microtubules, every line segment was assigned an angle in the interval from 0° to 180°. The bins had a width of 9° and were centered on 0°, 9°, etc., up to 171°.

For each image, the microtubule length density was obtained by dividing the total microtubule length by the area of the cortical section in the images. The angular distribution data are presented in contour plots produced with Origin (OriginLab, Northampton, MA, USA) as the fraction of microtubule length at each time point. For clarity, an extra 180° bin is depicted as a copy of the 0° bin in each graph. The angle bins are along the y-axis and time along the x-axis, and a rainbow color gradient indicates the cumulative microtubule length or fraction in 20 equal sized steps, ranging from blue (few microtubules) to red (maximum length or fraction). Plots of mean distributions of several experiments were produced by aligning the timing of individual cells to the moments of zero microtubules after breakdown or before re-polymerization, and averaging the fractions.

To calculate the increase in microtubule density after cytokinesis and oryzalin wash out, and the final plateau value, data from individual experiments were fitted with the linear function: if  $t > T_p$ , then density =  $P_1 + P_2 T_p$ , else density =  $P_1 + P_2 t$ , with  $T_p$  as the time to reach the plateau density. The time of emergence of diagonal (45° and 135°) and transverse (90°) microtubule ordering was analyzed by filtering the angle bins with two test functions:  $T$  for transverse ordering and  $D$  for diagonal ordering (see Supplementary

Information and Figure S8.5). Both functions have the property that a randomized system yields a value of zero. A system that is perfectly ordered (in the transverse direction for  $T$  and the diagonal direction for  $D$ ) produces a value of 1.

For the nucleation analysis we determined the position in the cell, the time point, the angle with respect to the cell axis, whether the nucleation was free or microtubule bound and the angle of the seed microtubule in case of branching nucleation. For further analysis we only used the microtubule nucleations that were unbound. To assess whether a bias exists for nucleation along diagonal directions, we defined  $15^\circ$  bins around the  $45^\circ$ ,  $135^\circ$ ,  $225^\circ$  and  $315^\circ$  degree directions, and scored microtubules in these bins as being diagonal. We introduced a diagonal biasing parameter  $\delta$  by equating the probability of a diagonal nucleation to a non-diagonal nucleation.

$$P_{diag}(\delta) = \frac{\frac{1}{6}\delta}{\frac{1}{6}\delta + \frac{5}{6}(1-\delta)} \quad (8.1)$$

This parameter is normalized such that  $\delta = 0$  implies there are no diagonal nucleations,  $\delta = 1$  implies all nucleations are diagonal, while  $\delta = \frac{1}{2}$  is the neutral case in which there is no bias, in which case the proper unbiased weight  $\frac{1}{6} = \frac{60^\circ}{360^\circ}$  is accorded to the diagonal bins. We then performed a maximum likelihood estimate of  $\delta$  by evaluating the likelihood ratio

$$\frac{L(\delta)}{L_{\frac{1}{2}}} = \frac{P_{diag}(\delta)^M (1 - P_{diag}(\delta))^{N-M}}{(\frac{1}{6})^M (\frac{5}{6})^{N-M}} \quad (8.2)$$

where  $M$  is the number of diagonal microtubules observed out of a total of  $N$ . For the nucleations after cytokinesis we have  $M = 66$  and  $N = 274$ , yielding  $\delta = 0.61$ . For the nucleations after oryzalin washout we have  $M = 26$  and  $N = 73$ , yielding  $\delta = 0.73$  (see Figure S6 a and b). Note that a standard one-tailed binomial analysis also rejects the null hypothesis of no bias with  $p < 0.001$  for the post-cytokinesis case and  $p < 0.0001$  for the oryzalin washout case.

### 8.5.5 Simulation methods

We performed simulations of interacting cortical microtubules using the event-based algorithm [133]. The simulations are implemented on a cylindrical cell geometry with a length of  $80 \mu\text{m}$  and a radius of  $40 \mu\text{m}$ . Microtubules that impinge on the edges of the cylinder undergo catastrophes, a boundary condition that was shown to robustly select a transverse orientation of the steady-state array (Allard et al., 2010; Eren et al., 2010).

The kinetic parameters for the dynamics of the microtubule plus-ends are based on Vos et al. (2004): growth speed  $v^+ = 0.08 \mu\text{m s}^{-1}$ , shrinkage speed  $v^- = 0.16 \mu\text{m s}^{-1}$ , spontaneous catastrophe rate (switch from growing to shrinking state)  $r_c = 0.003 \text{ s}^{-1}$  (a value slightly lower than that of Vos et al. 2004, consistent with a likely overestimation of this quantity in that work due to undetected collision-induced catastrophes), and rescue rate (switch from shrinking to growing state)  $r_r = 0.007 \text{ s}^{-1}$ . The minus-ends of microtubules shrink with a constant treadmilling speed of  $v_t = 0.01 \mu\text{m s}^{-1}$ , following Shaw et al. (2003) and identical to Deinum et al. (2011).

The results of angle-dependent collisions between growing microtubules and obstructing ones, follow the simplified scheme also employed by Allard et al. (2010), Eren et al. (2010) and Deinum et al. (2011). All collisions with an incidence angle below  $40^\circ$  result in collision induced bundling, where the incoming microtubule changes direction and continues to grow along the obstructing one. The outcomes of steep angle encounters vary greatly from cell type and stage [296], therefore we measured these outcomes in our 2s dataset after cytokinesis in BY-2 cells. We found that of 70 encounters  $> 40^\circ$  in 4 cells, 14 (20%) encounters induced a catastrophe and 56 (80%) resulted in a crossover. Therefore in our simulations collisions with an incidence angle larger than  $40^\circ$  have a 20% probability of undergoing an induced catastrophe, where they switch to a shrinking state, and a 80% probability of simply crossing over the obstructing microtubule.

New microtubules are nucleated at a constant overall rate of  $r_n = 0.0002 \text{ s}^{-1} \mu\text{m}^{-2}$ , which we estimated from our observations of the nucleations after cytokinesis [289]. Nucleations occur either at an arbitrary location in the model cortex or from a microtubule. We modeled the portioning of nucleation events between microtubule-free and microtubule-bound by a density-dependent chemical equilibrium, which accounts for the affinity of nucleation complexes for the microtubules. The fraction of microtubule-bound nucleations is given by

$$f_{\text{bound}} = \frac{\rho}{\rho + \rho_{\frac{1}{2}}} \quad (8.3)$$

where  $\rho$  is the (time-dependent) length density ( $\mu\text{m} \mu\text{m}^{-2}$ ) of the microtubules, and the cross-over density  $\rho_{\frac{1}{2}} = 0.1 \mu\text{m} \mu\text{m}^{-2}$ , determines the location of the equilibrium, which we chose in order to match the observed timescale of the crossover towards the final transversely ordered state. The microtubule-bound nucleations have an orientational distribution with respect to the parent microtubule, which is a coarse-grained representation [289] of the experimentally observed patterns [137]. We have reduced the rate of unbound nucleations by the a factor of 10 to  $r_{n,\text{free}} = 0.00002 \text{ s}^{-1} \mu\text{m}^{-2}$ , following the data presented by Nakamura et al. (2010) for a steady state microtubule array.

At the start of the simulations we add a finite pool of microtubule fragments with the density of  $0.1 \mu\text{m}^{-2}$  and an activation rate of  $r_s 0.003 \text{ s}^{-1}$ . These values were based on the free nucleation rate of BY-2 cells after cytokinesis. Only these reactivating microtubule fragments have a bias towards the diagonal directions of  $45^\circ$  and  $135^\circ$ . This bias was implemented by drawing the direction of nucleation with respect to the parent microtubule from the following distribution

$$\psi(\theta) = \frac{1}{2\pi I_0 \alpha} \exp \left\{ \alpha \cos \left( 4 \left( \theta - \frac{\pi}{4} \right) \right) \right\} \quad (8.4)$$

where the angle  $\theta$  is expressed in radians,  $\alpha$  is a parameter that sets the degree of bias, and  $I_0$  is a modified Bessel function of the first kind (see e.g. Abramowitz and Stegun, 1970). We chose  $\alpha = 1.5$ , which reproduces the experimentally determined ratio between the nucleations in  $15^\circ$  bins around the diagonal directions and those in the remaining directions, for the case after cytokinesis. In the control simulations, this pool of microtubule nucleations was not present.

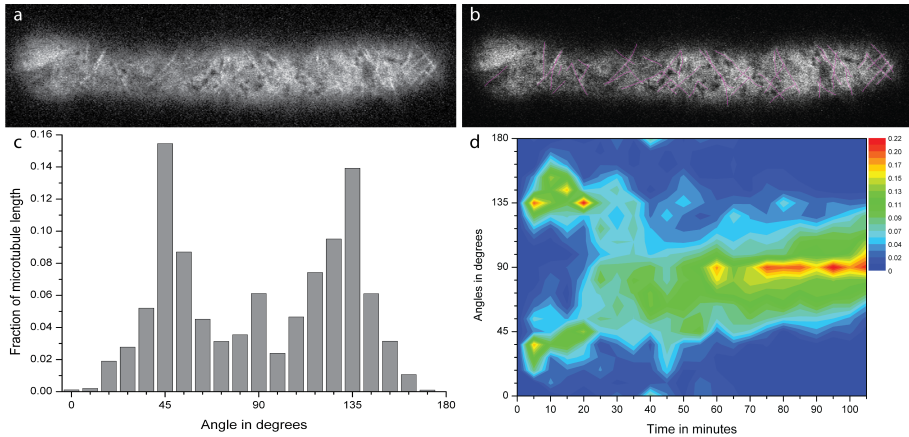
All simulations were started from an initially empty cortex. The time evolution of the angular distributions of microtubules was analyzed using the same filters also used for the

experiments (see Figure S8.5). The microtubule density is reported in terms of an ‘optical density’ in which overlapping microtubules in bundles do not separately contribute to the density, but only the bundle as a whole, mimicking the values measured in the experiments. All simulation results are the average of 500 independent simulations performed with the same parameters. The results were also used for subsequent calculations of  $D$  and  $T$  and Figure 4c.

## 8.6 Acknowledgements

We thank Seiichiro Hasezawa (University of Tokyo) for the generous gift of the tobacco GFP-TUA construct and Tijs Ketelaar (Wageningen University) for the BY-2 cell line expressing the GFP-FABD. We also thank Tijs Ketelaar for helpful discussions.

## 8.7 Supplementary information



**Figure S8.1: Microtubule ordering after cell division in two daughter cells.** (a) Snapshot of the two cells at  $T_{20}$ , and (b) the same image with the tracings of the microtubules in purple (see also Movie S1). Scale bar is  $10\ \mu\text{m}$ . (c) Angle distribution histogram of the microtubules in the two daughter cells at  $T_{20}$  (as indicated in c with an arrow). The fraction of microtubule segments that is diagonally oriented (at  $45^\circ$  and  $135^\circ$ ) is larger than that at  $90^\circ$ . (d) Angle distribution plot of cortical microtubules over time of the left daughter cell in a. In this cell, diagonal ordering is visible when the first microtubules appear in the cortex. After 30 minutes, the transverse ordering becomes dominant and increases in strength.

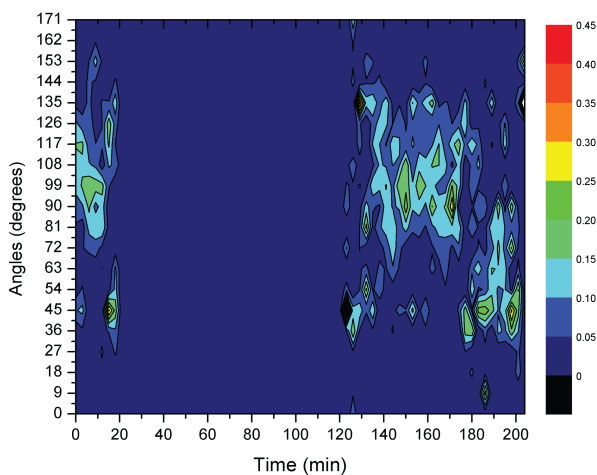
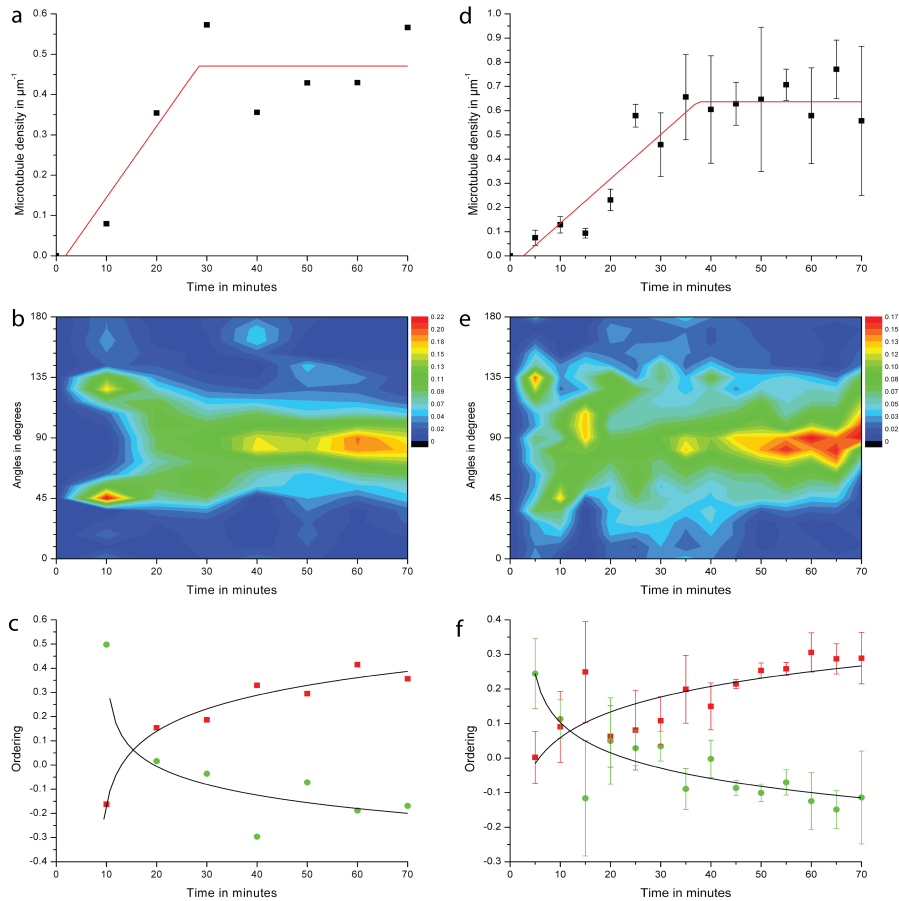


Figure S8.2: **Contour plot with the angular distribution of the microtubule length fractions over time** of a BY-2 cell expressing 35s-GFP-TUA that progresses into prophase after oryzalin washout. The oryzalin wash-in started at  $T_0$ , after which the microtubules depolymerized. During this depolymerization, the  $45^\circ$  and  $135^\circ$  angles emerged as dominant angles. This was also the case during recovery from the oryzalin treatment, which started at  $T_{120}$ . The cell formed a transverse cortical microtubule array at about  $T_{140}$ . At about  $T_{170}$  the interphase cortical array started to breakdown as the cell entered prophase, again, microtubule angles of  $45^\circ$  and  $135^\circ$  became dominant ( $T_{180}$ ). The microtubules inside the forming preprophase band were not measured.





**Figure S8.3 Cortical microtubule density and angle distribution after oryzalin treatment** in the presence of latrunculin B (a, b and c) or isoxaben (d, e and f). (a and d) The microtubule length density increased to a plate density (red line). (b and e) The angular distribution of the microtubule length fractions over time. In the absence of filamentous actin or functional cellulose synthase complexes, the diagonal ordering of the first cortical microtubules is still visible. (c and f) The transverse order parameter (red squares) surpassed the diagonal one (green circles) after  $15 \pm 10$  minutes.

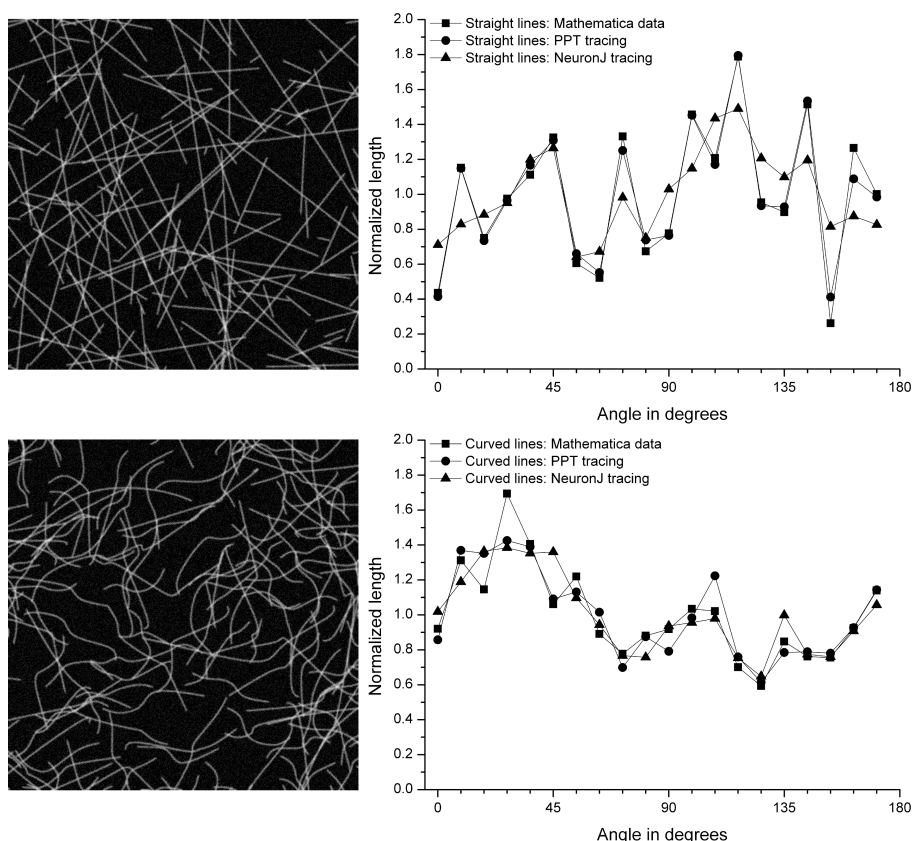


Figure S8.4: **Verification of the Perl script through two different line drawings.** In black the ‘original’ angle distribution of the vector drawing of straight lines (a) and curved lines (b) that were produced with Mathematica (black squares in the graphs); tracings of the Mathematica image using PowerPoint (red circles in the graphs) and the NeuronJ-Perl script tracing results (blue triangles in the graphs).

To confirm the accuracy of our analysis methods, we have generated three randomized line graphs using Mathematica (Wolfram Research, Inc., Champaign, IL, USA) containing straight lines and random curves. Gaussian noise was added using Photoshop (Adobe Systems Inc., San Jose, CA, USA). The images were analyzed by different people using two different methods. First, they were manually traced with curved lines using Microsoft PowerPoint. The traced curves were digitally extracted from a PDF document and analyzed using Mathematica to obtain a normalized length distribution in 20 bins. The generated images were also analyzed using NeuronJ and the subsequent processing steps as used for the experimental data and as described in the Materials and Methods. In Figure S8.4, the results from both methods are compared to the reference values that were computed directly from the original data. From this comparison, we conclude that the results stemming from the semi-automated NeuronJ tracing closely resemble the true distribution. We estimate the error of the NeuronJ tracings to be around 1 bin in the angle direction and  $\pm 14\%$  in amplitude. In addition, we rotated a movie in ImageJ by 27

degrees and did the microtubule tracking again. The pattern after rotation was similar as before, but shifted 27 degrees. The differences found were within the error margin mentioned before.

To analyze the appearance and disappearance of the diagonal and transverse microtubule orderings, we defined two filter functions:  $T$  for transverse ordering and  $D$  for diagonal ordering. A numerical value for the degree of transverse ( $T$ ) or diagonal ( $D$ ) ordering was obtained by multiplying the normalized density data by the relevant filter function and summing over all bins. Both filters were constructed such that an isotropic orientation distribution yields a value of zero, whereas a distribution that is fully contained within the three bins surrounding the target direction returns a value of one. The filter functions have a value of one over a width of  $27^\circ$  (3 bins), centered on  $90^\circ$  in the case of the transverse filter and centered on  $45^\circ$  and  $135^\circ$  in the case of the diagonal filter. The remaining values were chosen such that the sum of all weights is zero (Figure S8.5).

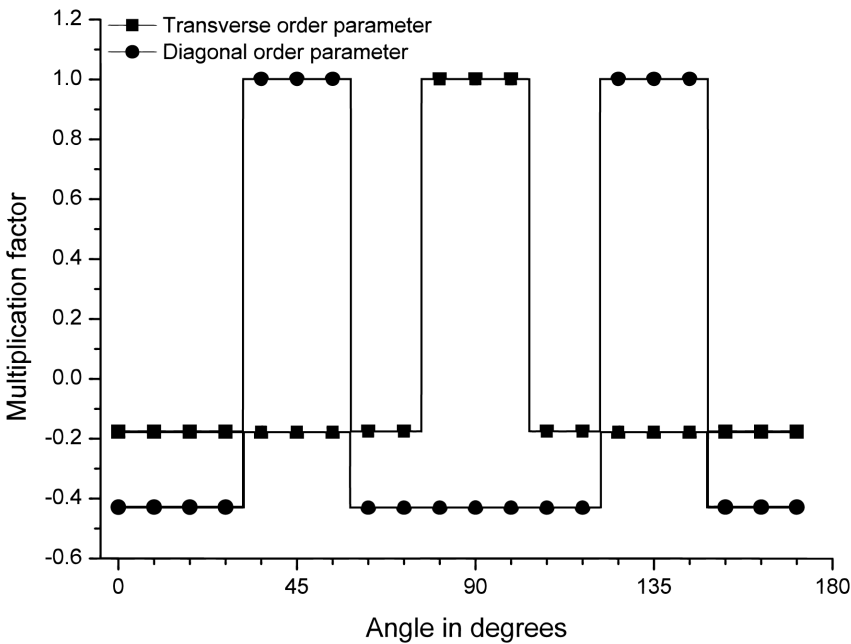


Figure S8.5: Depiction of the filter functions used to calculate the weighted ordering parameters,  $D$  and  $T$ , from the microtubule density angle fractions.

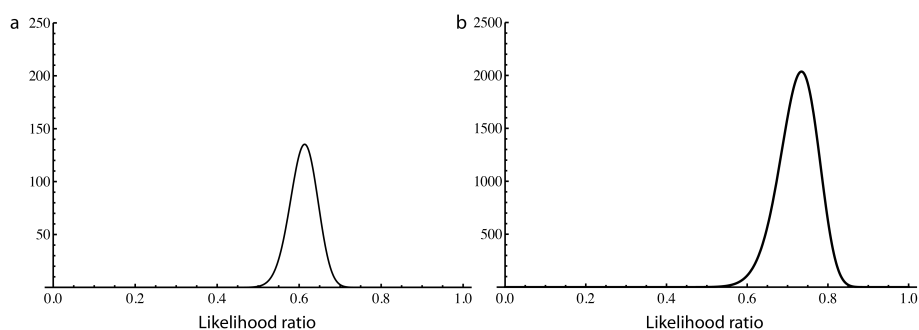


Figure S8.6: Plot of the likelihood ratio for a biased versus an unbiased model of diagonal nucleations as a function of the bias parameter  $\delta$  on the basis of the data for cytokinesis (a), and oryzalin washout (b), showing significant contrast for selecting the maximum likelihood estimate of  $\delta$ .

---

## Which way to go? Role of CLASP and MAP65 in the orientation of the cortical array

---

*This chapter is based on part of [135], with additional data and discussion.*

How is the cortical array oriented? In previous chapters we sort of skipped over this question. We picked up on it when colleagues from Utrecht asked for our help in understanding the cytoskeletal phenotype of particular mutants with impaired auxin responses.

The PLETHORA family of transcription factors is responsible for, literally, a plethora of responses to the plant hormone auxin. Part of the phenotype of the PLETHORA double mutant *plt1plt2* is a decreased number of cell layers in the lateral root cap. This deviation from the normally very regular patterning of the root originates from errors in the orientation of the cell division plane in the epidermis/lateral root cap stem cells. This is invariably linked to the orientation of the cortical microtubules during interphase. The experiments of [135] pointed towards the involvement of microtubule associated protein MAP65 and CLASP, indicated in microtubule-cortex interactions, in translating the auxin/PLETHORA signals to actual microtubule orientation. Using computer simulations we tried to gain further mechanistic understanding of the role of these proteins in the orientation of the cortical microtubule array.

## 9.1 Introduction

The orientation of cell division plane is key to the generation of multicellular organisms as their randomization often leads to morphogenetic defects [336–338]. In plants, neighboring cells cannot relocate due to shared cell walls, and cell divisions have to be oriented parallel to the surface (“periclinal”) to create new layers. Asymmetric periclinal cell divisions, where daughter cells acquire distinct identities, have been termed “formative divisions” (Gunning *et al.*, 1978)[]. Most formative divisions occur at early embryo stages when the body plan is established [339], but others take place when lateral organs are generated [340]. New layers are repeatedly established in the ground tissue and epidermis/lateral root cap (LRC) stem cells of *Arabidopsis* roots [341]. Several transcription factors required for these divisions have been identified [20, 342, 343] but mechanisms by which the orientation of cell division planes are controlled have remained unknown.

Plant cell division planes are specified prior to mitosis by formation of a cortical microtubular band called preprophase band (PPB) [344]. The cortical division site remains marked throughout mitosis and cytokinesis after the PPB has disassembled [345], with negative and positive markers of the cortical division site memorizing PPB position to guide the cell plate [346]. Most of those proteins follow the localization of PPB microtubules and seem to operate downstream [347, 348]. These observations indicate how the microtubular PPB can be coupled with cytokinesis. The PPB forms from the (late) interphase cortical array, likely by a search-and-capture mechanism [298], adopting its orientation. This, however, only moves the question from PPB to interphase array orientation, but does not reveal how either orientation is controlled by the cell.

Cell divisions associated with the *Arabidopsis* root stem cell niche are sustained by the activity of PLETHORA (PLT) proteins, members of the AP2 transcription factor family [349, 350]. Initial induction of PLT gene expression is regulated by distal accumulation of the plant growth regulator auxin [63, 349]. Auxin distribution patterns have been linked with altered cell division planes during embryo development [351], lateral root initiation [266], and in primary roots [352]. In addition, auxin accumulation in cultured cells alters PPB orientation and cell division planes [353]. How auxin influences cell division planes and whether this directs stem cells and their daughters to divide in specific orientations has remained unknown.

Dhonukshe *et al.* [135] have shown that PLT proteins induce root epidermal cells to orient cell division planes through TIR1-dependent auxin signaling [64, 65], which enhances expression of microtubule-associated MAP65 proteins [354, 355]. MAP65 guides localization of CLASP, a microtubule cortex interaction mediator [318], and we postulate a mechanism by which this precisely orients cell division planes. This chapter focusses on the contribution of computer simulations of the cortical microtubules in understanding array orientation.

CLASP has been identified as a protein that affects the orientation of the cortical array [318]. The presumed mechanism is that the cell’s edges form barriers of variable degree to microtubule crossing, as microtubules are stiff polymer tubes ( $l_p$  in the order of micrometers) and the local curvature can be quite high. Without CLASP these edges would induce extra catastrophes on incoming microtubules, with probabilities depending on the edge’s local curvature. It is assumed that the edges generated in the last cell division are sharper than the old edges, which would, without facilitation, typically result in conservation of

the division plane and thus the creation of cell files. CLASP would be able to reduce the catastrophe inducing effect of the edge, to such an extent that its localization could prescribe the array orientation [318]. Indeed, CLASP is found at the edges that are crossed by the aligned microtubules, localizing at the sites where microtubule (bundles) cross the edge [135]. We have used a large number computer simulations to test the reliability of this mechanism on cuboid cells, representative of the meristem cells of our interest.

MAP65 is assumed to be a microtubule bundling protein. The genetic analysis from [135] showed that its expression is enhanced by PLT signaling and it is required for the reorientation of the array, together with CLASP. Two possible scenarios arise:

1. The bundling activity of MAP65 is required for array orientation
2. The only MAP65 function needed for array orientation is linking CLASP to microtubules

It is extremely hard, or at least very time consuming, to genetically engineer different versions of MAP65 proteins, showing only one of presumed functions. In computer simulations, however, it is easy to disentangle them and distinguish between these two scenarios.

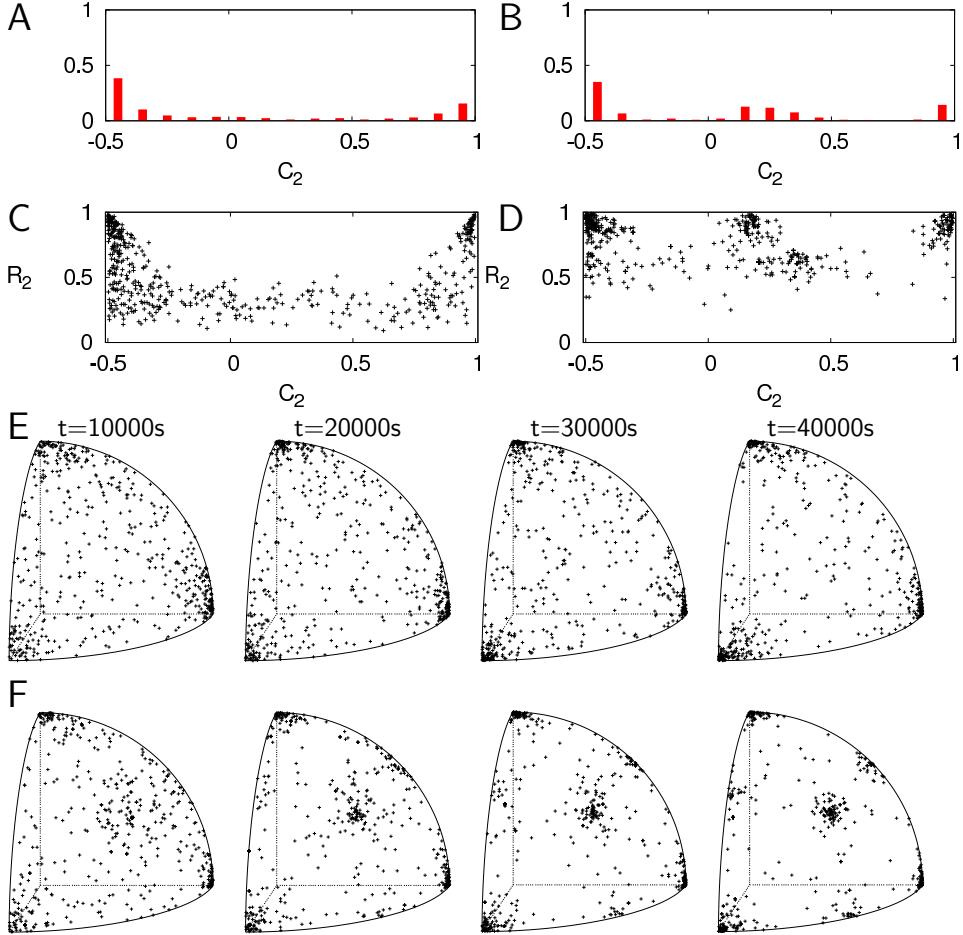
To investigate the reliability of edge induced catastrophes for the orientation of the cortical array and the role(s) of CLASP and MAP65 therein, we performed many simulations of the cortical array using a previously developed algorithm [133] on cubic cells with a size representative for the root meristem. The edges of these cubes induce catastrophes for incoming microtubule + ends with probabilities  $P_{PC}$  for the periclinal and  $P_{AC}$  for the anticlinal edges (figure 9.2A). By changing these probabilities, we simulate the combined effect of differences in edge curvature and CLASP presence.

## 9.2 Results

### 9.2.1 Edge-induced catastrophes can reliably orient the cortical array

Ambrose *et al.* reported a catastrophe probability of 0.26 for microtubules crossing “easy” edges [318]. Without any difference between the anticlinal and periclinal edges ( $P_{AC} = P_{PC} = 0.26$ ), the cube should favour either anticlinal or periclinal array orientation over the other. We indeed found that in this case the three orientations (1x periclinal and 2x anticlinal) occurred with roughly equal probability (figure 9.1A,E). Interestingly, intermediate (oblique) orientations were suppressed by the cube geometry and the runs that happened to be oriented differently showed a markedly lower degree of alignment ( $R_2$ , figure 9.1C). When we repeated the simulations without any penalties for crossing the edges ( $P_{AC} = P_{PC} = 0$ ), however, we additionally found a distinct fraction of the runs with specific oblique angles (figure 9.1B,F). Of these, the full diagonal orientation (the spot in the middle of figure 9.1F at later time points) obtained the same degree of alignment as the transverse and longitudinal arrays (figure 9.1D), whereas the plane diagonal orientation (spots in the middle of the edges in figure 9.1F) resulted in  $R_2$  values indistinguishable from cells with “random” orientations. This implies that the cube geometry

by itself favours specific orientations. Of these, oblique orientations are suppressed by (small) edge crossing penalties.



**Figure 9.1: Geometry and orientation.** Histogram of  $C_2$  values for  $P_{AC} = P_{PC} = 0.26$  (**A**) showing a bimodal distribution with peaks at  $C_2 \approx 1$  and  $C_2 \approx -0.5$  with the latter roughly twice as high as the former, indicating that most simulations end up in one of the three possible orientations with roughly equal probability, consistent with the cubic symmetry of the cell. Without any penalties for crossing the cell's edges ( $P_{AC} = P_{PC} = 0$ ; **B**) other orientations occur in a significant fraction of the runs. **C+D** show the orientation vectors of individual runs mapped to the positive octant of a unit sphere at four time points with  $P_{AC} = P_{PC} = 0.26$  (**C**) and  $P_{AC} = P_{PC} = 0$  (**D**). The cubes showing one of the preferred orientations typically have a larger degree of global alignment (at  $t=40000s$ ), as measured with order parameter  $R_2$ ;  $P_{AC} = P_{PC} = 0.26$  (**E**) and  $P_{AC} = P_{PC} = 0$  (**F**).



### 9.2.2 The only MAP65 function relevant for orientation control is linking CLASP and MTs

On changing the ratio of  $P_{AC} : P_{PC}$  (while keeping  $P_{PC} = 0.26$  fixed), the predominant orientation changed towards transverse/anticlinal ( $P_{AC}$  large) or towards longitudinal/periclinal ( $P_{AC} < P_{PC}$ ) (figure 9.2A). Histograms showing the distribution of array orientations from individual simulations show that towards the extremes for  $P_{AC}$ , almost all cells had an orientation in the most extreme bin (figure 9.2B,C). This implies that edge crossing penalties can reliably enforce a single particular orientation of the cortical array (if the edges ( $P_{AC}$  and  $P_{PC}$ ) are sufficiently different).

We observed the same trend with and without bundling/zippering (figure 9.2A,F,G). Only the effective edge penalties ( $P_{AC}$  and  $P_{PC}$ ) determine which array orientations will occur (and their relative frequency). This implies that the proposed bundling activity of MAP65 per se is not required for the orientation of the array. Along the same lines, the orientation bias on symmetrical cubes ( $P_{AC} = P_{PC}$ ) also showed without zippering (figure 9.3), with only differences in the precision of the selected orientations (specially clear when comparing 9.1B,F and 9.3B,F).

## 9.3 Discussion

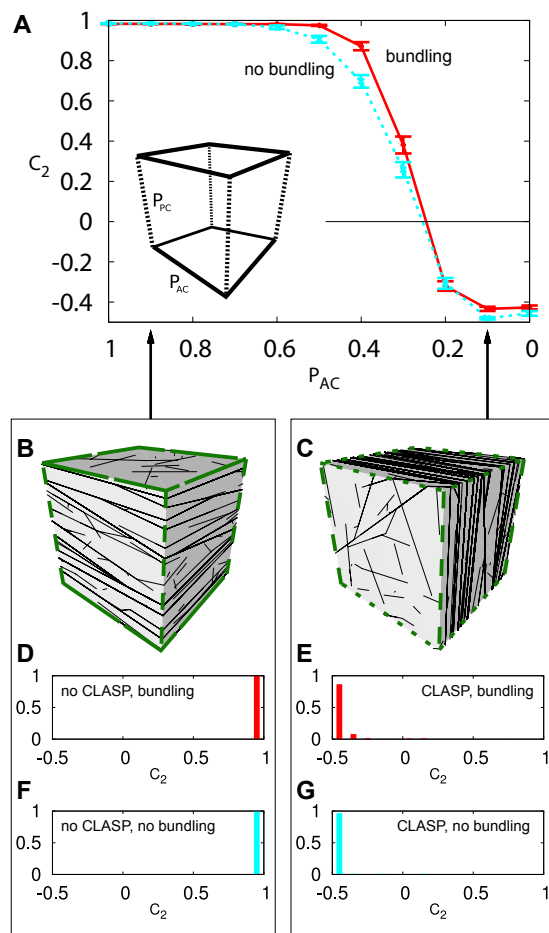
### 9.3.1 Bundling and orientation

Our results clearly show that the proposed bundling functionality of MAP65 per se is not important for array orientation. We could abolish all zippering interactions (replace them by cross overs, in terms of our model “non-interactions”) and still reliably orient the array to the desired orientation through differences in the probabilities for edge induced catastrophes. So, even though bundles can form *in planta* without MAP65 [313] and MT dynamics are the same within and outside bundles [356], MAP65 function within the orientation of the division plane in response to auxin signaling remains.

From earlier theoretical work, this finding is perhaps not that surprising. Tindemans *et al.* found that zippering, in the absence of MT treadmilling, did not affect the location of the bifurcation point  $G^*$  and resulted in a lower degree of alignment in ordered arrays [133, 357]. In this light, zippering can be considered as a “nuisance factor” rather than an ordering principle. Similar observations occur throughout. Compare for example the scatter of  $R_2$  values in figures 9.1D (with zippering) and 9.3D (no zippering). In chapter 7, the average  $S_2$  value in figure 7.3A does not approach the theoretical maximum of 1 for  $G_c \uparrow 0$ , but appears to saturate at a lower level (of course, one should note the finite simulation time). Perhaps the potential to smear local orientations together could explain why the observed orientations can be more precise without zippering (compare figures 9.2E and G and figures 9.1D,F and 9.3D,F). The interaction of local alignment and global array orientation forms an interesting topic for further study.

### 9.3.2 CLASP based orientation mechanism and cell size

The CLASP based orientation mechanism proposed in [318] is fully based on edge induced catastrophes. If the cell size increases, the growing MT ends will experience fewer



**Figure 9.2: CLASP, bundling and auxin signaling.** **A:** simulation setup: the edges of the simulation cell (cube) are divided in two sets: “periclinal” and “anticlinal”. MTs impinging on these edges undergo an induced catastrophe with probabilities  $P_{PC}$  and  $P_{AC}$ , respectively. With  $P_{PC} = 0.26$  fixed and decreasing  $P_{AC}$ , the predominant array orientation changes from always transverse to periclinal, both with (red solid) and without (cyan dashed lines) bundling interactions. **B,C:** example cells for  $P_{AC} = 0.9$  (“no CLASP”) and  $P_{AC} = 0.1$  (“with CLASP”). **D,E:** distributions of array orientations with and without (anticlinal) CLASP show the reliability of this orientation mechanism. **F,G:** the same holds without bundling interactions, implying that the essential function of MAP65 in array orientation is only the facilitation of CLASP-MT interactions.  $n=500$  runs per parameter combination.

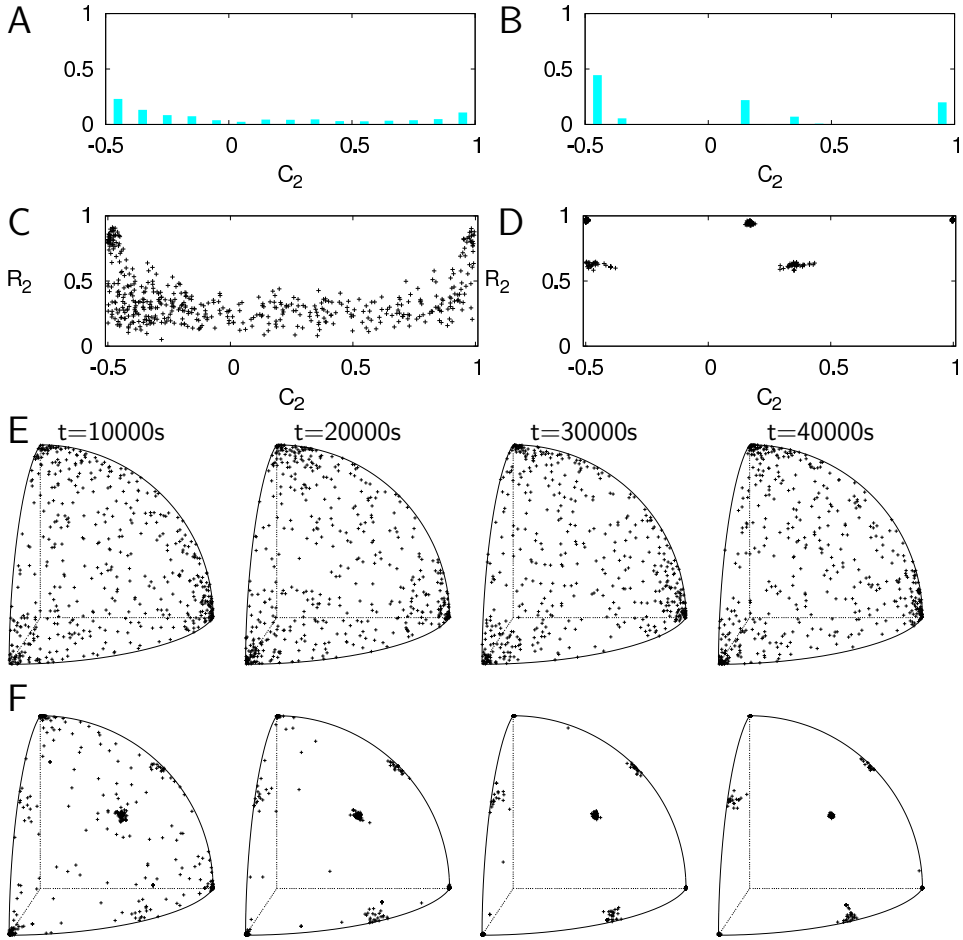


Figure 9.3: As figure 9.1, but without zippering/bundling

encounters with the edges and so the effect of the edges will decrease. To put these simulations in perspective: with the parameters we used ( $G = -0.007$ , see equation 7.1), the mechanism worked on the  $15 \times 15 \times 15 \mu m$  cubes. However, to obtain spontaneous alignment with all values of  $P_{AC}$  used, we had to use a somewhat lower spontaneous catastrophe rate  $r_c = 0.003s^{-1}$  in stead of  $r_c = 0.0045s^{-1}$  based on [298] (but within the reasonable range and the range used in [289]).

This means that for cell sizes typical for the root meristem, it is possible to have reliable CLASP-based orientation of the cortical array with reasonable parameters for microtubule dynamics.

From our starting point we could increase the cell size, possibly to a point that the orientation mechanism loses its reliability because the information of the edges no longer reaches the whole cell, and decrease it, to a point that spontaneous alignment would be impaired for an increasing range of  $P_{AC}$  and  $P_{PC}$  values, because the microtubules would

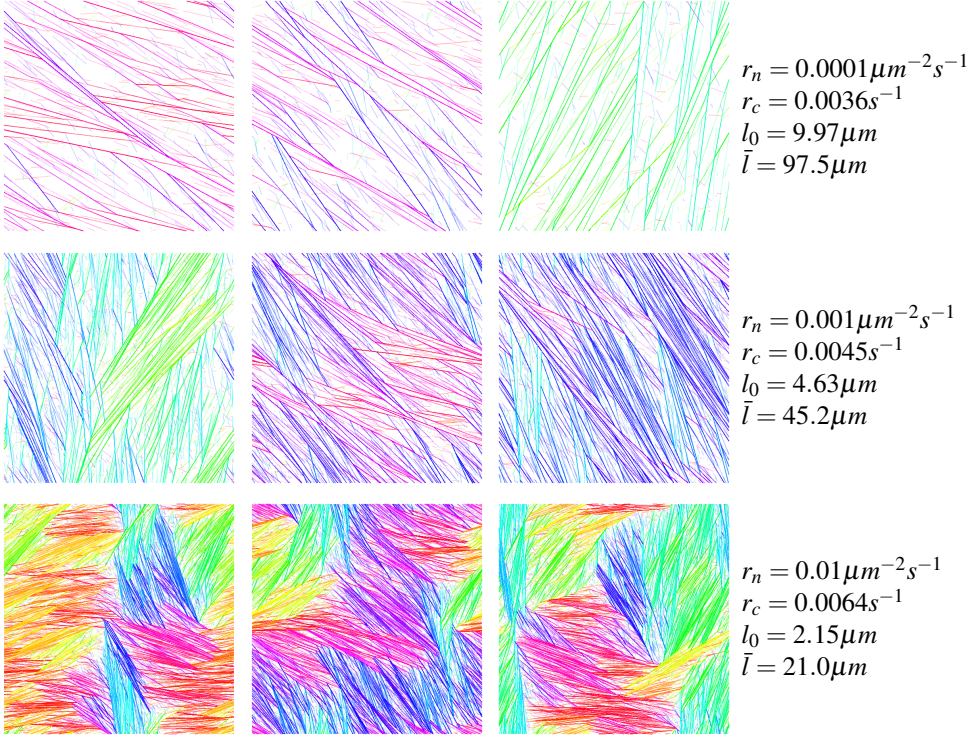


Figure 9.4: **Same  $G$ , but different microtubule length scales ( $l_0$  and  $\bar{l}$ ).** To enhance the visual detection of different domains, the MTs are coloured according to their angle. Base parameters: grid size  $150 \times 150 \mu m^2$ , defaults ( $G = -0.10$ ). Snapshots at  $T=100000s$ .

become too short to “communicate” enough to “coordinate” their orientation. This could be compensated by reducing the spontaneous catastrophes (decreasing  $r_c$ ), but that is only possible until the limit of  $r_c = 0$ .

To understand why edges may not be sufficient to orient arrays on large scales, reconsider control parameter  $G$ . For interpretation, Tindemans *et al.* rewrite  $G$  as the ratio of two length scales:  $G = -l_0/\bar{l}$ , with (adapted for treadmilling)  $1/\bar{l} = \left( \frac{r_c}{v^+ - v^-} - \frac{r_r}{v^- + v^+} \right)$  the average length of microtubules without any interactions. This implicitly defines  $l_0$ , the cube root part of the  $G$  equation, as an interaction length scale [133]. By multiplying both length scales with the same factor,  $G$  remains unchanged, but the MT lengths change. As a result, also for the same  $G$ , the orienting effect of catastrophe inducing boundaries can be stronger or weaker, depending on the values of  $\bar{l}$  and  $l_0$ . If  $\bar{l} \ll \text{system size}$ , the system seems no longer able reach a global alignment, at least not on biological relevant time scales (figure 9.4). The relationship between domain size and intrinsic microtubule lengths is an interesting topic for further research. This relationship will probably depend strongly on the interaction function of colliding microtubules, as this affects how far competing domains will typically penetrate each other and thus determine the energetic cost

of a boundary.

To understand how the decrease of the cell size can lead to a loss of spontaneous alignment, we could try to find an effective catastrophe rate including the edges to cross for a given orientation. For example, with a perfect periclinal orientation, a growing end encounters the edge every  $v^+/L$  seconds (with  $L$  the length of a cube's edge). This translates to an additional catastrophe rate of  $\frac{v^+P_{AC}}{L}$  and thus an effective catastrophe rate of  $r_{c,eff} = r_c + \frac{v^+P_{AC}}{L}$ . This we can plug into the equation of  $G$ , resulting in

$$G_{eff,xx} = \left\{ \frac{2(v^+ - v^t)^2(v^- + v^t)}{r_n v^+ (v^+ + v^-)} \right\}^{\frac{1}{3}} \left( \frac{r_r}{v^- + v^t} - \frac{r_c + \frac{v^+ P_{yy}}{L}}{v^+ - v^t} \right) \quad (9.1)$$

with  $xx$  either  $AC$  or  $PC$  and  $yy$  the other, depending on the orientation of the array. With the interaction function used (figure 7.1), the phase diagram of  $G$  and the alignment (quantified using order parameter  $S_2$ , see equation 7.8) is as follows: spontaneous alignment occurs if  $G < 0$  is larger than some critical value  $G^*$ , but not for smaller  $G$  (see also figure 7.4a). It is easy to see from equation 9.1 that  $G_{eff,xx} < G$  and that  $G_{eff,xx}$  decreases (becomes more negative) with decreasing cell size ( $L$ ). This implies that for each parameter combination that would lead to spontaneous alignment without obstructing edges and any value of the relevant  $P_{xx}$ , there is a minimum cell size ( $L$ ) required for alignment.

Along the same line we can also understand why oblique orientations are suppressed on the cube with a given (not too large) penalty on all edges: a diagonally oriented array would cross six edges in stead of four, with an average distance of  $\frac{1}{2}\sqrt{2}L$  between consecutive crossings. This means a factor  $\sqrt{2} \approx 1.41$  times more edge-induced catastrophes. With the parameters used, the effective catastrophe rate is 13% higher for a diagonal array compared to a transverse of longitudinal array at  $P_{AC} = P_{PC} = 0.26$  and the same for both all orientations for  $P_{AC} = P_{PC} = 0$ .

### 9.3.3 Chicken and egg: how to position CLASP?

In our simulations, we have incorporated the combined effects of CLASP presence and edge curvature into a single parameter  $P_{xx}$  per edge, typically fixed for the simulation. With this, we have implicitly postulated that CLASP simply sits on particular edges. The experiments show, however, that CLASP is associated with microtubule bundles, implying that CLASP assistance for crossing the edge won't be available before there are any bundles crossing. This creates a chicken-and-egg problem, at least apparently: for a large probability of crossing of the sharp edge, CLASP is needed, but CLASP positioning seems to require microtubule bundles already crossing that edge. As cells manage to adjust their orientation, a mechanism exists for resolving this paradox. Unraveling this mechanism means going into the details of dynamic CLASP localization. This is likely affected by other regulatory mechanisms coordinating cell polarity in the growing and developing plant. In the end, a mechanism is required that effectively "kicks" CLASP from one set of edges to another.

Further computer simulations could be useful to determine under what conditions proposed mechanisms could do the job, for example the minimum strength of a (temporal) bias in likelihood that CLASP molecules attach to microtubules at particular edges.

## 9.4 Conclusions

CLASP and MAP65 were identified in a genetic/cell biological analysis as key components in the translation of auxin signaling to the developmental orientation of the cell division plane, through the orientation of the cortical microtubules. Using computer simulations of the cortical microtubule array we have been able to disentangle the contributions of different biological functionalities of MAP65, that are hard to separate experimentally. This is a step forward in understanding the physical mechanism(s) of array orientation[, division plane orientation and plant development.]

## 9.5 Simulation methods

The simulations of the cortical microtubule array were performed using the event-based algorithm also employed in [133]. The microtubule dynamic parameters are based on [298] (growth speed  $v^+ = 4.8\mu\text{m}/\text{min}$ , shrinkage speed  $v^- = 9.6\mu\text{m}/\text{min}$ , and rescue rate  $r_r = 0.42/\text{min}$ ) and [291] (treadmilling speed  $v^t = 0.6\mu\text{m}/\text{min}$ ), as used in [289].

The nucleation rate of  $r_n = 0.06\text{min}^{-1}\mu\text{m}^{-2}$  is based on casual observations of interphase cells, and is equal to that used in [289, 294]. It gives rise to an aligned stationary state in combination with the chosen dynamical parameters. The simulation domain is the surface of a  $15\mu\text{m} \times 15\mu\text{m} \times 15\mu\text{m}$  cube, representing the cell cortex. We designated the two cell faces parallel to the XY plane of our reference system as the apical and basal planes. The remaining four faces, two parallel to the XZ plane and two parallel to the YZ are designated as longitudinal. The spontaneous catastrophe rate on the microtubules was chosen to be  $r_c = 0.18\text{min}^{-1}$ , a value still consistent with observations, but chosen slightly lower than in previous simulations to be compatible with the requirement of allowing for spontaneous alignment of the array for all values of the parameter  $P_{AC}$  that sets the probability of catastrophe when impinging on an anticlinal edge. For the microtubule collisional interactions we follow the simplified scheme first adopted by [293], also followed by [289, 294] (see figure 7.1): all collisions with angles below  $\theta_c = 40^\circ$  result in zippering (also called entrainment). For collision angles larger than  $\theta_c$  the result is either a collision induced catastrophe, with probability  $p_{cat}$  or a cross-over with probability  $1 - p_{cat}$ . While different values of  $p_{cat}$  have been reported [132, 299] and various values have been used in the simulations published so far, we chose to adopt the intermediate value  $p_{cat} = 0.5$ , as in [289], which falls between the reported values.

The order parameter we use to characterize the orientation of the ordered array is defined with the aid of the second-rank ordering tensor  $Q_{ij} = \langle u_i u_j \rangle - \frac{1}{3} \delta_{ij}$ , where  $i, j = X, Y, Z$  label the components in our reference frame,  $u = (u_X, u_Y, u_Z)$  is the 3-vector along a straight microtubule segment, the angular brackets  $\langle \dots \rangle$  denote a length-weighted configurational average over the whole surface, and  $\delta_{ij}$  is the 3-D isotropic tensor. We consider the normalized eigenvector corresponding to the dominant negative eigenvalue of  $Q_{ij}$  (i.e. the most negative one), corresponding to the direction on average most perpendicular to the microtubules. We denote its components by  $(\xi, \eta, \zeta)$ , where  $\xi^2 + \eta^2 + \zeta^2 = 1$  and we are free to choose  $\zeta > 0$ . The order parameter  $C_2$  is then defined through these components as  $C_2 = \zeta - \sqrt{\xi^2 + \eta^2}$ . It is straightforward, but tedious, to check that this parameter indeed produces the required characterization, i.e.  $C_2 = 1$

(eigenvector  $(0,0,1)$ ) for perfect anticlinal order,  $C_2 = -\frac{1}{2}$  (eigenvector  $(1,0,0)$  or  $(0,1,0)$ ) for perfect periclinal order, and  $C_2 = 0$ , for an equal mixture of the three possible orientations for ordered arrays on the cube. The degree of global alignment of the cube is indicated with  $R_2$ , the (absolute value of) the dominant negative eigenvalue of  $Q_{ij}$  []. This has the same properties as the planar order parameter  $S_2$  described in chapter 7, equation 7.8: 0 indicates no net (global) alignment, 1 indicates perfect global alignment e.g. an array of only perfectly transverse microtubules.

At each distinct set of parameter settings we perform  $N = 500$  independent simulations, each run for  $T = 40000s$  (11.1 hours) “biological” time to allow for full relaxation to a steady state. The reported values of  $C_2$  are averages over these sets of runs.





## **Part IV**

# **Concluding considerations**



---

## General discussion

---

*In general terms, the aim of this discussion is to put the results of the previous parts in a bigger picture, or more general scientific context. How big a bigger picture is, however, is subject to interpretation. I have therefore chosen to present several disjunct bigger pictures, embedded as examples in even bigger pictures. – With thanks to Bela Mulder and Victor Gijssbers for helpful suggestions.*

### 10.1 Biological systems from a design perspective

Why are we nowadays so often confronted with – by and large ineffective – anti-obesity propaganda? In other words: why is it so hard to refrain from eating too many sweet and/or fatty snacks? Why do all plants use the same enzyme, rubisco, that can greatly reduce photosynthetic yields by regularly incorporating oxygen rather than CO<sub>2</sub>? Or why do we have to keep losing our loved ones to cancer?

Why, why, why? From a rational design perspective, none of this makes any sense. There is an answer though, that we generally accept: *“Nothing in biology makes sense except in the light of evolution”* (Theodosius Dobzhansky). Accepting this, an important question arises: does it make any sense to view biological problems from a design perspective, as no living organism<sup>i</sup> originated from a designer’s drafting table, but all were shaped by evolution?

As I have used the designer’s perspective throughout this thesis, it is not surprising that my answer to this question is “yes”. Understanding the consequences of different design “choices” can help us understand what were/are the critical features for certain desirable functionally. This in turn can help us understand why, *given the starting conditions*, things evolved the way they did. Sometimes we will have to accept that it just happens to have evolved this particular way, but by being the way it is, it now shapes the current (im)possibilities of the organism or species. Striking deviations from what seems a “rational design” could also hint towards processes or components that are evolutionary so essential, that there is no way of changing them<sup>ii</sup>. In short: thinking about design properties could help us understand what functional solutions have been selected for.

---

<sup>i</sup>Except perhaps for the first surviving creations from the emerging field of synthetic biology.

<sup>ii</sup>Economy uses the term “lock-in” for similar situations – hypothetical according to some – that the market gets stuck on some “inferior” technology, because this was established and well spread before a (somewhat) better technology came along [358].

Adopting a design perspective is all about comparing and understanding different mechanisms. Understanding the mechanism behind some process makes it easier to predict or understand its response to challenges, for example the application of a herbicide to a plant. The possible uses of this depend on how much we know. If we know the mechanism, we could think of ways to optimally exploit some of its properties to our advantage. If we do not know the mechanism, but have a few likely candidates, understanding these mechanisms can help design experiments that are most likely to discriminate between the candidates. It may also help us understand why the same problems are solved in very different ways by different groups of organisms (see also chapter 3).

Models can be great tools in thinking about different mechanisms and design properties, but not all models are equally suitable for this.

## 10.2 Reinventing the wheel: the systems biology cycle

Anyone currently working on biological problems using models must have encountered the term “systems biology”, certainly when also collaborating with experimentalists. So why isn’t this thesis called: “Multilevel systems biology of plant development”?

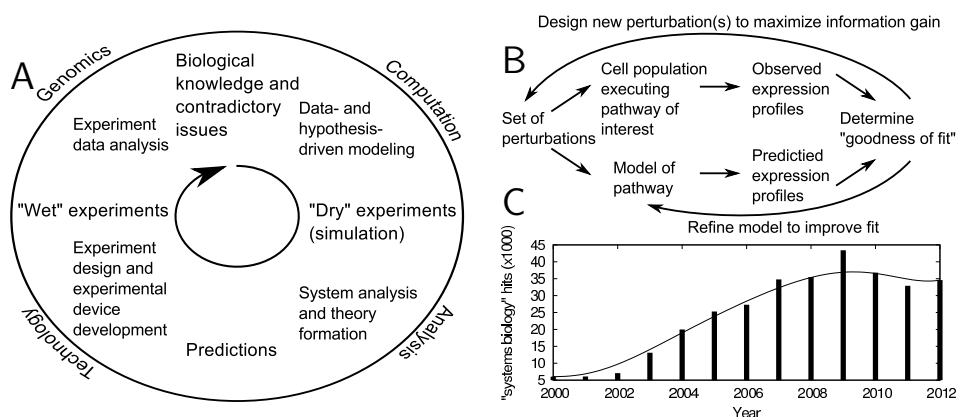
Curiously, for a field that defines itself by its approaches, very few people are able to provide a definition of systems biology (and those who can, do not necessarily agree with each other). This, for one thing, makes every systems biology meeting a surprise, either pleasant or unpleasant. Nevertheless, there appears to be some consensus on stereotypical systems biology as a combination of high throughput data and computationally heavy computer models. In such studies, the idea is that the experiments help improve the model(s) and through them our understanding of the system, which in turn inspires further experiments to challenge the model(s) and discriminate between model variants. This is presented as an iterative process, often called the “systems biology cycle”. Two versions of this cycle, as found in two key papers at the foundation of systems biology, are presented in figure 10.1.

For the moment ignoring the suggestion of strict temporal separation of “wet” and “dry” experiments (figure 10.1A), probably an artefact of representation, or the very specific nature of the experiments, models and tools suggested (figure 10.1B), this seems like a pretty generic description of current scientific methods: developing hypotheses (with models as their (not necessarily much) more explicit incarnations) and testing them, etc. If this abstraction is correct, then what is so new about systems biology?

### 10.2.1 A little historical context

The systems biology endeavour can best be seen as a counter-reaction against the classical genetic approach of studying single genes at a time, assessing their functions from the defects caused by impairing mutations. The first successes of this genetic approach were the unraveling of linear metabolic pathways. In those cases, the subsequent steps could be ordered based on the nutritional supplements that would allow different mutants to grow. This became the foundation of the “one gene, one enzyme” hypothesis, later updated into “one gene, one protein” and rewarded with a Nobel prize in 1958 [361].

After this many more genes and functions followed, but more and more studies got



**Figure 10.1: Famous systems biology cycles.** **A:** after Kitano 2002. Original caption: *“Hypothesis-driven research in systems biology. A cycle of research begins with the selection of contradictory issues of biological significance and the creation of a model representing the phenomenon. Models can be created either automatically or manually. The model represents a computable set of assumptions and hypotheses that need to be tested or supported experimentally. Computational “dry” experiments, such as simulation, on models reveal computational adequacy of the assumptions and hypotheses embedded in each model. Inadequate models would expose inconsistencies with established experimental facts, and thus need to be rejected or modified. Models that pass this test become subjects of a thorough system analysis where a number of predictions may be made. A set of predictions that can distinguish a correct model among competing models is selected for “wet” experiments. Successful experiments are those that eliminate inadequate models. Models that survive this cycle are deemed to be consistent with existing experimental evidence. While this is an idealized process of systems biology research, the hope is that advancement of research in computational science, analytical methods, technologies for measurements, and genomics will gradually transform biological research to fit this cycle for a more systematic and hypothesis-driven science.”* [359] **B:** after Ideker et al. 2001. Original caption: *“Overview of the systems biology approach, involving pathway verification and refinement through systematic, successive perturbations. The pathway of interest is perturbed genetically by gene deletion or overexpression and/or biologically by modulation of metabolite levels, temperature, or other pathway components. Gene expression profiles measured in response to each perturbation, obtained using microarrays or related technologies, are compared to those predicted by a model of the pathway mechanism. Perturbations are initially selected to target known pathway components and are thereafter chosen to distinguish between alternative models that are consistent with the present set of observations. All aspects of the process are amenable to automation (laboratory or computational), including model refinement and choice of perturbations.”* [360] **C:** Popularity of systems biology, as measured by the number of hits per year using google scholar (excluding citations and patents) on the term “systems biology” (data retrieved: January 23, 2013).

stuck on what is called genetic redundancy: knocking out of a single (or even multiple) genes does not produce a very clear phenotype, because other, similar genes, can compensate for the loss – at least partially. Other genes are so important, that their loss is simply lethal, the knock-out providing little more information about their function than that it is important. Moreover, the number of simple linear pathways in biological systems is limited. It would do no justice to the inventiveness of many great biologists to state that they all got stuck after the last linear pathway was solved or upon encountering genetic redundancy or lethality of mutations. There is no denying, however, that it is becoming increasingly difficult to learn more from studying genes/proteins in isolation. Was Tolkien perhaps thinking of genetics when he wrote that “*he that breaks a thing to find out what it is has left the path of wisdom*” [362]<sup>iii</sup>, foreseeing the limitations of this once revolutionary field?

With the progression of the human genome project – and other key genomes unraveled at the same time – the estimates of the numbers of genes per haploid genome were reduced time and again. For example, in 1993 this number was estimated for human and mouse at 80 000, refining the estimates of that time of 50 000 - 100 000 [363]. At the time the first full drafts were published in 2001, the estimates were down to 26 588 certain and up to 12 000 weakly predicted [364] or 30 000 - 40 000 [365] protein coding genes. This was a very threatening development for minds shaped by the one gene, one protein hypothesis. The discovery of alternative splicing could stretch the limits of the number of available proteins a bit, but it became inevitable to accept the end of the comfort of explaining all mysterious phenomena, missing links, etc by hypothesizing that there would be some yet undiscovered protein performing exactly the required task. With the decreasing estimates of gene numbers, the available “unidentified genes” to fix the problem seemed to be running out fast. This problem was resolved, however, by the realization that with increasing gene numbers, the number of possible interactions would increase combinatorially, restoring the damage to mankind’s pride from the observation that “we” have no more than twice the number of genes of fruit flies (*Drosophila melanogaster*) or worms (*Caenorhabditis elegans*). And indeed, the number of genes with regulatory functions increases faster than proportional with genome size [366].

Besides the exhaustion of genetically accessible problems, recent years have seen an explosion of high-throughput techniques, such as ever cheaper DNA sequencing, mRNA microarrays, metabolic profiling and many others. After “genomics”, the dictionaries have been expanded with many other words ending with “-omics”. These tools have inspired the idea of studying whole systems at once rather than their components in isolation. The resulting increase in the number of components alone made it simply impossible for the human brain to discover any system behind the data. This has made (computer) models an absolutely essential tool in making at least some sense out of the huge amounts of data. Fortunately, computer power had become available to do so – or to at least make an attempt.

At the beginning of the millennium the term “systems biology” was coined for integrating computer modeling and wet experiments addressing multiple components to-

---

<sup>iii</sup>If Tolkien were indeed thinking of genetics when he wrote down these words of his wizard Gandalf, this would have been more likely out of jealousy of its successes than inspired by his worries about its limitations, as he was no friend of scientific progress, or even lamp-posts. *The fellowship of the ring* was published 4 years before Beadle, Tatum and Lederberg received their Nobel prize.

gether [359, 360]. Along with the term came the prescription of an iterative method of integrating models and experiments, including the often reappearing “systems biology cycle” (figure 10.1A,B). Systems biology became a real buzzword, rapidly increasing in popularity in the scientific literature (figure 10.1C). This optimism resulted in the availability of lots of money from diverse funding bodies. Systems biology being very interdisciplinary from its definition, this money attracted people with diverse backgrounds, such as theoretical biology, physics, mathematics, computer science and, of course, diverse areas of biology including genetics. For some this was a jump into an entirely new field, others just found a new source of funding for the kind of work they had already been doing for a long time. With such a diversity in backgrounds and approaches, it is not strange that a decade later *“there is as yet no firm consensus as to what is meant by ‘systems biology’, although as our colleague Marc Kirschner has said, ‘we all seem to know it when we see it.’<sup>iv</sup>”* as stated by [367].

## 10.2.2 Stereotypical systems biology

What is it that we “know when we see it”? I think that most of us recognize something that fits a stereotypical conception of systems biology. Anything that shows a systems biology cycle or is presented as a step towards some very ambitious agenda of building a fully predictive model of a whole organism<sup>v</sup> or organ system, such as a “virtual cell” [369, 370], “virtual plant” [371], “virtual liver” and “virtual blood-brain barrier”<sup>vi</sup> certainly fits the stereotype. Common elements are lots of data and a combination of models and experiments. For a better impression of what this stereotype is, let’s take a close look at the method as described in [360], “A framework for systems biology” (box 10.1).

Although a general consensus on the definition of systems biology is lacking, the stereotype seems much easier to define<sup>vii</sup>: creating a model that, after repeated refinements based on (new) measurements, resembles the experimental system as closely as possible and, when successful, is able to reproduce the results or perturbations. Such an aim could be rephrased as creating a virtual clone of the experimental system, which typically is a very ambitious project because of the large number of components involved.

In any new field, particularly if it attracts people with completely different backgrounds, the initial optimism is typically accompanied by some naive ideas. This is perhaps best illustrated by the frequent occurrence of words such as “verification” and “validation”, reminiscent of the optimism of the logical positivists of the first half of the last century. To further illustrate the naivety of the agenda of this stereotype, I have marked some passages in italics (A-D in box 10.1) for discussion below.

The method does not state why we would like to build a particular model, or what

<sup>iv</sup>Kirschner himself was most likely referring to Associate Justice at the US supreme court Potter Stewart: *“I shall not today attempt further to define the kinds of material I understand to be embraced within that shorthand description [hard-core pornography]; and perhaps I could never succeed in intelligibly doing so. But I know it when I see it, and the motion picture involved in this case is not that.”* in the case *Jacobellis v. Ohio*, 378 U.S. 184 (1964).

<sup>v</sup>A list of flux balance models [368] describing “whole organisms” is maintained at <http://systemsbiology.ucsd.edu/InSilicoOrganisms/OtherOrganisms>.

<sup>vi</sup><http://www.epa.gov/heasd/edrb/comptox.html>

<sup>vii</sup>I have the impression that it is this kind of research that is most often presented together with a picture of the systems biology cycle.

1. **Define all of the components of the system.** Use these components, along with prior biochemical and genetic knowledge, to formulate an initial model. *Ideally, a global approach is the most powerful (i.e., defining all genes in the genome, all mRNAs and proteins expressed in a particular condition, or all protein-protein interactions occurring in the cell) because it does not require any prior assumptions about system components.<sup>A</sup>* Constructing a model by interrogating these components will ultimately accomplish two objectives: (a) to describe the structure of the interactions that govern the system's behavior and (b) to predict accurately relevant properties of the system given specified perturbations. If prior knowledge about the system is limited, the initial model may be rough and may involve purely hypothetical interactions.
2. **Systematically perturb and monitor components of the system.** Specific perturbations may be genetic (e.g., gene deletions, gene overexpressions, or undirected mutations) or environmental (e.g., changes in growth conditions, temperature, or stimulation by hormones or drugs). The corresponding response to each perturbation is measured using large-scale discovery tools to capture changes at relevant levels of biological information (e.g., mRNA expression, protein expression, protein activation state, overall pathway function). Once observed, data from all levels are integrated with each other and with the current model of the system. *As in step 1, an approach in which all components are systematically perturbed and globally monitored is the most desirable.<sup>B</sup>*
3. **Reconcile the experimentally observed responses with those predicted by the model.** Refine the model such that its predictions most closely agree with experimental observations. Agreement between the observed and predicted responses is evaluated qualitatively and/or quantitatively using a goodness-of-fit measure. When predictions and observations disagree, alternative hypotheses are proposed to alleviate the discrepancies (*maximize the goodness-of-fit<sup>C</sup>*), resulting in a refined model for each competing hypothesis. If the initial model is largely incomplete or is altogether unavailable, the observed responses may be used to directly infer the particular components required for system function and, among these, the components most likely to interact. If the model is relatively well defined, its predictions may already be in good qualitative agreement with the observations, differing only in the extent of their predicted changes.
4. **Design and perform new perturbation experiments to distinguish between multiple or competing model hypotheses.** Even for a moderate number of observations, the proposed refinements may result in several distinct models whose predictions fit equally well with the observations. These models are indistinguishable by the current data set, requiring new perturbations and measurements to discriminate among them. New perturbations are informative only if they elicit different systems responses between models, with the most desirable perturbations resulting in model predictions that are most dissimilar from one another. After choosing the set of new perturbations, repeat steps 2 through 4, thereby expanding and refining the model continually, over successive iterations. *The idea is to bring the theoretical predictions and experimental data into close apposition by repeated iterations of this process so that the model predictions reflect biological reality.<sup>D</sup>*

**Box 10.1:** Systems biology method as described in [360]. Italics mine, marked with capitals A-D.



questions we would like to address with it, but nevertheless assumes that a global approach including all genes/mRNAs/proteins is ideal (A+B). The motivation is that this saves the model from a priori biases. This seems noble, perhaps even heroic, but at step one of this method, there is already a strong bias introduced, as it appears that – even before reaching step 1 of this method – an implicit decision has already been made about the kind of model to use. The proposed measurements (A) destroy all spatial information of individual samples and it seems that correspondingly space is deemed irrelevant in the model. Such a choice would definitely affect the model's behaviour.

Even at the single cell level, this can have a dramatic impact. For example, there is no way of understanding the positioning of the division wall in fission yeast as in [372] using a non-spatial model, yet without this system cell division (and thus culture growth) is heavily impaired, if not impossible (80% of the cells arrested in a failed attempt at cell division in a temperature sensitive *mid1* mutant [373]). In more general terms: there is a trade-off between the number of components one can include in a model and the “realism” with which each component can be modelled. This holds for spatial resolution, but also the kind of equations that can be used. Essential properties of the system may be lost by choosing for example a linear ODE system because of tractability (as is used in flux balance analysis [368]) rather than implementing the well established Michaelis-Menten kinetics for enzymatic reactions, resulting in “unnatural” behaviour [374]<sup>viii</sup>.

Another possible issue with including all components becomes clear when considering step 3. The authors suggest that different models or model variants should be compared by maximizing a goodness-of-fit measure (C). Parameter fitting, however, is regularly called an art or even (black) magic. For one thing, there is the risk of overfitting the model to noise in the data, particularly if the number of parameters is large relative to the available constraints. Every realistic experiment involves some degree of uncertainty on every measured value. Some variables may fluctuate a lot due to intrinsic noise, or processes unrelated to the one being studied, such as circadian fluctuations. These potentially distract from the information of actual interest in the experiment. The more “irrelevant” variables are fitted along with the pathway of interest, the more the evaluation criterion will be dominated by reducing the differences between experimental and model values for variables that do not matter. Recall the advice against a priori assumptions (A), which implies no a priori knowledge about which variables matter most, or how to weight the fitting errors on individual parameters to obtain a single goodness-of-fit measure.

Depending on the kind of model used, the fitting procedure may be further complicated if the model parameters are not all independent. The model behaviour may, for example, depend on the ratio of two parameters rather than the value of one of the two in isolation, as illustrated by the example in box 10.2. If we were to fit that model to some data, the value of parameters  $\beta$  and  $N_0$  would seem unconstrained, perhaps making us conclude that their precise values do not matter. In this particular case, it is still relatively easy to discover from the formula of the full time dependent solution  $R(t)$  that the ratio of these two parameters matters, but what if the model had several orders of magnitude

<sup>viii</sup> “As long as rates are the only concern, no feedback loop is needed, but it becomes absolutely necessary when one recognizes that metabolite concentrations need to be taken into account as well: without feedback inhibition (and other classical regulatory mechanisms), flux control would be achieved at the expense of huge uncontrolled variations in the concentrations of intermediates (Cornish-Bowden and Cárdenas 2001b); these would normally be very harmful, even lethal, to the organism, and explain why suppressing regulatory mechanisms is not normally a useful way of achieving biotechnological aims.” [374]

more variables and parameters and the functional relationships between subsets of parameters giving the same behaviour were more involved? What would be the probability, for example, of discovering control parameter  $G$  (equation 7.1) from comparing experiments measuring behaviour of the cortical array under different experimental conditions and in different mutants to simulations with different parameter sets?

All this illustrates why more data does not necessarily lead to more understanding. The same is beautifully illustrated by Thomas Pynchon in “The crying of lot 49” [375]. Contrary to a classical detective story, on the last page the pieces of the puzzle do not all fit together in a grand unified theory of the truth. Instead, the discovery of additional clues causes ever greater confusion to main character Oedipa Maas. This, of course, is a work of fiction. Could it be of any relevance for scientific reality? A thought experiment:

Envision a far future, with a perfect scientific literature – highly accurate measurements of every quantity, under every relevant condition we could think of, cured from all mistakes ever made in the past – summarized in computational models that correctly predict every conceivable input-output relationship. Could we then say that we understand the biological systems?

If we accept the “criterion for the intelligibility of theories” (CIT) by De Regt and Dieks [376]:

*“CIT: A scientific theory  $T$  is intelligible for scientists (in context  $C$ ) if they can recognise qualitatively characteristic consequences of  $T$  without per-<sup>ix</sup>forming exact calculations.*

as a definition of scientific understanding, the only possible answer is: “No”. We might have to accept that we would have simply replaced one black box by another, albeit no longer necessarily constrained by the basic laws of physics.<sup>x</sup>

Meant as a general method, the description in box 10.1 naturally did not mention a particular biological question, or a reason for building such kind of a model. The applications the author had in mind only surface in the last sentence (D): to build a reliable *in silico* replica of the exact experimental system used to create it. If the resulting model is to be used as a (partial) replacement of expensive or undesirable experiments in drug development, for example, this seems indeed a desirable end product. In that case correct predictions are all valuable and understanding is of much less importance. But how often is that the case?

Recently, a very impressive virtual cell model was published combining different processes and modelling approaches [370]. This model accounted for every gene and protein of *Mycoplasma genitalium*, a bacterium known for its very small genome of only 525 genes, compared to over 4000 genes of *E. coli*. The authors made use of over 900 published data sources and the resulting model has more than 1900 parameters. With this model, called “first draft” by the authors, they were able to correctly predict if a gene was essential to sustain growth and cell division for 79% of all genes. Most of the other model results are also reported in terms of mass statistics, scatter plots and cartoons. The

<sup>ix</sup> “If one wants to apply our analysis to non-mathematical, qualitative theories, we suggest to replace ‘exact calculation’ by ‘complete logical argumentation’. Intelligibility of such theories then implies the ability to recognise consequences without following all the steps the ‘formalism’ of the theory requires.” [376]”

<sup>x</sup> Compliance with the basic laws of physics, of course, would be more relevant if the models were slightly less than perfect.

Auxin production may be measured by incubating plants for some time with heavy water and comparing the ratios of labeled and unlabeled auxin using mass spectroscopy (e.g. [75]). In an attempt to write down the simplest possible model for the production of labelled and unlabelled auxin, we assume that the plant is a structureless, well mixed bag of constant size, without any regulation on the production and no changes of the parameters over time.

We assume that auxin is produced with constant rate  $\beta$ , of which a fraction  $f \in (0, 1]$  is labelled ( $L$ ) and the remaining fraction non-labelled ( $N$ ). Degradation occurs with rate  $\delta$ , which is the same for both labelled and unlabelled auxin. This results in the following system of two differential equations:

$$\frac{d}{dt}L(t) = f\beta - \delta L(t) \quad (10.1)$$

$$\frac{d}{dt}N(t) = (1-f)\beta - \delta N(t) \quad (10.2)$$

Assuming that no labelled auxin is present at the beginning of the experiment ( $L(0) = 0$ ) and the amount of non-labelled auxin is known ( $N(0) = N_0$ ), this system has the following solution:

$$L(t) = \frac{f\beta}{\delta} \left(1 - e^{-\delta t}\right) \quad (10.3)$$

$$N(t) = \frac{(1-f)\beta}{\delta} \left(1 - e^{-\delta t} \left(1 - \frac{N_0\delta}{(1-f)\beta}\right)\right) \quad (10.4)$$

Define  $R(t) = L(t)/N(t)$  as the ratio measured in the experiments.

$$R(t) = \frac{f}{1-f} \left( \frac{1 - e^{-\delta t}}{1 - e^{-\delta t} \left(1 - \frac{N_0\delta}{(1-f)\beta}\right)} \right) \quad (10.5)$$

$$\frac{d}{dt}R(t) = \frac{N(t)\frac{d}{dt}L(t) - L(t)\frac{d}{dt}N(t)}{N(t)^2} = \frac{N(t)f\beta - L(t)(1-f)\beta}{N(t)^2} \quad (10.6)$$

$$= \frac{f\beta e^{-\delta t} N_0}{\left(\frac{(1-f)\beta}{\delta} \left(1 - e^{-\delta t} \left(1 - \frac{N_0\delta}{(1-f)\beta}\right)\right)\right)^2} \quad (10.7)$$

This function has four parameters:  $f$ ,  $\delta$ ,  $\beta$  and  $N_0$ . All solutions tend to the same asymptotic value of  $R = \frac{f}{1-f}$ , independent of the other parameters. How fast this value is reached, however, does depend on all parameters. In the beginning ( $t$  close to 0), the solutions follow

$$R(\text{early}) \approx \frac{f\beta e^{\delta t}}{\delta} \quad (10.8)$$

and **two solutions  $R_1(t)$  and  $R_2(t)$  are identical if and only if  $f_1 = f_2$ ,  $\delta_1 = \delta_2$ ,  $\beta_1/N_{0,1} = \beta_2/N_{0,2}$ .**

**Box 10.2: Example of parameter dependencies that may complicate curve fitting.** A very simple model of auxin production measurements.

authors end with three examples of discoveries at the level of individual genes that resulted from resolving discrepancies between model predictions and experimental results (on gene essentiality). From this they conclude that “[t]hese results support the assertion that large-scale modeling can be used to guide biological discovery.”

They have examples to support their claim, yes, but let’s return once more to the thought experiment. How far in the future would it be that our measurements could be considered “complete”? Is it conceivable at all, given that new discoveries typically result in more rather than fewer open questions?

The systems biology cycle as depicted always lacks an exit condition. The exit condition is also never mentioned in stereotypical systems biology talks. Nevertheless, scientists do move on to new topics at some point, either using the existing model as a building block, or moving to something independent. This makes me wonder if the lack of exit condition means in practice: repeat *ad nauseam*, or until the money runs out? Consider the following words by Herbert A. Simon<sup>xi</sup>: “An ant, viewed as a behaving system, is quite simple. The apparent complexity of its behavior over time is largely a reflection of the complexity of the environment in which it finds itself.” and the even more quoted variant: “Human beings, viewed as behaving systems, are quite simple. The apparent complexity of our behavior over time is largely a reflection of the complexity of the environment in which we find ourselves.” The former version is accepted by most people without problems, but depending on their background they may feel somewhat offended by the latter. If we take the description of a human as a behavioural system for granted, the importance of an exit condition becomes apparent. Without it, the behavioural system would simply keep iterating the same cycle, with the same type of experiment and model of it, continually refining the model. The crude, and perhaps cynical, way out is often paraphrased as: “Science advances one funeral at a time” (Max Planck).<sup>xii</sup> Compared to funerals, exhaustion of (financial) resources may be a more humane and faster driver of scientific progress, although this mechanism does cause some collateral damage by the premature termination of valuable projects.

### 10.2.3 Beyond the stereotype

The first years of systems biology might be characterized by a great optimism and the availability of lots of money. Judging from figure 10.1C, though, the chances of getting money by simply calling something “systems biology” seem to be declining.

The stereotypical systems biology and its great promises – ambitious, optimistic, but naive – probably have helped to attract a lot of money to biological research integrating “wet” and “dry” experiments. The people in charge of this money, however, slowly seem to become aware that these promises might not be met that soon. It may be wise to compare the current situation to the human genome project. When the first drafts were published, there was a lot of skepticism about the use of these long lists of As, Cs, Ts and Gs. I think it is safe to say that nowadays no scientist doubts the many benefits brought

<sup>xi</sup> 1978 Winner of the Nobel prize in economics.

<sup>xii</sup> A common paraphrased version of Max Planck’s original words: “Eine neue wissenschaftliche Wahrheit pflegt sich nicht in der Weise durchzusetzen, daß ihre Gegner überzeugt werden und sich als belehrt erklären, sondern vielmehr dadurch, daß ihre Gegner allmählich aussterben und daß die heranwachsende Generation von vornherein mit der Wahrheit vertraut gemacht ist.”

about by the human genome project. These include technological advances, new research tools and evolutionary understanding, to name a few. Many of this happened because the effort was broadened to include other species very early on, which greatly helped for making sense of the sequence data and also for decreasing the costs of sequencing itself. One of the main promises, however, that we would soon know the genetic causes of a great number of diseases, is still not met and will not be met in the near future. If this is what the public remembers, it will backfire on public support for funding further scientific research.<sup>xiii</sup>

There is a lot of research funded in the name of systems biology that is very far from the stereotype I described and does not suffer from the same naivety either. Many researchers have made different choices on the number of components to study simultaneously and the features to incorporate, such as spatial structures or non-linear interactions. When it comes to valuable results, the lack of a consensus definition for systems biology – or rather, the diversity of approaches already taken to integrate models and experiments – will most likely be a great benefit. In this light the past decade can be seen a broad collective exploration, discovering more and less successful approaches.

Modern disciplines of biology such as bioinformatics and systems biology are often coined as the future of biology. The current education of the people who like to contribute to these fields, however, is in a way absurd: students (e.g. in the Netherlands) desiring a career in such fields typically have to choose between biology on the one hand, or physics/mathematics/computer science on the other hand and the few who like to learn a lot from both sides have to overcome an increasing number of bureaucratic and financial hurdles. In this light the popularity of the word “systems biology” may have yet another advantage: it probably contributed to the realization that the biology education of the future, that delivers students that are able to understand their own field, simply requires a much stronger basis in mathematics, computer science and related subjects [378]<sup>xiv</sup>. This may be an unwelcome message in a system with a strong financial stimuli towards degrees without delay, but the change will come in the end<sup>xv</sup>. Bioinformatics tools have already established themselves in many labs for molecular biology, genetics, etc. In the end, there will be hardly any leading edge biology left for those who fear mathematics. I think that already now the students who seriously want to contribute to modern biology

<sup>xiii</sup> Paul Noble in an editorial: “As Paul Nurse (15) says, ‘our past successes have led us to underestimate the complexity of living organisms.’ Proponents of the systems approach should not make the same public-relations mistake. I prefer to shock people in the opposite way by saying that it might even take centuries to achieve the aims! The second is that, although the task may appear to be ‘mission impossible’, it is also ‘mission imperative’ in the sense that we cannot make complexity disappear merely by saying that the task is impossible. The history of science is littered with incorrect claims to impossibility. Faced with complexity, there is no choice but to try to unravel it.” [377].

<sup>xiv</sup> “It is not enough for physicists to come into biology and bring their quantitative and analytical skills. Quantitative skills must be a fundamental part of the training of all biologists. No longer can biology be the refuge of those (like myself) who were no good at mathematics.” [378]

<sup>xv</sup> This confidence is based on the assumption that there are sufficient incentives to have the proper education. It is not merely important to interdisciplinary research in academia, but also essential to keep – for example – leading biotech companies in this country. They will disappear if it is impossible to find enough good people for their more demanding positions. Needless to say that the economic impact of such a trend would be far bigger than the costs of (in practice) somewhat longer educational programs. Unfortunately, the precise costs are impossible to calculate exactly (even in retrospect), so typically politicians (etc) tend to treat the quality of higher education and the strength of a knowledge based economy as independent. I am afraid that here a change is needed.

(having both the capacities and the motivation) will welcome an adequate education.

### 10.3 Comparing different scenarios – uses and limitations of this method

The work in this thesis certainly does not qualify as stereotypical systems biology as described in the previous section – the total number of variables in the whole thesis is easily dwarfed by a single stereotypical study – but that *by itself* does not make it any more useful. At this point it would be only fair to take a step back and critically review our own approaches. For this I will focus on the approach of comparing different scenarios, taken very explicitly in chapter 4 and more implicitly in a number of other places.

In chapter 4 we used models to compare different scenarios for local auxin accumulation in the context of nodule primordium formation. The use of models allows for a much more rigorous assessment of the different scenarios than intuition alone, strongly increasing our discriminating power. Moreover, if evaluation of the model is cheaper and/or faster than performing an experiment, it can help focus on the most promising hypotheses and measurements that will most likely be helpful. Potentially, this seems a powerful approach, but under what conditions could it really be so?

To answer that question, we will dissect the approach into several steps. In general terms it can be described as follows:

1. generate a list of hypotheses that intuitively seem able to produce the observed phenomena
2. translate the hypotheses to explicit scenarios, preferably implemented in the same model framework
3. discard scenarios that are unable to yield the experimentally observed phenomena
4. to discriminate among remaining scenarios, use the models to find conditions or new kinds of measurements for which the predicted differences are large(st)
5. repeat until one scenario remains

To answer our question, we have to understand what it means when we complete step 5. Strictly speaking, we can only conclude that of the *scenarios* tested, scenario X is best able to generate the phenomena under study. To translate this to the conclusion that corresponding hypothesis Y matches what happens in the system, we would make some implicit assumptions.

First of all, we would assume that the initial list of hypotheses is exhaustive. When considering all possible details (that is, by equating hypotheses and scenarios), it can never be the case. This philosophical problem won't stop real life scientists from putting more trust in a hypothesis that beats a long list of alternatives. Inevitably, there is a risk that this increased trust is based on a false dichotomy: the "winning" hypothesis was only

compared to alternatives that could not work in the first place (e.g. see [379]<sup>xvi</sup>). From this it becomes obvious that the approach of scenario comparison only makes sense if multiple serious hypotheses/scenarios exist.

The second assumption would be that no hypothesis was discarded unjustly. Translating a hypothesis to a scenario for the modelling step requires us to make all assumptions very explicit, as otherwise the scenario is impossible to implement. There must be a value for each and every parameter, a mathematical function for each (sub)process and, most importantly, a long list of things to ignore for the sake of tractability, for example natural variation, space (whether the third dimension or space in general), (certain) time scales and/or numerous intermediate components. Consequently, there are most likely so many ways to translate a hypothesis to a scenario, that it would be theoretically impossible to try them all before deciding that a scenario is discarded. Again, scientists are sufficiently pragmatic to increase their understanding of the world without obtaining absolute certainty, but this does imply that a certain rigorousness is required to obtain results of any significance. The smaller the number of different hypotheses, the easier this can be achieved.

In summary, the approach of testing different scenarios could be most useful and conclusive if there is a natural way of (apparently) exhausting the “space” of possibly sensible hypotheses: apparently plausible alternatives exist, but their number is sufficiently small and they yield obvious differences that can be translated to experimental observations.

### 10.3.1 Case study: On determinate and indeterminate nodules

As discussed in chapter 4, different legumes produce anatomically different root nodules. The model legume *Medicago* produces indeterminate nodules, which maintain a meristem for the entire nodule life span, which results in a zoned nodule structure, with from tip to base a meristem, invasion, fixation and – when old enough – senescence zone. This results in elongated nodule morphology. Another model legume, *Lotus*, on the other hand, produces determinate nodules. Their meristem terminates during nodulation and nodules remain spherical structures, with senescence starting at their core [28]. The differences between these two nodule types comprise more than the persistence or termination of the nodule meristem. A from our perspective very interesting difference is that *Medicago* nodules originate from the inner cortex, endodermis and pericycle [27], whereas *Lotus* nodules originate from the middle cortex [28]. Neither determinate or indeterminate nodule type define a monophyletic group [251, 252], suggesting that the mechanism underlying the determination of nodule type is something that is easy to vary on evolutionary time scales. Additionally it has to be root autonomous, as grafting experiments show that the shoot does not affect the nodule type formed [253]. In this light we investigated the impact of an inward/outward/neutral bias in cortical PIN distribution on the

<sup>xvi</sup>The authors compare two modes for senescence in hypotrichous ciliates. These ciliates have very high chromosome copy numbers in their (macro)nuclei. The authors aim to assess whether copy number imbalance could cause senescence and clonal death in lab cultures. They use a model of macronuclear division that consists of exact duplication of all chromosomes present, followed by random redistribution of the chromosomes over daughter cells. They compare two scenarios: (I) if at least a single copy of each chromosome is inherited, original copy numbers are restored and (II) no regulation of copy numbers. Senescence is assumed as soon as any chromosome is missing in the propagated cell line (1 cell). A simple back of the envelope calculation would have been sufficient to show senescence is a very rare event in scenario I, making it hard to claim that scenario II is tested against anything but itself.

position of the auxin maximum resulting from homogeneous reduction of the effective efflux permeability (figure 4.4).

Based on these simulations, an inward bias seems to fit more with indeterminate nodules and an outward or no bias with determinate nodules. It would be very premature (and possibly wrong), however, to conclude that this really is the difference determining between the two nodule types based on these scenarios alone. The differential response to the epidermal (“cytokinin”) signal in both backgrounds (figure 6.1) in line with the first observation is consistent with this and thus may increase confidence, but that does not change the fact that several other plausible scenarios are still unexplored. It is, of course, conceivable to compare different legumes and see if this hypothetical difference indeed discriminates between determinate and indeterminate nodule types. That, however, would require a lot of work, not even considering technical challenges. Moreover, there are other possibilities that could potentially yield similar differences. Other differences than the distribution of PIN proteins could cause differences in the available auxin supply, such as ABCB auxin efflux carriers [60, 61], or differences in the pattern of symplastic permeabilities (see also chapter 6). Moreover, the sensitivity to the epidermal signal might be different, for example because of differences in the distribution of (cytokinin) receptors, or general differences in auxin sensitivity (chapter 6). Given the current state of experimental and theoretical possibilities, it would probably be more fruitful to test several more hypotheses *in silico* first, before setting up particular experiments.

It would be interesting, though ambitious, to extent the question of what determines nodule type and morphology to other less common model legumes, to allow for differentiation between specific differences between *Lotus* and *Medicago* and more general trends. For example, the root nodules of the tropical legume *Sesbania rostrata* originate predominantly from the middle cortex<sup>xvii</sup> and developmentally are said to seem “intermediate between indeterminate and determinate types”: the meristem terminates, but is maintained markedly longer than in determinate (*Lotus*-like) nodules and fixation starts before the nodule has matured [380]. This might not be the easiest organism to work on, though, as the invasion may either occur via root hairs or intercellularly via crack entry, depending on environmental conditions (in an ethylene dependent way) [381]. Please note that I have chosen *Sesbania* as a first, not necessarily the most fruitful suggestion of how a broad knowledge of biodiversity can increase our general understanding, even of a particular model organism.

Another application of comparing scenarios is to obtain a larger mechanistic understanding of different possible mechanisms rather than determining the single “true” one, which was a key aim in chapter 5 and is also illustrated by the following case study.

### 10.3.2 Case study: Different scenarios for cortical microtubule (re)orientation

In chapter 9 we have considered one mechanism for the (re)orientation of the cortical microtubule array: differential penalties for crossing the cell’s edges. These penalties were implemented by different probabilities of growing microtubules undergoing an induced catastrophe when arriving at an edge. These probabilities reflected assumptions on the sharpness (local curvature) of the edge and the presence or absence of crossing assistance by CLASP proteins. In a crude way we used the same mechanism for enforcing a



transverse orientation of the steady state array in chapter 8: we had set the catastrophe probability of the cylinders edges to 1, that is: no crossing. This effectively separates the caps from the rest of the cell surface and therefore we dropped them altogether from the simulations.

Differences in edge crossing probabilities, however, is not the only conceivable mechanism for array orientation. Currently, several mechanisms circulate in the community<sup>xviii</sup>. Other mechanisms are differences in the microtubule dynamic instability parameters on different faces of the cell and different nucleation rates for the different faces, possibly in combination with differences in dynamic instability parameters. Both these mechanisms would result in different values of control parameter  $G$  on different cell faces and are therefore likely to work most reliably (require the smallest bias) in a regime close to the critical value  $G^*$ : in that case a small decrease of  $G$  could result in some faces that do ( $G > G^*$ ) and some that do not ( $G < G^*$ ) allow for spontaneous alignment.

For all three proposed mechanisms for array (re)orientation, some simulations exist that show that at least in some regime they can orient the array. At the same time, it is to be expected that the different mechanisms will not behave the same in every aspect. For example, an array established in the most favourable orientation given the edge penalties, will remain affected by the (mild) penalties belonging to that direction (see discussion in 9.3.2). This will not be the case if the array is oriented by less favourable dynamics on two faces: once these faces are avoided, the array density can increase as if there were no extra penalties in the system.

What is missing is a consistent comparison of these different scenarios, addressing questions such as the (relative) time scales of (re)orientation and how the reliability of the mechanism depends on cell size and aspect ratio (for different  $G$  and  $l_0$ ). The primary aim of such a study would not be to find the one “winning” scenario – as there is no biological necessity that the same mechanism controls array orientation in all cases – but to provide a valuable resource of mechanistic understanding to the community.

## 10.4 The warders of our prison of space and time

A recurring theme in this thesis is that the mechanisms described are effective only on a limited range of length and time scales. This theme is so very common in biology and physics, that it would go too far to review the many ways that life is enslaved by space and time. The reason is simple: the space and time that could possibly be dedicated to the reviewing process are strongly restricted themselves<sup>xix</sup>.

### 10.4.1 Numbers

Think of the last glass of water you drank: thin and watery to us, yet highly viscous from the perspective of the microorganisms living in it while you drank it. Now think of the Gierer-Meinhardt model we varied upon in chapter 2. This model can produce patterns with a characteristic length scale in the micrometer range, but just as easily at the kilometer, femtometer, or terameter scale. We could go far beyond the yocto ( $10^{-24}$ )

<sup>xix</sup>Disregarding thesis deadlines: a human life would be equally insufficient.

and yotta ( $10^{24}$ ), the current boundaries of our naming scheme<sup>xx</sup>, and the mechanism would work just as fine by a simple rescaling of the parameters. The same holds for the mean field theory we used in part III for describing the transition between the isotropic and aligned state: no matter how the length scales of the microtubules are changed, the transition is predicted at the same value  $G$ . The simulations in figure 9.4 show that this only holds for local, not global alignment. The mean field theory does not include this spatial dimension, so can say nothing about it. But even with our microtubule simulations it would be possible to “teleport” the same behaviour to a km or fm scale by consistently replacing  $\mu\text{m}$  with km or fm. For our model it does not matter that a km is about  $10^9$  times the persistence length of a microtubule, or that a fm is less than millionth of the size of a single tubulin subunit, because we model microtubules as (series of) *straight line segments*. This gets to the heart of the problem: a line segment is a *continuous* object *without thickness*.

To illustrate the implications of this observation, consider something very simple: a line segment  $\mathcal{L}$  of length  $l > 0$ . We shall consider it as a convex subset of the infinite line of real numbers, or more precisely:  $\mathcal{L} \subset \mathbb{R} = \{x | x \in [0, l]\}$ . **Claim:** the number of points on this line segment is independent of its length  $l$ . This is counterintuitive and perhaps hard to grasp for non-mathematicians, but very easy to prove. Consider a second line  $\mathcal{L}'$  of any arbitrary length  $l' > 0$  defined in the same way. There is a very simple 1-to-1 map from any point  $x$  on  $\mathcal{L}$  to a unique point  $y$  on  $\mathcal{L}'$ : multiply  $x$  by  $l'/l$  for the forward step and  $y$  by  $l/l'$  for the inverse. As this holds for *all* points on  $\mathcal{L}$  and thus for all points on  $\mathcal{L}'$ , the number of points on them is exactly the same  $\square$ .

Simple, isn't it? Then why is it so counterintuitive? To many of us, a line is something one can draw on a piece of paper, something *with* a certain thickness and, if we were to zoom in far enough, something consisting of a precise number of molecules of ink. The same holds a microtubule: approximately 25 nm in diameter and at any particular moment in time consisting of a discrete number of building blocks, whether accounted as tubulin subunits, atoms, or quarks. Everything is at some level build up of discrete particles and this number of particles is more than trivial property of the system. A continuum description may often be very close to reality if numbers are sufficiently large, but when numbers get fewer, systems may show fundamentally different behaviour because of their discreteness.

In a classical example, a residual density of one rabies infected atto-fox per square kilometer would cause recurring waves of the disease upon a single introduction, whereas a discrete model would predict that the disease would disappear after an initial wave upon introduction [382]. The key difference is that the – deterministic – partial differential equation model would never reach a true zero “concentration” of infected individuals. Another process strongly affected by the noise arising from small copy numbers is gene expression, with often but tens of copies of a particular transcription factor, having to find the right spots in a spatial environment [383]. Though often seen as detrimental in terms of information conservation, noise can also create heterogeneities in a clonal population, increasing the chance that at least some individuals will survive an unfavourable change of the environment [384]. Discreteness can also be exploited in astonishing ways using for example a “Brownian ratchet” to bias to movement of molecules or even large objects, such as the entropic *sorting* of particles of different size [385], weight carried forward by a

<sup>xx</sup>Officially introduced no earlier than 1991.

string of beads on a vibrating plate [386], or, back to biology, foxtails (the spikes/spikelets of grass such as *Hordeum murinum*) that because of their surface structure move unidirectionally when, for example, deposited in the collar of another kid (hence the Dutch name “Kruipertje”, literally translated into “crawler”).

In parts I and II we have used continuum models throughout. In chapter 6 we mentioned the trade-off between gradient steepness and molecule number available for sensing positional information, as also discussed by [158]. Along the same lines, it would be worth asking what is a reasonable (relative) concentration difference over an auxin gradient (chapter 2, figures 2.7, 2.10, 2.8 and 2.11). Detailed mass spectroscopy measurements yielded an IAA concentration in the order of  $50\mu\text{M}$  in the QC (the location of the root tip auxin maximum) of 8 day old *Arabidopsis* seedlings [77]. To put this in perspective: a concentration of  $0.06\text{ nM}$  is equivalent to an average of 1 auxin molecule per  $10 \times 10 \times 10\mu\text{m}^3$  cell, likely too little for reliable signaling. This would leave perhaps a  $10^4$  meaningful relative range. In practise this range might not be fully exploited, given that many concentrations for whole root and stem segments are in the range of  $10^{-7}\text{M}$  [246, 387]<sup>xxi</sup> or more [76], leaving an exploited range of  $10^2 - 10^3$ .

Our consideration of symplastic transport through individual plasmodesmata (chapter 3 could well be affected by finite size/number effects, given the small size of plasmodesmata. In this light it is interesting to note that the measured translational diffusion coefficients for free GFP in different organisms increase with cell size from  $8\text{--}9\mu\text{m}^2/\text{s}$  in *E. coli* [389, 390] via  $20\mu\text{m}^2/\text{s}$  in PTK2 cell lines of *Potorous tridactylis* (rat kangaroo) [391] to  $40\text{--}50\mu\text{m}^2/\text{s}$  in plant cells (cowpea protoplasts and tobacco BY-2 [392] and tobacco leaf cells [393]), the latter approaching the water value of  $90\mu\text{m}^2/\text{s}$  [392, 394]. Given the close match between our calculations and experimentally measured effective wall permeabilities without assuming a reduced diffusion constant inside the plasmodesmata (chapter 3), it is highly unlikely that this trend can be, or has to be, extrapolated to the inner volume of plasmodesmata (at least not for fluorescein).

In the light of exotic finite size effects it seems tempting to investigate if the very asymmetrical structure of plasmodesmata in some tissues, i.e. a single channel in one side and (highly) branched on the other in the other half of the wall (e.g. see [395]), could function as a passive Brownian ratchet too, thus providing “free” directionality to the transport of molecules of particular sizes. For many molecule sizes, however, this would require a much finer surface structure, which would have to be built completely from proteins coating the desmotubule and/or plasma membrane, as the membrane itself is far too stiff at the relevant length scales. All in all, this seems highly unlikely.

## 10.4.2 Scaling laws

An entirely different reason why many mechanisms function only for a limited range of length scales is that at least some of their properties do not scale linearly with system size or distance. This is an important reason why symplastic transport of the kind investigated

<sup>xxi</sup> 1cm of *Medicago truncatula* root 24h after inoculation with *Rhizobium* ( $0.3\mu\text{M}$ ) or control ( $0.4\mu\text{M}$ ), i.e. differentiated root tissue [246];  $0.1\mu\text{M}$  in stems young of *Arabidopsis* plants, 2 days after decapitation and removal of lateral organs [387]. Lower IAA concentrations were reported in old measurements of phloem and xylem sap (the latter of root origin):  $0.023\mu\text{M}$  and  $0.019\mu\text{M}$  respectively and  $0.06\mu\text{M}$  in bark of *Ricinus communis* [388].

in part I is only suitable for local transport: as it behaves similar to ordinary diffusion, the time required to travel a certain distance  $L$  scales quadratic with  $L$ .

As the plants get larger, a directional system for the transport of signals and metabolites becomes essential. The measured values reported for the linear velocity of a pulse of (labeled) auxin are in the order of 1 cm/h. If these are the same for mature trees, it may take a few days for a signal from the top of tree to reach the roots, but if it were traveling by pure diffusion, it probably wouldn't arrive in time to confer a relevant message.

[153] measured linear velocities of 90 - 140 cm/h for the phloem sap in plant stems and 580 - 1800 cm/h for the corresponding xylem sap (these values are much slower in small organs, such as petioles or seedling stems [154]). This may seem slow in comparison with humans – our total blood volume is circulated approximately every minute –, but is sufficient for a plant's much lower metabolic demand.

Plants and animals both use gradients for conferring positional gradients. What mechanisms are suitable, however, strongly depends on the length of the required gradient.

### 10.4.3 Case study: Different mechanisms (and models) for auxin gradients in the plant root

Gradients play a role in many developmental processes, as they are means of communicating positional information. There are different mechanisms that can form a gradient. That it is not trivial to determine the mechanism actually responsible for a particular gradient is nicely illustrated by the bicoid gradient in *Drosophila*. This gradient is the initial source of anterior-posterior positional information and originates from maternal mRNA deposited at the anterior end of the embryo [155–157]. Gradient formation takes place in early stages of *Drosophila* development, before individual nuclei are surrounded by their own cell membrane. This morphogen gradient has received much attention from modelers and has long been modelled as a simple diffusion process in a homogeneous medium (e.g. [158, 159]). This has then been replaced by a model based on mRNA transport, with the bicoid gradient as a direct readout of the mRNA gradient [160, 161], which was disputed again by more precise measurements of the mRNA gradient, which restored the need for bicoid diffusion, or another form of bicoid transport [162] *et cetera*...

Similarly, different models have been proposed for the auxin gradient found in roots (nicely compared in [171]). They compare three mechanisms for gradient formation in an (approximately) linear tissue reminiscent of the *Arabidopsis* root: a source-decay model (with a source at the maximum of the gradient), a linear transport model (comparable to early 1D models of auxin transport [84, 85]) and a reflux loop [91]. In chapter 2 we have also considered the impact of symplastic transport on these gradient formation mechanisms<sup>xxii</sup>

We found that symplastic transport alters the length and steepness of a gradient in a linear transport model (figures 2.7, 2.10), but does not destroy the potential to form ascending gradients in a simple 1D model (for realistic parameters). The reflux loop seemed even more resistant to symplastic transport, particularly in the longitudinal direction. In the latter case the total concentration decreased, but other characteristics of the gradient were surprisingly little affected, including the time scales of building up the gradient. These findings could relieve a concern in the community that symplastic transport could be detrimental to the efficiency of polar auxin transport (particularly with long cells) [163].

In the linear transport model, the profile can be changed in a similar way with an apoplastic rather than symplastic backflux. In this, a symplastic backflux is adaptive over time (relatively lower while the gradient is established) and only maximal in the final bit of the ascending part of the gradient, whereas an apoplastic backflux is always a static and fixed fraction of the forward flux (figure 2.7G,H). The consequence of this difference is that a symplastic backflux outperforms an apoplastic backflux on optimizing both the length of the gradient and total relative increase of the concentration over this gradient (figures 2.7F, 2.10). The difference is rather small for long cells and high forward transport, but increases with shorter cells or a lower effective efflux permeability for the forward transport. The speed of forming a gradient differed correspondingly (figure 2.7I,J). The similarity between these two processes is perhaps best described as a matter of choice: in potential they can result in similar combinations of gradient length and gradient steepness, reached on similar time scales (specially for long cells and high forward transport). Depending on the parameters, however, a large part of this potential (towards longer, but shallow gradients) will be unavailable using symplastic backflux, because it would require symplastic permeabilities larger than resulting from free diffusion over the thickness of the wall.

Looking at the (numerical) steady state solutions of the 1D models with apoplastic and symplastic backflux and the reflux loop as in [91] (concentration measured in one cell file), the solutions look remarkably similar. All three seem to be the sum of two exponentials. This suggests that it should be possible to map the reflux loop to a much simpler 1D model with a single vascular and cortical compartment per “cell”. For the fairest and most comprehensible comparison, this should be in a system with uniform cell length and PIN distributions in the whole root, except for a root cap with redistributing function that joins the vascular and cortical counterfluxes.

With such a mapping, the three mechanisms could be ranked as follows in terms of steady state desirabilities (long but steep) and time scales of gradient establishment (keeping other model parameters constant as much as possible). A linear transport model with apoplastic backflux would perform worst, because the ratio of forward/backward fluxes per interface is fixed over space (position in the “tissue”) and time. This would be followed by the symplastic backflux, which has the same ratio forward/backward only towards the end of the gradient and in the steady state. During gradient establishment and always at some distance from the end the ratio of forward/backward flux is larger. As a result more auxin is available for the total gradient and it is established faster. The reflux loop would perform best, because with its increased number of parameters it is possible to find a regime with even further decoupled forward and backward fluxes and thus even faster gradient establishment.

This consideration begs the question whether these three really are fundamentally different mechanisms, or just different positions along some scale of variation and decoupling of the forward and backward fluxes? After all, the ratios of total forward and total backward flux over an interface (particularly near the maximum of the gradient) must become similar upon approaching the steady state to obtain similar gradient steepnesses<sup>xxiii</sup>.

## 10.5 What are realistic parameters? – Lessons from cortical microtubule simulations

Why care about the laws of physics, when considering a biological problem? Sure, it makes no sense to explicitly consider the strong and weak nuclear force in our thinking of a biological system at the cellular, tissue or organismal level. Nevertheless, other basic principles, such as conservation of mass or energy, are key concepts in, for example ecology.

The parameter choices made by different groups simulating the cortical microtubule array form a very nice example illustrating the importance of physical constraints in biology. In 2010, two groups independently published simulations of the cortical array [293, 294]. They based their dynamic instability parameters directly on a few sets of published measurements [291, 396] and used these sets throughout their work. The justification for directly using published values is that – given a certain degree of uncertainty on these measured values – taking the measured averages or distributions for individual parameters yields the most realistic parameter choices. Curiously, for some of these parameter sets, the average microtubule lengths do not seem to saturate in the data shown (runs up to 1000 minutes  $\approx$  17 hours). Our choice, on the other hand, has always been to put a joint constraint on all dynamic instability parameters by demanding that control parameter  $G < 0$ . This constraint translates 1-to-1 in the requirement that there is a natural limit on the average microtubule life time and hence length and total density. Parameters with  $G \geq 0$  do not allow for a steady state array, because the microtubule density would simply continue increasing beyond the number of atoms in the universe. Within this constraint we aim for parameters in agreement with experimental observations, taking into account how precisely the different parameter values are known [133, 135, 289, 306]. The choices may be further constrained by considering additional measurements, such as the dynamic increase of the total microtubule length density (e.g. [306]).

The interesting question is: which of these two ways of choosing the parameter values brings us closer to reality? With either approach, not a single individual parameter has a distinctly unrealistic value. The competing models use three rather two states for the microtubule +end, also including a pausing state. It is possible, however, to map this model to our two state model (Bela Mulder, unpublished results). Using this mapping, it turns out that most of their parameter sets are with  $G > 0$ .

How unrealistic is this? The obvious answer is that a parameter set that cannot produce a bound on microtubule density cannot be realistic. Does that imply that the measurements that produced these parameters are wrong? Not necessarily. It only does under the assumption that the dynamic instability parameters are constant over time. These parameters are often measured in early, sparse microtubule arrays, because already in those the systems are so crowded that no one has yet succeeded in producing a reliable automated pipeline for image analysis. Even under “easy” circumstances those analysis typically involve a lot of manual work and therefore the numbers of analyzed microtubules and events are relatively small. The joint parameters have to be sufficiently close to  $G = 0$  to allow for spontaneous alignment, that cumulative errors may easily switch the sign of  $G$ . But even if the numbers are right, it is not physically impossible. As the microtubule density increases, the concentration of free tubulin decreases. This will likely affect the incorporation rate and thus the growth speed, as well as the nucleation rate. Slower growth is likely

to result in on average shorter GTP caps on the +ends, which makes the microtubules less stable (i.e. increasing the castastrophe rate). The rescue rate is probably also affected by the microtubule density, at least by the extreme that rescues are not possible without free tubulin. These joint effects could allow for a system that starts with an empty array and  $G > 0$ , which is naturally driven towards  $G < 0$  as the microtubule density increases.

These changing rates and velocities, of course, are harder to implement than constant parameters. For the moment assuming that the (near) empty system indeed has  $G > 0$ , what would then be the more realistic choice of constant parameters? Using near steady state values ( $G < 0$ ) from the beginning, perhaps with a somewhat slower initial accumulation of microtubule density, or using representative early ( $G > 0$ ) values and refrain from claiming any predictive power over the later stages of the array? The answer, of course, would depend on the – unknown – time scales of approaching the steady state parameters.

As an advocate of the devil, one might ask: “Why care about the steady state; does it make much of a difference for the early stages if no steady state can exist?” Well, probably yes. For this we should focus on different claims made by the different “camps”. Both [293] and [294] claim that (i) zippering alone is sufficient for alignment and (ii) induced catastrophes are not necessary for alignment. We rather claim the opposite: catastrophes alone are sufficient [133, 135] and zippering (without -end treadmilling) has a negative rather than positive effect on alignment [133]. The mechanism of alignment through collision dependent induced castastrophes is dubbed “survival of the aligned”. If the parameters are such that  $G \gg 0$ , the disaligned microtubules undergo somewhat more induced catastrophes than their more aligned counterparts, but still maintain very long life times (all the time obstructing the ones in the majority direction), if bound at all. This way the “weeding out” of microtubules with minority orientations is slowed down, if not impared. This effect may have its strongest impact on the initial symmetry breaking that is essential for spontaneous alignment, as initially the differences between “majority” and “minority” orientations will be nothing but chance fluctuations. The stability of the isotropic state, and thus the average time before symmetry breaking, will be even larger when using low induced catastrophe probabilities ( $P_{cat} = 0.09$  is the smallest value used in [293] and [294] uses  $P_{cat} = 0.30$ ). In those cases, zippering may result in apparent alignment, particularly when an – inappropriate – “entropy” measure is used for the degree of alignment of the array [294] (this “entropy” weights the microtubule density in bins with different angular orientation. As zippering is likely to increase the differences in density per angle bin, this will decrease “entropy”, giving the illusion of alignment even if the dominant angles are not at all similar).

I hope to have illustrated that “realistic” parameter values can not necessarily be judged on the level of individual parameters in isolation. Assessing parameter values on a “population” level, however, does require understanding of the system with some composite parameter(s), typically resulting from rescaling efforts (which is near impossible for overly complex models). This is only possible with a combined analytical and simulation approach.

This consideration also shows two advantages of the real experimental system over any model of it: it naturally makes the correct assumptions for all choices, including those we ourselves would make so implicitly that we are not even aware of them and it always obeys the basic laws of physics and biology. The only thing that might apparently

contradict the latter is a failure in our measurements (e.g. neutrinos that for a few days appeared to be able to travel faster than the speed of light).

## 10.6 Seeing the invisible

“Seeing is believing,” they say. For the majority of phenomena currently studied by biologists, however, our naked eye is insufficient to observe. We could not possibly build a complex understanding of the interesting phenomena if we could not – having put enough effort, for practical purposes – take our measurements for granted. Sometimes, though, it is good to consider again what we really have measured. Even something as straightforward as the size of an object can be far from trivial, when it is either very large or very small. Plasmodesmata, for example, as so small, that the fixation technique used in preparation of the electron microscopy can have a very significant impact on the sizes in the final microscopy sample [190], to a degree that would heavily affect the calculated values for effective wall permeability from such data (as in chapter 3). Measuring the amounts, distributions and properties of individual molecules (hormones, proteins, mRNAs, etc) is typically even more involved and indirect. Despite the difficulties of individual measurements, nature itself has to be consistent. This can be exploited using models in improving our understanding of the thing(s) hardest to measure. In a computational model, for example, we can know exactly where how much of each substance is at any moment in time. This way, a model can be used to predict the whereabouts of something invisible, using as inputs the data on the easier to visualize<sup>xxiv</sup>. The reliability of such a prediction will, off course, depend on the quality of the input data and how much is already known about the system.

### 10.6.1 Case study: Symplastic transport: the rise of the conveniently ignored

The field of symplastic transport is currently still relatively small. Despite the great importance of its regulation for normal development – e.g. the lethality of several regulatory mutations [115–117] –, symplastic transport is by and large ignored in current models of plant development. Our results in chapters 2, 5 and 6, however, show that it can have a significant impact on a variety of developmental processes (although auxin gradient formation in the root, which is based on a reflux loop, was remarkably robust against symplastic backfluxes over transverse walls).

One possibly important reason that symplastic transport is often ignored in such models is that the relevant transport parameters are hard to address with current technology. In chapter 3 we have developed an approach to calculate effective wall permeabilities for symplastic transport from the density, distribution and geometrical dimensions of individual plasmodesmata. With this, a larger amount of data and experimental approaches becomes available to assess effective wall permeabilities – important for assessing how far (and fast) different signaling molecules will travel (see chapter 2) – and allows for a

<sup>xxiv</sup>One review on auxin and computer models has the beautiful title: “Computer simulation: the imaginary friend of auxin transport biology”. [83]



more accurate translation of measurements based on single substances (so far all on fluorescein [163, 168, 169]) to other biologically relevant molecules if additional data on the microscopic level is available.

Symplastic permeability is altered during development [121, 122, 148, 187, 198]. This is one way that proteins that at some stage can move throughout the whole plant (embryo) become restricted in their movement [115, 117, 122, 223]. In a molecule(size) dependent manner this gives rise to so called symplastic domains: groups of cells that are symplastically connected *with respect to the movement of particular molecules*. This is of developmental importance, as it provides a means to isolate markers of a particular developmental “fate” to the respective cells. A beautiful example of what happens when this isolation is impaired is the *chorus (chor)* mutant. This weak allele of callose synthase NN results in larger than usual plasmodesmata opening in the leaf epidermis. As a consequence, stomatal fate markers such as SPEECHLESS move into neighbouring cells, which results in clusters of – normally isolated – stomata [149]. Symplastic domains are also dynamically reorganized in normal development, as is demonstrated by the formation of a new symplastic domain in the process of nodule primordium formation in *Medicago*, that connects the phloem and nodule initials (with respect to GFP) [282].

A very interesting open question is how such significant alterations in symplastic permeability are coordinated, possibly in response to the same signals that they affect. With our conceptual approach at the end of chapter 2 we have taken but a very small step in this exciting direction.

In addition to getting a grasp of something “invisible”, models could also aid in understanding what is actually observed (the example model in box 10.2 was originally set up for this purpose, but merely uncovered that the problem as posed is underconstrained, even with perfect data).

### 10.6.2 Case study: Indirect markers and time series

All plant hormones are small molecules, active in minute concentrations. They are therefore notoriously hard to monitor. A commonly used strategy is to monitor the activity of a hormone using marker promoters that drive either a fluorescent protein (e.g. GFP) with a nuclear localization signal, or the GUS enzyme. These are then visualized in their respective ways. With GUS this implies sacrificing the plant, staining and embedding and sectioning for more precise cytological localization. As the GUS assay always results in a blue color, the interaction of two hormones would have to be studied in different plant lines, with different plants for both for all time points. Besides labour intensive, it may be hard to exactly determine the “developmental time” of each sample. This is, for example, an important issue when dating root nodules/primordia. The time of inoculation (addition of Rhizobia) is only an upper bound to developmental time, particularly with systemic inoculation.

When studying the interaction of different hormones in nodule formation, another timing issue occurs. This can be well illustrated with the hormone pair auxin and strigolactone, another hormone indicated to affect nodulation [397]. For both hormones, promotor-GUS studies are possible, but the markers used are in different relations to the hormone they monitor. The most used marker for strigolactone, D27, is an enzyme involved early in its biosynthesis (the first step in strigolactone synthesis from  $\beta$ -carotene [398]), i.e.

something that is already active before strigolactone is present. DR5, currently the most used auxin marker, is an artificial promoter with an auxin responsive element, i.e. something that is activated in response to auxin signaling (see also 1.4.1). If in an experiment both DR5 and D27 are monitored, for example using promoter::GUS constructs, what does it mean when D27 activity is found first? How much time between the D27 signal and DR5 signal is required to be certain that strigolactone was produced before an increase of the local auxin concentration? Using a model it is possible to derive the signals of the different markers from the computed spatio-temporal distributions of the different hormones. This could be a tremendous aid in the interpretation of the data.

Next to thinking of ways improve the usefulness of a set of markers, it could be useful to reconsider the markers used. For one thing, D27 is a marker of strigolactone biosynthesis, which is not the same as hormone activity. The use as D27 as marker for activity thus depends on the assumption that strigolactone acts locally. Locally applied strigolactone has a direct inhibiting effect on local bud outgrowth [399], but the root to shoot movement of strigolactones through the xylem has also been demonstrated [400]. Recently developed fluorescent strigolactones (e.g. [401]) could help determine the relative importance of local and long distance action. The need for external application, combined with their hormonal activity, however, make them unfit for studying normal (“unperturbed”) development.

On the auxin side, recently a new marker was developed: dII-venus, which is based on the Aux/IAA proteins involved in auxin perception ([81] see also 1.4.1). Unfortunately, this is not a real alternative for studying nodulation. Given the high turnover of the dII-venus proteins, this negative marker of auxin increase requires live (confocal) monitoring, which in roots is limited to the outer  $\approx 50 - 100\mu m$ , that is, up to the center of an *Arabidopsis* root and only the outer few layers in other plants. Besides, for this interaction the switch of the auxin marker would at best decrease the time difference with D27.

## 10.7 Too little of a good thing can be wonderful<sup>xxv</sup>

In my experience, a common conception among biologists, when they first start thinking about the use of models in biology, is that a good model should be realistic, which in their eyes often implies including as many known components as possible (see also highlights A and B in box 10.1 and discussion thereof). Using some “classical” examples, I would like to illustrate not only that this is not the case (as would be a repetition of much of this thesis), but moreover, that “more wrong” can be “more better”, or simply: wonderful.

One such example of a model that became paradigmatic we have encountered in chapter 2: the Gierer-Meinhardt model [167], it in turn being an application of a Turing model [164]. These models are very famous for producing spots and stripes [176, 402]. Not all stripes, however, originate from a Turing instability. This is beautifully illustrated by the stripes of pair rule genes in the *Drosophila* embryo, now known to be regulated all in a different way rather than by a single activator/inhibitor pair (reviewed by [403]). The very right question to ask is how something with such a track record could ever be called “wonderful”<sup>xxvi</sup>?

<sup>xxv</sup> Mae West: “Too much of a good thing can be wonderful.”

<sup>xxvi</sup> Actually, it is not. This line of reasoning, that something that can produce bad results must be bad itself,

The paradigmatic models thank their great value to the universality of the mathematical language that describes them: the model's behaviour is invariant to whether variable  $C$  – to randomly pick one – represents “Cow” (Consumer), “Christian fundamentalist” (non-vaccinated individual), or Cytokinin concentration. The additional value of having a few *simple* paradigmatic models is that a huge body of analytical work can accumulate around each of them. The simpler the model is, the closer this could come an “exhaustive” bifurcation analysis. This way the simple models can tell which generic types of behaviour might be expected from the more complex systems of interest and under what (approximate) conditions. All understanding of the generic behaviours can be translated along, albeit perhaps in a “fuzzy” way if the mapping is imprecise.

Much of this is illustrated by the FitzHugh-Nagumo model [404, 405], originally formulated as a phenomenological simplification of the Hodgkin-Huxley model for neuronal membrane currents [406] and nowadays used as a standard example of an excitable medium [407]. As such<sup>xxvii</sup>, it is very valuable in understanding many different problems, for example the migration of *Dictyostelium* slugs by cells responding to cAMP waves [408], or simple heart models [409, 410]. Other systems that can be understood as excitable media include forest fires, predator-prey systems and disease epidemics.

The mapping to a paradigmatic model does not have to be 1-to-1 on the component level to benefit from the concepts developed for a “classic” (e.g. see [176]). For example, in the shoot apical meristem the modulation of auxin transport (in the continual generation of auxin maxima for phyllotaxis) fulfills the “inhibitor” function, rather than an explicit inhibitor molecule produced from the local auxin maxima [288].

Even though they often do not faithfully recapitulate the biological mechanism underlying the phenomena they are used for, simple models did and do shape our thinking on a conceptual level, for example on what is required for pattern formation. Perhaps the different heuristic rules used in models for dynamic PIN localization serve a similar role: they helped uncover the need of positive feedback to obtain and maintain asymmetrical PIN distribution patterns and primed our thinking to what information a cell actually has to sense fluxes and/or gradients, reviewed below.

### 10.7.1 Case study: On dynamic PIN localization

The polar distribution of PIN proteins has made them a popular object in theoretical and computational studies focusing on auxin. The distribution of these proteins seems to determine where the auxin goes and where it will accumulate (to induce further developmental steps). Interestingly, auxin itself seems to affect the polar distribution of these proteins [411]. The details of the underlying mechanism are still a matter of ongoing debate.

PIN proteins are not delivered to the cell membrane in a once-only manner. The polar distribution of PIN proteins is maintained by regulated exo- and endocytosis of PIN containing membrane vesicles [411, 412].

On a molecular level, the phosphorylation state of PIN proteins seems to determine to what cell face they are recycled [413]. In roots, PIN1 is located mostly in the cell

would instantly disqualify widely appreciated concepts such as life and love and even the Gods that support so many in their daily lives. Oh, and science too.

<sup>xxvii</sup>Possibly with minor modifications respecting the mathematical features that are essential for obtaining an excitable medium.

membrane at the basal (rootward) side of the cell and PIN2 at the apical (shootward) side. Phosphorylation by PINOID results in basal targeting of recycling PINs (PIN1-like) and dephosphorylation by PP2A in (PIN2-like) apical targeting [413, 414]. This molecular mechanism, however, requires that the cell polarity is already set up (and does not easily explain PIN distributions deviating from the basic top/bottom pattern, for example the L-shaped distribution in endodermis cells [63]).

Several heuristic rules have been proposed in modelling studies to link auxin concentrations and/or fluxed to the dynamic redistribution of the localization of PIN proteins that (particularly in those models) held responsible for the auxin transport and distribution. One published rule is sometimes called “up-the-gradient”: PINs are localized preferentially to the cell face next to the neighbouring cell with the highest auxin concentration. This rule is able to produce patterns of auxin maxima representative of phyllotactic patterns found in the shoot apical meristem [3–5]. An often heard critique on this rule is that it is hard to envision a way that plant cells could sense the auxin concentration in their neighbours [82]. A competing rule is sometimes called “with-the-flux”: PINs are localized preferentially to the cell face that already sustains the largest auxin flux [415, 416]. This rule is successful in producing strands (“veins”) of cells pumping auxin towards some sink [6, 417]. The older “canalization” hypothesis for vein formation [418] – that a positive feedback reinforcing the flux through a series of cells would canalize auxin transport into channels – is very similar to this rule. A critique on this rule is that this would require a plant to sense fluxes [89], although this might be achieved indirectly by sensing the intracellular gradient or end-to-end concentration differences [84]. Another issue is that this rule results in veins with a low auxin concentration, whereas the parts of (pre)vascular tissue transporting the auxin are assumed to have a high auxin concentration (relative to the surrounding tissue) [7].

What both rules have in common is that they exaggerate biases in the cell’s PIN distribution and that way make the uniform distribution unstable. Rules that would do the opposite, dampen deviations from the uniform distribution, would not be able to produce stable polarized patterns [288]. From the very nature of the rules, up-the-gradient results in polarization towards auxin maxima, whereas with-the-flux results in polarization away from sources (possibly maxima) to sinks. As both polarization patterns occur in nature, it has been attempted to combine both rules using some concentration based switching mechanism between the two [7]. This made the heuristic rules more complicated, but did not bring us closer towards any mechanism.

A more mechanistic view came from combining links between the orientation of cortical microtubules and wall stress [134], and cortical microtubules and tissue coordination of PIN polarization [419] in a single model that was able to recapitulate the PIN1 localization response to cell ablation in the shoot apical meristem [8]. Interestingly, mathematically this model behaves as up-the-gradient [8]. Further supporting this mechanism, [420] found that the link between wall stress and PIN polarity could run through wall strain via membrane strain, membrane tension and resulting decrease of endocytosis rates, leaving more PINs at the membrane.<sup>xxviii</sup> The experimental evidence so far suggests that this mechanism can account for responses to mechanical perturbations (e.g. ablation experiments as in [134]), but it is highly unlikely that the differences in wall strain are sufficient to explain all observed patterns. For example, it seems unlikely to expect large differences between apical and basal cell faces in provascular strands. Moreover, modeling wall me-

chanical properties (for example using finite element models) is computationally heavy, explaining a current preference among many modelers to ignore them.

In a completely different attempt to bring in a mechanism, one model has put forward Auxin Binding Protein 1 (ABP1) to link auxin and PIN recycling rates [90]. ABP1 is a secreted protein with a high affinity for auxin [421] essential for embryo development [422]. At the plasma membrane it stimulates the endocytosis of PIN proteins, but this stimulation is inhibited by auxin [72]. In pavement cells the action of ABP1 has been linked to the ROP-GTPases (ROPs) [423] that are important in the establishment of cell polarity [424], for example the multiple “neck” and “lobe” regions of pavement cells [423]; What is still missing, however, is a link between the outside (ABP1) and inside (clatrin, ROPs) of the cell.<sup>xxix</sup> Interestingly, ABP1 has been suggested as a candidate “mechanism” for both “up-the-gradient” [89] and “with-the-flux” rules [417], illustrating that its function in PIN polarity is not a priori obvious. Although the link between ABP1 and PIN recycling rates is not complete yet from a biochemical perspective, an extracellular receptor may be what in the future will link the two. The current ABP1-based model, however, will not be the end of the debate. Upon close inspection it uses an artefact to exaggerate minute auxin concentration gradients over the (0.2  $\mu\text{m}$  thick) cell wall: whenever an ABP1 molecule binds an auxin molecule, it immediately and reliably jumps to the plasma membrane of the corresponding half of the cell wall, on that side reducing the PIN recycling rate. A resulting curiosity in several of the figures is that the (ABP1 bound) auxin concentration in part of the half-walls is much higher than the (free) auxin concentration in the cells [90]. This artefactual rather than real mechanism puts it on the pile of the heuristic rules that simply provide some positive feedback that exaggerates deviations from a uniform PIN distribution.

Although (or because of) being “wrong”, such models have been very useful in inspiring our thinking, both on mechanistic requirements of the polarization of auxin transport and what possibilities plant cells could have to sense subcellular auxin gradients and movement.

In this violent debate, we chose to use static bias in the distribution of efflux carriers (PINs) over the different cell faces (in this following [54, 91–93] and others). Although perhaps the best option until the dust settles, it does limit our approach (chapters 4 - 6) to the early stages of primordium formation, as with a large number of divisions and organ outgrowth a whole new PIN layout is established. This of course is not a severe limitation when working on a fixed tissue layout, which poses the same, if not more stringent limitations.

When the mechanism(s) of dynamic PIN localization is(are) finally unravelled, the very first requirement for their implementation in large scale developmental models will be to simplify them. The resulting description may end up curiously close to some of the current heuristic rules, with a single difference: it will be founded on a mechanism rather than “intuition” – a great step forward.

To conclude on the use of “classics”, I would like to point to one final example of an overly simplified, but very relevant model: the “Tragedy of the Commons” [425]. The model can be explained in one simple differential equation, which by no means captures the richness and complexity of our world. At a conceptual level, however, the model very clearly explains why it is so hard to change certain aspects of our global society, that are

so obviously destructive in the long run – as well as the need to keep trying.

The tragedy has also been applied to many biological problems, including root competition among plants [426]. Interestingly, many biological systems are able to resolve this tragedy: they may perform suboptimally, but populations do not typically collapse and the example species did not go extinct [427]. We are still here, too. Does that imply that all “hippies” should “shut up” and better worry about “things that actually matter” (e.g. economic growth and unlimited individual freedom to exploit whatever “needs” to be exploited for maximum personal gain)? Before rejoicing, there is one key difference that should not too quickly be overlooked: the scale of things. If the sole cause for (partially) resolving the tragedy the commons in “natural” systems is natural selection at a group level [428], what is left to save a globalised population, with but a single, all comprising “commons”?

## 10.8 A final word on hammers

Different questions call for different models. Interesting biological questions span a large range of space and time scales, but also different levels of abstraction. Reducing the number of animal tests through *in silico* predictions sets very different requirements than investigating the fundamental properties of a generic mechanism. We have shown through many examples that the most useful model is most often not the most faithful representation of reality, even in cases that understanding is of no importance.

In the introduction I have compared models to hammers, praising both. The same hammer that is used to carve a statue from an anonymous piece of stone, however, has the power to destroy that very statue. Creation and destruction with a single tool. Is this also true for models? I think so. Whatever way a model is built, whatever its aims, there will always be many things not included. Possibly crucial aspects of the system. If the model is successful nonetheless, it will divert our attention from these “forgotten” aspects, possibly delaying our proper understanding of the system for a long time.

This is not a reason to be afraid of models, though, just a reason for ongoing critical evaluation of what we think is right, or better: useful – whether model, “fact” or experimental procedure. For after all, creation inherently is a form of destruction: it is the destruction of all that has the potential to become in favour of a single things that do get realised.

---

## So, what was the use of all this?

---

*FOM strongly encourages PhD students to include in their thesis a chapter on valorization. To further support the student's thinking on the valorization aspects of their work, FOM organizes a "valorization workshop" and a "valorization chapter contest" specially for them. The latter only the small counterpart of the "real" valorization contest. With so many incentives to think about this matter, I of course accepted the challenge and now sit down to write this chapter.*

So, what was the use of all this? Had this been a grant application, I might have felt obliged to link the study of biological nitrogen fixation to solutions for the global food challenge, perhaps through the long term dream of engineering it into other crop species, and by the energy thus saved to the looming energy crisis. Along the same lines, understanding plant development could aid in "educated plant breeding", answering to the call of food challenge as – directly or indirectly – all we eat comes from plants. The organisation of cortical microtubules tunes the mechanics of plant development and growth, but moreover, through the (un)ease of biofuel extraction from wall material could benefit energy research too. Plasmodesmata, last but not least, are not only essential for any plant development and – thanks to the existence of gap junctions, cytoplasmic connections between animal cells – who knows, my general modelling approach might one day form the foundation of a cure to cancer!

Thank goodness I don't have to write such nonsense here. If anything, I have the feeling such words are detrimental to the public support of science in the long run. People might remember that such claims have been made for quite some time, yet still suffer from losing their loved ones to cancer, see the poor children in Africa with their big bellies and hollow eyes, while fuel prices keep increasing. They would *rightfully* ask what is the use of spending all this money on science. From the scientist's point of view, however, there is a strong pressure to make such claims anyhow, as those who do write promising proposals survive in the struggle for scarce funding money. The result is like an evolutionary deadlock, perhaps as gloom as the political theatre to revert global warming and climate change.

Would there be a solution in modesty? That would be as least as far from the truth. It is easy to see how almost every aspect of our daily life is shaped by science and technology. Einstein certainly could not have foreseen that his theory of relativity would prove

essential to the functioning of the GPS system\* – as essential, by the way, as the discovery of the transistor, or the ancient study of the planet's orbits across the sky. In the long run, a single discovery can have *huge* impact on many things, yet it would never be fair to credit only that discovery for it. This example illustrates nicely that the unpredictability of the impact of a single scientific discovery does not imply uselessness. Unfortunately for all control freaks, the world is a chaotic system and science just a part of that. In particle physics, no one would ever think of trying to predict the trajectory of a single atom in the air – even the three body problem can not be solved analytically – yet the behaviour of a large body of gas can be very well described. This is perfectly acceptable. Then why, I wonder, is it so hard to accept that the impact of a particular tiny bit of research is much less predictable than the impact of investing more, or less, money in science?

On days of overexposure to valorization, patent attorneys and economical benefits, I sometimes feel tempted to write down: “my work has no use at all.” That, however, would be a massive lie. Only if the usefulness would be measured exclusively in the number of patents and spin-off companies, my work would most certainly be useless. This I can write down now, long before I will hand in my thesis, and still be completely safe. It simply is inherent to the kind of work I have been doing. We need different measures to express the value of this work.

I think a key aim of theoretical work is to provide insight into the mechanisms underlying our observations and help understand the consequences of proposed hypothetical mechanisms. The study of the different signatures of different mechanisms for increasing the local auxin concentration, initiated in chapter 4, aimed exactly at this. The patterns discovered are of a generic nature, so this insight is also useful in other areas of plant biology. This was a good reason to put extra effort into a more general study of these patterns (chapter 5).

Along the way, the software I developed for this investigation has been used in the development of a computer case on development now used in the education of biology students at Wageningen university. This will help students understand the basics of auxin transport and modelling and specifically how different factors contribute to the information gradient that controls the growth and differentiation of the root tissues. The story of branched nucleation in plant cortical microtubule arrays (chapter 7) has been welcomed by people working on animal embryos, as the giant egg cells also have a cortical microtubule array.

The popular picture of knowledge flow is that from fundamental science, via applied science, to actual applications. Whilst this might well be the main direction of the flow, this is not always the case. In the initial phase of my work on symplastic transport I found myself reading literature from analytical chemistry, catalysis and porous membranes: much closer to industrial application than my own work. Let's call it “reverse valorization” of knowledge. At the beginning of my PhD project I could never have predicted that such information would be of any relevance to my work. And the insights from this work may in turn spread into unexpected directions: when I explained the difference between a straight channel and a plasmodesma with a constricted neck region and a wider central cavity, a colleague suddenly remarked: “Now I understand the use of these wider areas in rivers (“uiterwaarden” in Dutch).”

---

\*Thanks to Vincent Icke for his illustrative calculation of the stock value of Einstein Inc in the science and society workshop at AMOLF, September 26, 2012



The fancy word “serendipity” is frequently used for such cross topic inspiration. A popular conception of serendipity is that these often praised odd associations arise by sheer chance. They do not. It is the same as stating that winning a Nobel prize is the same as winning a lottery, with identical chances for every researcher / lottery ticket. Pulling in ideas from other fields requires an open mind and many, diverse inputs. No miracles happen from a hyper focus on one’s particular very specific field, or, similarly, patentable research only.

I could think of many more examples to write about, things I have learned and experienced during my PhD, but I hope my point is clear now.



Let me conclude with a familiar question: *So, what was the use of writing all this?* Another thing I have learned over the years, is that confronting problems sometimes is a risky business. Nevertheless, if nobody is willing to confront this problem, the damage could be much worse.

Sometimes I envision a dark future, with a brain drain to those contries that do value science in a broad sense and this part of the world sinking to the low-tech level of un(der)paid mass production, with people as the easily replaceable, versatile machines. I hope we do not need to sink that far.

For the individual idealistic researcher though, there might be better ways than waiting for miracles. Spreading word about their research, not only through the conventional channels, could perhaps increase the number of people knowing about it enough to let it make a critical difference. Why not help serendipity a bit – together with your own findings?



# A

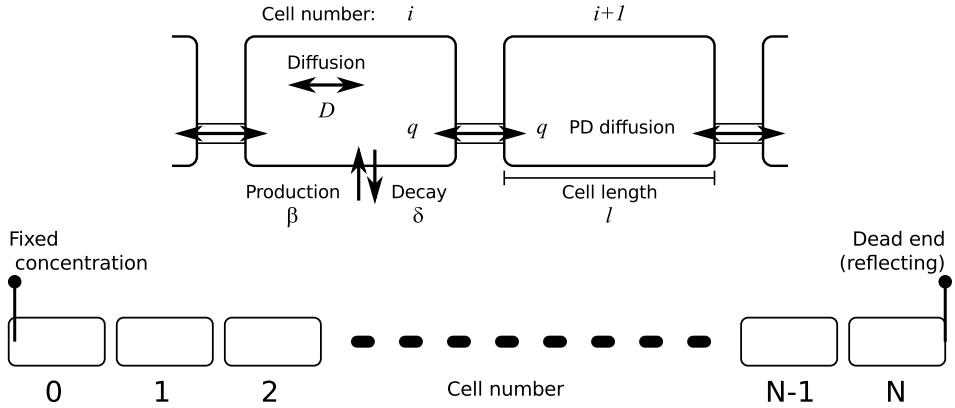
## Walking the back alleys: a modeling study of symplastic transport

### A.1 Mathematical derivations

#### A.1.1 1D analytical model: coordinate system

We track both concentration ( $C_{i,x}$ ) and flux, in the positive direction, ( $J_{i,x}$ ) with subcellular precision. The cell number ( $i$ ) and position ( $x \in [0, l]$ ) are indicated with subscripts.

#### A.1.2 1D steady state profile for purely diffusive symplastic transport



With pure symplastic transport, the flux over a wall is given by:

$$J_{i,0} = J_{i-1,l} = q(C_{i-1,l} - C_{i,0}) \quad (\text{A.1})$$

To link one end of the cell to the next, we compute the intracellular concentration profile. With (only) decay with rate  $\delta$  this profile must obey:

$$\frac{d}{dt}f(x,t) = D \frac{\partial^2}{\partial x^2}f(x,t) - \delta f(x,t), \quad x \in (0, l) \quad (\text{A.2})$$

Which has the general steady state solution

$$f(x) = \kappa e^{-\sqrt{\frac{\delta}{D}}x} + \eta e^{\sqrt{\frac{\delta}{D}}x} \quad (\text{A.3})$$

with  $\kappa$  and  $\eta$  constants. For a given cell  $i$ :

$$C_{i,0} = f_i(0) = \kappa_i + \eta_i \quad (\text{A.4})$$

$$C_{i,l} = f_i(l) = \kappa_i e^{-\sqrt{\frac{\delta}{D}}l} + \eta_i e^{\sqrt{\frac{\delta}{D}}l} \quad (\text{A.5})$$

$$J_{i,0} = -Df'_i(0) = \sqrt{\delta D}\kappa_i - \sqrt{\delta D}\eta_i \quad (\text{A.6})$$

$$J_{i,l} = -Df'_i(l) = \sqrt{\delta D}\kappa_i e^{-\sqrt{\frac{\delta}{D}}l} - \sqrt{\delta D}\eta_i e^{\sqrt{\frac{\delta}{D}}l} \quad (\text{A.7})$$

Choosing the least complicated equations we start from  $C_{i,0}$  and  $J_{i,0}$ :

$$\eta_i = \frac{-J_{i,0}}{\sqrt{\delta D}} + \kappa_i \quad (\text{A.8})$$

$$\kappa_i = \frac{1}{2} \left( C_{i,0} + \frac{J_{i,0}}{\sqrt{\delta D}} \right) \quad (\text{A.9})$$

$$\eta_i = \frac{1}{2} \left( C_{i,0} - \frac{J_{i,0}}{\sqrt{\delta D}} \right) \quad (\text{A.10})$$

$$C_{i,x} = \frac{1}{2} \left( C_{i,0} + \frac{J_{i,0}}{\sqrt{\delta D}} \right) e^{-\sqrt{\frac{\delta}{D}}x} + \frac{1}{2} \left( C_{i,0} - \frac{J_{i,0}}{\sqrt{\delta D}} \right) e^{\sqrt{\frac{\delta}{D}}x} \quad (\text{A.11})$$

$$C_{i,l} = \frac{1}{2} \left( C_{i,0} + \frac{J_{i,0}}{\sqrt{\delta D}} \right) e^{-\sqrt{\frac{\delta}{D}}l} + \frac{1}{2} \left( C_{i,0} - \frac{J_{i,0}}{\sqrt{\delta D}} \right) e^{\sqrt{\frac{\delta}{D}}l} \quad (\text{A.12})$$

Matter is conserved, so the flux over a given wall is the same as the flux over the previous wall minus the decay in that cell:

$$J_{i,0} = J_{i-1,0} - \delta \int_0^l f_{i-1}(x) dx \quad (\text{A.13})$$

$$= J_{i-1,0} - \sqrt{\delta D} \left( \kappa_{i-1} (1 - e^{-\sqrt{\frac{\delta}{D}}l}) + \eta_{i-1} (e^{\sqrt{\frac{\delta}{D}}l} - 1) \right) \quad (\text{A.14})$$

$$= J_{i-1,0} - \frac{\sqrt{\delta D}}{2} \left( \left( C_{i-1,0} + \frac{J_{i-1,0}}{\sqrt{\delta D}} \right) (1 - e^{-\sqrt{\frac{\delta}{D}}l}) + \left( C_{i-1,0} - \frac{J_{i-1,0}}{\sqrt{\delta D}} \right) (e^{\sqrt{\frac{\delta}{D}}l} - 1) \right) \quad (\text{A.15})$$

$$J_{i,0} = C_{i-1,0} \frac{\sqrt{\delta D}}{2} \left( e^{-\sqrt{\frac{\delta}{D}}l} - e^{\sqrt{\frac{\delta}{D}}l} \right) + \frac{J_{i-1,0}}{2} \left( e^{-\sqrt{\frac{\delta}{D}}l} + e^{\sqrt{\frac{\delta}{D}}l} \right) \quad (\text{A.16})$$

We introduce the ratios

$$\Delta_i = \frac{C_{i,0}}{C_{i-1,0}} \quad (\text{A.17})$$

With these we can search for homogeneous solutions, i.e.  $\Delta_i = \Delta_{i+1} = \Delta$ . Introducing the short hand notations

$$\ominus = \left( \frac{e^{\sqrt{\frac{\delta}{D}}l} - e^{-\sqrt{\frac{\delta}{D}}l}}{2} \right) = \sinh\left(\sqrt{\frac{\delta}{D}}l\right) \quad (\text{A.18})$$

$$\boxplus = \left( \frac{e^{\sqrt{\frac{\delta}{D}}l} + e^{-\sqrt{\frac{\delta}{D}}l}}{2} \right) = \cosh\left(\sqrt{\frac{\delta}{D}}l\right) \quad (\text{A.19})$$

we can rewrite equations A.16 and A.1:

$$J_{i,0} = -C_{i-1,0}\sqrt{\delta D}\ominus + J_{i-1,0}\boxplus \quad (\text{A.20})$$

$$J_{i,0} = q(C_{i-1,l} - C_{i,0}) \quad (\text{A.21})$$

$$= q\left(C_{i-1,0}\boxplus - \frac{J_{i-1,0}}{\sqrt{\delta D}}\ominus\right) - q\Delta C_{i-1,0} \quad (\text{A.22})$$

$$= q(\boxplus - \Delta)C_{i-1,0} - \frac{q}{\sqrt{\delta D}}\ominus J_{i-1,0} \quad (\text{A.23})$$

So

$$J_{i-1,0} = C_{i-1,0} \frac{q\boxplus + \sqrt{\delta D}\ominus - \Delta q}{\boxplus + \frac{q}{\sqrt{\delta D}}\ominus} \quad (\text{A.24})$$

At the same time

$$J_{i-1,0} = -C_{i-2,0}\sqrt{\delta D}\ominus + J_{i-2,0}\boxplus \quad (\text{A.25})$$

$$= C_{i-2,0} \left( -\sqrt{\delta D}\ominus + \boxplus \frac{q\boxplus + \sqrt{\delta D}\ominus - \Delta q}{\boxplus + \frac{q}{\sqrt{\delta D}}\ominus} \right) \quad (\text{A.26})$$

$$= \frac{C_{i-1,0}}{\Delta} \left( -\sqrt{\delta D}\ominus + \boxplus \frac{q\boxplus + \sqrt{\delta D}\ominus - \Delta q}{\boxplus + \frac{q}{\sqrt{\delta D}}\ominus} \right) \quad (\text{A.27})$$

Combining A.24 and A.27 and solving for  $\Delta$  we obtain two homogeneous solutions:

$$\Delta_- = \frac{2q\boxplus + \sqrt{\delta D}\ominus - \sqrt{(2q\boxplus + \sqrt{\delta D}\ominus)^2 - 4q^2}}{2q} \quad (\text{A.28})$$

$$\Delta_+ = \frac{2q\boxplus + \sqrt{\delta D}\ominus + \sqrt{(2q\boxplus + \sqrt{\delta D}\ominus)^2 - 4q^2}}{2q} \quad (\text{A.29})$$

This means that the general steady state profile must be a linear combination of these two solutions:

$$C_{i,0} = \bar{\kappa}\Delta_-^i + \bar{\eta}\Delta_+^i \quad (\text{A.30})$$

We use a no flux boundary at the last cell ( $N$ ), so at steady state:

$$J_{N,0} = \delta \int_0^l C_{N,x} dx \quad (\text{A.31})$$

$$= J_{N,0} (1 - \boxplus) + C_{N,0} \sqrt{\delta D} \ominus \quad (\text{A.32})$$

$$J_{N,0} = C_{N,0} \sqrt{\delta D} \frac{\ominus}{\boxplus} \quad (\text{A.33})$$

and

$$J_{N,0} = q(C_{N-1,l} - C_{N,0}) \quad (\text{A.34})$$

$$= q \left( C_{N-1,0} \boxplus - \frac{J_{N-1,0}}{\sqrt{\delta D}} \ominus \right) - q C_{N,0} \quad (\text{A.35})$$

$$= q \left( C_{N-1,0} \boxplus - \frac{(J_{N,0} + \sqrt{\delta D} C_{N-1,0} \ominus) \ominus}{\sqrt{\delta D} \boxplus} \right) - q C_{N,0} \quad (\text{A.36})$$

$$J_{N,0} \left( 1 + \frac{q \ominus}{\sqrt{\delta D} \boxplus} \right) = q \left( \frac{1}{\boxplus} C_{N-1,0} - C_{N,0} \right) \quad (\text{A.37})$$

$$= q C_{N,0} \left( \frac{1}{\boxplus \Delta_N} - 1 \right) \quad (\text{A.38})$$

$$J_{N,0} = q \sqrt{\delta D} C_{N,0} \frac{1/\Delta_N - \boxplus}{\sqrt{\delta D} \boxplus + q \ominus} \quad (\text{A.39})$$

Combining A.33 and A.39 and solving for  $\Delta_N$ :

$$\Delta_N = \frac{q}{q \left( \boxplus + \frac{\ominus^2}{\boxplus} \right) + \sqrt{\delta D} \ominus} \quad (\text{A.40})$$

We now have

$$C_{0,0} = \bar{\kappa} + \bar{\eta} \quad (\text{A.41})$$

$$\Delta_N = \frac{C_{N,0}}{C_{N-1,0}} = \frac{\bar{\kappa} \Delta_-^N + (C_{0,0} - \bar{\kappa}) \Delta_+^N}{\bar{\kappa} \Delta_-^{N-1} + (C_{0,0} - \bar{\kappa}) \Delta_+^{N-1}} \quad (\text{A.42})$$

So

$$\bar{\kappa} = C_{0,0} \frac{\Delta_+^{N-1} (\Delta_+ - \Delta_N)}{\Delta_N (\Delta_-^{N-1} - \Delta_+^{N-1}) + \Delta_+^N - \Delta_-^N} \quad (\text{A.43})$$

$$\bar{\eta} = C_{0,0} \frac{\Delta_-^{N-1} (\Delta_N - \Delta_-)}{\Delta_N (\Delta_-^{N-1} - \Delta_+^{N-1}) + \Delta_+^N - \Delta_-^N} \quad (\text{A.44})$$

### Characteristic length

It is straightforward to show that  $\Delta_- < 1$  and  $\Delta_+ > 1$ . This means that in the limit of  $N \rightarrow \infty$ ,  $\bar{\kappa} \rightarrow C_{0,0}$  and  $\bar{\eta} \rightarrow 0$ , so

$$C_{i,0}^- = \lim_{N \rightarrow \infty} C_{i,0} = C_{0,0} \Delta_-^i \quad (\text{A.45})$$

This we can rewrite as a single negative exponential:

$$C_{i,0}^- = e^{\log(\Delta_-)i} \quad (\text{A.46})$$

In the literature of animal morphogen gradients the characteristic length of a gradient is defined as  $\lambda$  in

$$C_0 e^{-x/\lambda} \quad (\text{A.47})$$

with  $C_0$  the concentration at the source and  $x$  a spatial coordinate. On an infinite line of cells our profile thus has the characteristic length

$$\lambda = \frac{-1}{\log(\Delta_-)} \quad (\text{A.48})$$

in number of cells or

$$\lambda' = \frac{-l}{\log(\Delta_-)} \quad (\text{A.49})$$

in real length ( $\mu m$ ).

### Useful limits

To verify the formulas, we compute a few physically meaningful limits. By taking the limit for  $D \rightarrow \infty$  (using l'Hôpital's rule) we arrive at the expressions that can be found without taking into account the intracellular gradients.

$$\lim_{D \rightarrow \infty} \Delta_- = \frac{2q + \delta l - \sqrt{(2q + \delta l)^2 - 4q^2}}{2q} \quad (\text{A.50})$$

$$\lim_{D \rightarrow \infty} \Delta_+ = \frac{2q + \delta l + \sqrt{(2q + \delta l)^2 - 4q^2}}{2q} \quad (\text{A.51})$$

$$\lim_{D \rightarrow \infty} \Delta_N = \frac{q}{\delta l + q} \quad (\text{A.52})$$

If we consider the walls as interfaces of vanishing thickness and let the diffusive permeability  $q \rightarrow \infty$  we obtain:

$$\lim_{q \rightarrow \infty} \Delta_- = \boxminus - \ominus = e^{-\sqrt{\delta/D}l} \quad (\text{A.53})$$

$$\lim_{q \rightarrow \infty} \lambda = \frac{-1}{\log(e^{-\sqrt{\delta/D}l})} = \sqrt{D/\delta}/l \quad (\text{A.54})$$

for position expressed in cell number. This can be changed to actual length by multiplying by the cell length, obtaining  $\lambda' = \sqrt{D/\delta}$ , exactly the characteristic length found for diffusion/decay gradients.

Inspired by these limits, we could write an “effective diffusion constant”  $D_{eff}$  from the characteristic length:

$$D_{eff} \equiv \lambda^2 \delta = \frac{\delta}{(\log(\Delta_-))^2} \quad (\text{in \#cells}) \quad (\text{A.55})$$

$$D'_{eff} \equiv (\lambda')^2 \delta = \frac{\delta l^2}{(\log(\Delta_-))^2} \quad (\text{in } \mu m) \quad (\text{A.56})$$

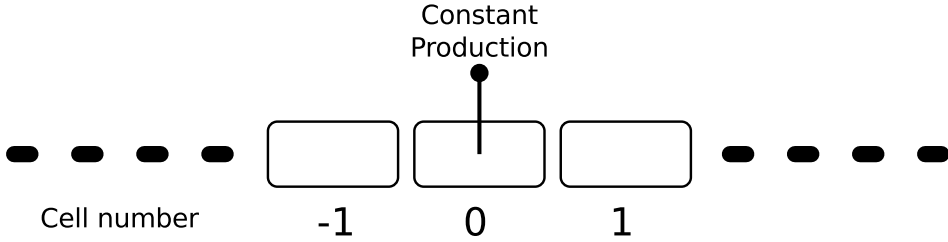
These are dependent on  $\delta$ , which seems odd. Taking the limits for  $\delta \downarrow 0$ , we obtain:

$$D_{S,eff} = \frac{Dq}{l(D+ql)} \quad (\text{in \#cells}) \quad (\text{A.57})$$

$$D'_{S,eff} = \frac{Dql}{D+ql} \quad (\text{in } \mu m) \quad (\text{A.58})$$

The latter expression is also found by [166], describing effective diffusion in an animal tissue (1D). We therefore tested if these formulas were also useful for  $\delta > 0$  to map our system (in a coarse grained way) to ordinary diffusion/decay system. This worked surprisingly well (e.g. figure 2.2A), but the more elaborate formulas performed better for high  $\delta$  in combination with low  $q$  and long cells (high  $l$ ) (e.g. figure 2.2B).

### A.1.3 1D: time resolved solution for purely diffusive symplastic transport (approximation)



Assume an infinite file of cells,  $k \in (-\infty, \infty)$ , with production in the middle cell ( $k = 0$ ) with rate  $\beta$ . In an attempt to obtain the full time dependent solution, we exploit that the steady state can be rescaled to a homogeneous diffusion problem. We assume that all matter produced in cell 0 at time  $t$  will spread outward following a Gaussian profile with  $\sigma^2 = 2\alpha t$ ,  $\alpha$  some yet unknown constant. Including homogeneous decay with a constant rate  $\delta$ , this will be:

$$g(k, t) = \beta \frac{1}{\sqrt{4\pi\alpha t}} e^{-\frac{k^2}{4\alpha t}} e^{-\delta t} \quad (\text{A.59})$$

Integrating over all time till moment  $T$ :

$$f(k, T) = \beta \int_0^T g(k, t) dt \quad (\text{A.60})$$

$$= \beta \int_0^T \frac{1}{\sqrt{4\pi\alpha t}} e^{-\frac{k^2}{4\alpha t}} e^{-\delta t} dt \quad (\text{A.61})$$

$$= \beta \frac{1}{4\sqrt{\alpha\delta}} \left\{ e^{-\sqrt{\delta/\alpha}|k|} \left( 1 + \operatorname{erf} \left( \frac{2\sqrt{\alpha\delta}T - |k|}{2\sqrt{\alpha T}} \right) \right) + e^{\sqrt{\delta/\alpha}|k|} \left( -1 + \operatorname{erf} \left( \frac{2\sqrt{\alpha\delta}T + |k|}{2\sqrt{\alpha T}} \right) \right) \right\} \quad (\text{A.62})$$

As  $\lim_{x \rightarrow \infty} \operatorname{erf}(x) = 1$ ,

$$f(k, T \rightarrow \infty) = \frac{\beta}{2\sqrt{\alpha\delta}} e^{-\sqrt{\delta/\alpha}|k|} \quad (\text{A.63})$$



We also know that without boundaries, similar to equation A.46, the steady state profile must follow

$$h(k) = \kappa e^{\log(\Delta_-)|k|} \quad (\text{A.64})$$

with  $\kappa$  some constant and

$$\Delta_- = \frac{2q_{\boxplus} + \sqrt{\delta D_{\ominus}} - \sqrt{(2q_{\boxplus} + \sqrt{\delta D_{\ominus}})^2 - 4q^2}}{2q} \quad (\text{A.65})$$

We can thus solve for  $\alpha$ :

$$\alpha = \left( \frac{-\sqrt{\delta}}{\log(\Delta_-)} \right)^2 = D_{eff} \quad (\text{A.66})$$

so

$$f(k, \infty) = \frac{\beta |\log(\Delta_-)|}{2\delta} e^{\log(\Delta_-)|k|} \quad (\text{A.67})$$

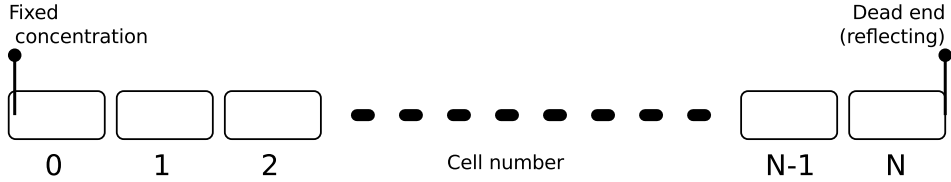
$$f(k, \infty) = \frac{\beta}{2\sqrt{D_{eff}\delta}} e^{-\sqrt{\delta/D_{eff}}|k|} \quad (\text{A.68})$$

$$f(k, T) = \frac{\beta |\log(\Delta_-)|}{2\delta} \left\{ e^{\log(\Delta_-)|k|} \left( 1 + \operatorname{erf} \left( \sqrt{\delta T} - \frac{|k| |\log(\Delta_-)|}{2\sqrt{\delta T}} \right) \right) + e^{-\log(\Delta_-)|k|} \left( -1 + \operatorname{erf} \left( \sqrt{\delta T} + \frac{|k| |\log(\Delta_-)|}{2\sqrt{\delta T}} \right) \right) \right\} \quad (\text{A.69})$$

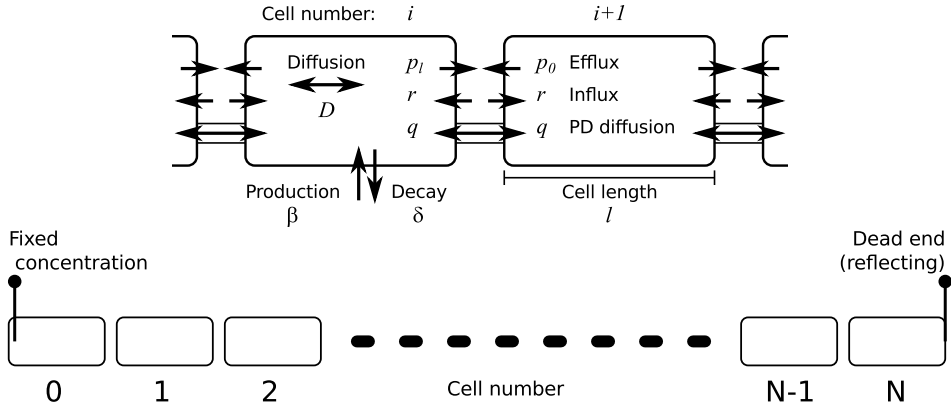
$$f(k, T) = \frac{\beta}{2\sqrt{D_{eff}\delta}} \left\{ e^{-\sqrt{\delta/D_{eff}}|k|} \left( 1 + \operatorname{erf} \left( \sqrt{\delta T} - \frac{|k|}{2\sqrt{D_{eff}T}} \right) \right) + e^{\sqrt{\delta/D_{eff}}|k|} \left( -1 + \operatorname{erf} \left( \sqrt{\delta T} + \frac{|k|}{2\sqrt{D_{eff}T}} \right) \right) \right\} \quad (\text{A.70})$$

Note that in this approach we implicitly assume that within each cell, the concentration profile follows a steady state distribution. This is, of course, only true in the actual steady state. If, however, the deviations from the steady state profile are sufficiently small, equation A.69 will be a good approximation for the tissue profile. Moreover, the difference between this profile and the actual non-steady state profile (obtained from numerical simulations with subcellular precision) will decrease with time and will eventually vanish (figure 2.2A,B). A correction for the tails can be obtained by taking into account the actual size (1 cell) of the source. This results in fatter tails in early stages and converges to the same steady state profile (except for the source cell, which actually is an improvement too) for the tissue (figure 2.2C). Unfortunately, there is no analytical expression for the corrected solution, so one has to resort to numerical integration.

### A.1.4 1D steady state profile for combined symplastic transport and apoplastic transport



This is a single derivation for the two processes, symplastic and apoplastic transport, combined. Equations for either process can be obtained by setting the parameters for the other process to zero. For apoplastic transport this is only possible with efflux on both sides (possibly very small on one side), otherwise the resulting formulas contain a division by zero. In essence the derivation is the same as for only symplastic transport (appendix A.1.2), except for a more complicated expression for the flux over the wall, naturally affecting the resulting expressions.



In the setting we chose, only diffusion and decay take place inside a cell. That means that the intracellular profiles are the same as before:

$$C_{i,x} = C_{i,0} \frac{e^{\sqrt{\delta/D}x} + e^{-\sqrt{\delta/D}x}}{2} - \frac{J_{i,0}}{\sqrt{\delta D}} \frac{e^{\sqrt{\delta/D}x} - e^{-\sqrt{\delta/D}x}}{2} \quad (\text{A.71})$$

So, using the shorthand notation introduced before (equations A.28 and A.29):

$$C_{i,l} = C_{i,0} \boxplus - \frac{J_{i,0}}{\sqrt{\delta D}} \ominus \quad (\text{A.72})$$

The fluxes over the wall follow

$$J_{i-1,w} = (p_l + q)C_{i-1,l} - rw - qC_{i,0} \quad (\text{A.73})$$

$$J_{w,i} = rw - (p_0 + q)C_{i,0} + qC_{i-1,0} \quad (\text{A.74})$$

$$w = \frac{p_l C_{i-1,l} + p_0 C_{i,0}}{2r} \quad (\text{A.75})$$

$$J_{i-1,l} = J_{i,0} = (p_l/2 + q)C_{i-1,l} - (p_0/2 + q)C_{i,0} \quad (\text{A.76})$$

Moreover

$$J_{i,0} = J_{i-1,0} - \delta \int_0^l f_{i-1}(x) dx \quad (\text{A.77})$$

$$= C_{i-1,0} \frac{\sqrt{\delta D}}{2} \left( e^{-\sqrt{\frac{\delta}{D}}l} - e^{\sqrt{\frac{\delta}{D}}l} \right) + \frac{J_{i-1,0}}{2} \left( e^{-\sqrt{\frac{\delta}{D}}l} + e^{\sqrt{\frac{\delta}{D}}l} \right) \quad (\text{A.78})$$

$$= -C_{i-1,0} \sqrt{\delta D} \ominus + J_{i-1,0} \boxplus \quad (\text{A.79})$$

We again compute the ratios

$$\Delta_i = \frac{C_{i,0}}{C_{i-1,0}} \quad (\text{A.80})$$

and search for homogeneous solutions  $\Delta_i = \Delta_{i+1} = \Delta \forall i$

$$J_{i,0} = -C_{i-1,0} \sqrt{\delta D} \ominus + J_{i-1,0} \boxplus \quad (\text{A.81})$$

$$J_{i,0} = (p_l/2 + q) C_{i-1,l} - (p_0/2 + q) C_{i,0} \quad (\text{A.82})$$

$$= (p_l/2 + q) \left( C_{i-1,0} \boxplus - \frac{J_{i-1,0}}{\sqrt{\delta D}} \ominus \right) - (p_0/2 + q) \Delta C_{i-1,0} \quad (\text{A.83})$$

$$= ((p_l/2 + q) \boxplus - (p_0/2 + q) \Delta) C_{i-1,0} - \frac{p_l/2 + q}{\sqrt{\delta D}} \ominus J_{i-1,0} \quad (\text{A.84})$$

So

$$J_{i-1,0} = C_{i-1,0} \frac{(p_l/2 + q) \boxplus + \sqrt{\delta D} \ominus - \Delta(p_0/2 + q)}{\boxplus + \frac{p_l/2 + q}{\sqrt{\delta D}} \ominus} \quad (\text{A.85})$$

$$J_{i-1,0} = -C_{i-2,0} \sqrt{\delta D} \ominus + J_{i-2,0} \boxplus \quad (\text{A.86})$$

$$= C_{i-2,0} \left( -\sqrt{\delta D} \ominus + \boxplus \frac{(p_l/2 + q) \boxplus + \sqrt{\delta D} \ominus - \Delta(p_0/2 + q)}{\boxplus + \frac{p_l/2 + q}{\sqrt{\delta D}} \ominus} \right) \quad (\text{A.87})$$

$$= \frac{C_{i-1,0}}{\Delta} \left( -\sqrt{\delta D} \ominus + \boxplus \frac{(p_l/2 + q) \boxplus + \sqrt{\delta D} \ominus - \Delta(p_0/2 + q)}{\boxplus + \frac{p_l/2 + q}{\sqrt{\delta D}} \ominus} \right) \quad (\text{A.88})$$

Combining these two expressions and solving for  $\Delta$ :

$$\Delta_- = \quad (\text{A.89})$$

$$\frac{(p_0/2 + p_l + 2q) \boxplus + \sqrt{\delta D} \ominus - \sqrt{\left( (p_0/2 + p_l + 2q) \boxplus + \sqrt{\delta D} \ominus \right)^2 - 4(p_0/2 + q)(p_l/2 + q)}}{2(p_0/2 + q)}$$

$$\Delta_+ = \quad (\text{A.90})$$

$$\frac{(p_0/2 + p_l + 2q) \boxplus + \sqrt{\delta D} \ominus + \sqrt{\left( (p_0/2 + p_l + 2q) \boxplus + \sqrt{\delta D} \ominus \right)^2 - 4(p_0/2 + q)(p_l/2 + q)}}{2(p_0/2 + q)}$$

At steady state we have because of the no flux boundary of the last cell:

$$J_{N,0} = \delta \int_0^l C_{N,x} dx \quad (\text{A.91})$$

$$= J_{N,0}(1 - \boxplus) + C_{N,0}\sqrt{\delta D} \ominus \quad (\text{A.92})$$

$$J_{N,0} = C_{N,0}\sqrt{\delta D} \frac{\ominus}{\boxplus} \quad (\text{A.93})$$

and

$$J_{N,0} = (p_l/2 + q)C_{N-1,l} - (p_0/2 + q)C_{N,0} \quad (\text{A.94})$$

$$= (p_l/2 + q) \left( C_{N-1,0} \boxplus - \frac{J_{N-1,0}}{\sqrt{\delta D}} \ominus \right) - (p_0/2 + q)C_{N,0} \quad (\text{A.95})$$

$$= (p_l/2 + q) \left( C_{N-1,0} \boxplus - \frac{\left( J_{N,0} + \sqrt{\delta D} C_{N-1,0} \ominus \right) \ominus}{\sqrt{\delta D} \boxplus} \right) - (p_0/2 + q)C_{N,0} \quad (\text{A.96})$$

$$J_{N,0} \left( 1 + \frac{(p_l/2 + q) \ominus}{\sqrt{\delta D} \boxplus} \right) = \frac{C_{N-1,0}}{\boxplus} (p_l/2 + q) - C_{N,0} (p_0/2 + q) \quad (\text{A.97})$$

$$= C_{N,0} \left( -(p_0/2 + q) + \frac{p_l/2 + q}{\boxplus \Delta_N} \right) \quad (\text{A.98})$$

$$J_{N,0} = \sqrt{\delta D} C_{N,0} \frac{-(p_0/2 + q) \boxplus + (p_l/2 + q)/\Delta_N}{\sqrt{\delta D} \boxplus + (p_l/2 + q) \ominus} \quad (\text{A.99})$$

Combining A.93 and A.99 and solving for  $\Delta_N$ :

$$\Delta_N = \frac{p_l/2 + q}{(p_0/2 + q) \boxplus + \frac{\ominus^2}{\boxplus} (p_l/2 + q) + \sqrt{\delta D} \ominus} \quad (\text{A.100})$$

We now have

$$C_{i,0} = \kappa \Delta_-^i + \eta \Delta_+^i \quad (\text{A.101})$$

$$C_{0,0} = \kappa + \eta \quad (\text{A.102})$$

$$\Delta_N = \frac{C_{N,0}}{C_{N-1,0}} = \frac{\kappa \Delta_-^N + (C_{0,0} - \kappa) \Delta_+^N}{\kappa \Delta_-^{N-1} + (C_{0,0} - \kappa) \Delta_+^{N-1}} \quad (\text{A.103})$$

So

$$\kappa = C_{0,0} \frac{\Delta_+^{N-1} (\Delta_+ - \Delta_N)}{\Delta_N (\Delta_-^{N-1} - \Delta_+^{N-1}) + \Delta_+^N - \Delta_-^N} \quad (\text{A.104})$$

$$\eta = C_{0,0} \frac{\Delta_-^{N-1} (\Delta_N - \Delta_-)}{\Delta_N (\Delta_-^{N-1} - \Delta_+^{N-1}) + \Delta_+^N - \Delta_-^N} \quad (\text{A.105})$$

Considering that  $\Delta_- < 1 < \Delta_+$ , it is not hard to see that for  $N$  sufficiently large,  $\kappa \approx C_{0,0}$  (slightly smaller than  $C_{0,0}$ ) and that  $\eta \approx 0$  (but strictly positive). In other words,

in a sufficiently long “tissue” the near end of the profile will be dominated by  $\kappa\Delta_-^i$ . With directed apoplastic transport ( $p_l > p_0$ ), the far end will be dominated by  $\eta\Delta_+^i$  ( $i \approx N$ ).

Note that (using l’Hôpital’s rule)

$$\lim_{D \rightarrow \infty} \Delta_- = \frac{\frac{p_0+p_l}{2} + 2q + \delta l - \sqrt{\left(\left(\frac{p_0+p_l}{2} + 2q\right) + \delta l\right)^2 - 4(p_0/2 + q)(p_l/2 + q)}}{2(p_0/2 + q)} \quad (\text{A.106})$$

$$\lim_{D \rightarrow \infty} \Delta_+ = \frac{\frac{p_0+p_l}{2} + 2q + \delta l + \sqrt{\left(\left(\frac{p_0+p_l}{2} + 2q\right) + \delta l\right)^2 - 4(p_0/2 + q)(p_l/2 + q)}}{2(p_0/2 + q)} \quad (\text{A.107})$$

$$\lim_{D \rightarrow \infty} \Delta_N = \frac{p_l/2 + q}{\delta l + p_0/2 + q} \quad (\text{A.108})$$

i.e. the same as can be calculated without intracellular gradients.

### Length of the “informative gradient”

We define the distance  $d(X)$  as the distance between the far end and the point where both parts contribute equally to the solution (i.e.  $X$  in  $\kappa\Delta_-^X = \eta\Delta_+^X$ ):

$$\frac{\Delta_+^{N-1}(\Delta_+ - \Delta_N)}{\Delta_N(\Delta_-^{N-1} - \Delta_+^{N-1}) + \Delta_+^N - \Delta_-^N} \Delta_-^X = \frac{\Delta_-^{N-1}(\Delta_N - \Delta_-)}{\Delta_N(\Delta_-^{N-1} - \Delta_+^{N-1}) + \Delta_+^N - \Delta_-^N} \Delta_+^X \quad (\text{A.109})$$

Solving for  $X$  yields:

$$X = N - 1 + \log\left(\frac{\Delta_+ - \Delta_N}{\Delta_N - \Delta_-}\right) / \log\left(\frac{\Delta_+}{\Delta_-}\right) \quad (\text{A.110})$$

So

$$d(X) = N - X = 1 - \log\left(\frac{\Delta_+ - \Delta_N}{\Delta_N - \Delta_-}\right) / \log\left(\frac{\Delta_+}{\Delta_-}\right) \quad (\text{A.111})$$

Note that this distance  $d(X)$  is independent of the number of cells. This means that the length of the informative gradient is independent of the total tissue length (provided that it is long enough, i.e.  $N > d(X)$ ).

### A.1.5 1D: Reconstructing intracellular gradients and local fluxes from analytical steady state profiles

The tissue scale profiles calculated in appendices A.1.2 and A.1.4 yield the concentrations  $C_{i,0}$  at the “upstream” side of each cell. This contains enough information for reconstructing all intracellular profiles and intercellular fluxes.

### Intracellular profiles

Inside the cell we have:

$$C_{i,x} = C_{i,0} \cosh\left(\sqrt{\delta/D}x\right) - \frac{J_{i,0}}{\sqrt{\delta D}} \sinh\left(\sqrt{\delta/D}x\right) \quad (\text{A.112})$$

Combining this with

$$J_{i,0} = C_{i,0} \frac{(p_l/2 + q) \boxplus + \sqrt{\delta D} \ominus - \Delta_{i+1}(p_0/2 + q)}{\boxplus + \frac{p_l/2 + q}{\sqrt{\delta D}} \ominus} \quad (\text{A.113})$$

$$J_{i,0} = C_{i,0} \frac{(p_l/2 + q) \boxplus + \sqrt{\delta D} \ominus}{\boxplus + \frac{p_l/2 + q}{\sqrt{\delta D}} \ominus} - C_{i+1,0} \frac{(p_0/2 + q)}{\boxplus + \frac{p_l/2 + q}{\sqrt{\delta D}} \ominus} \quad (\text{A.114})$$

found during the derivation in A.1.4, we get:

$$\begin{aligned} C_{i,x} = C_{i,0} & \frac{\sqrt{\delta D} \cosh\left(\sqrt{\delta/D}(l-x)\right) + (p_l/2 + q) \sinh\left(\sqrt{\delta/D}(l-x)\right)}{\sqrt{\delta D} \boxplus + (p_l/2 + q) \ominus} \\ & + C_{i+1,0} \frac{(p_0/2 + q) \sinh\left(\sqrt{\delta/D}x\right)}{\sqrt{\delta D} \boxplus + (p_l/2 + q) \ominus} \end{aligned} \quad (\text{A.115})$$

which describes the profile within a cell based on the concentration at its 0-end and the concentration at the beginning of the next cell.

### Intercellular fluxes

Using the above formula, the concentration at the far end of cell  $i$  is:

$$C_{i,l} = \frac{C_{i,0} \sqrt{\delta D} + C_{i+1,0}(p_0/2 + q) \ominus}{\sqrt{\delta D} \boxplus + (p_l/2 + q) \ominus} \quad (\text{A.116})$$

The total flux over the walls at both ends are given by:

$$J_{i,0} = (p_l/2 + q)C_{i-1,l} - (p_0/2 + q)C_{i,0} \quad (\text{A.117})$$

$$J_{i,l} = (p_l/2 + q)C_{i,l} - (p_0/2 + q)C_{i+1,0} \quad (\text{A.118})$$

Filling in the expression of  $C_{i,l}$  in  $J_{i,l}$  to obtain the full expression:

$$J_{i,l} = (p_l/2 + q) \frac{C_{i,0} \sqrt{\delta D} + C_{i+1,0}(p_0/2 + q) \ominus}{\sqrt{\delta D} \boxplus + (p_l/2 + q) \ominus} - (p_0/2 + q)C_{i+1,0} \quad (\text{A.119})$$

$$J_{i,l} = \sqrt{\delta D} \frac{C_{i,0}(p_l/2 + q) - C_{i+1,0}(p_0/2 + q) \boxplus}{\sqrt{\delta D} \boxplus + (p_l/2 + q) \ominus} \quad (\text{A.120})$$

Of this, the net flux through the plasmodesmata is:

$$J_{i,l}^q = q(C_{i,l} - C_{i+1,0}) \quad (\text{A.121})$$

$$= q \frac{C_{i,0} \sqrt{\delta D} - C_{i+1,0} \left( \sqrt{\delta D} \boxplus + \frac{p_l - p_0}{2} \ominus \right)}{\sqrt{\delta D} \boxplus + (p_l/2 + q) \ominus} \quad (\text{A.122})$$

Note that this is not the same as simply dropping  $p_l$  and  $p_0$  from the numerator of the full flux equation  $J_{i,l}$

Similarly the forward apoplastic flux is:

$$J_{i,l}^{p_l} = \frac{p_l C_{i,l}}{2} \quad (\text{A.123})$$

$$= \frac{p_l}{2} \frac{C_{i,0} \sqrt{\delta D} + C_{i+1,0} (p_0/2 + q) \ominus}{\sqrt{\delta D} \boxplus + (p_l/2 + q) \ominus} \quad (\text{A.124})$$

and the reverse apoplastic flux:

$$J_{i,l}^{p_0} = -\frac{p_0 C_{i+1,0}}{2} \quad (\text{A.125})$$

For completion we write down the same fluxes for the near end of the cell:

$$J_{i,0} = \sqrt{\delta D} \frac{C_{i-1,0} (p_l/2 + q) - C_{i,0} (p_0/2 + q) \boxplus}{\sqrt{\delta D} \boxplus + (p_l/2 + q) \ominus} \quad (\text{A.126})$$

$$J_{i,0}^q = q \frac{C_{i-1,0} \sqrt{\delta D} - C_{i,0} (\sqrt{\delta D} \boxplus + \frac{p_l - p_0}{2} \ominus)}{\sqrt{\delta D} \boxplus + (p_l/2 + q) \ominus} \quad (\text{A.127})$$

$$J_{i,0}^{p_l} = \frac{p_l}{2} \frac{C_{i-1,0} \sqrt{\delta D} + C_{i,0} (p_0/2 + q) \ominus}{\sqrt{\delta D} \boxplus + (p_l/2 + q) \ominus} \quad (\text{A.128})$$

$$J_{i,0}^{p_0} = -\frac{p_0 C_{i,0}}{2} \quad (\text{A.129})$$

## A.2 Overview of mathematical symbols

A

Parameter	Default(s)	Comments
$\beta$	$2\delta/\text{volume}$	Production rate per unit volume
$D$	$300\mu\text{m}^2/\text{s}$	Intracellular diffusion constant
$\delta$	$0.001 ; 1 \cdot 10^{-5} \text{s}^{-1}$	Degradation constant
$l$	$10 ; 100\mu\text{m}$	Cell length
$q$	$1 ; 10\mu\text{m}/\text{s}$	Effective wall permeability for symplastic transport
$p$		Effective efflux permeability for apoplastic transport; often different values are used for different cell faces, which is then indicated with subscripts.
$p_0$	$0 ; 1 ; 10\mu\text{m}/\text{s}$	1D only: the low $p$ value, on the “left” side of the cell
$p_l$	$20\mu\text{m}/\text{s}$	1D only: the high $p$ value, on the “right” side of the cell
$r$	$\max(p)$	Effective influx permeability for apoplastic transport; typically equals the (highest) value of $p$ used in a simulation, i.e. 2 or $20\mu\text{m}/\text{s}$ .

**B**

Quantity	Units	Comments
$C_{i,x}$	a.u.	Local concentration (in this case (1D) in cell $i$ at point $x$ )
$J_{i,x}$	$(a.u./\mu m^2/s)$	Flux through cell $i$ at point $x$ within the cell ( $x \in (0, l)$ ) (positional information as used in 1D)
$D_{eff}$	$\#cells^2/s$	effective diffusion constant ( $\delta$ dependent) (see appendix A.1.2)
$D'_{eff}$	$\mu m^2/s$	effective diffusion constant ( $\delta$ dependent) (see appendix A.1.2)
$D_{S,eff}$	$\#cells^2/s$	$= \frac{Dq}{l(D+ql)}$ ; “simple” effective diffusion constant (see appendix A.1.2)
$D'_{S,eff}$	$\mu m^2/s$	$= \frac{Dql}{D+ql}$ ; “simple” effective diffusion constant (see appendix A.1.2)
$\lambda$	$\# cells$	characteristic length (see appendix A.1.2)
$\lambda'$	$\mu m$	characteristic length (see appendix A.1.2)
$\ominus$	$\sinh\left(\sqrt{\frac{\delta}{D}}l\right)$	short hand notation used in appendices
$\boxplus$	$\cosh\left(\sqrt{\frac{\delta}{D}}l\right)$	short hand notation used in appendices
$\log$	–	natural logarithm

**C**

Parameter	Default(s)	Comments
$D_A$	variable	Diffusion constant of $A$ (“activator”)
$D_H$	$100\mu m^2/s$	Diffusion constant of $H$ (“inhibitor”)
$\kappa$	0.3 a.u.	Saturation term of $A$ production
$i_A$	$0.0001 a.u./s$	Constant base production of $A$ (to render the $A, H = 0, 0$ equilibrium unstable)
$i_H$	$0.0001 a.u./s$	idem for $H$
$\mu_A$	$1 s^{-1}$	Degradation rate of $A$
$\nu_H$	$1 s^{-1}$	Degradation rate of $H$
$\rho$	$1 a.u./s$	Base rate of $A$ -dependent production (of both $A$ and $H$ )
$X$	$50 - 200\mu m$	Size of simulation domain (square, periodic)
$T$	$1000, 10000 s$	Time

Table A.1: **Overview of model parameters and mathematical symbols** **A**: parameters for symplastic and/or apoplastic transport. **B**: other quantities. **C**: Turing like model (figure 2.9).



# B

---

## Playing the auxin pipeline – consequences of different mechanisms for local auxin accumulation

---

### B.1 1D model

#### B.1.1 Definition and notation

For an overview of the model and parameters, see figure 5.1A. Notations:

$c_{i,x}$	[IAA] in cell $i$ at position $x \in [0, l_i]$
$\bar{c}_i$	average [IAA] in cell $i$ . At steady state and without production $\bar{c}_i = \frac{c_{i,0} + c_{i,l_i}}{2}$
$\bar{c}$	Resting state concentration, dependent on the resting state flux $\bar{J}$ and most model parameters (see ....) (average concentration)
$P_{inf}$	assuming $P_{inf} = P_{in,i} = P_{in,j} \forall i, j$ (in the embedding tissue)
$P_{eff,0}$	assuming $P_{eff,0} = P_{eff,i,L} = P_{eff,j,L} \forall i, j$ (in the embedding tissue)
$P_{eff,l}$	assuming $P_{eff,l} = P_{eff,i,R} = P_{eff,j,R} \forall i, j$ (in the embedding tissue)
$\bar{J}_{i,x}$	[IAA] flux through cell $i$ at position $x$ . Indices may be dropped as above for steady states if it is constant over a cell or region of cells (without production/decay).
$\hat{P}_{in}$	assuming $P_{inf} = P_{in,i} = P_{in,j} \forall i, j$ (in the CA)
$\hat{P}_{eff,0}$	assuming $P_{eff,0} = P_{eff,i,L} = P_{eff,j,L} \forall i, j$ (in the CA)
$\hat{P}_{eff,l}$	assuming $P_{eff,l} = P_{eff,i,R} = P_{eff,j,R} \forall i, j$ (in the CA)
$\hat{c}$	Target concentration for a given change (average concentration)

#### B.1.2 General steady state solution for a homogeneous tissue (no production or decay)

In this section we derive a general solution for the average concentration (equivalently: the concentration in the middle of the cell) in each cell in a tissue (segment) of identical cells with identical parameters.

The flux over a wall can be observed from two sides:

$$J_{i,l} = P_{eff,l}c_{i,l} - P_{inf}w_{i,i+1} \quad (\text{B.1})$$

$$J_{i+1,0} = P_{inf}w_{i,i+1} - P_{eff,0}c_{i+1,0} \quad (\text{B.2})$$

As we consider a 1D system, these two fluxes have to be the same. Equating them gives the steady state concentration in the wall ( $w_{i,i+1}$ ):

$$w_{i,i+1} = \frac{P_{eff,l}c_{i,l} - P_{eff,0}c_{i+1,0}}{2P_{inf}} \quad (\text{B.3})$$

This we can fill in in either of the equations for the flux over the wall:

$$J_{i,l} = J_{i+1,0} = \frac{1}{2}P_{eff,l}c_{i,l} - \frac{1}{2}P_{eff,0}c_{i+1,0}. \quad (\text{B.4})$$

Interestingly, as  $P_{inf}$  no longer appears in this equation, it implies that the effective influx permeability  $P_{inf}$  does not affect the steady state flux through the wall, as long as it is the same on both sides of the wall and larger than zero.

Within the cell, the flux obeys

$$J_{D_{i,x}} = -D \frac{\partial}{\partial x} c_{i,x}. \quad (\text{B.5})$$

Without production or decay, mass conservation requires that this flux is constant everywhere in the cell, so

$$J_{D_i} = \frac{-D}{l} (c_{i,l} - c_{i,0}). \quad (\text{B.6})$$

At steady state, the flux must be constant everywhere, so we drop the indices and replace all fluxes by  $\bar{J}$ , a flux of yet undetermined magnitude and direction. Combining the two equations, we obtain:

$$\bar{J} = \frac{1}{2}P_{eff,l} \left( c_{i,0} - \bar{J} \frac{l}{D} \right) - \frac{1}{2}P_{eff,0}c_{i+1,0}. \quad (\text{B.7})$$

Which is equivalent to the following expression for  $c_{i+1,0}$ :

$$c_{i+1,0} = \frac{P_{eff,l}}{P_{eff,0}} c_{i,0} - \left( \frac{lP_{eff,l}}{DP_{eff,0}} + \frac{2}{P_{eff,0}} \right) \bar{J} \quad (\text{B.8})$$

With the following substitutions this can be rewritten as:

$$\xi = \frac{P_{eff,l}}{P_{eff,0}} \quad (\text{B.9})$$

$$\zeta = \frac{lP_{eff,l}}{DP_{eff,0}} + \frac{2}{P_{eff,0}} \quad (\text{B.10})$$

$$c_{i+1,0} = \xi c_{i,0} - \zeta \bar{J} \quad (\text{B.11})$$

Using this expression to calculate the concentration at the beginning of consecutive cells, it is straightforward to see:

$$c_{i+2,0} = \xi^2 c_{i,0} - \zeta \bar{J}(1 + \xi) \quad (\text{B.12})$$

$$\vdots$$

$$c_{i+n,0} = \xi^n c_{i,0} - \zeta \bar{J} \sum_{k=0}^{n-1} \xi^k \quad (\text{B.13})$$

Using that  $\sum_{k=0}^{n-1} \xi^k = \frac{1-\xi^n}{1-\xi}$ ,  $\forall \xi \neq 1$  the expression for  $c_{i+n,0}$  becomes:

$$c_{i+n,0} = \begin{cases} \xi^n c_{i,0} - \zeta \bar{J} \frac{1-\xi^n}{1-\xi} & , \quad \xi \neq 1 \\ c_{i,0} - n \zeta \bar{J} & , \quad \xi = 1 \quad (P_{eff,0} = P_{eff,l}) \end{cases} \quad (\text{B.14})$$

Note that if the steady state flux is set by the same tissue,  $\bar{J} = 0$  if  $P_{eff,0} = P_{eff,l}$ .

To translate this to average concentrations we use the linear intracellular gradient of this case (no production/decay):

$$\bar{c}_{i+n} = c_{i+n,0} - \bar{J} \frac{l}{2D} \quad (\text{B.15})$$

$$c_{i,0} = \bar{c}_i + \bar{J} \frac{l}{2D} \quad (\text{B.16})$$

$$\bar{c}_{i+n} = \begin{cases} \xi^n \bar{c}_i - \bar{J}(1 - \xi^n) \frac{l}{2D} - \zeta \bar{J} \frac{1-\xi^n}{1-\xi} & , \quad \xi \neq 1 \\ \bar{c}_i - n \zeta \bar{J} & , \quad \xi = 1 \quad (P_{eff,0} = P_{eff,l}) \end{cases} \quad (\text{B.17})$$

Removing  $\xi$  and  $\zeta$  by reversing the substitutions, this is:

$$\bar{c}_{i+n} = \begin{cases} \left( \frac{P_{eff,l}}{P_{eff,0}} \right)^n \bar{c}_i + \bar{J} \left( 1 - \left( \frac{P_{eff,l}}{P_{eff,0}} \right)^n \right) \left( \frac{\frac{l}{2D}(P_{eff,0} + P_{eff,l}) + 2}{P_{eff,l} - P_{eff,0}} \right) & , \quad P_{eff,0} \neq P_{eff,l} \\ \bar{c}_i - n \bar{J} \left( \frac{l}{D} + \frac{2}{P_{eff}} \right) & , \quad P_{eff,0} = P_{eff,l} \end{cases} \quad (\text{B.18})$$

From this we can learn several things. If both effective efflux permeabilities are the same, all cells will have the same concentration precisely if there is no net flux. Otherwise, the concentration will increase or decrease linearly from cell to cell, depending on the direction of the flux. Equivalently, the concentration will increase linearly with every cell further upstream.

Moreover, if  $\frac{P_{eff,l}}{P_{eff,0}} \neq 1$  is close to 1, the concentration can change only with small steps from cell to cell, because  $\xi^n$  only slowly deviates from 1 and  $(1 - \xi^n)$  long remains close to 0. Along the same lines, the concentration will likely change faster towards a fixed point of the flux  $\bar{J}$  is large.

### B.1.3 Resting state

We saw in the previous section that flux and (average) concentration are related. In this section we will show that along a tissue, the concentration will tend to a certain level,

determined by flux and the other parameters. If there is no net production or decay, the concentration will tend towards this level and it is (mathematically) possible to construct an infinitely long tissue with the same concentration in every cell, if and only if it obeys this relation between flux and average concentration. This relation we call the *resting state*.

The concept of a resting state makes sense only if there is no net production or decay. We will restrict ourselves to the simple case without any production or decay. Any combination of flux and concentration obeying this definition of the resting state would also be a fixed point of the recursive formula B.18. This will serve as a check in the end.

As in the previous section, the flux over the wall *within a segment of identical cells* follows

$$J_{i,l} = J_{i+1,0} = \frac{1}{2}P_{eff,l}c_{i,l} - \frac{1}{2}P_{eff,0}c_{i+1,0}. \quad (B.19)$$

and within the cell, the flux obeys

$$J_{D_i} = \frac{-D}{l}(c_{i,l} - c_{i,0}). \quad (B.20)$$

Equating the diffusive flux to the flux over the wall, we can obtain an expression for  $c_{i,l}$  in terms of other concentrations:

$$c_{i,l} = \frac{\frac{D}{l}c_{i,0} + \frac{1}{2}P_{eff,0}c_{i+1,0}}{\frac{D}{l} + \frac{1}{2}P_{eff,l}} \quad (B.21)$$

We defined the resting state as the concentration that an infinitely long tissue would settle on. This means that at the resting state  $c_{i,0} = c_{i+1,0}$ , so

$$c_{i,l} = c_{i,0} \frac{\frac{D}{l} + \frac{1}{2}P_{eff,0}}{\frac{D}{l} + \frac{1}{2}P_{eff,l}} \quad (B.22)$$

With this relation, the (diffusive) flux becomes:

$$J = c_{i,0} \frac{D}{l} \left( \frac{\frac{1}{2}P_{eff,l} - \frac{1}{2}P_{eff,0}}{\frac{D}{l} + \frac{1}{2}P_{eff,l}} \right) \quad (B.23)$$

To express this in terms of the average concentration, we use that without production and decay

$$\bar{c} = \frac{c_{i,0} + c_{i,l}}{2} = \frac{c_{i,0}}{2} \left( \frac{2\frac{D}{l} + \frac{1}{2}P_{eff,l} + \frac{1}{2}P_{eff,0}}{\frac{D}{l} + \frac{1}{2}P_{eff,l}} \right) \quad (B.24)$$

and inversely

$$c_{i,0} = \bar{c} \left( \frac{2\frac{D}{l} + P_{eff,l}}{2\frac{D}{l} + \frac{1}{2}P_{eff,l} + \frac{1}{2}P_{eff,0}} \right) \quad (B.25)$$

Resulting in the resting state relationship:

$$\bar{J} = \bar{c} \left( \frac{P_{eff,l} - P_{eff,0}}{2 + \frac{l}{2D}(P_{eff,l} + P_{eff,0})} \right) \quad (B.26)$$

or its inverse:

$$\bar{c} = \bar{J} \left( \frac{2 + \frac{1}{2D}(P_{eff,l} + P_{eff,0})}{P_{eff,l} - P_{eff,0}} \right) \quad (\text{B.27})$$

Substituting the latter in equation B.18 shows that if  $\bar{c}_i$  is at resting state, so will be  $\bar{c}_{i+n}$ . This shows that the resting state is indeed a fixed point of equation B.18.

### Deviations from the resting state

If the concentration in cell  $i$  deviates from the resting state, how does this affect the steady state profile? For simplicity we rewrite the general expression for the tissue level concentration profile (equation B.18). For  $P_{eff,l} \neq P_{eff,0}$ , this has the following general shape:

$$\bar{c}_{i+n} = \left( \frac{P_{eff,l}}{P_{eff,0}} \right)^n \bar{c}_i + \bar{J} \left( 1 - \left( \frac{P_{eff,l}}{P_{eff,0}} \right)^n \right) K \quad (\text{B.28})$$

with  $K$  some constant depending on the model parameters. It is straightforward to see that the resting state concentration  $\bar{c} = \bar{J}K$ . For the non-resting state concentration  $\bar{c}_i$  we write:  $\bar{c}_i = \bar{c} + \varepsilon = \bar{J}K + \varepsilon$ , ( $\varepsilon \neq 0$ ). We get:

$$\bar{c}_{i+n} = \left( \frac{P_{eff,l}}{P_{eff,0}} \right)^n \varepsilon + \bar{J}K = \bar{c} + \left( \frac{P_{eff,l}}{P_{eff,0}} \right)^n \varepsilon. \quad (\text{B.29})$$

This means that if  $P_{eff,l} > P_{eff,0}$ , the deviation from the resting state increases with increasing  $i$  (or: decreases with decreasing  $i$ ) and vice versa the deviation decreases with increasing  $i$  if  $P_{eff,l} < P_{eff,0}$ . If the resting state flux  $\bar{J}$  is towards the side with the largest  $P_{eff}$  (the “natural” direction), deviations increase when following the concentration further downstream.

This formulation makes it easy to see that the closer  $\frac{P_{eff,l}}{P_{eff,0}}$  is to 1, the more cells are needed to halve a deviation from the resting state.

### B.1.4 Target concentration

We define the *target concentration* ( $\hat{c}$ ) as the equivalent of the resting state in the CA: the concentration that would be reached in the CA if it were infinitely long, with the steady state flux  $\bar{J}$  set by an embedding tissue at resting state, with concentration  $\bar{c}$ . Writing  $\hat{P}_{eff,0}$  etc for parameters within the CA and  $P_{eff,0}$  etc for the embedding tissue, the target concentration follows directly from the definition:

$$\hat{c} = \bar{J} \left( \frac{2 + \frac{1}{2D}(\hat{P}_{eff,l} + \hat{P}_{eff,0})}{\hat{P}_{eff,l} - \hat{P}_{eff,0}} \right) \quad (\text{B.30})$$

$$\hat{c} = \bar{c} \frac{P_{eff,l} - P_{eff,0}}{\hat{P}_{eff,l} - \hat{P}_{eff,0}} \cdot \frac{\frac{1}{2D}(\hat{P}_{eff,l} + \hat{P}_{eff,0}) + 2}{\frac{1}{2D}(P_{eff,l} + P_{eff,0}) + 2} \quad (\text{B.31})$$

### B.1.5 Adding symplastic transport

To assess the impact of symplastic transport, we will model the collective effect of all plasmodesmata in a cell-cell interface as an effective permeability,  $P_{sym}$ . This approach is also used by [163]. We again consider the case without production or decay. The resulting fluxes over the wall are:

$$J_{i,l} = (P_{eff,l} + P_{sym})c_{i,l} - P_{inf}w_{i,i+1} - P_{sym}c_{i+1,0} \quad (B.32)$$

$$J_{i+1,0} = P_{sym}c_{i,l}P_{inf}w_{i,i+1} - (P_{eff,0} + P_{sym})c_{i+1,0} \quad (B.33)$$

As we consider a 1D system, these two fluxes have to be the same. Equating them gives the steady state concentration in the wall ( $w_{i,i+1}$ ):

$$w_{i,i+1} = \frac{P_{eff,l}c_{i,l} - P_{eff,0}c_{i+1,0}}{2P_{inf}} \quad (B.34)$$

This we can fill in in either of the equations for the flux over the wall:

$$J_{i,l} = J_{i+1,0} = \left( \frac{1}{2}P_{eff,l} + P_{sym} \right) c_{i,l} - \left( \frac{1}{2}P_{eff,0} + P_{sym} \right) c_{i+1,0}. \quad (B.35)$$

Again,  $P_{inf}$  no longer appears in this equation, as without symplastic transport.

The transport mechanism inside the cell remains simple diffusion, with the following intracellular flux:

$$J_{Di} = \frac{-D}{l}(c_{i,l} - c_{i,0}). \quad (B.36)$$

At steady state, the flux must be constant everywhere, so we drop the indices and replace all fluxes by  $\bar{J}$ , a flux of yet undetermined magnitude and direction. Combining the two equations, we obtain:

$$\bar{J} = \left( \frac{1}{2}P_{eff,l} + P_{sym} \right) \left( c_{i,0} - \bar{J} \frac{l}{D} \right) - \left( \frac{1}{2}P_{eff,0} + P_{sym} \right) c_{i+1,0}. \quad (B.37)$$

Which is equivalent to the following expression for  $c_{i+1,0}$ :

$$c_{i+1,0} = \frac{P_{eff,l} + 2P_{sym}}{P_{eff,0} + 2P_{sym}} c_{i,0} - \left( \frac{\frac{l}{D}(P_{eff,l} + 2P_{sym}) + 2}{P_{eff,0} + 2P_{sym}} \right) \bar{J} \quad (B.38)$$

With the following substitutions this can be rewritten as:

$$\xi = \frac{P_{eff,l} + 2P_{sym}}{P_{eff,0} + 2P_{sym}} \quad (B.39)$$

$$\zeta = \frac{\frac{l}{D}(P_{eff,l} + 2P_{sym}) + 2}{P_{eff,0} + 2P_{sym}} \quad (B.40)$$

$$c_{i+1,0} = \xi c_{i,0} - \zeta \bar{J} \quad (B.41)$$

Which is exactly the same expression as without symplastic transport, so

$$c_{i+n,0} = \begin{cases} \xi^n c_{i,0} - \zeta \bar{J} \frac{1-\xi^n}{1-\xi} & , \quad \xi \neq 1 \\ c_{i,0} - n \zeta \bar{J} & , \quad \xi = 1 \quad (P_{eff,0} = P_{eff,l}) \end{cases} \quad (\text{B.42})$$

Note that if the steady state flux is set by the same tissue,  $\bar{J} = 0$  if  $P_{eff,0} = P_{eff,l}$ .

To translate this to average concentrations we use the linear intracellular gradient of this case (no production/decay):

$$\bar{c}_{i+n} = c_{i+n,0} - \bar{J} \frac{l}{2D} \quad (\text{B.43})$$

$$c_{i,0} = \bar{c}_i + \bar{J} \frac{l}{2D} \quad (\text{B.44})$$

$$\bar{c}_{i+n} = \begin{cases} \xi^n \bar{c}_i - \bar{J} (1 - \xi^n) \frac{l}{2D} - \zeta \bar{J} \frac{1-\xi^n}{1-\xi} & , \quad \xi \neq 1 \\ \bar{c}_i - n \zeta \bar{J} & , \quad \xi = 1 \quad (P_{eff,0} = P_{eff,l}) \end{cases} \quad (\text{B.45})$$

Removing  $\xi$  and  $\zeta$  by reversing the substitutions, this is:

$$\bar{c}_{i+n} = \begin{cases} \left( \frac{P_{eff,l} + 2P_{sym}}{P_{eff,0} + 2P_{sym}} \right)^n \bar{c}_i + \bar{J} \left( 1 - \left( \frac{P_{eff,l} + 2P_{sym}}{P_{eff,0} + 2P_{sym}} \right)^n \right) \left( \frac{\frac{l}{2D} (P_{eff,0} + P_{eff,l} + 4P_{sym}) + 2}{P_{eff,l} - P_{eff,0}} \right) & , \quad P_{eff,0} \neq P_{eff,l} \\ \bar{c}_i - n \bar{J} \left( \frac{l}{D} + \frac{2}{P_{eff} + 2P_{sym}} \right) & , \quad P_{eff,0} = P_{eff,l} \end{cases} \quad (\text{B.46})$$

Because  $\xi = \frac{P_{eff,l} + 2P_{sym}}{P_{eff,0} + 2P_{sym}} \rightarrow 1$  for  $P_{sym} \rightarrow \infty$  increasing symplastic transport results in increasingly slower changes in the concentration. This means that with symplastic transport a larger number of cells is required to reach the resting state or target concentration, compared to without symplastic transport (equation B.46).

Again, the resting state  $\bar{c}$  is a fixed point of equation B.46, so with symplastic transport:

$$\bar{c} = \bar{J} \left( \frac{\frac{l}{2D} (P_{eff,0} + P_{eff,l} + 4P_{sym}) + 2}{P_{eff,l} - P_{eff,0}} \right) \quad (\text{B.47})$$

Analogously to the case without symplastic transport, the target concentration in the CA ( $\hat{c}$ ) becomes:

$$\hat{c} = \bar{c} \frac{P_{eff,l} - P_{eff,0}}{\hat{P}_{eff,l} - \hat{P}_{eff,0}} \cdot \frac{\frac{l}{2D} (\hat{P}_{eff,l} + \hat{P}_{eff,0} + 4P_{sym}) + 2}{\frac{l}{2D} (P_{eff,l} + P_{eff,0} + 4P_{sym}) + 2} \quad (\text{B.48})$$

with  $\hat{P}_{eff,l}$  etc parameters for inside the CA and  $P_{eff,l}$  etc for outside. As before, this does not include the influx permeability ( $P_{inf}$ ). For Effl $\downarrow$  the target concentration increases with increasing  $P_{sym}$ .





# References

- [1] C. Kuhlemeier, *Phyllotaxis.*, Trends Plant Sci **12**, 143 (2007).
- [2] J. Traas, *Phyllotaxis.*, Development **140**, 249 (2013).
- [3] H. Jonsson, M. G. Heisler, B. E. Shapiro, E. M. Meyerowitz, and E. Mjolsness, *An auxin-driven polarized transport model for phyllotaxis.*, Proc Natl Acad Sci U S A **103**, 1633 (2006).
- [4] M. G. Heisler and H. Jonsson, *Modeling auxin transport and plant development*, Journal of Plant Growth Regulation **25**, 302 (2006).
- [5] R. S. Smith, S. Guyomarc'h, T. Mandel, D. Reinhardt, C. Kuhlemeier, and P. Prusinkiewicz, *A plausible model of phyllotaxis.*, Proc Natl Acad Sci U S A **103**, 1301 (2006).
- [6] S. Stoma, M. Lucas, J. Chopard, M. Schaedel, J. Traas, and C. Godin, *Flux-based transport enhancement as a plausible unifying mechanism for auxin transport in meristem development.*, PLoS Comput Biol **4**, e1000207 (2008).
- [7] E. M. Bayer, R. S. Smith, T. Mandel, N. Nakayama, M. Sauer, P. Prusinkiewicz, and C. Kuhlemeier, *Integration of transport-based models for phyllotaxis and midvein formation.*, Genes Dev **23**, 373 (2009).
- [8] M. G. Heisler, O. Hamant, P. Krupinski, M. Uyttewaal, C. Ohno, H. Jonsson, J. Traas, and E. M. Meyerowitz, *Alignment between PIN1 polarity and microtubule orientation in the shoot apical meristem reveals a tight coupling between morphogenesis and auxin transport.*, PLoS Biol **8**, e1000516 (2010).
- [9] D. Müller and O. Leyser, *Auxin, cytokinin and the control of shoot branching.*, Ann Bot **107**, 1203 (2011).
- [10] M. A. Domagalska and O. Leyser, *Signal integration in the control of shoot branching.*, Nat Rev Mol Cell Biol **12**, 211 (2011).
- [11] P. Prusinkiewicz, S. Crawford, R. S. Smith, K. Ljung, T. Bennett, V. Ongaro, and O. Leyser, *Control of bud activation by an auxin transport switch.*, Proc Natl Acad Sci U S A **106**, 17431 (2009).
- [12] B. D. Rybel, B. Möller, S. Yoshida, I. Grabowicz, P. B. de Reuille, S. Boeren, R. S. Smith, J. W. Borst, and D. Weijers, *A bhlh complex controls embryonic vascular tissue establishment and indeterminate growth in arabidopsis.*, Dev Cell , (2013).
- [13] C. Kidner, V. Sundaresan, K. Roberts, and L. Dolan, *Clonal analysis of the arabidopsis root confirms that position, not lineage, determines cell fate.*, Planta **211**, 191 (2000).
- [14] S. Artavanis-Tsakonas, M. D. Rand, and R. J. Lake, *Notch signaling: cell fate control and signal integration in development.*, Science **284**, 770 (1999).
- [15] V. Bolós, J. Grego-Bessa, and J. L. de la Pompa, *Notch signaling in development and cancer.*, Endocr Rev **28**, 339 (2007).
- [16] J. R. K. Seifert and M. Mlodzik, *Frizzled/pcp signalling: a conserved mechanism regulating cell polarity and directed motility.*, Nat Rev Genet **8**, 126 (2007).
- [17] H. Strutt and D. Strutt, *Long-range coordination of planar polarity in drosophila.*, Bioessays **27**, 1218 (2005).
- [18] B. Aigouy, R. Farhadifar, D. B. Staple, A. Sagner, J.-C. Röper, F. Jülicher, and S. Eaton, *Cell flow reorients the axis of planar polarity in the wing epithelium of drosophila.*, Cell **142**, 773 (2010).

- [19] M. Grebe, *The patterning of epidermal hairs in arabidopsis—updated.*, *Curr Opin Plant Biol* **15**, 31 (2012).
- [20] Y. Helariutta, H. Fukaki, J. Wysocka-Diller, K. Nakajima, J. Jung, G. Sena, M. T. Hauser, and P. N. Benfey, *The short-root gene controls radial patterning of the arabidopsis root through radial signaling.*, *Cell* **101**, 555 (2000).
- [21] H. Cui, M. P. Levesque, T. Vernoux, J. W. Jung, A. J. Paquette, K. L. Gallagher, J. Y. Wang, I. Blilou, B. Scheres, and P. N. Benfey, *An evolutionarily conserved mechanism delimiting shr movement defines a single layer of endodermis in plants.*, *Science* **316**, 421 (2007).
- [22] R. Bernal, E. Rojas, and J. Dumais, *The mechanics of tip growth morphogenesis: What we have learned from rubber balloons*, *J Mech Mater Struct* **2**, 1157 (2007).
- [23] F. Batenburg, R. Jonker, and J. Kijne, *Rhizobium induces marked root hair curling by redirection of tip growth: a computer simulation*, *Physiologia Plantarum* **66**, 476 (1986).
- [24] S. Bartnicki-Garcia, F. Hergert, and G. Gierz, *Computer simulation of fungal morphogenesis and the mathematical basis for hyphal (tip) growth*, *Protoplasma* **153**, 46 (1989).
- [25] J. Esseling, F. Lhuissier, and A. Emons, *Nod factor-induced root hair curling: Continuous polar growth towards the point of nod factor application*, *Plant Physiology* **132**, 1982 (2003).
- [26] K. M. Jones, H. Kobayashi, B. W. Davies, M. E. Taga, and G. C. Walker, *How rhizobial symbionts invade plants: the Sinorhizobium-Medicago model*, *Nature Reviews Microbiology* **5**, 619 (2007).
- [27] A. Timmers, M. Auriac, and G. Truchet, *Refined analysis of early symbiotic steps of the rhizobium-medicago interaction in relationship with microtubular cytoskeleton rearrangements*, *Development* **126**, 3617 (1999).
- [28] A. Hirsch, *Developmental biology of legume nodulation*, *New Phytologist* **122**, 211 (1992).
- [29] R. V. Penmetse, J. A. Frugoli, L. S. Smith, S. R. Long, and D. R. Cook, *Dual genetic pathways controlling nodule number in Medicago truncatula.*, *Plant Physiol* **131**, 998 (2003).
- [30] S. Magori, E. Oka-Kira, S. Shibata, Y. Umehara, H. Kouchi, Y. Hase, A. Tanaka, S. Sato, S. Tabata, and M. Kawaguchi, *TOO MUCH LOVE, a Root Regulator Associated with the Long-Distance Control of Nodulation in Lotus japonicus.*, *Mol Plant Microbe Interact* **22**, 259 (2009).
- [31] A. M. Hirsch, T. V. Bhuvaneswari, J. G. Torrey, and T. Bisseling, *Early nodulin genes are induced in alfalfa root outgrowths elicited by auxin transport inhibitors.*, *Proc Natl Acad Sci U S A* **86**, 1244 (1989).
- [32] J. B. Cooper and S. R. Long, *Morphogenetic Rescue of Rhizobium meliloti Nodulation Mutants by trans-Zeatin Secretion.*, *Plant Cell* **6**, 215 (1994).
- [33] J. D. Murray, B. J. Karas, S. Sato, S. Tabata, L. Amyot, and K. Szczygłowski, *A cytokinin perception mutant colonized by Rhizobium in the absence of nodule organogenesis.*, *Science* **315**, 101 (2007).
- [34] J. Plet, A. Wasson, F. Ariel, C. Le Signor, D. Baker, U. Mathesius, M. Crespi, and F. Frugier, *MtCRE1-dependent cytokinin signaling integrates bacterial and plant cues to coordinate symbiotic nodule organogenesis in Medicago truncatula.*, *Plant J* **65**, 622 (2011).
- [35] R. H. M. O. den Camp, S. D. Mita, A. Lillo, Q. Cao, E. Limpens, T. Bisseling, and R. Geurts, *A phylogenetic strategy based on a legume-specific whole genome duplication yields symbiotic cytokinin type-a response regulators.*, *Plant Physiol* **157**, 1203 (2011).
- [36] C. Pacios-Bras, H. R. Schlaman, K. Boot, P. Admiraal, J. M. Langerak, J. Stougaard, and H. P. Spaink, *Auxin distribution in Lotus japonicus during root nodule development.*, *Plant Mol Biol* **52**, 1169 (2003).
- [37] K. Takanashi, A. Sugiyama, and K. Yazaki, *Involvement of auxin distribution in root nodule development of Lotus japonicus*, *Planta* **234**, 73 (2011).

- [38] R. Dello Ioio, K. Nakamura, L. Moubayidin, S. Perilli, M. Taniguchi, M. T. Morita, T. Aoyama, P. Costantino, and S. Sabatini, *A genetic framework for the control of cell division and differentiation in the root meristem.*, Science **322**, 1380 (2008).
- [39] P. Marhavy, A. Bielach, L. Abas, A. Abuzeineh, J. Duclercq, H. Tanaka, M. Pařezová, J. Petrášek, J. Friml, J. Kleine-Vehn, and E. Benková, *Cytokinin modulates endocytic trafficking of pin1 auxin efflux carrier to control plant organogenesis.*, Dev Cell **21**, 796 (2011).
- [40] B. Jones, S. A. Gunnerås, S. V. Petersson, P. Tarkowski, N. Graham, S. May, K. Dolezal, G. Sandberg, and K. Ljung, *Cytokinin regulation of auxin synthesis in arabidopsis involves a homeostatic feedback loop regulated via auxin and cytokinin signal transduction.*, Plant Cell **22**, 2956 (2010).
- [41] W. J. Lucas, B. C. Yoo, and F. Kragler, *Rna as a long-distance information macromolecule in plants.*, Nat Rev Mol Cell Biol **2**, 849 (2001).
- [42] V. Haywood, F. Kragler, and W. J. Lucas, *Plasmodesmata: pathways for protein and ribonucleoprotein signaling.*, Plant Cell **14 Suppl**, S303 (2002).
- [43] K. Furuta, R. Lichtenberger, and Y. Helariutta, *The role of mobile small rna species during root growth and development.*, Curr Opin Cell Biol **24**, 211 (2012).
- [44] S. Bloemendal and U. Kück, *Cell-to-cell communication in plants, animals, and fungi: a comparative review.*, Naturwissenschaften **100**, 3 (2013).
- [45] G. Coruzzi and D. R. Bush, *Nitrogen and carbon nutrient and metabolite signaling in plants.*, Plant Physiol **125**, 61 (2001).
- [46] R. Benjamins and B. Scheres, *Auxin: the looping star in plant development.*, Annu Rev Plant Biol **59**, 443 (2008).
- [47] A. N. Stepanova, J. Yun, L. M. Robles, O. Novak, W. He, H. Guo, K. Ljung, and J. M. Alonso, *The arabidopsis yucca1 flavin monooxygenase functions in the indole-3-pyruvic acid branch of auxin biosynthesis.*, Plant Cell **23**, 3961 (2011).
- [48] Y. Mano and K. Nemoto, *The pathway of auxin biosynthesis in plants.*, J Exp Bot **63**, 2853 (2012).
- [49] A. N. Stepanova, J. Robertson-Hoyt, J. Yun, L. M. Benavente, D. Y. Xie, K. Dolezal, A. Schlereth, G. Jurgens, and J. M. Alonso, *TAA1-mediated auxin biosynthesis is essential for hormone crosstalk and plant development.*, Cell **133**, 177 (2008).
- [50] Y. Cheng, X. Dai, and Y. Zhao, *Auxin biosynthesis by the YUCCA flavin monooxygenases controls the formation of floral organs and vascular tissues in Arabidopsis.*, Genes Dev **20**, 1790 (2006).
- [51] Y. Cheng, X. Dai, and Y. Zhao, *Auxin synthesized by the yucca flavin monooxygenases is essential for embryogenesis and leaf formation in arabidopsis.*, Plant Cell **19**, 2430 (2007).
- [52] A. Gallavotti, S. Barazesh, S. Malcomber, D. Hall, D. Jackson, R. J. Schmidt, and P. McSteen, *sparse inflorescence1 encodes a monocot-specific yucca-like gene required for vegetative and reproductive development in maize.*, Proc Natl Acad Sci U S A **105**, 15196 (2008).
- [53] A. W. Woodward and B. Bartel, *Auxin: regulation, action, and interaction.*, Ann Bot **95**, 707 (2005).
- [54] R. Swarup, E. M. Kramer, P. Perry, K. Knox, H. M. Leyser, J. Haseloff, G. T. Beemster, R. Bhalarao, and M. J. Bennett, *Root gravitropism requires lateral root cap and epidermal cells for transport and response to a mobile auxin signal.*, Nat Cell Biol **7**, 1057 (2005).
- [55] R. Swarup, J. Friml, A. Marchant, K. Ljung, G. Sandberg, K. Palme, and M. Bennett, *Localization of the auxin permease aux1 suggests two functionally distinct hormone transport pathways operate in the arabidopsis root apex.*, Genes & Development **15**, 2648 (2001).
- [56] R. Swarup, J. Kargul, A. Marchant, D. Zadik, A. Rahman, R. Mills, A. Yemm, S. May, L. Williams, P. Millner, S. Tsurumi, I. Moore, R. Napier, I. D. Kerr, and M. J. Bennett,

- Structure-function analysis of the presumptive arabidopsis auxin permease aux1*, Plant Cell Online **16**, 3069 (2004).
- [57] J. Kleine-Vehn, P. Dhonukshe, R. Swarup, M. Bennett, and J. Friml, *Subcellular trafficking of the arabidopsis auxin influx carrier aux1 uses a novel pathway distinct from pin1*, Plant Cell Online **18**, 3171 (2006).
- [58] L. Galweiler, C. Guan, A. Muller, E. Wisman, K. Mendgen, A. Yephremov, and K. Palme, *Regulation of polar auxin transport by AtPIN1 in Arabidopsis vascular tissue.*, Science **282**, 2226 (1998).
- [59] I. A. Paponov, W. D. Teale, M. Trebar, I. Blilou, and K. Palme, *The pin auxin efflux facilitators: evolutionary and functional perspectives.*, Trends Plant Sci **10**, 170 (2005).
- [60] B. Noh, A. S. Murphy, and E. P. Spalding, *Multidrug resistance-like genes of Arabidopsis required for auxin transport and auxin-mediated development.*, Plant Cell **13**, 2441 (2001).
- [61] J. Mravec, M. Kubes, A. Bielach, V. Gaykova, J. Petrasek, P. Skupa, S. Chand, E. Benkova, E. Zazimalova, and J. Friml, *Interaction of PIN and PGP transport mechanisms in auxin distribution-dependent development.*, Development **135**, 3345 (2008).
- [62] E. Benkova, M. Michniewicz, M. Sauer, T. Teichmann, D. Seifertova, G. Jurgens, and J. Friml, *Local, efflux-dependent auxin gradients as a common module for plant organ formation.*, Cell **115**, 591 (2003).
- [63] I. Blilou, J. Xu, M. Wildwater, V. Willemsen, I. Paponov, J. Friml, R. Heidstra, M. Aida, K. Palme, and B. Scheres, *The PIN auxin efflux facilitator network controls growth and patterning in Arabidopsis roots.*, Nature **433**, 39 (2005).
- [64] S. Kepinski and O. Leyser, *The arabidopsis f-box protein tir1 is an auxin receptor.*, Nature **435**, 446 (2005).
- [65] N. Dharmasiri, S. Dharmasiri, and M. Estelle, *The f-box protein tir1 is an auxin receptor.*, Nature **435**, 441 (2005).
- [66] W. M. Gray, S. Kepinski, D. Rouse, O. Leyser, and M. Estelle, *Auxin regulates scf(tir1)-dependent degradation of aux/iaa proteins.*, Nature **414**, 271 (2001).
- [67] E. H. Rademacher, B. Möller, A. S. Lokerse, C. I. Llavata-Peris, W. van den Berg, and D. Weijers, *A cellular expression map of the arabidopsis auxin response factor gene family.*, Plant J **68**, 597 (2011).
- [68] E. H. Rademacher, A. S. Lokerse, A. Schlereth, C. I. Llavata-Peris, M. Bayer, M. Kientz, A. F. Rios, J. W. Borst, W. Lukowitz, G. Jürgens, and D. Weijers, *Different auxin response machineries control distinct cell fates in the early plant embryo.*, Dev Cell **22**, 211 (2012).
- [69] L. I. A. C. Villalobos, S. Lee, C. D. Oliveira, A. Ivetac, W. Brandt, L. Armitage, L. B. Sheard, X. Tan, G. Parry, H. Mao, N. Zheng, R. Napier, S. Kepinski, and M. Estelle, *A combinatorial tir1/afb-aux/iaa co-receptor system for differential sensing of auxin.*, Nat Chem Biol **8**, 477 (2012).
- [70] A. Chini, S. Fonseca, G. Fernández, B. Adie, J. M. Chico, O. Lorenzo, G. García-Casado, I. López-Vidriero, F. M. Lozano, M. R. Ponce, J. L. Micol, and R. Solano, *The jaz family of repressors is the missing link in jasmonate signalling.*, Nature **448**, 666 (2007).
- [71] B. Thines, L. Katsir, M. Melotto, Y. Niu, A. Mandaokar, G. Liu, K. Nomura, S. Y. He, G. A. Howe, and J. Browse, *Jaz repressor proteins are targets of the scf(coi1) complex during jasmonate signalling.*, Nature **448**, 661 (2007).
- [72] S. Robert, J. Kleine-Vehn, E. Barbez, M. Sauer, T. Paciorek, P. Baster, S. Vanneste, J. Zhang, S. Simon, M. Čovanová, K. Hayashi, P. Dhonukshe, Z. Yang, S. Y. Bednarek, A. M. Jones, C. Luschig, F. Aniento, E. Zažímalová, and J. Friml, *Abp1 mediates auxin inhibition of clathrin-dependent endocytosis in arabidopsis.*, Cell **143**, 111 (2010).

- [73] D. Lin, S. Nagawa, J. Chen, L. Cao, X. Chen, T. Xu, H. Li, P. Dhonukshe, C. Yamamuro, J. Friml, B. Scheres, Y. Fu, and Z. Yang, *A rop gtpase-dependent auxin signaling pathway regulates the subcellular distribution of pin2 in arabidopsis roots.*, *Curr Biol* **22**, 1319 (2012).
- [74] X. Chen, S. Naramoto, S. Robert, R. Tejos, C. Löffke, D. Lin, Z. Yang, and J. Friml, *Abp1 and rop6 gtpase signaling regulate clathrin-mediated endocytosis in arabidopsis roots.*, *Curr Biol* **22**, 1326 (2012).
- [75] K. Ljung, R. P. Bhalerao, and G. Sandberg, *Sites and homeostatic control of auxin biosynthesis in Arabidopsis during vegetative growth.*, *Plant J* **28**, 465 (2001).
- [76] A. Marchant, R. Bhalerao, I. Casimiro, J. Eklof, P. J. Casero, M. Bennett, and G. Sandberg, *AUX1 promotes lateral root formation by facilitating indole-3-acetic acid distribution between sink and source tissues in the Arabidopsis seedling.*, *Plant Cell* **14**, 589 (2002).
- [77] S. V. Petersson, A. I. Johansson, M. Kowalczyk, A. Makoveychuk, J. Y. Wang, T. Moritz, M. Grebe, P. N. Benfey, G. Sandberg, and K. Ljung, *An auxin gradient and maximum in the Arabidopsis root apex shown by high-resolution cell-specific analysis of IAA distribution and synthesis.*, *Plant Cell* **21**, 1659 (2009).
- [78] M. Goldsmith, *Movement of pulses of labeled auxin in corn coleoptiles*, *Plant Physiology* **42**, 258 (1967).
- [79] M. Goldsmith, *The polar transport of auxin*, *Annual Review of Plant Physiology* **28**, 439 (1977).
- [80] T. Ulmasov, J. Murfett, G. Hagen, and T. J. Guilfoyle, *Aux/IAA proteins repress expression of reporter genes containing natural and highly active synthetic auxin response elements.*, *Plant Cell* **9**, 1963 (1997).
- [81] G. Brunoud, D. M. Wells, M. Oliva, A. Larrieu, V. Mirabet, A. H. Burrow, T. Beeckman, S. Kepinski, J. Traas, M. J. Bennett, and T. Vernoux, *A novel sensor to map auxin response and distribution at high spatio-temporal resolution.*, *Nature* **482**, 103 (2012).
- [82] E. M. Kramer, *Computer models of auxin transport: a review and commentary.*, *J Exp Bot* **59**, 45 (2008).
- [83] P. Garnett, A. Steinacher, S. Stepney, R. Clayton, and O. Leyser, *Computer simulation: the imaginary friend of auxin transport biology.*, *Bioessays* **32**, 828 (2010).
- [84] G. Mitchison, *The dynamics of auxin transport*, *Proceedings of the Royal Society of London. Series B. Biological Sciences* **209**, 489 (1980).
- [85] M. H. Goldsmith, T. H. Goldsmith, and M. H. Martin, *Mathematical analysis of the chemosmotic polar diffusion of auxin through plant tissues.*, *Proc Natl Acad Sci U S A* **78**, 976 (1981).
- [86] M. H. Martin, M. H. Goldsmith, and T. H. Goldsmith, *On polar auxin transport in plant cells.*, *J Math Biol* **28**, 197 (1990).
- [87] K. Bainbridge, S. Guyomarc'h, E. Bayer, R. Swarup, M. Bennett, T. Mandel, and C. Kuhlemeier, *Auxin influx carriers stabilize phyllotactic patterning.*, *Genes Dev* **22**, 810 (2008).
- [88] A. Rolland-Lagan and P. Prusinkiewicz, *Reviewing models of auxin canalization in the context of leaf vein pattern formation in Arabidopsis*, *Plant Journal* **44**, 854 (2005).
- [89] R. M. Merks, Y. Van de Peer, D. Inze, and G. T. Beemster, *Canalization without flux sensors: a traveling-wave hypothesis.*, *Trends Plant Sci* **12**, 384 (2007).
- [90] K. Wabnik, J. Kleine-Vehn, J. Balla, M. Sauer, S. Naramoto, V. Reinohl, R. M. Merks, W. Govaerts, and J. Friml, *Emergence of tissue polarization from synergy of intracellular and extracellular auxin signaling.*, *Mol Syst Biol* **6**, 447 (2010).
- [91] V. A. Grieneisen, J. Xu, A. F. Maree, P. Hogeweg, and B. Scheres, *Auxin transport is sufficient to generate a maximum and gradient guiding root growth.*, *Nature* **449**, 1008 (2007).

- [92] M. Laskowski, V. A. Grieneisen, H. Hofhuis, C. A. Hove, P. Hogeweg, A. F. Maree, and B. Scheres, *Root system architecture from coupling cell shape to auxin transport.*, PLoS Biol **6**, e307 (2008).
- [93] A. R. Jones, E. M. Kramer, K. Knox, R. Swarup, M. J. Bennett, C. M. Lazarus, H. M. Leyser, and C. S. Grierson, *Auxin transport through non-hair cells sustains root-hair development.*, Nat Cell Biol **11**, 78 (2009).
- [94] A. Bishopp, H. Help, S. El-Showk, D. Weijers, B. Scheres, J. Friml, E. Benkova, A. P. Mahonen, and Y. Helariutta, *A Mutually Inhibitory Interaction between Auxin and Cytokinin Specifies Vascular Pattern in Roots.*, Curr Biol **21**, 917 (2011).
- [95] H. Sakakibara, *Cytokinins: activity, biosynthesis, and translocation.*, Annu Rev Plant Biol **57**, 431 (2006).
- [96] B. Muller and J. Sheen, *Advances in cytokinin signaling.*, Science **318**, 68 (2007).
- [97] K. Caesar, A. M. K. Thamm, J. Witthöft, K. Elgass, P. Huppenberger, C. Grefen, J. Horak, and K. Harter, *Evidence for the localization of the arabidopsis cytokinin receptors ahk3 and ahk4 in the endoplasmic reticulum.*, J Exp Bot **62**, 5571 (2011).
- [98] A. Cedzich, H. Stransky, B. Schulz, and W. B. Frommer, *Characterization of cytokinin and adenine transport in arabidopsis cell cultures.*, Plant Physiol **148**, 1857 (2008).
- [99] B. Gillissen, L. Bürkle, B. André, C. Kühn, D. Rentsch, B. Brandl, and W. B. Frommer, *A new family of high-affinity transporters for adenine, cytosine, and purine derivatives in arabidopsis.*, Plant Cell **12**, 291 (2000).
- [100] L. Burkler, A. Cedzich, C. Dopke, H. Stransky, S. Okumoto, B. Gillissen, C. Kuhn, and W. B. Frommer, *Transport of cytokinins mediated by purine transporters of the PUP family expressed in phloem, hydathodes, and pollen of Arabidopsis.*, Plant J **34**, 13 (2003).
- [101] N. Hirose, N. Makita, T. Yamaya, and H. Sakakibara, *Functional characterization and expression analysis of a gene, osent2, encoding an equilibrative nucleoside transporter in rice suggest a function in cytokinin transport.*, Plant Physiol **138**, 196 (2005).
- [102] N. Hirose, K. Takei, T. Kuroha, T. Kamada-Nobusada, H. Hayashi, and H. Sakakibara, *Regulation of cytokinin biosynthesis, compartmentalization and translocation.*, J Exp Bot **59**, 75 (2008).
- [103] A. Bishopp, S. Lehesranta, A. Vaten, H. Help, S. El-Showk, B. Scheres, K. Helariutta, A. P. Mahonen, H. Sakakibara, and Y. Helariutta, *Phloem-transported cytokinin regulates polar auxin transport and maintains vascular pattern in the root meristem.*, Curr Biol **21**, 927 (2011).
- [104] A. Vátén, J. Dettmer, S. Wu, Y.-D. Stierhof, S. Miyashima, S. R. Yadav, C. J. Roberts, A. Campilho, V. Bulone, R. Lichtenberger, S. Lehesranta, A. P. Mähönen, J.-Y. Kim, E. Jokitalo, N. Sauer, B. Scheres, K. Nakajima, A. Carlsbecker, K. L. Gallagher, and Y. Helariutta, *Callose biosynthesis regulates symplastic trafficking during root development.*, Dev Cell **21**, 1144 (2011).
- [105] A. Levy, M. Erlanger, M. Rosenthal, and B. L. Epel, *A plasmodesmata-associated beta-1,3-glucanase in arabidopsis.*, Plant J **49**, 669 (2007).
- [106] S. Dashevskaya, R. B. Kopito, R. Friedman, M. Elbaum, and B. L. Epel, *Diffusion of anionic and neutral gfp derivatives through plasmodesmata in epidermal cells of nicotiana benthamiana.*, Protoplasma **234**, 13 (2008).
- [107] B. Terry and A. Robards, *Hydrodynamic radius alone governs the mobility of molecules through plasmodesmata.*, Planta **171**, 145 (1987).
- [108] A. J. Maule, *Plasmodesmata: structure, function and biogenesis.*, Curr Opin Plant Biol **11**, 680 (2008).

- [109] T. M. Burch-Smith and P. C. Zambryski, *Plasmodesmata paradigm shift: regulation from without versus within.*, *Annu Rev Plant Biol* **63**, 239 (2012).
- [110] Y. Benitez-Alfonso, C. Faulkner, C. Ritzenthaler, and A. J. Maule, *Plasmodesmata: gateways to local and systemic virus infection.*, *Mol Plant Microbe Interact* **23**, 1403 (2010).
- [111] P. Kankanala, K. Czymmek, and B. Valent, *Roles for rice membrane dynamics and plasmodesmata during biotrophic invasion by the blast fungus.*, *Plant Cell* **19**, 706 (2007).
- [112] R. Zavaliev, S. Ueki, B. L. Epel, and V. Citovsky, *Biology of callose ( $\beta$ -1,3-glucan) turnover at plasmodesmata.*, *Protoplasma* **248**, 117 (2011).
- [113] B. Ding, M. Kwon, and L. Warnberg, *Evidence that actin filaments are involved in controlling the permeability of plasmodesmata in tobacco mesophyll.*, *Plant Journal* **10**, 157 (1996).
- [114] S. Su, Z. Liu, C. Chen, Y. Zhang, X. Wang, L. Zhu, L. Miao, X.-C. Wang, and M. Yuan, *Cucumber mosaic virus movement protein severs actin filaments to increase the plasmodesmal size exclusion limit in tobacco.*, *Plant Cell* **22**, 1373 (2010).
- [115] I. Kim, F. D. Hempel, K. Sha, J. Pfluger, and P. C. Zambryski, *Identification of a developmental transition in plasmodesmatal function during embryogenesis in arabidopsis thaliana.*, *Development* **129**, 1261 (2002).
- [116] Y. Benitez-Alfonso, M. Cilia, A. S. Roman, C. Thomas, A. Maule, S. Hearn, and D. Jackson, *Control of arabidopsis meristem development by thioredoxin-dependent regulation of intercellular transport.*, *Proc Natl Acad Sci U S A* **106**, 3615 (2009).
- [117] M. Xu, E. Cho, T. M. Burch-Smith, and P. C. Zambryski, *Plasmodesmata formation and cell-to-cell transport are reduced in decreased size exclusion limit 1 during embryogenesis in arabidopsis.*, *Proc Natl Acad Sci U S A* **109**, 5098 (2012).
- [118] T. Zhu, W. Lucas, and T. Rost, *Directional cell-to-cell communication in the arabidopsis root apical meristem i. an ultrastructural and functional analysis.*, *Protoplasma* **203**, 35 (1998).
- [119] T. Zhu, R. O'Quinn, W. Lucas, and T. Rost, *Directional cell-to-cell communication in the arabidopsis root apical meristem ii. dynamics of plasmodesmatal formation.*, *Protoplasma* **204**, 84 (1998).
- [120] I. M. Roberts, P. Boevink, A. G. Roberts, N. Sauer, C. Reichel, and K. J. Oparka, *Dynamic changes in the frequency and architecture of plasmodesmata during the sink-source transition in tobacco leaves.*, *Protoplasma* **218**, 31 (2001).
- [121] K. Ehlers and A. J. E. van Bel, *Dynamics of plasmodesmal connectivity in successive interfaces of the cambial zone.*, *Planta* **231**, 371 (2010).
- [122] R. Stadler, C. Lauterbach, and N. Sauer, *Cell-to-cell movement of green fluorescent protein reveals post-phloem transport in the outer integument and identifies symplastic domains in arabidopsis seeds and embryos.*, *Plant Physiol* **139**, 701 (2005).
- [123] K. J. Oparka, A. G. Roberts, P. Boevink, S. S. Cruz, I. Roberts, K. S. Pradel, A. Imlau, G. Kotlizky, N. Sauer, and B. Epel, *Simple, but not branched, plasmodesmata allow the nonspecific trafficking of proteins in developing tobacco leaves.*, *Cell* **97**, 743 (1999).
- [124] K. Nakajima, G. Sena, T. Nawy, and P. N. Benfey, *Intercellular movement of the putative transcription factor shr in root patterning.*, *Nature* **413**, 307 (2001).
- [125] A. Paredez, C. Somerville, and D. Ehrhardt, *Visualization of Cellulose Synthase Demonstrates Functional Association with Microtubules.*, *Science* **312**, 1491 (2006).
- [126] R. Gutierrez, J. J. Lindeboom, A. R. Paredez, A. M. Emons, and D. W. Ehrhardt, *Arabidopsis cortical microtubules position cellulose synthase delivery to the plasma membrane and interact with cellulose synthase trafficking compartments.*, *Nat Cell Biol* **11**, 797 (2009).
- [127] H. Li, D. J. DeRosier, W. V. Nicholson, E. Nogales, and K. H. Downing, *Microtubule structure at 8 Å resolution.*, *Structure* **10**, 1317 (2002).

- [128] M. A. Welte, *Bidirectional transport along microtubules.*, Curr Biol **14**, R525 (2004).
- [129] J. Howard and A. A. Hyman, *Dynamics and mechanics of the microtubule plus end.*, Nature **422**, 753 (2003).
- [130] J. Sedbrook, *MAPs in plant cells: delineating microtubule growth dynamics and organization*, Current Opinion in Plant Biology **7**, 632 (2004).
- [131] D. Ehrhardt, *Straighten up and fly right – microtubule dynamics and organization of non-centrosomal arrays in higher plants*, Current Opinion in Cell Biology **20**, 107 (2008).
- [132] R. Dixit and R. Cyr, *Encounters between Dynamic Cortical Microtubules Promote Ordering of the Cortical Array through Angle-Dependent Modifications of Microtubule Behavior*, Plant Cell Online **16**, 3274 (2004).
- [133] S. H. Tindemans, R. J. Hawkins, and B. M. Mulder, *Survival of the aligned: ordering of the plant cortical microtubule array.*, Phys Rev Lett **104**, 058103 (2010).
- [134] O. Hamant, M. G. Heisler, H. Jonsson, P. Krupinski, M. Uyttewaal, P. Bokov, F. Corson, P. Sahlin, A. Boudaoud, E. M. Meyerowitz, Y. Couder, and J. Traas, *Developmental patterning by mechanical signals in Arabidopsis.*, Science **322**, 1650 (2008).
- [135] P. Dhonukshe, D. A. Weits, A. Cruz-Ramirez, E. E. Deinum, S. H. Tindemans, K. Kakar, K. Prasad, A. P. Mähönen, C. Ambrose, M. Sasabe, G. Wachsmann, M. Luijten, T. Bennett, Y. Machida, R. Heidstra, G. Wasteneys, B. M. Mulder, and B. Scheres, *A PLETHORA-auxin transcription module controls cell division plane rotation through MAP65 and CLASP.*, Cell **149**, 383 (2012).
- [136] T. Murata, S. Sonobe, T. Baskin, S. Hyodo, S. Hasezawa, T. Nagata, T. Horio, and M. Hasebe, *Microtubule-dependent microtubule nucleation based on recruitment of big gamma-tubulin in higher plants*, Nature Cell Biology **7**, 961 (2005).
- [137] J. Chan, A. Sambade, G. Calder, and C. Lloyd, *Arabidopsis Cortical Microtubules Are Initiated along, as Well as Branching from, Existing Microtubules.*, Plant Cell **12**, 2298 (2009).
- [138] S. H. Tindemans and B. M. Mulder, *Microtubule length distributions in the presence of protein-induced severing.*, Phys Rev E Stat Nonlin Soft Matter Phys **81**, 031910 (2010).
- [139] D. Burk, B. Liu, R. Zhong, W. Morrison, and Z. Ye, *A Katanin-like Protein Regulates Normal Cell Wall Biosynthesis and Cell Elongation*, PLANT CELL **13**, 807 (2001).
- [140] A. Bichet, T. Desnos, S. Turner, O. Grandjean, and H. Höfte, *Boterol1 is required for normal orientation of cortical microtubules and anisotropic cell expansion in arabidopsis.*, Plant J **25**, 137 (2001).
- [141] M. Webb, S. Jouannic, J. Foreman, P. Linstead, and L. Dolan, *Cell specification in the arabidopsis root epidermis requires the activity of ectopic root hair 3-a katanin-p60 protein*, Development **129**, 123 (2002).
- [142] T. Bouquín, O. Mattsson, H. Naested, R. Foster, and J. Mundy, *The arabidopsis lue1 mutant defines a katanin p60 ortholog involved in hormonal control of microtubule orientation during cell growth.*, J Cell Sci **116**, 791 (2003).
- [143] W. J. Lucas, S. Bouché-Pillon, D. P. Jackson, L. Nguyen, L. Baker, B. Ding, and S. Hake, *Selective trafficking of knotted1 homeodomain protein and its mrna through plasmodesmata.*, Science **270**, 1980 (1995).
- [144] G. Schönknecht, J. E. Brown, and J. Verchot-Lubicz, *Plasmodesmata transport of gfp alone or fused to potato virus x tgbp1 is diffusion driven.*, Protoplasma **232**, 143 (2008).
- [145] P. Zambryski and K. Crawford, *Plasmodesmata: gatekeepers for cell-to-cell transport of developmental signals in plants.*, Annu Rev Cell Dev Biol **16**, 393 (2000).
- [146] X. M. Xu, J. Wang, Z. Xuan, A. Goldshmidt, P. G. M. Borrell, N. Hariharan, J. Y. Kim, and D. Jackson, *Chaperonins facilitate knotted1 cell-to-cell trafficking and stem cell function.*, Science **333**, 1141 (2011).



- [147] W. J. Lucas, *Plant viral movement proteins: agents for cell-to-cell trafficking of viral genomes.*, Virology **344**, 169 (2006).
- [148] A. Levy, D. Guenoun-Gelbart, and B. L. Epel, *beta-1,3-glucanases: Plasmodesmal gate keepers for intercellular communication.*, Plant Signal Behav **2**, 404 (2007).
- [149] J. M. Guseman, J. S. Lee, N. L. Bogenschutz, K. M. Peterson, R. E. Virata, B. Xie, M. M. Kanaoka, Z. Hong, and K. U. Torii, *Dysregulation of cell-to-cell connectivity and stomatal patterning by loss-of-function mutation in arabidopsis chorus (glucan synthase-like 8).*, Development **137**, 1731 (2010).
- [150] J. R. Blake, *On the hydrodynamics of plasmodesmata.*, J Theor Biol **74**, 33 (1978).
- [151] B. Gunning and J. Hughes, *Quantitative assessment of symplastic transport of pre-nectar into the trichomes of abutilon nectaries*, Functional Plant Biology **3**, 619 (1976).
- [152] E. Waigmann and P. Zambryski, *Tobacco mosaic virus movement protein-mediated protein transport between trichome cells.*, Plant Cell **7**, 2069 (1995).
- [153] C. W. Windt, F. J. Vergeldt, P. A. de Jager, and H. van As, *Mri of long-distance water transport: a comparison of the phloem and xylem flow characteristics and dynamics in poplar, castor bean, tomato and tobacco.*, Plant Cell Environ **29**, 1715 (2006).
- [154] M. J. Clearwater, Z. Luo, M. Mazzeo, and B. Dichio, *An external heat pulse method for measurement of sap flow through fruit pedicels, leaf petioles and other small-diameter stems.*, Plant Cell Environ **32**, 1652 (2009).
- [155] W. Driever and C. Nüsslein-Volhard, *A gradient of bicoid protein in drosophila embryos.*, Cell **54**, 83 (1988).
- [156] W. Driever and C. Nüsslein-Volhard, *The bicoid protein determines position in the drosophila embryo in a concentration-dependent manner.*, Cell **54**, 95 (1988).
- [157] W. Driever and C. Nüsslein-Volhard, *The bicoid protein is a positive regulator of hunchback transcription in the early drosophila embryo.*, Nature **337**, 138 (1989).
- [158] F. Tostevin, P. R. ten Wolde, and M. Howard, *Fundamental limits to position determination by concentration gradients.*, PLoS Comput Biol **3**, e78 (2007).
- [159] O. Grimm, M. Coppey, and E. Wieschaus, *Modelling the bicoid gradient.*, Development **137**, 2253 (2010).
- [160] A. Spirov, K. Fahmy, M. Schneider, E. Frei, M. Noll, and S. Baumgartner, *Formation of the bicoid morphogen gradient: an mrna gradient dictates the protein gradient.*, Development **136**, 605 (2009).
- [161] H. D. Lipshitz, *Follow the mrna: a new model for bicoid gradient formation.*, Nat Rev Mol Cell Biol **10**, 509 (2009).
- [162] S. C. Little, G. Tkačik, T. B. Kneeland, E. F. Wieschaus, and T. Gregor, *The formation of the bicoid morphogen gradient requires protein movement from anteriorly localized mrna.*, PLoS Biol **9**, e1000596 (2011).
- [163] H. L. Rutschow, T. I. Baskin, and E. M. Kramer, *Regulation of solute flux through plasmodesmata in the root meristem.*, Plant Physiol **155**, 1817 (2011).
- [164] A. Turing, *The chemical basis of morphogenesis*, Philosophical Transactions of the Royal Society of London. Series B, Biological Sciences **237**, 37 (1952).
- [165] L. Wolpert, *Positional information and the spatial pattern of cellular differentiation*, Journal of Theoretical Biology **25**, 1 (1969).
- [166] F. Crick, *Diffusion in embryogenesis*, Nature **225**, 420 (1970).
- [167] A. Gierer and H. Meinhardt, *A theory of biological pattern formation.*, Kybernetik **12**, 30 (1972).

- [168] P. B. Goodwin, V. Shepherd, and M. G. Erwee, *Compartmentation of fluorescent tracers injected into the epidermal cells of <i>Egeria densa</i> leaves*, *Planta* **181**, 129 (1990). 10.1007/BF00202335.
- [169] J. Liesche and A. Schulz, *Quantification of plant cell coupling with three-dimensional photoactivation microscopy*, *J Microsc* **247**, 2 (2012).
- [170] K. Krynicki, C. D. Green, and D. W. Sawyer, *Pressure and temperature dependence of self-diffusion in water*, *Faraday Discuss. Chem. Soc.* **66**, 199 (1978).
- [171] V. A. Grieneisen, B. Scheres, P. Hogeweg, and A. F. M. Maree, *Morphogengeneering roots: comparing mechanisms of morphogen gradient formation*, *BMC Syst Biol* **6**, 37 (2012).
- [172] E. A. Rennie and R. Turgeon, *A comprehensive picture of phloem loading strategies*, *Proc Natl Acad Sci U S A* **106**, 14162 (2009).
- [173] A. Steinacher, O. Leyser, and R. H. Clayton, *A computational model of auxin and ph dynamics in a single plant cell*, *J Theor Biol* **296**, 84 (2012).
- [174] M. Coppey, A. M. Berezhevskii, Y. Kim, A. N. Boettiger, and S. Y. Shvartsman, *Modeling the bicoid gradient: diffusion and reversible nuclear trapping of a stable protein*, *Dev Biol* **312**, 623 (2007).
- [175] J. Szymanski, A. Patkowski, A. Wilk, P. Garstecki, and R. Holyst, *Diffusion and viscosity in a crowded environment: from nano-to macroscale*, *J. Chem. Phys. B* **110**, 25593 (2006).
- [176] S. Kondo and T. Miura, *Reaction-diffusion model as a framework for understanding biological pattern formation*, *Science* **329**, 1616 (2010).
- [177] X.-Y. Chen, L. Liu, E. Lee, X. Han, Y. Rim, H. Chu, S.-W. Kim, F. Sack, and J.-Y. Kim, *The arabidopsis callose synthase gene gsl8 is required for cytokinesis and cell patterning*, *Plant physiology* **150**, 105 (2009).
- [178] M. Pesch and M. Hülskamp, *Creating a two-dimensional pattern de novo during arabidopsis trichome and root hair initiation*, *Curr Opin Genet Dev* **14**, 422 (2004).
- [179] J. D. Masucci, W. G. Rerie, D. R. Foreman, M. Zhang, M. E. Galway, M. D. Marks, and J. W. Schiefelbein, *The homeobox gene glabra2 is required for position-dependent cell differentiation in the root epidermis of arabidopsis thaliana*, *Development* **122**, 1253 (1996).
- [180] D. B. Szymanski, R. A. Jilk, S. M. Pollock, and M. D. Marks, *Control of gl2 expression in arabidopsis leaves and trichomes*, *Development* **125**, 1161 (1998).
- [181] C. Duckett, K. Oparka, D. Prior, L. Dolan, and K. Roberts, *Dye-coupling in the root epidermis of arabidopsis is progressively reduced during development*, *Development* **120**, 3247 (1994).
- [182] E. E. Deinum, R. Geurts, T. Bisseling, and B. M. Mulder, *Modeling a cortical auxin maximum for nodulation: different signatures of potential strategies*, *Front Plant Sci* **3**, 96 (2012).
- [183] D. Peaceman and H. Rachford, *The numerical solution of parabolic and elliptic differential equations*, *Journal of the Society for Industrial and Applied Mathematics* **3**, 28 (1955).
- [184] K. H. Jensen, D. L. Mullendore, N. M. Holbrook, T. Bohr, M. Knoblauch, and H. Bruus, *Modeling the hydrodynamics of phloem sieve plates*, *Front Plant Sci* **3**, 151 (2012).
- [185] P. Hepler, *Endoplasmic reticulum in the formation of the cell plate and plasmodesmata*, *Protoplasma* **111**, 121 (1982).
- [186] D. A. Barton, L. Cole, D. A. Collings, D. Y. T. Liu, P. M. C. Smith, D. A. Day, and R. L. Overall, *Cell-to-cell transport via the lumen of the endoplasmic reticulum*, *Plant J* **66**, 806 (2011).
- [187] B. E. S. Gunning, *Age-related and origin-related control of the numbers of plasmodesmata in cell walls of developing Azolla roots*, *Planta* **143**, 181 (1978). 10.1007/BF00387789.
- [188] K. Bell and K. Oparka, *Imaging plasmodesmata*, *Protoplasma* **248**, 9 (2011).

- [189] J. Fitzgibbon, K. Bell, E. King, and K. Oparka, *Super-resolution imaging of plasmodesmata using three-dimensional structured illumination microscopy.*, *Plant Physiol* **153**, 1453 (2010).
- [190] P. Olesen, *The neck constriction in plasmodesmata*, *Planta* **144**, 349 (1979).
- [191] A. M. Berezhkovskii, M. I. Monine, C. B. Muratov, and S. Y. Shvartsman, *Homogenization of boundary conditions for surfaces with regular arrays of traps.*, *J Chem Phys* **124**, 036103 (2006).
- [192] H. Berg and E. Purcell, *Physics of chemoreception*, *Biophysical journal* **20**, 193 (1977).
- [193] D. Shoup and A. Szabo, *Role of diffusion in ligand binding to macromolecules and cell-bound receptors*, *Biophysical journal* **40**, 33 (1982).
- [194] D. Champion, H. Hervet, G. Blond, and D. Simatos, *Comparison between two methods to measure translational diffusion of a small molecule at subzero temperature*, *Journal of agricultural and food chemistry* **43**, 2887 (1995).
- [195] H. Corti, G. Frank, and M. Marconi, *An alternate solution of fluorescence recovery kinetics after spot-bleaching for measuring diffusion coefficients. 2. diffusion of fluorescein in aqueous sucrose solutions*, *Journal of solution chemistry* **37**, 1593 (2008).
- [196] A. Pluen, Y. Boucher, S. Ramanujan, T. McKee, T. Gohongi, E. Di Tomaso, E. Brown, Y. Izumi, R. Campbell, D. Berk, et al., *Role of tumor–host interactions in interstitial diffusion of macromolecules: cranial vs. subcutaneous tumors*, *Proc. Natl. Acad. Sci.* **98**, 4628 (2001).
- [197] A. Ekani-Nkodo and D. Fygenson, *Size exclusion and diffusion of fluoresceinated probes within collagen fibrils*, *Phys. Rev. E* **67**, 021909 (2003).
- [198] K. M. Crawford and P. C. Zambryski, *Non-targeted and targeted protein movement through plasmodesmata in leaves in different developmental and physiological states.*, *Plant Physiol* **125**, 1802 (2001).
- [199] B. Epel and M. Erlanger, *Light regulates symplastic communication in etiolated corn seedlings*, *Physiologia Plantarum* **83**, 149 (1991).
- [200] S. Stonebloom, T. Burch-Smith, I. Kim, D. Meinke, M. Mindrinos, and P. Zambryski, *Loss of the plant dead-box protein *ise1* leads to defective mitochondria and increased cell-to-cell transport via plasmodesmata.*, *Proc Natl Acad Sci U S A* **106**, 17229 (2009).
- [201] T. M. Burch-Smith and P. C. Zambryski, *Loss of increased size exclusion limit (*ise1*) or *ise2* increases the formation of secondary plasmodesmata.*, *Curr Biol* **20**, 989 (2010).
- [202] S. Stonebloom, J. O. Brunkard, A. C. Cheung, K. Jiang, L. Feldman, and P. Zambryski, *Redox states of plastids and mitochondria differentially regulate intercellular transport via plasmodesmata.*, *Plant Physiol* **158**, 190 (2012).
- [203] W. Rawicz, K. C. Olbrich, T. McIntosh, D. Needham, and E. Evans, *Effect of chain length and unsaturation on elasticity of lipid bilayers.*, *Biophys J* **79**, 328 (2000).
- [204] B. Lewis, D. Engelman, et al., *Lipid bilayer thickness varies linearly with acyl chain length in fluid phosphatidylcholine vesicles.*, *Journal of molecular biology* **166**, 211 (1983).
- [205] D. Guenoune-Gelbart, M. Elbaum, G. Sagi, A. Levy, and B. L. Epel, *Tobacco mosaic virus (*tmv*) replicase and movement protein function synergistically in facilitating *tmv* spread by lateral diffusion in the plasmodesmal desmotubule of *nicotiana benthamiana*.*, *Mol Plant Microbe Interact* **21**, 335 (2008).
- [206] P. Goodwin, *Molecular size limit for movement in the symplast of the elodea leaf*, *Planta* **157**, 124 (1983).
- [207] C. Faulkner and A. Maule, *Opportunities and successes in the search for plasmodesmal proteins.*, *Protoplasma* **248**, 27 (2011).
- [208] J. Tilsner, K. Amari, and L. Torrance, *Plasmodesmata viewed as specialised membrane adhesion sites.*, *Protoplasma* **248**, 39 (2011).

- [209] K. Ehlers and R. Kollmann, *Primary and secondary plasmodesmata: structure, origin, and functioning.*, *Protoplasma* **216**, 1 (2001).
- [210] C. Faulkner, O. E. Akman, K. Bell, C. Jeffree, and K. Oparka, *Peeking into pit fields: a multiple twinning model of secondary plasmodesmata formation in tobacco.*, *Plant Cell* **20**, 1504 (2008).
- [211] M. Levin, *Isolation and community: a review of the role of gap-junctional communication in embryonic patterning.*, *J Membr Biol* **185**, 177 (2002).
- [212] G. E. Sosinsky and B. J. Nicholson, *Structural organization of gap junction channels.*, *Biochim Biophys Acta* **1711**, 99 (2005).
- [213] M. P. Schwartz and A. Matouschek, *The dimensions of the protein import channels in the outer and inner mitochondrial membranes.*, *Proc Natl Acad Sci U S A* **96**, 13086 (1999).
- [214] P. Paine, L. Moore, S. Horowitz, et al., *Nuclear envelope permeability.*, *Nature* **254**, 109 (1975).
- [215] A. Rustom, R. Saffrich, I. Markovic, P. Walther, and H.-H. Gerdes, *Nanotubular highways for intercellular organelle transport.*, *Science* **303**, 1007 (2004).
- [216] H.-H. Gerdes and R. N. Carvalho, *Intercellular transfer mediated by tunneling nanotubes.*, *Curr Opin Cell Biol* **20**, 470 (2008).
- [217] R. E. Waugh and R. M. Hochmuth, *Mechanical equilibrium of thick, hollow, liquid membrane cylinders.*, *Biophys J* **52**, 391 (1987).
- [218] G. Koster, M. VanDuijn, B. Hofs, and M. Dogterom, *Membrane tube formation from giant vesicles by dynamic association of motor proteins.*, *Proc Natl Acad Sci U S A* **100**, 15583 (2003).
- [219] J. Hu, Y. Shibata, C. Voss, T. Shemesh, Z. Li, M. Coughlin, M. M. Kozlov, T. A. Rapoport, and W. A. Prinz, *Membrane proteins of the endoplasmic reticulum induce high-curvature tubules.*, *Science* **319**, 1247 (2008).
- [220] K. M. Crawford and P. C. Zambryski, *Subcellular localization determines the availability of non-targeted proteins to plasmodesmatal transport.*, *Curr Biol* **10**, 1032 (2000).
- [221] Z. Hong, A. J. Delauney, and D. P. Verma, *A cell plate-specific callose synthase and its interaction with phragmoplastin.*, *Plant Cell* **13**, 755 (2001).
- [222] M. A. Hink, R. A. Griep, J. W. Borst, A. van Hoek, M. H. Eppink, A. Schots, and A. J. Visser, *Structural dynamics of green fluorescent protein alone and fused with a single chain fv protein.*, *J Biol Chem* **275**, 17556 (2000).
- [223] R. Stadler, K. M. Wright, C. Lauterbach, G. Amon, M. Gahrtz, A. Feuerstein, K. J. Oparka, and N. Sauer, *Expression of gfp-fusions in arabidopsis companion cells reveals non-specific protein trafficking into sieve elements and identifies a novel post-phloem domain in roots.*, *Plant J* **41**, 319 (2005).
- [224] D. Smith, *Restricted diffusion through pores with periodic constrictions*, *AIChE journal* **32**, 1039 (1986).
- [225] R. Zwanzig, *Diffusion past an entropy barrier*, *J. Chem. Phys.* **96**, 3926 (1992).
- [226] J. Douglas and J. Gunn, *A general formulation of alternating direction methods*, *Numerische Mathematik* **6**, 428 (1964).
- [227] B. Rolfe, M. Djordjevic, J. Weinman, U. Mathesius, C. Pittock, E. Gartner, K. Ride, Z. Dong, M. McCully, and J. McIver, *Root morphogenesis in legumes and cereals and the effect of bacterial inoculation on root development*, *Plant and Soil* **194**, 131 (1997). Meeting on Opportunities for Biological Nitrogen Fixation in Rice and Other Non-Legumes, Natl Inst Biotechnol & Genet Engn, Faisalabad, Pakistan, Oct 13-15, 1996.

- [228] P. J. Larkin, J. M. Gibson, U. Mathesius, J. J. Weinman, E. Gartner, E. Hall, G. J. Tanner, B. G. Rolfe, and M. A. Djordjevic, *Transgenic white clover. Studies with the auxin-responsive promoter, GH3, in root gravitropism and lateral root development.*, Transgenic Res **5**, 325 (1996).
- [229] U. Mathesius, H. R. Schlaman, H. P. Spaink, C. Of Sautter, B. G. Rolfe, and M. A. Djordjevic, *Auxin transport inhibition precedes root nodule formation in white clover roots and is regulated by flavonoids and derivatives of chitin oligosaccharides.*, Plant J **14**, 23 (1998).
- [230] L. Blakely and T. Evans, *Cell dynamics studies on the pericycle of radish seedling roots*, Plant Science Letters **14**, 79 (1979).
- [231] S. Gonzalez-Rizzo, M. Crespi, and F. Frugier, *The medicago truncatula cre1 cytokinin receptor regulates lateral root development and early symbiotic interaction with sinorhizobium meliloti.*, Plant Cell **18**, 2680 (2006).
- [232] L. Tirichine, N. Sandal, L. H. Madsen, S. Radutoiu, A. S. Albrechtsen, S. Sato, E. Asamizu, S. Tabata, and J. Stougaard, *A gain-of-function mutation in a cytokinin receptor triggers spontaneous root nodule organogenesis*, Science **315**, 104 (2007).
- [233] L. Laplace, E. Benkova, I. Casimiro, L. Maes, S. Vanneste, R. Swarup, D. Weijers, V. Calvo, B. Parizot, M. B. Herrera-Rodriguez, R. Offringa, N. Graham, P. Doumas, J. Friml, D. Bogusz, T. Beeckman, and M. Bennett, *Cytokinins act directly on lateral root founder cells to inhibit root initiation.*, Plant Cell **19**, 3889 (2007).
- [234] J. E. Malamy and P. N. Benfey, *Organization and cell differentiation in lateral roots of Arabidopsis thaliana.*, Development **124**, 33 (1997).
- [235] I. Casimiro, T. Beeckman, N. Graham, R. Bhalerao, H. Zhang, P. Casero, G. Sandberg, and M. J. Bennett, *Dissecting Arabidopsis lateral root development.*, Trends Plant Sci **8**, 165 (2003).
- [236] A. Hirota, T. Kato, H. Fukaki, M. Aida, and M. Tasaka, *The auxin-regulated AP2/EREBP gene PUCHI is required for morphogenesis in the early lateral root primordium of Arabidopsis.*, Plant Cell **19**, 2156 (2007).
- [237] T. Mallory, S. Chiang, E. Cutter, and E. Gifford, *Sequence and pattern of lateral root formation in 5 selected species*, American Journal of Botany **57**, 800 (1970).
- [238] T. V. Bhuvaneswari, A. A. Bhagwat, and W. D. Bauer, *Transient susceptibility of root cells in four common legumes to nodulation by rhizobia.*, Plant Physiol **68**, 1144 (1981).
- [239] V. A. Grieneisen and B. Scheres, *Back to the future: evolution of computational models in plant morphogenesis.*, Curr Opin Plant Biol **12**, 606 (2009).
- [240] H. Jonsson and P. Krupinski, *Modeling plant growth and pattern formation.*, Curr Opin Plant Biol **13**, 5 (2010).
- [241] K. Ljung, A. K. Hull, M. Kowalczyk, A. Marchant, J. Celenza, J. D. Cohen, and G. Sandberg, *Biosynthesis, conjugation, catabolism and homeostasis of indole-3-acetic acid in Arabidopsis thaliana.*, Plant Mol Biol **49**, 249 (2002).
- [242] W. C. Yang, C. de Blank, I. Meskiene, H. Hirt, J. Bakker, A. van Kammen, H. Franssen, and T. Bisseling, *Rhizobium nod factors reactivate the cell cycle during infection and nodule primordium formation, but the cycle is only completed in primordium formation.*, Plant Cell **6**, 1415 (1994).
- [243] E. M. Kramer, *Pin and aux/lax proteins: their role in auxin accumulation*, Trends in Plant Science **9**, 578 (2004).
- [244] K. Libbenga and P. Harkes, *Initial proliferation of cortical cells in the formation of root nodules in pisum sativum l.*, Planta **114**, 17 (1973).

- [245] A. P. Rightmyer and S. Long, *Pseudonodule formation by wild type and symbiotic mutant Medicago truncatula in response to auxin transport inhibitors.*, Mol Plant Microbe Interact **24**, 1372 (2011).
- [246] G. E. van Noorden, J. J. Ross, J. B. Reid, B. G. Rolfe, and U. Mathesius, *Defective long-distance auxin transport regulation in the Medicago truncatula super numeric nodules mutant.*, Plant Physiol **140**, 1494 (2006).
- [247] F. Frugier, S. Kosuta, J. D. Murray, M. Crespi, and K. Szczygłowski, *Cytokinin: secret agent of symbiosis*, Trends in Plant Science **13**, 115 (2008).
- [248] R. Dello Ioio, F. S. Linhares, E. Scacchi, E. Casamitjana-Martinez, R. Heidstra, P. Costantino, and S. Sabatini, *Cytokinins determine Arabidopsis root-meristem size by controlling cell differentiation.*, Curr Biol **17**, 678 (2007).
- [249] K. Ruzicka, M. Simaskova, J. Duclercq, J. Petrasek, E. Zazimalova, S. Simon, J. Friml, M. C. Van Montagu, and E. Benkova, *Cytokinin regulates root meristem activity via modulation of the polar auxin transport.*, Proc Natl Acad Sci U S A **106**, 4284 (2009).
- [250] M. Pernisova, P. Klima, J. Horak, M. Valkova, J. Malbeck, P. Soucek, P. Reichman, K. Hoyerova, J. Dubova, J. Friml, E. Zazimalova, and J. Hejatkó, *Cytokinins modulate auxin-induced organogenesis in plants via regulation of the auxin efflux.*, Proc Natl Acad Sci U S A **106**, 3609 (2009).
- [251] J. Doyle, *Phylogeny of the legume family: an approach to understanding the origins of nodulation*, Annual Review of Ecology and Systematics **25**, 325 (1994).
- [252] P. Mergaert, K. Nikovics, Z. Kelemen, N. Maunoury, D. Vaubert, A. Kondorosi, and E. Kondorosi, *A novel family in Medicago truncatula consisting of more than 300 nodule-specific genes coding for small, secreted polypeptides with conserved cysteine motifs.*, Plant Physiol **132**, 161 (2003).
- [253] D. P. Lohar and K. A. VandenBosch, *Grafting between model legumes demonstrates roles for roots and shoots in determining nodule type and host/rhizobia specificity.*, J Exp Bot **56**, 1643 (2005).
- [254] J. Friml, X. Yang, M. Michniewicz, D. Weijers, A. Quint, O. Tietz, R. Benjamins, P. B. F. Ouwkerk, K. Ljung, G. Sandberg, P. J. J. Hooykaas, K. Palme, and R. Offringa, *A pinoid-dependent binary switch in apical-basal pin polar targeting directs auxin efflux.*, Science **306**, 862 (2004).
- [255] M. Michniewicz, M. K. Zago, L. Abas, D. Weijers, A. Schweighofer, I. Meskiene, M. G. Heisler, C. Ohno, J. Zhang, F. Huang, R. Schwab, D. Weigel, E. M. Meyerowitz, C. Luschnig, R. Offringa, and J. Friml, *Antagonistic regulation of PIN phosphorylation by PP2A and PINOID directs auxin flux.*, Cell **130**, 1044 (2007).
- [256] Z. Ding, C. S. Galván-Ampudia, E. Demarsy, Łukasz Łangowski, J. Kleine-Vehn, Y. Fan, M. T. Morita, M. Tasaka, C. Fankhauser, R. Offringa, and J. Friml, *Light-mediated polarization of the pin3 auxin transporter for the phototropic response in arabidopsis.*, Nat Cell Biol **13**, 447 (2011).
- [257] O. Leyser, *Auxin, self-organisation, and the colonial nature of plants.*, Curr Biol **21**, R331 (2011).
- [258] A. Delbarre, P. Muller, V. Imhoff, and J. Guern, *Comparison of mechanisms controlling uptake and accumulation of 2,4-dichlorophenoxy acetic acid, naphthalene-1-acetic acid, and indole-3-acetic acid in suspension-cultured tobacco cells*, Planta **198**, 532 (1996).
- [259] W. Grunewald and J. Friml, *The march of the PINs: developmental plasticity by dynamic polar targeting in plant cells*, EMBO Journal **29**, 2700 (2010).
- [260] H. Tanaka, P. Dhonukshe, P. B. Brewer, and J. Friml, *Spatiotemporal asymmetric auxin distribution: a means to coordinate plant development.*, Cell Mol Life Sci **63**, 2738 (2006).

- [261] P. Hutangura, U. Mathesius, M. G. Jones, and B. G. Rolfe, *Auxin induction is a trigger for root gall formation caused by root-knot nematodes in white clover and is associated with the activation of the flavonoid pathway*, Australian journal of plant physiology **26**, 221 (1999).
- [262] W. Grunewald, G. van Noorden, G. Van Isterdael, T. Beeckman, G. Gheysen, and U. Mathesius, *Manipulation of auxin transport in plant roots during Rhizobium symbiosis and nematode parasitism.*, Plant Cell **21**, 2553 (2009).
- [263] K. Kobayashi, M. S. Otegui, S. Krishnakumar, M. Mindrinos, and P. Zambryski, *Increased size exclusion limit 2 encodes a putative devh box rna helicase involved in plasmodesmata function during arabidopsis embryogenesis.*, Plant Cell **19**, 1885 (2007).
- [264] P. Hosek, M. Kubes, M. Lanková, P. I. Dobrev, P. Klíma, M. Kohoutová, J. Petrásek, K. Hoyerová, M. Jirina, and E. Zazimalová, *Auxin transport at cellular level: new insights supported by mathematical modelling.*, J Exp Bot **63**, 3815 (2012).
- [265] M. J. Laskowski, M. E. Williams, H. C. Nusbaum, and I. M. Sussex, *Formation of lateral root meristems is a two-stage process.*, Development **121**, 3303 (1995).
- [266] B. Péret, B. D. Rybel, I. Casimiro, E. Benková, R. Swarup, L. Laplace, T. Beeckman, and M. J. Bennett, *Arabidopsis lateral root development: an emerging story.*, Trends Plant Sci **14**, 399 (2009).
- [267] J. G. Dubrovsky, M. Sauer, S. Napsucially-Mendivil, M. G. Ivanchenko, J. Friml, S. Shishkova, J. Celenza, and E. Benková, *Auxin acts as a local morphogenetic trigger to specify lateral root founder cells.*, Proc Natl Acad Sci U S A **105**, 8790 (2008).
- [268] M. A. Moreno-Risueno, J. M. V. Norman, A. Moreno, J. Zhang, S. E. Ahnert, and P. N. Benfey, *Oscillating gene expression determines competence for periodic arabidopsis root branching.*, Science **329**, 1306 (2010).
- [269] I. D. Smet, S. Vanneste, D. Inzé, and T. Beeckman, *Lateral root initiation or the birth of a new meristem.*, Plant Mol Biol **60**, 871 (2006).
- [270] L. M. Blakely, M. Durham, T. A. Evans, and R. M. Blakely, *Experimental studies on lateral root formation in radish seedling roots. i. general methods, developmental stages, and spontaneous formation of laterals*, Botanical Gazette **143**, 341 (1982).
- [271] P. Dart and J. Pate, *Nodulation studies in legumes iii. the effects of delaying inoculation on the seedling symbiosis of barrel medic, medicago tribuloides desr.*, Australian journal of biological sciences **12**, 427 (1959).
- [272] R. o. d. Camp, Ph.D. thesis, [Sl: sn], 2012.
- [273] R. Dello Ioio, F. S. Linhares, and S. Sabatini, *Emerging role of cytokinin as a regulator of cellular differentiation.*, Curr Opin Plant Biol **11**, 23 (2008).
- [274] X. Huo, E. Schnabel, K. Hughes, and J. Frugoli, *RNAi phenotypes and the localization of a protein :: GUS fusion imply a role for Medicago truncatula PIN genes in nodulation*, Journal of Plant Growth Regulation **25**, 156 (2006).
- [275] G. E. van Noorden, T. Kerim, N. Goffard, R. Wiblin, F. I. Pellerone, B. G. Rolfe, and U. Mathesius, *Overlap of proteome changes in medicago truncatula in response to auxin and sinorhizobium meliloti*, Plant Physiology **144**, 1115 (June 2007).
- [276] J. Prayitno, B. G. Rolfe, and U. Mathesius, *The Ethylene-insensitive sickle mutant of Medicago truncatula shows altered auxin transport regulation during nodulation.*, Plant Physiol **142**, 168 (2006).
- [277] A. P. Wasson, F. I. Pellerone, and U. Mathesius, *Silencing the flavonoid pathway in Medicago truncatula inhibits root nodule formation and prevents auxin transport regulation by rhizobia.*, Plant Cell **18**, 1617 (2006).
- [278] H. Koltai, E. Dor, J. Hershenhorn, D. M. Joel, S. Weininger, S. Lekalla, H. Shealtiel, C. Bhattacharya, E. Eliahu, N. Resnick, et al., *Strigolactones' effect on root growth and root-hair*

- elongation may be mediated by auxin-efflux carriers*, Journal of Plant Growth Regulation **29**, 129 (2010).
- [279] S. Crawford, N. Shinohara, T. Sieberer, L. Williamson, G. George, J. Hepworth, D. Müller, M. A. Domagalska, and O. Leyser, *Strigolactones enhance competition between shoot branches by dampening auxin transport.*, Development **137**, 2905 (2010).
- [280] D. Koren, N. Resnick, E. M. Gati, E. Belausov, S. Weininger, Y. Kapulnik, and H. Koltai, *Strigolactone signaling in the endodermis is sufficient to restore root responses and involves short hypocotyl 2 (shy2) activity.*, New Phytol , (2013).
- [281] R. N. Beachy and M. Heinlein, *Role of p30 in replication and spread of tmv.*, Traffic **1**, 540 (2000).
- [282] A. Complainville, L. Brocard, I. Roberts, E. Dax, N. Sever, N. Sauer, A. Kondorosi, S. Wolf, K. Oparka, and M. Crespi, *Nodule initiation involves the creation of a new symplasmic field in specific root cells of medicago species.*, Plant Cell **15**, 2778 (2003).
- [283] A. B. Heckmann, N. Sandal, A. S. Bek, L. H. Madsen, A. Jurkiewicz, M. W. Nielsen, L. Tiri-chine, and J. Stougaard, *Cytokinin induction of root nodule primordia in Lotus japonicus is regulated by a mechanism operating in the root cortex.*, Mol Plant Microbe Interact , (2011).
- [284] Y. Ito and N. Kurata, *Identification and characterization of cytokinin-signalling gene families in rice.*, Gene **382**, 57 (2006).
- [285] R. V. Penmetse and D. R. Cook, *A Legume Ethylene-Insensitive Mutant Hyperinfected by Its Rhizobial Symbiont*, Science **275**, 527 (1997).
- [286] R. V. Penmetse, P. Uribe, J. Anderson, J. Lichtenzveig, J.-C. Gish, Y. W. Nam, E. Engstrom, K. Xu, G. Sckisel, M. Pereira, J. M. Baek, M. Lopez-Meyer, S. R. Long, M. J. Harrison, K. B. Singh, G. B. Kiss, and D. R. Cook, *The medicago truncatula ortholog of arabidopsis ein2, sickle, is a negative regulator of symbiotic and pathogenic microbial associations.*, Plant J **55**, 580 (2008).
- [287] R. Heidstra, W. C. Yang, Y. Yalcin, S. Peck, A. M. Emons, A. van Kammen, and T. Bisseling, *Ethylene provides positional information on cortical cell division but is not involved in Nod factor-induced root hair tip growth in Rhizobium-legume interaction.*, Development **124**, 1781 (1997).
- [288] P. Sahlin, B. Soderberg, and H. Jonsson, *Regulated transport as a mechanism for pattern generation: capabilities for phyllotaxis and beyond.*, J Theor Biol **258**, 60 (2009).
- [289] E. Deinum, S. Tindemans, and B. Mulder, *Taking directions: the role of microtubule-bound nucleation in the self-organization of the plant cortical array.*, Phys Biol **8**, 056002 (2011).
- [290] D. Ehrhardt and S. Shaw, *Microtubule Dynamics and Organization in the Plant Cortical Array*, Annual review of plant biology **57**, 859 (2006).
- [291] S. Shaw, R. Kamyar, and D. Ehrhardt, *Sustained Microtubule Treadmilling in Arabidopsis Cortical Arrays*, Science **300**, 1715 (2003).
- [292] A. Desai and T. J. Mitchison, *Microtubule polymerization dynamics*, Annu. Rev. Cell Dev. Biol. **13**, 83 (1997).
- [293] J. F. Allard, G. O. Wasteneys, and E. N. Cytrynbaum, *Mechanisms of self-organization of cortical microtubules in plants revealed by computational simulations.*, Mol Biol Cell **21**, 278 (2010).
- [294] E. C. Eren, R. Dixit, and N. Gautam, *A 3D Computer Simulation Model Reveals the Mechanisms for Self-Organization of Plant Cortical Microtubules into Oblique Arrays.*, Mol. Biol. Cell **21**, 2674 (2010).
- [295] R. J. Hawkins, S. H. Tindemans, and B. M. Mulder, *Model for the orientational ordering of the plant microtubule cortical array.*, Phys. Rev.. E, Statistical, nonlinear, and soft matter physics **82**, 011911 (2010).



- [296] G. O. Wasteneys and J. C. Ambrose, *Spatial organization of plant cortical microtubules: close encounters of the 2D kind.*, Trends Cell Biol **19**, 62 (2009).
- [297] J. Chan, G. Calder, S. Fox, and C. Lloyd, *Cortical microtubule arrays undergo rotary movements in Arabidopsis hypocotyl epidermal cells.*, Nature Cell Biology **9**, 171 (2007).
- [298] J. Vos, M. Dogterom, and A. Emons, *Microtubules become more dynamic but not shorter during preprophase band formation: A possible "search-and-capture" mechanism for microtubule translocation*, Cell Motility and the Cytoskeleton **57**, 246 (2004).
- [299] R. Wightman and S. Turner, *Severing at sites of microtubule crossover contributes to microtubule alignment in cortical arrays*, Plant Journal **52**, 742 (2007).
- [300] M. Nakamura, D. W. Ehrhardt, and T. Hashimoto, *Microtubule and katanin-dependent dynamics of microtubule nucleation complexes in theacentrosomal arabidopsis cortical array*, Nature Cell Biology **12**, 1064 (2010).
- [301] N. A. Eckardt, *High-resolution imaging of cortical microtubule assays.*, Plant Cell **20**, 817 (2008).
- [302] H. W. Xiang, *The Corresponding-States Principle and its Practice: Thermodynamic, Transport and Surface Properties of Fluids* (Elsevier, Amsterdam, 2005).
- [303] P. W. Anderson, *Concepts in Solids* (World Scientific, Singapore, 1997).
- [304] D. Burk, R. Zhong, and Z. Ye, *The Katanin Microtubule Severing Protein in Plants*, Journal of Integrative Plant Biology **49**, 1174 (2007).
- [305] V. Stoppin-Mellet, J. Gaillard, and M. Vantard, *Katanin's severing activity favors bundling of cortical microtubules in plants*, Plant Journal **46**, 1009 (2006).
- [306] J. J. Lindeboom, A. Lioutas, E. E. Deinum, S. H. Tindemans, D. W. Ehrhardt, A. M. C. Emons, J. W. Vos, and B. M. Mulder, *Cortical microtubule arrays are initiated from a non-random pre-pattern driven by atypical microtubule initiation.*, Plant Physiol , (2013).
- [307] M. C. Ledbetter and K. R. Porter, *A "microtubule" in plant cell fine structure*, Journal of Cell Biology **19**, 239 (1963).
- [308] P. B. Green, *Mechanism for Plant Cellular Morphogenesis.*, Science **138**, 1404 (1962).
- [309] C. Weerdenburg and R. W. Seagull, *The effects of taxol and colchicine on microtubule and microfibril arrays in elongating plant cells in culture* , Can J Bot **66**, 1707 (1988).
- [310] T. I. Baskin, *On the alignment of cellulose microfibrils by cortical microtubules: A review and a model*, Protoplasma **215**, 150 (2001).
- [311] A. T. Whittington, O. Vugrek, K. J. Wei, N. G. Hasenbein, K. Sugimoto, M. C. Rashbrooke, and G. O. Wasteneys, *Mor1 is essential for organizing cortical microtubules in plants.*, Nature **411**, 610 (2001).
- [312] H. Buschmann and C. W. Lloyd, *Arabidopsis mutants and the network of microtubule-associated functions.*, Molecular plant **1**, 888 (2008).
- [313] J. R. Lucas, S. Courtney, M. Hassfurder, S. Dhingra, A. Bryant, and S. L. Shaw, *Microtubule-associated proteins map65-1 and map65-2 positively regulate axial cell growth in etiolated arabidopsis hypocotyls.*, Plant Cell **23**, 1889 (2011).
- [314] C. Somerville, *Cellulose synthesis in higher plants.*, Annual review of cell and developmental biology **22**, 53 (2006).
- [315] G. Wasteneys. *Microtubule organization in the green kingdom: chaos or self-order?*, (2002).
- [316] F. Bartolini and G. G. Gundersen, *Generation of noncentrosomal microtubule arrays.*, Journal of Cell Science **119**, 4155 (2006).
- [317] A. R. Hardham and B. E. Gunning, *Structure of cortical microtubule arrays in plant cells*, Journal of Cell Biology **77**, 14 (1978).

- [318] C. Ambrose, J. F. Allard, E. N. Cytrynbaum, and G. O. Wasteneys, *A clasp-modulated cell edge barrier mechanism drives cell-wide cortical microtubule organization in arabidopsis.*, Nat Commun **2**, 430 (2011).
- [319] G. O. Wasteneys and R. E. Williamson, *Reassembly of Microtubules in Nitella Tasmanica - Quantitative-Analysis of Assembly and Orientation*, European Journal of Cell Biology **50**, 76 (1989).
- [320] G. O. Wasteneys and R. E. Williamson, *Reassembly of microtubules in Nitella tasmanica: assembly of cortical microtubules in branching clusters and its relevance to steady-state microtubule assembly*, Journal of Cell Science **93**, 705 (1989).
- [321] F. Kumagai, A. Yoneda, T. Tomida, T. Sano, T. Nagata, and S. Hasezawa, *Fate of nascent microtubules organized at the M/G1 interface, as visualized by synchronized tobacco BY-2 cells stably expressing GFP-tubulin: time-sequence observations of the reorganization of cortical microtubules in living plant cells.*, Plant and Cell Physiology **42**, 723 (2001).
- [322] J. Chan, G. Calder, J. Doonan, and C. Lloyd, *EB1 reveals mobile microtubule nucleation sites in Arabidopsis.*, Nature Cell Biology **5**, 967 (2003).
- [323] M. Pastuglia, J. Azimzadeh, M. Goussot, C. Camilleri, K. Belcram, J. Evrard, A. Schmit, P. Guerche, and D. Bouchez,  *$\gamma$ -Tubulin Is Essential for Microtubule Organization and Development in Arabidopsis*, Plant Cell **18**, 1412 (2006).
- [324] M. Nakamura, D. W. Ehrhardt, and T. Hashimoto, *Microtubule and katanin-dependent dynamics of microtubule nucleation complexes in theacentrosomal Arabidopsis cortical array.*, Nature Cell Biology **12**, 1064 (2010).
- [325] J. Chan, M. Eder, E. F. Crowell, J. Hampson, G. Calder, and C. Lloyd, *Microtubules and CESA tracks at the inner epidermal wall align independently of those on the outer wall of light-grown Arabidopsis hypocotyls.*, Journal of Cell Science **124**, 1088 (2011).
- [326] E. F. Crowell, H. Timpano, T. Desprez, T. Franssen-Verheijen, A.-M. Emons, H. Höfte, and S. Vernhettes, *Differential regulation of cellulose orientation at the inner and outer face of epidermal cells in the Arabidopsis hypocotyl.*, Plant Cell Online **23**, 2592 (2011).
- [327] M. Fujita, R. Himmelspach, C. H. Hocart, R. E. Williamson, S. D. Mansfield, and G. O. Wasteneys, *Cortical microtubules optimize cell-wall crystallinity to drive unidirectional growth in Arabidopsis.*, Plant journal **66**, 915 (2011).
- [328] L. C. Morejohn, T. E. Bureau, J. Mol Bajer, A. S. Bajer, and D. E. Fosket, *Oryzalin, a dinitroaniline herbicide, binds to plant tubulin and inhibits microtubule polymerization in vitro*, Planta **172**, 252 (1987).
- [329] A. Kirik, D. W. Ehrhardt, and V. Kirik, *TONNEAU2/FASS regulates the geometry of microtubule nucleation and cortical array organization in interphase Arabidopsis cells.*, Plant Cell **24**, 1158 (2012).
- [330] D. Job, O. Valiron, and B. Oakley, *Microtubule nucleation.*, Current Opinion in Cell Biology **15**, 111 (2003).
- [331] D. K. Fygenson, E. Braun, and A. Libchaber, *Phase diagram of microtubules*, Phys. Rev. E **50**, 1579 (1994).
- [332] T. Ketelaar, E. G. Allwood, R. Anthony, B. Voigt, D. Menzel, and P. J. Hussey, *The actin-interacting protein AIP1 is essential for actin organization and plant development*, Current Biology **14**, 145 (2004).
- [333] P. Thevenaz, U. E. Ruttimann, and M. Unser, *A pyramid approach to subpixel registration based on intensity*, Ieee Transactions on Image Processing **7**, 27 (1998).
- [334] E. Meijering, M. Jacob, J. C. F. Sarria, P. Steiner, H. Hirling, and M. Unser, *Design and validation of a tool for neurite tracing and analysis in fluorescence microscopy images.*, Cytometry. Part A **58**, 167 (2004).

- [335] M. Abramowitz and I. A. Stegun, *Handbook of mathematical functions with formulas, graphs, and mathematical tables* (U.S. Govt. Print. Off., Washington., 1970).
- [336] L. A. Baena-López, A. Baonza, and A. García-Bellido, *The orientation of cell divisions determines the shape of drosophila organs.*, *Curr Biol* **15**, 1640 (2005).
- [337] R. torres Ruiz and G. Jurgens, *Mutations in the fass gene uncouple pattern-formation and morphogenesis in Arabidopsis development*, *Development* **120**, 2967 (1994).
- [338] J. Traas, C. Bellini, P. Nacry, J. Kronenberger, D. Bouchez, and M. Caboche, *Normal differentiation patterns in plants lacking microtubular preprophase bands*, *Nature* **375**, 676 (1995).
- [339] G. Jurgens, *Axis formation in plant embryogenesis - cues and clues*, *Cell* **81**, 467 (1995).
- [340] I. De Smet and T. Beeckman, *Asymmetric cell division in land plants and algae: the driving force for differentiation*, *Nature reviews molecular cell biology* **12**, 177 (2011).
- [341] L. Dolan, K. Janmaat, V. Willemsen, P. Linstead, S. Poethig, K. Roberts, and B. Scheres, *Cellular organization of the Arabidopsis thaliana root*, *Development* **119**, 71 (1993).
- [342] L. Di Laurenzio, J. Wysocka Diller, J. Malamy, L. Pysh, Y. Helariutta, G. Freshour, M. Hahn, K. Feldmann, and P. Benfey, *The SCARECROW gene regulates an asymmetric cell division that is essential for generating the radial organization of the Arabidopsis root*, *Cell* **86**, 423 (1996).
- [343] V. Willemsen, M. Bauch, T. Bennett, A. Campilho, H. Wolkenfelt, J. Xu, J. Haseloff, and B. Scheres, *The nac domain transcription factors fez and sombrero control the orientation of cell division plane in arabidopsis root stem cells.*, *Dev Cell* **15**, 913 (2008).
- [344] J. D. Pickett-Heaps and D. H. Northcote, *Organization of microtubules and endoplasmic reticulum during mitosis and cytokinesis in wheat meristems.*, *J Cell Sci* **1**, 109 (1966).
- [345] L. Smith, *Plant cell division: Building walls in the right places*, *Nature reviews molecular cell biology* **2**, 33 (2001).
- [346] S. Muller, A. J. Wright, and L. G. Smith, *Division plane control in plants: new players in the band.*, *Trends Cell Biol* , (2009).
- [347] C. G. Rasmussen, B. Sun, and L. G. Smith, *Tangled localization at the cortical division site of plant cells occurs by several mechanisms*, *Journal of cell science* **124**, 270 (2011).
- [348] C. G. Rasmussen, J. A. Humphries, and L. G. Smith, *Determination of symmetric and asymmetric division planes in plant cells.*, *Annu Rev Plant Biol* **62**, 387 (2011).
- [349] M. Aida, D. Beis, R. Heidstra, V. Willemsen, I. Blilou, C. Galinha, L. Nussaume, Y.-S. Noh, R. Amasino, and B. Scheres, *The plethora genes mediate patterning of the arabidopsis root stem cell niche.*, *Cell* **119**, 109 (2004).
- [350] C. Galinha, H. Hofhuis, M. Luijten, V. Willemsen, I. Blilou, R. Heidstra, and B. Scheres, *PLETHORA proteins as dose-dependent master regulators of Arabidopsis root development*, *Nature* **449**, 1053 (2007).
- [351] J. J. Petricka, J. M. Van Norman, and P. N. Benfey, *Symmetry Breaking in Plants: Molecular Mechanisms Regulating Asymmetric Cell Divisions in Arabidopsis*, *Cold Spring Harbor perspectives in biology* **1**, (2009).
- [352] S. Sabatini, D. Beis, H. Wolkenfelt, J. Murfett, T. Guilfoyle, J. Malamy, P. Benfey, O. Leyser, N. Bechtold, P. Weisbeek, and B. Scheres, *An auxin-dependent distal organizer of pattern and polarity in the Arabidopsis root*, *Cell* **99**, 463 (1999).
- [353] P. Dhonukshe, J. Mathur, M. Hulskamp, and T. Gadella, *Microtubule plus-ends reveal essential links between intracellular polarization and localized modulation of endocytosis during division-plane establishment in plant cells*, *BMC Biology* **3**, (2005).

- [354] J. Chan, C. Jensen, L. Jensen, M. Bush, and C. Lloyd, *The 65-kDa carrot microtubule-associated protein forms regularly arranged filamentous cross-bridges between microtubules*, PNAS **96**, 14931 (1999).
- [355] A. Smertenko, N. Saleh, H. Igarashi, H. Mori, I. Hauser-Hahn, C. Jiang, S. Sonobe, C. Lloyd, and P. Hussey, *A new class of microtubule-associated proteins in plants*, Nature cell biology **2**, 750 (2000).
- [356] S. L. Shaw and J. Lucas, *Intrabundle microtubule dynamics in the arabidopsis cortical array*, Cytoskeleton **68**, 56 (2011).
- [357] S. H. Tindemans, Ph.D. thesis, 2009.
- [358] S. Liebowitz and S. Margolis, *Path dependence, lock-in, and history*, Journal of Law, Economics, & Organization, 205 (1995).
- [359] H. Kitano, *Systems biology: a brief overview*, Science **295**, 1662 (2002).
- [360] T. Ideker, T. Galitski, and L. Hood, *A new approach to decoding life: systems biology*, Annu Rev Genomics Hum Genet **2**, 343 (2001).
- [361] P. Berg and M. Singer, *George Beadle, an uncommon farmer: The emergence of genetics in the 20th century* (CSHL Press, 2003).
- [362] J. Tolkien, *The Fellowship of the Ring* (Unwin, 1954).
- [363] F. Antequera and A. Bird, *Number of cpg islands and genes in human and mouse*, Proc Natl Acad Sci U S A **90**, 11995 (1993).
- [364] J. C. Venter, M. D. Adams, E. W. Myers, and *et al.*, *The sequence of the human genome*, Science **291**, 1304 (2001).
- [365] E. S. Lander, L. M. Linton, B. Birren, *et al.*, and I. H. G. S. Consortium, *Initial sequencing and analysis of the human genome*, Nature **409**, 860 (2001).
- [366] E. van Nimwegen, *Scaling laws in the functional content of genomes*, Trends Genet **19**, 479 (2003).
- [367] P. Nurse and J. Hayles, *The cell in an era of systems biology*, Cell **144**, 850 (2011).
- [368] J. D. Orth, I. Thiele, and B. O. Palsson, *What is flux balance analysis?*, Nat Biotechnol **28**, 245 (2010).
- [369] M. Castellanos, D. B. Wilson, and M. L. Shuler, *A modular minimal cell model: purine and pyrimidine transport and metabolism*, Proc Natl Acad Sci U S A **101**, 6681 (2004).
- [370] J. R. Karr, J. C. Sanghvi, D. N. Macklin, M. V. Gutschow, J. M. Jacobs, B. Bolival, N. Assad-Garcia, J. I. Glass, and M. W. Covert, *A whole-cell computational model predicts phenotype from genotype*, Cell **150**, 389 (2012).
- [371] R. A. Gutiérrez, D. E. Shasha, and G. M. Coruzzi, *Systems biology for the virtual plant*, Plant Physiol **138**, 550 (2005).
- [372] N. N. Padte, S. G. Martin, M. Howard, and F. Chang, *The cell-end factor pom1p inhibits mid1p in specification of the cell division plane in fission yeast*, Curr Biol **16**, 2480 (2006).
- [373] M. Sohrmann, C. Fankhauser, C. Brodbeck, and V. Simanis, *The dmfl/mid1 gene is essential for correct positioning of the division septum in fission yeast*, Genes Dev **10**, 2707 (1996).
- [374] A. Cornish-Bowden, *Putting the systems back into systems biology*, Perspect Biol Med **49**, 475 (2006).
- [375] T. Pynchon, *The crying of lot 49* (J. B. Lippincott & Co., 1966).
- [376] H. W. De Regt and D. Dieks, *A contextual approach to scientific understanding*, Synthese **144**, 137 (2005).
- [377] D. Noble, *Systems: What's in a name?*, Physiology **26**, 126 (2011).
- [378] A. A. Hyman, *Whither systems biology*, Philos Trans R Soc Lond B Biol Sci **366**, 3635 (2011).

- [379] H. P. Duerr, M. Eichner, and D. Ammermann, *Modeling senescence in hypotrichous ciliates.*, Protist **155**, 45 (2004).
- [380] I. Ndoye, F. de Billy, J. Vasse, B. Dreyfus, and G. Truchet, *Root nodulation of Sesbania rostrata.*, J Bacteriol **176**, 1060 (1994).
- [381] S. Goormachtig, W. Capoen, E. K. James, and M. Holsters, *Switch from intracellular to intercellular invasion during water stress-tolerant legume nodulation.*, Proc Natl Acad Sci U S A **101**, 6303 (2004).
- [382] D. Mollison, *Dependence of epidemic and population velocities on basic parameters*, Mathematical biosciences **107**, 255 (1991).
- [383] J. S. van Zon, M. J. Morelli, S. Tănase-Nicola, and P. R. ten Wolde, *Diffusion of transcription factors can drastically enhance the noise in gene expression.*, Biophys J **91**, 4350 (2006).
- [384] M. Kaern, T. C. Elston, W. J. Blake, and J. J. Collins, *Stochasticity in gene expression: from theories to phenotypes.*, Nat Rev Genet **6**, 451 (2005).
- [385] D. Reguera, A. Luque, P. S. Burada, G. Schmid, J. M. Rubí, and P. Hänggi, *Entropic splitter for particle separation.*, Phys Rev Lett **108**, 020604 (2012).
- [386] K. Chen, Y. C. Chou, and K. To, *Force generation by granular chains moving randomly on periodic ratchet plates.*, Phys Rev E Stat Nonlin Soft Matter Phys **87**, 012711 (2013).
- [387] S. E. Jones, J. S. Demeo, N. W. Davies, S. E. Noonan, and J. J. Ross, *Stems of the arabidopsis pin1-1 mutant are not deficient in free indole-3-acetic acid.*, Planta **222**, 530 (2005).
- [388] S. M. Hall and G. Medlow, *Identification of iaa in phloem and root pressure saps of ricinus communis l. by mass spectrometry*, Planta **119**, 257 (1974).
- [389] C. W. Mullineaux, A. Nenninger, N. Ray, and C. Robinson, *Diffusion of green fluorescent protein in three cell environments in escherichia coli.*, J Bacteriol **188**, 3442 (2006).
- [390] M. B. Elowitz, M. G. Surette, P. E. Wolf, J. B. Stock, and S. Leibler, *Protein mobility in the cytoplasm of escherichia coli.*, J Bacteriol **181**, 197 (1999).
- [391] Z. Wang, J. V. Shah, Z. Chen, C.-H. Sun, and M. W. Berns, *Fluorescence correlation spectroscopy investigation of a gfp mutant-enhanced cyan fluorescent protein and its tubulin fusion in living cells with two-photon excitation.*, J Biomed Opt **9**, 395 (2004).
- [392] M. A. Hink, J. W. Borst, and A. J. W. G. Visser, *Fluorescence correlation spectroscopy of gfp fusion proteins in living plant cells.*, Methods Enzymol **361**, 93 (2003).
- [393] P. Schwille, U. Haupts, S. Maiti, and W. W. Webb, *Molecular dynamics in living cells observed by fluorescence correlation spectroscopy with one- and two-photon excitation.*, Biophys J **77**, 2251 (1999).
- [394] E. O. Potma, W. P. de Boeij, L. Bosgraaf, J. Roelofs, P. J. van Haastert, and D. A. Wiersma, *Reduced protein diffusion rate by cytoskeleton in vegetative and polarized dictyostelium cells.*, Biophys J **81**, 2010 (2001).
- [395] M.-J. Gagnon and D. U. Beebe, *Minor vein differentiation and the development of specialized plasmodesmata between companion cells and contiguous cells in expanding leaves of moricandia arvensis (l.) dc.(brassicaceae)*, International Journal of Plant Sciences , 685 (1996).
- [396] E. Kawamura and G. O. Wasteneys, *MOR1, the Arabidopsis thaliana homologue of Xenopus MAP215, promotes rapid growth and shrinkage, and suppresses the pausing of microtubules in vivo.*, J Cell Sci **121**, 4114 (2008).
- [397] W. Liu, W. Kohlen, A. Lillo, R. O. den Camp, S. Ivanov, M. Hartog, E. Limpens, M. Jamil, C. Smaczniak, K. Kaufmann, W.-C. Yang, G. J. E. J. Hooiveld, T. Charnikhova, H. J. Bouwmeester, T. Bisseling, and R. Geurts, *Strigolactone biosynthesis in medicago truncatula and rice requires the symbiotic gras-type transcription factors nsp1 and nsp2.*, Plant Cell **23**, 3853 (2011).

- [398] A. Alder, M. Jamil, M. Marzorati, M. Bruno, M. Vermathen, P. Bigler, S. Ghisla, H. Bouwmeester, P. Beyer, and S. Al-Babili, *The path from  $\beta$ -carotene to carlactone, a strigolactone-like plant hormone.*, Science **335**, 1348 (2012).
- [399] E. A. Dun, P. B. Brewer, and C. A. Beveridge, *Strigolactones: discovery of the elusive shoot branching hormone.*, Trends Plant Sci **14**, 364 (2009).
- [400] W. Kohlen, T. Charnikhova, Q. Liu, R. Bours, M. A. Domagalska, S. Beguerie, F. Verstappen, O. Leyser, H. Bouwmeester, and C. Ruyter-Spira, *Strigolactones are transported through the xylem and play a key role in shoot architectural response to phosphate deficiency in nonarbuscular mycorrhizal host arabidopsis.*, Plant Physiol **155**, 974 (2011).
- [401] A. Rasmussen, T. Heugebaert, C. Matthys, R. V. Deun, F.-D. Boyer, S. Goormachtig, C. Stevens, and D. Geelen, *A fluorescent alternative to the synthetic strigolactone gr24.*, Mol Plant **6**, 100 (2013).
- [402] J. D. Murray, *Mathematical biology: II: spatial models and biomedical applications* (Springer, 2003).
- [403] J. Jaeger, *Modelling the drosophila embryo.*, Mol Biosyst **5**, 1549 (2009).
- [404] R. Fitzhugh, *Impulses and physiological states in theoretical models of nerve membrane*, Biophysical journal **1**, 445 (1961).
- [405] J. Nagumo, S. Arimoto, and S. Yoshizawa, *An active pulse transmission line simulating nerve axon*, Proceedings of the IRE **50**, 2061 (1962).
- [406] A. L. Hodgkin and A. F. Huxley, *A quantitative description of membrane current and its application to conduction and excitation in nerve*, Journal of physiology **117**, 500 (1952).
- [407] C. Jones, *Stability of the travelling wave solution of the fitzhugh-nagumo system*, Trans. Amer. Math. Soc **286**, 431 (1984).
- [408] A. F. Marée, A. V. Panfilov, and P. Hogeweg, *Migration and thermotaxis of Dictyostelium discoideum slugs, a model study*, Journal of theoretical biology **199**, 297 (1999).
- [409] A. M. Pertsov, J. M. Davidenko, R. Salomonsz, W. T. Baxter, and J. Jalife, *Spiral waves of excitation underlie reentrant activity in isolated cardiac muscle*, Circulation research **72**, 631 (1993).
- [410] R. R. Aliev and A. V. Panfilov, *A simple two-variable model of cardiac excitation*, Chaos, Solitons & Fractals **7**, 293 (1996).
- [411] T. Paciorek, E. Zazimalová, N. Ruthardt, J. Petrásek, Y.-D. Stierhof, J. Kleine-Vehn, D. A. Morris, N. Emans, G. Jürgens, N. Geldner, and J. Friml, *Auxin inhibits endocytosis and promotes its own efflux from cells.*, Nature **435**, 1251 (2005).
- [412] J. Kleine-Vehn and J. Friml, *Polar targeting and endocytic recycling in auxin-dependent plant development.*, Annu Rev Cell Dev Biol **24**, 447 (2008).
- [413] F. Huang, M. K. Zago, L. Abas, A. van Marion, C. S. Galván-Ampudia, and R. Offringa, *Phosphorylation of conserved pin motifs directs arabidopsis pin1 polarity and auxin transport.*, Plant Cell **22**, 1129 (2010).
- [414] J. Kleine-Vehn, F. Huang, S. Naramoto, J. Zhang, M. Michniewicz, R. Offringa, and J. Friml, *PIN auxin efflux carrier polarity is regulated by PINOID kinase-mediated recruitment into GNOM-independent trafficking in Arabidopsis.*, Plant Cell **21**, 3839 (2009).
- [415] F. G. Feugier, A. Mochizuki, and Y. Iwasa, *Self-organization of the vascular system in plant leaves: inter-dependent dynamics of auxin flux and carrier proteins.*, J Theor Biol **236**, 366 (2005).
- [416] H. Fujita and A. Mochizuki, *Pattern formation of leaf veins by the positive feedback regulation between auxin flow and auxin efflux carrier.*, J Theor Biol **241**, 541 (2006).
- [417] E. M. Kramer, *Auxin-regulated cell polarity: an inside job?*, Trends Plant Sci **14**, 242 (2009).

- [418] T. Sachs, *Polarity and the induction of organized vascular tissues*, Annals of Botany **33**, 263 (1969).
- [419] Y. Boutte, M. T. Crosnier, N. Carraro, J. Traas, and B. Satiat-Jeunemaitre, *The plasma membrane recycling pathway and cell polarity in plants: studies on PIN proteins.*, J Cell Sci **119**, 1255 (2006).
- [420] N. Nakayama, R. S. Smith, T. Mandel, S. Robinson, S. Kimura, A. Boudaoud, and C. Kuhlemeier, *Mechanical regulation of auxin-mediated growth.*, Curr Biol , (2012).
- [421] A. M. Jones, *Auxin-binding proteins*, Annual review of plant biology **45**, 393 (1994).
- [422] J. G. Chen, H. Ullah, J. C. Young, M. R. Sussman, and A. M. Jones, *Abp1 is required for organized cell elongation and division in arabidopsis embryogenesis.*, Genes Dev **15**, 902 (2001).
- [423] T. Xu, M. Wen, S. Nagawa, Y. Fu, J.-G. Chen, M.-J. Wu, C. Perrot-Rechenmann, J. Friml, A. M. Jones, and Z. Yang, *Cell Surface- and Rho GTPase-Based Auxin Signaling Controls Cellular Interdigitation in Arabidopsis*, Cell **143**, 99 (2010).
- [424] J. Xu and B. Scheres, *Cell polarity: Roping the ends together.*, Curr Opin Plant Biol **8**, 613 (2005).
- [425] G. Hardin, *The tragedy of the commons*, Science **162**, 1243 (1968).
- [426] M. Gersani, E. E. O'Brien, G. M. Maina, Z. Abramsky, et al., *Tragedy of the commons as a result of root competition*, Journal of Ecology **89**, 660 (2001).
- [427] D. J. Rankin, K. Bargum, and H. Kokko, *The tragedy of the commons in evolutionary biology.*, Trends Ecol Evol **22**, 643 (2007).
- [428] D. S. Wilson, *A theory of group selection.*, Proc Natl Acad Sci U S A **72**, 143 (1975).

# English summary

Plant growth and development can be understood at different levels, from the whole plant adapting its morphology to its environment to processes at the cellular and subcellular level (further described in 1.2).

Each level has its own interesting questions. A common theme over the different levels is the distribution of information to coordinate the relevant processes. The fact that plant cells are separated by thick cell walls constrains the possibilities for intercellular communication. As a consequence, plants have evolved a number of unique ways of solving the general communication challenges arising from multicellularity. We have selected several questions on different levels. For each we have used different modelling approaches, tailored to the nature of the respective system and the questions asked.

In part I we address a mechanism for the intercellular communication of biochemical signals: non-targeted symplastic transport. Although mutations affecting the regulation of symplastic transport are often lethal, this mechanism is often overlooked. For this reason we started from the beginning. With a simple tissue level model (chapter 2) we addressed the basic biophysical properties of communication by non-targeted symplastic transport: how far and how fast will a biochemical signal move? We started in one dimension (1D), which allowed for the derivation of an effective diffusion constant at the tissue level and thus greatly aided in understanding the basic biophysical properties. Using the same tissue level model we investigated how it affects key communication processes in plants. For this we focussed on two canonical systems: first, the formation of auxin gradients, which coordinate many processes in plant growth and development, and second, reaction-diffusion patterning systems, using a modified Gierer-Meinhardt model, on a more conceptual level.

A key quantity in this is the effective wall permeability for the symplastic route. In chapter 3 we derive a method of calculating this parameter from first principles: a geometrical description of the plasmodesmata, their density and distribution and the size of the symplastically moving particle. The effective permeabilities calculated using parameters based on diverse ultrastructural studies are well in line with experimentally measured values, confirming the validity of our approach. The method also allows us to assess the impact of several plasmodesmatal features, such as the desmotubule, that occupies the center of the plasmodesma, and the central cavity, the wider central region of the channel.

In part II we investigate the initiation of nodule primordia in model legumes. The axial position of the first cell divisions differs among legumes and is strongly correlated with the type of nodules they form. In all cases, however, a local accumulation of the plant hormone auxin is observed at the location of the first divisions. We started out by investigating conceptual different mechanisms for local auxin accumulation – increased influx, decreased efflux and local production – and related this to the most likely mechanism behind the auxin accumulation observed in nodulation (chapter 4). These mechanisms all yield distinct signatures of auxin accumulation. For example, the local maximum formed



after locally increasing the effective influx permeability is much more confined than after locally decreasing the effective efflux permeability. Of these different mechanisms, a local reduction of efflux is most compatible with nodulation. Moreover, the signatures are modified by the distribution of efflux carriers (such as PIN proteins) in the unaffected root. Little is known about this distribution in the relevant region of the roots of model legumes. We therefore used a published *Arabidopsis* model as a starting point. Varying from this starting point resulted in the observation that the initial distribution of the efflux carriers affects the axial position of the induced auxin maximum through changing auxin availability.

We further investigated the biophysical properties of the different mechanisms to increase their applicability and to become able to address questions about why evolution “chose” different mechanisms for different processes (chapter 5). Here we compared the signatures in the complicated root context with a simple 1D model, thus separating the influence of the environment from the “core signatures”. Our current understanding of the PIN distribution in roots is that auxin flows in opposite directions in the vascular tissue and cortex. As a consequence, it is locally recycled to some degree. Increasing the influx can strongly enhance this local recycling and thus increase the resulting local auxin accumulation beyond what is expected from a 1D model, making it particularly suitable for lateral root initiation, which occurs predominantly (or fully, depending on the species) from the pericycle. Decreasing the efflux, on the other hand, has either little or a negative effect on local recycling.

Next we returned to nodulation. In model legume *Medicago truncatula* the initial auxin accumulation and cell divisions occur in the inner root layers (inner cortex, endodermis and pericycle), but the signal that induces the divisions is of epidermal origin. To investigate how this is possible, we assumed a simple interaction between the epidermal signal, presumably cytokinin, and the amount of efflux carriers in the cell membrane based on experimental observations in other contexts. With this simple interaction we could easily find a parameter regime that yielded auxin accumulation patterns reminiscent of different legumes. We further discuss how other components, not included in the current version of the model, could increase the robustness of the mechanism to variations in rates and root geometry as well as intrinsic noise originating from low numbers of signaling molecules.

As the plant hormones auxin and cytokinin are small molecules, we also investigated in chapters 5 and 6 the impact of symplastic transport on our findings.

In part III we zoom in again, now into the subcellular level. The cell wall is key to the diverse shapes of plant cells. It consists for a large part of cellulose microfibrils. These long fibers are highly aligned and deposited layer by layer by cellulose synthase complexes. This alignment is thought to dictate the anisotropic mechanical properties of the cell wall. The movement of the wall depositing complexes in turn is controlled by the orientation of cortical microtubules. In dividing cells, the orientation of the microtubule array is also a predictor of the orientation of the next division plane. Cortical microtubules are highly dynamic protein filaments attached to the cell membrane that interact through frequent collisions. It has been shown that the angle dependent outcomes of these collisions can result in spontaneous alignment of the array. In plant cells, cortical microtubules are controlled in far more elaborate ways than would be required based on

the core mechanism alone. At the same time, the core mechanism does not reliably orient the array.

In chapter 7 we investigate the impact of microtubule-bound nucleation and the particular distribution of nucleation angles found in experiments. The impact on coarse grained statistics such as order parameter  $S_2$  (which quantifies alignment) can be explained from the Fourier transform of the angle distribution, in biological terms: the average degree of alignment between parent and nascent microtubule. The very peculiar measured distribution, including peaks centered around a relative angle of  $35^\circ$  to either side of the parent, however, results in a more homogeneous distribution of microtubule density over the whole array.

The nucleation complexes have a strong affinity for existing microtubules and their nucleation rate is about 10-fold higher when attached to one. After every cell division, however, the array starts empty. In chapter 8 we address the early stages of array formation. It turns out that in the earliest stages, the microtubule density is biased towards diagonal angles, which results from a diagonal bias on nucleations. Using computer simulations we investigated the impact of these observations and addressed the question how such initial conditions can be compatible with the consistent establishment of a transverse array at later stages.

Finally we address a mechanism of array orientation (chapter 9) based on differences in the crossing probabilities of different edges of cuboid cells. These probabilities are assumed to be affected by the edge's curvature and the differential presence of proteins, in this case CLASP, facilitating edge crossing. This work was embedded in a study linking auxin signaling and the auxin responsive PLETHORA transcription factors to cell division plane orientation through the orientation of the interphase cortical microtubules, linking the cortical microtubules to developmental questions at the level of whole tissues and organs.

Taken together, the different parts illustrate that simple models can provide insight into many questions related to plant growth and development. We do not advocate a single modelling approach as the best possible: the best way is to tailor the approach to the research questions.

# Nederlandse samenvatting

Er zijn veel manieren om tegen de groei en ontwikkeling van planten aan te kijken. Op het niveau van de gehele plant is de plant een organisme dat zich al groeiende voortdurend aanpast aan zijn omgeving. Verder inzoomend spelen er processen zoals het coördineren van functies binnen en tussen weefsels, en het ontwikkelen van de eigenschappen van individuele cellen en delen ervan, zodat deze hun taken binnen de plant kunnen uitvoeren. Deze niveaus worden nader beschreven in 1.2.

Elk niveau kent zijn eigen interessante vraagstukken. Wat op alle niveaus belangrijk is, is het verspreiden van informatie ter coördinatie van de processen die op dat niveau relevant zijn. Plantencellen zijn omgeven door dikke celwanden, wat de mogelijkheden voor communicatie tussen cellen beperkt. Als gevolg hiervan zijn er verschillende communicatiemethoden geëvolueerd die uniek zijn voor planten, hoewel intercellulaire communicatie voor alle meercellige organismen van belang is.

De vragen in dit proefschrift haken in op verschillende niveaus. De gemeenschappelijke component is het gebruik van wiskundige modellen en computermodellen, steeds aangepast aan het desbetreffende systeem en, niet onbelangrijk, de vragen zelf.

In deel I bestuderen we een mechanisme voor intercellulaire communicatie via biochemische signalen: “non-targeted” symplastisch transport. Dit is het transport door nauwe kanaaltjes tussen plantencellen, plasmodesmata genaamd, van alle moleculen die daar klein genoeg voor zijn. Mutaties die de regulatie van dit transportmechanisme verstoren zijn vaak dodelijk. Desalniettemin wordt doorgaans weinig aandacht aan dit mechanisme besteed. Om die reden zijn we met de basis begonnen. We hebben een eenvoudig model op weefselniveau (zie hoofdstuk 2) opgesteld om de basale biofysische eigenschappen van communicatie via non-targeted symplastisch transport te onderzoeken: hoe ver en hoe snel beweegt een biochemisch signaal via dit mechanisme? We begonnen de analyse in één dimensie (1D), omdat dit wiskundig het makkelijkst is. Hiermee hebben we een effectieve diffusieconstante afgeleid voor het weefselniveau, wat zeer nuttig is voor het begrijpen van de basale eigenschappen van het systeem.

Vervolgens hebben we dit model gebruikt om te bepalen hoe symplastisch transport enkele belangrijke communicatieprocessen in planten beïnvloedt. We hebben ons daarbij gericht op twee veelvuldig bestudeerde systemen: ten eerste op de vorming van gradiënten van het plantenhormoon auxine, die vele processen met betrekking tot de groei en ontwikkeling van planten coördineren, en ten tweede – op een meer conceptueel niveau – op reactie-diffusie mechanismen voor patroonvorming. Specifiek gebruikten we voor dit laatste een nieuwe variant van het Gierer-Meinhardt model.

Een zeer belangrijke grootte in dit weefselniveau-model is de effectieve permeabiliteit (doorlaatbaarheid) van de celwand voor de symplastische transportroute. In hoofdstuk 3 leiden we een methode af om deze modelparameter te berekenen aan de hand van een geometrische beschrijving van individuele plasmodesmata, hun dichtheid en verdeling, en de grootte van het signaalmolecuul. De effectieve permeabiliteitswaarden die we op deze manier berekenen, met getallen gebaseerd op de beschikbare exper-

imentele literatuur, komen goed overeen met directe metingen van de effectieve permeabiliteit. Daarnaast is het op deze manier mogelijk om te berekenen wat het effect is van verschillende eigenschappen van de plasmodesmata, zoals de desmotubulus, een nauwe membraanbuis die een behoorlijk deel van de beschikbare ruimte inneemt, en een veel geobserveerde kanaalopbouw bestaande uit een centrale holte in combinatie met twee nauwere 'nek'-gebieden aan de uiteinden.

Deel II gaat in op de vorming van knolprimordia in vlinderbloemen. De plaats van de eerste celdelingen ten opzichte van het centrum van de wortel verschilt per soort vlinderbloemige en hangt sterk samen met het type wortelknollen dat de soort vormt. In alle onderzochte gevallen vindt echter lokaal accumulatie plaats van het plantenhormoon auxine, en wel op de plek waar deze delingen plaatsvinden. Om te kunnen begrijpen hoe dit belangrijke hormoon daar ophoopt zijn we begonnen met een inventarisatie van conceptueel verschillende mechanismen die leiden tot de lokale ophoping van auxine, en de eigenschappen hiervan. Hoofdstuk 4 gaat over de vraag welk van deze mechanismen het best past bij bestaande experimentele observaties met betrekking tot knolvorming. Hierbij zijn drie mechanismen onderzocht: het verhogen van de influx (zodat er meer auxine de cel ingepompt kan worden), het verlagen van de efflux (zodat er meer in de cel achterblijft) en lokale productie van het hormoon (zodat er totaal meer beschikbaar is). Elk van deze mechanismen geeft een eigen karakteristiek accumulatiepatroon. Aan de hand hiervan hebben we geconcludeerd dat afname van de efflux het meest waarschijnlijke mechanisme is voor de eerste stadia van knolvorming. De karakteristieke patronen worden beïnvloed door de plaatsing van de eiwitten die auxine de cel uit pompen (PINs), voorafgaand aan de lokale veranderingen. Over de verdeling van deze PINs is onvoldoende bekend in het relevante gedeelte van de wortel van vlinderbloemen. Daarom hebben we een bestaand model voor zandraket (*Arabidopsis thaliana*) gebruikt als uitgangspunt, dit aangepast aan de geometrie van modelvlinderbloemen, en mogelijke variaties onderzocht. Hieruit blijkt dat de initiële verdeling van de PINs effect heeft op de axiale positie van het auxinmaximum doordat deze verdeling de beschikbaarheid van auxine in verschillende cellen bepaalt.

In het volgende hoofdstuk, hoofdstuk 5, hebben we de biofysische eigenschappen van de verschillende mechanismen uitgebreider onderzocht, voor een bredere toepasbaarheid van deze kennis en om inzicht te krijgen in de vraag waarom evolutie verschillende "keuzes gemaakt heeft" voor verschillende processen. Hiervoor hebben we de mechanismen ook bestudeerd in een overeenkomstig 1D model, zodat we de eerder gevonden patronen konden splitsen in een "basispatroon" en de invloed van de wortelarchitectuur hierop. De huidige hypothese over auxinestromen in dit deel van de plantenwortel gaat uit van een neerwaartse stroom – preciezer: richting de punt van de wortel – in het vaatweefsel en een opwaartse in de cortex. Deze tegengestelde stromen zijn in zekere mate gekoppeld, waardoor ook lokale circulatie optreedt. Het vergroten van de influx, vooral rond het grensvlak van de stroomrichtingen, versterkt deze circulatie behoorlijk, resulterend in een lokaal hogere flux en daardoor meer auxineophoping dan verwacht op basis van het 1D vergelijkingsmodel. Dit maakt het een bijzonder geschikt mechanisme voor de vorming van zijwortels, die namelijk begint in de pericykel, oftewel bij het grensvlak. Het verlagen van de efflux heeft daarentegen een beperkt of zelfs negatief effect op de lokale circulatie.

Na deze biofysische uitdieping gaat hoofdstuk 6 verder in op de knolvorming. In de

modelvlinderbloemige *Medicago truncatula* vinden de initiële auxineaccumulatie en de eerste celdelingen plaats in centrale wortellagen, om precies te zijn: in de pericykel, de endodermis en de binnenste cortex. Het signaal dat deze delingen aanstuurt, waarschijnlijk het plantenhormoon cytokinine, is zelf echter afkomstig uit de epidermis, de buitenste cellaag. Om deze paradox op te lossen introduceerden we een simpele interactie tussen dit signaal en de PIN-eiwitten, gebaseerd op experimenten in andere contexten (voornamelijk *Arabidopsis*). Met deze interactie konden we gemakkelijk een regime vinden dat de “Medigoparadox” oplost, alsook een regime dat patronen geeft die optreden in een ander type modelvlinderbloemigen. Daarnaast bevat dit hoofdstuk een uitgebreide discussie hoe verschillende observaties, die op dit moment niet meegenomen worden in het model, het patroonvormingsmechanisme betrouwbaarder kunnen maken in het licht van natuurlijke variatie en fluctuaties die intrinsiek horen bij kleine aantallen signaalmoleculen.

De plantenhormonen auxine en cytokinine zijn kleine moleculen. We hebben daarom in de hoofdstukken 5 en 6 ook de effecten van symplastisch transport op onze bevindingen onderzocht.

Deel III beslaat het niveau van de cel en kleiner. De celwand is essentieel in het ontstaan en vasthouden van de verschillende vormen die plantencellen kunnen aannemen. De celwand bestaat uit lange dunne vezels, microfibrillen van cellulose, die laag na laag afgezet worden door cellulosesynthasecomplexen en sterk opgelijnd zijn. Dit is belangrijk voor de mechanische eigenschappen van de celwand. De oplijning zelf wordt gestuurd door de oriëntatie van corticale microtubuli, lange dynamische eiwitbuizen aan de binnenkant van het celmembraan. De oriëntatie van deze eveneens opgelijnde microtubuli voorspelt de oriëntatie van het delingsvlak bij de eerstvolgende celdeling.

De corticale microtubuli wisselen veelvuldig tussen fases van groei en krimp en interacteren met elkaar door frequente botsingen. Omdat het effect van de botsing afhangt van de hoek tussen de twee microtubuli, is deze interactie voldoende is voor spontane oplijning, zo blijkt uit computersimulaties. Het basismechanisme geeft echter onvoldoende tot geen controle over de collectieve oriëntatie van de corticale microtubuli.

In hoofdstuk 7 onderzoeken we het effect van nucleatie van nieuwe microtubuli vanaf bestaande microtubuli en de ogenschijnlijk eigenaardige verdeling van hoeken waarmee dit gebeurt. De effecten op de snelheid en mate van oplijning kunnen eenvoudig verklaard worden aan de hand van de fouriergetransformeerde van de verdeling van nucleatiehoeken. In simpele woorden is dit een maat voor de gemiddelde overeenstemming in oriëntatie van de bestaande en de nieuwe microtubulus. De eigenaardigheden van de gemeten verdeling, zoals een grote hoeveelheid nucleaties met een relatieve hoek rond gemiddeld  $35^\circ$ , zorgt voor een gelijkmatigere spreiding van microtubuli over de celcortex.

De eiwitcomplexen die de nieuwe microtubuli nucleëren hebben een sterke affiniteit voor bestaande microtubuli. Wanneer ze daaraan gebonden zijn, is hun activiteit circa tien keer zo hoog. Direct na een celdeling zijn er echter geen corticale microtubuli aanwezig. In hoofdstuk 8 bestuderen we dit initiële stadium. Het blijkt dat de dichtheid van microtubuli in het begin ongelijk verdeeld is over verschillende hoeken: de diagonale oriëntaties zijn oververtegenwoordigd. Dezelfde voorkeursrichtingen hebben we gevonden bij de nucleaties in dit stadium. Met behulp van computersimulaties hebben we onderzocht

hoe deze beginsituatie samen kan gaan met de uiteindelijke transversale oriëntatie van de microtubuli, die consistent optreedt in deze cellen.

Tenslotte behandelen we een mechanisme voor de oriëntatie van de corticale microtubuli (hoofdstuk 9), gebaseerd op verschillen in de waarschijnlijkheid waarmee microtubuli de randen van kubusvormige cellen oversteken. Volgens de laatste inzichten is dit afhankelijk van de kromming van de rand en variaties in de beschikbaarheid van eiwitten die helpen bij het oversteken, zoals CLASP. Dit werk was onderdeel van een studie waarin werd aangetoond dat het effect van de auxinegevoelige PLETHORA transcriptiefactoren op de oriëntatie van het celdelingsvlak loopt via CLASP en de oriëntatie van corticale microtubuli in de interfase. Zo staan de corticale microtubuli in individuele cellen in verband met plantenontwikkeling op het niveau van weefsels en organen.

Als geheel tonen de verschillende onderdelen van dit proefschrift dat simpele modellen op diverse niveaus kunnen bijdragen aan het beter begrijpen van plantengroei en -ontwikkeling. Daarbij is er *à priori* niet één juiste manier van modelleren voor te schrijven: de vraag bepaalt de antwoordstrategie.

# Acknowledgements

*Mein Führer, I can walk!*

It is said that this perhaps most famous scene of *Dr. Strangelove* was created by accident. The lame man was never supposed to leave his wheelchair. What a pity it would have been if Kubric had strictly adhered to his script for the final cut! Along the same lines I am very grateful that my supervisors allowed me the freedom to deviate from the original “script” and explore interesting but unforeseen directions.

Bela, you’ve been very supportive in many ways. You are always full of ideas and often come up with interesting references, to scientific literature and much beyond. This often made for very enjoyable work discussions. Although discussing several topics in limited time could sometimes be a challenge, your broad interests always proved very useful when exploring new directions.

Ton, you’ve been a great source of information, from old legume literature to grant applications and much in between. You could do much with a well timed smile, such as reinterpret the urgency of work that *had* to be finished over the weekend. In a way, I really got to appreciate that style. I hope for you I won’t become too proficient at sometimes using it myself. Thank you for both your criticism and kind support.

René, thank you for supplying me with lots of useful information and explaining the languages and working habits of others, if needed with a joke.

During the whole of my PhD I have had the pleasure of frequent interactions with experimentalists. It is a great way of learning about the details that nobody ever writes down. I’ve learned a lot from the work discussions and at the coffee table in Wageningen. What I liked most, however, is the synergy of working together on the same problem: combining our different perspectives to get to the heart of the problem. The coffee slide that I’ve used in many presentations, always in the first half, is a tribute to all collaborators.



Tingting, thank you for the frequent discussions based on our pictures. It’s always good to learn what does and, equally interesting, does not fit the picture. Marijke, thank

you for actually getting me into the lab and turning my plants upside down. Rik op den Camp, I've always enjoyed discussing with you over data and mechanisms. Unfortunately you were long gone when I finally managed to implement cytokinin. When I did, it immediately resulted in very interesting discussions with René, Arjan, Ton and Tingting.

Anne-Mie, thank you for pulling me in (again) on the nucleation project. It took a lot more time than the two weeks you initially anticipated, but it was time well spent. For a long time, the discussions with Jelmer were a weekly recurring phenomenon and something I often looked forward to. Jelmer, your drive to really understand the problem is contagious. Thank you, too, for explaining many things about imaging and image analysis along the way.

Ben and Pankaj, thank you for another interesting microtubule project.

Every beginning is said to be difficult, but I don't remember many difficulties at the start of my PhD. I think I owe that largely to Simon. Thank you for the excellent "Bela manual", orally transmitted of course, and the discussions on life, science and career over the years that followed. I've really enjoyed the extended projects we continued working on together. Also in Wageningen I found good "starting conditions". Gerben, Silvester, Marijke en Rik op den Camp, thank you for helping me find my way and making me feel at home in the lab.

Theoretical work often involves just sitting behind a desk. Fortunately, I've had many nice room mates at AMOLF. Niels, discussing politics and speculating about hidden agendas with you was always interesting. Almost as interesting as goldfishes ;-). Ioana, thank you for keeping me up to date with everything that happened at AMOLF in times that I was away a lot – almost the last two years. Best of luck with your grant and visa applications and don't worry too much about Wageningen University. You can always contact me for outdated advice. Mirjam, Roland, Pier, Anne-Mie, Yvette, Takis, Wilfried, Leander and Xuji, thank you for making working conditions in the office more interesting.

Many thanks to all the bio-people for the good atmosphere for discussing science and everything else. Dancing, swimming and regular visits to the local pubs are just a few examples that illustrate this supportive atmosphere. Jose, Ioana, Laurens, Leon, Niels and Pier, thank you for finding your way all the way to Utrecht (specially for Pier this must have been a big step!).

Thank you Stan and Veronica for the nice place you have created in Norwich and the warm welcome you gave me there. Your enthusiasm is so close to infinity, that it sometimes even scares me. Enjoy teaching it to the next generation! Yoselin and Veronica, it has been a great experience working with you! My stay in Norwich wouldn't have been the same without everybody in the lab. No late night burger dinners downstairs without you. Matthew, our defense against computing and always a helping hand. George, don't lose that silver lining! Ramiro, tried dancing yet? Claire, keep up the coffee breaks! Yara, sorry for the cheese... Sander, Job, Sedeer, Erika, Robert, Marian and others: thank you very much! Esther and Dorina, thanks for being great house mates. Thank you Yoselin for cheering me up and giving strategic advice when my creativity would run out on that part.

A great thing about science is meeting many interesting people in the lab and all over the world. The NVTB meetings have been a very nice way of keeping in touch with the TBB people after many, including myself, found new places to work. I specially like to thank Klaartje for some very insightful discussions.



Somewhere between science and friendship I've always found a great source of mental energy in my involvement in the Biology Olympiad. Many thanks to my fellow board members, co-organizers and the ever enthusiastic participants. Of course I'm not forgetting my dearest family members of the IBO jury! It's fantastic to see how much has changed since I participated in the olympiad myself. The growing network of former participants and the increasing number of social, scientific and professional activities is really something special. Keep it up! I am looking forward to our upcoming journey to Bern. For me, it will be a spectacular way of saying goodbye – to organizing.

I'd like to thank Dikkie and my paranimfen Victor and Rob for scrutinizing parts of my thesis; Jelmer and Michiel for valuable latex files; and Michiel for technical support and reflecting on minute changes in cover design. These are the most direct contributions you made to my thesis, but arguably the smallest and least important ones.

Over the past two years I've been away really a lot. This made me realize how much I appreciate my friends: the people who are always there, even if they are far away in a physical sense.



Finally I'd like to thank my brother, my parents, my "second parents" Boets and Dikkie, and, most of all, Michiel for many years of moral support and encouragement.

# List of publications

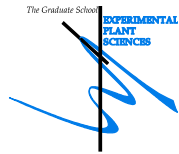
- »» E. E. Deinum, S. H. Tindemans, and B. M. Mulder, *Taking directions: the role of microtubule-bound nucleation in the self-organization of the plant cortical array.*, Phys Biol **8**, 056002 (2011).
- »» P. Dhonukshe, D. A. Weits, A. Cruz-Ramirez, E. E. Deinum, S. H. Tindemans, K. Kakar, K. Prasad, A. P. Mähönen, C. Ambrose, M. Sasabe, G. Wachsmann, M. Luijten, T. Bennett, Y. Machida, R. Heidstra, G. Wasteneys, B. M. Mulder, and B. Scheres, *A PLETHORA-auxin transcription module controls cell division plane rotation through MAP65 and CLASP.*, Cell **149**, 383 (2012).
- »» E. E. Deinum, R. Geurts, T. Bisseling, and B. M. Mulder, *Modeling a cortical auxin maximum for nodulation: different signatures of potential strategies.*, Front Plant Sci **3**, 96 (2012).
- »» J. J. Lindeboom, A. Lioutas, E. E. Deinum, S. H. Tindemans, D. W. Ehrhardt, A. M. C. Emons, J. W. Vos, and B. M. Mulder, *Cortical microtubule arrays are initiated from a non-random pre-pattern driven by atypical microtubule initiation.*, Plant Physiol , (2013).
- »» E. E. Deinum, Y. Benitez-Alfonso, and V. A. Grieneisen, *Walking the back alleys: a modeling study of symplastic transport.*, Manuscript in preparation
- »» E. E. Deinum, Y. Benitez-Alfonso, and B. M. Mulder, *Modeling symplastic transport: from single channels to effective wall permeability.*, Manuscript in preparation
- »» E. E. Deinum, and B. M. Mulder, *Playing the auxin pipeline: consequences of different mechanisms for local auxin accumulation.*, Manuscript in preparation
- »» S. H. Tindemans, J. J. Lindeboom, E. E. Deinum, B. M. Mulder, *Identifying drivers of alignment and orientation of the cortical microtubule array in plant cells.* Manuscript in preparation

# Curriculum Vitae

Eva Elisabeth Deinum was born in the Hague, The Netherlands, on October 12, 1982. From 1995 to 2001 she attended high school at “Stedelijk gymnasium Leiden”, The Netherlands. After that she studied biology and mathematics at Utrecht University, The Netherlands, obtaining BSc degrees in both. The two combined well in a MSc degree in Theoretical biology and bio-informatics, also at Utrecht University. For this she completed two research projects: “*Evolutionary consequences of the ciliate nuclear dualism*” with Prof. dr. Paulien Hogeweg at Utrecht University and “*Modelling self organisation of cortical microtubules*” with Dr. Simon Tindemans and Prof. dr. Bela Mulder at FOM institute AMOLF. After graduating in 2009, she started a PhD in the labs of Prof. dr. Bela Mulder and Prof. dr. Ton Bisseling at Wageningen University for a PhD on the formation of root nodules in the legume-rhizobium symbiosis. For this she also spend 2,5 months in the lab of Dr. Verónica Grieneisen at the John Innes Institute in Norwich, UK, for a biophysical study of symplastic transport. During these years, she remained involved in the research on plant cortical microtubules.

Throughout her studies and PhD Eva has been involved in the organisation of the Dutch biology olympiad. This was inspired by participation in the finals of the junior olympiad (BOJ) in 1998 and the national and international biology olympiads in both 2000 and 2001. From 2004 she has been a regular jury member for The Netherlands in the international biology olympiad and an official member of the Stichting Biology Olympiade Nederland (SBON) board since 2008.

# Education Statement of the Graduate School Experimental Plant Sciences



Issued to: Eva Deinum  
Date: 1 July 2013  
Group: Molecular Biology and Theory of Biomolecular Matter (AMOLF)  
Wageningen University & Research Centre

1) Start-up phase	date
► <b>First presentation of your project</b> Modelling nodulation	Sep 2009
► <b>Writing or rewriting a project proposal</b> A modelling study of the fundamental properties of non-targeted symplastic transport and its impact on plant developmental pattern formation. (EMBO short term fellowship for internship at JIC, Awarded: EMBO ASTF 105-2012)	Jan 2012
► <b>MSc courses</b>	
► Laboratory use of isotopes	
<i>Subtotal Start-up Phase</i>	<i>5.5 credits*</i>

2) Scientific Exposure	date
► <b>EPS PhD student days</b> EPS PhD student day, Utrecht University, Utrecht EPS PhD student day, University of Amsterdam, Amsterdam	Jun 01, 2010 Nov 30, 2012
► <b>EPS theme symposia</b> EPS theme symposium 1 'Developmental Biology of Plants', Wageningen EPS theme symposium 1 'Developmental Biology of Plants', Leiden	Jan 28, 2010 Jan 17, 2013
► <b>NWO Luntenen days and other National Platforms</b> ALW meeting Lunteren 2009 (one day only) Dutch Meeting on Molecular and Cellular Biophysics, Veldhoven Dutch Meeting on Molecular and Cellular Biophysics, Veldhoven Dutch Meeting on Molecular and Cellular Biophysics, Veldhoven NVTB meeting 2009 NVTB meeting 2011 NVTB meeting 2012 NCSB meeting 2010 NCSB meeting 2011	Apr 06, 2009 Sep 28-29, 2009 Oct 04-05, 2010 Oct 03-04, 2011 May 07-08, 2009 May 19-20 2011 May 24-25 2012 Oct 21-22, 2010 Nov 01, 2011
► <b>Seminar plus</b>	
► <b>Seminars (series), workshops and symposia</b> AMOLF weekly colloquia (>50) KNAW biophysics meetings 2009 – 2013 NISb meeting 2009 NCSB kick-off symposium CBSG kick-off meeting EU COST E50 Workshop 'Systems Biology for Plant Design' (1 day) EMBO Workshop 'Systems biology of development', Ascona, Switzerland Various JIC seminars EPS seminar Peter Coole WEES seminar Fiona Jordan + master class	2009-2013 2009-2013 Mar 27, 2009 Oct 15-16, 2009 Feb 17, 2010 Jul 09, 2009 Aug 16-20, 2010 Feb-May, 2012 Oct 27, 2010 Nov 18, 2010
► <b>International symposia and congresses</b> Biophysical circle meeting 2010, Amsterdam Biophysical circle meeting 2011, Saarbrücken, Germany EMBO Conference Series on Morphogenesis and Dynamics of Multicellular Systems Lindau meeting 2010 Interdisciplinary CSHA conference 'Plant Cell and Developmental Biology', Suzhou, China ECMTB 2011 meeting, Krakow, Poland Auxin 2012 meeting, Waikoloa, USA Biophysical circle meeting 2013, Heidelberg, Germany	Apr 22-23, 2010 Apr 14-15, 2011 Oct 02-06, 2009 Jun 27-Jul 02, 2010 May 31-Jun 04, 2011 Jun 27-Jul 02, 2011 Dec 09-14, 2012 Apr 04-05, 2013
► <b>Presentations</b> Oral + poster: "Cell shape changes" 2009 Oral: NVTB meeting 2009 Poster: Heraeus seminar "Physics of biological function" Oral: CBSG kick-off meeting 2010 Poster: Circle meeting 2010, Amsterdam Poster: 'Systems biology of Development', Ascona, Switzerland Oral: NCSB meeting 2010 Oral: AMOLF Kleyn colloquium, Amsterdam Oral: NCSB meeting 2011 Oral: Biophysical circle meeting 2011, Saarbrücken, Germany Oral: NVTB meeting 2011 Oral + Poster: CSHA conference 'Plant Cell and Developmental Biology', Suzhou, China Oral: ECMTB 2011 meeting, Krakow, Poland Oral (invited): Contribution to web-based course 'Embryogenesis explained' Oral (invited): at Carnegie institute, Stanford, USA Oral (invited): Computational and systems biology departmental seminar; JIC, Norwich, UK Oral NVTB meeting 2012 Oral (invited): Soft Condensed Matter, Biological Physics Experiment & Statistical Physics Seminar, Edinburgh University, Edinburgh Oral: EPS PhD students day, Amsterdam, NL Poster: 'Auxin 2012', Waikoloa, USA Oral: AMOLF Kleyn colloquium, Amsterdam Oral: EPS theme 1 meeting, Leiden Oral: Biophysical circle meeting, Heidelberg, Germany	Oct 19, 2009 May 07, 2009 Jun 21-25, 2009 Feb 17, 2010 Apr 22-23, 2010 Aug 16-20, 2010 Oct 21, 2010 Feb 28, 2011 Nov 01, 2011 Apr 15 2011 May 20, 2011 Jun 01, 2011 Jul 01, 2011 Oct 26, 2011 Jan 26, 2012 Mar 06, 2012 May 24, 2012 Oct 22, 2012 Nov 30, 2012 Dec 09-14, 2012 Jan 07, 2013 Jan 17, 2013 Apr 2013 Feb 18, 2011
► <b>IAB interview</b>	
► <b>Excursions</b>	
<i>Subtotal Scientific Exposure</i>	<i>52.0 credits*</i>

<b>3) In-Depth Studies</b>	<u>date</u>
► <b>EPS courses or other PhD courses</b> Physics of biological function (Heraeus seminar 435, Bad Honnef) Cell shape changes 2009 (school, Institut Curie, Paris, France)	Jun 21-25, 2009 Oct 19-23, 2009
► <b>Journal club</b>	
► <b>Individual research training</b> John Innes Centre, Norwich	Feb 27-May 18, 2012

*Subtotal In-Depth Studies 5.7 credits\**

<b>4) Personal development</b>	<u>date</u>
► <b>Skill training courses</b> Promotie in eigen regie Write it right (academic writing) FOM valorisatie workshop The art of presenting science Business Orientation Week (Nyenrode University) FOM loopbaanplanning	Feb-Mar 2010 Apr 15-16, 2010 Jun 15, 2010 Nov-Dec 2011 Apr 2012 Feb-Mar 2013
► <b>Organisation of PhD students day, course or conference</b> Organisation + coaching + development of tests for national biology olympiade	2009-2013
► <b>Membership of Board, Committee or PhD council</b> member SBON board (biology olympiade foundation)	2009-2013

*Subtotal Personal Development 8.6 credits\**

<b>TOTAL NUMBER OF CREDIT POINTS*</b>	<b>71.8</b>
---------------------------------------	-------------

Herewith the Graduate School declares that the PhD candidate has complied with the educational requirements set by the Educational Committee of EPS which comprises of a minimum total of 30 ECTS credits

\* A credit represents a normative study load of 28 hours of study.

# Notes

---



# Notes

---



The research described in this thesis was financed by the Centre for Biosystems Genomics (CBSG) under the auspices of the Netherlands Genomics Initiative (NGI). The research was carried out at FOM institute AMOLF in Amsterdam, the Netherlands and at Wageningen University, the Netherlands. The work described in chapters 2 and 3 was initiated at the John Innes Centre in Norwich, UK. An 83 days stay there was financed by EMBO short term fellowship ASTF 105-2012.

Financial support for the printing of this thesis was kindly provided by the Foundation for Fundamental Research on Matter (FOM) and the Laboratories of Molecular Biology and Cell Biology, both at Wageningen University.

Cover art: Eva E. Deinum